University of Alberta

Temperature Distribution in Waste Rock Piles in Permafrost Regions

by

Renata Klassen

A thesis submitted to the Faculty of Graduate Studies and Research
in partial fulfillment of the requirements for the degree of

Master of Science

in

Geotechnical Engineering

Civil and Environmental Engineering

Spring 2014

Edmonton, Alberta

ABSTRACT

The GeoStudio 2007 convection module a finite element program was used to examine convection in porous embankments and waste rock piles. Conduction modeling was carried out for comparison. The results from the GeoStudio modeling were compared to each other, to literature numerical and experimental examples and to the field data from the Diavik waste rock test piles. Comparison of GeoStudio results to literature examples was for the purpose of testing GeoStudio 2007 convection module.

A roadway embankment geometry reported on by Goering and Kumar (1996) and Goering (2000) was modeled with GeoStudio 2007 convection module. The purpose of the modeling was to compare modeling results between full and half geometries, various mesh sizes, to examine repeatability of modeling results, and to compare modeling results to the results from the two studies. Comparisons were made using snapshots of isotherms and air flow vectors, and using temperature trends. Modeling results were found to be similar and repeatable in the spring and summer when the embankment was conduction dominated. The modeling results were found to vary and not repeatable during the fall and winter when convection dominates. Chaotic sinking of air during convection was observed. Comparison to the two literature examples both numerical and experimental showed good agreement when the boundaries were closed but not as good when the sideslopes were open. When the sideslopes were open, the agreement was better when compared to the experimental literature example.

Another roadway embankment geometry presented by Sun et al. (2005) was modeled. The purpose of this modeling was to compare modeling results at various Rayleigh numbers. The modeled embankment was free standing with either closed boundaries or

open sideslopes exposed to isothermal or adiabatic conditions. The modeling results showed that Sun's modeling cases can be matched with GeoStudio model when Rayleigh numbers were decreased to about half of these used by Sun. Panda Waste Rock Storage Area at the Ekati Diamond Mine was used to compare field measured data to GeoStudio model of similar geometry and representative parameters. The modeling results showed that convection exists in the modeled Ekati waste rock pile. The effect of compacted layers in the waste rock pile was not observed in the GeoStudio model.

The Diavik waste rock test pile project was described including the author's involvement. Installation of bedrock ground temperature cables was described as observed by the author. Relevant temperature data from the test piles was described. The location of thermistor beads located on ground temperature cables in the Type 1 and Type 3 pile were found. The Type 3 Pile face 2 was modeled using the parameters measured in the waste rock test piles. The thermistor bead locations found was used for comparison of modeled to measured temperature data. The modeled data do not compare well to the measured data although cooling trends were reproduced. Wind forcing of air movement in the test piles prevents modeled data to be compared with measured data.

ACKNOWLEDGEMENTS

My sincere thanks and deep appreciation goes to my thesis supervisor Dr. Dave Sego P.Eng. His continued advice, support and encouragement inspired me to complete this thesis to the best of my ability. Also, I would like to acknowledge Dr. Dave Chan P.Eng. for his trust and belief that I was able complete this thesis within the allotted time.

Special thanks go to my parents, my daughter and my family for their unquestioning support for me as I worked tirelessly on my thesis. Not forgetting, my mother's dedication to looking after my daughter during this period. Seeing this chapter of my life is over, I am now looking forward to spending more time with my family – Thanks ☺.

Last, but by no means least, thanks to my friends, peers, colleagues and fellow students who were inspirational in helping me achieve this major goal.

TABLE OF CONTENTS

LIST OF TABLES

LIST OF FIGURES

Appendix B Figures:

Appendix C Figures:

Appendix D Figures:

Appendix E Figures:

Appendix F Figures:

Appendix G Figures:

Appendix H Figures:

Appendix I Figures:

1.0 INTRODUCTION

1.1 Background

Past studies indicate that open-graded highly permeable embankments constructed in permafrost regions allow for natural air convection to develop that cools the underlying permafrost foundation soils. This passively cooling of high porous materials was applied to waste rock storage areas in the northern mines. Passive cooling could restrain the potential of acid rock drainage from sulphide bearing waste rock stockpiles.

Numerical and experimental studies have been carried out to provide insight into thermal performance of highly porous roadway embankments to minimize or eliminate thaw. Temperatures have been measured in waste rock piles to examine the internal thermal behaviour of waste rock storage areas. Finally, a "large-scale" waste rock test pile project was initiated at the Diavik Diamond Mine to better understand the thermal regime that develops in the waste rock piles. Continuous thermal data is collected from the Diavik test pile project and studies are conducted to apply the measured data to the full scale waste rock piles.

The initiation of the Diavik test pile project triggered this work. The author had the opportunity to be involved in some aspects of project planning and installation of ground temperature cables in early stages of the test pile construction in 2004. Unfortunately, the test pile construction did not continue in 2005 and no ground temperature data was available for analysis to continue supporting the experimental aspect of this work. The focus was changed to numerical modeling of the waste rock test piles. A GeoStudio convection module, a finite element numerical program was just launched for testing by GeoSlope International Ltd. The author received the copy of the GeoStudio convection module in December 2005 and started learning numerical modeling. Dr. Lukas Arenson, a post-doctoral fellow at the University of Alberta, lead the testing of the GeoStudio convection module. GeoSlope International Ltd. modified the numerical module based on the test results. Testing of the GeoStudio convection module was carried out for about one year until spring 2007. By this time, the candidate started a full time employment with EBA Engineering Consultants Ltd. to regain financial stability after two and a half years of full time studies at the University of Alberta.

The author resumed work on this thesis in 2009 and attempted its completion numerous times. Detail by detail was put together to finally complete the first draft by July 2010. The first draft, however, lacked solid findings and required additional effort. In the spring of 2011, the findings were weak and not sufficient to finalize this work. Major development took place between fall 2011 and winter 2012 after the discovery that GeoStudio modeling results are not repeatable during convection dominated months. This finding accelerated the work to its completion in February 2012. No further modelling was required past this completion date and was no modelling was conducted past this date. The edits mainly required the incorporation of new findings by Pham (2013) and papers prepared for the 2012 ICARD conference, and were completed in August 2013.

This thesis combines the results of numerical modeling with the findings of thermal regime from the Diavik waste rock test piles. A large part of this work is devoted to further testing of GeoStudio convection module.

1.2 Scope

The scope of this work included the following:

- Modeling natural convection using the GeoStudio convection module. Wind, seepage or climatic conditions other than varying air temperatures were not considered in the modeling.

- Testing of the GeoStudio convection module for an embankment on top of a foundation or waste rock pile geometry. The geometry of the tested embankments as well as input parameters were limited to match those reported in the literature or experimental examples provided in these reports.

- Modeling Diavik waste rock test piles using GeoStudio convection module. Wind action was not considered irrespective of significant wind action in the test piles.

- Modeling open and closed sideslopes in embankments.

1.3 Information Supplied and Author's Involvement

Information supplied by others was used during the preparation of this thesis. The information supplied, their source, and their application in this work is listed in Table 1.1.

The author participated in thermal aspects of the Diavik test pile project execution. The author's time on site for the purpose of the Diavik test pile project is summarized in Table 1.2.

1.0 LITERATURE REVIEW

Selected literature examples were reviewed for this work. The main purpose of the literature review was to highlight findings from the past research discussing cooling capabilities and significance of natural air convection in highly porous construction materials. The reviewed literature also provided technical information needed for preparation of studies carried out in this thesis. The literature review included numerical modeling and experimental studies. Some of the literature reviewed below was used during testing of GeoStudio 2007 convection module. Table 2.1 summarizes the literature reviewed identifying source, research type, pressure boundary conditions and research area. Figures are only being presented once and this chapter will refer to figures from Chapter 3.

Goering from the University of Alaska, Fairbanks conducted extensive numerical simulations and experimental studies with air convection embankment (ACE) on permafrost. One of the purposes of his work was to develop a nonconventional construction practice that would contribute to maintaining the integrity of permafrost foundation by minimizing or eliminating its thaw. This technology could be applied to construction on warm ice rich permafrost as a means of reducing mean permafrost surface temperatures after construction thus eliminating thaw of the underlying permafrost. The embankments consisted of highly porous rock/gravel materials that allow for the natural convection to develop in response to temperature boundary conditions and their geometry is shown in Figure 3.1A. The embankments worked like one-way heat transfer devices transferring cold air into the embankment during winter due to unstable pore-air density gradients without allowing warm air to enter during summer. Goering developed a non-steady state two-dimensional finite element model described by Goering and Kumar (1996) and Kumar (1984). The numerical code used equations governing transient energy transport and fluid motion in a two-phase system consisting of a porous matrix filled with a mobile fluid (air). Three coupled equations for mass, energy, and momentum had to be solved simultaneously to provide the solution. Boussinesq approximation was used to couple air flow with the temperature field. Pore-air convection occurred only within the embankment and the foundation soil transferred heat only via conduction. Goering's results show instantaneous isotherms and air flow vectors for selected dates for the modeled embankment and full-scale field experiments involving an ACE having the same cross section as his modeled embankment (Goering, 1998 and 2000).

Modeled results from Goering and Kumar (1996) were used for testing of GeoStudio convection module. Goering and Kumar (1996) described numerical simulations conducted to examine the long term state of a closed ACE and the underlying foundation (Case 1) in comparison with the same but a low permeability embankment where conduction dominates (Case 2), all under periodic thermal boundary conditions. The modeling was for 25 years to allow for the development of annual cycles that would determine if the foundation thaws or remains frozen. In Case 1, the foundation under the embankment did not thaw. The artificial permafrost table in the embankment area rose from its native state (approximately 1.5 m) reaching more or less the original ground level on October 2 (Figure 3.92A). Yearly minimum temperature extremes under the

embankment were similar to those in the native ground (Figure 3.100A). In Case 2, the foundation under the embankment thawed. The permafrost table under the embankment reached into the foundation below the 5 m depth while the native ground retained the permafrost table at approximately 1.5 m. Yearly minimum temperature extremes in Case 2 show that the foundation under the embankment never froze forming a large area of near 0°C temperatures.

Goering (1998) described an experimental ACE. The ACE was constructed during the summer and fall of 1993 at Brown's Hill Quarry near Fairbanks, Alaska, and the experiment was conducted between October 1993 and October 1995. The experiment consisted of continuous temperature measurements in the embankment and the underlying subgrade. The embankment cross section was the same as geometries modeled numerically by Goering and Kumar (1996) and later by Goering (2000). Open and closed sideslope boundary conditions were created in the ACE during the experiment as follows:

- Open sideslope for the first winter (driving surface closed);
- Closed sideslope during the first spring, summer and fall (driving surface closed);
- Closed sideslope for the second winter (driving surface closed); and
- Open sideslope and driving surface for the spring and summer of the second year.

The impermeable driving surface condition was achieved by building an ice sheet from the first snow for the winter, and placing plastic sheeting after the snow melted. The impermeable sideslope condition was achieved by placing plastic sheeting on the slopes. Goering (1998) presented instantaneous isotherms and air flow vectors for selected months during the first and second year, and plots of subgrade temperatures over the two-year study. The experiment confirmed the presence of natural convection in the embankment during winter months. In winter, the isotherms have downward/inward plume shapes and smaller temperature gradients due to convective mixing of the air. In summer, the isotherms were flat horizontal profiles and the embankment had much higher temperature gradient compared to the winter indicating conduction as the dominant heat transfer mechanism. The presence of the ACE embankment depressed the mean annual temperatures in the underlying foundation. Mean annual temperatures at the upper surfaces of the embankment were approximately 2°C during the two year test and mean annual temperatures at the subgrade surface ranged from -1.2°C to -3.6°C during the same period.

Goering (2000) was used for testing of GeoStudio convection module. Goering (2000) examined ACEs with respect to their fluid, mechanical and thermal properties through experimental and numerical studies. The examined ACEs were subjected to boundary conditions of closed and open sideslope. Under the closed sideslope boundary condition no air entered the embankments and only internal convection took place. When the sideslope boundary was open, air exchange took place through the sideslope. Goering

simulated closed and open sideslope by defining pressure boundary conditions at the sideslope. To simulate the closed sideslope, he applied Neumann pressure boundary condition on the sideslope boundary. To simulate the open sideslope, the pressure boundary condition at the sideslope was based on the pressure in the surrounding ambient air mass according to the equation:

$$P_{boundary} = P'_0 + \rho_0 \beta (T_{amb} - T_0) gy$$

Where

$P_{boundary}$	pressure on boundary
$P'_0 =$	arbitrary background pressure set to zero
$\rho_0 =$	density of air
$\beta =$	pore fluid expansion coefficient
$T_0 =$	temperature
$T_{amb} =$	ambient air temperature
$g =$	acceleration of gravity
$y =$	elevation variable

Numerical simulations showed convective activity in the embankment. Simulations on the closed sideslope resulted in instantaneous isotherms exhibiting a downward plume under the driving lane on February 1 (Figure 3.101A). Winter temperatures under the embankment are similar to those in the surrounding native permafrost and temperatures under the sideslope are slightly higher. When the sideslopes were open, the isotherms also exhibited a downward plume near the embankment centerline but also an inward dipping along the sideslope (Figure 3.81B). The foundation was slightly warmer under the embankment centerline than in the native ground. The warmest foundation condition was under the sideslope. Thermal conditions on August 1 are similar for the open and closed sideslope boundary conditions resulting in straight line isotherms signifying conduction dominated heat transfer (Figures 3.79C and 3.103B). The experimental results showed convective activity in the embankment. When the sideslope was closed, the isotherms in the experimental embankment were almost identical to those simulated numerically in winter (February 1) (Figures 3.102A and B) and summer (August 1) (Figure 3.103A and B). The changes in isotherms were visible when the sideslope is open during the winter. The experiment does not exhibit a downward plume (Figure 3.81C). Instead, dipping of the isotherms under the sideslope penetrates deeper into the embankment and moves towards the embankment centerline. The underlying top of the foundation is the coldest under the embankment sideslope contrary to the numerical simulations where it occurred under the driving lane.

Some numerical results from Sun et al. (2005) were used during testing of the GeoStudio 2007 convection module. Sun et al. (2005) discussed various aspects of natural convection associated with the Qinghai-Tibet railway. The results of numerical modeling were based on using a numerical model proposed by Goering and Kumar (1996). Methods to measure natural convection were one of the topics discussed. Nusselt number and Rayleigh number were defined as means to represent the cooling effect and triggering

of natural convection. Natural convection was examined in a two dimensional rectangular enclosure with isothermal top and bottom, adiabatic sides, and all impermeable boundaries. Two width-to-height ratios of 1:1 and 2:1 were employed to show patterns of convective cells for varying Rayleigh numbers. The influence of pressure and thermal boundary conditions on natural convection in an embankment (Figure 3.111) including its triggering was also presented. Five cases were modeled with boundary conditions as follows:

- Case 1 - All boundaries isothermal and impermeable;
- Case 2 - All boundaries isothermal, only sideslopes permeable;
- Case 3 - All boundaries isothermal, only sideslopes and pavement permeable;
- Case 4 - All boundaries isothermal, only pavement permeable; and,
- Case 5 - All boundaries impermeable, only sideslopes adiabatic.

Sun et al. (2005) modeling results were presented in terms of isotherms and air flow vectors for two Rayleigh numbers of 50 and 80. Sun et al. (2005) introduced a formula for the natural convection index A_0, a cumulative temperature parameter which implies natural convection when it is greater than zero and is a measure of convection intensity. The natural convection index was defined as an area representing total time exceeding a critical temperature difference on a sinusoidal temperature graph within a yearly temperature cycle. The critical temperature difference was that temperature difference between an upper and lower boundary in the embankment that triggered natural convection under prescribed embankment properties, geometry, and under given harmonic surface temperature. The critical temperature difference between the lower and upper boundaries was calculated based on conduction alone because the basic solution of heat conduction dominates the time up until natural convection is triggered. Based on the definition of the natural convection index, Sun et al. (2005) calculated minimum and maximum heights of fractured rock layer in an embankment for the Qinghai-Tibet railway. The minimum height was the height that triggers natural convection and the maximum height corresponded to 80% of the maximum convection index. Four grain sizes of fractured rock materials were evaluated based on natural convection index (2-4 cm, 4-6 cm, 6-8 cm, and 8-10 cm) under two temperature amplitudes of 20°C and 15°C, and for two Rayleigh numbers of 20 and 40. At amplitude 20°C, fractured rock layer minimum heights were between 0.6 m - 1.1 m and 0.4 m - 0.8 m; and maximum heights between 2.4 m – 3.7 m and 2.0 m – 2.6 m, for critical Rayleigh numbers of 40 and 20, respectively. At amplitude 15°C, fractured rock layer minimum heights were between 0.7 m - 1.3 m and 0.5 m - 0.9 m; and maximum heights between 2.5 m – 5.4 m and 2.1 m – 2.9 m, for critical Rayleigh numbers of 40 and 20, respectively. These heights were then verified using a numerical model proposed by Goering and Kumar (1996). A pair of critical embankment heights existed for each temperature amplitude with smaller values corresponding to the higher temperature amplitude. The higher temperature amplitude required smaller embankment height to trigger natural convection. The embankment heights increased with

increasing Rayleigh numbers. It was more difficult to trigger natural convection in cases possessing higher Rayleigh numbers. Critical embankment heights decreased with increasing particle size.

Various methods aimed to prevent permafrost degradation were explored for the Qinghai-Tibet railway project in China. The railway is 1118 km long with 275 km constructed on warm permafrost with mean annual ground temperatures above -1.0°C, 221 km on permafrost with high ice content, and 134 km on the combination of both conditions (Ma et al., 2006). Ma et al. (2006) described field experiments with three methods of permafrost protection including embankment of crushed rock slope protection, the crushed rock embankment and ventilated duct embankment. Sections of the railway project were selected to carry out these experiments. Crushed rock embankments were installed in other geographical parts for comparison. The temperature profiles were measured over two warm and two cold seasons. The results were shown on October 19 and compared to the common embankments located in similar regions. The embankment of crushed rock slope protection varied in height between 4.1 m to 4.9 m. Small (5-8 cm) and large (40 to 50 cm) diameter rock were used for the experiment. The rock covered both sideslopes of the embankment to the thickness of 80 cm. The ventilated duct embankment was about 3 m high. The ducts with the diameter of either 30 cm or 40 cm were installed horizontally 0.5 m and at 1.5 m above the original ground surface at two times the duct diameter interval. The crushed rock embankment was a total of 6 m high and contained a 1.5 m thick crushed rock layer at the base. Rock diameter varied between 20 cm and 40 cm. The small and large diameter crushed rock slope protection embankments caused the 0°C isotherm to raise under the embankment generally reaching the original ground level. This rise was asymmetrical and slightly higher under the shady slope. This rise peaked under the shady slope covered with small diameter rock penetrating into the embankment material by about 1 m. The least significant rise took place under the sunny slope covered with the large diameter rock. Rising of the artificial permafrost table was associated with warming of the underlying permafrost under the embankment indicating cold energy consumption. Temperatures 0.7 m under the crushed rock layer were measured. The measured temperatures indicated that the smaller rock had better shielding effects in the summer and the bigger rock had better cooling effects in the winter resulting in gradual cooling with time under both rock sizes. It was concluded that the crushed rock slope protection embankment is an effective method of cooling but results in asymmetrical enhancement. If deformations of the embankment were to occur, they would be asymmetrical as well. The common embankment used for the comparison exhibited some rising of the permafrost table under the shady slope that was insufficient to protect permafrost under the embankment. The ventilated duct embankment has generally a symmetrical temperature distribution. The thaw depth was limited to embankment material reaching more or less the original ground surface. When installed in the embankment middle, smaller diameter ducts had limited cooling effect while larger diameter ducts provided some cooling effect. When installed at 0.5 m above the original ground surface, both diameter ducts provide remarkable cooling effect to the embankment, with large diameter ducts performing better. The embankment with 40 cm diameter ducts maintained the frozen state throughout the year after construction of the roadbed. The average ground temperature in this embankment at 3 m stayed near -1°C in the first and

second construction period. The crushed rock embankment had proven to have cooling capabilities of the underlying permafrost. In comparison to the common embankment, the crushed rock layer was colder during colder months and warmer during the warmer months. On average, however, the crushed rock layer stayed near and below zero year round. Crushed rock embankment installed in other geographical locations showed similar results.

Zhang et al. (2006) numerically investigated an embankment of 2 m and 5 m height containing a 1.5 m thick layer of crushed rock. The crushed rock layer sat on the ground surface and was overlain by conventional low permeability embankment fill, and somewhat permeable railway ballast. The crushed rock was 10 cm diameter and its intrinsic permeability was k=1.58x10^{-6} m^2. The railway ballast also was permeable with intrinsic permeability k=6.32x10^{-7} m^2. The foundation soil had very low permeability and was composed of metamorphic schist. The sideslope of the crushed rock layer was either closed or opened, with the remaining boundaries always closed. The closed boundary condition relied on convection due to ambient temperature. Wind was considered in the simulations because the permafrost regions of Qinghai-Tibetan Plateau are windy. The open boundary condition allowed air and wind to enter the embankment. Sinusoidal temperature functions were applied to the surface boundaries of the model reflecting thermal air and ground surface conditions in the regions of the Qinghai-Tibet railway project. The discussion of the numerical method used for this simulation can be found in Tao (2004). The embankment was constructed in mid-July and the total simulation time was 50 years using a 6 hour time step. The simulations included global warming of 2.6°C over the 50 years. The results were shown for July 15 and January 15 in the 50th year of simulation. The results of natural convection are summarized below as forced convection is beyond the scope of the work learned from the present study. The 2 m closed embankment exhibits convective patterns in winter and slightly in summer in the crushed rock layer. The convective pattern in the summer helps remove heat energy from the bottom of the embankment by one outward eddy but the flow velocities are too small to be significant. In the winter, the convective pattern near the sideslope is inward which helps cold air enter the embankment. In total three convective cells develop in winter and the flow speed is double that in summer. One convective cell is visible in both winter and summer in the 5 m closed embankment. The direction of the flow near the sideslope is similar as in the 2 m embankment. However, the small air flow speed is maintained throughout the year. The embankment fill overlying the crushed rock layer reduce the temperature gradient within it, being significantly more noticeable in 5 m embankment in the winter. Embankment temperatures show that the embankment with less fill can counteract global warming effect and refreeze the embankment by January 15 when the natural ground still has a thaw zone. The permafrost table rose by almost 2 m under the embankment with less fill. The embankment with more fill, however, does not refreeze by January 15. Although the permafrost table moves up, the temperature beneath the embankment is warmer than in the native ground. In conclusion, for a closed embankment to be effectively cooling permafrost, the fill thickness should be minimized.

Linklater (2004) predicted heat and gas transport in a Diavik test pile using the SULFIDOX numerical code. The cross section of the model resembled the 15 m high Diavik test pile

situated on solid granite bedrock with 20 m driving surface and 1.3 sideslopes. Input parameters selected were from earlier ANSTO work described in Ritchie and Plotnikoff (1997) and Ritchie et al. (1998). The intrinsic permeability was 10^{-10} m^2, bulk density 1600 kg/m^2, and the porosity 0.4. The simulations included a rainfall infiltration of 50 mm/year of. Sinusoidal temperature boundary with MAST of -10.2°C and amplitude of 21.1°C developed by Kuo and Noël (1998) was applied to the model external surfaces. The underlying bedrock was assumed to maintain -8°C temperature. Pyrrhotite was assumed as a dominant sulphide in the waste rock. The modeling results included temperature profiles complete with flow vectors, and oxygen concentrations every six months for the five years. The oxygen concentrations were predicted to stay close to ambient throughout the pile at all times. The bottom 10 m of the pile froze after the first year and remained frozen for the five years of modeling. Temperatures after the first year fluctuated approximately between -30°C and 10°C near the pile surface, and between -8°C and -5°C at 5 m to 10 m depth. The pile base stayed between -5°C and 0°C after the first year. Instantaneous isotherms in the five winters and five summers resemble conduction patterns. The air flow vectors near the sideslope are in a downward direction in the winter and in the upward direction in summer. Small eddies have developed near the sideslope in summers but no eddies are present in winters. This concludes that convection does not occur in this model.

SRK (2003) supplied temperature data from waste rock storage areas (WRSA) at the Ekati Diamond Mine. The SRK report was provided to the author by Ray Eskelson, Water Management Coordinator (DDMI) on February 22, 2006 by posting it on the Diavik public ftp site. Ekati Diamond Mines is located about 30 km northeast of Diavik Diamond Mine. Ekati has several open pits and developed underground mining operations. Ekati generates waste rock during mining operations that is stored on site in waste rock storage areas such as Panda WRSA. The temperature profiles from Panda WRSA show convective activity in the waste rock. The profiles show sinking of cold air and the effects of the compacted layers during construction. Details of this experimental example are provided in Section 3 during testing of GeoStudio 2007 convection module.

Smith et al. (2009) describes waste rock test piles construction. Three large scale waste rock test piles (Type 1 Pile, Type 3 Pile, and TC Covered Pile) were construction between 2004 and 2007 at Diavik Diamond Mine. Generally, Diavik waste rock has low sulfur content but the amounts vary making some of the waste rock potentially acid generating. Waste rock comprising the Type 1 Pile (Type I rock) is granite with sulfur content of less than 0.04 wt%S classified as non-acid generating. This pile is to provide baseline information. Waste rock comprising the Type 3 Pile (Type III rock) is granite with some amounts of biotite schist responsible for sulfur content exceeding 0.08 wt%S and is considered potentially acid generating. This pile is considered the worst case scenario. The TC Covered Pile represents the closure plan where the Type III rock is covered with 1.5 m thick layer of till overlain by 3 m of the Type I rock to encapsulate and promote freezing of the Type III rock within. The test pile dimensions were established using numerical modeling with the reactive transport code SULFIDOX. SULFIDOX determined test pile dimensions so the permafrost at the pile base would not be affected by thermal conditions at the top of the pile. The Type 1 and Type 3 Piles were designed to 15 m

height with 20 m wide driving surface and 1:1.3 (V:H) slopes. The TC Covered Pile had a 1:3 (V:H) slopes. Instrumentation was installed on the angle-of-repose faces as the construction of the test piles progressed. The location of the four instrumentation planes was determined by SULFIDOX modeling as 5 m apart and 5 m from the final slope surface. The test pile instrumentation was designed to contribute to characterization of physicochemical process on multiple scales. Instruments at the pile base included ground temperature cables, gas sampling lines, different-sized basal collection lysimeters and the basal drains. Instruments on the pile faces included ground temperature cables, time domain reflectometry (TDR) probes, soil water solution samplers (SWSS), gas sampling lines, air permeability probes, access ports for thermal conductivity measurements, and access ports for microbiological characterization. The foundation and bedrock under the test piles were also instrumented with ground temperature cables reaching approximately 10 m below the test pile base. The test piles were constructed in stages including the construction of test pile foundation, the test pile base, and the test pile faces using standard mining equipment. The foundation was the Type I rock placed over bedrock and covered with a thin layer of esker sand or processed kimberlite to provide bedding under the high density polyethylene (HDPE) liner. The liner became a part of the basal drain collection system together with 150 mm perforated PVC pipes. Type I crushed 300 mm minus rock layer was placed on top of the liner as top liner bedding material and base for the construction of base instrumentation. The instrumented base was covered with a 2 m thick run-of-mine layer consistent with each pile type before the construction of the pile faces proceeded. The test pile faces were built using a push-dump and end-dump construction method. The waste rock was push dumped or end dumped from the 15 m high access ramp. The construction was stopped as the design instrumentation angle-of-repose faces were reached and the required instrumentation was installed. An excavator placed between 0.5 m and 1 m run-of-mine layer over the complete instrumented faces to protect the instruments before construction resumed. Instrument cables were protected at the top of the test piles until the construction was complete. Instrument leads were then excavated to allow data collection. The TC Covered Pile was sloped after construction to achieve the design 3:1 (H:V) slopes. Fala et al. (2003) recognizes four ways how the waste rock may be placed to form a waste rock pile: (1) end-dumping, (2) push-dumping, (3) free-dumping and (4) deposition with dragline. End-dumping is a method of waste rock deposition where waste rock is dumped over the crest of the pile directly from the truck. In this method, due to high angular velocity of the rock, 75 % of the largest grain size falls to the bottom of the pile (Morin et al., 1991). Push-dumping is a method where waste rock is dumped near the crest from the haul truck and then pushed over the crest with a dozer or equivalent. In this method, as the angular velocity is less than during end-dumping, only 40 per cent of the largest size reaches the bottom of the pile (Morin et al., 1991). Free-dumping is a method of forming small piles of waste rock that are later spread and compacted. Dumping with dragline is a method where waste rock is deposited with a dragline bucket.

Pham (2013) examined thermal regime within and under the Diavik waste rock test piles. Pham (2013) compared measured temperatures in bedrock beneath the Type 3 Pile and adjacent to the Type 3 Pile. Maximum and minimum temperatures in bedrock surface adjacent to the Type 3 Pile were 15°C and -25°C, respectively and the MAST was -5°C

between September 2004 and April 2009. The bedrock underneath the Type 3 Pile was generally below 0°C since construction with some temperatures remaining at 0°C due to latent heat effects from September to December during both 2007 and 2008. Temperatures cooled below 0°C between December and July in both 2007 and 2008 due to convective cooling effects. A cooling trend was observed since construction between 2007 and 2008 with temperatures between 0°C and -3°C, and -1°C and -5°C in 2007 and 2008, respectively. The maximum active layer in bedrock adjacent to the Type 3 Pile was found to be 4 m deep. Since construction, the bedrock temperatures beneath the Type 3 Pile remained below 0°C and temperatures at 10 m depth varied between -3°C and -5.5°C.

Pham (2013) created two dimensional isotherm plots in the Type 3 Pile on Face 1 and Face 4 and on a longitudinal cross section through the pile centerline perpendicular to the test pile faces. Average surface temperatures for the Type 3 Pile were established using temperature data from locations less than 0.05 m below the surface of the Type 1 and Type 3 Piles. The average surface temperatures vary sinusoidally with amplitude of 20°C, maximum and minimum value of 15°C and -25°C in July and January/February, respectively, and a MAST of -5°C. The measured temperature data available from the Type 3 Pile were used to create the isotherm plots. The isotherm plots were then used to calculate air velocity vectors in the pore space that resulted from density differences. Darcy law, ideal gas law and waste rock properties were used to create air velocity vectors. Intrinsic permeability for the waste rock was assumed to change linearly between $2.0x10^{-9}$ m^2 at the surface (Amos et al., 2009a) with the assigned value of $2.0\ x10^{-8}$ m^2 (Chi, 2010) at the bottom of the pile. Material segregation during construction was the reason for this segregation.

Isotherms on Face 1 and Face 4 indicated that 0°C isotherm progressed deeper into the pile under the sideslopes than under the surface. Pham suggests that greater water infiltration into the batters (Neuner et al., 2012) and subsequent freezing and/or wind induced/natural convection under the sideslopes are responsible for this phenomenon. The isotherms were found to be symmetrical on each sideslope indicating similar amount of energy entering from each sideslope. Two metres below the pile surface on each face exhibited a cooling trend of 4°C during each winter since 2006 and above 0°C temperatures each summer. Similarly, the longitudinal section indicated decrease in internal temperatures between 2007 and 2008. Temperatures at the same depth on most outer Face 4 were colder than on Face 1 indicating that more heat was released in the winter from the most outer face due to close proximity to the outside boundary of the pile.

Calculated air flow vectors indicated that in the winter air flows from the inside up to the surface carrying new air into the pile through the bottom of the sideslopes. In the summer, the air flows in the opposite direction entering through the surface and exiting the pile near the bottom of the sideslopes. Pham predicted a similar air flow patterns in the longitudinal section. The average air velocity values in the winter on all sections were about three times larger than in the summer suggesting that heat transfer is greater in the winter.
Pham (2013) also prepared temperature profiles with depth in the Type 3 Pile along the centerline of Face 1 and Face 4. Temperatures on both faces varied from 3°C to 6°C after construction in 2006. The active layer reached to the bottom of the pile in 2007 on both

faces. In 2008, the active layer thinned on both faces. Face 1 had the active layer reaching 13 m and Face 4 11.9 m below the surface of the pile. Thus, the frozen zone at the pile base grew 1 m on Face 1 and 2.1 m on Face 4. Temperature profiles had similar shape on both faces.

Pham (2013) prepared heat budget for the Type 3 Pile to determine heat gain/loss on annual basis through a control volume. Conduction and convection constituted heat transfer mechanisms and were assumed only at the perimeters of the control volume. Heat release due to oxidation in the Type 3 Pile was negligible (Amos et al., 2009) and was not considered in the heat budget calculations. The convective heat transfer was assumed only through the sideslopes and was calculated using a horizontal inward flux through the sideslopes based on internal pressure measurements (Amos, 2009). The conductive heat transfer was assumed through the surface and through the base and was calculated using monthly average temperature gradient using two dimensional isotherms constructed for Face 1 and Face 4. Thermal properties of waste rock acquired during the test pile study were used in the heat budget calculations and are summarized in Table 2.2. Thermal conductivity was measured at various depths in a test pile using a transient probe and the bulk volumetric heat capacity was calculated based on measured fractions of air, water and solids. Between January and March, heat was released on Face 1 and Face 4 in 2007 and 2008. On Face 1, the total amount of this released heat was -1.2×10^4 MJ in 2007 and -1.8×10^4 in 2008; and on Face 4 -1.3×10^4 MJ in 2007 and -2.1×10^4 MJ in 2008. Face 4 released more heat due to its proximity to the edge of the pile that allowed for longitudinal air inflow due to natural convection, and wind induced inflow of cold air. The heat was released in a similar manner between October and December in 2007 and 2008. Between May and September, smaller amounts of heat were gained on Face 1 and Face 4 in 2007 and 2008. On Face 1, the total heat gained was 4.8×10^3 MJ in 2007 and 9.2×10^3 MJ in 2008; and on Face 4 3.8×10^3 MJ in 2007 and 9.3×10^3 MJ in 2008. Almost double heat gain in 2008 is attributed to wind induced warm air inflow. In summary, average total heat transfer was similar in 2007 and 2008 despite of monthly heat transfer variations.

Pham (2013) also conducted numerical heat transfer simulation of the waste rock test piles for the purpose of examining the Air Convection Cover (ACC) concept to select the optimum thickness of the cover and permeability for the waste rock test piles. Relevant to this work are the thermal conductivity measurements in the Type 3 and Type 1 Piles (Table 2.3) and in-situ measurements used by Pham (2013) in Type 3 Pile modeling (Table 2.4).

3.0 GEOSTUDIO 2007 CONVECTION MODULE EXAMINATION

GeoStudio 2007 convection module part of a finite element numerical program was used to carry out the numerical modeling studies described in this thesis. The convection module was first tested and then applied to modeling a Diavik waste rock test pile to develop an understanding of temperature variations within the pile. Testing of the convection module was a part of this work and consisted of examining full versus half geometries, various mesh sizes, repeatability of modeling results and similarities and differences between examples from the literature and field data. GeoStudio 2007 was also used in thermal conduction mode for comparison to convection mode.

GeoStudio 2007 convection module combines two independent modules TEMP/W used to solve thermal conduction, and SEEP/W module used to solve fluid flow that was modified using a dependant module AIR/W to modify the flowing fluid as unsaturated flow of water and air. Description of the equations used by GeoStudio 2007 convection module and the solution scheme are presented in Appendix A.

Testing of the GeoStudio 2007 convection module utilized embankments and a waste rock pile to establish geometry and to vary air permeability of the materials. The embankment base was either underlain by a foundation or had no heat/air flow through it. Natural convection in roadway embankments underlain by a foundation has been discussed in the literature (Goering and Kumar (1996), Goering (2000)). The roadway embankments were highly permeable gravel/rock material where natural convection could develop. These permeable embankments were modeled as a two-phase system filled with a mobile air surrounding a coarse soil skeleton. The void spaces were assumed to be dry. The waste rock pile is a field example from the Ekati Diamond Mine. Panda Waste Rock Storage Area at Ekati was modeled using GeoStudio and the results were compared to in-situ field temperature data. The examples selected for testing the model are shown in Table 3.1. The table identifies the model example, air embankment boundary conditions and modeling duration.

Studies by Goering and Kumar (1996) and Goering (2000) were selected to examine embankment geometry underlain by a foundation. Closed boundaries were modeled using data presented by Goering and Kumar (1996) and Goering (2000), and open sideslopes using results shown in Goering (2000). The same embankment geometry was modeled to compare full versus half geometry and examine repeatability of modeling results.

Goering and Kumar's (1996) and Goering's (2000) embankment geometry consisted of a roadway embankment rested on a foundation, as shown in Figure 3.1A. The driving surface was 6 m wide and the embankment had 1V:2H sideslopes. The upper boundaries of the model comprised the driving surface, sideslopes and the native ground extending horizontally away from the embankment toe. The computational domain was extended 9 m away from the embankment toe and 9 m below the embankment base. These dimensions would eliminate the influence of the model boundaries on modeling results according to Goering and Kumar (1996).

Material properties of the embankment and foundation differed between the two studies, as shown in Tables 3.2 and 3.3. However, both studies describe the embankment as highly permeable gravel and the foundation as "uniform ice-rich silt with moisture content of 45% and dry density of 1442 kg/m^3" (Goering and Kumar, 1996 and Goering, 2000).

Volumetric water contents were calculated from the porosities while assuming full saturation. A functional relationship was created in GeoStudio between volumetric water content and matric suction and applied to the foundation material. The matric suction corresponding to the volumetric water content was applied in the form of pressure head over the foundation area to saturate it to particular volumetric water content. The phase change took place only in the foundation soil. The highly permeable embankment was filled with air and was assumed to be dry. Goering (2000) foundation porosity of 0.078 was not used in GeoStudio modeling. This parameter was adjusted to either 0.78 or 0.65 to better represent literature description of the actual foundation material. Comparison models were run with the foundation porosity decreasing to 0.45 in case the foundation "moisture content of 45%" (Goering and Kumar, 1996; and Goering, 2000) was actually volumetric not gravimetric. Thus, some modeling examples contain results with the foundation porosity of 0.45.

Generally, foundation volumetric water content changed with temperature according to a build-in function for silt in the GeoStudio. This gradual change was preferred in GeoStudio models used in this thesis to eliminate possible numerical instabilities related to sharper instantaneous changes in material properties. A step function was also used in some GeoStudio models to simulate instantaneous change in foundation volumetric water content. Goering and Kumar (1996) and Goering (2000) do not discuss this aspect of their modeling. However, the results from both studies suggest that this instantaneous change might have been used in their modeling.

Air pressure boundary conditions varied to simulate either closed boundaries or open sideslopes. Goering and Kumar (1996) simulated no air flow across the boundaries by setting the normal pressure gradient to zero at each boundary. Goering (2000) specified open sideslope condition based on the pressure in the surrounding air mass. No air flow boundary was used in GeoStudio to simulate Goering and Kumar's and Goering's impermeable condition because by default no air boundary specification means no flow in GeoStudio. Transient state air pressure boundary condition was applied for the closed boundary condition. GeoStudio's ad-in function was applied on the sideslopes to simulate open sideslopes in the transient state. Pressures were applied throughout the whole model grid to maintain the desired air/water saturation in both the steady and transient states.

Temperature boundary conditions were the same in both studies from the literature and were used without changes in GeoStudio embankment modeling. Temperature boundary conditions were applied in the steady and transient states. Steady state temperature boundary condition consisted of -2°C temperature applied across the entire model grid as suggested in Goering (1994). Transient boundary conditions consisted of

sinusoidal temperature functions applied to the model surface boundaries, as shown in Table 3.4. The heat flux boundary condition consisted of a geothermal flux applied to the base of the foundation as a unit flux of 0.06 W/m^2 (5.2 kJ/day-m^2).

The three sinusoidal curves were derived by Goering based on conditions that are typical of interior Alaska and using the n-factors approach to account for surface conditions. The n-factors accounted for the energy balance of the three surface covers such as snow, surface moisture conditions and radiant properties based on Lunardini (1998). The time variable t in the sinusoidal function is a Julian day. Yearly mean temperatures for the pavement, sideslopes, and native ground surface are 1.1°C, 2.7°C, and -1.9°C, respectively. The sideslope is the warmest out of the three surfaces, and the mean annual temperature of -1.9°C signifies the presence of permafrost in the native ground. The GeoStudio embankment models described in this chapter were started on April 1.

Modeling results from the GeoStudio embankment study were compared in terms of snapshots or trends or both. Snapshots were taken of isotherms and air flow vectors on selected days. Temperature trends were extracted for a modeling time. Sixteen locations were selected to extract temperature trends, as shown in Figure 3.1B. These 16 locations were used consistently in this chapter to extract temperature trends. These locations were mainly in the embankment subjected to convective flow. Three locations were in the foundation under the embankment.

Mesh size was varied in GeoStudio models to examine mesh dependency. A mesh is automatically generated by GeoStudio given element shape and global element size specified by the user. A mesh can be additionally modified by specifying constraints on the regions or regions' boundaries. GeoStudio does not generate meshes for given modeling particulars.

SRK (2003) supplied information to compare a GeoStudio model study to field data collected at the Ekati Diamond Mine from a waste rock storage area. Data from Diavik waste rock test piles was used as input parameters to this model, as shown in Table 3.5.

The parameters measured at Diavik differ substantially from the parameters used by Goering and Kumar (1996) and Goering (2000). Thermal conductivity was increased five times and volumetric heat capacity almost doubled. Nevertheless, these higher values were chosen for the Ekati model under the assumption that Ekati waste rock is best represented by Diavik waste rock due to close proximity of the two mine sites (about 30 km).

Sun (2005) also provided information on an embankment with both closed and open boundary conditions but without a foundation. Input parameters for this modeling study were selected to achieve Sun's Rayleigh numbers of 50 and 80, as shown in Table 3.6, and a Rayleigh number of 25 for additional comparison.

GeoStudio 2007 convection module modeling results were compared to these case records along with recommendations for future work presented later.

3.1 Full Versus Half Models

An embankment geometry used by Goering and Kumar (1996) and later by Goering (2000) was modeled as a full and half geometry of the symmetrical embankment with either closed boundaries or open sideslopes. The purpose of the modeling was to establish if half geometries could be modeled instead of full geometries to limit computation time. Modeling results were compared in terms of snapshots of isotherms and air flow vectors, and trends of temperatures.

The symmetry principle was not met in the half geometries because neither vertical nor horizontal flow was allowed on/across the symmetry line. The horizontal no-flow condition was a result of applying no pressure boundary on the symmetry line. By default, no pressure boundary in GeoStudio equals to no flow in either direction. Creating a boundary condition with just vertical flow was not explored because this option is not easily available in GeoStudio.

Input parameters for the GeoStudio models to examine full and half geometries are shown in Table 3.7. Foundation parameters differed in the models because the models were created at different times. The newer models replaced a step function to represent unfrozen volumetric water content changes with temperature with GeoStudio built-in functions, and used the lower value of 0.65 for volumetric water content.

3.1.1 Full Versus Half Models in Terms of Snapshots

Three full models and their corresponding half models were created, as shown in Figures 3.2 to 3.4, to examine in terms of snapshots of isotherms and air flow vectors full versus half geometries with either closed boundaries or open sideslopes. The corresponding half models were created by deleting materials from the full models that were on the right side of the symmetry line. Modeling with closed boundaries was undertaken using coarse and fine mesh models (Figure 3.2 and 3.3) to examine mesh dependency. Modeling with open sideslopes was undertaken using one model with an adequate mesh (Figure 3.4). All three meshes were built using triangles. The coarse full model mesh consisted of 1574 nodes and 1138 elements, and the fine full model mesh consisted of 4259 nodes and 3202 elements. The full model created with open sideslopes consisted of 3124 nodes and 1712 elements. The selected models with applied pressure and temperature boundary conditions are shown in Appendix B. Steady state pressure, steady state temperature and transient state temperature boundary conditions were the same in the three models.

Modeling results were compared in terms of snapshots of isotherms and air flow vectors. The full models were compared to their corresponding half models, and the three models were compared to each other on the days when snapshots were taken. The results from this section are not compared to other modeling available from the literature or conducted in this thesis.

Results

The three evaluations were started on April 1 and run for 426 days to include May 1 after one year of modeling. The comparative results consisted of snapshots of isotherms and air flow vectors on August 4, November 14, January 31 and May 1 representing summer, fall, winter and spring condition, respectively. These dates were selected arbitrarily to represent each season in a consistent manner.

The results are summarized below:

- In August and May, the two closed boundary and one open sideslope models show similar results for full and half models, as shown in Figures 3.5, through 3.7 and 3.14 through 3.16. The results are also similar between the two close boundary coarse and fine mesh models for either the full or half model. Isotherms are straight indicating that conduction dominates the heat transfer.

- In May, embankment temperatures in the full and half model with open sideslopes are warmer than embankment temperatures in the models with closed boundaries.

- In August, embankment temperatures in the full and half model with open sideslopes are similar to embankment temperatures in the models with closed boundaries.

- On November 14 in the embankment, all three models and their corresponding half models are different, as shown in Figures 3.8 through 3.10. The embankment experiences chaotic sinking of cold air and neither isotherms nor air flow vectors develop consistent patterns that can be compared.

- On January 31 in the embankment, the two closed boundary full size models are similar but differ from their corresponding half models which also are similar to each other. One downward plume exists in the full models but it also exists in the half models, as shown in Figures 3.11 and 3.12. One plume in a half model implies two plumes in the corresponding full model contrary to the results from the full models. The open sideslope model, on the other hand, shows a close match for the embankment between the half and full models, as is shown in Figure 3.13. In the foundation, isotherms vary in all the three models both for full and half models. Differences mostly relate to distribution of unfrozen zones as the foundation undergoes freezing.

- Air flow vector distribution for the full models on January 31, as shown in Figure 3.11 through 3.13 indicate the symmetrical nature of heat flow for the embankment problem. The open sideslope half model confirmed this symmetry but the closed boundary half models did not, as shown in Figures 3.11 and 3.12. On January 31, both closed boundary coarse and fine mesh half models have air flow vector patterns that are different than the corresponding full models but similar to each other.

Discussion

Isotherms and air flow vectors match between the full and half models in the three models when heat transfer via conduction dominates. They become chaotic during chaotic sinking of air in the fall for all the three models. Isotherm and air flow vector patterns develop in the winter but they match only for the case of open sideslopes. The closed sideslopes full and half models develop patterns that differ from each other.

Stabilizing conditions must be present in the embankment with open sideslopes. This could be the combination of high air flow and open sideslopes. The high air flow is either pushed against the open sideslopes or towards the embankment centerline. In either case, the air does not have a chance to redistribute itself inside the embankment. This is not the case when the boundaries and closed. The air is trapped inside the embankment and redistributes itself within the embankment. This redistribution of air is different in the full embankment than in half embankment. This redistribution may be different if vertical air flow was allowed along the symmetry line of the half model.

There is evidence in the full models, however, that the embankment problem is of a symmetrical nature. This symmetry is partially confirmed by the half model with open sideslopes, but not by the half models with closed boundaries. The symmetry in the half model with open sideslopes could be misleading as the majority of the air flow is concentrated near the sideslopes. Lack of symmetry in half models could be a result of GeoStudio no-flow boundary condition along the symmetry line, or a consequence of the chaotic sinking of air that initiates the patterns for development of plumes in the winter.

Conclusion

GeoStudio models conduction dominated cases well. Half models could be modeled instead of full models for conduction dominated cases to save computing time and effort based on the results in this study.

In the winter, the open sideslope model is more robust during the convection heat transfer modeling. This open sideslope model geometry can almost be modeled using the half model. The closed boundary models cannot be modeled using the half geometries. Further examination of a half model with closed boundaries is recommended to determine if the plume is always singular under these modeling conditions.

In the fall, comparison cannot be made based on these snapshots as no snapshots were similar for comparison.

Further modeling should be conducted to examine smaller meshes in the models with closed boundaries.

It was concluded that snapshots at a particular time cannot be used for comparing GeoStudio convection modeling results. Temperature trends should be compared instead of snapshots showing temperatures on a particular date for GeoStudio convection modeling.

3.1.2 Full Versus Half Models in Terms of Trends

A half model and corresponding full model were both created, as shown in Figure 3.17, to examine in terms of temperature trends full versus half geometry with closed boundaries. The full model was created by adding a symmetrical half across the symmetry line to the existing half model. The mesh in the half model and corresponding full model consisted of quads and triangles. The half model and the corresponding full model consisted of 1661 nodes and 1241 elements, and 3286 nodes and 2482 elements, respectively. The half model and corresponding full model with applied pressure and temperature boundary conditions are shown in Appendix C.

The results were compared in terms of temperature trends comparing a half model to the corresponding full model. The results from this section are comparable to other modeling described in later sections. Comparison in term of snapshots of isotherms and air flow vectors on selected days was also included for completeness.

Results

The models were started on April 1 and run for 730 days. The results as temperature trends are presented at the 16 locations described earlier (Figure 3.1B). The snapshots are presented as isotherms and air flow vectors on August 4, November 14, January 31 and May 1. A complete set of time-temperature plots and snapshots is included in Appendix C.

The results are summarized below:

- Temperature trends are similar in the warm months when conduction dominates (Figure 3.18 through 3.20).
- Temperature trends differ when convection dominates. Negative temperatures fluctuate in the embankment locations, as shown in Figures 3.18 through 3.20A. Most fluctuation occurs when the temperatures are cooling. Both half and full models show these temperature fluctuations that reach up to about 11°C in a relatively short time at Location 7 near the embankment centerline (Figure 3.19A).
- Temperature trends are similar in the foundation and no fluctuations are observed, as shown in Figure 3.20B.

Discussion

Temperature fluctuations are greatest in the fall, decrease during the winter and end around mid-March. This is consistent with the snapshot results presented earlier in Section 3.1.1 where differences are greatest in the fall when chaotic sinking of air begins to occur. The differences decrease during the winter and disappear in May.

The snapshot results in the previous section also indicate that the closed boundary model is more susceptible to differences than the open sideslope model. The GeoStudio model modeled in this section had closed boundaries.

Temperature fluctuations of this magnitude within a short time suggest that modeling results are not repeatable.

Conclusions

The modeling carried out in this section establishes that differences exist between temperature trends in GeoStudio convection modeling but is not sufficient to draw definite conclusions related to the causes and how to adjust the model to overcome the differences.

It was concluded that additional modeling is required to examine the trends and snapshots from the various GeoStudio convection models. The models should include open sideslopes and closed boundaries with varying mesh size. Repeatability of modeling results should be investigated as well.

3.2 Repeatability of Modeling Results

An embankment geometry used by Goering and Kumar (1996) and later by Goering (2000) was modeled using GeoStudio to examine repeatability of modeling results. Half of the symmetrical embankment geometry was modeled. The models varied in mesh size and had either closed boundaries or open sideslopes. The models were run twice without changes and the modeling results were compared in terms of snapshots of isotherms and air flow vectors, and/or temperature trends. Input parameters were adapted after Goering (2000), as summarized in Table 3.8.

Two foundation volumetric water contents were used in the models. The foundation volumetric water content of 0.78 was used in the models to compare snapshots, and of 0.65 to compare trends. The higher volumetric water content was derived using latent heat presented by Goering (2000), and the lower using moisture content and dry density presented by Goering (2000). The volumetric water content derived using the two sets of values was not the same.

3.2.1 Repeatability of Modeling Results in Terms of Snapshots

Three models were created in GeoStudio, as shown in Figure 3.21, to examine repeatability of modeling results in terms of snapshots. The three models had coarse, medium and fine meshes and closed boundaries. These models were run twice without changes and snapshots of isotherms were compared on one day in each season. The three models with applied boundary conditions are shown in Appendix D.

The number of nodes in the coarse, medium and fine models was 1661, 3250 and 6907, respectively, and the number of elements was 1241, 1876 and 3323, respectively. All the three meshes were created out of quads and triangles.

Each model was compared to itself and to the remaining two models.

Results

The three evaluations were started on April 1 and run for 426 days to include May 1 after one year of modeling. Each evaluation was run twice without changes. The first run in each evaluation was called run A and the second run B. Each evaluation was saved under a different name prior to performing run B. Snapshots of isotherms were compared on August 4, November 14, January 31, and May 1. Modeling results are discussed below:

- Snapshots of isotherms in the embankment and foundation in the spring and summer are similar between run A and run B in the three models, and between the three mesh sizes, as shown in Appendix D.

- Snapshots of isotherms in the embankment differ between run A and run B in all the three models in the fall and winter, as shown in Figures 3.22 through 3.27. On November 14, the thaw zones are present in the embankment and have different shapes and sizes, and the isotherm locations differ. The fine mesh model shows the closest comparison between run A and run B. On January 31, isotherms differ in the number of downward plumes and their shapes between run A and run B in the three models. The coarse mesh and fine mesh models have one-and-a-half plumes in run A and one downward plume in run B. The medium mesh model has one downward plume in both runs; however, the plume shapes differ between each other.

- Snapshots of temperature isotherms in the foundation are similar between run A and run B, and between the three mesh sizes in the fall and winter as these temperatures are controlled by conductive heat transfer.

Discussion

The chaotic sinking observed on November 14 is consistent with the results reported in Section 3.1.1. The greatest differences in temperature isotherms are present during fall

when chaotic sinking of air occurs. Differences still occur during the winter but some patterns develop.

Temperature isotherms are not repeatable when the same half model is run twice.

Conclusions

GeoStudio modeling results are not repeatable when compared during the fall and winter. The differences in the modeling should be examined by evaluating temperature trends.

3.2.2 Repeatability of Modeling Results in Terms of Trends

Two models were created in GeoStudio, as shown in Figure 3.28, to examine repeatability of modeling results in terms of temperature trends. The difference between the two models is the mesh size in the embankment and in the underlying part of the foundation. A finer mesh was used in the second model. Both had either closed boundaries or open sideslopes. The two models were run twice without changes between the runs and the trends of daily temperatures were presented and compared. The two models with applied boundary conditions are shown in Appendix E. Steady state pressure, steady state temperature and transient state temperature boundary conditions were the same for the two models.

Except for the foundation porosity, as illustrated earlier in Table 3.8, the two models are the same as the coarse and fine mesh models with closed boundaries discussed in previous Section 3.2.1. The coarse mesh model had 1661 nodes and 1241 elements, and the fine mesh model had 6907 nodes and 3323 elements. The mesh was created out of quads and triangles.

The following boundary conditions and runs were compared:

- Run A and run B with the coarse and fine mesh model with closed boundaries;
- Run A and run B with the coarse and fine mesh model with open sideslopes;
- Run A and run B with the coarse mesh model with closed boundaries; and,
- Run A and run B with the fine mesh model with closed boundaries.

Results

The two evaluations were started on April 1 and were run twice as run A and run B for 730 days. The results are presented as daily time-temperature plots from the 16 selected locations described earlier (Figure 3.1B). Run A with the coarse mesh model is called “Coarse A” and run B with the coarse mesh model is called “Coarse B” on the

plots. The same applies to runs with the fine mesh models. The results are presented and discussed below:

- Embankment temperatures in the two models with closed boundaries differ between run A and run B, as shown in Figures 3.29 through 3.35A. Differences between temperatures from run A and run B exist when temperatures are negative. The greatest differences exist when the temperatures are cooling during the late fall. Daily fluctuations of the negative temperatures are observed. These fluctuations are greatest when the temperatures are cooling rapidly, e.g. Location 7, as shown in Figure 3.32A. The locations near the embankment centerline and under the driving lane exhibit most significant daily fluctuations. No or insignificant differences are observed when temperatures are warming or above 0°C.

- Embankment temperatures in the two models with open sideslopes differ between run A and run B, as shown in Figures 3.37 through 3.43A. The nature of the differences is similar to the ones in the two models with closed boundaries but the differences are less and observed at fewer locations. Daily fluctuations of the negative temperatures are observed as well but are also less and at fewer locations. No or insignificant differences or fluctuations are observed when temperatures are positive, as in the two models with closed boundaries.

- Differences were calculated between run A and run B temperatures in the coarse and fine mesh model with either closed boundaries or open sideslopes (four models). The differences are between daily temperature readings in the 16 locations for the modeling duration. The differences between run A and run B temperatures in the coarse and fine mesh model with closed boundaries were plotted, as shown in Figures 3.45 through 3.52 (coarse mesh model) and Figures 3.53 and 3.60 (fine mesh model) to show their distribution with time. The differences for the models with open sideslopes were not plotted because they were small. Generally, differences are higher in the models with closed boundaries.

- Standard deviation for these differences was calculated in each location, as shown in Table 3.9. It should be noted that these differences occur on different days and the time dependency was not factored out of the standard deviation calculation. The standard deviation ranges for each model are included at the bottom of the table. Standard deviations are highest in the coarse mesh model with closed boundaries. When sideslopes are open, the situation reverses and the standard deviations in the fine mesh model are higher than the standard deviations in the coarse mesh model.

- Differences between run A and run B temperatures also differ between locations. This is illustrated with standard deviations shown in Table 3.9. The six embankment locations near the centerline (Location 3, 7, and 13) and under the driving lane (Location 2, 6, and 12) have highest standard deviations in both closed boundary and open sideslope models. These locations are exposed most to the chaotic sinking of the cool or cold air. Location 8 in the embankment toe exhibits the least

standard deviations out of all the four models. This location is closest to the sideslope temperature boundary. The foundation locations (Location 14, 15 and 16) have least standard deviations out of all the locations in all the models.

- Foundation temperatures behave differently than the embankment temperatures. The foundation temperatures do not fluctuate and are similar for the two models with closed boundaries and two with open sideslopes, as shown in Figures 3.35B through 3.36 (closed boundaries) and Figures 3.43B through 3.44 (open sideslopes). Temperature differences are near zero indicated by maximum standard deviation of 0.3 in the coarse and fine mesh models, as shown in Table 3.9.

- Temperature trends for the coarse mesh model with either closed boundaries or open sideslopes were plotted against each other for the 16 locations to illustrate how temperatures differ in the closed boundary versus open sideslope models. Except for Location 8, the open sideslope model is generally colder in the summer and colder in the winter, as shown in Figure 3.61 through 3.67A. The colder temperatures in the summer are most visible in the top and middle locations. In the bottom locations, the same pattern exists but generally temperatures are much colder in the winter. The three foundation locations are similar in the summer but significantly colder in the winter when the sideslopes are open, as shown in Figures 3.67B through 3.68.

Discussion

Temperature trends can be compared. The comparison is better in the model with open sideslopes because daily fluctuations are less. Trends give a better understanding of temperature changes in the embankment than snapshots that can differ significantly from day to day as discussed earlier.

The open sideslope model shows colder temperatures at different locations in the embankment. The open sideslope model is colder due to greater amounts of cold air flowing through the embankment in the winter. This cold air remains in the embankment during warm summer months.

Conclusions

GeoStudio modeling results can be repeated when conduction dominates the heat flow but cannot be repeated when convection dominates. This is true for both closed boundary and open sideslope models with either coarse or fine mesh.

Trends can be used as a tool for comparing GeoStudio convection modeling results despite of lack of their repeatability. For example, daily temperature data can be plotted over temperature trends for comparison. This conclusion is used in the following section to compare GeoStudio modeling results from examples presented in the literature.

3.3 Studies by Goering and Kumar (1996) and Goering (2000)

Four full models were created in GeoStudio based on numerical models described by Goering and Kumar (1996) and Goering (2000). The purpose of the models was to model a long term effect of natural convection in a highly porous road embankment with either closed boundaries or open sideslopes and compare the results to both studies. A study by Goering (2000) was used to compare modeling results for the embankment with either closed boundaries or open sideslopes, and by Goering and Kumar (1996) for the embankment with closed boundaries. In addition to numerical modeling, Goering (2000) describes a field experiment with either closed boundaries or open sideslopes conducted to allow for back analysis of the numerical simulations and comparison. Goering's field experiment was short term lasting between October 1993 and October 1995 (Goering, 1998). However, Goering (2000) compares the field experiment to his long term modeling results. The same approach was used during the GeoStudio modeling reported here where the long term GeoStudio results were compared to Goering's field experiment data.

Goering and Kumar's (1996) and Goering's (2000) embankment geometry consisted of a roadway embankment rested on a foundation, as described earlier and shown in Figure 3.1A. The experimental embankment had the same cross section as used in the numerical studies reported by Goering and Kumar (1996) and Goering (2000) and was 40 m long.

Full geometries were modeled with GeoStudio to eliminate an additional variable from the modeling related to full versus half geometries. Both studies from the literature modeled half geometries. The main assumptions used in the GeoStudio modeling are identified below:

- Initial temperature condition for the steady state analysis was assumed to be -2°C throughout the entire model grid (the embankment and foundation); this assumption was made based on Goering (1984); the initial condition was not addressed in Goering and Kumar (1996) and Goering (2000).

- Impermeable condition was simulated by not specifying any pressure condition because no flow is a default in GeoStudio 2007; Goering represented impermeable condition by setting the normal pressure gradient to zero along each boundary.

- The start date of the modeling was assumed as April 1, each year having 365 days and a leap year every four years; these details were not discussed in Goering and Kumar (1996) and Goering (2000).

Input parameters used in the four GeoStudio models are summarized in Tables 3.10 and 3.11. The parameters in Table 3.10 were applied to one model based on Goering and Kumar (1996) and parameters in Table 3.11 to three models based on Goering (2000). The foundation in the three models based on Goering (2000) was examined for two porosities of 0.65 and 0.45 because neither Goering and Kumar (1996) nor Goering

(2000) report on the definition of the moisture content of 45% assumed for the foundation. The porosity of 0.65 represents a gravimetric moisture content of 45%, and of 0.45 represents a volumetric moisture content of 45%. The foundation in the model based on Goering and Kumar (1996) was examined for porosity of 0.65. A GeoStudio ad-in function was used to model unfrozen water content change with temperature in the foundation expect for one modeling case where a stepped function was used. Goering and Kumar (1996) and Goering (2000) did not consider wind in the numerical modeling.

Mesh element size and shape was adjusted for each model to limit the number of iterations during the computations. Each model was composed of regions representing the embankment, the top 2 m of the foundation, and the remaining deeper portion of the foundation. Coarser mesh was used in the deeper portion of the foundation.

The four GeoStudio models were run for 25 years and the results extracted during the 25th year of modeling. The results were presented as trends of temperatures or snapshots of isotherms and air flow vectors or both. The trends were of daily temperatures extracted in the last year of modeling at the 16 locations within the embankment discussed earlier (Figure 3.1B). Snapshots were of isotherms and air flow vectors on the days listed in the literature. GeoStudio snapshots were compared to the literature snapshots. GeoStudio temperature trends were compared to temperatures estimated from literature snapshots. Snapshots from the literature were enlarged and temperatures were estimated at the 16 locations from the isotherms. These estimated temperatures are listed in Table 3.12. Experimental results were not available in all 16 locations. Temperatures could not be estimated when isotherms were missing in proximity of the horizontal isotherms.

3.3.1 Embankment with Open Sideslopes – Goering (2000)

Two full models differing in mesh size were created in GeoStudio based on a numerical model described by Goering (2000), as shown in Figure 3.69, to model the embankment with open sideslopes. The results were examined and compared to Goering (2000) numerical and experimental results. The input parameters were adapted after Goering (2000) and are shown in Table 3.11. Foundation porosities of 0.45 and 0.65 were used in both models. The coarse mesh model was also evaluated using a stepped function for the unfrozen water content change with temperature in the foundation. The coarse mesh model had 2286 nodes and 1286 elements, and the fine mesh model had 5829 nodes and 3190 elements. The mesh was created out of quads and triangles. The two models with applied boundary conditions are shown in Appendix F.

Compared were snapshots of isotherms and air flow vectors and temperature trends. The two models were compared to each other and to Goering (2000) numerical and experimental field temperature results.

The five cases modeled are listed below and summarized in Table 3.13:

- Case 1 - A coarse mesh model with the foundation porosity of 0.65;

- Case 2 - A coarse mesh model with the foundation porosity of 0.45;
- Case 3 - A fine mesh model with the foundation porosity of 0.65;
- Case 4 - A fine mesh model with the foundation porosity of 0.45; and
- Case 5 - A coarse mesh model with the foundation porosity of 0.65 and stepped function for the unfrozen water content change with temperature.

Results

The results are presented as snapshots of isotherms and air flow vectors and trends of temperatures, and are summarized below. The snapshots were taken on February 1 and August 1, representing winter and summer condition, respectively.

Comparison between GeoStudio Modeling Cases

- The comparison of snapshots on February 1 for Cases 1 through 4 shows that generally, embankment and foundation temperature isotherms in winter are similar between the coarse and fine mesh models with either porosity, as shown in Figure 3.70. Minor differences exist near the center of the embankment. These differences are believed to be related to the lack of repeatability of modeling results shown earlier in this chapter. The embankment center seems to be least robust; thus allowing for the development of unstable air reflected by varying isotherm distribution. The area under the sideslopes does not experience as much unstable air and the isotherms remain similar. These differences are believed to be unrelated to mesh size or foundation porosity.

- The comparison of temperature trends for Cases 1 through 4 confirms the pattern found in the temperature trends examined earlier for this embankment geometry with open sideslopes, but Case 5 expands on the findings. The five temperature trends (Cases 1 through 5) in the locations near the centerline (Location 3, 7 and 13) and under the driving lane (Locations 2, 6 and 12), exhibit daily fluctuation and differences when negative temperatures are cooling, as shown in Figures 3.71B and 3.72A; 3.73B and 3.74A; and 3.76B and 3.77A. These differences cease for the remaining locations, as shown in Figures 3.71A, 3.72B, 3.73A, 3.74B, 3.75, 3.76A, 3.77B and 3.78. The trend for Case 5 differs from the four modeling cases by having increased temperatures between June and November at the locations near the embankment base (Locations 8 through 13) and in the foundation (Location 14 through 16), as shown in Figures 3.74B through 3.78. This warmer condition results in zero temperatures in the foundation between August and November, as shown in Figures 3.77B and 3.78, contrary to the remaining four modeling cases where the temperatures remain near -2°C. The coldest temperatures in winter are the same in the five modeling cases and are not affected by this warmer condition in late summer and early fall.

- Embankment and foundation isotherms in summer are similar between coarse and fine mesh models, as shown on two snapshots illustrated in Figure 3.79A and B. The foundation porosity was 0.65 in both models.

- Air flow vectors are similar in the winter, as shown on the snapshots illustrated in Figures 3.80A and B. The number of air flow vectors is greater in the model with the finer mesh but the pattern is similar.

Comparison between GeoStudio Modeling Cases and Goering (2000) Numerical and Experimental Results

- The snapshots of isotherms taken on August 1 show good agreement between Goering's numerical results and the GeoStudio models, as shown in Figure 3.79. There is also agreement in the shapes of the isotherms in Goering's experimental embankment. However, Goering's field experiment shows warmer temperatures near the embankment base of around 6°C comparing to the GeoStudio models and Goering's numerical results showing near zero temperatures.

- The snapshots of air flow vectors taken on February 1 show different air flow vector pattern between the GeoStudio model and Goering's numerical results, as shown in Figure 3.80. Goering's air enters near the embankment toe and exits near the embankment crest. The GeoStudio air flow is reversed. The air enters through the crest and exits through the toe. In addition, Goering's numerical results show localized air flow where a downward plume is observed. This localized air flow is absent in the GeoStudio models.

- The snapshots of isotherms taken on February 1 show similarities and differences between the selected GeoStudio modeling case and Goering's (2000) numerical and experimental results. The GeoStudio coarse mesh model with foundation porosity of 0.65 and gradual change in foundation water content was selected for this comparison. Temperature isotherms under the sideslope have shapes similar to Goering's numerical and experimental results, as shown in Figure 3.81. The isotherms are concave towards the centerline and progress towards the centerline. This pattern can be observed in both Goering's experimental and numerical results. Except for Goering's numerical results, this pattern continues towards the centerline. A downward plume develops under the driving lane in Goering's numerical model. This plume is not observed either in Goering's experiment or the GeoStudio models. Goering's experimental and numerical embankment warms towards the centerline contrary to GeoStudio models that cool towards the centerline. The value of the isotherm under the sideslope, however, is -16°C in both numerical simulations but only -13°C in the experimental embankment.

- The snapshots of isotherms taken on February 1 also show that GeoStudio and Goering's studies differ with respect to coldest area in the underlying foundation. The experimental embankment indicates that the coldest zone under the

embankment is under the sideslope, as shown in Figure 3.81C. In Goering's numerical model there is a warm zone in the foundation under the embankment crest with temperature isotherms dipping up. None of Goering's results were reproduced using the GeoStudio models. GeoStudio foundation is coldest under the driving lane in the center. The temperature isotherms in the foundation are colder in the GeoStudio model (Goering's -8°C near the foundation surface versus GeoStudio -14°C). The native ground temperatures, however, are in good agreement. These colder temperatures are expected to reflect how the GeoStudio model translates air flow resulting from the intrinsic permeability. The air flow corresponding to Goering's intrinsic permeability of 6.3 x 10-7 m^2 was 40,481 m/d following the Rayleigh number calculation.

- The comparison of temperature trends shows that temperatures estimated from Goering numerical and experimental results more or less follow the pattern of GeoStudio temperature trends. The embankment top (Locations 1 through 3) is colder in the summer than Goering's numerical results, as shown in Figures 3.71 through 3.72A. Experimental results were not available for these locations during the summer. In the winter, the top of the embankment is generally colder than Goering's numerical and experimental results. Goering's experimental results are the warmest in the winter compared to the numerical results. The horizontal center of the embankment (Locations 4 through 7) show good agreement with Goering's experimental results in the summer; Goering's numerical results, however, are warmer during this time, as shown in Figures 3.72B through 3.74A. The same figures show that in the winter, Goering's numerical results are closer to GeoStudio trends than the experimental results but are still generally warmer. In the winter, Goering's experimental results are the warmest and thus show greater differences from the GeoStudio trends. At the embankment base (Location 8 through 13) the temperatures are generally colder in the summer and winter compared to Goering's numerical and experimental results, as shown in Figures 3.74B through 3.77A. The differences are greater when comparing to Goering's experimental results especially in the winter. Except for modeling Case 5, the foundation under the embankment (Location 14 through 16) is consistently colder in the summer and winter than Goering's numerical results, as shown in Figures 3.77B through 3.78. The temperature trend from Case 5 matches Goering's numerical results during the late summer and early fall maintaining zero temperatures as shown in Goering's studies. Goering's experimental results were not available for this period at the foundation.

Discussion

The GeoStudio models with open sideslopes show differences mainly in the center of the embankment. The examined foundation porosity and mesh size have no or little influence on the results either in terms of snapshots or temperature trends.

Temperature trends give better understanding of how the temperatures vary during either summer or winter compared to the temperature snapshots. Trends show daily variations in temperatures between models during chaotic sinking of air. This is confirmed by

snapshots having varying temperature isotherms in the embankment center. Snapshots confirm the results from trends and expand our knowledge of isotherm distributions. Snapshots are a good tool to compare air flow vectors to alter designers how to adjust the constructed product to enhance cooling.

Best agreement with Goering's experimental results was achieved at the horizontal center of the embankment in the summer. Best agreement with Goering's numerical results was achieved in the foundation in late summer. It was surprising to see that the agreement with Goering's numerical results was poor during the summer when conduction dominates but matched Goering's field experimental results. A good match with Goering's numerical results in the foundation confirmed the fact that Goering used instantaneous water content change with temperature in the foundation. This information might be helpful for future comparative studies involving Goering's work.

The open sideslope boundary condition produces isotherm distribution in the foundation that is unique to the GeoStudio model indicating the coldest area is located in area different than shown by Goering's numerical and experimental results.

GeoStudio embankment is colder than Goering's embankment. The colder embankment could represent the embankment's true condition. This could be caused by GeoStudio definition of air flow. The GeoStudio air flow (m/d) was equated to hydraulic conductivity. To find air flow corresponding to Goering's intrinsic permeability of 6.32×10^{-7} m^2, Rayleigh number formula was used. Air flow of 40,481 m/d calculated in such manner was applied to the GeoStudio model to simulate Goering's embankment. It is speculated that this calculated air flow might not exactly represent the intrinsic permeability defined by Goering in his model. The GeoStudio convection module does not provide Rayleigh numbers. Rayleigh number calculation is external to the program and might not exactly represent the combination of input parameters within the program. The Rayleigh number calculation within GeoStudio is not known.

The coldest embankment condition under the centre of the driving lane found in the experimental results further indicates that open sideslope may further distort the air flow from the GeoStudio model.

Conclusions

Further studies are recommended to examine relation between intrinsic permeability and air flow in the GeoStudio 2007 convection module. This is beyond the scope of this thesis.

Unique solution to open sideslope boundary condition suggests additional investigation of open sideslope embankments with GeoStudio models to evaluate the effect of the open sideslope on the underlying foundation.

3.3.2 Embankment with Closed Boundaries – Goering and Kumar (1996) and Goering (2000)

Two full models differing in mesh size and input parameters were created in GeoStudio based on numerical models described by Goering and Kumar (1996) and Goering (2000), as shown in Figure 3.82, to model the embankment with closed boundaries. The results were examined and compared to Goering and Kumar (1996) and Goering (2000) numerical and experimental results. Both studies were selected for this comparison because the embankments in both studies had closed boundaries and input parameters varied slightly. The model based on Goering and Kumar (1996) (GeoStudio 1996 Model) had a finer mesh in the embankment and used input parameters adapted after Goering and Kumar (1996) shown in Table 3.10. The model based on Goering (2000) (GeoStudio 2000 Model) had coarser mesh in the embankment and used input parameters adapted after Goering (2000) shown in Table 3.11. Foundation porosities of 0.45 and 0.65 were used in GeoStudio 2000 Model. Foundation porosity of 0.65 was used in GeoStudio 1996 Model. GeoStudio 1996 Model had 5177 nodes and 2561 elements, and GeoStudio 2000 Model had 3286 nodes and 2482 elements. The meshes were different to facilitate computations during modeling time. Both meshes were created out of quads and triangles. The two models with applied boundary conditions are shown in Appendix F.

The three cases modeled are listed below and summarized in Table 3.14:

- GeoStudio 2000 Model with the foundation porosity of 0.65;
- GeoStudio 2000 Model with the foundation porosity of 0.45; and,
- GeoStudio 1996 Model with the foundation porosity of 0.65.

Compared were both snapshots of isotherms and air flow vectors, and temperature trends. Comparison was first made between the two GeoStudio models and then the two GeoStudio models were compared to Goering and Kumar (1996) and Goering (2000). Comparison between the two GeoStudio models was made in terms of temperature trends and included two foundation porosities for GeoStudio 2000 Model. Comparison between the two GeoStudio models and both literature studies was made in terms of snapshots of isotherms and air flow vectors, and temperature trends. GeoStudio 1996 Model snapshots were compared to Goering and Kumar (1996) snapshots, and GeoStudio 2000 Model snapshots were compared to Goering (2000) snapshots. Snapshot comparison was made for the foundation porosity of 0.65.

Results

The results are summarized below. Snapshots of isotherms and air flow vectors from the GeoStudio 1996 Model were taken on June 2, October 2, November 2, December 2, January 1, March 3 and April 2. Snapshots of isotherms and air flow vectors from the GeoStudio 2000 Model were taken on February 1 and August 1.

Comparison between GeoStudio Modeling Cases

- The comparison of temperature trends for GeoStudio 1996 and GeoStudio 2000 Models with two porosities confirm the patterns observed for this embankment geometry with closed sideslopes, as shown in Figures 3.83 through 3.90. Summer temperatures show good agreement between the two models. Slight differences exist between GeoStudio 1996 Model that is finer and GeoStudio 2000 Models that are coarser. This difference is related to the actual locations were the trends were taken. The nodes in the fine and coarse mesh models did not fall in exactly the same locations and hence the differences. This is best illustrated in Location 8, as shown in Figure 3.86B. Except for the locations in the foundation, negative temperatures especially when cooling result in daily fluctuations and temperature variations between the three modeling cases.

- The comparison of trends also shows that the foundation temperatures are similar in the three modeling cases. The foundation porosity does not appear to influence the results.

Comparison between GeoStudio and Goering and Kumar (1996) and Goering (2000)

- Figure 3.91 shows the behaviour of the isotherms and air flow vectors on June 2. By this date, Goering and Kumar's embankment is entirely thawed contrary to the GeoStudio embankment which is thawed down to only 1.7 m at the centerline. The rapid thaw of the embankment is explained by the lack of moisture associated with phase change in the near-dry embankment material. The native ground away from the embankment had thawed by about 0.5 m in both studies. The -2°C isotherm reaches deeper for Goering and Kumar than for the GeoStudio model where it remained closer to the surface. Both models have straight isotherms indicating that conduction dominates the heat flow. Goering and Kumar's air flow vectors exhibit gentle counter-clockwise rotation which occupies most of the embankment. This airflow vector pattern is also present in the GeoStudio model.

- By October 2, as shown in Figure 3.92, the thawed zone at the surface still exists in Goering and Kumar's model but had disappeared in the GeoStudio model. Goering and Kumar's zero degree isotherm under the embankment is replaced by -2°C isotherm in the GeoStudio model. Hence, the GeoStudio native ground is colder than the Goering and Kumar's. The embankment cools in similar manner between the two models indicated by similar temperature isotherm pattern. The air flow vectors have one small eddy in both embankments.

- Figure 3.93 shows the progress of refreezing on November 2. Goering and Kumar's embankment sideslope has refrozen by this date contrary to the GeoStudio embankment that still shows a thick layer of unfrozen material. Earlier intrusion of cold air is also visible under the driving lane. The intrusion of cold temperatures at

the pavement surface is more pronounced in Goering and Kumar's model than shown by the GeoStudio model. The native ground has an unfrozen layer in Goering and Kumar's model but the GeoStudio native ground is all frozen.

- On December 2, as shown in Figure 3.94, a large downward plume develops centered under the driving lane in Goering and Kumar's model – a sign of natural convection. This downward plume is also present in the GeoStudio model but is closer to the centerline. In both models, this plume penetrates to the bottom of the embankment. The cold isotherms penetrate into the foundation under the embankment. The convective action under the sideslope is similar in both models marked by two downward plumes. No unfrozen zones exist in the native ground and under the embankment in the GeoStudio model. Only a small unfrozen bulb exists under the Goering and Kumar's model. The air flow vectors increase and create eddies in both models. The air flow vectors exhibit the symmetrical nature in the GeoStudio full model.

- On January 1, as shown in Figure 3.95, the convective action continues in both models. The downward plume in the embankment is still present in both models. The isotherms in the foundation are similar dipping down under the embankment driving lane. The foundation under the Goering and Kumar's embankment is at -6°C and warms to -2°C with depth becoming similar to the temperatures in the adjacent native ground that warm with depth as well. The foundation under the GeoStudio embankment is at -4°C but it does warm with depth to achieve -2°C. However, the adjacent native ground temperatures stay at the same temperature as well resulting in foundation temperatures staying close to the native ground as in Goering and Kumar's model.

- By March 3, as shown in Figure 3.96, the large convective plume found in the embankment in both models stretches towards the sideslopes replacing the small plumes found under the sideslopes on January 1. The centerline of the plumes falls in the embankment centerline for both models. GeoStudio model shows the foundation temperatures under the embankment are slightly warmer than under the native ground contrary to Goering and Kumar's model that maintains the pattern of January 1. The air flow vectors show the symmetrical nature of the problem.

- On April 2, as shown in Figure 3.97, the isotherms straighten out and the magnitude of air flow vectors decrease. Isotherms are almost identical between the two models including the foundation under the centerline where temperatures are similar to those in the native ground.

- Average annual temperatures were compared in 12 areas in the embankment and foundation area, as shown in Figure 3.98. Goering and Kumar's simulation resulted in average annual temperature contours. Such contours are not achievable in GeoStudio model. Instead, average temperatures in the last year of modeling were calculated in various areas and presented in Figure 3.98B. A good match of results was found between the two models. Coldest temperatures were confirmed in the

foundation under the pavement. Slightly warmer temperatures were confirmed under the embankment sideslope. The warmest temperatures were under the pavement and under the top of the sideslope. Areas showing near-zero temperatures were in the centre of the embankment.

- The active layer depth was identified in GeoStudio model by plotting zero isotherms every day in the last year of modeling. The isoline 0°C, as shown in Figure 3.99B, is a lower boundary for all the zero temperatures plotted. This line is at the native ground surface level under the embankment in the GeoStudio model but falls below this level in Goering and Kumar's model indicating a colder foundation in the modeling results using GeoStudio.

- Yearly minimum temperature extremes were found for -10°C and -14°C in the GeoStudio model, as shown in Figures 3.100B and C. GeoStudio isoline -10°C does not reach as high into the embankment as Goering and Kumar's data shown in Figure 3.100A. GeoStudio isoline -14°C, however, reaches almost to the driving lane, contrary to Goering and Kumar's results that do not reach as high. The shapes of the isolines in both models are similar.

- The comparison of snapshots (numerical results) on February 1 show different isotherm distribution in the embankment as well as in the foundation, as shown in Figure 3.101. The number of plumes is different in the numerical study. Goering has one plume in his half model and GeoStudio has one plume in its full model. GeoStudio air flow vectors show a symmetrical nature and form one distinct circle in the embankment. This is not reflected in Goering's study that has air flow vectors corresponding to the formation of the one plume in the half model. In the foundation, Goering shows warming under the sideslope that does not occur in GeoStudio 2000 Model. Both models agree on the coldest area under the centerline of the embankment.

- The comparison of snapshots (numerical and experimental results) on February 1 shows that one GeoStudio plume does not match Goering's experimental and numerical results, as shown in Figure 3.102. However, warming under the sideslope is visible in Goering's and GeoStudio's numerical results and in Goering's experimental results. The GeoStudio embankment base is colder reaching about -14°C and Goering's embankment is at -9°C (experimental) and -12° (numerical).

- The snapshots (numerical and experimental results) taken on August 1 show good agreement between Goering's numerical results and the GeoStudio models, as shown in Figure 3.103. There is also agreement in the shapes of the isotherms in Goering's experimental embankment. However, Goering's experiment data shows warmer temperatures near the embankment base of around 4°C compared to the GeoStudio models and Goering's numerical results showing near zero temperatures.

- In the summer, except for the locations in the foundation (Location 14 through 16), the comparison of trends show agreement between GeoStudio trends and Goering's numerical results, as shown in Figures 3.83 through 3.90. The numerical results that match GeoStudio trends come from both Goering and Kumar (1996) and Goering (2000). No match with the experimental results was achieved in any of the locations during the summer. The experimental results are consistently colder on the horizontal centerline and consistently warmer at the base. No summer experimental results were available at the top of the embankment.

- In the winter, the comparison of trends shows some agreement with Goering's numerical results but no agreement with Goering's experiment (Figure 3.83 through 3.90). Goering's numerical results at the bottom of the embankment near the centerline (Location 13) were consistently warmer and matched least the GeoStudio trends. Goering's numerical results fell close to the fluctuating GeoStudio temperatures. The available experimental temperatures were consistently warmer. The winter experimental temperatures were not available at the base of the embankment under the sideslope (Locations 8, 9 and 10).

- The comparison of snapshots may lead to conclusions different than the comparison of trends. For example, the comparison of snapshots of isotherms in the embankment on November 2 (Figure 3.93) indicates significantly different pattern and progression of refreezing in Goering and Kumar's model comparing to the GeoStudio 1996 Model. The comparison of trends, however, shows an overall good match between the two numerical studies with the exception of one location in the centre of the embankment at the top where the temperature differs significantly by about 5°C (Figure 3.83B).

- The comparison of trends in the foundation locations show that Goering's numerical temperatures are near zero in late summer and early fall (Figure 3.89B through 2.90). The GeoStudio model does not show this and is colder for this period. This is consistent with the findings from the previous section when instantaneous change in foundation volumetric water content was examined and compared to a GeoStudio add-in function. It can be speculated that near zero temperatures would be achieved in GeoStudio 1996 and 2000 Models if this instantaneous change in foundation volumetric water content was used instead of the add-in function, as illustrated earlier in Figures 3.77B and 3.78. Temperature trends in the foundation in the winter matched closely Goering's numerical results.

Discussion

Temperature trends reported as daily time-temperature plots show daily temperature development in a point. Daily temperature development reveals temperature fluctuations and temperature progressions. Such ranges of values broaden the comparison criteria.

Close agreement with Goering and Kumar (1996) and Goering (2000) numerical results was achieved except in the winter and in the foundation during late summer and early fall.

Daily temperatures fluctuated higly in the GeoStudio models in the winter. The literature values plotted against these fluctuating temperatures fall close to these temperatures and indicate matching temperature trends. These temperature fluctuations are most likely not repeatable based on the findings described earlier and a better/worse match could be achieved if the GeoStudio models were re-run.

The foundation during late summer and early fall is consistently colder. It can be speculated that better comparison in the foundation would be achieved if the foundation was modeled with instantaneous water content changes with temperature. The speculation is based on the results from the previous section where zero temperatures were achieved in the foundation when a stepped function was used to represent water content changes with temperature. This stepped function was not used in the GeoStudio models described in this section because water content does not instantaneously change at zero temperature. A GeoStudio ad-in function modeled water content changes more realistically.

Warming under the sideslope on February 1 is the only similarity discovered between Goering's experimental data and GeoStudio modeling.

Conclusions

Plotting isolated temperature values supplied by Goering and Kumar (1996) and Goering (2000) over GeoStudio temperature trends shows where the literature values fall within GeoStudio modeling results. This allows for a high level comparison that is not available when comparing snapshots.
Further studies are recommended to examine relation between intrinsic permeability and air flow in the GeoStudio 2007 convection module. This is beyond the scope of this thesis.

3.3.3 Discussion

The GeoStudio models with closed boundaries are less robust than the models with open sideslopes. Snapshots of isotherms in the open sideslope models compare better than in closed boundary models. On the other hand, snapshots of air flow vectors compare better in the closed boundary models.

GeoStudio temperature trends revealed that in the winter temperatures fluctuate on daily bases making temperature snapshots difficult to compare. These daily temperature fluctuations are higher in the closed boundary than in the open sideslope GeoStudio models. The two GeoStudio open sideslope and closed boundary models confirmed the findings described earlier in this chapter.

The mesh size and foundation porosity did not appear to influence the results.

Modeling volumetric water content changes with temperature with a stepped function did influence the modeling results and made temperature trends in the foundation more comparable to the two literature studies.

3.3.4 Conclusions

Further studies are recommended to understand the relationship between intrinsic permeability of the material and air flow in GeoStudio modeling. It is not known how the GeoStudio model translates air flow resulting from intrinsic permeability of the material. Differences between modeling results using GeoStudio and literature examples may be related to this translation.

Further studies are also recommended to understand how GeoStudio models air flow in open sideslope models. The understanding of direction and patterns for air flow vectors would be one of them.

GeoStudio modeling results in form of temperature trends are better suited for making comparisons due to temperature fluctuations in the winter that are higher in closed boundary models. Snapshots can be compared in the summer months.

3.4 Ekati Diamond Mine Experimental Example

GeoStudio 2007 convection module was used to model the Panda Waste Rock Storage Area (WRSA) at Ekati Diamond Mine. The data to build the GeoStudio model of this waste rock pile was extracted from the SRK seepage report (SRK, 2003), and the modeling results were compared to a vertical ground temperature profile measured at Panda WRSA as reported in SRK (2003) and shown in Figure 3.104. The purpose of the modeling was to establish whether the evidence of convection can be found in the GeoStudio model of the Panda WRSA. The data from Site 4 was used for this comparison.

The Ekati model was built on the assumption that Panda WRSA was constructed in two lifts and the surfaces of these lifts were compacted (low permeable) due to traffic during placement using heavy haul trucks. A modified version of this model was also created to see what would happen if the compacted surfaces did not exists and the pile was homogenous rather than layered. A conduction heat transfer case was modeled as well.

The model cross section was estimated from a Site 4 plan provided in SRK (2003) and shown in Figure 3.105. The model was composed of two 15 m waste rock lifts rested on a foundation of rock, as shown in Figure 3.106A. Each bench was 30 m wide. The compacted layer was the top 3 m of each lift. The ground temperature cable at Site 4 was estimated to be 30 m back from the crest of the upper lift. The material properties were assumed the same as for the Diavik model due to the proximity of the two mine sites and similarity of host rock types. Maximum air flow used was 6,000 m/d which was

the best match in the modeling of the Diavik test pile that will be discussed later in Chapter 5. The model had 27,670 nodes and 27,750 elements. The mesh was composed of quads and triangles. Surface boundaries of the model were composed of two horizontal surfaces and the two sideslopes. The Ekati model with applied boundary conditions is shown in Appendix G.

Thermal boundary conditions were composed of steady state initial temperatures and a sinusoidal temperature function applied to the top surfaces. The initial temperature condition was approximated from Site 4 temperature profile (SRK, 2003) for late summer of 2000, as shown in Table 3.15. A geothermal gradient of 4.3 kJ/day-m was applied to the bottom boundary of the foundation rock.

The sinusoidal waste rock surface temperature function used in the transient state was estimated using correlation between temperatures at Diavik as follows:

- Average monthly air temperatures at Diavik between August 2006 and October 2008 were collected from Diavik weather database;
- Average monthly waste rock surface temperatures at the Diavik waste rock test piles between August 2006 and October 2008 were acquired from field measurements;
- A difference between average monthly air temperatures and average monthly surface waste rock surface temperatures at Diavik was calculated;
- Average monthly air temperatures at Ekati between August 2000 to October 2002 were collected from Environment Canada website;
- The difference between average monthly air temperatures and average monthly surface waste rock surface temperatures at Diavik was applied to average monthly air temperatures at Ekati to calculate average monthly waste rock surface temperatures at Ekati between August 2000 and October 2002.

Average monthly air temperatures, waste rock surface temperatures and calculated differences are shown in Table 3.16. Ekati surface temperatures 2000-2002 were applied in the transient state. Temperatures in the last column are for information only and show air temperatures at Diavik between August 2000 and October 2002. These are similar to Ekati air temperatures for this period.

Atmospheric pressure was applied to the two horizontal top surfaces of the model in the steady state to allow air to move into the modeling area. Atmospheric pressure was applied to the two horizontal top surfaces of the model and GeoStudio ad-in function was applied to the two sideslopes in the transient state.

The variability in compaction of waste rock was expressed by varying air flow. The air flow of 6,000 m/d represents high convective activity. The air flow of 1 m/d and

1,000 m/d represent two different levels of compaction associated with these layers. The cases modeled included various combinations of air flow. The 4 cases were modeled, as summarized in Table 3.17. Case 1 has the same high permeability in all the waste rock. Case 2 introduces compaction in the compacted top layers. Case 3 increases this compaction to an almost impermeable condition. Case 4 is a conduction case only.

Results

The model was started on August 1, 2000 and was run for 822 days until October 31, 2002. Temperatures were extracted from 16 locations located 30 m from the pile crest, as shown in Figure 3.106B, at depths corresponding to the depths where temperatures were measured. The temperatures were extracted on two dates in each year representing summer and winter and corresponding to days when field temperatures were measured. Temperature-depth plots (trumpet curves) were created using these temperatures from various depths. The trumpet curves were compared to Ekati field data extracted from Site 4 temperature profile, as shown in Table 3.18. Additional information from the modeling is included in Appendix G.

The symbols on the trumpet curves (Figures 3.107 through 3.110) are as follows:

- Green and black curves are for the measured temperatures;
- Red is for the modeled temperatures;
- Squares are for winter temperatures and triangles for summer temperatures, respectively;
- Squares and triangles that are filled are for the first year;
- Squares and triangles that are opened are for the second year.

These are the results:

- The convective activity in the measured data is present in the two winters indicated by cold air present in the two lifts, as shown in Figures 3.107 through 3.110. The coldest air creates bulges in the trumpet curves. Two bulges are present in the measured data during the two winters. The bulges are near the bottom of each waste rock lift.
- Case 1 shows convective activity in the modeled data during both winters (Figure 3.107). This bulging in the measured data is not observed in the GeoStudio modeling data. However, cold air persists throughout the depth of the waste rock.
- This is consistent with the assumption that no compacted layers exist in Case 1. The GeoStudio trumpet curve shows warming near the bottom of the waste rock. This is likely an indication of the chaotic sinking of air into the pile that is

unobstructed by the compacted layer. The temperatures are similar in the measured and modeled data. In Case 1, the GeoStudio summer temperatures are warmer by about 10°C in the middle of the pile. No convective air movement is observed during the summer. The GeoStudio active layer is about 17 m in both years. The measured active layer is about 12 m in the first year decreases to about 9 m in the second year. The GeoStudio model did not reproduce this important field result.

- Case 2 shows convective activity in the GeoStudio model that is different from Case 1. The cold air sinks to the bottom of the upper lift but not into the lower lift, as shown in Figure 3.108. Temperatures in the middle of the pile are positive in year two. The active layer is slightly thinner than in Case 1 and remains the same for the two years.

- Case 3 is similar to Case 4. These cases are dominated by conduction, as shown in Figures 3.109 and 3.110. The active layer is 15 m in the first year and thins to about 5 m in the second year.

Discussion

None of the GeoStudio modeling cases could reproduce the shapes of the measured trumpet curves from the Ekati WRSA. The results from Case 1 are the closest to the measured data. Although the GeoStudio model did not reproduce the measured trumpet curve shapes, it showed convective activity through the waste rock pile.

Conclusion

The purpose of the modeling was achieved because the convective activity was shown to exist in the Ekati waste rock pile.

3.5 Sun et al. (2005) – Comparison of Isotherms and Air Flow Vectors

Sun et al. (2005) used a numerical model proposed by Goering and Kumar (1996) to examine the effects of temperature and pressure boundary conditions on triggering natural convection in a roadway embankment. The examined embankment had no heat/air flow through its base. The embankment was 1 unit high, with the pavement 2 units wide, and a base 5 units wide, as shown in Figure 3.111.

Although Sun investigated conditions of triggering natural convection, he presented the results of his investigation as isotherms and air flow vectors for the full embankment for Raleigh numbers of 50 and 80. These graphic representations were used in this work for comparison with the GeoStudio 2007 convection module model. Finding the onset of natural convection with GeoStudio convection module was not attempted.

The following boundary conditions were investigated by Sun in his numerical embankment model:

- Case 1 - All boundaries isothermal and impermeable;
- Case 2 - All boundaries isothermal, only sideslopes permeable;
- Case 3 - All boundaries isothermal, only sideslopes and pavement permeable;
- Case 4 - All boundaries isothermal, only pavement permeable; and,
- Case 5 - All boundaries impermeable, only sideslopes adiabatic.

Isothermal and adiabatic conditions were present in the Sun's model. Sun's isothermal conditions consisted of -1°C applied over the pavement and sideslopes and 0°C at the base. Sun's isothermal condition placed the embankment at inside temperature of about -1°C. No boundary conditions were applied for adiabatic condition.

One model was created in GeoStudio to model Sun et al. (2005). It was a full embankment geometry composed of 4,812 nodes and 9,268 elements. The mesh was built of triangles. The model had boundary conditions and parameters applied to model each Sun's case. The GeoStudio model with applied boundary conditions is shown in Appendix H. Additional modeling was performed with the GeoStudio model to illustrate that all five Sun's cases can be matched with the GeoStudio model. This was the additional modeling:

- The GeoStudio model was modeled with Rayleigh number of 25;
- The GeoStudio model was modeled under modified isothermal conditions consisting of 10°C applied over the pavement and sideslopes and 11°C at the base; the new isothermal conditions placed the inside of the embankment near GeoStudio default temperature of 10°C; the 1°C temperature difference between the top and bottom boundaries was maintained throughout the modeling.

Input to GeoStudio model consisted of material properties selected to achieve the desired Rayleigh numbers of 25, 50 and 80, as shown in Table 3.19. Thermal conductivity was adapted after Goering and Kumar (1996) and Goering (2000). Porosity was adapted after Goering (2000).

The Rayleigh numbers were calculated according to:

$$R_a = \frac{C_a \times g \times \beta_a \times K \times H \times \Delta t}{k \times \nu_a}$$

Where

C_a	=	volumetric heat capacity
g	=	acceleration of gravity
β_a	=	thermal expansion coefficient
K	=	intrinsic permeability

H = height
Δt = temperature difference
k = thermal conductivity
v_a = kinematic viscosity

GeoStudio 2007 convection module does not have an option of Rayleigh number input. Rayleigh numbers were calculated beforehand for the combination of input parameters and these parameters were input into the model to represent the Rayleigh number calculated. Driving potential for GeoStudio air flow depends on air pressure and elevation. The pore-air total head is calculated according to:

$$H_a = \frac{P_a}{\gamma_{ref}} + y \times \frac{\gamma_{actual}}{\gamma_{ref}}$$

Where

H_a = Pore-air total head
γ_{actual} = pore-air actual density
γ_{ref} = pore-air reference density
P_a = pore-air pressure
y = elevation

The default air temperature in GeoStudio is 10°C and corresponding air density is about 1245 kg/m^3. This can be observed in GeoStudio initial conditions for SEEP/AIR.

Results

The GeoStudio model was run for either 100 or 500 days. The longer modeling time was used for models that did no stabilize within the 100 days. The comparison was made either on the 100th or the 500th day. Sun's isotherms and air flow vectors were compared to GeoStudio results at Sun's Rayleigh numbers and then at Rayleigh numbers less than Sun's. This comparison was made at both Sun's and modified isothermal conditions. The modified isothermal conditions were used because they produced matching results for all the five Sun's cases. GeoStudio modeling results at the modified isothermal conditions and at Sun's isothermal conditions were compared as well. The comparison was arranged in this sequence for each case:

- Sun's instantaneous isotherms and air flow vectors at Rayleigh number of 50 are compared to GeoStudio results at Rayleigh number of 25 for the modified isothermal conditions;

- Sun's instantaneous isotherms and air flow vectors at Rayleigh number of 50 are compared to GeoStudio results at Rayleigh number of 50 at modified isothermal conditions;

- Sun's instantaneous isotherms and air flow vectors at Rayleigh number of 80 are compared to GeoStudio results at Rayleigh number of 50 at modified isothermal conditions;

- Sun's instantaneous isotherms and air flow vectors at Rayleigh number of 80 are compared to GeoStudio results at Rayleigh number of 80 at modified isothermal conditions;

- GeoStudio instantaneous isotherms and air flow vectors at Rayleigh number of 50 at modified isothermal conditions are compared to another GeoStudio simulation with the same Rayleigh number but at Sun's isothermal conditions;

- GeoStudio instantaneous isotherms and air flow vectors at Rayleigh number of 80 at modified isothermal conditions are compared to another GeoStudio simulation with the same Rayleigh number but at Sun's isothermal conditions;

The results of the comparison are listed below:

- The GeoStudio model can match Sun's Cases 1 through 5 (both Rayleigh numbers 50 and 80) at Rayleigh numbers less than Sun's and at modified isothermal condition, as shown in Figures 3.112 and 3.114 (Case 1), 3.118 and 3.120 (Case 2); 3.124 and 1.126 (Case 3); 3.130 and 3.132 (Case 4); 3.136 and 3.138 (Case 5). The GeoStudio model can match Sun's Cases 1, 4 and 5 also at Sun's isothermal conditions contrary to Cases 2 and 3 that cannot be matched at Sun's isothermal conditions.

- The GeoStudio model cannot match Cases 1 through 5 (both Rayleigh numbers 50 and 80) at Sun's Rayleigh numbers for either the modified or Sun's isothermal condition, as shown in Figures 3.113 and 3.115 (Case 1); 3.119 and 3.121 (Case 2); 3.125 and 3.127 (Case 3); 3.131 and 1.133 (Case 4); and 3.137 and 1.139 (Case 5). However, GeoStudio results for Rayleigh number of 50 can match Sun's results at Rayleigh number of 80, for the modified isothermal conditions.

- The results of GeoStudio simulations are the same at Sun's and modified isothermal conditions for Sun's Cases 1, 4 and 5 that have closed sideslopes. The GeoStudio model has numerical instabilities when modeling Cases 2 and 3 (both Rayleigh numbers 50 and 80) at Sun's isothermal conditions, as shown in Figures 3.122 and 3.123 (Case 2) and 3.128 and 3.129 (Case 3). The model is stable for the modified isothermal conditions, as shown in the same figures. The air flow vectors enter the embankment from the top and exit near the base of the sideslope when the numerical instabilities occur.

- Some GeoStudio results do not stabilize after 500 days. GeoStudio results stabilize at Rayleigh number of 25 for all five cases. Except for Cases 2 and 3, GeoStudio results stabilize at Rayleigh number of 50. Except for Cases 1 through 4, GeoStudio stabilizes at Rayleigh number of 80.

- Differences between isotherms in GeoStudio and Sun models both at number of 50 include:
  - isotherms reaching deeper into the embankment and sideslopes for Case 1, as shown in Figure 3.113;
  - isotherms reaching deeper under the sideslopes for Case 2, as shown in Figure 3.119;
  - isotherms becoming wavy for Case 3, as shown in Figure 3.125;
  - isotherms dipping under the top centre in Case 4, as shown in Figure 3.131; and
  - isotherms have two dips under the top in Case 5, as shown in Figure 3.137.
  - The air flow vectors reflect these isotherm shapes.
- GeoStudio air pressures and air densities were examined along the open sideslopes in Case 2 (Ra=50) and Case 3 (Ra=50), and compared to air pressures and air densities along the closed sideslopes in Case 4 (Ra=50) for both Sun's and modified isothermal conditions. The air pressures were found to be quite similar (between 0.012 kPa and 0 kPa) for all the examined embankments, as shown in Figures 3.142 through 3.144. The air densities were found to be similar at Sun's isothermal conditions (between 1296.2 g/m^3 and 1296.4 g/m^3) and similar at the modified isothermal conditions (1245.9 g/m^3 and 1246.0 g/m^3).

Discussion

Similar air pressures along the open or closed sideslopes suggest that the pressures observed are hydrostatic and, independent of air temperatures. This is explained by the fact that very high air flow values used over these short distances do not allow air to remain in the embankment long enough to increase pressure. Thus, the unit flux rates will be controlled by air density. Air densities are also similar along the open and closed sideslopes. However, air density in the cold embankment is about 1296.3 g/m^3 and air density in the warm embankment is about 1245 g/m^3. The warm embankment is at the default GeoStudio air density of 1245 g/m^3 calculated at 10°C.

In many instances the solutions were unstable. The instability of the solutions occurred when stabilizing conditions were weakened or not achieved. The same stabilizing conditions, such as temperature specified over the sideslope, work for lower but not for higher Rayleigh numbers. For example, solutions to all five cases are stable at Rayleigh number of 25, but only for one case at Rayleigh number of 80. The lower Rayleigh numbers promote stable solutions. For example, all five cases stabilize at Rayleigh number of 25. As Rayleigh number increases, the solutions become less stable. At Rayleigh number of 80, only Case 5 is stable. This might suggest that adiabatic

conditions promote stable solutions best. Open sideslopes are less stable as seen in Cases 2 and 3 that destabilized once Rayleigh number increases to 50.

A solution to GeoStudio 2007 model with open sideslopes is dependent on the inside temperature of the embankment. Only under inside temperatures equal to the default GeoStudio temperature of 10°C can numerical instabilities be avoided. Temperatures in the embankment higher or lower than the default 10°C result in numerical instabilities. This behaviour in GeoStudio should be further investigated.

GeoStudio models behave as if they were subjected to a higher Rayleigh number than calculated using the input from other studies.

Conclusion

GeoStudio 2007 works for problems involving convection and the main points are summarized below:

- Convection in high permeability embankments with closed sideslopes can be closely compared to literature examples while open sideslope boundary condition produces results that differ from those reported in literature. Generally, the high permeability embankment produces stronger convective cooling effects at corresponding intrinsic permeabilities. The high permeability embankment with open sideslopes allows air to sink during the winter. Air enters through the crest and exits near the embankment toe. Literature examples suggest an opposite air pattern where air enters near the toe and exits near the crest.
- Uncertainty exists as to how GeoStudio 2007 translates intrinsic permeability into air flow. Further research is proposed to enhance understanding of the relationship between intrinsic permeability and GeoStudio air flow and inclined open boundary condition such as an embankment sideslope.

4.0 DIAVIK WASTE ROCK TEST PILE RESEARCH PROJECT

Diavik Diamond Mine Inc. (DDMI) hosts and partially funds a challenging multidisciplinary research project directed at the study of the thermal, hydrological, geochemical and physical behaviour of large scale waste rock stockpiles in the Canadian Arctic. The results of the study will aid sustainable mining practices as a knowledge base to minimize acid rock drainage potential from sulphide bearing mine waste rock stockpiles located in permafrost regions.

Instrumented large scale waste rock test piles were constructed at the Diavik mine site (FDA, 2006). The construction and instrumentation of the test piles started in 2004 and was completed in 2007. To date, three test piles were constructed and instrumented. The project is under constant development as new information becomes available. The design layout of the test piles was undertaken by FDA Engineering Ltd. (FDA) under the direction of DDMI, and the test pile construction was managed by FDA during the 2006 construction season.

The test piles were constructed primarily by on-site contractors (LDG Construction, Tli Cho Projects, and Norpo) and DDMI departments. FDA provided survey control to the project.

The research personnel were provided by the University of Waterloo (UW), University of Alberta (UA), University of British Columbia (UBC), Carleton University (CU), and the Australian Nuclear Science and Technology Organization (ANSTO). The instrumentation installation, sample collection, and grain size analysis were primarily carried out by students and technical staff from the participating Universities.

The funding for the project was provided by DDMI, the International Network for Acid Prevention (INAP), Mine Environment Neutral Drainage (MEND) program, Natural Science and Engineering Research Council of Canada (NSERC), and the Canadian Foundation for Innovation (CFI).

4.1 Diavik Diamond Mine Overview and Waste Rock Management

Diavik Diamond Mine is a diamond mine in northern Canada. It is located in the Northwest Territories, about 300 km northeast of Yellowknife—the territory capital. The mine operates on the island in Lac de Gras (Figure 4.1A)) in the area of continuous permafrost.

Diavik uses surface and underground mining techniques to mine diamond bearing deposits, and underground mining has been producing in 2009. At present, there are two open surface pits at Diavik. Pit A154 (Figure 4.1B)) was opened first and has been in production since 2003. The second pit A418 has just finished production. Both pits were constructed inside Lac de Gras by constructing impermeable separation dykes to allow mining in the dry.

Diamonds are found in carrot shaped kimberlite pipes that erupted to the surface from the earth's core bringing diamonds with them. To reach the diamond bearing kimberlite, large amounts of waste rock have to be excavated. The projected waste rock production during 2009 was 25.9 million tonnes. The waste rock does not leave the island but is hauled and stored in waste rock piles. A small percent of waste rock is used for building mining infrastructure. Figure 4.2A) shows a waste rock pile at Diavik.

Waste rock properties after excavation are determined by its chemical composition. Sulphide-bearing waste rock when exposed to air and water has acid generating potential and release of contaminated to the environment water may be detrimental to fish and wildlife. Generating acid from rock is called acid rock drainage (ARD). The chemical composition determines whether the excavated waste rock becomes harmful to the environment or remains benign. Waste rock management must evaluate potential to cause environmental harm. This is a challenge when the amount of waste rock is large.

Great efforts have been undertaken at the Diavik Diamond Mine to limit or remove the possibility of acid impacted waters being released into the environment. Managing acid generating waste rock is an important part of Progressive Closure Strategy (PCS) being a component of the Interim Closure and Reclamation Plan (ICRP). Rock excavated as waste is tested prior to being separated according to its sulphur content. Sulphur content of 0.08 wt%S is the threshold for potential acid rock drainage to occur. Waste rock stockpiles with minimal and low (less than 0.08 wt%S) sulphur content are exposed and allowed to drain while the seepage water quality is monitored. Waste rock stockpiles with high sulphur content (greater than 0.08 w%S) drain to collection ponds where the water is tested against the discharge criteria prior to being either discharged to Lac de Gras either directly or treated.

Long term approach to on-site storing of acid generating waste rock includes capping the waste rock stockpiles with 1.5 m impermeable layer of till overlain by a thicker layer (about 3 m) of non-acid generating waste rock for thermal protection after re-sloping (FDA, 2006). The acid-generating waste rock protected in this manner is intended to be sealed from water infiltration and left to freeze in place and remain frozen into the future.

4.2 Waste Rock Test Pile Project Concept

Waste rock at Diavik is primarily granite and biotite schist. Diavik waste rock has been classified into three categories according to its acid generating potential (Smith et al., 2012):

Type I waste rock (T1) – sulphur content of less than 0.04 wt%S; considered non-acid generating; composed primarily of granite with granitic pegmatite and diabase.

Type II waste rock (T2) – sulphur content of between 0.04 and 0.08 wt%S; considered non or low acid-generating; composed primarily of granite with minimal amounts of biotite schist.

Type III waste rock (T3) – sulphur content of greater than 0.08 wt%S; considered acid-generating; composed of granite and biotite schist.

The waste rock test pile project triggered by the need for best management of acid-generating waste rock was to build large scale waste rock piles and instrument them during their construction. The instrumentation would allow data collection from within the test piles to better understand the thermal, hydrological, and geochemical and gas transport processes inside these test piles. The summary of the instrumentation in the test piles is included in Table 4.1 Instrumentation around the test piles was also installed.

In addition to instrumentation, a sampling program was initiated to examine the physical, biological and geochemical characteristics of waste rock such as grain size distribution, microbial populations, mineralogy, moisture content, sulphur content, acid generating potential and whole rock composition.

Three configurations and types of test piles were built to create an environment of:

(1) Benign rock Type I Pile (Type 1 Pile); test pile composed of only Type I waste rock, sulphur concentrations in the Type 1 Pile are low at 0.035 wt%S (Smith et al., 2012).

(2) Acid-generating rock Type III Pile (Type 3 Pile), test pile composed of only Type III waste rock; sulphur concentrations in the Type 3 Pile are low at 0.058 wt%S (Smith et al., 2012) composed of predominantly granite, pegmatitic granite, and biotite schist (Chi, X., et al., 2012).

(3) Hybrid pile following the configuration of the long term closure plan Covered Pile (TC Pile).

4.3 Test Pile Description and Relevant Construction Aspects

The test pile site is located in a designated area at Diavik Diamond Mine. The test pile site is located away from the production pit but close to major haul roads and the process plant, about 1 km west of the south accommodation camp. The water from the test piles discharges to a collection pond. The test piles built are Type 1 Pile, Type 3 Pile, and TC (Covered) Pile (Figure 4.2B left side, centre, and right side, respectively)). The piles are oriented towards the north (Type1 Pile), west (Type 3 Pile), and south (TC Pile). The piles are composed of Type1 Rock (Type 1 Pile), T3 Rock (Type 3 Pile), and T3 Rock capped with a layer of till and a layer of Type 1 Rock (TC Pile).

The plan view and as-built cross sections through Type 1 and Type 3 Piles are shown in Figure 4.3A) and Figure 4.4A), respectively. The piles were constructed to approximately 15 m height above the geomembrane liner, with the top horizontal surface about 20 m wide, and the slope at 1:1.3 (V:H). The test piles have four instrumented faces spread about 5 m apart. Face 0 is the ramp face of the pile and Face 5 is the final, outside face of the pile. There is minor instrumentation on Face 0, and no instrumentation on Face 5. The plan view of Type 1 and Type 3 Piles showing as-built ground temperature cable locations are shown in Figure 4.3B) and Figure 4.4B), respectively. This information was later used during the modeling of the waste rock test piles. Table 4.2 summarizes general information about the test piles and the faces where ground temperature cables are located.

The components for the Type 3 Pile are shown in Figures 4.5. The components for the Type 1 and Type 3 Piles included the following (FDA, 2006):

- ROM fill over the tundra to design base elevation (Type 1 Rock);
- 50 mm minus liner bedding material under and over the liner;
- High density polyethylene (HDPE) liner;
- Basal collection lysimeters (BCL) with drainage lines on top of the liner cover material;
- ROM protective layer over BCLs (Type 1 Rock for Type 1 Pile, and Type 3 Rock for Type 3 Pile);
- ROM fill from Face 0 to Face 5 (Type 1 Rock for Type 1 Pile, and Type 3 Rock for Type 3 Pile); and
- Base and face instrumentation.

TC Pile is a hybrid pile containing Type 3 Rock core, overlain with a layer of till and a layer of Type 1 Rock. TC Pile has been reshaped. The design components for TC Pile include:

- ROM fill over the tundra to design base elevation (Type 1 Rock)
- 50 mm liner bedding material under and over the liner;
- High density polyethylene (HDPE) liner;
- Basal collection lysimeters (BCL) with drainage lines on top of liner cover material;
- ROM fill protective layer over BCLs (Type 1 Rock for Type 1 Pile, and Type 3 Rock for Type 3 Pile);

- ROM core fill from Face 0 to Face 5 (Type 3 Rock);
- Till layer on top of Type 3 Rock;
- Type 1 Rock layer on top of Till layer; and
- Base and face instrumentation.

The ground temperature cables are connected to dataloggers for continuous data collection.

The Type 3 Pile was constructed using standard mining equipment and end dumping and push dumping methods from the access ramp adjacent to the pile from the east (Chi, X., et al., 2012). The rock was brought in by Komatsu 830 and CAT 785 haul trucks and dumped near the crest of the piles. The rock was pushed onto the slope with either Komatsu 375 or CAT D9 or D10 dozers.

4.4 Bedrock Ground Temperature Cable Installation Under Type 1 Pile

The author carried out the installation of four ground temperature cables into bedrock under the supervision of DDMI. Three out of the four ground temperature cables (T1J1, T1J2, and T1J3) were drilled into bedrock from the construction pad under the future Type 1 Pile. The one ground temperature cable (T1J0), later destroyed during construction, was installed into the tundra away from the test piles to provide background temperatures for the project. The contractor was WT Rock Services Ltd.

Five out of twelve thermistor beads present on T1J1, T1J2, and T1J3 were lowered into the drill holes. The remaining seven thermistor beads were extended within the pad surface. Figure 4.3B) shows the seven extended thermistor beads for T1J1, T1J2, and T1J3. Figure 4.6A) and Figure 4.6B) show ground temperature cables under Type 1 and Type 3 Piles, respectively including their depths below the pad surface.

Drilling proceeded on September 22 and 23, 2004. Drilling was carried out using an air track drill available on site (Figure 4.7A)). The drill log is included in Table 4.3.

The location of the control string J0 was adjusted to the ground conditions. The staked out J0 location was devoid of rock containing peat and saturated silt closing immediately after drilling. The new location was established about 10 m away from the pad in line with the remaining ground temperature cable. J1 was moved about 2 m to the west due to collapsing hole. All boreholes were wet at some point of installation. It was difficult to keep the boreholes open after drilling. This was due to water and pad material sloughing in the boreholes.

Neither the thermistor string lead ends nor the opposite-to-lead ends of the ground temperature cables were lowered to the bottom of the drill holes. The ground

temperature cables was folded part way and these folds were lowered to the bottom of the drill holes. This method of installation utilized 2-metre spacing present between six thermistor beads near the lead end of the thermistor cable. The spacing between the remaining thermistor beads was 5 m and was better suited for placement within the pad (Figure 4.6A)). A weight was attached to the fold in each ground temperature cable before dropping it into a drill hole (Figure 4.7B)). Processed kimberlite was used as backfill around the ground temperature cables in the drill holes. After installation into bedrock, the remaining thermistor cable was temporarily covered with barrels to protect the cables from wildlife (Figure 4.8A)) until pad construction was completed.

After the ground temperature cables were backfilled, a trench was dug into the pad spanning between the newly installed ground temperature cables and extending towards the north, past the north pad edge, to reach T1J0 installed into the tundra (Figure 4.8A)). The purpose of the trench was to protect the ground temperature cables from damage by traffic travelling on the access road located near the north pad edge. A section of T1J0 passing under this access road was strung through a steel conduit for additional protection (Figure 4.8B)). The trench was then backfilled with processed kimberlite (Figure 4.9A) immediately around the cables topped with gravel for the driving surface. The pad was then covered with a layer of processed kimberlite.

The ground temperature cables were then stretched along the pad in excavated trenches in processed kimberlite. The lead ends for T1J1, T1J2, and T1J3 were installed bare in the kimberlite trench (Figure 4.9B) dug between the installed ground temperature cables and along the pads north edge to leave at the pad`s northwest corner. The opposite-to-lead ends containing thermistor beads for T1J1 and T1J2, running perpendicular to the line spanning between the three ground temperature cable drill holes, were strung through protective steel conduit (Figure 4.10A). The opposite-to-lead end for T1J3 containing thermistor beads was stretched bare together with the lead ends in the same trench. The trenches were backfilled with processed kimberlite. Fluorescent spray paint was used to mark the location of the backfilled cables. Survey lath was used to mark the location of the thermistor beads (Figure 4.10B) until their location could be surveyed.

The lead ends were connected to dataloggers for continuous data collection. The dataloggers were positioned inside two Nema containers (Figure 4.10B) covered with a wooden box through the winter. The dataloggers were left over winter in this configuration. They functioned as intended without damage. The dataloggers were programmed by the author.

4.5 Ground Temperature Cable Naming

Each ground temperature cable was identified with a unique name. The names were to reflect their locations for the cables on the test pile faces. The original design had cables spanning between up to two levels at design elevations of 2 m, 5 m, 10 m, and 15 m from the test pile surface. As an example, cable 2 m - 5 m was intended to stretch between two levels positioned at 2 m and 5 m from the test pile surface. To

distinguish between cables with the same spacing, numbers in brackets were added (e.g., 2m - 5m (1)). The cables to span two levels usually had one large spacing to allow the cable to reach the second level. Each thermistor bead was identified by a number preceded by a letter T. The lowest number (T1) was located at the end opposite to the cable lead. The maximum number of beads on one ground temperature cable was twelve.

4.6 Ground Temperature Cable Preparation

As-manufactured thermistor bead spacing was preserved for ground temperature cables installed into bedrock under Type 1 Pile. Factory spacing between thermistor beads was adjusted for some ground temperature cables installed on the test pile faces. This adjustment was required to reflect changes in ground temperature cable placement. The thermistor bead spacing was adjusted by folding and taping the excess cable to itself. The pig-tailed thermistor beads, originally intended to serve as inserts into rock voids, were taped to the main cable as well.

All the ground temperature cables were strung through 50 mm PVC flexible protective tubing before installation (FDA, 2006) (Figure 4.11A)). Three holes were drilled in the PVC tubing in and around each thermistor bead location prior to stringing (Figure 4.11B)). After the cable was strung, foam insulation was placed in the two holes around the beads to limit convective heat transfer between the beads via the tubing.

4.7 Ground Temperature Cable Calibration

The author calibrated ground temperature cables that were delivered to site in 2004 and 2005. The calibration was performed in the University of Alberta laboratory before they were shipped to the Diavik site. The calibration was carried out by immersing each thermistor bead in an ice bath and recording the resistance readings while in the bath. This number was taken as calibration number that could be added to the temperature readings to establish a true reading.

4.8 Relevant Test Pile Data

The thermal data from the test piles has been collected since October 2004. Description of the thermal data can be found in Pham (2013). This section describes thermal data relevant to modeling of the waste rock test piles with GeoStudio 2007 convection module.

4.8.1 Waste Rock Surface Temperatures

Temperatures were measured at various proximities to the test piles surface. Type 1 Pile had three thermistor beads located within 0.5 m of the pile surface (11WBthm00 – T1 at 0.4 m, 12W5thm00 – T1 at 0.3 m, 12E5thm00 – T4 at 0.5 m). These average monthly temperatures cover the period between October 2006 and November 2008, as shown in Figure 4.12A. Type 3 Pile had 6 thermistor beads located within 0.3 m depth

of the pile surface (31NBthm00 – T1 at 0.1 m and T2 at 0.2 m, 31N5thm00 – T1 at 0.1 m and T2 at 0.3 m, 31S5thm00 - T1 at 0.2 m and T2 at 0.4 m, 31SBthm00 – T1 at 0.2 m and T2 at 0.3 m, 34S5thm00 – T3 at 0.3 m). These average monthly temperatures cover the same time period as for Type 1 Pile, as shown in Figure 4.12B.

The TC Pile had two surface thermistor beads that belonged to two ground temperature cables identified as East and West. The surface temperatures from these two thermistor beads located at 0.1 m below the pile surface are shown in Figure 4.13A. Near and below surface temperatures in the TC Pile are shown in Figure 3.13B for comparison.

4.8.2 Waste Rock Inner Temperatures

Inner temperatures in the Type 3 on the face 2 were received from Nam Pham in an excel spreadsheet are shown in Figure 4.14A and B. The face 2 contained two ground temperature cables (32N5thm00 and 32S5thm00). The data was arranged according to thermistor bead locations and depths described in Section 5.0.

4.8.3 Bedrock Temperatures

T1J1, T1J2, and T1J3 were ground temperature cables installed into bedrock under the Type 3 Pile. Data for T3J3 was selected to represent ground temperatures under the Type 3 Pile. The data was available from September 1005 and is presented until October 2008, a shown in Figure 4.15A and B. Figure 4.15A shows average monthly temperatures from the surface thermistor beads and Figure 4.15B from the deep thermistor beads on T3J3. Daily and monthly averages were calculated based on data obtained from Nam Pham in an excel spreadsheet.

4.8.4 Tundra Surface Temperatures

Surface tundra temperatures have been collected from the surface thermistor bead on T3J0 installed into the tundra near the test pile site. This ground temperature cable replaced T1J0 installed by the author in 2004 and destroyed during construction. Raw data from T3J0 was provided by Nam Pham in an excel spreadsheet. The raw data was between September 14, 2005 and March 11, 2008 consisting of four daily measurements.

Daily and monthly averages were calculated based on the raw data available. Monthly temperature averages between October 2005 and October 2008 measured at the tundra surface are shown in Figure 4.13A). These monthly averages were not used in the GeoStudio test pile model because the tundra was not found in the modeled cross section.

T3J0 contained six thermistor beads at 2-metre spacing. The thermistor beads were located at 10 m, 8 m, 6 m, 4 m, 2 m, and 0 m depths below the tundra surface.

5.0 GROUND TEMPERATURE CABLE BEAD LOCATIONS IN THE TEST PILES

Thermistor bead depths below the finished surface of the Type 1 and Type 3 Piles were found (Figures 5.1 through 5.20) using as-built survey information provided by FDA, along with Surfer and AutoCAD 2010 software. As-manufactured, adjusted and as-built thermistor bead spacing for each ground temperature cable were compared to the properly identify thermistor bead and its position on a thermistor cable. The acquired depths of the thermistor beads were used to model the Diavik waste rock test pile using GeoStudio 2007 convection module.

The purpose was to determine vertical and horizontal position on a vertical plane. The process of finding thermistor bead depths can be summarized as follows:

- As-built thermistor bead coordinates were drawn in AutoCAD 2010.
- The position of the thermistor beads drawn in AutoCAD was analysed and each thermistor bead was matched with a proper bead identification number and assigned to a particular thermistor cable; as-manufactured and field adjusted thermistor bead spacing, was used in this matching process.
- Once the thermistor bead sequence and thermistor bead ID was established Surfer files were created for each ground temperature cable representing vertical projections of each thermistor bead onto the XY plane.
- The finished 3-dimensional configuration for Type 1 and Type 3 Piles was found (Figure 5.21) using drawing information provided by FDA (FDA, 2006).
- The finished surface data and the Surfer projection files were used to make slices through the Type 1 and Type 3 Piles containing the projections of the thermistor beads on the XY plane; the slices through the two piles provided coordinates of the vertical projections of the thermistor beads onto the finished surface of the Type 1 and Type 3 Piles.
- Subtracting as-built elevations from the elevations of these projections gave the actual depths for each thermistor bead.

Assumptions had to be made in the process of finding thermistor bead depths due to missing information. First, the survey information was incomplete and some thermistor beads were not surveyed following placement during construction. Secondly, the order in which survey information listed thermistor bead coordinates did not always correspond to the true order of the thermistor beads on a cable. Moreover, the survey did not always pick up the location of the beads as they were concealed by the PVC tubing. Finally, some ground temperature cables were shortened before installation and this information was not always provided. As a result, multiple comparisons and best judgement were used to determine the position of each thermistor bead on a particular cable. The necessary

assumptions made as to thermistor bead locations do not influence the temperature profiles along the test pile faces.

As-manufactured thermistor bead spacing was as prepared by the manufacturer. This as-manufactured spacing was further adjusted in the field as required before installation in the test piles. The cables with adjusted spacing were strung through PVC flexible tubing before installation. The adjusted as-manufactured thermistor bead spacing is shown in Figures 5.1 through 5.20-As Manufactured. Numbers in brackets are the true as-manufactured distances for the sections that were field adjusted.

Adjusted for installation thermistor bead spacing was not recorded for all of the cables installed in the test piles. The cables with missing adjusted spacing information were installed regardless, and the adjusted bead spacing on those cables can only be speculated. Table 5.1 summarizes adjusted (strung) and as-manufactured thermistor bead spacing for the cables prepared for installation as of September 2006.

The as-built thermistor bead spacing is the true distance between the beads in 3-dimensional space as installed in the test piles. Figures 5.1 through 5.20-Plan show a plan view of each ground temperature cable drawn in AutoCAD. The distances shown between the thermistor beads are the true distances projected onto the XY plane. The numbers written above or besides the spacing are the true distances between the thermistor beads in a 3-dimensional space.

Figures 5.1 through 5.20-Section show a cross section along a cable. The distances between the thermistor beads are the true distances show between the thermistor beads on Figures 5.1 through 5.20-Plan.

5.1 Ground Temperature Cable 12E5THM00

Verification of bead locations for ground temperature cable 12E5thm00 in the test pile was required because the number of thermistor beads surveyed was less than the number of beads manufactured on this cable, and the adjusted spacing of 12E5thm00 was unknown. Figure 5.6 shows the selected sequence of the thermistor beads. Figures 5.6a and 5.6b show two other combinations that were considered but rejected.

Option shown in Figure 5.6 was selected to represent ground temperature cable 12E5thm00. This assumption assumes that the three as-manufactured three-metre sections (T9-T8-T7-T6) correspond to the three as-built three-metre sections (Figure 5.6-Plan). This reasoning suggests that the as-manufactured section T10-T9 was surveyed improperly (5 m versus 5.73 m), and as-manufactured section T2-T3 was folded before installation. Bead T1 was not surveyed. This reasoning points to as-built T2 as a first available bead from this string.

Option shown in Figure 5.6a assumes that the as-manufactured six-metre section T11-T10 is located at the end of the as-built cable. This assumption suggests that sections T10-T9, T7-T6, and T4-T3 were folded to three-metre, two-metre, and one-metre sections,

respectively. Making this type of field adjustment is unlikely. Examination of the thermal data from the thermistor beads confirmed this conclusion, and this option was rejected.

Option shown in Figure 5.6b assumes that the last section on the as-built cable (Figure 5.6b-Plan) corresponds to as-manufactured section T9-T8. This assumption was rejected because the as-built section cannot be longer than the as-manufactured section.

5.2 Summary and Conclusions

The tedious process of identifying and locating thermistor beads in the test piles was required to continue with the work presented in this thesis.

It is believed that the depths of the thermistor beads in the Type 1 and Type 3 Piles were correctly identified. However, it is recommended that these depths are verified by others to confirm that no errors were made during the identification process.

6.0 DIAVIK WASTE ROCK TEST PILE NUMERICAL MODEL

A Diavik waste rock test pile was modeled using GeoStudio using a typical geometry of the Type 3 Pile. Input parameters consisted of values measured in Diavik waste rock test piles. The thermal regime between August 1, 2006 and October 30, 2008 was modeled and compared to temperatures measured in the Type 3 Pile and findings from the Type 3 Pile described by Pham (2013). A pure conduction case was modeled as well. The conduction results were compared to cases that included air movement into, within and out of the pile. Wind action was not included in this modeling study as it was beyond the scope of this thesis.

The calibration analysis was carried out prior to modeling the Type 3 Pile to examine thermal properties of the Type 3 Pile foundation. The best match parameters from the calibration analysis were not used in the modeling of the Diavik waste rock test pile to stay consisted with the parameters that were measured.

6.1 Calibration Analysis

A one-dimensional model of the Type 3 Pile foundation was built in GeoStudio 2007 convection module (Figure 6.1). The model consisted of a waste rock pad underlain by bedrock. The waste rock pad was 5 m thick and bedrock was assumed to extend to a depth of 100 m. Average measured temperatures in the foundation in October 2005 were applied to the model and the model was run from October 2005 through to June 2006 subjected to average measured surface temperatures in the waste rock pad over this period. The comparison between modeled and measured temperatures was made in June 2006. The calibration analysis was carried out with two sets of input parameters. The first set was provided by Pham (personal communication, May 2011) and the second set was developed to create the best match scenario.

Average measured temperatures from Ground Temperature Cable T3J3 were selected for the calibration analysis. Out of the twelve thermistor beads located in this cable (T3J3), seven were located below the waste rock pad surface at 0.5 m (T6), 5.5 m (T7), 7.5 m (T8), 9.5 m (T9), 11.5 m (T10), 13.5 m (T11), and 15.5 m (T12) depth. Average measured temperatures from these thermistor beads in October 2005, and June, July and August 2006 are provided in Table 6.1. The October 2005 average measured temperatures were used as initial temperatures in the calibration model. The measured temperatures in June 2006 were used for comparison with the modeling results. The initial temperature boundary conditions applied to the GeoStudio model are shown in Table 6.1. The temperature at 100 m depth was calculated to be -1.55°C using a temperature gradient of 1.9°C/100 m of depth. The remaining five thermistor beads on Ground Temperature Cable T3J3 were stretched along the waste rock pad surface to the south from the T3J3 borehole location (FDA, 2006). Measured temperatures from these five surface thermistor beads were averaged to represent surface temperatures of the waste rock pad. Average measured surface temperatures between October 2005 and September 2006 are provided in Table 6.2. These average measured surface temperatures were applied to the model surface during the transient analysis. Thermal boundary conditions for the transient

analysis are shown in Figure 6.3. A geothermal gradient of 4.6 kJ/day-m was applied at 100 m depth.

Material thermal properties used in the calibration analysis are shown in Table 6.3. The modeling was first conducted using thermal properties provided by Pham shown in Table 6.3 (personal communication, May 2011). Then, thermal parameters for the waste rock pad were varied to come up with parameters that provided the best match with the measured subsurface rock temperatures. Best match representation was achieved for thermal properties shown in Table 6.3.

Pham's thermal conductivity of 241.9 kJ/day-m-C for granite bedrock is greater than 216.0 kJ/day-m-C quoted by Cote and Konrad (2005), but within the range of 146.9 kJ/day-m-C and 345.6 kJ/day-m-C quoted by Andersland and Ladanyi (1994). Assuming the density of the granite is 2750 kg/m^3 (Cote and Konrad, 2005), the volumetric heat capacity of the granite would be 2,170 kJ/m3-C. Pham's volumetric heat capacity of 2,130 kJ/m3-C is close to this value. As for the waste rock pad, Pham's values are closer to literature examples for granite bedrock. However, Goering and Kumar (1996) assume thermal conductivity for high permeability embankment to be equal to 30 kJ/day-m-C with volumetric heat capacity to 1006 kJ/m3-C. The best match values are closer to Goering and Kumar's than to Pham's. The waste rock composing the waste rock pad is not homogenous. Coarser waste rock around the Ground Temperature Cable T3J3 could have caused the temperatures to be representative of the coarser waste rock such as used by Goering and Kumar (1996).

The results of the calibration analysis are presented in Table 6.4 and Figure 6.4. Temperatures measured by Ground Temperature Cable T3J3 are compared in June 2006 to temperatures modeled with GeoStudio using both Pham's parameters and best match parameters.

The difference between the average measured and modeled temperatures is up to 1.56°C using Pham's parameters and up to 0.55 °C using best match parameters. The results using the best match parameters varied by less than one degree from the temperature profile measured in June 2006 and exhibited warming trend in the bedrock and cooling trend in overlying waste rock pad.

6.2 Diavik Test Pile Model Description

The temperatures from face 2 of the Type 3 Pile were selected to be modeled using GeoStudio. The face cross section was 14 m high, 30 m wide at the top, 70 m wide at the bottom resting on the foundation. This cross section may be considered typical for the T3 Pile. The foundation consisted of 5 m thick waste rock pad and underlying bedrock. The model was extended 70 m in each horizontal direction from the pile toe and 30 m below the pile base, as shown in Figure 6.5. Both slopes were 1:1.3 (vertical to horizontal). The model consisted of 32,332 nodes and 32,840 elements. The mesh was composed of quads and triangles. The model with applied boundary conditions is shown in detail in Appendix I.

Waste rock was modeled using three air permeabilities selected to achieve a best match with the measured temperatures. Modeled versus measured temperatures were compared at 23 locations in the pile and 7 locations in bedrock shown in Figure 6.6. Twelve locations in the north portion of the Type 3 Pile (T1 through T12) are the locations of thermistor beads from Ground Temperature Cable 32NBthm00. Eleven locations in the south portion of the Type 3 Pile are the locations of thermistor beads (T2 through T12) on Ground Temperature Cable 32SB thm00.

Temperature boundary conditions were applied for the steady and transient states. Initial temperature boundary conditions were average measured temperatures in the foundation during August 2006 (Table 6.5) and the waste rock pile was assumed to be at 3°C throughout the model grid.

Ground Temperature Cable T3J3 was selected to provide foundation temperatures because it was located closest to the face 2 and away from lysimeters that were heat traced (Figure 6.7). Transient boundary conditions consisted of surface temperatures applied over top surface and a geothermal gradient applied at the lower boundary. The uppermost thermistor bead T1 on Ground Temperature Cable 31NBthm00 located 0.1 m below the pile surface was selected to provide the surface temperature function for the modeling. Ground Temperature Cable 31NBthm00 started recording temperatures in October 2006 and estimates were projected back to August 2006. The estimate was carried out by comparison with air temperatures, as shown in Figure 6.8. Surface temperatures were applied at the waste rock surface because surface climatic conditions affecting surface temperatures were not considered in the modeling.

Pressure boundary conditions were applied during the steady and transient states as well. A negative pressure was applied to the waste rock pile in the steady and transient states to suck the water out of waste rock resulting in a dry waste rock condition at the assumed porosity of 30%. An atmospheric pressure was applied over the driving surface to let the air into the pile to aerate the pile. This atmospheric air was maintained during the transient state. A GeoStudio ad-on function was applied over the sideslope in the transient state to model open sideslope condition. The ad-on function accounted for pressure changes with elevation.

Material properties consisted of properties for waste rock, waste rock pad and bedrock provided by Pham (personal communication May 2011) and shown in Table 6.6. Table 6.6 also shows three air permeability values were used in the modeling. Pham's properties were used to compare the modelling results to the results from Pham's (2013) modeling.

A Diavik waste rock test pile was also modeled using conductive heat transfer. The purpose of conduction modeling was to compare the results to modeling involving convection. The Temp/W component of the GeoStudio 2007 convection module was used for the conduction modeling. Temp/W analysis was set to "transient" instead of "convective heat transfer" thus eliminating convective component. Steady state analysis used for the initial condition was the same as used for the convection module. With

exception of air flow, the conduction model utilized the same input parameters as the convection model described above.

6.3 Rayleigh Number

Rayleigh numbers were calculated in the centre and under the crest in the pile (Table 6.7) for the three air permeabilities on March 15, 2008. The two locations were selected to show how Rayleigh numbers vary in the pile between the centre and the crest locations. A snapshot of isotherms in mid-March in 2007 and 2008 is shown in Figure 6.9. The Rayleigh numbers decrease with increased permeability under the crest and increase with increased permeability in the centre of the pile.

6.4 Results

The model was run for just over two years between August 1, 2006 and October 30, 2008. The results were saved every 7.5 days. The temperatures were extracted from the locations within the pile where thermistor beads were located. Three locations around each thermistor bead were selected to better represent the measuring locations and the extracted temperatures were averaged. The locations were 3 m, 5 m and 7 m to the left and 3 m, 5 m and 7 m to the right from the pile design centerline. These distances were selected to match the general location of the thermistor beads in the pile face (FDA, 2006). Yearly temperature trends were plotted against the measured temperatures. Then, temperatures on March 15 to represent the coldest month and August 15 to represent the warmest month were extracted for each year modeled and compared. The modeled temperatures were compared to the temperatures measured in Type 3 Pile on the face 2.

These are the results:

- Between March 15, 2007 and March 15, 2008, the test pile is mainly cooling for the 4,000 m/d permeability, warming in bottom portions for the 6,000 m/d permeability and warming throughout for the 8,000 m/d permeability (Tables 6.8, 6.9 and 6.10). Deeper portions of the foundation are slightly warming at 4,000 m/d. The foundation is cooling at the two higher air permeabilities. The majority of the cooling takes place at the foundation top reaching a cooling value of 3.7°C when permeability is the highest. When conduction is modeled, the entire pile cools but the foundation is warming, as shown in Table 6.11.

- Between March 15, 2007 and March 15, 2008, most significant cooling at the 2 m depth occurs for permeability of 4,000 m/d with the cooling value of 2.5°C, as shown in Table 6.8. Cooling is 0.8°C for the permeability of 6,000 m/d and the pile is warming by 0.5°C for the permeability of 8,000 m/d, as shown in Tables 6.9 and 6.10, respectively. Thus, the cooling described by Pham (2013) of 4°C at the 2 m depth is not observed in the GeoStudio model. However, the lowest permeability compares best to the data reported by Pham (2013).

- Between August 15, 2007 and August 15, 2008, the test pile is mainly warming at the three permeabilities. However, the foundation cools. The highest cooling is at the foundation top and maintains its intensity to greater depths with increased permeability. For conduction, although the pile cools, almost the entire foundation is warming.

- During the first August after construction (2007), the test pile thawed to a depth of 5.8 m, 5.8 m and 6.8 m for permeability of 4,000 m/d, 6,000 m/d and 8,000 m/d, respectively. During the second August (2008), the thaw depth remains similar with the lower permeabilities but increases slightly to 7 m for permeability of 8,000 m/d. In conduction, the thaw depth reaches 3.3 m in August 2007 and 2008.

- The frozen zone at the bottom of the pile did not grow for any of the three permeabilities between August 15, 2007 and August 15, 2008, as shown in Tables 6.12 through 6.14. The frozen zone remains at about 7 m for both 4,000 m/d and 6,000 m/d permeabilities and slightly less at 8.8 m at permeability of 8,000 m/d. This does not agree with Pham (2013) who reports a frozen zone growing at the pile base by an average of 1.5 m between 2007 and 2008. However, the frozen zone that is maintained in the GeoStudio model at the two lower permeabilities results in shallower than Pham's average active layer depth (12.5 m below the pile surface) in 2008.

- The foundation freezes during the second winter and remains frozen during the summer for all three permeabilities and for conduction modeling, as shown in Figures 6.22 through 6.25. The foundation is cooling between the two winters and the two summers for permeabilities of 6,000 m/d and 8.000 m/d. Permeability of 4,000 m/d causes slight warming in the foundation. The conduction case causes warming between the two winters and summers. However, the foundation temperatures are the lowest when permeability is the highest.

- The top of the foundation in 2007 ranges between 0.6°C and -0.5°C (4,000 m/d), 0.3°C and -4.3°C (6,000 m/d); and -0.4°C and -6.4°C (8,000 m/d) on March 15 and August 15, as shown in Tables 6.8 through 6.10 and Tables 6.12 through 6.14. In 2008, these ranges are -1.0°C and -2.5°C (4,000 m/d), -3.0°C and -6.7°C (6,000 m/d) and -4.0°C and -8.1°C (8,000 m/d), as shown in the same tables. The shift towards colder temperatures in 2008 was observed for all the permeabilities. This is consistent with the results reported by Pham (2013).

- The GeoStudio 6,000 m/d permeability compares best to the temperatures measured in the Type 3 Pile on the face 2, as shown in Figures 6.10 through 6.25. Measured temperatures are colder in the winter and warmer in summer down to about 2 m depth. At about 3 m depth, modeled temperatures are closest to matching the measured temperatures, as shown in Figure 6.13. At about 4.5 m depth, modeled temperatures become colder than measured in the first winter after construction. This pattern continues to the bottom of the pile. At about 5.5 m depth, modeled temperatures become colder than measured in the two summers. This pattern occurs

until the pile bottom and continues under the pile base, as shown in Figures 6.14 through 6.21.

6.5 Discussion

The results of the GeoStudio 2007 test pile model with input parameters as measured in the test piles show that:

- Measured temperatures in the summer reach above 0°C for all embankment measuring locations. This is most likely due to wind that penetrates the entire pile in the summer. Wind was not included in the GeoStudio modeling and this warming effect was not observed. Summer thawing reaches to about 9 m and is less than measured. The modeled temperatures could be more representative of a full scale waste rock pile that is so large that wind does not penetrate deep into it.

- Cooling in the foundation is observed in the measured and modeled data. This cooling is more pronounced near the top than deeper in the foundation for both data sets. However, the cooling modeled is more than was measured. This is most likely the effect of warm air penetrating the pile in the summer due to wind.

- Modeled summer warming reaches to about 9 m into the test pile but the foundation continues cooling for all three permeabilities. This might indicate the cold air remains in the bottom of the pile thus providing cooling to the foundation.

- Even though according to the calculated Rayleigh number there is little or no convection in the test pile, cooling was observed in the model. The cooling modeled is more than the cooling measured in the test piles.

- Except for the conduction case, all the foundation measuring locations exhibit cooling in the modeled and measured data. This indicates that convection is present and is effective despite the Rayleigh numbers.

6.6 Conclusions

- The lack of wind action and lack of consideration for snow in the GeoStudio model indicates that modeling results are not comparable to temperatures measured in the test pile experiment. Even though the test pile experiment is “large scale”, the experiment is dependent on prevailing winds and snow accumulation (Pham, 2013) not accounted for in the GeoStudio model.

- Wind moves air into the pile deep enough to influence its entire volume. The influence of prevailing winds is also visible in the test piles (Pham, 2013). This factor was not included in the GeoStudio model. Further modeling is suggested to observe these influences. More and more data will be available from the test piles and can be helpful for this future modeling.

- The GeoStudio model showed that the thermal regime under the permeability of 6,000 m/d most closely represents temperatures measured in the test piles. Increased GeoStudio permeability triggers convection that manifests itself by warming in the pile and cooling under the pile. Warming in the pile shows that the warm air moves through the pile and cooling under the pile indicates cold air sinks into the pile.

- Snow cover is another influencing factor that was not considered in the GeoStudio model. Snow accumulation can influence temperatures through its insulating properties. Snow drifts accumulate around the test piles in various amounts. Snow also penetrates into the surface voids in waste rock creating an insulating effect on the pile surface. The investigation of these conditions could be also considered as a topic for further modeling.

- The GeoStudio 2007 model represents production waste rock piles where wind action and snow accumulation are not as significant. The results from the GeoStudio model quite likely describe thermal regime in the production waste rock piles. This could be a topic for future modeling.

7.0 SUMMARY, CONCLUSIONS AND RECOMMENDATIONS

The initial stages associated with the Diavik waste rock test pile project at the Diavik Diamond Mine are described in this thesis. The anticipated in 2004 thesis focus on construction and instrumentation of the test piles was shifted to numerical modeling in 2005 because the test pile construction was delayed until summer 2006. In 2005, a GeoStudio convection module finite element numerical program was launched for testing. The completion of the testing in spring 2007 was a milestone that allowed the GeoStudio convection module to be used for modeling. The author started building models in the GeoStudio convection module representing literature examples and comparing the results. This modeling phase of the work was the most difficult and time consuming. The author's models were crashing and the results could not be successfully compared to the literature examples. The modeling was successfully completed in early 2012 and the thesis was submitted for review in February 2012. Two milestones contributed to this successful submission: a discovery that GeoStudio modeling results are not repeatable and that temperature trends instead of isotherm snapshots can be used to compare GeoStudio results. The edits to the February 2012 version allowed producing this final version. The edits to the February 2012 version did not require any further modeling.

The conclusions from this thesis include:

- GeoStudio convection in high permeability embankments with closed boundaries can be closely compared to literature examples while the open sideslopes produce results that differ from the literature. When the sideslope is open in the embankment, the GeoStudio air enters through the crest and leaves through the embankment toe contrary to literature examples where air flow exhibits the opposite pattern.

- Convective cooling has manifested itself in the GeoStudio embankment models either for closed boundaries or open sideslopes.

- GeoStudio half models instead of full models can be modeled for conduction dominated cases. Models with open sideslopes are more robust than models with closed boundaries and modeling half models instead of full models might give good results.

- Convection dominated GeoStudio models are not repeatable in the fall and winter in either full or half models due to chaotic sinking of air. Temperature trends instead of isotherm snapshots can be used to examine temperatures during this time.

- The direction of air flow vectors in the convection dominated GeoStudio models of an embankment with open sideslopes match literature examples only under GeoStudio default temperatures. For temperatures other than the default temperatures, air flow vector direction cannot be matched.

- The best match with measured temperatures in the Diavik test pile was achieved for GeoStudio model with permeability of 6,000 m/d. Warming in the GeoStudio model

indicated that air moves through the pile and cooling under the pile indicated sinking of cold air.

- The lack of wind action and lack of consideration for snow in the GeoStudio model indicate that modeling results are not comparable to temperatures measured in the "large scale" Diavik test piles.

- This modeling of the Diavik test pile most likely represents temperatures in a production large scale pile where wind action and snow accumulation are insignificant.

Based on the findings from this thesis, it is recommended that:

- GeoStudio convection module is further investigated for modeling embankments with open sideslopes under default and non-default GeoStudio temperatures and the direction of air flow vectors is assessed.

- Modeling half models instead of full models with open sideslopes using GeoStudio is further examined.

- A Diavik test pile is modeled with the consideration for wind action and snow cover.

- A relation between material intrinsic permeability and GeoStudio air flow is established.

- A Rayleigh number can be readily extracted from the GeoStudio models to give immediate indication of the presence or absence of convection in the modeling cases.

REFERENCES

Beck, J.V., Cole, K.D., Haji-Sheikh, A., and Litkouhi, B. (1992), "Heat Conduction Using Green's Functions", Hemisphere publishing corporation.

Fala, O., Aubertin, M., Molson, J., Bussière, B., Wilson, G.W., Chapuis, R.P., Martin, V., 2003. Numerical modeling of unsaturated flow in uniform and heterogeneous waste rock piles". 6th International Conference on Acid Rock Drainage. Cairns, Australia.

FDA Engineering Ltd., 2006, Test Piles Project 2006 Construction Summary, Prepared for Diavik Diamond Mines Inc.

Goering, D.J., 1984. Unsteady-state heat conduction by the finite element method. M.Sc. thesis, University of Alaska, Fairbanks.

Goering, D.J. and Kumar, P., 1996, "Winter-time convection in open-graded embankments", Cold Reg. Sci. Technol.

Goering, D.J., 1998, "Experimental Investigation of Air Convection Embankments for Permafrost-resistant Roadway design Proceedings, 7th International Conference on Permafrost, Yellowknife, NWT.

Goering, D.J. 2000, "Passive Cooling of Permafrost Foundation Soils Using Porous Embankment Structures", American Society of Mechanical Engineers, HTD 366-5, 103-111.

Kuo, E.Y. and Noël M.M., 1998. The Feasibility of Maintaining an Ice-filled Cover Layer in an oxidising stockheap in the Lac de Gras Basin. ANSTO Technical Report, ANSTO/C542.

Linklater, C, 2004, "Prediction of Heat and Gas Transport in a Test Heap at Diavik Diamond Mines: Results from SULFIDOX 'Base Case' Simulations for 15 m Heap". ANSTO Technical Report.

Ma, W., Shi C., Wu Q., Zhang L., Wu Z., 2006. Monitoring Study on Technology of the Cooling Roadbed in Permafrost Region of Qinghai-Tibet Plateau. Cold Regions Science and Technology.

Morin, K.A., Gerencher, E, Jones, C.E. and Konasewich, D.E., 1991, "Critical Literature Review of Acid Drainage from waste Rock, MEND Report 1.11.1.

Neild, D.A. and Bejan, A., 1992, "Convection in Porous Media".

Lunardini, V.J., 1981, "Heat Transfer in Cold Climates", Van Nostrand Reinhold, New York.

Pham, N. H., 2013, "Heat Transfer in Waste-Rock Piles Constructed in a Continuous Permafrost Region". A thesis submitted to the Faculty of Graduate Studies and Research for the degree of Doctor of Philosophy in Geotechnical Engineering at the University of Alberta, Edmonton.

Ritchie, A.I.M. and Plotnikoff, W.W., 1997. Preliminary Estimates of the Sulphate Production Rate in Granite Stockheaps. ANSTO Technical Report, ANSTO/C524.

Ritchie, A.I.M., Plotnikoff, W.W. and Miskelly, P, 1998. The Impact of a Low, Temperature Dependent IOR on Sulphur Oxidation Rates in a Granite Stockheap. ANSTO Technical Report, ANSTO/C560.

Smith, L.J.D., Neuner, M., Gupton, M., Moore, M., Bailey, B.L., Blowes, D.W., Smith, L., and Sego, D.C., 2009. Diavik Waste Rock Project: From the Laboratory to the Canadian Arctic. Presented at Securing the Future and 8th ICARD, June 23-26, 2009, Skellefteå, Sweden.

Smith, L.J., Macdonald, G., Blowes, D.W., Smith, L., Sego, D.C., and Amos, R.T. 2012. Diavik Waste Rock Project: Objectives, Construction, Current Conclusions and Implications. 9th ICARD, 2012, Ottawa, Canada.

Steffen, Robertson and Kirsten (Canada) Inc., 2003. 1CB009.04, 2002 Waste Rock Storage Area, Seepage and Waste Rock Survey Report. Submitted to BHP Billiton Diamonds Inc., March 2003.

Sun, B., Xu, X., Lai, Y., and Fang, M., 2005. "Evaluation of Fractured Rock Layer Heights in Ballast Railway Embankment Based on Cooling Effect of Natural Convection in Cold Regions". Cold Regions Science and Technology 42, 120-144.

Tao, W.Q., 2004. Numerical Heat Transfer, second edition. Xi'an Jiaotong University Press, Xi'an, China.

Zhang, M., Lai Y., Gao Z., Yu W., 2006. Influence of Boundary Conditions on the Cooling Effect of Crushed-rock Embankment in Permafrost Regions of Qinghai-Tibet Plateau. Cold Regions Science and Technology 44, 225-239.

TABLES

Table 1.1: Information Supplied

Information	Source	Application
Survey Data	FDA (2006)	Finding thermistor bead depths
Test Pile Drawings	FDA (2006)	Finding thermistor bead depths

Table 1.2: Author's Time on Site for the Purpose of Diavik Test Pile Project

Trip	Time	Comment
Trip 1	September 21 - 28, 2004	Installed bedrock ground temperature cables under Type 1 Pile and one control ground temperature cable.
Trip 2	May 16 - 19, 2005	Participated in establishing field tasks for the test pads including safety and logistics.
Trip 3	June 9 - 16, 2005	Was unable to install bedrock ground temperature cables under Type 3 Pile due to equipment unavailability. Retrieved and processed existing data and maintained liaison with DDMI.
Trip 4	July 7 - 12, 2005	Participated in construction of Type 1 Pile pad. Prepared instrumentation to be placed in the Type 3 Pile.
Trip 5	July 28 - August 4, 2005	Worked with the Waterloo group on construction of lysimeters for Type 3 Pile.
Trip 6	September 1 – 15, 2005	Experiments with rock dumps to establish a feasible method for instrumentation installation.
Trip 7	September 22 - 29, 2005	Strung ground temperature cables through a spa hose for installation.
Trip 8	October 12 - 27, 2006	Connected selected ground temperature cables to dataloggers

Table 2.1: Literature Review Summary

Source	Research Type	Pressure Boundary Conditions	Research Area
Goering, D.J. and Kumar, P. 1996, "Winter-time Convection in Open-graded Embankments"	Numerical	Closed	A high permeability and low permeability roadway embankment subjected to long term periodic boundary conditions
Goering, D.J., 1998. "Experimental Investigation of Air Convection Embankments for Permafrost-Resistant Roadway Design"	Experimental	Open and closed	A high permeability roadway embankment constructed on permafrost and monitored for two years
Goering, D.J., 2000. "Passive Cooling of Permafrost Foundation Soils Using Porous Embankment Structures"	Experimental and numerical	Open and closed	A high permeability roadway embankment constructed on permafrost, monitored for two years and then modeled numerically
Sun et al., 2005. "Evaluation of Fractured Rock Layer Heights in Ballast Railway Embankment Based on Cooling Effect of Natural Convection in Cold Regions"	Numerical	Open and closed	Critical embankment heights are evaluated based on natural convection index, and then verified numerically. The evaluation is for varying temperature amplitude, embankment materials and Rayleigh numbers
Ma et al., 2006. "Monitoring Study on Technology of the Cooling Roadbed in Permafrost Region of Qinghai-Tibet Plateau"	Experimental	Open	Field experiments on railway sections with three methods of permafrost protection including embankment of crushed rock slope protection, the crushed rock embankment and ventilated duct embankment
Zhang et al., 2006. "Influence of Boundary Conditions on the Cooling Effect of Crushed-rock Embankment in Permafrost Regions of Qinghai-Tibet Plateau"	Numerical	Open and closed	1.5 m crushed rock layer embankment with various amounts of fill
Linklater, C, 2004. "Prediction of Heat and Gas Transport in a Test Heap at Diavik Diamond Mines: Results from SULFIDOX 'base case' simulations for 15 m heap"	Numerical	Closed	Diavik test pile under periodic boundary conditions modeled for five years
SRK, 2003. Water License.	Experimental	Open	Results of temperature measurements inside a production waste rock pile at Ekati Diamond Mine
Smith et al., 2009. "Diavik Waste Rock Project: From the Laboratory to the Canadian Arctic"	Experimental	Open	Waste rock test pile construction procedures

Table 2.1: Literature Review Summary

Source	Research Type	Pressure Boundary Conditions	Research Area
Pham, 2013. "Heat Transfer in Waste Rock Piles Constructed in a Continuous Permafrost Region"; PhD Thesis.	Experimental and numerical	Open and closed	Selected thermal data from Diavik waste rock test piles used to calculate heat budgets for the piles

Table 2.2: Waste Rock Properties Used by Pham (2013) in Heat Budget Calculations (References in Table)

Property	Thermal Conductivity (Amos et al., 2009) (Measured)	Air Permeability (Amos et al., 2009) (Measured)	Bulk Volumetric Heat Capacity (Calculated)	Bulk Density (Smith, 2012) (Assumed)	Porosity (Neuner et al., 2012) (Measured)	Volumetric Water Content (Neuner et al., 2012) (Measured)
Unit	**J/(s-m-°K)**	**m^2**	**$J/(m^3-K)$**	**kg/m^3**		
Value	1.9	2.0×10^{-9}	2.1×10^{6}	2060	0.25	0.06

Table 2.3: Thermal Conductivity Measurements in Diavik Test Piles (Pham, 2013)

Material	Thermal Conductivity (Pham, 2013) (J/s-m-°K)	
	Type 1 Pile	Type 3 Pile
2006		1.2
2007	1.4	1.6
2008	1.7	1.9
2009	2.0	1.9
2010	2.0	2.2
Average	1.7	1.8

Table 2.4: In-situ Measurements Used by Pham (2013) for Type 3 Pile Numerical Simulations

Material	Thermal Conductivity	Air Permeability (Amos et al., 2009)	Frozen Bulk Volumetric Heat Capacity	Thawed Bulk Volumetric Heat Capacity	Porosity (Neuner et al., 2012)	Volumetric Water Content (Neuner et al., 2012)
Unit	**J/(s-m-°K)**	**m^2**	**J/(m^3-K)**	**J/(m^3-K)**		
Type 3 Pile	1.8	2.0×10^{-9}	2.2×10^{6}	2.3×10^{6}	0.25	0.06

Table 3.1: Literature Used for Verification of GeoStudio Convection Module

Literature	Type of Work	Air Boundary Conditions	Experiment Duration
Goering and Kumar (1996)	Numerical	Closed	Long term
Goering (2000)	Numerical and experimental	Closed and open	Long term
Sun et al. (2005)	Numerical	Closed and open	Short term
SRK (2003)	Field Investigation	Open	Short term

Table 3.2: Input Parameters (Goering and Kumar, 1996)

Material	Thermal Conductivity (kJ/d-m-°C)		Specific Heat (kJ/m³-°C)		Porosity	Intrinsic Permeability (m²)	Latent Heat (kJ/m³)
	Frozen	Unfrozen	Frozen	Unfrozen			
Embankment (high permeability)	30	30	1006	1006	0.4	6.3×10^{-7}	~0
Foundation (silt)	200	129	2380	3740	0.65	~0	2.17×10^{5}
Closed boundaries							

Table 3.3: Input Parameters (Goering, 2000)

Material	Thermal Conductivity (kJ/d-m-°C) Specific Heat		Specific Heat (kJ/m3-oC)		Porosity	Intrinsic Permeability (m²)	Latent Heat (J/m³)
	Frozen	Unfrozen	Frozen	Unfrozen			
Embankment (high permeability)	30	30	1020	1020	0.3	6.3×10^{-7}	~0
Foundation (silt)	186	173	1640	2010	0.078	~0	26.2×10^{6}
Closed boundaries or open sideslopes							

Table 3.4: Temperature Boundary Conditions (Goering and Kumar, 1996 and Goering, 2000)

Surface	Thaw n Factor	Freeze n Factor	Sinusoidal Function
Asphalt surface	1.9	0.9	1.1-26.1cos(2π/365(t-9))
Gravel sideslope	1.7	0.6	2.7-20.9cos(2π/365(t-9))
Native surface	0.5	0.5	-1.9-10.0cos(2π/365(t-9))
Bottom boundary	Geothermal gradient 5.2 (kJ/d-m^2)		

Table 3.5: Input Parameters Used in GeoStudio Ekati Model

Material	Thermal Conductivity (Frozen/Unfrozen) (kJ/d-m-°C)	Volumetric Heat Capacity (Frozen/Unfrozen) (kJ/m^3-°C)	Air Permeability (m/d)	Porosity (%)
Waste Rock	155.5	2170	6,000	30
Compacted Waste Rock	155.5	2170	1, 1,000 and 6,000 (assumed)	30
Bedrock	241.9	2130	~0	~0

Table 3.6: Input Parameters Used to Simulate Rayleigh Numbers of 50 and 80

Material	Thermal Conductivity (kJ/d-m-°C)		Specific Heat (kJ/m³-°C)		Porosity	Intrinsic Permeability (m²)	Latent Heat (kJ/m³)
	Frozen	Unfrozen	Frozen	Unfrozen			
Embankment Ra=25	31	31	2170	2170	0.3	5.1×10^{-5}	~0
Embankment Ra=50	31	31	2170	2170	0.3	2.51×10^{-6}	~0
Embankment Ra=80	31	31	2170	2170	0.3	8.16×10^{-6}	~0

Table 3.7: Input Parameters Adapted after Goering (2000) Used in GeoStudio Models to Examine Full Versus Half Geometries

Material	Thermal Conductivity (kJ/d-m-°C)		Specific Heat (kJ/m³-°C)		Porosity	Intrinsic Permeability (m²)	Latent Heat (kJ/m³)
	Frozen	Unfrozen	Frozen	Unfrozen			
Embankment (high permeability)	30	30	1020	1020	0.3	6.3×10^{-7}	~0
Foundation (silt)	186	173	1640	2010	0.78* 0.65**	~0	2.62×10^{5} 2.17×10^{5}
*Unfrozen volumetric water content changes at 0°C according to step function							
**Unfrozen volumetric water content changes as per GeoStudio ad-in functions							
Boundaries closed or sideslopes open							
Note: * used in models for comparing snapshots ** used in models for comparing trends							

Table 3.8: Input Parameters Adapted after Goering (2000) Used in GeoStudio Models to Examine Repeatability of Modelling Results

Material	Thermal Conductivity (kJ/day-m-°C)		Specific Heat (kJ/m³-°C)		Porosity	Intrinsic Permeability (m²)	Latent Heat (kJ/m³)
	Frozen	Unfrozen	Frozen	Unfrozen			
Embankment (high permeability)	30	30	1020	1020	0.3	6.3×10^{-7}	~0
Foundation (silt)	186	173	1640	2010	0.78* 0.65**	~0	2.62×10^{5} 2.17×10^{5}
Unfrozen volumetric water content changes as per GeoStudio ad-in functions							
Either closed boundaries or open sideslopes							
Note: * used in models for comparing snapshots ** used in models for comparing trends							

Table 3.9: Standard Deviation for Temperature Differences between Runs in the Four Models

Location	Model 1 Coarse Mesh	Model 2 Fine Mesh	Model 1 Coarse Mesh	Model 2 Fine Mesh
	Closed Boundaries		Open Sideslopes	
1	0.8	0.4	0.0	0.0
2	2.2	1.2	0.8	0.9
3	1.6	1.1	0.5	1.2
4	1.3	0.8	0.1	0.0
5	0.9	0.4	0.1	0.0
6	1.3	0.6	0.5	0.6
7	2.0	0.6	0.3	1.3
8	0.5	0.0	0.0	0.0
9	0.9	0.2	0.0	0.0
10	1.7	0.9	0.0	0.1
11	1.3	1.6	0.1	0.1
12	1.8	0.8	0.3	0.6
13	1.2	0.5	0.2	1.1
14	0.0	0.0	0.0	0.0
15	0.3	0.1	0.0	0.1
16	0.2	0.1	0.0	0.3
Range	0.0 to 2.2	0.0 to 1.6	0.0 to 0.8	0.0 to 1.3

Table 3.10: Input Parameters Adapted after Goering and Kumar (1996)

Material	Thermal Conductivity (kJ/d-m-°C)		Specific Heat (kJ/m³-°C)		Porosity	Intrinsic Permeability (m²)	Latent Heat (kJ/m³)
	Frozen	Unfrozen	Frozen	Unfrozen			
Embankment (high permeability)	30	30	1006	1006	0.4	6.3×10^{-7}	~0
Foundation (silt)	200	129	2380	3740	0.65*	~0	2.17×10^{5}
Closed boundaries							
*Unfrozen volumetric water content changes as per GeoStudio ad-in functions							

Table 3.11: Input Parameters Adapted after Goering (2000)

Material	Thermal Conductivity (kJ/d-m-°C)		Specific Heat (kJ/m³-°C)		Porosity	Intrinsic Permeability (m²)	Latent Heat (kJ/m³)
	Frozen	Unfrozen	Frozen	Unfrozen			
Embankment (high permeability)	30	30	1020	1020	0.3	6.3×10^{-7}	~0
Foundation (silt)	186	173	1640	2010	0.65 0.45	~0	2.17×10^{5} 1.50×10^{5}
Closed boundaries							
Open sideslopes							

Table 3.12: Temperature Estimates from Snapshots Presented in Goering and Kumar (1996) and Goering (2000)

ID	1	2	3	4	5	6	7	8	9	10	11	12	13	14	15	16
CLOSED BOUNDARIES																
Goering and Kumar (1996)																
Apr	-4	-6	-6	-6	-8	-8.5	-9	-4	-6.5	-8	-8.5	-9	-9	-7	-8	-8
Jun	17	16	16	12	10	9	9	4	1	0	0	-2	-2	-2	-3	-3
Oct	7	7.5	7.5	6.5	7	7	7	3	2	2	1.5	1.5	1.5	0	-1	-1
Nov	0	-5	0	-1	1	0	1	-2	-1.5	-0.5	0	0	0	-0.5	-0.5	-0.5
Dec	-6	-12	-6	-6	-6	-12	-4	-6	-4	-4	-6	-8	-2	-1	-2	-3
Jan	-13	-18	-12	-12	-12	-18	-12	-10	-8	-6	-12	-14	-9	-2	-6	-7
Mar	-12	-15	-14	-11	-13.5	-15	-13	-9.5	-8	-10	-12	-14	-12	-7.5	-9	-10
Goering (2000) Numerical Results																
Aug	22	22	22	18	17.5	17.5	17.5	8	6	5	4	4	4	0	0	0
Feb	-14	-20	-16	-12	-14	-19.5	-14	-12	-9	-9	-14	-17	-13	-7	-9	-10
Goering (2000) Experimental Results																
Aug	n/a	n/a	n/a	13	12	11.5	11.5	n/a	8.5	7.5	7	6	5.5	n/a	n/a	n/a
Feb	-10	-14	-10.5	-10	-10	-13	-9.5	n/a	n/a	-9.5	-9.5	-11	-9	n/a	n/a	n/a
OPEN SIDESLOPES																
Goering (2000) Numerical Results																
Aug	20	21	21	18	15	15	15	12	6	4	4	4	4	0	0	0
Feb	-15	-14	-16	-16	-15	-14	-14	-14	-12	-11	-10	-15	-11	-8	-6	-8
Goering (2000) Experimental Results																
Aug	21	20	20	17	17	16.5	16	n/a	9	9	8	7	7	n/a	n/a	n/a
Feb	-12.5	-11.5	-10.5	-13	-13	-11.5	-10.5	n/a	-11	-12	-11.5	-9.5	-9	n/a	n/a	n/a

Table 3.13: Modeling Cases for Embankment with Open Sideslopes

Case	Mesh	Foundation Porosity	Foundation Volumetric Water Content Change
1	Coarse	0.65	Gradual according to GeoStudio ad-in function
2	Coarse	0.45	Gradual according to GeoStudio ad-in function
3	Fine	0.65	Gradual according to GeoStudio ad-in function
4	Fine	0.45	Gradual according to GeoStudio ad-in function
5	Coarse	0.65	Instantaneous according to a step function

Table 3.14: Modeling Cases for Embankment with Closed Boundaries

Case	Parameters Adapted After	Mesh	Foundation Porosity	Foundation Volumetric Water Content Change
GeoStudio 1996 Model	Goering and Kumar (1996)	Fine	0.65	Gradual according to GeoStudio ad-in function
GeoStudio 2000 Model	Goering (2000)	Coarse	0.65	Gradual according to GeoStudio ad-in function
GeoStudio 2000 Model	Goering (2000)	Coarse	0.45	Gradual according to GeoStudio ad-in function

Table 3.15: Initial Temperature Condition for Ekati Model

Waste Rock Pile Height (m)	Temperature (°C)	Comment
27	9	Bottom of higher compacted waste rock layer
15	-1	Top of lower compacted waste rock layer
12	-3	Bottom of lower compacted waste rock layer

Table 3.16: Average Monthly Air and Surface Temperatures

Month	Temperature (°C) 2006-2008		Difference (°C)	Temperature (°C) 2000-2002		Temperature (°C) 2000-2002
	Diavik Air	Diavik Surface		Ekati Air	Ekati Surface	Diavik Air
August	15.8	17.5	-1.7	9.7	11.4	10.1
September	9.1	9.0	0.1	1.9	1.8	2.5
October	-2.0	1.7	-3.7	-7.3	-3.6	-6.5
November	-17.9	-13.9	-4.0	-18.1	-14.1	-17.1
December	-12.0	-15.0	3.1	-31.1	-34.2	-30.3
January	-24.6	-16.7	-7.9	-24.7	-16.8	-24.0
February	-27.8	-21.2	-6.6	-27.6	-21.0	-27.1
March	-27.0	-22.8	-4.2	-22.4	-18.2	-21.8
April	-11.8	-12.2	0.4	-14.5	-14.9	-14.5
May	-3.3	-0.8	-2.5	-3.2	-0.7	-3.0
June	6.9	3.5	3.4	6.6	3.2	6.7
July	14.4	15.4	-1.0	14.4	15.4	14.1
August	8.2	9.8	-1.6	9.8	11.4	9.9
September	3.2	3.8	-0.5	6.6	7.1	6.9
October	-4.7	-1.0	-3.7	-8.3	-4.6	-7.4
November	-20.3	-10.1	-10.2	-19.5	-9.3	-18.8
December	-26.5	-12.7	-13.8	-23.4	-9.6	-23.3
January	-28.9	-16.3	-12.5	-28.0	-15.5	-27.3
February	-32.0	-22.2	-9.7	-30.2	-20.5	-29.8
March	-28.2	-21.7	-6.5	-25.5	-19.0	-25.3
April	-14.3	-14.0	-0.3	-19.2	-18.9	-18.9
May	-0.5	-1.2	0.7	-6.7	-7.4	-8.3
June	9.1	8.2	0.8	8.7	7.9	10.4
July	14.4	14.4	0.0	13.5	13.5	12.8
August	11.6	13.1	-1.5	9.4	10.9	9.5
September	2.0	4.2	-2.2	3.5	5.7	3.8
October	-3.7	0.7	-4.5	-8.5	-4.0	-7.6

Table 3.17: Cases Modeled with Ekati Model

Case	Air Permeability	
	Waste Rock (m/d)	Compacted Waste Rock Layers (Higher and Lower) (m/d)
Case 1	6,000	6,000
Case 2	6,000	1,000
Case 3	6,000	1
Case 4	Conduction only	

Table 3.18: Measured Temperatures at Site 4 on Four Days Used to Compare GeoStudio Modeling Temperatures

Depth	2001-04-14	2001-08-25	2002-04-02	2002-08-30
2.0	-11.6	7.2	-15.6	6.6
4.5	-8.1	3.6	-10.9	3.4
7.0	-10.0	3.8	-11.5	3.7
9.5	-12.2	1.8	-14.1	0.0
12.0	-16.2	-0.6	-18.2	-6.5
14.5	-15.8	-5.7	-19.6	-9.8
17.5	-13.4	-8.4	-13.2	-10.9
20.5	-15.8	-8.9	-10.7	-10.7
23.5	-20.0	-11.5	-11.9	-11.2
26.5	-22.6	-13.1	-14.0	-11.4
28.5	-22.9	-13.7	-14.4	-11.4
29.5	-22.4	-14.1	-14.3	-11.8
30.5	-20.6	-13.8	-13.3	-11.9
31.5	-18.4	-13.3	-12.3	-11.6
32.5	-16.3	-13.3	-12.0	-11.8
34.5	-12.8	-12.0	-10.9	-11.0

Table 3.19: Parameters Used for Input to GeoStudio Model to Achieve Rayleigh Numbers of 25, 50 and 80

Parameter	Symbol	Unit	Rayleigh Number		
			25	50	80
Specific heat capacity (air)	c	kJ/kg-K	1.005	1.005	1.005
Density (air)	ρ	Kg/m^3	1.293	1.293	1.293
Volumetric heat capacity (air)	C	KJ/m^3-K	1.299	1.299	1.299
0°C in Kelvin		K	273.0	273.0	273.0
Expansion coefficient (air)	β	1/K	0.00366	0.00366	0.00366
Kinematic viscosity (air)	v	m^2/s	0.0000133	0.0000133	0.0000133
Kinematic viscosity (air)	v	m^2/d	1.149	1.149	1.149
Acceleration of gravity	g	m/s^2	9.81	9.81	9.81
Acceleration of gravity	g	m/d^2	7.32E+10	7.32E+10	7.32E+10
Hydraulic conductivity (Kg/v)	h	m/s	3.762	1.852	6.019
Hydraulic conductivity (Kg/v)	h	m/d	325,000	160,000	520,000
Permeability	K	m^2	5.10E-05	2.51E-06	8.16-06
Height	H	m	1.0	1.0	1.0
Temperature difference	ΔT	°C	1.0	1.0	1.0
Thermal conductivity (mixture)	k	J/(s-m-C)	0.359	0.359	0.359
Thermal conductivity (mixture)	k	J/(d-m-C)	31	31	31

Table 4.1: Test Pile Instrumentation Summary (FDA, 2006)

Instrumentation	Target measured/purpose
Air permeability probes	Internal test pile permeability to air flow
Basal collection lysimeters (BCL)	Discrete collection of basal water flow and quality
Basal drain collection lines	Bulk basal water flow and quality
Gas sampling lines	Internal test pile gas phase composition
Microbiology access ports	Internal teat pile microbial populations
Soil-water suction samplers (SWSS)	Internal test pile water quality
Time-Domain Reflectometry (TDR) probes	Internal test pile moisture content
Tensiometers	Internal test pile matric water potential (unsaturated rock moisture tension)
Thermal conductivity probe access lines	Internal test pile thermal conductivity characteristics
Ground Temperature Cables (ground temperature cables)	Bedrock and internal test pile temperature
Upper collection lysimeters (UCL)	Active zone water flow and quality

Table 4.2: Test Pile Components Summary

Test Pile Name	Waste Rock Type (%)	Pile Orientation	Number of Instrumented Faces	Ground Temperature Cable Locations
Type 1 Pile	Type I	North	4	Face 1, 2, and 4
Type 3 Pile	Type III	West	4	Face 1, 2, and 4
TC Covered Pile	Type I, Type III and Till	South	4	Face 1, 2, 3, and 4

Table 4.3: Bedrock Ground Temperature Cable Installation Details

Item		Ground Temperature Cable			
		T1J0	**T1J1**	**T1J2**	**T1J3**
Installation Date		Sep 23, 2004	Sep 23, 2004	Sep 23, 2004	Sep 22, 2004
Borehole Location		Moved to pile centerline	Moved 2 m west from staked out location	As staked out by survey	As staked out by survey
Depth Drilled (m)		10	10	10	10
Depth of Slough (m)		9.9	8.7	8.5	9.8
Water after Completion (m)		Dry	8.2	8.0	6.1
Stratigraphy	Pad	0 m	0 m	0 m	0 m
	Bedrock	1.5 m	4 0 m	3.7 m	3. 5 m
	End of Borehole	10 m	10 m	10 m	10 m
Backfill		PK	PK	PK	PK

Table 5.1: Thermistor Bead Spacing as of September 2006

Strung and As-manufactured GTC Spacing Summary September 2006

Item	Type	Total Cable Length	Labeled	Status	Spacing starting from T1 (end opposite to lead)																														No. Beads
					Order 2005																														
				Bead ID	T1		T2		T3		T4		T5		T6		T7		T8		T9		T10		T11		T12								
					•	~	•	~	•	~	•	~	•	~	•	~	•	~	•	~	•	~	•	~	•	~	•								
1	pigtailed	205	2m-5m (1)	strung on site		1		2		2		2		2		3		3		2		2		2		2									12
2	pigtailed	205	2m-5m (2)	strung on site		1		2		2		2		2		3		3		2		2		2		2									12
3	pigtailed	205	2m-5m (3)	strung on site		1		2		2		2		2		3		3		2		2		2		2									12
4	pigtailed	205	2m-5m (4)	strung on site		1		2		2		2		2		3		3		2		2		2		2									12
5	pigtailed	205	2m-5m (5)	strung on site		1		2		2		2		2		3		3		2		2		2		2									12
6	pigtailed	205	2m-5m (6)	strung on site		1		2		2		2		2		3		3		2		2		2		2									12
7	pigtailed	205	2m-5m (7)	strung on site		1		2		2		2		2		3		3		2		2		2		2									12
8	pigtailed	205	2m-5m (8)	strung on site		1		2		2		2		2		3		3		2		2		2		2									12
9	pigtailed	225	5m-10m (1)	in trailer		1		2		41		3		3		3		2		2		2		2		1									12
10	pigtailed	225	5m-10m (2)	strung on site		1		2		3		3		3		3		2		2		1		1		1									12
11	pigtailed	225	5m-10m (3)	strung on site		1		2		3		3		3		3		2		2		1		1		1									12
12	pigtailed	225	5m-10m (4)	strung on site		1		2		3		3		3		3		2		2		2		2		1									12
13	pigtailed	225	5m-10m (5)	strung on site		1		2		3		3		3		3		2		2		2		2		1									12
14	pigtailed	225	5m-10m (6)	in trailer		1		2		41		3		3		3		2		2		2		2		1									12
15	pigtailed	225	5m-10m (7)	strung on site		1		1		3		3		3		3		2		2		2		2		1									12
16	pigtailed	225	5m-10m (8)	strung on site		1		1		3		3		3		3		2		2		1		1		1									12
17	in-line	200	10m-15m (1)	in trailer		1		2		2		2		2		3		3		3		5		6		23									12
18	in-line	200	10m-15m (2)	in trailer		1		2		2		2		2		3		3		3		5		6		23									12
19	in-line	200	10m-15m (3)	in trailer		1		2		2		2		2		3		3		3		5		6		23									12
20	in-line	200	10m-15m (4)	in trailer		1		2		2		2		2		3		3		3		5		6		23									12
21	in-line	200	10m-15m (5)	in trailer		1		2		2		2		2		3		3		3		5		6		23									12
22	in-line	200	10m-15m (6)	in trailer		1		2		2		2		2		3		3		3		5		6		23									12
23	in-line	200	10m-15m (7)	in trailer		1		2		2		2		2		3		3		3		5		6		23									12
24	in-line	200	10m-15m (8)	in trailer		1		2		2		2		2		3		3		3		5		6		23									12
					Order 2004																														
25	pigtailed	150	a1	in trailer		1		3		2		2		2		2		2		2		2		2		2									12
26	pigtailed	140	a2	in trailer		1		3		2		2		2		2		2		2		2		2		2									12
27	pigtailed	130	a3	in trailer		1		3		2		2		2		2		2		2		2		2		2									12
28	pigtailed	137	2m (A)	in trailer		1		2		2		2		2		3		3		3		3													10
29	pigtailed	137	2m (B)	in trailer		1		2		2		2		2		3		3		3		3													10
30	pigtailed	130	5m (A)	in trailer		1		2		2		2		2		3		3		3		3													10
31	pigtailed	130	5m (B)	in trailer		1		2		2		2		2		3		3		3		3													10
32	pigtailed	122	10m (A)	in trailer		1		2		2		2		2		3		3		3		5		6											11
33	pigtailed	122	10m (B)	in trailer		1		2		2		2		2		3		3		3		5		6											11
34	pigtailed	115	15m (A)	in trailer		1		2		2		2		2		3		3		3		5		6		6									12
35	pigtailed	115	15m (B)	in trailer		1		2		2		2		2		3		3		3		5		6		6									12
39	in-line	50	J0	installed		2		2		2		2		2																					6
36	in-line	170	J1	installed		5		5		5		5		5		5		2		2		2		2		2									12
37	in-line	160	J2	installed		5		5		5		5		5		5		2		2		2		2		2									12
38	in-line	190	J3	installed		5		5		5		5		5		5		2		2		2		2		2									12

Table 6.1: Average Monthly Measured Temperatures in Ground Temperature Cable T3J3

Depth Below Pad Surface (m)	Temperature (°C)			
T3J3	October 2005 (Initial)	June 2006	July 2006	August 2006
-0.5	1.95	-0.87	-0.22	0.09
-5.5	-1.57	-1.82	-1.66	-1.54
-7.5	-2.26	-1.94	-1.85	-1.74
-9.5	-2.7	-2.05	-2.03	-1.97
-11.5	-3.01	-2.24	-2.25	-2.23
-13.5	-2.66	-2.00	-2.00	-1.99
-15.5	-2.88	-2.59	-2.57	-2.56

Table 6.2: Averaged Measured Surface Temperatures in Ground Temperature Cable T3J3

Date	Temperature (°C)
October 2005	0.86
November 2005	-3.25
December 2005	-8.37
January 2006	-8.77
February 2006	-11.74
March 2006	-11.94
April 2006	-7.71
May 2006	-0.86
June 2006	1.89
July 2006	3.67
August 2006	4.27
September 2006	4.44

Table 6.3: Thermal Properties for Calibration Analysis

Material	Thermal Conductivity (kJ/day-m-˚C)		Volumetric Heat Capacity (kJ/m³-˚C)	
	Frozen	Unfrozen	Frozen	Unfrozen
Pham's Thermal Properties				
Waste rock pad	155.5	155.5	2170	2170
Bedrock	241.9	241.9	2130	2130
Best Match Thermal Properties				
Waste rock pad	29	29	1500	1500
Bedrock	241.9	241.9	2130	2130

Table 6.4: Calibration Analysis Results

Depth (m)	Average Measured By T3J3	Modelled with Pham's Parameters		Modelled with Best Match Parameters	
		Temperatures in June 2006	Difference	Temperatures in June 2006	Difference
0	1.89	1.95	-0.06	1.95	-0.06
-0.5	-0.87	-0.14	-0.73	-0.82	-0.05
-5.5	-1.82	-3.39	1.56	-1.89	0.07
-7.5	-1.94	-2.94	0.99	-2.09	0.14
-9.5	-2.05	-2.63	0.58	-2.27	0.22
-11.5	-2.24	-2.51	0.27	-2.42	0.18
-13.5	-2.00	-2.53	0.53	-2.55	0.55
-15.5	-2.59	-2.60	0.01	-2.65	0.06

Table 6.5: Initial Foundation Temperature Boundary Conditions

Depth Below Pad Surface (m)	Temperature (°C)
T3J3	**August 2006**
-0.5	0.09
-5.5	-1.54
-7.5	-1.74
-9.5	-1.94
-11.5	-2.33
-13.5	-1.99
-15.5	-2.56

Table 6.6: Material Properties for GeoStudio Diavik Test Pile Model

Material	Thermal Conductivity (Frozen/Unfrozen) (kJ/day-m-˚C)	Volumetric Heat Capacity (Frozen/Unfrozen) (kJ/m^3-˚C)	Air Permeability (m/d)	Corresponding Intrinsic Permeability (m^2)	Porosity (%)
Waste Rock	155.5	2170	4,000	6 x 10^{-8}	30
Waste Rock	155.5	2170	6,000	9 x 10^{-8}	30
Waste Rock	155.5	2170	8,000	1 x 10^{-7}	30
Waste Rock Pad	155.5	2170	128	2 x 10^{-9}	30
Bedrock	241.9	2130	~0		~0

Table 6.7: Rayleigh Numbers on March 15, 2008 in GeoStudio Diavik Test Pile Model

Parameter	Symbol	Unit	Rayleigh Number					
			29	24	39	23	48	17
Location on Face			Centre	Under Crest	Centre	Under Crest	Centre	Under Crest
Specific heat capacity (air)	c	kJ/kg-K	1.005	1.005	1.005	1.005	1.005	1.005
Density (air)	ρ	Kg/m^3	1.293	1.293	1.293	1.293	1.293	1.293
Volumetric heat capacity (air)	C	KJ/m^3-K	1.299	1.299	1.299	1.299	1.299	1.299
0°C in Kelvin		K	273.0	273.0	273.0	273.0	273.0	273.0
Expansion coefficient (air)	β	1/K	0.00366	0.00366	0.00366	0.00366	0.00366	0.00366
Kinematic viscosity (air)	v	m^2/s	1.33E-5	1.33E-5	1.33E-5	1.33E-5	1.33E-5	1.33E-5
Kinematic viscosity (air)	v	m^2/d	1.149	1.149	1.149	1.149	1.149	1.149
Acceleration of gravity	g	m/s^2	9.81	9.81	9.81	9.81	9.81	9.81
Acceleration of gravity	g	m/d^2	7.32E+10	7.32E+10	7.32E+10	7.32E+10	7.32E+10	7.32E+10
Hydraulic conductivity (Kg/v)	h	m/s	0.046	0.046	0.069	0.069	0.093	0.093
Hydraulic conductivity (Kg/v)	h	m/d	4,000	4,000	6,000	6,000	8,000	8,000
Permeability	K	m^2	6.28E-08	6.28E-08	9.41E-08	9.41E-08	1.26E-07	1.26E-07
Height	H	m	14	14	14	14	14	14
Temperature difference	ΔT	°C	17	14	15	9	14	5
Thermal conductivity (mixture)	k	J/(s-m-C)	1.8	1.8	1.8	1.8	1.8	1.8
Thermal conductivity (mixture)	k	J/(d-m-C)	155.5	155.5	155.5	155.5	155.5	155.5

Table 6.8: Temperatures in Coldest Month of 2007 and 2008 (Permeability 4,000 m/d)

Ground Temperature Cable	Thermistor Bead	Depth Below Surface (m)	Temperatures on March 15, 2007 (°C)	Temperatures on March 15, 2008 (°C)	Difference	Warming
32N5THM00	T1	0.68	-15.7	-17.2	-1.5	
	T2	1.12	-14.3	-16.3	-2.0	
	T3	2.14	-11.6	-14.0	-2.5	
	T4	3.31	-9.1	-11.6	-2.4	
	T5	4.54	-6.8	-9.1	-2.3	
	T6	5.75	-4.8	-6.9	-2.1	
	T7	7.01	-3.0	-5.0	-2.0	
	T8	8.78	-1.0	-3.0	-2.0	
	T9	10.24	0.1	-2.0	-2.1	
	T10	11.13	0.6	-1.7	-2.2	
	T11	11.59	-0.5	-2.4	-1.9	
	T12	11.63	-3.6	-4.4	-0.8	
32S5THM00	T2	1.15	-14.0	-16.1	-2.1	
	T3	2.10	-11.7	-14.1	-2.4	
	T4	3.16	-9.5	-11.9	-2.4	
	T5	4.26	-7.3	-9.7	-2.3	
	T6	5.34	-5.5	-7.7	-2.2	
	T7	6.82	-3.2	-5.3	-2.0	
	T8	8.71	-1.1	-3.1	-2.0	
	T9	10.18	0.1	-2.1	-2.1	
	T10	11.12	0.5	-1.7	-2.2	
	T11	11.66	1.2	-1.1	-2.4	
	T12	11.63	1.4	-0.9	-2.4	
T3J3	T6	0.5	0.6	-1.0	-1.6	
	T7	5.5	-1.1	-1.4	-0.3	
	T8	7.5	-1.4	-1.5	-0.1	
	T9	9.5	-1.7	-1.7	0.0	
	T10	11.5	-1.9	-1.8	0.1	Warming
	T11	13.5	-2.1	-1.9	0.2	Warming
	T12	15.5	-2.2	-2.0	0.2	Warming

Table 6.9: Temperatures in Coldest Month of 2007 and 2008 (Permeability 6,000 m/d)

Ground Temperature Cable	Thermistor Bead	Depth Below Surface (m)	Temperatures on March 15, 2007 (°C)	Temperatures on March 15, 2008 (°C)	Difference	Warming
32N5THM00	T1	0.68	-15.7	-16.4	-0.6	
	T2	1.12	-15.0	-15.7	-0.7	
	T3	2.14	-13.8	-14.6	-0.8	
	T4	3.31	-12.9	-13.7	-0.8	
	T5	4.54	-11.9	-12.6	-0.7	
	T6	5.75	-11.2	-11.7	-0.5	
	T7	7.01	-10.5	-10.6	-0.2	
	T8	8.78	-9.6	-9.1	0.5	Warming
	T9	10.24	-8.9	-7.7	1.1	Warming
	T10	11.13	-8.0	-6.7	1.3	Warming
	T11	11.59	-11.9	-9.6	2.3	Warming
	T12	11.63	-16.3	-14.4	1.9	Warming
32S5THM00	T2	1.15	-14.9	-15.6	-0.7	
	T3	2.10	-13.9	-14.7	-0.8	
	T4	3.16	-13.0	-13.8	-0.8	
	T5	4.26	-12.1	-12.9	-0.7	
	T6	5.34	-11.4	-12.0	-0.6	
	T7	6.82	-10.6	-10.8	-0.2	
	T8	8.71	-9.7	-9.2	0.5	Warming
	T9	10.18	-8.9	-7.8	1.1	Warming
	T10	11.12	-8.1	-6.8	1.3	Warming
	T11	11.66	-3.3	-4.0	-0.7	
	T12	11.63	-0.4	-2.9	-2.5	
T3J3	T6	0.5	0.3	-3.0	-3.3	
	T7	5.5	-1.1	-2.9	-1.8	
	T8	7.5	-1.4	-2.7	-1.3	
	T9	9.5	-1.7	-2.5	-0.8	
	T10	11.5	-1.9	-2.4	-0.5	
	T11	13.5	-2.1	-2.3	-0.2	
	T12	15.5	-2.2	-2.2	0.0	

Table 6.10: Temperatures in Coldest Month of 2007 and 2008 (Permeability 8,000 m/d)

Ground Temperature Cable	Thermistor Bead	Depth Below Surface (m)	Temperatures on March 15, 2007 (°C)	Temperatures on March 15, 2008 (°C)	Difference	Warming
32N5THM00	T1	0.68	-17.9	-17.5	0.4	Warming
	T2	1.12	-17.5	-17.1	0.4	Warming
	T3	2.14	-16.9	-16.4	0.5	Warming
	T4	3.31	-16.5	-15.8	0.7	Warming
	T5	4.54	-16.1	-15.3	0.8	Warming
	T6	5.75	-15.8	-14.9	0.9	Warming
	T7	7.01	-15.7	-14.7	1.0	Warming
	T8	8.78	-15.7	-14.6	1.1	Warming
	T9	10.24	-15.7	-14.8	1.0	Warming
	T10	11.13	-15.4	-14.5	0.9	Warming
	T11	11.59	-17.9	-17.7	0.2	Warming
	T12	11.63	-20.0	-20.3	-0.3	
32S5THM00	T2	1.15	-17.4	-17.0	0.5	Warming
	T3	2.10	-16.9	-16.4	0.5	Warming
	T4	3.16	-16.5	-15.9	0.6	Warming
	T5	4.26	-16.1	-15.4	0.8	Warming
	T6	5.34	-15.9	-15.0	0.9	Warming
	T7	6.82	-15.7	-14.7	1.0	Warming
	T8	8.71	-15.7	-14.7	1.1	Warming
	T9	10.18	-15.8	-14.8	1.0	Warming
	T10	11.12	-15.5	-14.6	0.9	Warming
	T11	11.66	-10.5	-10.0	0.6	Warming
	T12	11.63	-6.5	-6.4	0.1	Warming
T3J3	T6	0.5	-0.4	-4.0	-3.7	
	T7	5.5	-1.1	-3.5	-2.4	
	T8	7.5	-1.4	-3.2	-1.8	
	T9	9.5	-1.7	-3.0	-1.3	
	T10	11.5	-1.9	-2.7	-0.8	
	T11	13.5	-2.1	-2.5	-0.5	
	T12	15.5	-2.2	-2.4	-0.2	

Table 6.11: Temperatures in Coldest Month of 2007 and 2008 (Conduction)

Ground Temperature Cable	Thermistor Bead	Depth Below Surface (m)	Temperatures on March 15, 2007 (°C)	Temperatures on March 15, 2008 (°C)	Difference	Warming
32N5THM00	T1	0.68	-17.8	-17.4	0.4	Warming
	T2	1.12	-16.2	-16.2	0.0	
	T3	2.14	-11.7	-12.5	-0.8	
	T4	3.31	-7.1	-8.6	-1.5	
	T5	4.54	-3.5	-5.4	-2.0	
	T6	5.75	-1.0	-3.3	-2.3	
	T7	7.01	0.6	-1.9	-2.5	
	T8	8.78	1.6	-0.9	-2.5	
	T9	10.24	1.7	-0.6	-2.3	
	T10	11.13	1.6	-0.5	-2.1	
	T11	11.59	1.5	-0.5	-2.0	
	T12	11.63	1.5	-0.6	-2.0	
32S5THM00	T2	1.15	-15.8	-15.9	0.0	
	T3	2.10	-11.9	-12.7	-0.8	
	T4	3.16	-7.7	-9.1	-1.4	
	T5	4.26	-4.2	-6.1	-1.9	
	T6	5.34	-1.8	-4.0	-2.2	
	T7	6.82	0.4	-2.1	-2.4	
	T8	8.71	1.5	-1.0	-2.5	
	T9	10.18	1.7	-0.6	-2.3	
	T10	11.12	1.6	-0.5	-2.1	
	T11	11.66	1.5	-0.4	-1.9	
	T12	11.63	1.5	-0.4	-1.9	
T3J3	T6	0.5	0.6	-0.3	-0.9	
	T7	5.5	-1.1	-0.9	0.2	Warming
	T8	7.5	-1.4	-1.2	0.3	Warming
	T9	9.5	-1.7	-1.4	0.3	Warming
	T10	11.5	-1.9	-1.6	0.3	Warming
	T11	13.5	-2.1	-1.7	0.3	Warming
	T12	15.5	-2.2	-1.9	0.3	Warming

Table 6.12: Temperatures in Warmest Month of 2007 and 2008 (Permeability 4,000 m/d)

Ground Temperature Cable	Thermistor Bead	Depth Below Surface (m)	Temperatures on August 15, 2007 (°C)	Temperatures on August 15, 2008 (°C)	Difference	Warming
32N5THM00	T1	0.68	7.9	9.9	2.0	Warming
	T2	1.12	8.2	10.0	1.8	Warming
	T3	2.14	7.6	8.9	1.3	Warming
	T4	3.31	5.4	6.2	0.8	Warming
	T5	4.54	2.6	2.9	0.3	Warming
	T6	5.75	0.2	0.1	-0.1	
	T7	7.01	-1.6	-2.0	-0.4	
	T8	8.78	-3.1	-3.8	-0.7	
	T9	10.24	-3.7	-4.5	-0.8	
	T10	11.13	-3.9	-4.7	-0.8	
	T11	11.59	-5.1	-5.8	-0.7	
	T12	11.63	-6.7	-7.2	-0.5	
32S5THM00	T2	1.15	8.2	10.0	1.8	Warming
	T3	2.10	7.7	8.9	1.3	Warming
	T4	3.16	5.8	6.6	0.8	Warming
	T5	4.26	3.3	3.7	0.4	Warming
	T6	5.34	1.0	1.1	0.1	Warming
	T7	6.82	-1.3	-1.7	-0.4	
	T8	8.71	-3.0	-3.7	-0.7	
	T9	10.18	-3.7	-4.5	-0.8	
	T10	11.12	-3.9	-4.7	-0.8	
	T11	11.66	-2.7	-3.8	-1.1	
	T12	11.63	-1.9	-3.2	-1.3	
T3J3	T6	0.5	-0.5	-2.5	-2.0	
	T7	5.5	-1.0	-1.9	-0.9	
	T8	7.5	-1.3	-1.9	-0.6	
	T9	9.5	-1.5	-1.9	-0.4	
	T10	11.5	-1.7	-1.9	-0.2	
	T11	13.5	-1.9	-2.0	0.0	
	T12	15.5	-2.1	-2.0	0.1	Warming

Table 6.13: Temperatures in Warmest Month of 2007 and 2008 (Permeability 6,000 m/d)

Ground Temperature Cable	Thermistor Bead	Depth Below Surface (m)	Temperatures on August 15, 2007 (°C)	Temperatures on August 15, 2008 (°C)	Difference	Warming
32N5THM00	T1	0.68	8.2	10.3	2.1	Warming
	T2	1.12	8.8	10.7	1.9	Warming
	T3	2.14	9.0	10.4	1.4	Warming
	T4	3.31	7.3	8.3	1.0	Warming
	T5	4.54	4.4	5.2	0.8	Warming
	T6	5.75	1.2	2.0	0.7	Warming
	T7	7.01	-1.7	-1.1	0.5	Warming
	T8	8.78	-4.7	-4.6	0.1	Warming
	T9	10.24	-6.2	-6.5	-0.2	
	T10	11.13	-6.7	-7.2	-0.4	
	T11	11.59	-7.4	-7.8	-0.4	
	T12	11.63	-7.9	-8.3	-0.4	
32S5THM00	T2	1.15	8.9	10.8	1.9	Warming
	T3	2.10	9.0	10.4	1.4	Warming
	T4	3.16	7.7	8.7	1.0	Warming
	T5	4.26	5.1	6.0	0.9	Warming
	T6	5.34	2.4	3.1	0.8	Warming
	T7	6.82	-1.3	-0.7	0.6	Warming
	T8	8.71	-4.6	-4.4	0.1	Warming
	T9	10.18	-6.2	-6.4	-0.2	
	T10	11.12	-6.7	-7.1	-0.4	
	T11	11.66	-6.3	-7.0	-0.7	
	T12	11.63	-5.9	-6.7	-0.8	
T3J3	T6	0.5	-4.3	-6.0	-1.7	
	T7	5.5	-1.7	-3.6	-1.9	
	T8	7.5	-1.6	-3.2	-1.6	
	T9	9.5	-1.7	-2.9	-1.2	
	T10	11.5	-1.8	-2.7	-0.9	
	T11	13.5	-1.9	-2.5	-0.6	
	T12	15.5	-2.1	-2.4	-0.3	

Table 6.14: Temperatures in Warmest Month of 2007 and 2008 (Permeability 8,000 m/d)

Ground Temperature Cable	Thermistor Bead	Depth Below Surface (m)	Temperatures on August 15, 2007 (°C)	Temperatures on August 15, 2008 (°C)	Difference	Warming
32N5THM00	T1	0.68	8.4	10.5	2.1	Warming
	T2	1.12	9.2	11.1	1.9	Warming
	T3	2.14	9.8	11.2	1.4	Warming
	T4	3.31	8.7	9.6	0.9	Warming
	T5	4.54	6.1	7.0	0.9	Warming
	T6	5.75	3.0	3.9	0.9	Warming
	T7	7.01	-0.2	0.6	0.8	Warming
	T8	8.78	-4.2	-3.8	0.3	Warming
	T9	10.24	-6.5	-6.7	-0.2	
	T10	11.13	-7.5	-7.9	-0.5	
	T11	11.59	-7.9	-8.4	-0.5	
	T12	11.63	-8.0	-8.5	-0.4	
32S5THM00	T2	1.15	9.3	11.2	1.9	Warming
	T3	2.10	9.8	11.2	1.4	Warming
	T4	3.16	9.0	9.9	1.0	Warming
	T5	4.26	6.8	7.7	0.9	Warming
	T6	5.34	4.1	5.0	0.9	Warming
	T7	6.82	0.3	1.1	0.8	Warming
	T8	8.71	-4.0	-3.6	0.4	Warming
	T9	10.18	-6.4	-6.6	-0.1	
	T10	11.12	-7.4	-7.8	-0.4	
	T11	11.66	-7.6	-8.3	-0.7	
	T12	11.63	-7.5	-8.2	-0.8	
T3J3	T6	0.5	-6.4	-8.1	-1.7	
	T7	5.5	-2.6	-4.7	-2.1	
	T8	7.5	-2.2	-4.0	-1.9	
	T9	9.5	-2.0	-3.5	-1.5	
	T10	11.5	-1.9	-3.1	-1.2	
	T11	13.5	-2.0	-2.8	-0.8	
	T12	15.5	-2.1	-2.7	-0.6	

Table 6.15: Temperatures in Warmest Month of 2007 and 2008 (Conduction)

Ground Temperature Cable	Thermistor Bead	Depth Below Surface (m)	Temperatures on August 15, 2007 (°C)	Temperatures on August 15, 2008 (°C)	Difference	Warming
32N5THM00	T1	0.68	6.7	8.3	1.6	Warming
	T2	1.12	6.2	7.5	1.3	Warming
	T3	2.14	4.2	4.6	0.4	Warming
	T4	3.31	1.6	1.3	-0.3	
	T5	4.54	-0.5	-1.2	-0.8	
	T6	5.75	-1.4	-2.5	-1.1	
	T7	7.01	-1.5	-2.9	-1.4	
	T8	8.78	-1.0	-2.5	-1.6	
	T9	10.24	-0.4	-1.9	-1.5	
	T10	11.13	-0.2	-1.6	-1.4	
	T11	11.59	-0.2	-1.5	-1.3	
	T12	11.63	-0.5	-1.7	-1.2	
32S5THM00	T2	1.15	6.1	7.3	1.2	Warming
	T3	2.10	4.3	4.7	0.5	Warming
	T4	3.16	1.9	1.7	-0.2	
	T5	4.26	-0.1	-0.7	-0.7	
	T6	5.34	-1.1	-2.2	-1.0	
	T7	6.82	-1.5	-2.9	-1.4	
	T8	8.71	-1.0	-2.6	-1.6	
	T9	10.18	-0.5	-2.0	-1.5	
	T10	11.12	-0.2	-1.6	-1.4	
	T11	11.66	0.0	-1.3	-1.3	
	T12	11.63	0.0	-1.3	-1.3	
T3J3	T6	0.5	0.0	-0.5	-0.5	
	T7	5.5	-1.0	-0.9	0.1	Warming
	T8	7.5	-1.3	-1.1	0.1	Warming
	T9	9.5	-1.5	-1.3	0.2	Warming
	T10	11.5	-1.7	-1.5	0.2	Warming
	T11	13.5	-1.9	-1.7	0.3	Warming
	T12	15.5	-2.1	-1.8	0.3	Warming

FIGURES

FIGURE 3.1: EMBANKMENT GEOMETRY (GOERING AND KUMAR, 1996 AND GOERING, 2000) USED FOR GEOSTUDIO CONVECTION MODULE VERIFICATION AND 16 LOCATIONS USED FOR EXTRACTING TEMPERATURE TRENDS

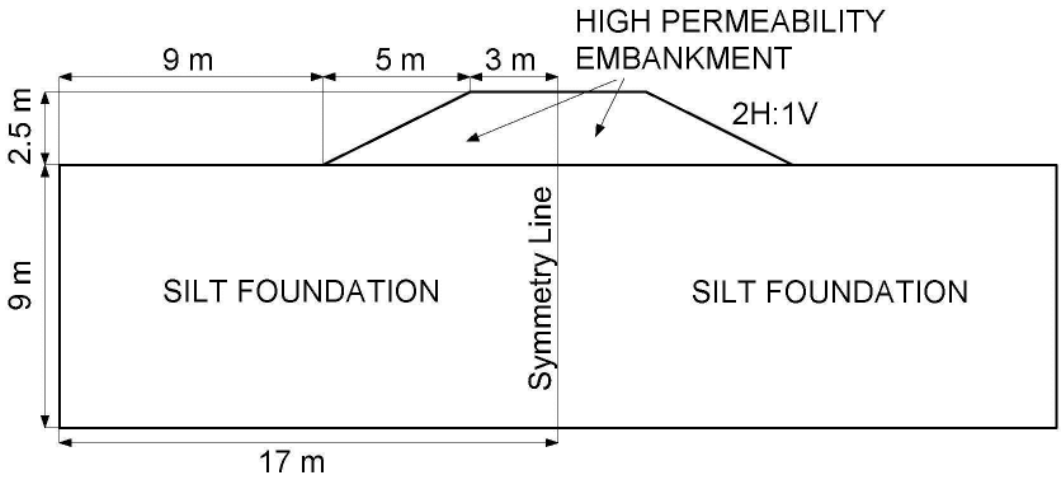

A) Embankment dimensions

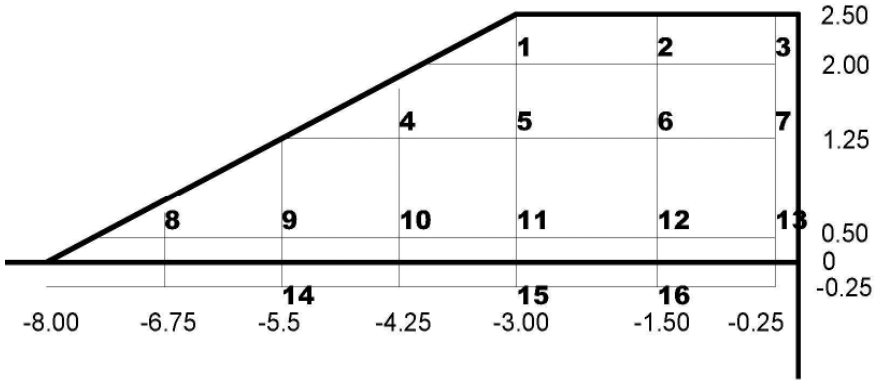

B) Sixteen locations used for extracting temperature trends

FIGURE 3.2: GEOSTUDIO COARSE MESH FULL MODEL WITH CLOSED BOUNDARIES AND CORRESPONDING HALF MODEL USED TO EXAMINE SNAPSHOTS

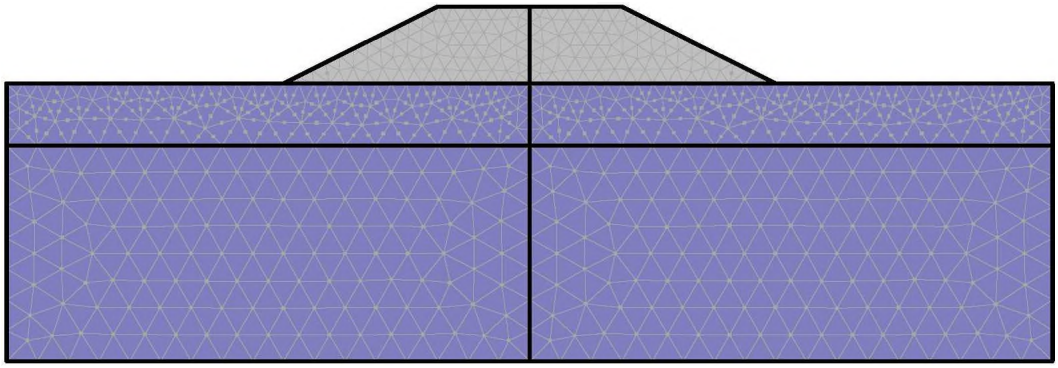

A) Coarse mesh full model; 1574 nodes and 1138 elements; triangles mesh

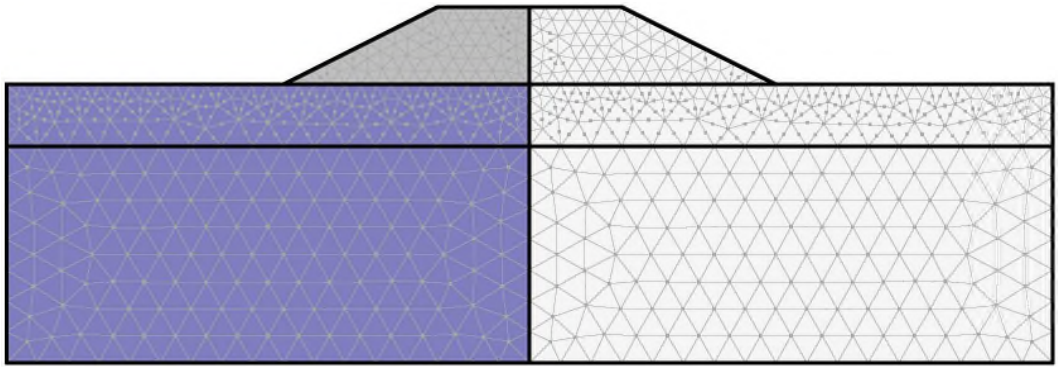

B) Corresponding half model

FIGURE 3.3: GEOSTUDIO FINE MESH FULL MODEL WITH CLOSED BOUNDARIES AND CORRESPONDING HALF MODEL TO EXAMINE SNAPSHOTS

GEOSTUDIO SIMULATION

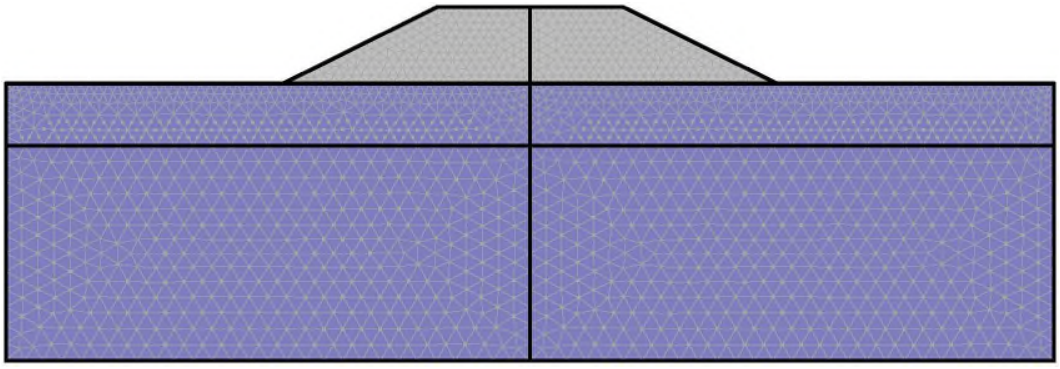

A) Fine mesh full model; 4259 nodes and 3202 elements; triangles mesh

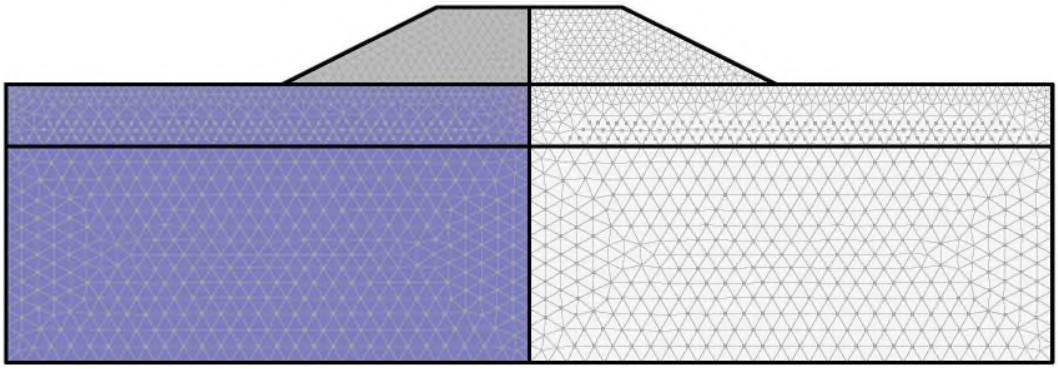

B) Corresponding half model

FIGURE 3.4: GEOSTUDIO FULL MODEL (NEITHER COARSE NOR FINE MESH) WITH OPEN SIDESLOPES AND CORRESPONDING HALF MODEL USED TO EXAMINE SNAPSHOTS

GEOSTUDIO SIMULATION

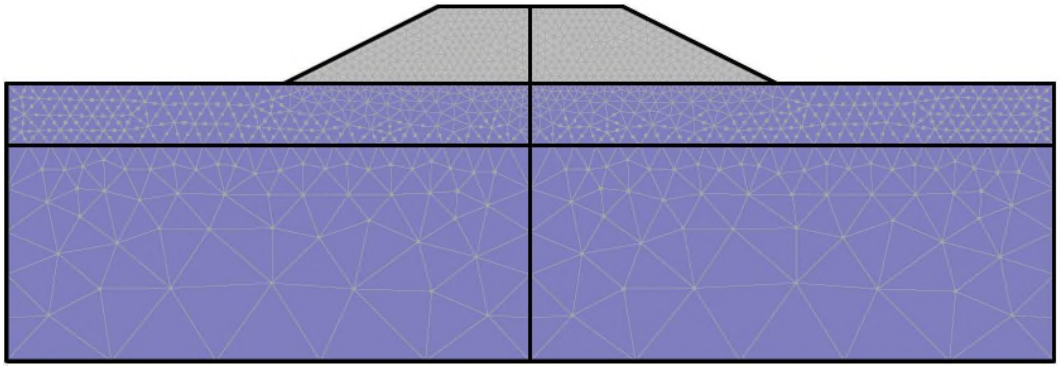

A) Full model (neither coarse nor fine mesh); 3124 nodes and 1712 elements; triangles mesh

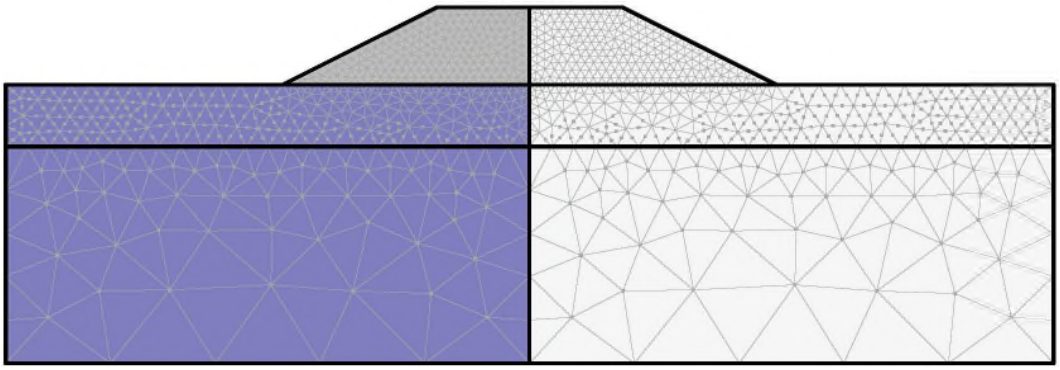

B) Corresponding half model

FIGURE 3.5: COMPARISON OF NUMERICAL RESULTS ON AUGUST 4 REPRESENTING SUMMER CONDITION FOR GEOSTUDIO COARSE MESH FULL MODEL WITH CLOSED BOUNDARIES AND CORRESPONDING HALF MODEL

GEOSTUDIO SIMULATION

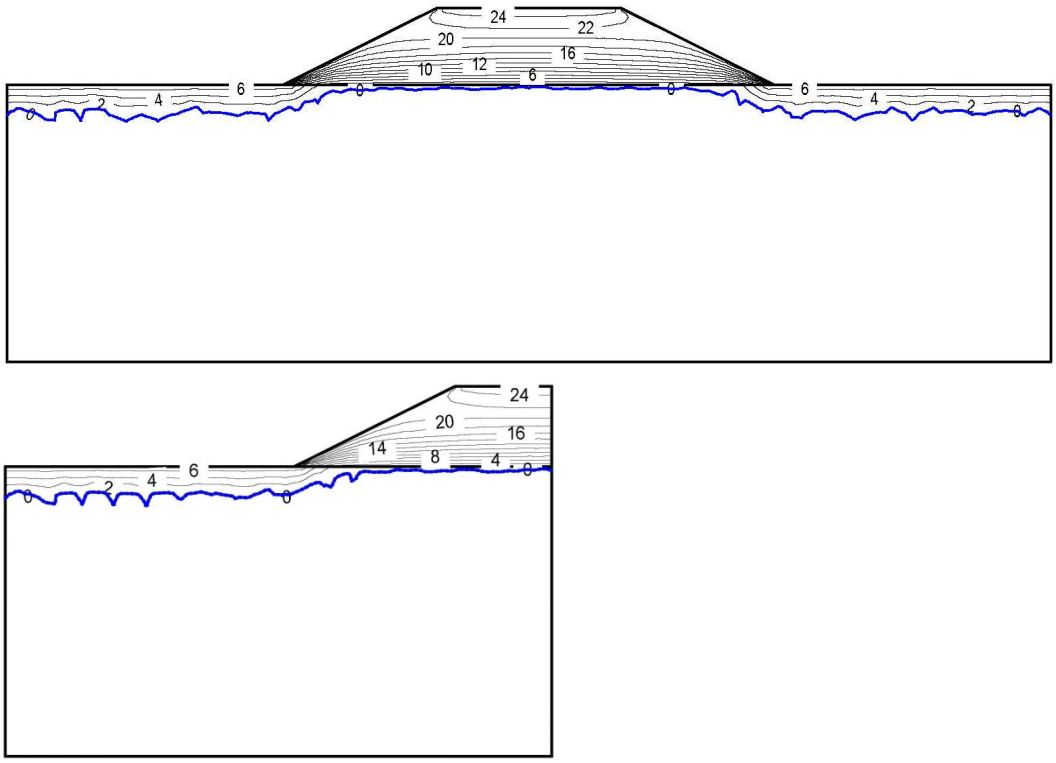

A) Isotherms in full model (top) and corresponding half model (bottom)

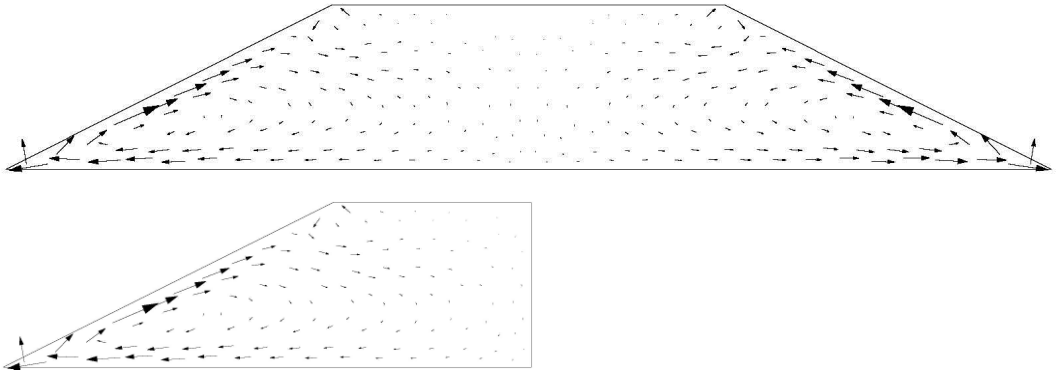

B) Air flow vectors in full model (top) and corresponding half model (bottom)

FIGURE 3.6: COMPARISON OF NUMERICAL RESULTS ON AUGUST 4 REPRESENTING SUMMER CONDITION FOR GEOSTUDIO FINE MESH FULL MODEL WITH CLOSED BOUNDARIES AND CORRESPONDING HALF MODEL

GEOSTUDIO SIMULATION

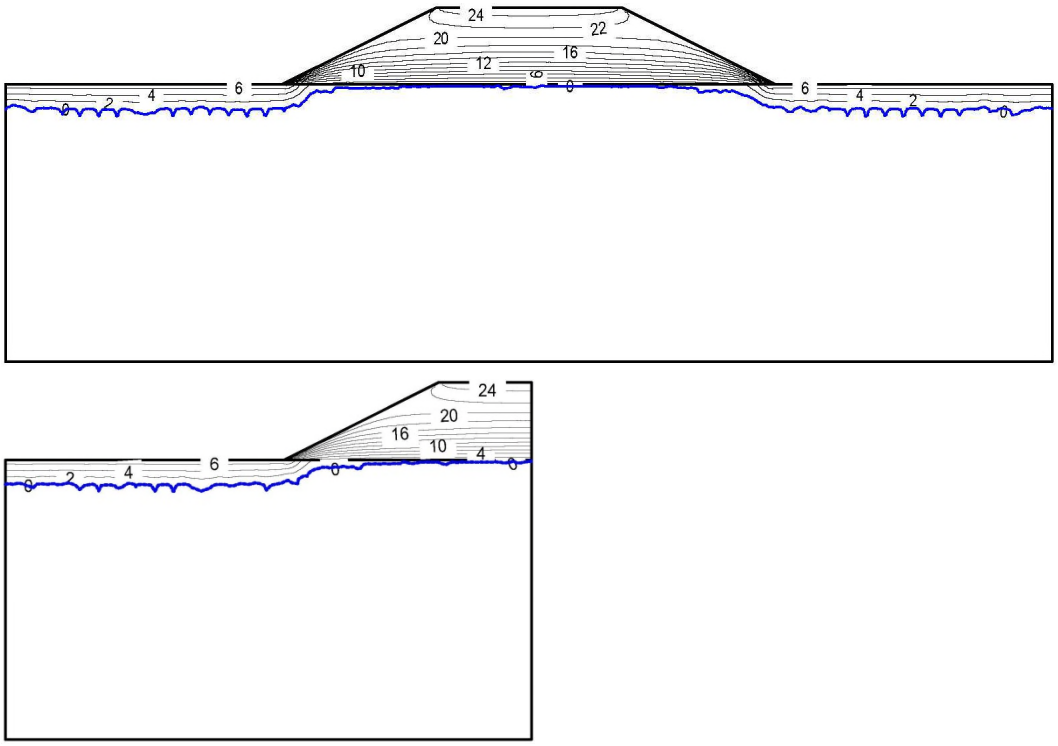

A) Isotherms in full model (top) and corresponding half model (bottom)

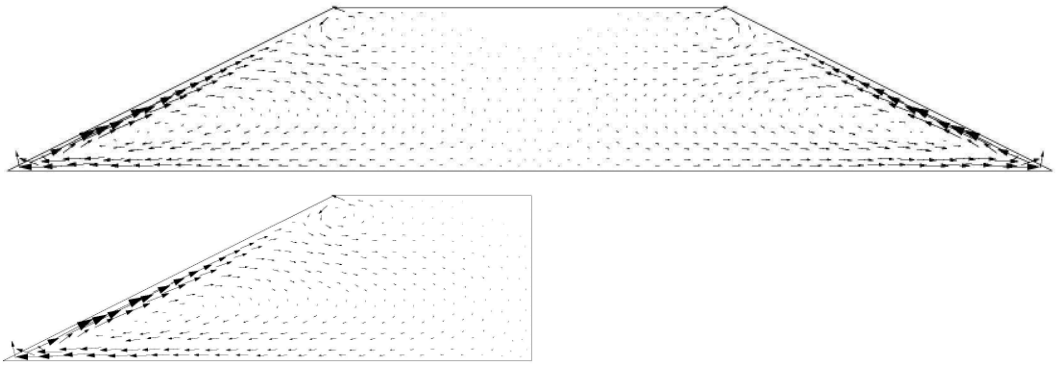

B) Air flow vectors in full model (top) and corresponding half model (bottom)

FIGURE 3.7: COMPARISON OF NUMERICAL RESULTS ON AUGUST 4 REPRESENTING SUMMER CONDITION FOR GEOSTUDIO FULL MODEL WITH OPEN SIDESLOPES AND CORRESPONDING HALF MODEL

GEOSTUDIO SIMULATION

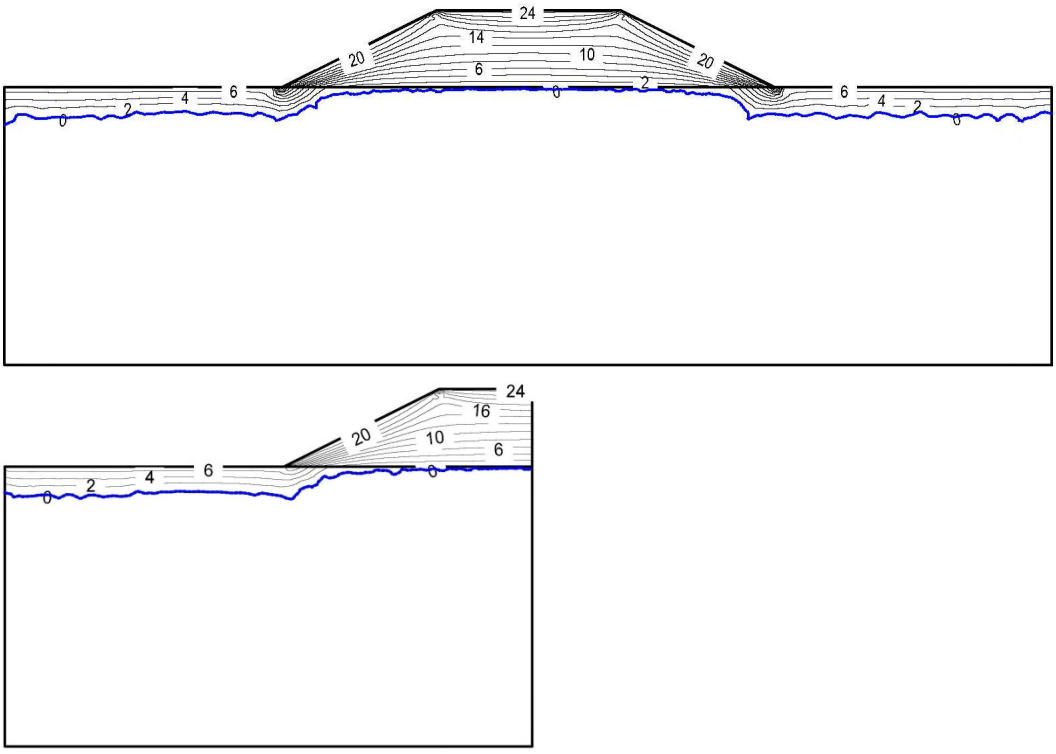

A) Isotherms in full model (top) and corresponding half model (bottom)

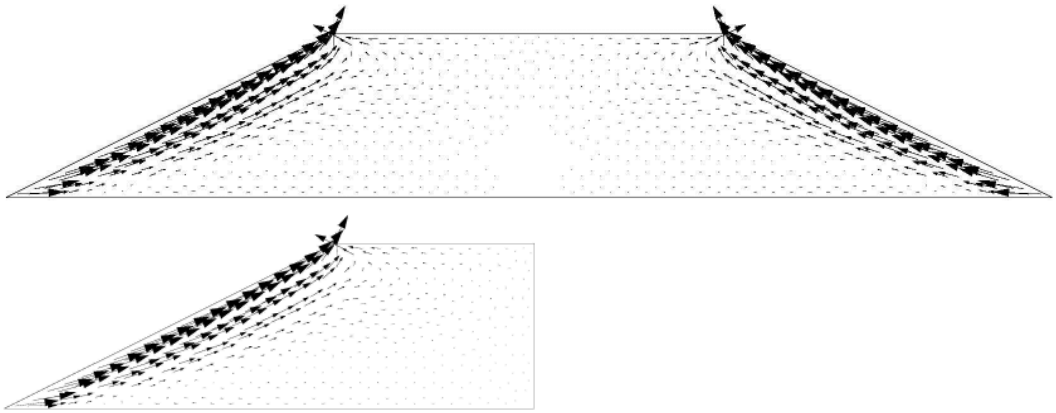

B) Air flow vectors in full model (top) and corresponding half model (bottom)

FIGURE 3.8: COMPARISON OF NUMERICAL RESULTS ON NOVEMBER 14 REPRESENTING FALL CONDITION FOR GEOSTUDIO COARSE MESH FULL MODEL WITH CLOSED BOUNDARIES AND CORRESPONDING HALF MODEL

GEOSTUDIO SIMULATION

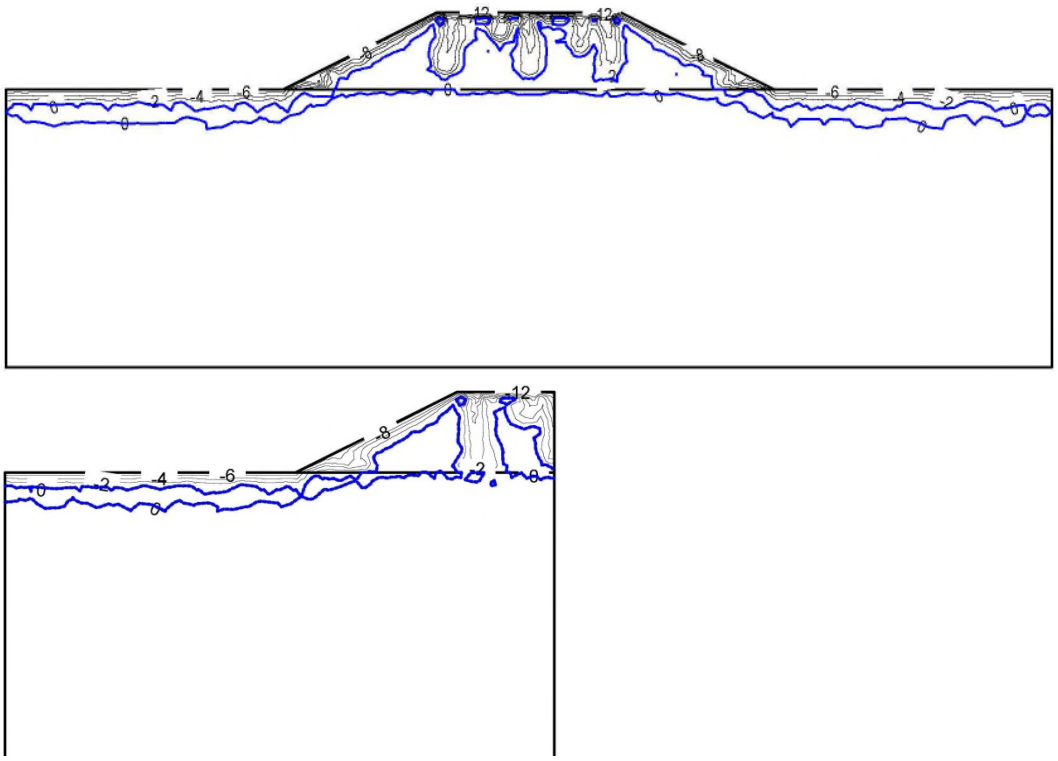

A) Isotherms in full model (top) and corresponding half model (bottom); Ra=225

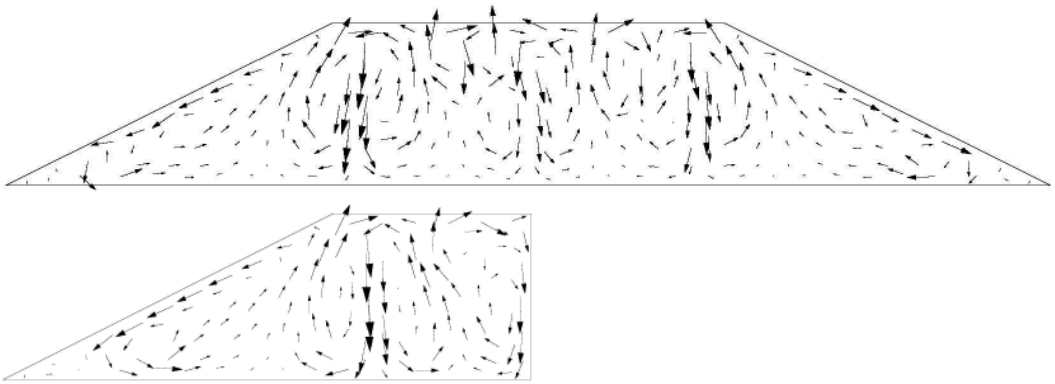

B) Air flow vectors in full model (top) and corresponding half model (bottom)

FIGURE 3.9: COMPARISON OF NUMERICAL RESULTS ON NOVEMBER 14 REPRESENTING FALL CONDITION FOR GEOSTUDIO FINE MESH FULL MODEL WITH CLOSED BOUNDARIES AND CORRESPONDING HALF MODEL

GEOSTUDIO SIMULATION

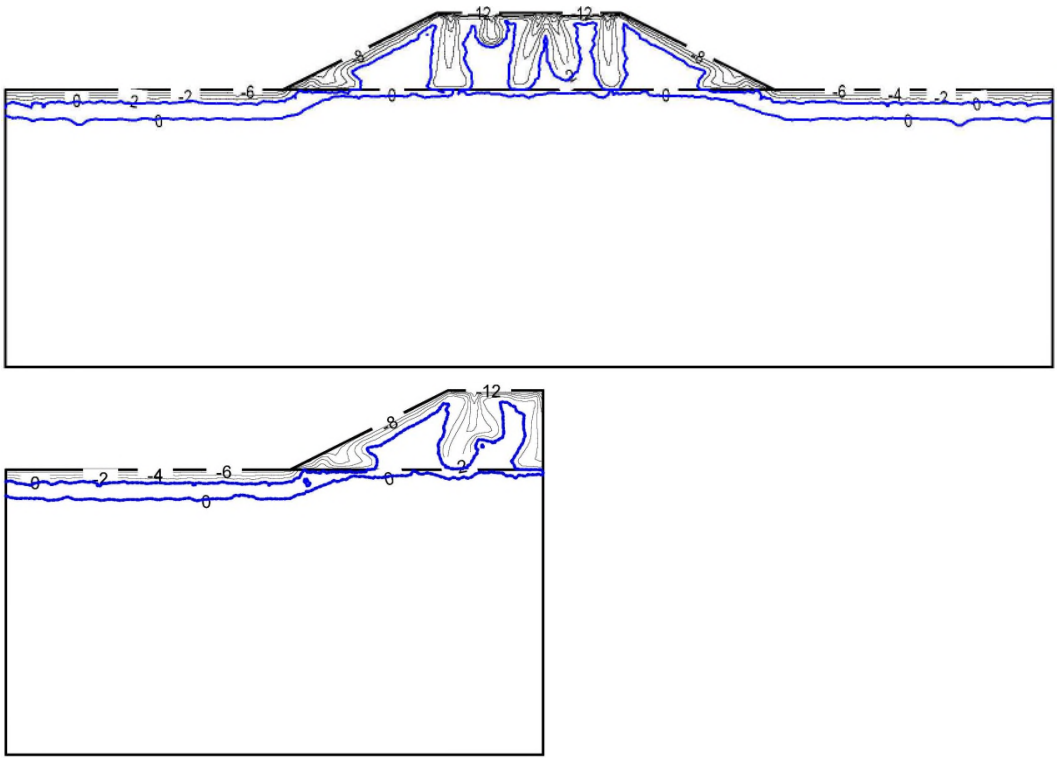

A) Isotherms in full model (top) and corresponding half model (bottom); Ra=225

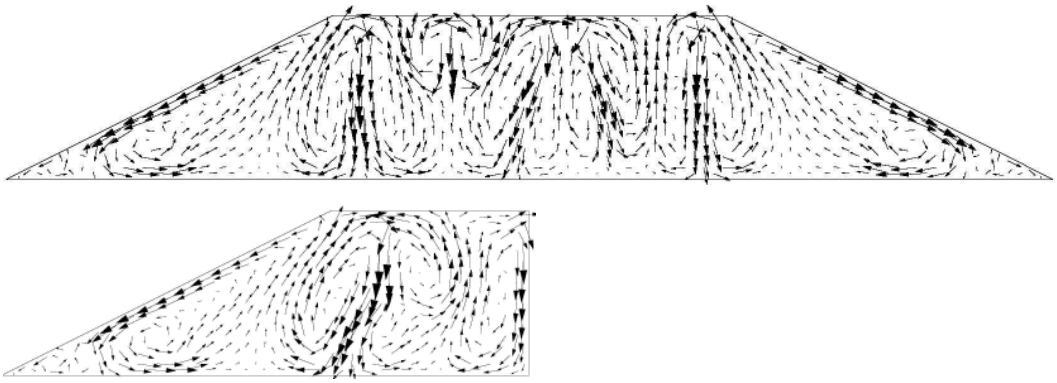

B) Air flow vectors in full model (top) and corresponding half model (bottom)

FIGURE 3.10: COMPARISON OF NUMERICAL RESULTS ON NOVEMBER 14 REPRESENTING FALL CONDITION FOR GEOSTUDIO FULL MODEL WITH OPEN SIDESLOPES AND CORRESPONDING HALF MODEL

GEOSTUDIO SIMULATION

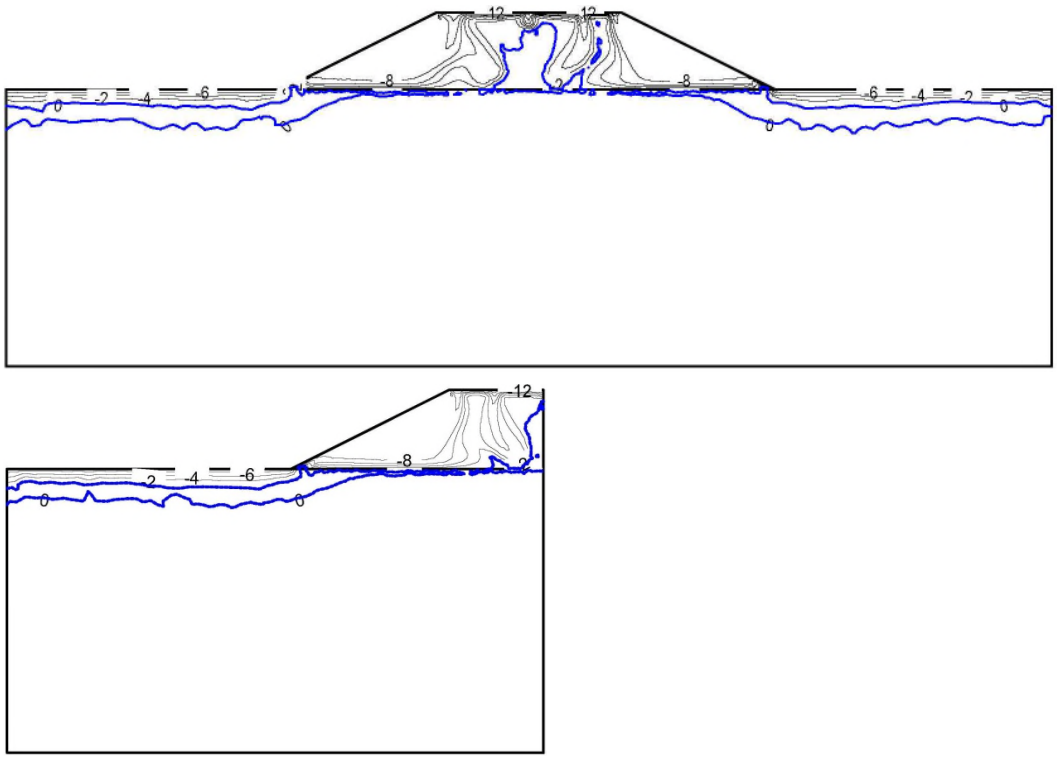

A) Isotherms in full model (top) and corresponding half model (bottom); Ra=225

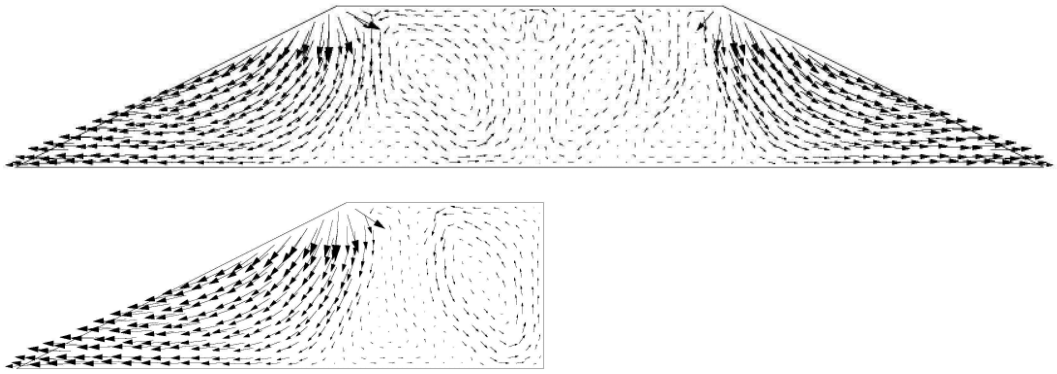

B) Air flow vectors in full model (top) and corresponding half model (bottom)

FIGURE 3.11: COMPARISON OF NUMERICAL RESULTS ON JANUARY 31 REPRESENTING WINTER CONDITION FOR GEOSTUDIO COARSE MESH FULL MODEL WITH CLOSED BOUNDARIES AND CORRESPONDING HALF MODEL

GEOSTUDIO SIMULATION

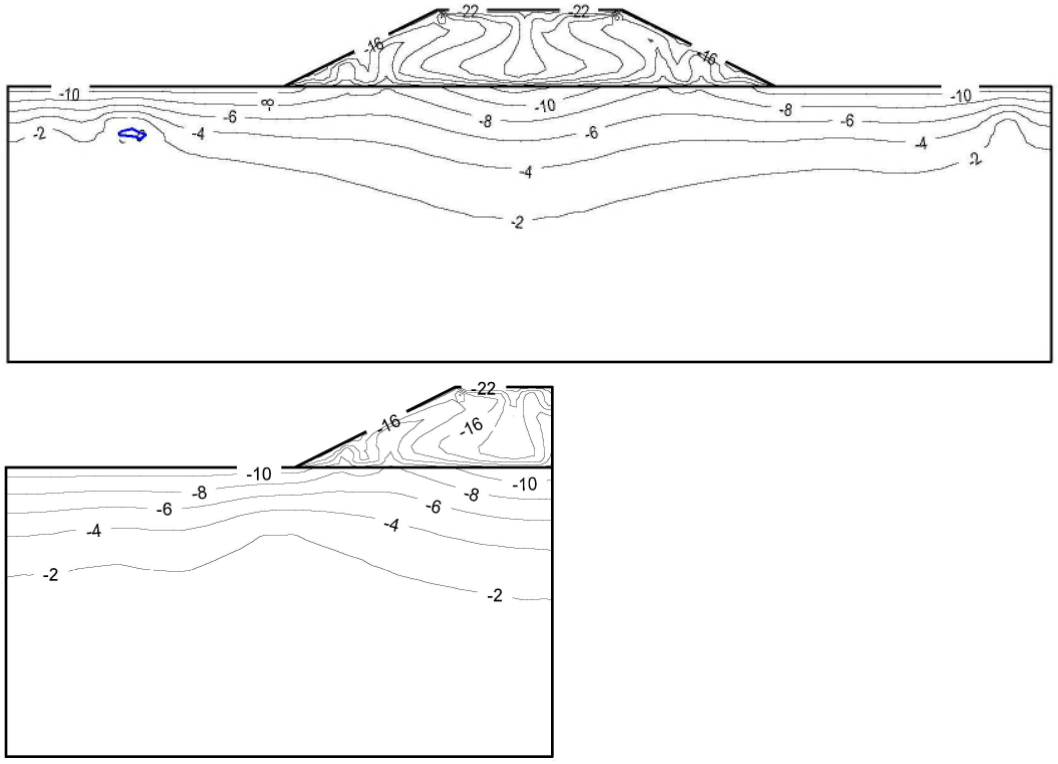

A) Isotherms in full model (top) and corresponding half model (bottom); Ra=175

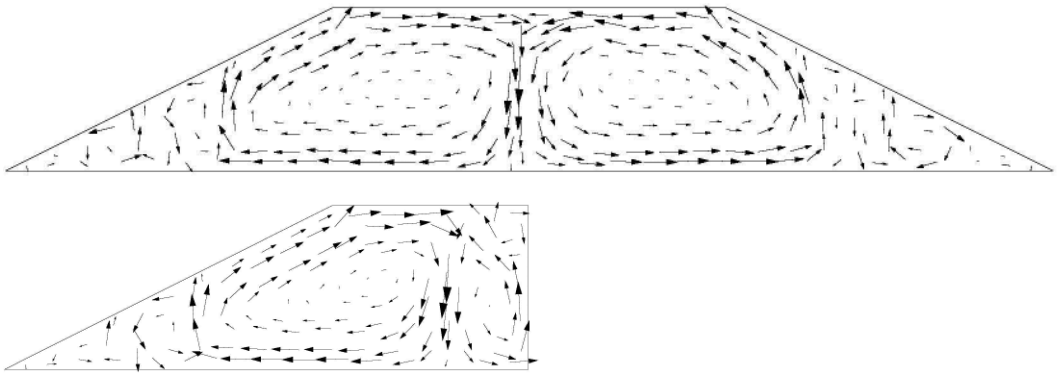

B) Air flow vectors in full model (top) and corresponding half model (bottom)

FIGURE 3.12: COMPARISON OF NUMERICAL RESULTS ON JANUARY 31 REPRESENTING WINTER CONDITION FOR GEOSTUDIO FINE MESH FULL MODEL WITH CLOSED BOUNDARIES AND CORRESPONDING HALF MODEL

GEOSTUDIO SIMULATION

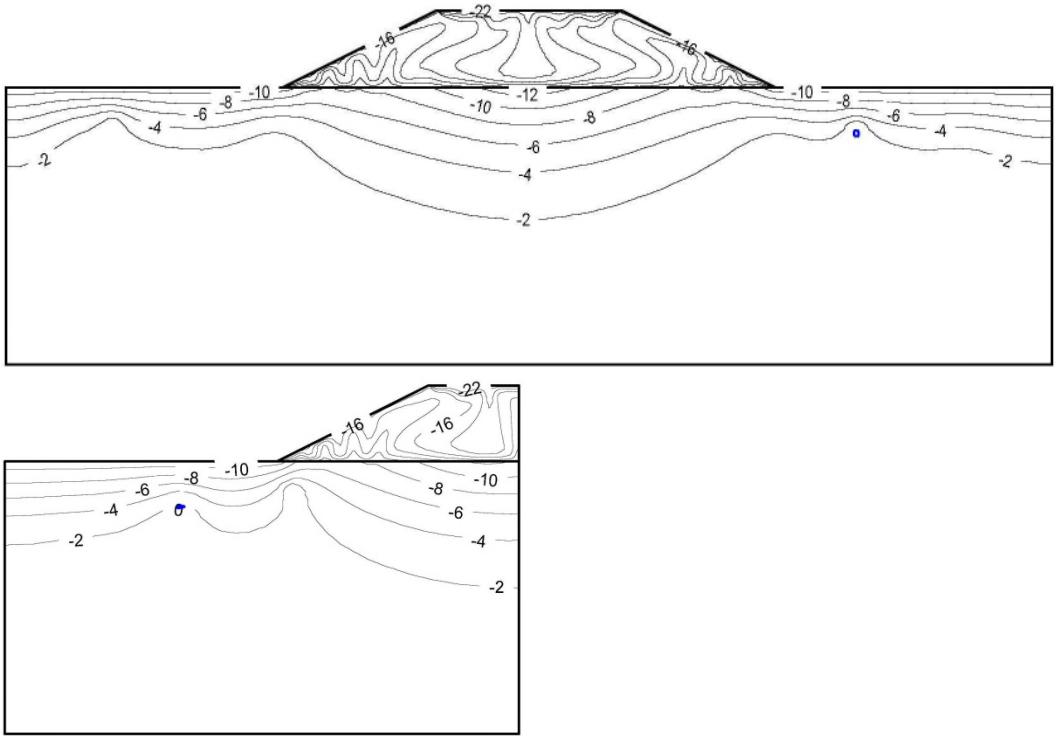

A) Isotherms in full model (top) and corresponding half model (bottom); Ra=175

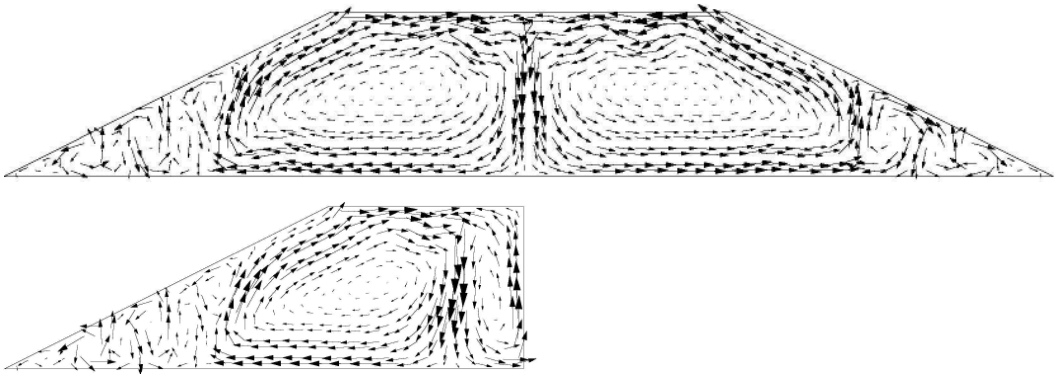

B) Air flow vectors in full model (top) and corresponding half model (bottom)

FIGURE 3.13: COMPARISON OF NUMERICAL RESULTS ON JANUARY 31 REPRESENTING WINTER CONDITION FOR GEOSTUDIO FULL MODEL WITH OPEN SIDESLOPES AND CORRESPONDING HALF MODEL

GEOSTUDIO SIMULATION

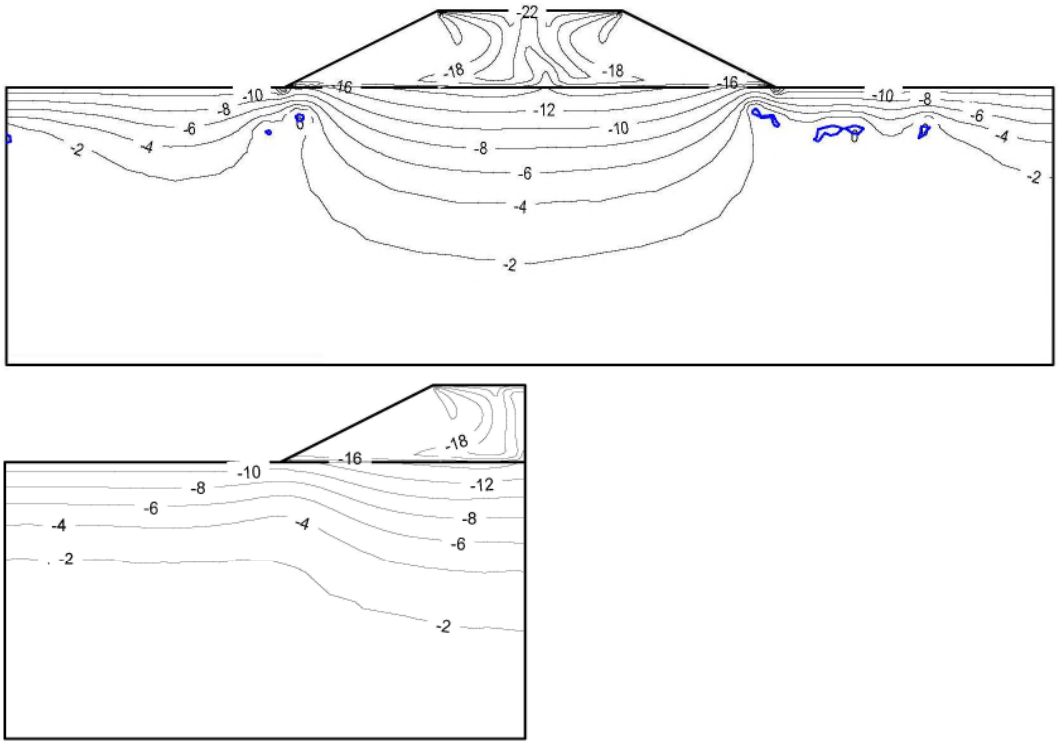

A) Isotherms in full model (top) and corresponding half model (bottom); Ra=175

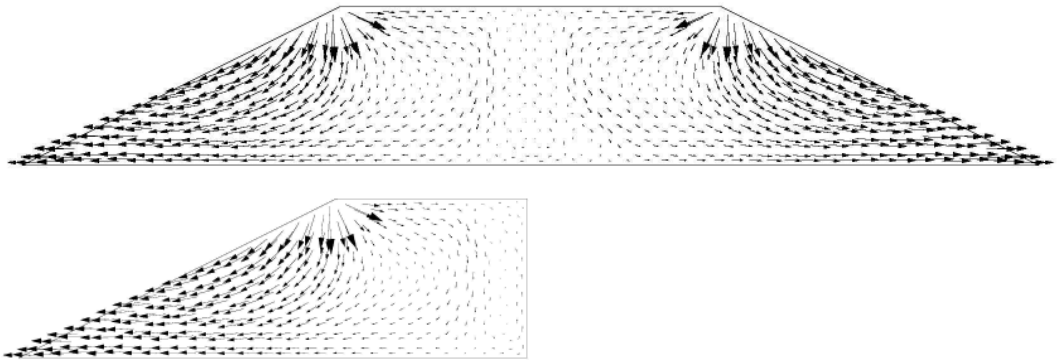

B) Air flow vectors in full model (top) and corresponding half model (bottom)

FIGURE 3.14: COMPARISON OF NUMERICAL RESULTS ON MAY 1 REPRESENTING SPRING CONDITION FOR GEOSTUDIO COARSE MESH FULL MODEL WITH CLOSED BOUNDARIES AND CORRESPONDING HALF MODEL

GEOSTUDIO SIMULATION

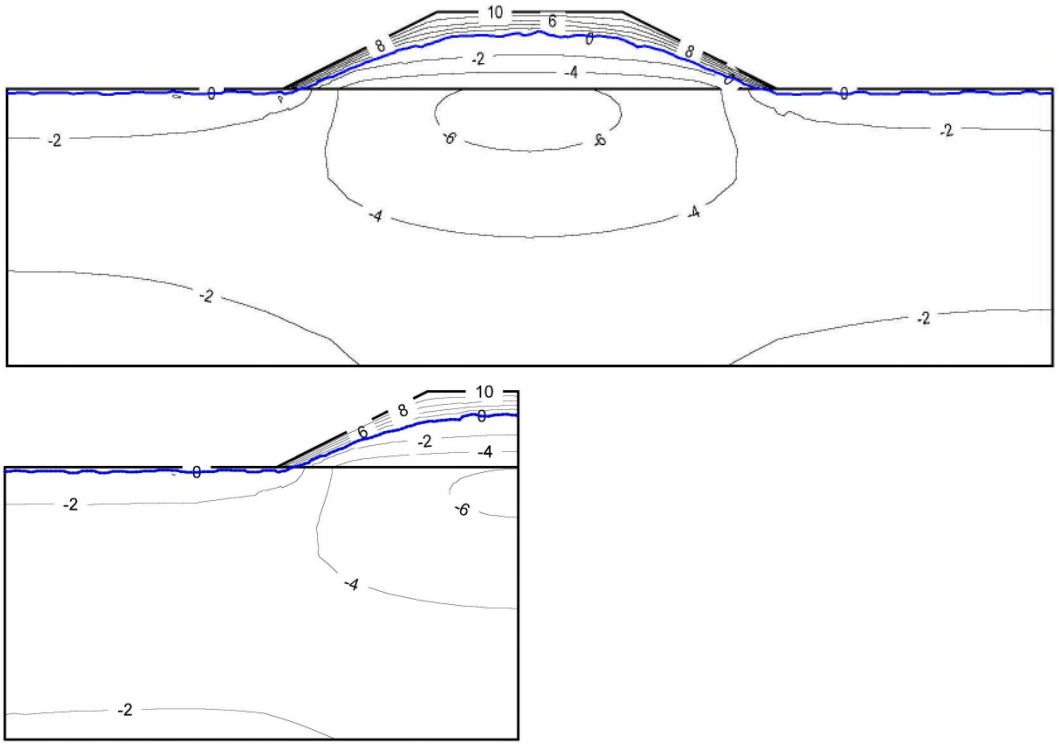

A) Isotherms in full model (top) and corresponding half model (bottom)

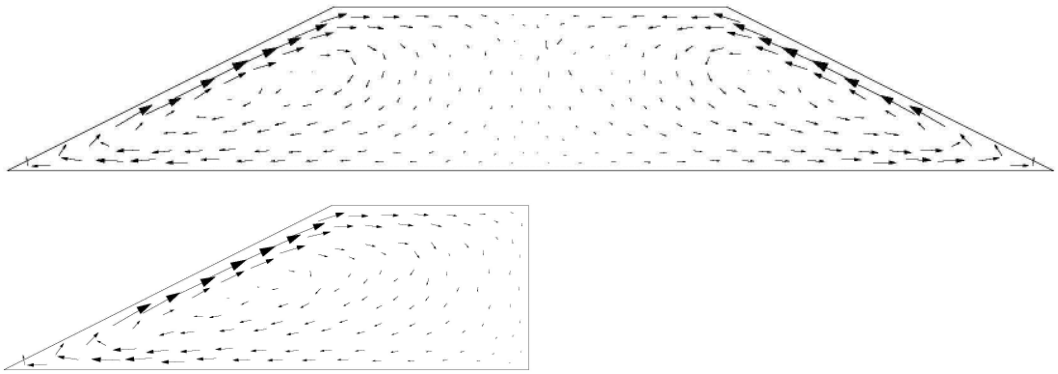

B) Air flow vectors in full model (top) and corresponding half model (bottom)

FIGURE 3.15: COMPARISON OF NUMERICAL RESULTS ON MAY 1 REPRESENTING SPRING CONDITION FOR GEOSTUDIO FINE MESH FULL MODEL WITH CLOSED BOUNDARIES AND CORRESPONDING HALF MODEL

GEOSTUDIO SIMULATION

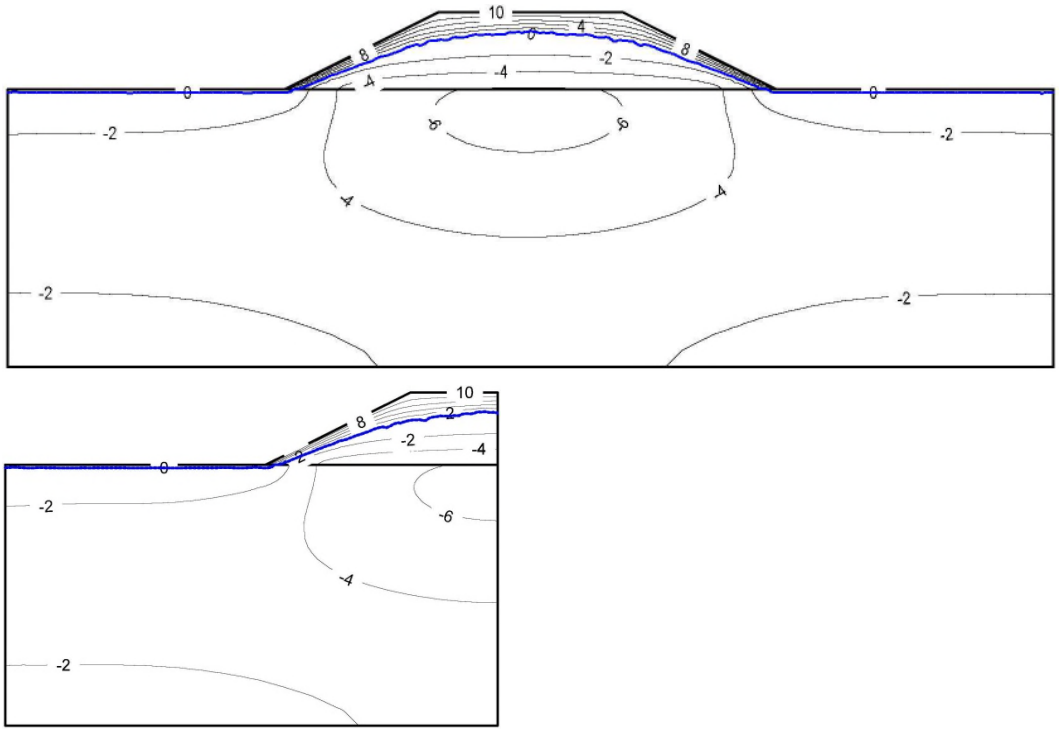

A) Isotherms in full model (top) and corresponding half model (bottom)

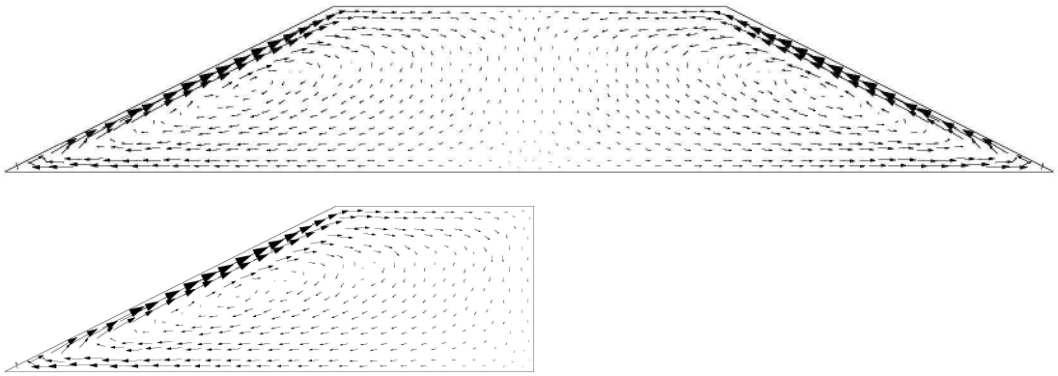

B) Air flow vectors in full model (top) and corresponding half model (bottom)

FIGURE 3.16: COMPARISON OF NUMERICAL RESULTS ON MAY 1 REPRESENTING SPRING CONDITION FOR GEOSTUDIO FULL MODEL WITH OPEN SIDESLOPES AND CORRESPONDING HALF MODEL

GEOSTUDIO SIMULATION

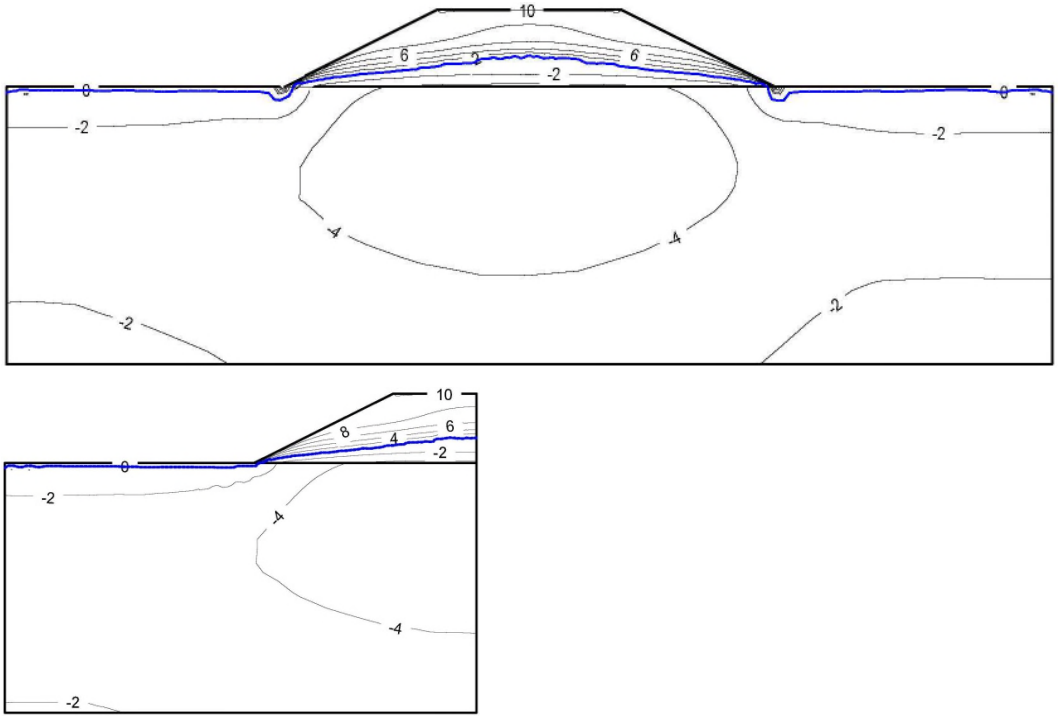

A) Isotherms in full model (top) and corresponding half model (bottom)

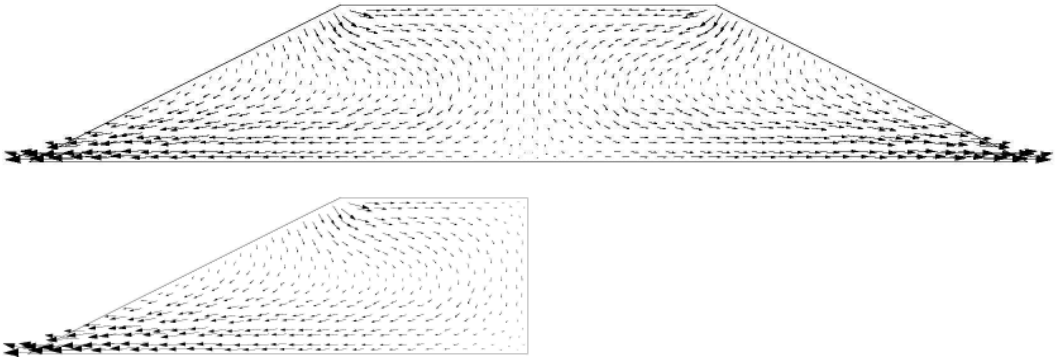

B) Air flow vectors in full model (top) and corresponding half model (bottom)

FIGURE 3.17: GEOSTUDIO HALF MODEL WITH CLOSED BOUNDARIES AND CORRESPONDING FULL MODEL TO EXAMINE TRENDS

GEOSTUDIO SIMULATION

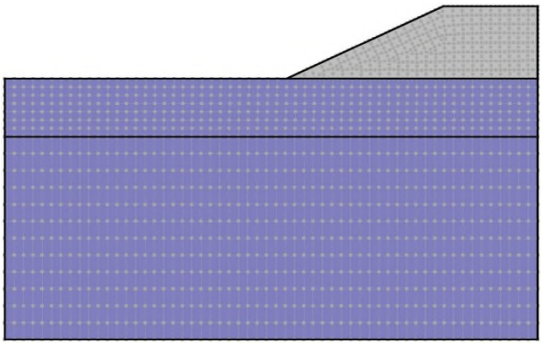

A) Half model; 1661 nodes and 1241 elements; quads and triangles mesh

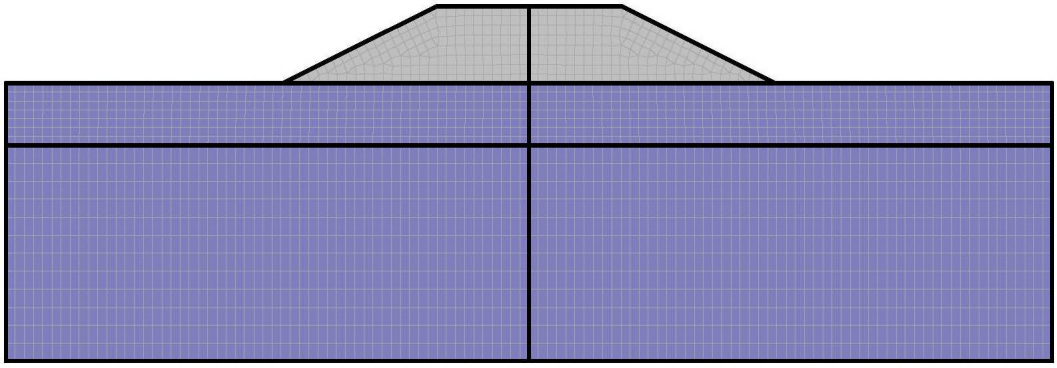

B) Corresponding full model; 3286 nodes and 2482 elements

FIGURE 3.18: TRENDS IN GEOSTUDIO HALF MODEL WITH CLOSED BOUNDARIES AND CORRESPONDING FULL MODEL – LOCATIONS 2 AND 5

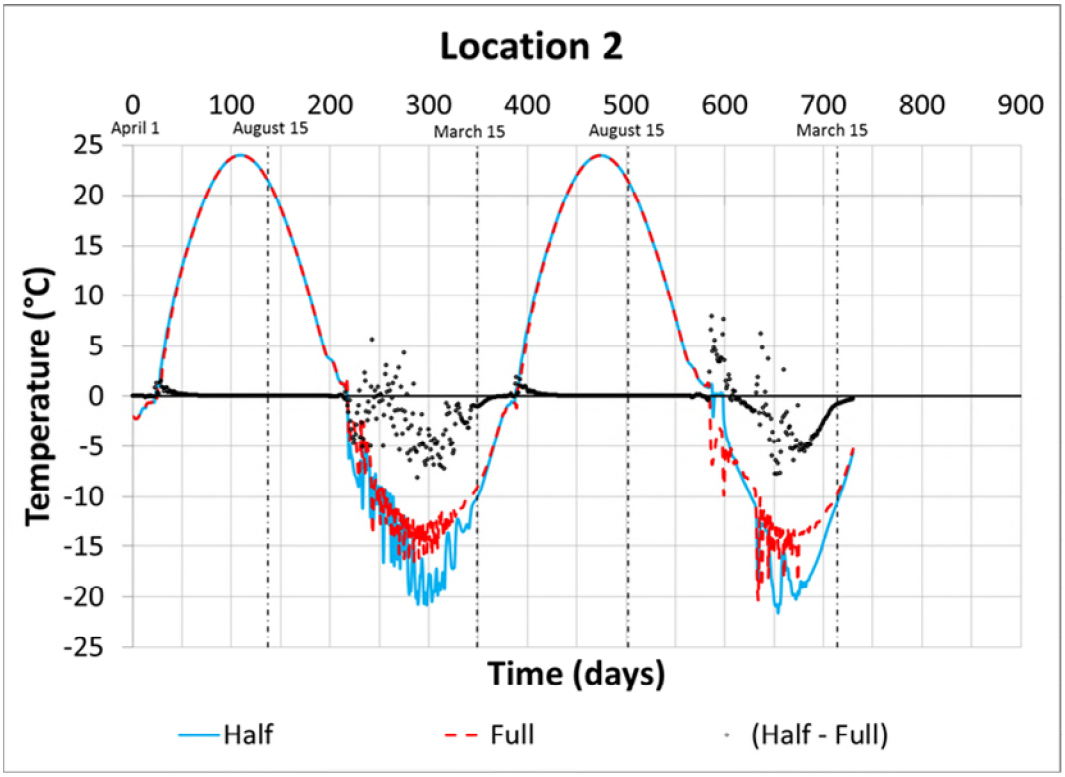

A) Time-temperature plots in Location 11

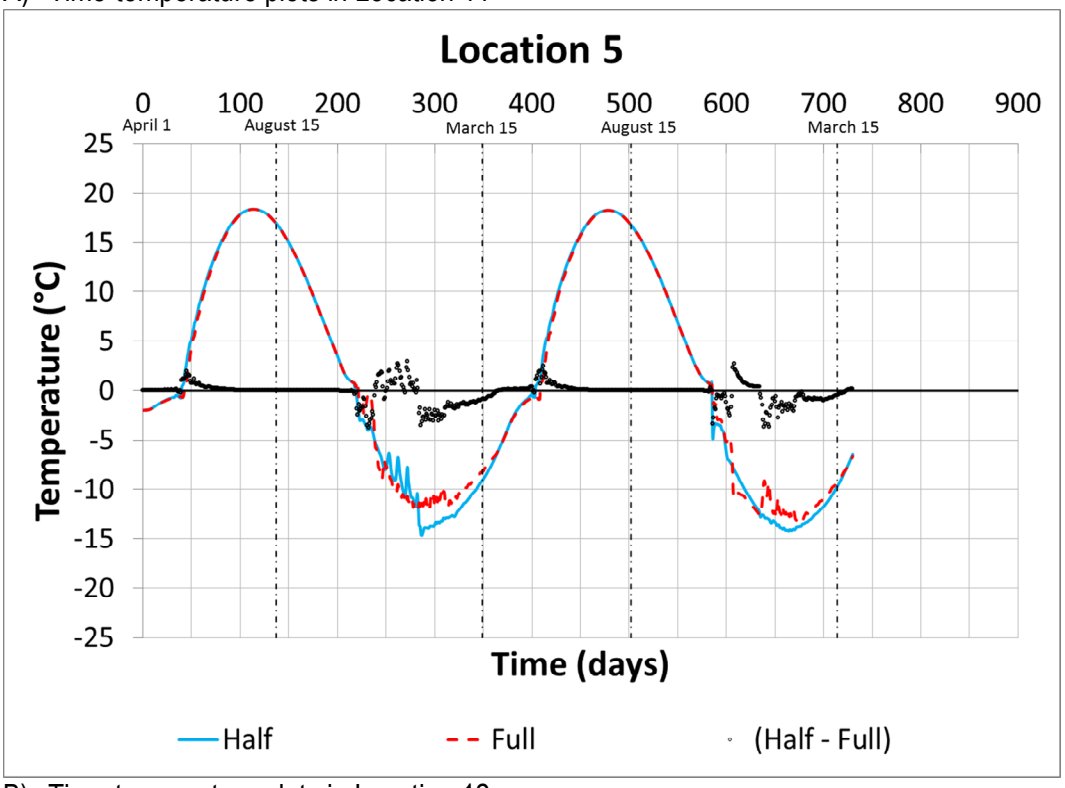

B) Time-temperature plots in Location 12

FIGURE 3.19: TRENDS IN GEOSTUDIO HALF MODEL WITH CLOSED BOUNDARIES AND CORRESPONDING FULL MODEL – LOCATIONS 7 AND 9

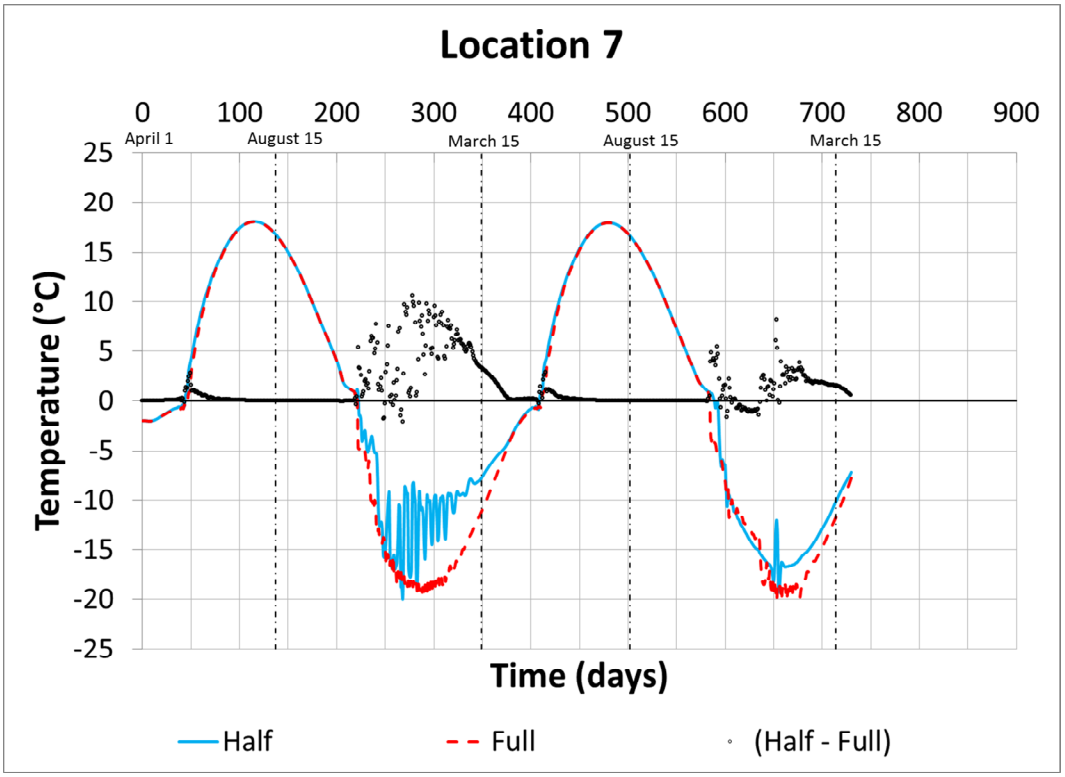

A) Time-temperature plots in Location 13

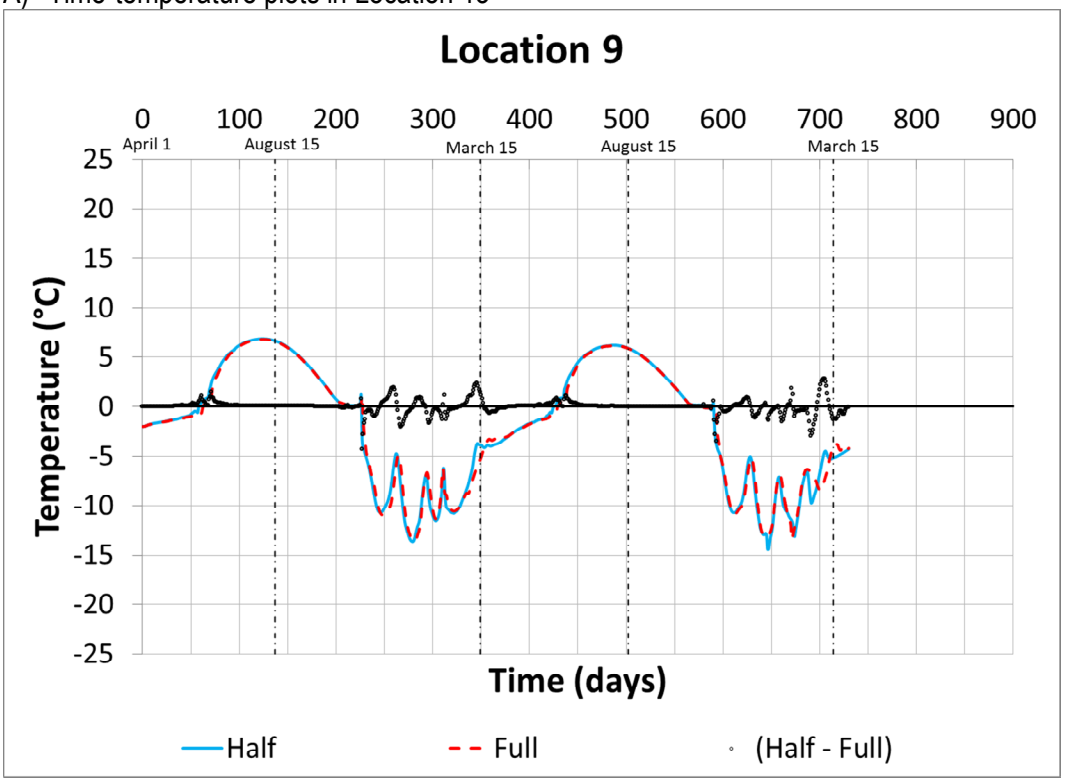

B) Time-temperature plots in Location 14

FIGURE 3.20: TRENDS IN GEOSTUDIO HALF MODEL WITH CLOSED BOUNDARIES AND CORRESPONDING FULL MODEL – LOCATIONS 11 AND 15

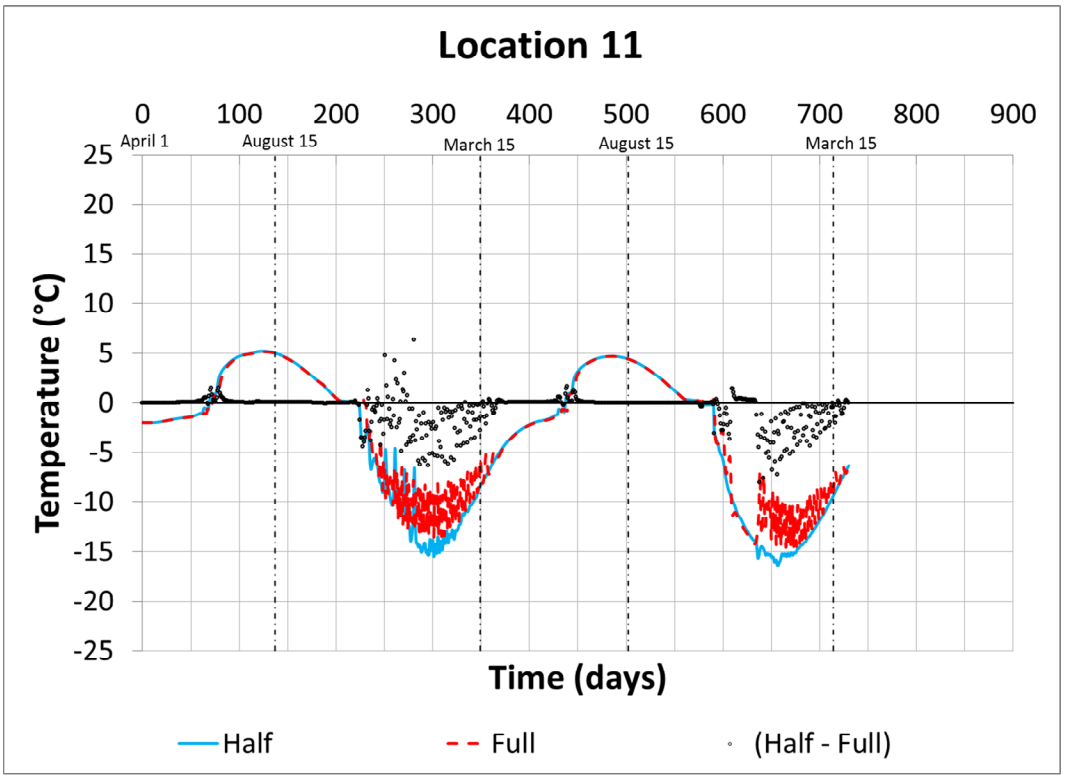

A) Time-temperature plots in Location 13

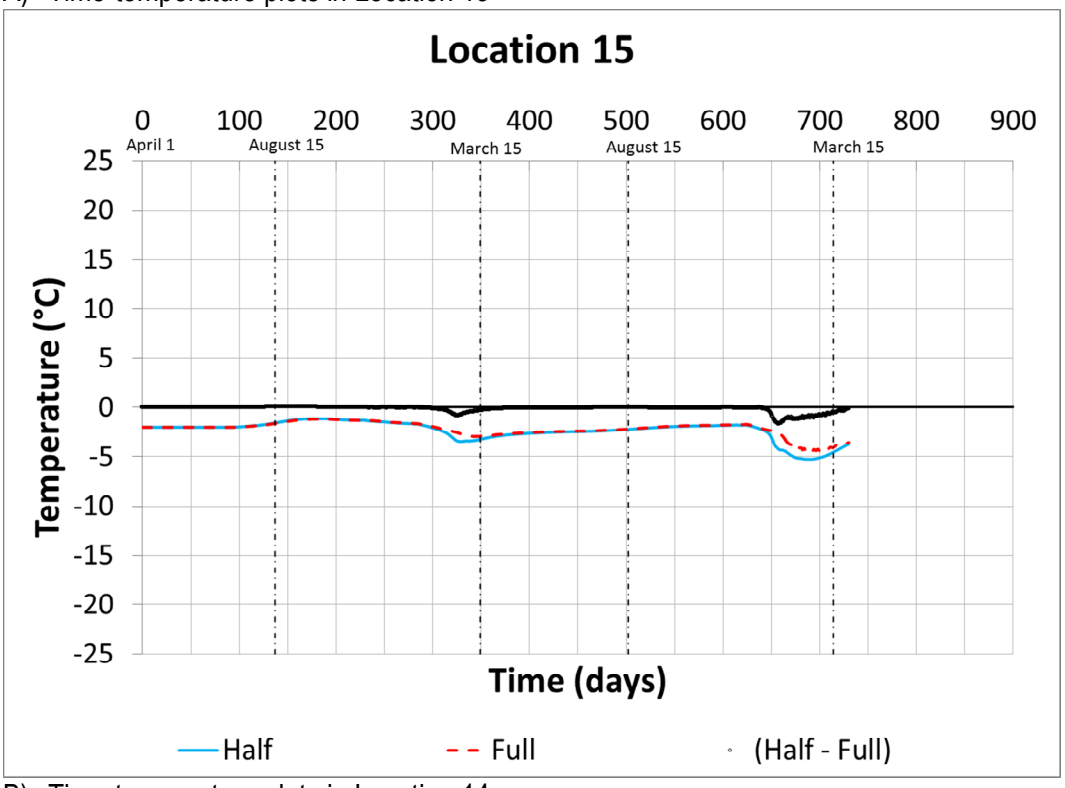

B) Time-temperature plots in Location 14

FIGURE 3.21: THREE GEOSTUDIO MODELS WITH CLOSED BOUNDARIES USED TO EXAMINE IN TERMS OF SNAPSHOTS REPEATABILITY OF MODELING RESULTS

GEOSTUDIO SIMULATION

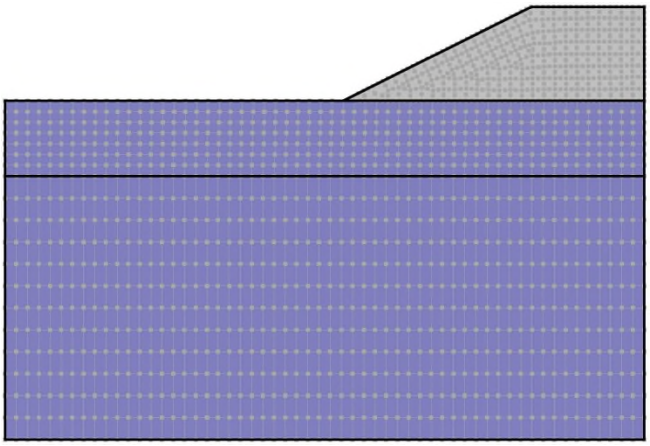

A) Coarse mesh model; 1661 nodes and 1241 elements; quads and triangles mesh

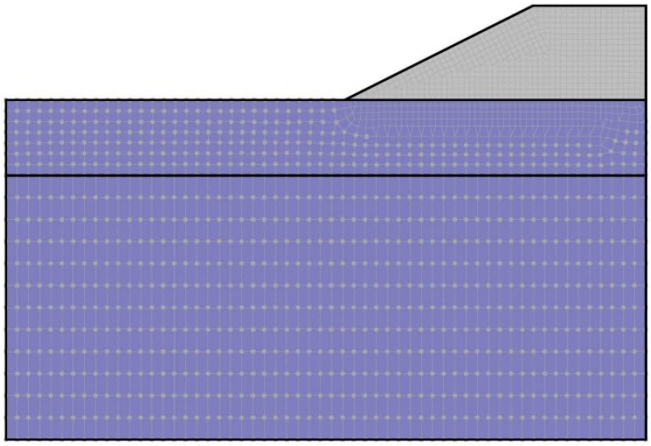

B) Medium mesh model; 3250 nodes and 1876 elements; quads and traingles mesh

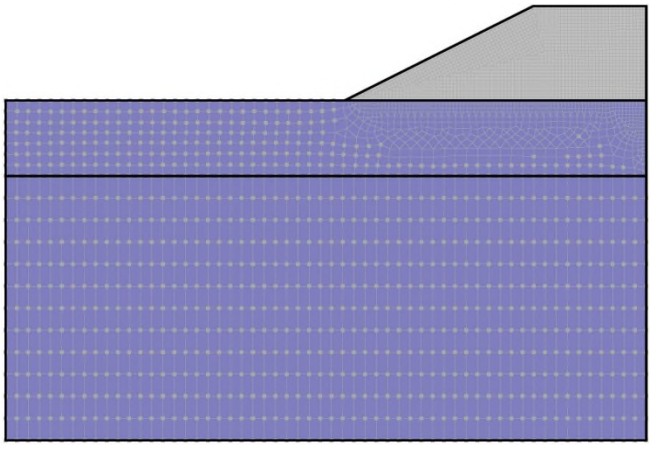

C) Fine mesh model; 6907 nodes and 3323 elements; quads and triangles mesh

FIGURE 3.22: COMPARISON OF NUMERICAL RESULTS ON NOVEMBER 14 REPRESENTING FALL CONDITION FOR GEOSTUDIO COARSE MESH MODEL WITH CLOSED BOUNDARIES

GEOSTUDIO SIMULATION

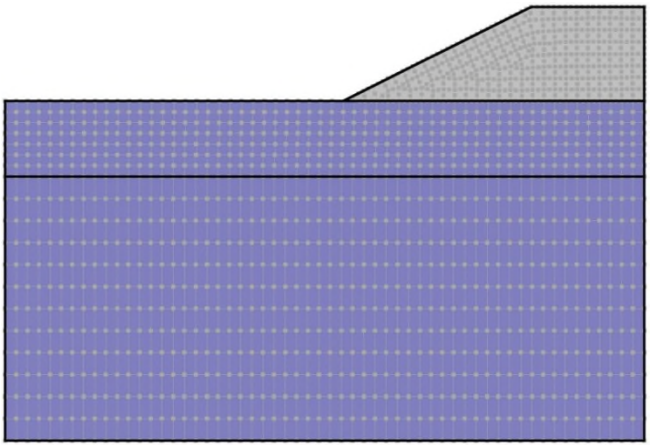

A) Coarse mesh model; 1661 nodes and 1241 elements

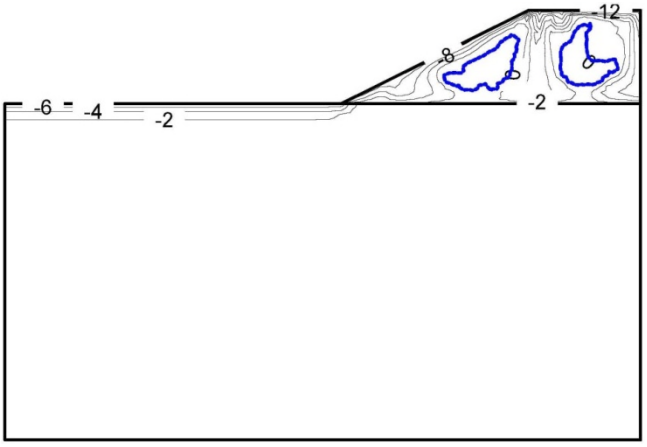

B) Temperature isotherms for run A; Ra=199

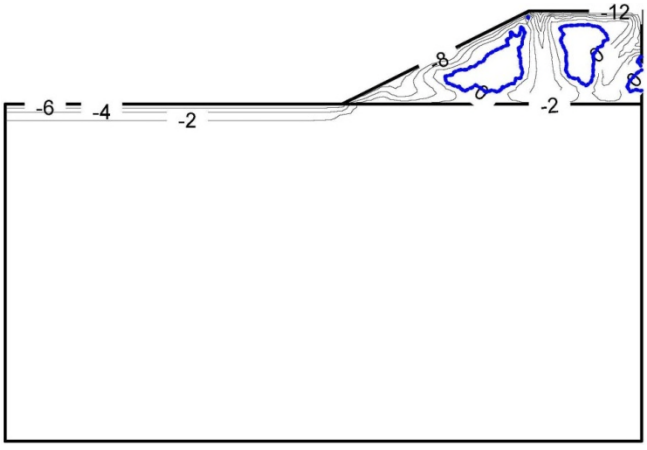

C) Temperature isotherms for run B; Ra=199

FIGURE 3.23: COMPARISON OF NUMERICAL RESULTS ON NOVEMBER 14 REPRESENTING FALL CONDITION FOR GEOSTUDIO MEDIUM MESH MODEL

GEOSTUDIO SIMULATION

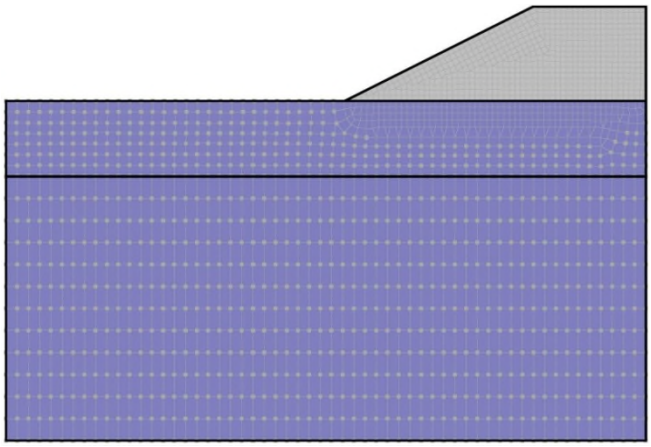

A) Medium mesh model; 3250 nodes and 1876 elements

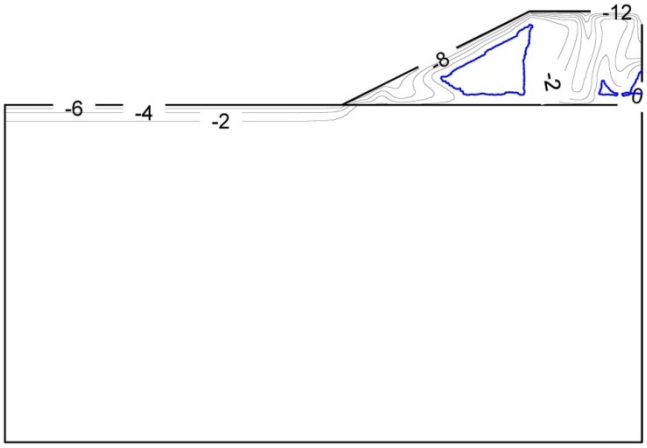

B) Temperature isotherms for run A; Ra=199

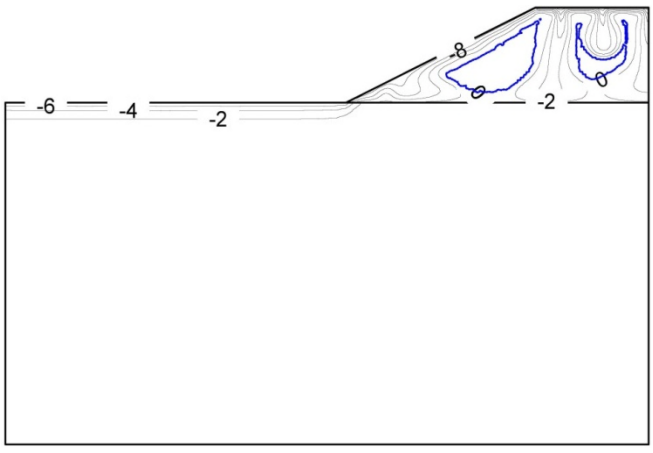

C) Temperature isotherms for run B; Ra=199

FIGURE 3.24: COMPARISON OF NUMERICAL RESULTS ON NOVEMBER 14 REPRESENTING FALL CONDITION FOR GEOSTUDIO FINE MESH MODEL

GEOSTUDIO SIMULATION

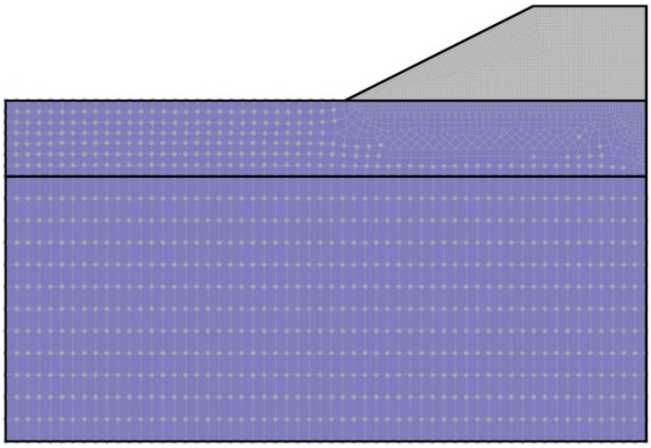

A) Fine mesh model; 6907 nodes and 3323 elements

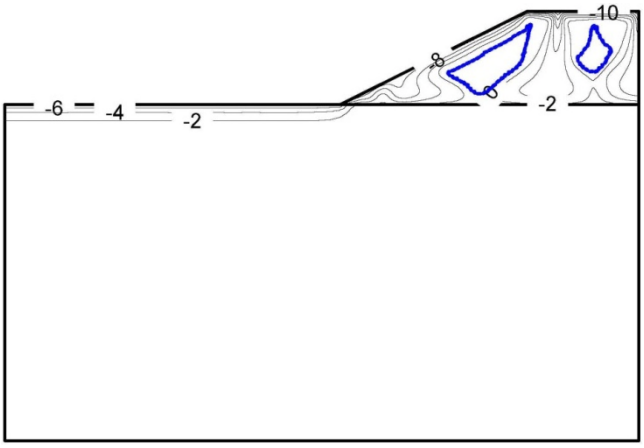

B) Temperature isotherms for run A; Ra=199

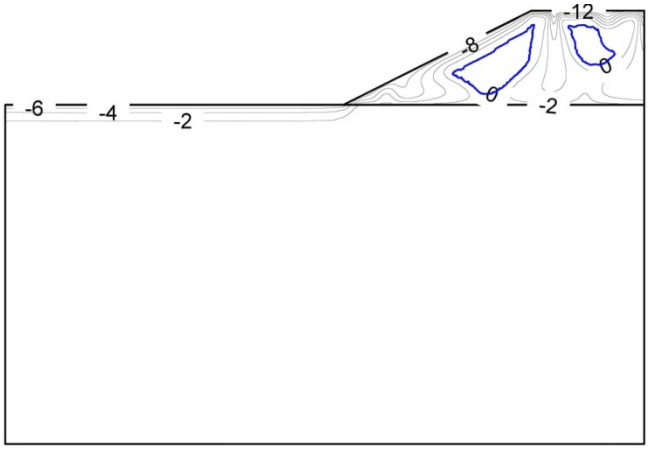

C) Temperature isotherms for run B; Ra=199

FIGURE 3.25: COMPARISON OF NUMERICAL RESULTS ON JANUARY 31 REPRESENTING WINTER CONDITION FOR GEOSTUDIO COARSE MESH MODEL

GEOSTUDIO SIMULATION

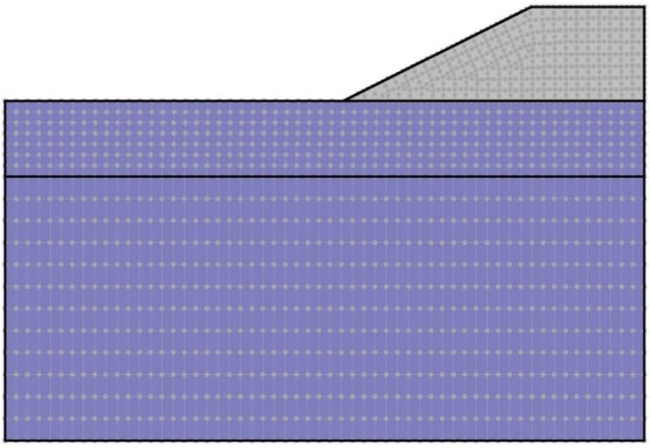

A) Coarse mesh model; 1661 nodes and 1241 elements

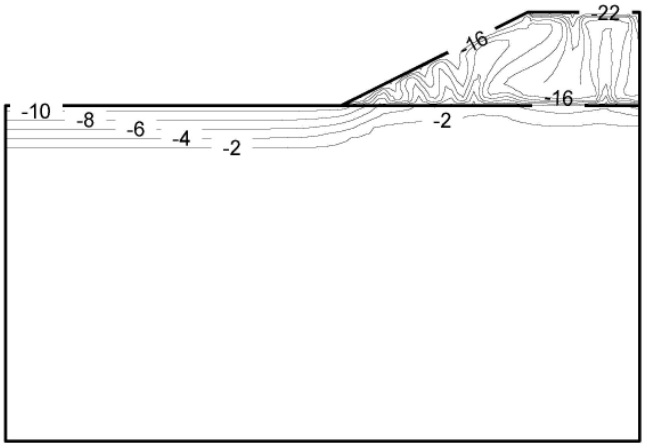

B) Temperature isotherms for run A; Ra=280

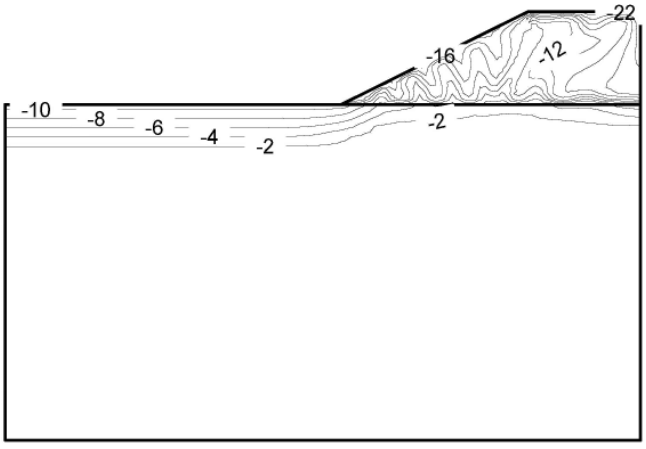

C) Temperature isotherms for run B; Ra=280

FIGURE 3.26: COMPARISON OF NUMERICAL RESULTS ON JANUARY 31 REPRESENTING WINTER CONDITION FOR GEOSTUDIO MEDIUM MESH MODEL

GEOSTUDIO SIMULATION

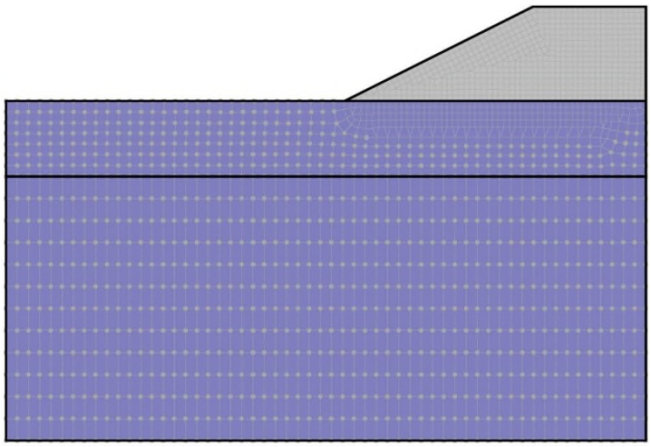

A) Medium mesh model; 3250 nodes and 1876 elements

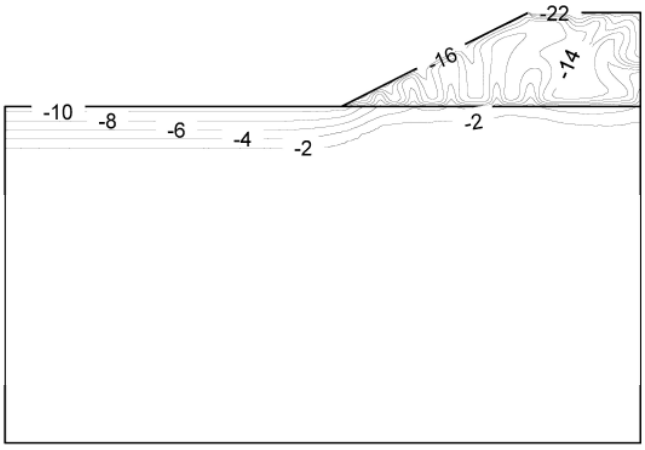

B) Temperature isotherms for run A; Ra=280

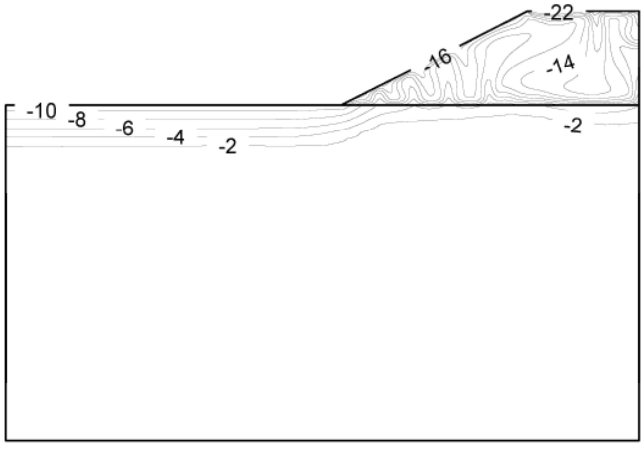

C) Temperature isotherms for run B; Ra=280

FIGURE 3.27: COMPARISON OF NUMERICAL RESULTS ON JANUARY 31 REPRESENTING FALL CONDITION FOR GEOSTUDIO FINE MESH MODEL

GEOSTUDIO SIMULATION

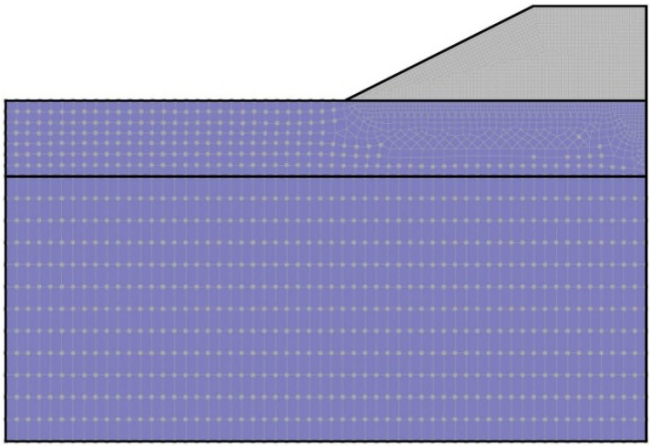

A) Fine mesh model; 6907 nodes and 3323 elements

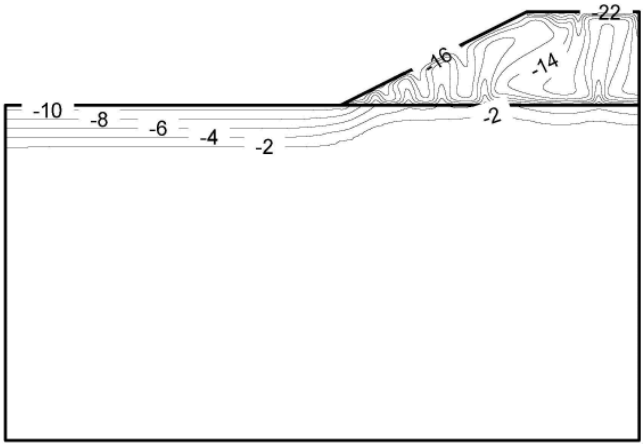

B) Temperature isotherms for run A; Ra=283

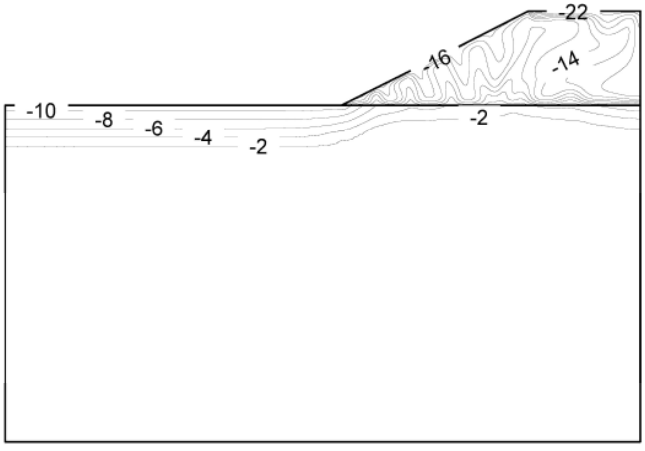

C) Temperature isotherms for run B; Ra=283

FIGURE 3.28: GEOSTUDIO COARSE AND FINE MESH MODELS USED TO EXAMINE IN TERMS OF TRENDS REPEATABILITY OF MODELING RESULTS

GEOSTUDIO SIMULATION

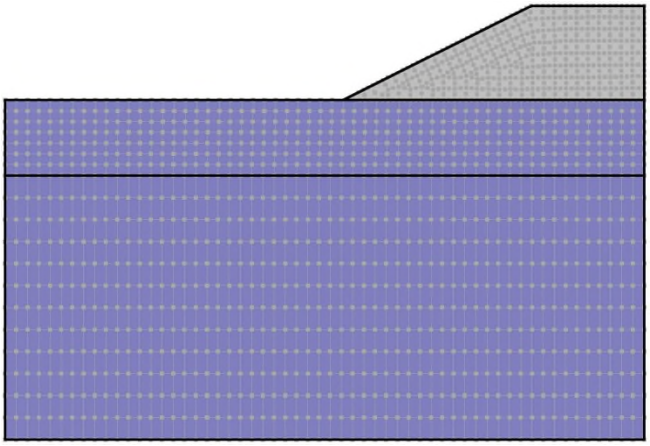

A) Coarse mesh model; 1661 nodes and 1241 elements; quads and triangles mesh

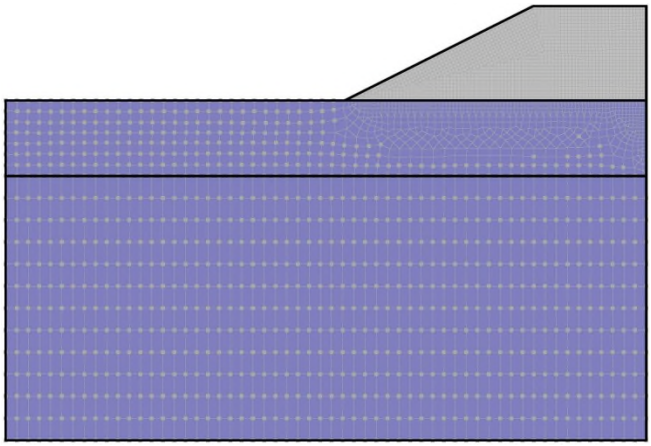

B) Fine mesh model; 6907 nodes and 3323 elements; quads and triangles mesh

FIGURE 3.29: TRENDS IN GEOSTUDIO COARSE AND FINE MESH MODEL BOTH WITH CLOSED BOUNDARIES – LOCATIONS 1 AND 2

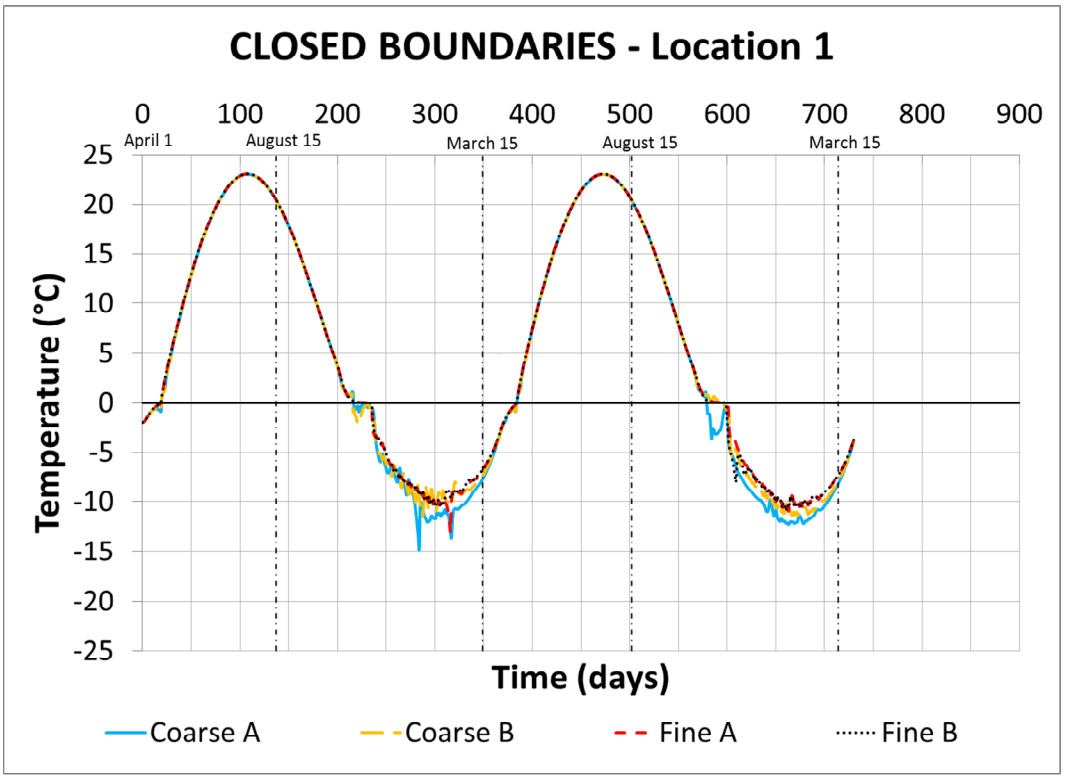

A) Time-temperature plots in Location 1

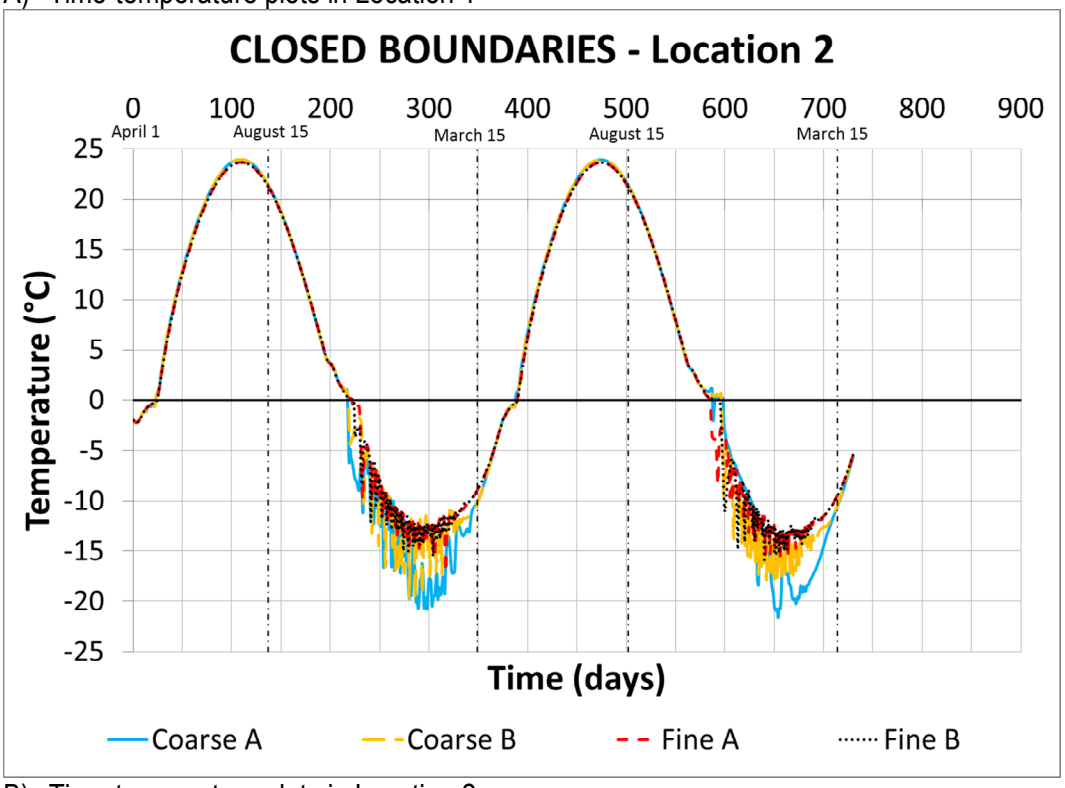

B) Time-temperature plots in Location 2

FIGURE 3.30: TRENDS IN GEOSTUDIO COARSE AND FINE MESH MODEL BOTH WITH CLOSED BOUNDARIES – LOCATIONS 3 AND 4

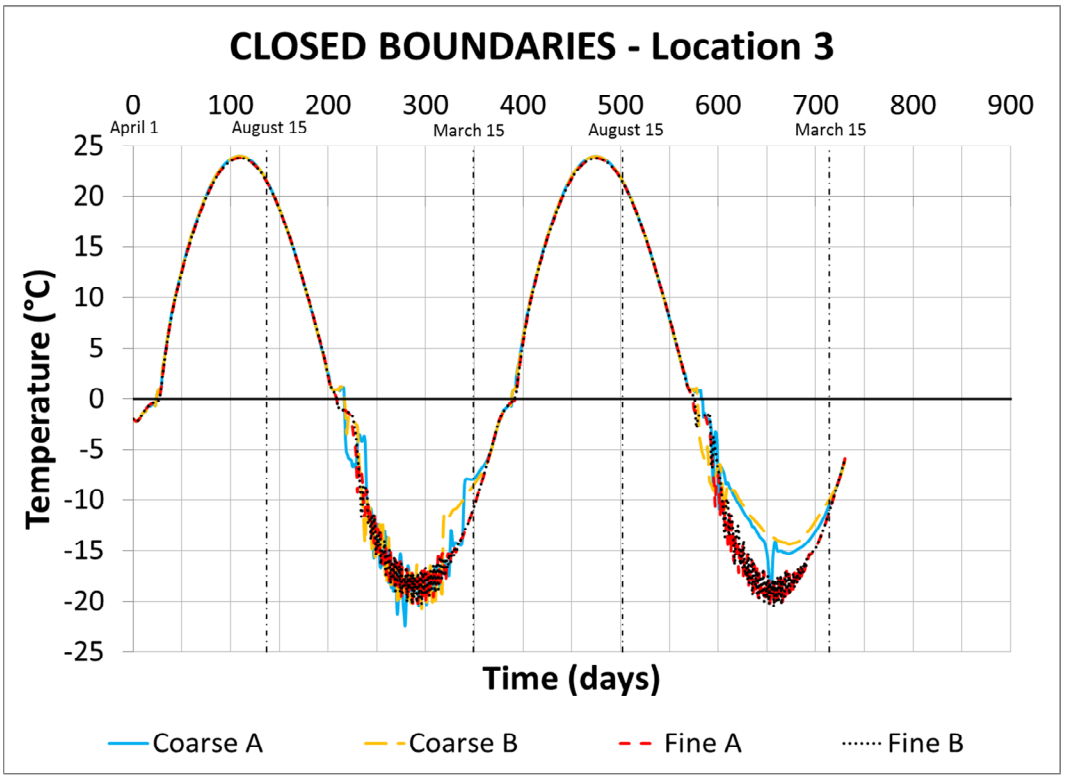

A) Time-temperature plots in Location 3

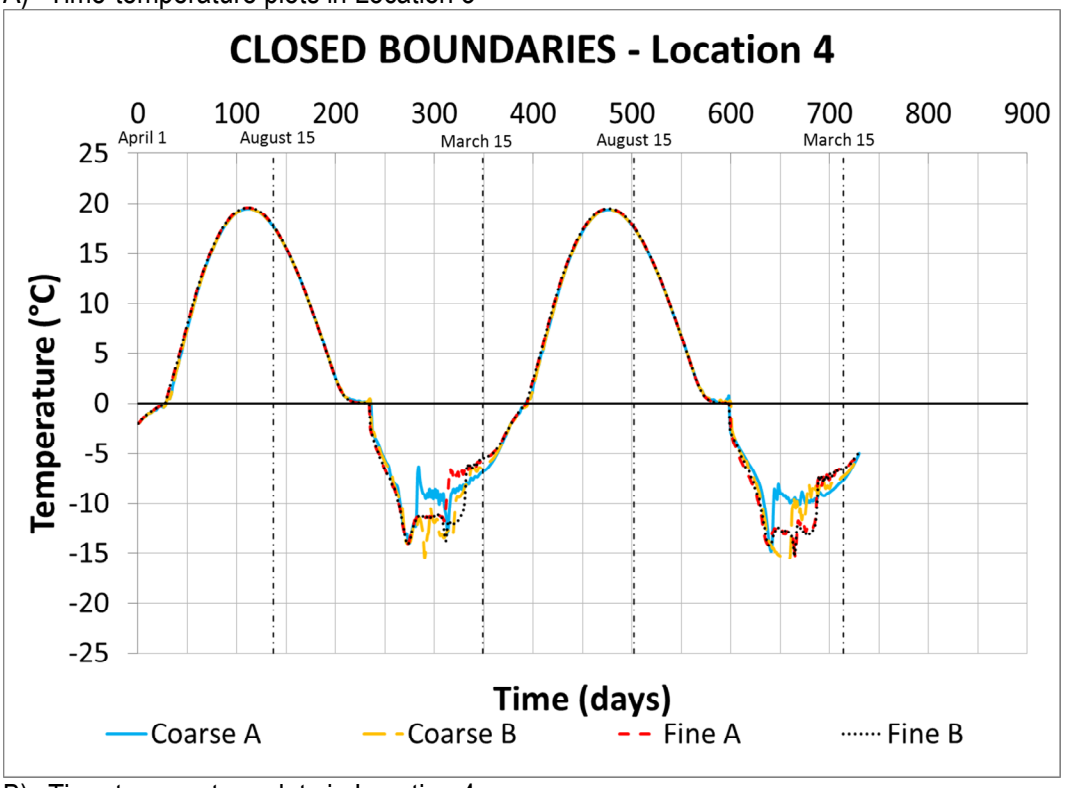

B) Time-temperature plots in Location 4

FIGURE 3.31: TRENDS IN GEOSTUDIO COARSE AND FINE MESH MODEL BOTH WITH CLOSED BOUNDARIES – LOCATIONS 5 AND 6

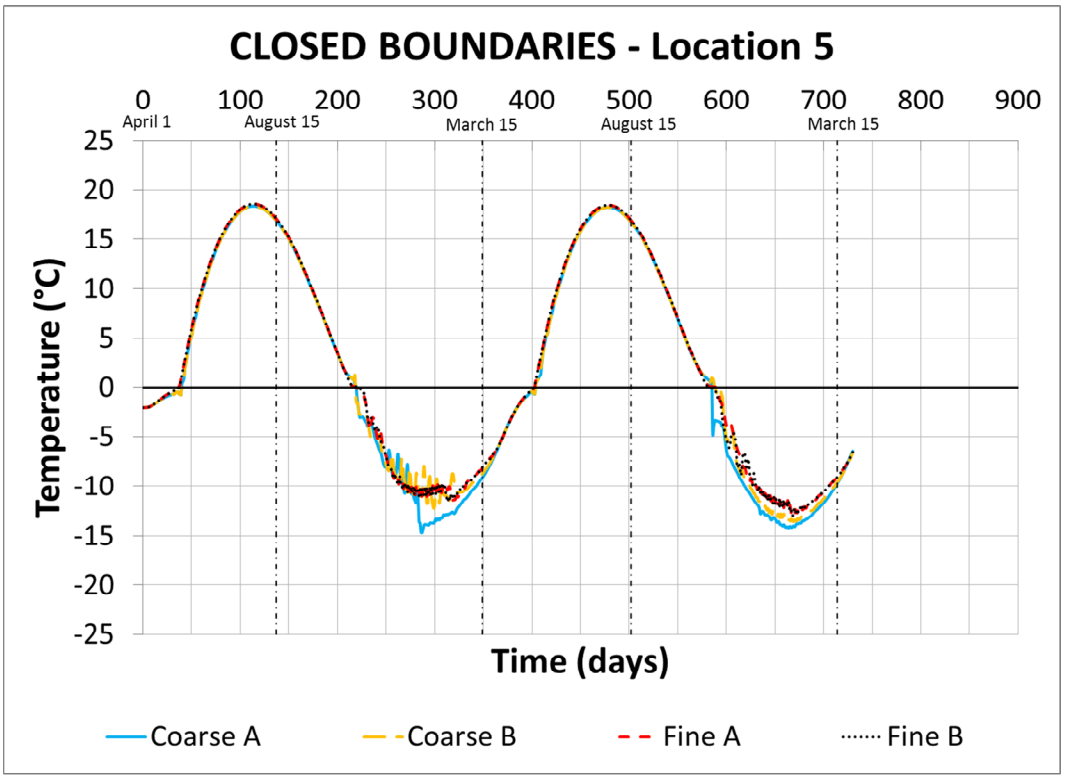

A) Time-temperature plots in Location 5

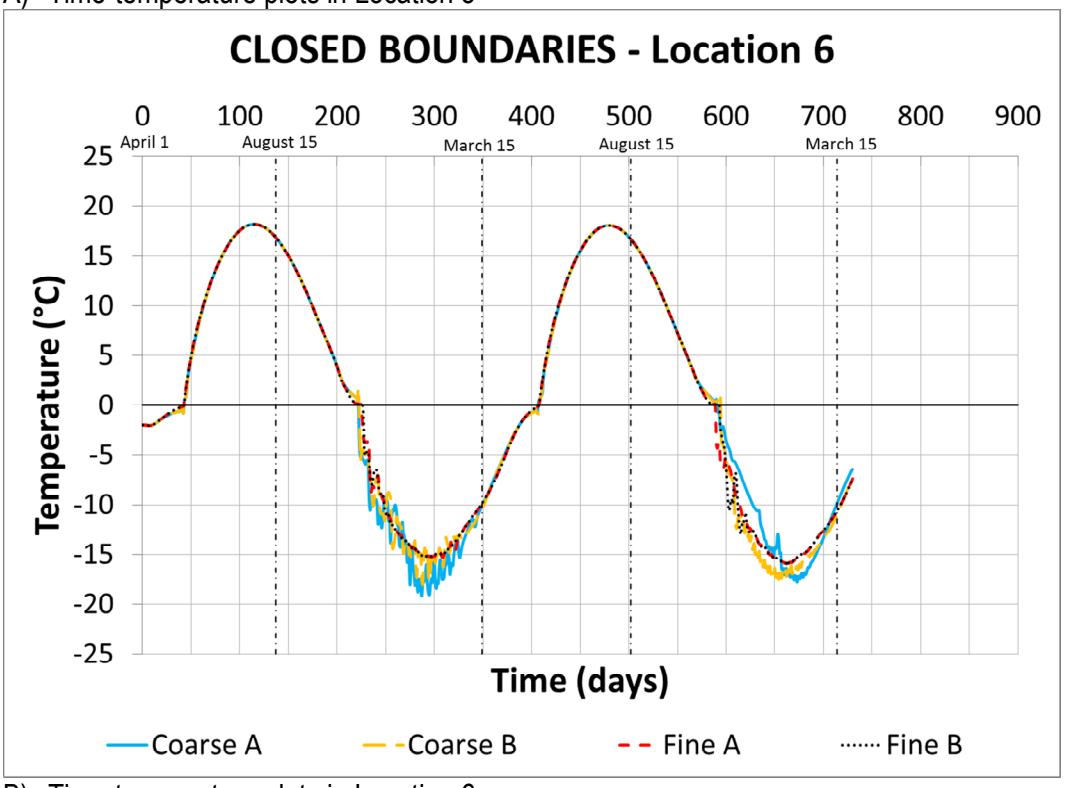

B) Time-temperature plots in Location 6

FIGURE 3.32: TRENDS IN GEOSTUDIO COARSE AND FINE MESH MODEL BOTH WITH CLOSED BOUNDARIES – LOCATIONS 7 AND 8

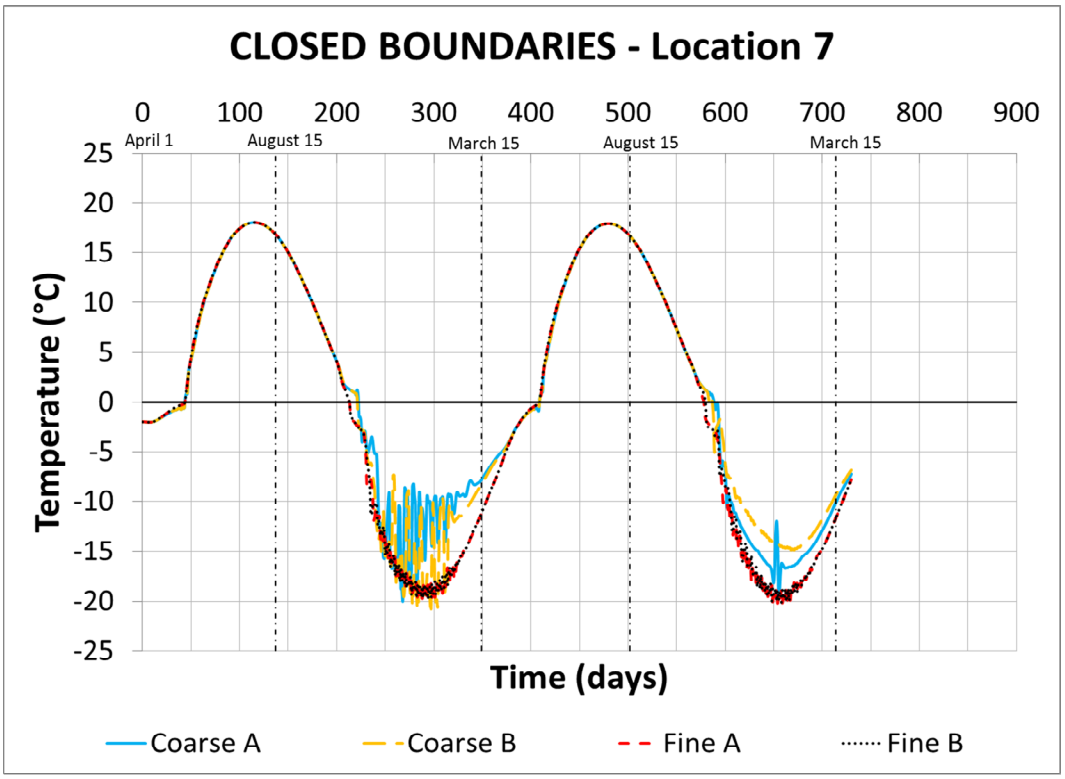

A) Time-temperature plots in Location 7

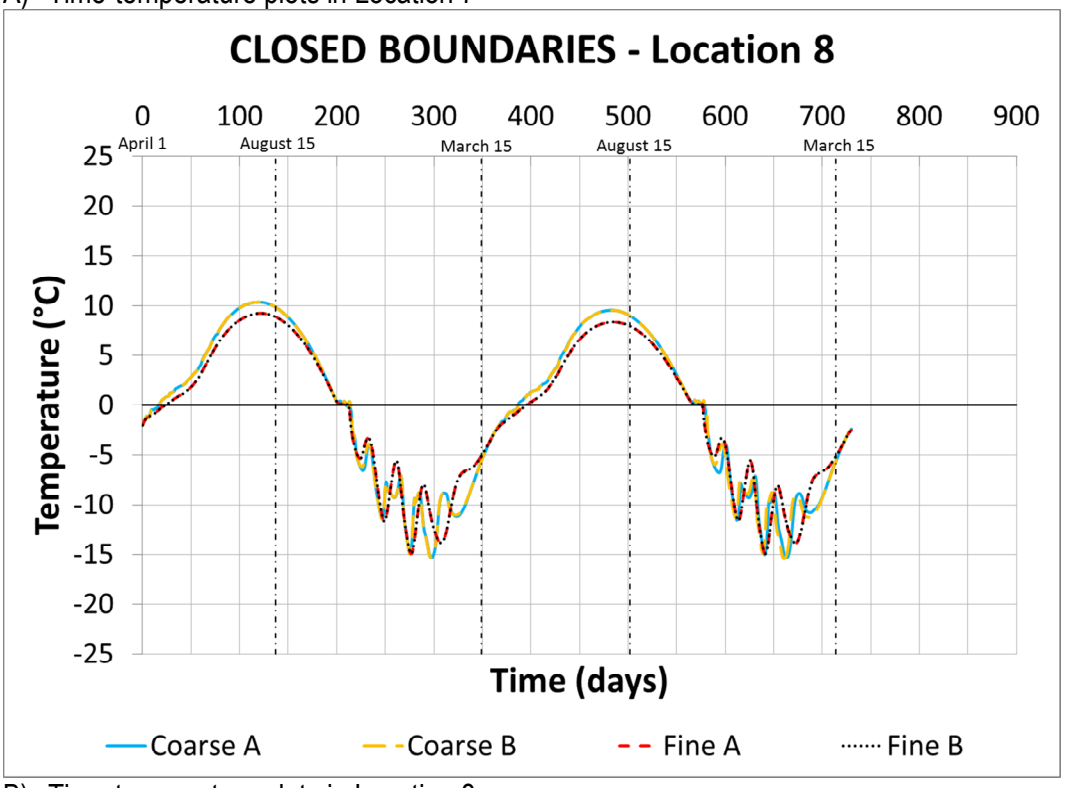

B) Time-temperature plots in Location 8

FIGURE 3.33: TRENDS IN GEOSTUDIO COARSE AND FINE MESH MODEL BOTH WITH CLOSED BOUNDARIES - LOCATIONS 9 AND 10

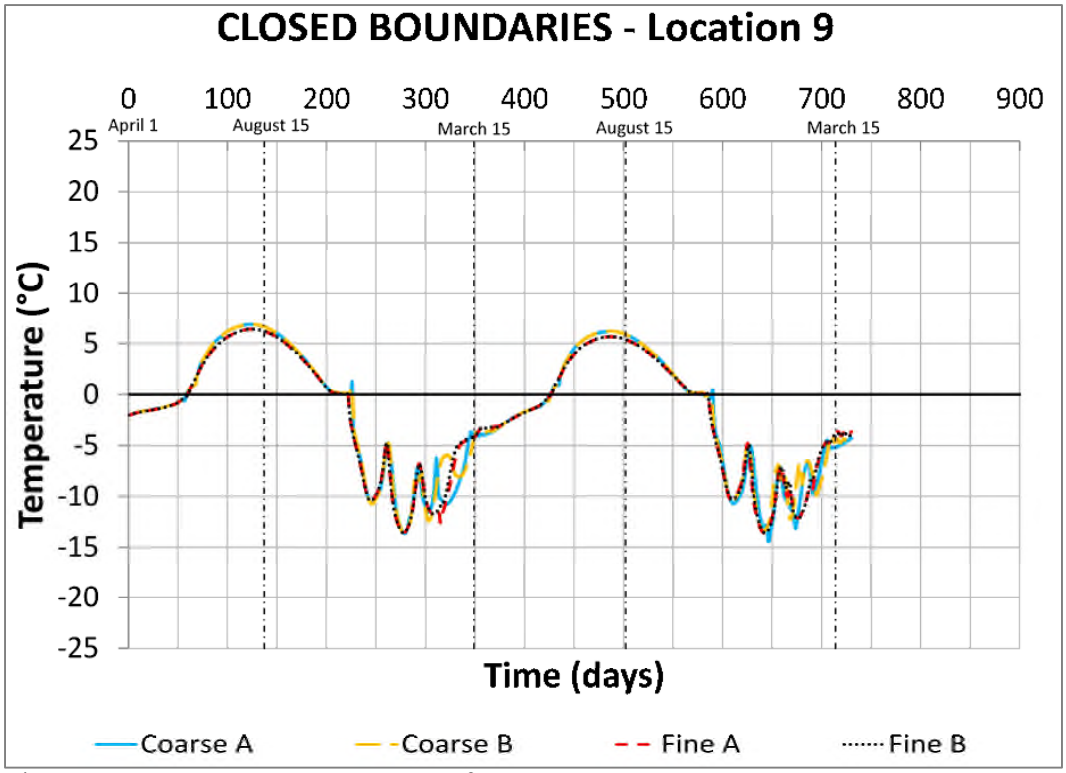

A) Time-temperature plots in Location 9

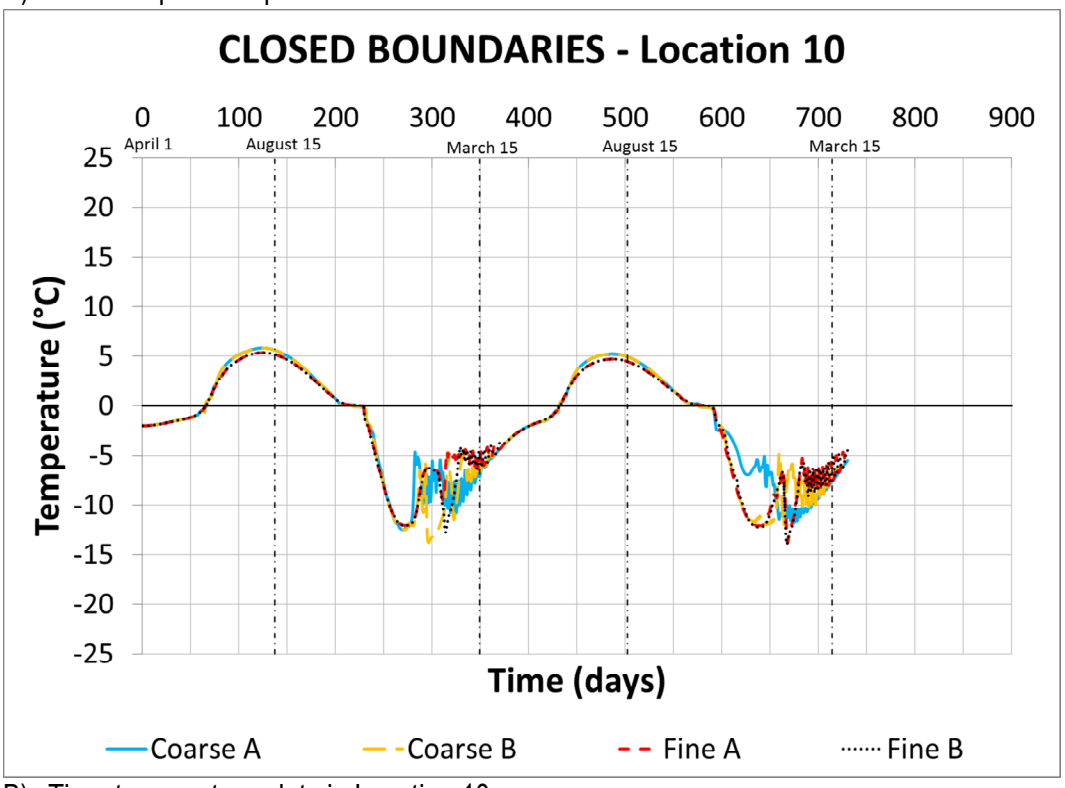

B) Time-temperature plots in Location 10

FIGURE 3.34: TRENDS IN GEOSTUDIO COARSE AND FINE MESH MODEL BOTH WITH CLOSED BOUNDARIES – LOCATIONS 11 AND 12

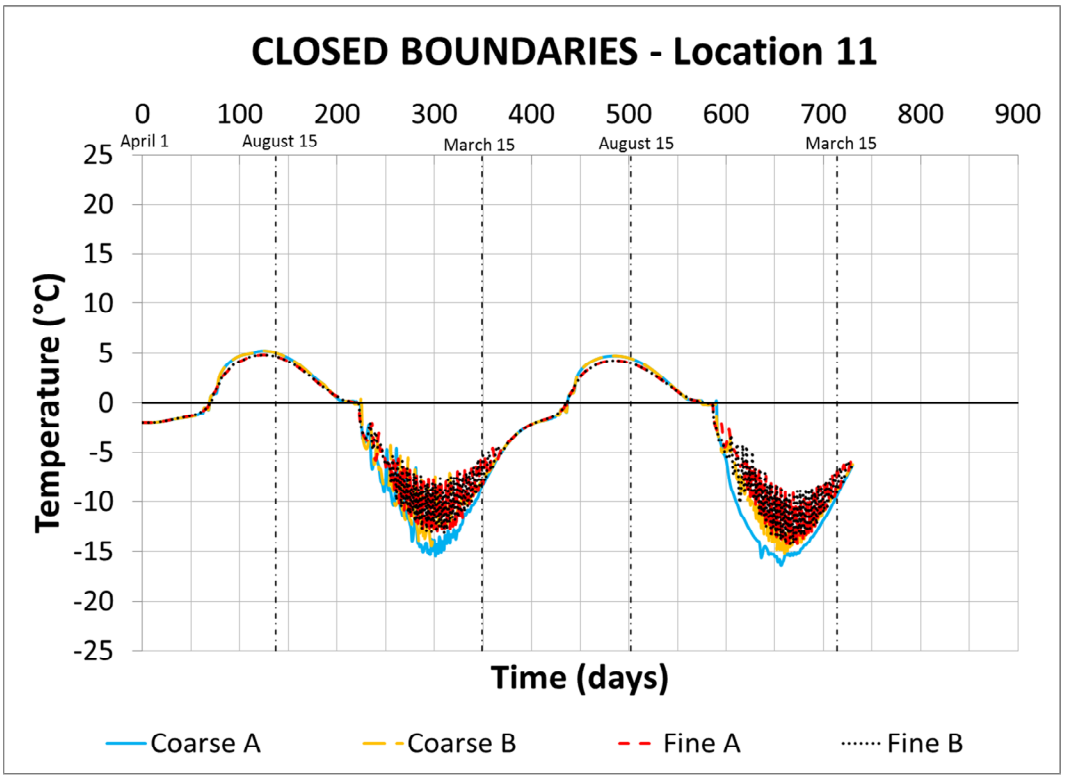

A) Time-temperature plots in Location 11

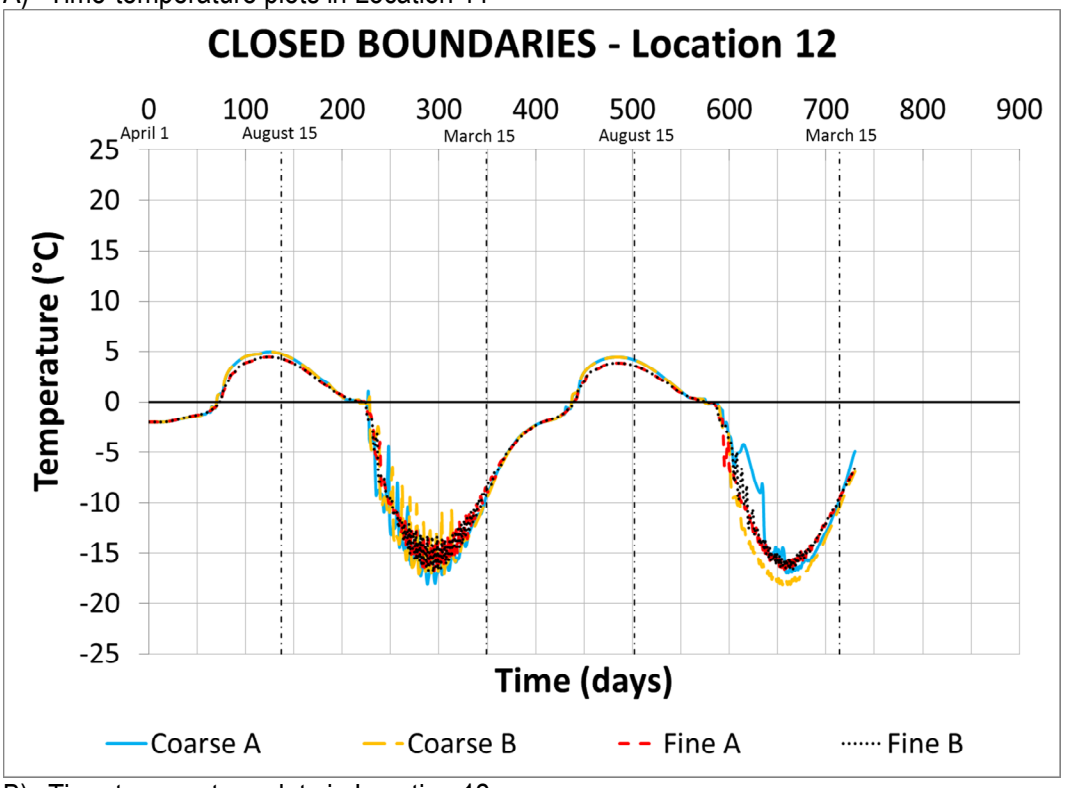

B) Time-temperature plots in Location 12

FIGURE 3.35: TRENDS IN GEOSTUDIO COARSE AND FINE MESH MODEL BOTH WITH CLOSED BOUNDARIES – LOCATIONS 13 AND 14

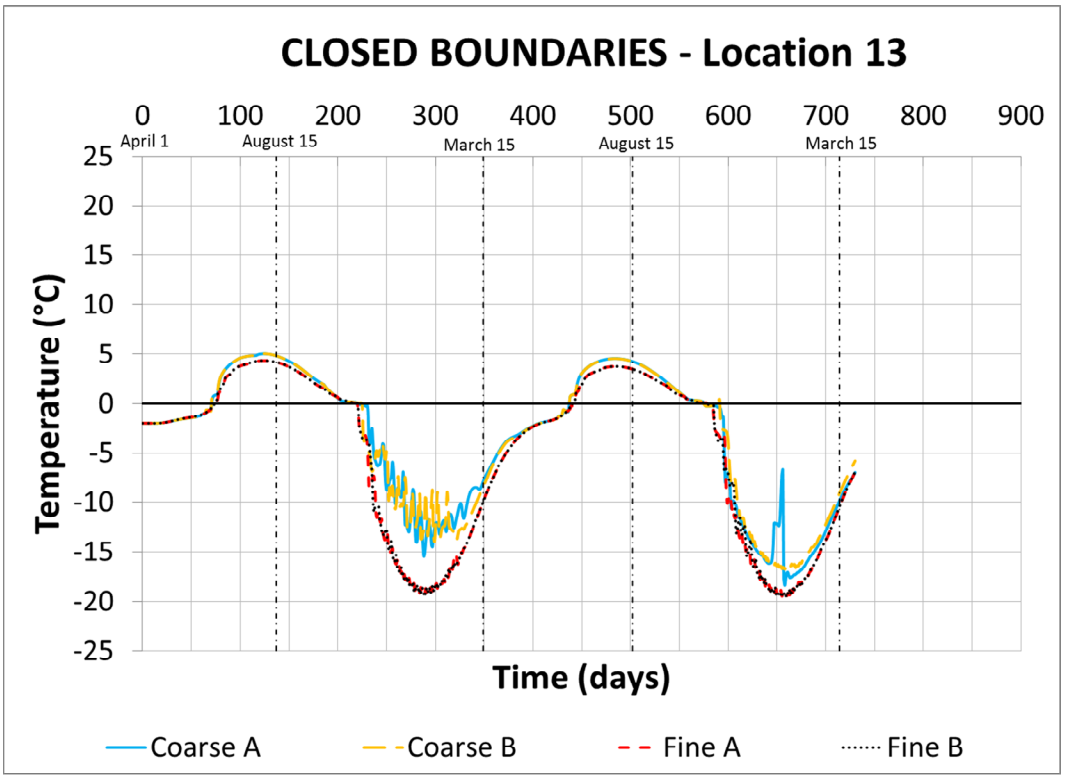

A) Time-temperature plots in Location 13

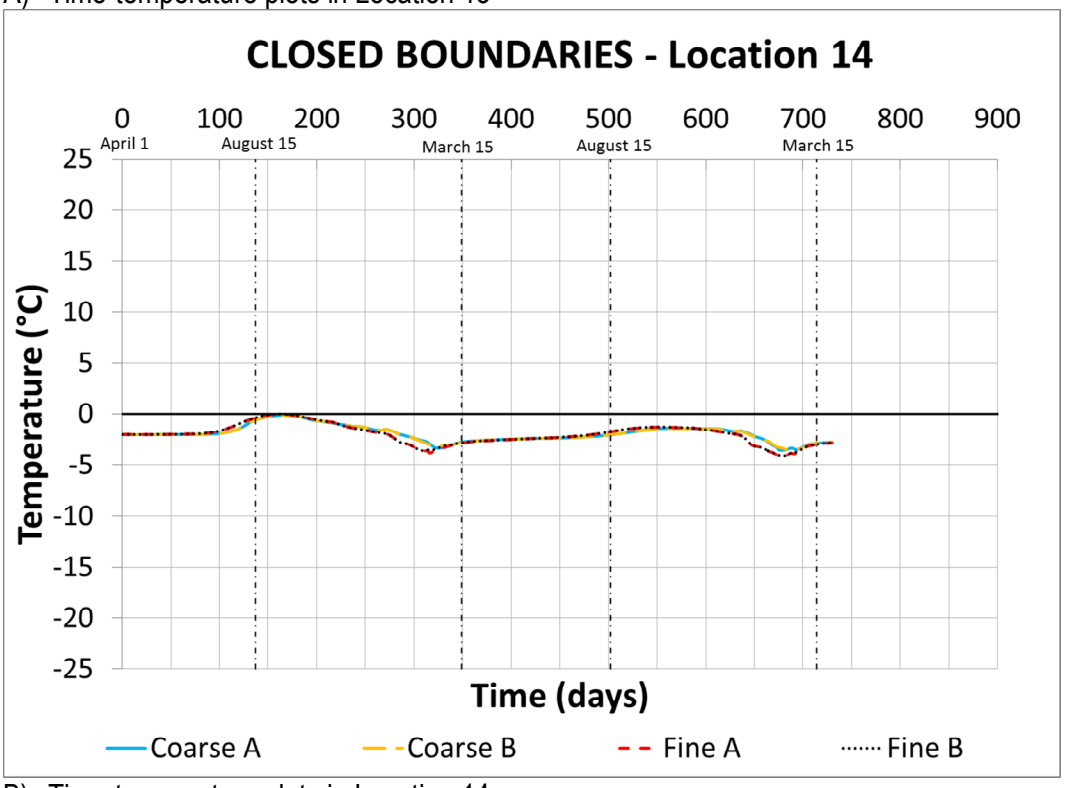

B) Time-temperature plots in Location 14

FIGURE 3.36: TRENDS IN GEOSTUDIO COARSE AND FINE MESH MODEL BOTH WITH CLOSED BOUNDARIES – LOCATIONS 15 AND 16

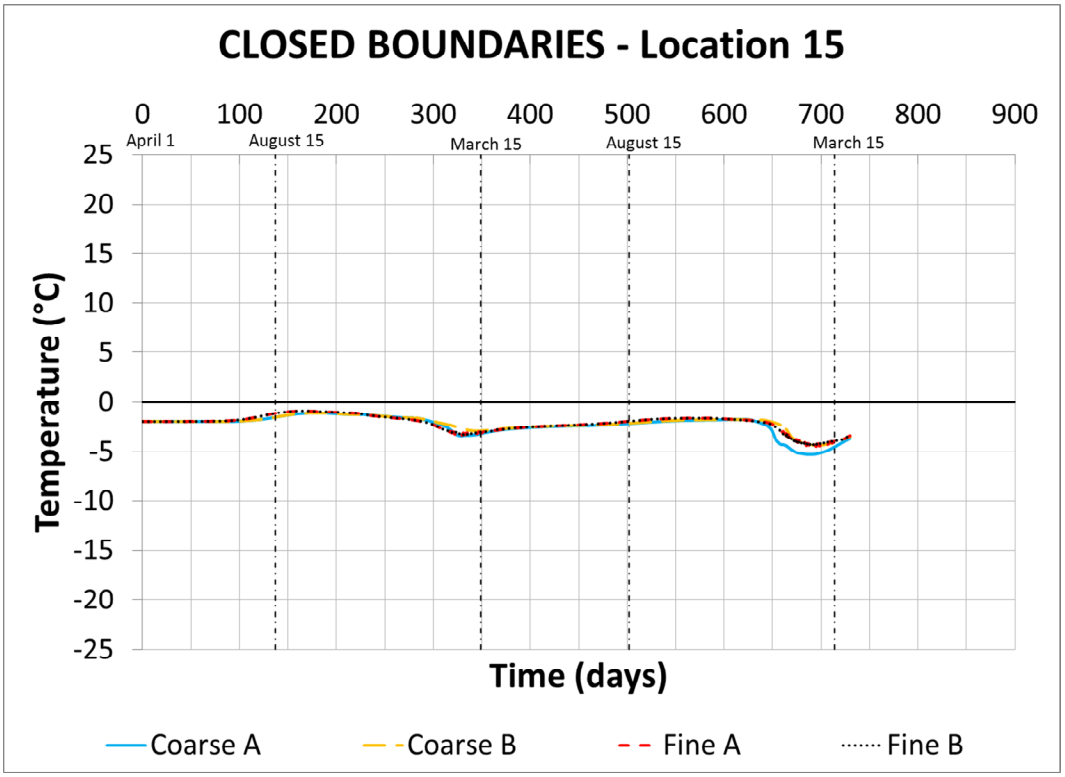

A) Time-temperature plots in Location 15

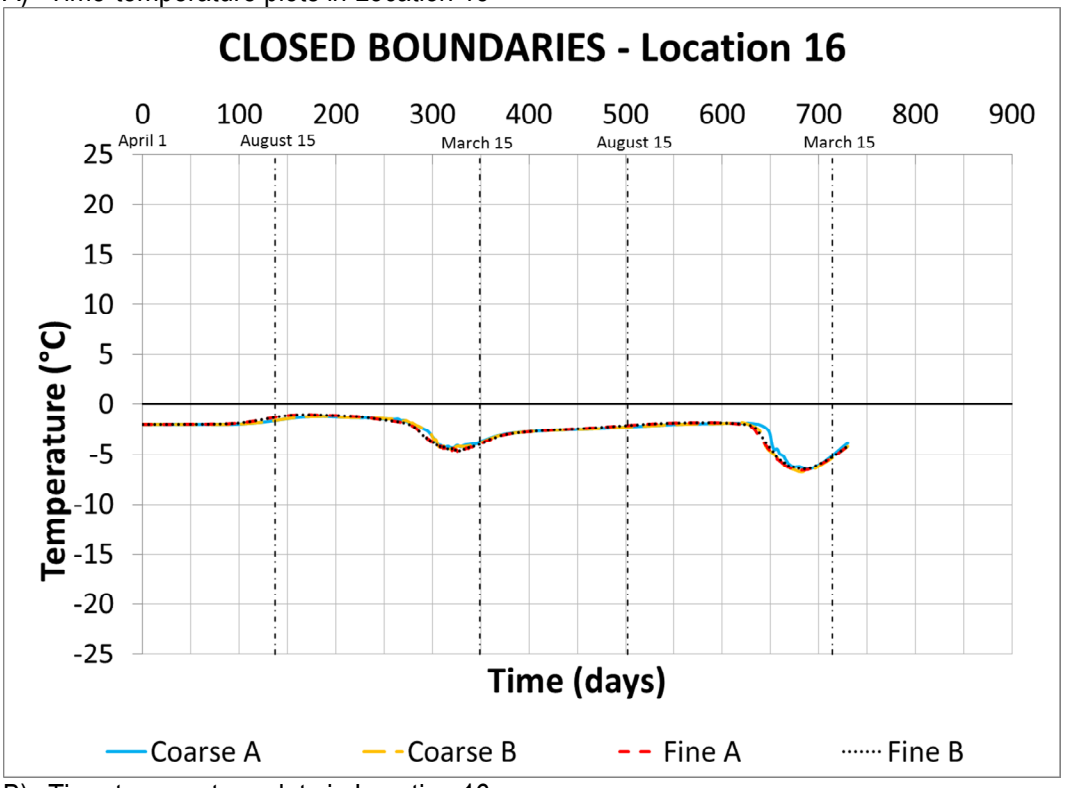

B) Time-temperature plots in Location 16

FIGURE 3.37: TRENDS IN GEOSTUDIO COARSE MESH MODEL AND FINE MESH MODEL BOTH WITH OPEN SIDESLOPES – LOCATIONS 1 AND 2

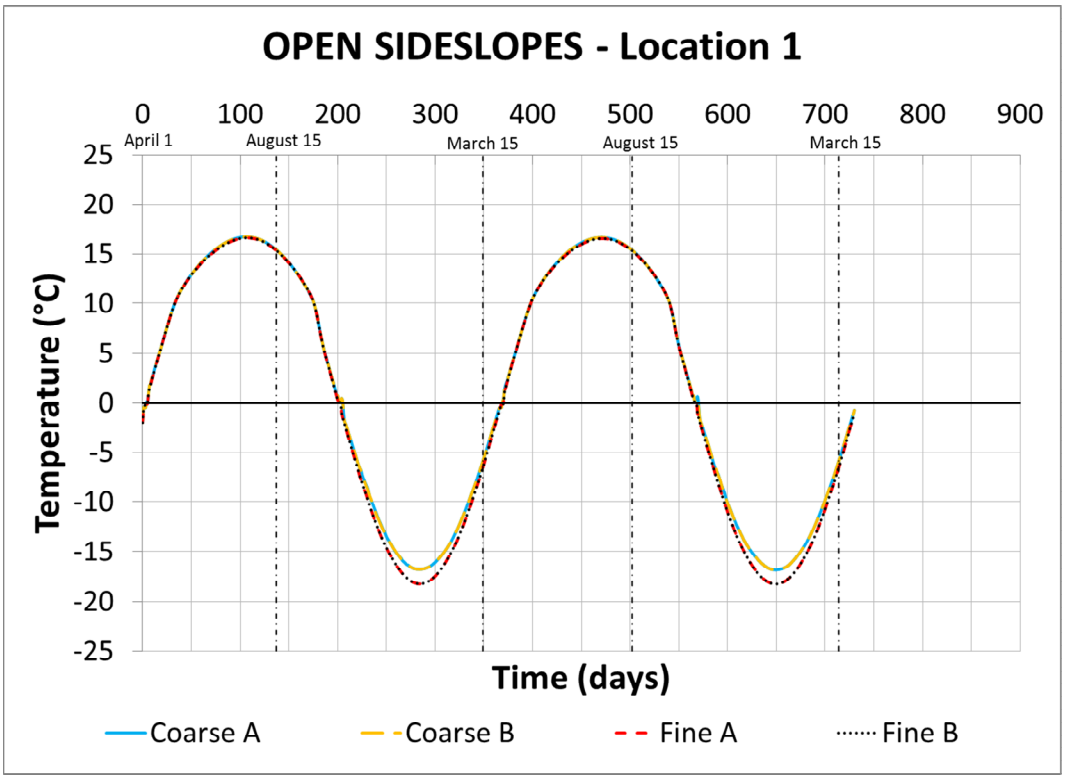

A) Time-temperature plots in Location 1

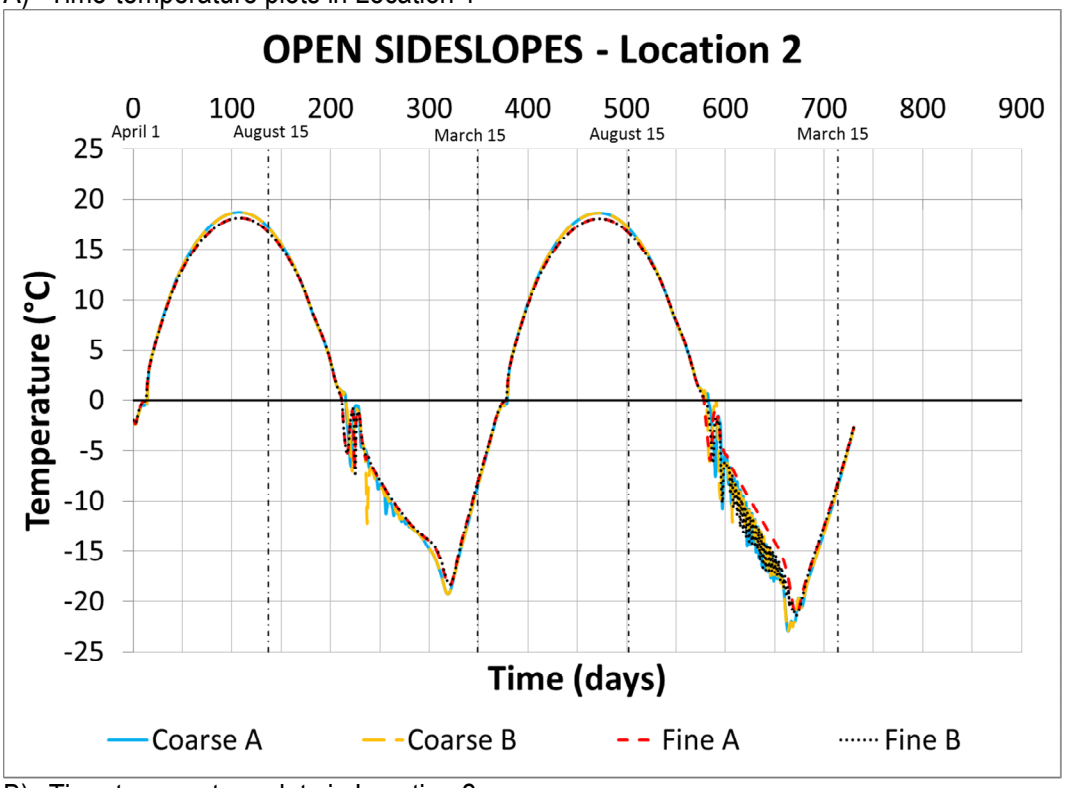

B) Time-temperature plots in Location 2

FIGURE 3.38: TRENDS IN GEOSTUDIO COARSE MESH MODEL AND FINE MESH MODEL BOTH WITH OPEN SIDESLOPES – LOCATIONS 3 AND 4

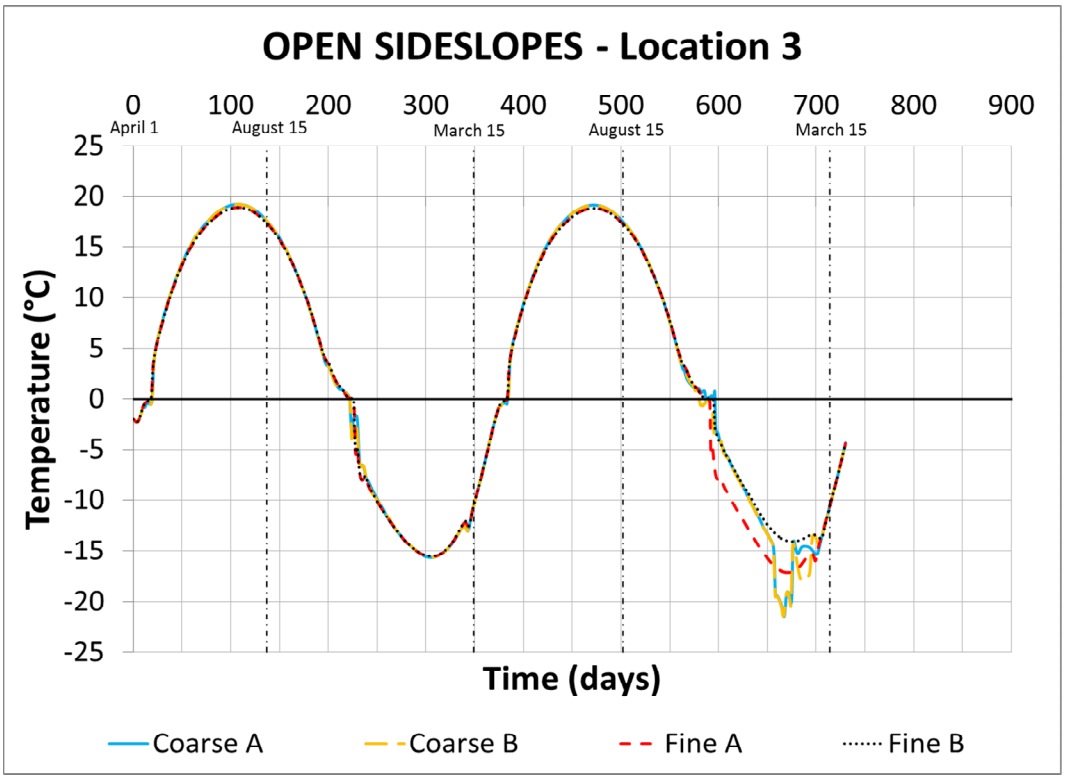

A) Time-temperature plots in Location 3

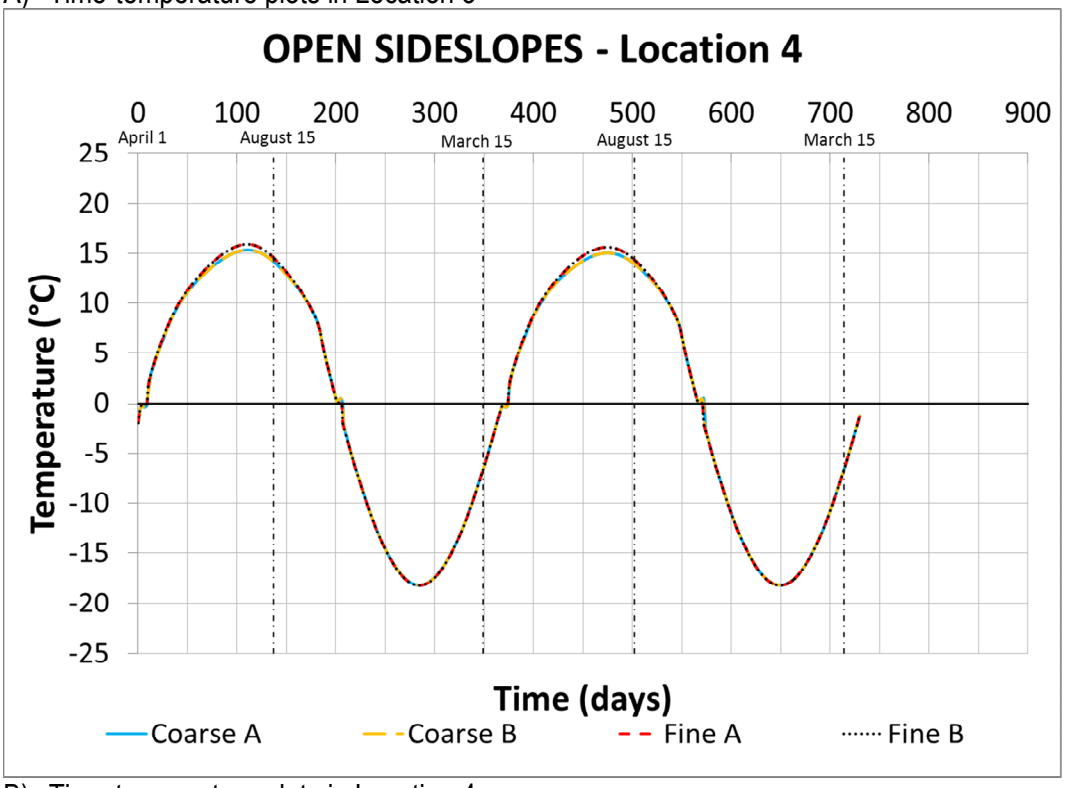

B) Time-temperature plots in Location 4

FIGURE 3.39: TRENDS IN GEOSTUDIO COARSE MESH MODEL AND FINE MESH MODEL BOTH WITH OPEN SIDESLOPES – LOCATIONS 5 AND 6

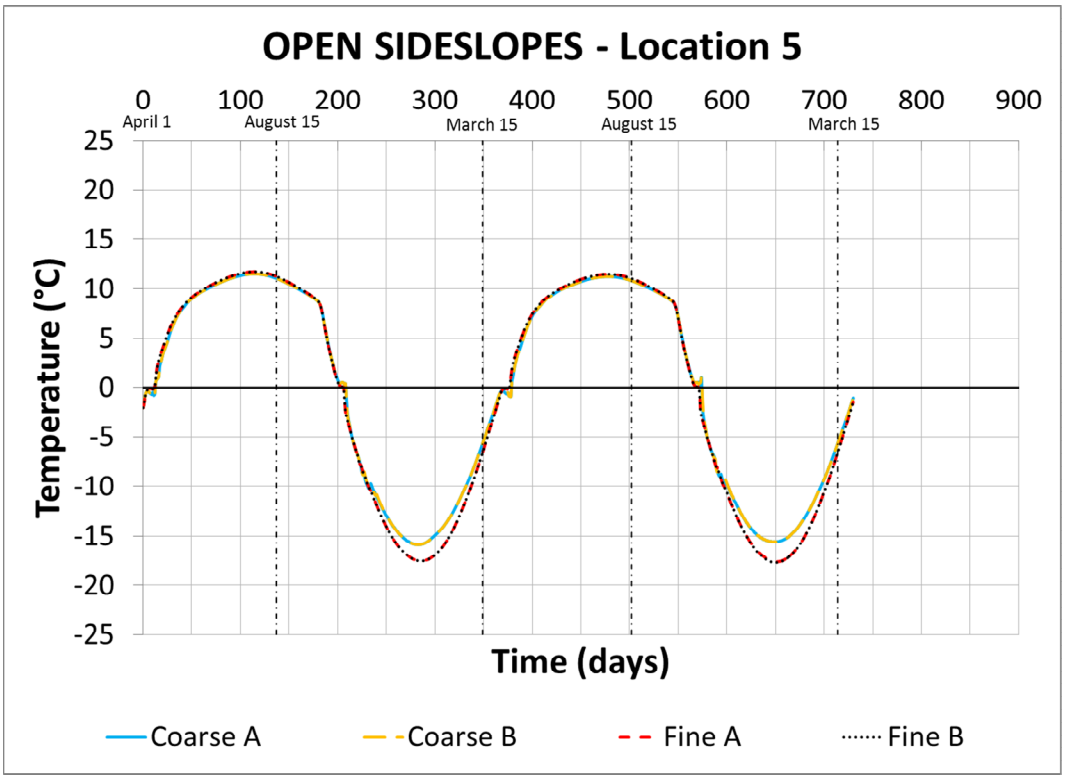

A) Time-temperature plots in Location 5

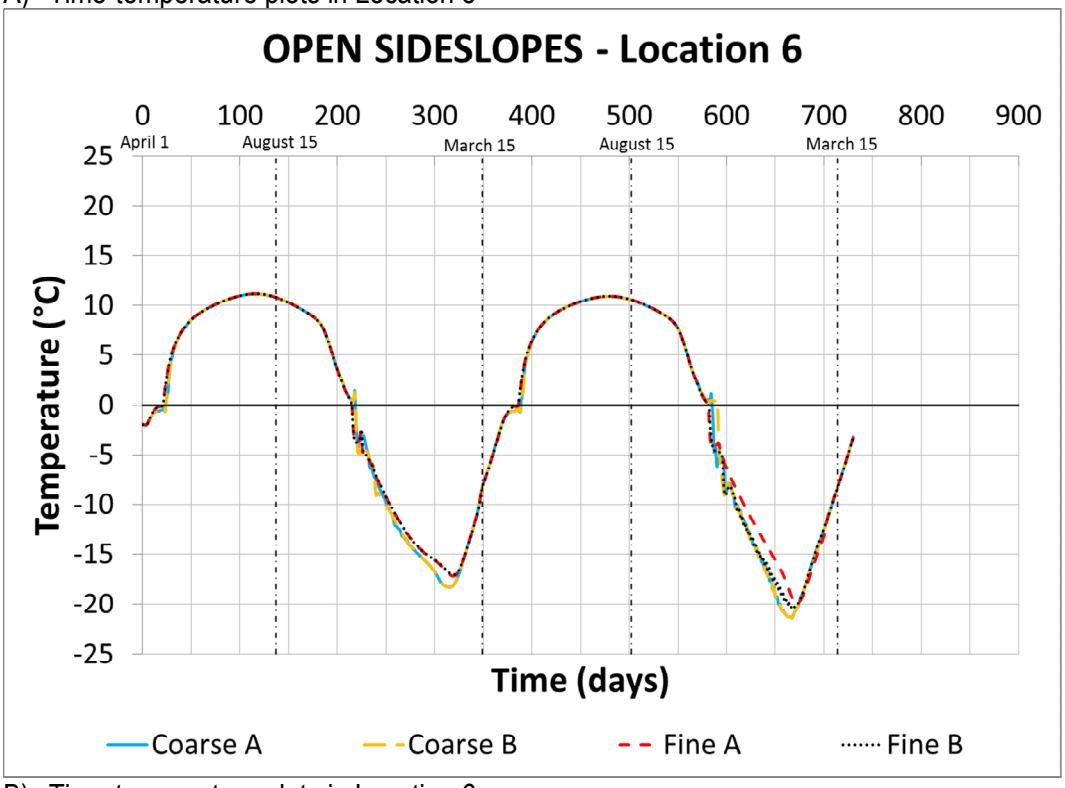

B) Time-temperature plots in Location 6

FIGURE 3.40: TRENDS IN GEOSTUDIO COARSE MESH MODEL AND FINE MESH MODEL BOTH WITH OPEN SIDESLOPES – LOCATIONS 7 AND 8

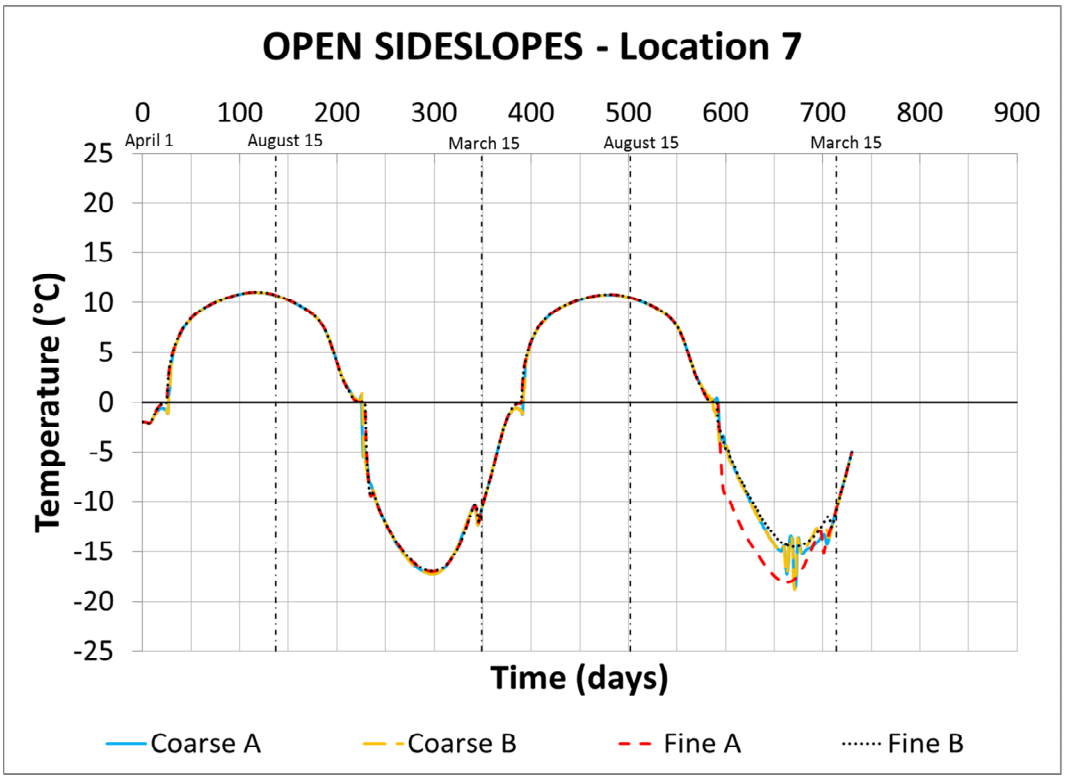

A) Time-temperature plots in Location 7

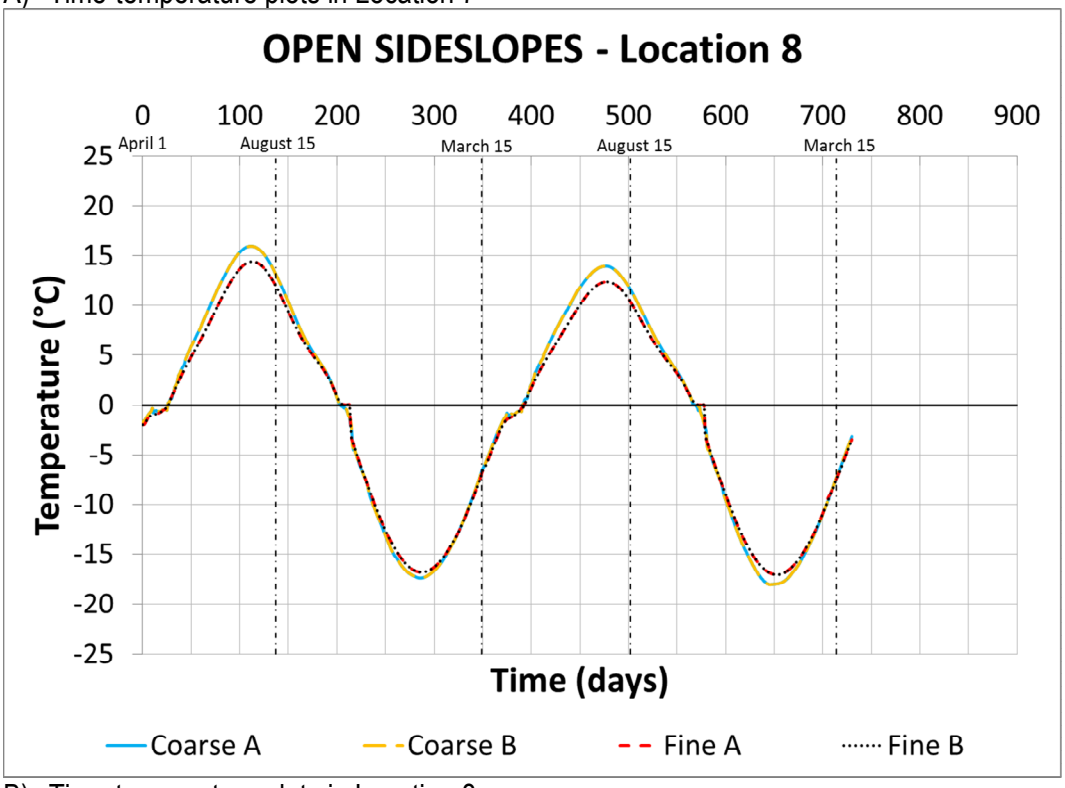

B) Time-temperature plots in Location 8

FIGURE 3.41: TRENDS IN GEOSTUDIO COARSE MESH MODEL AND FINE MESH MODEL BOTH WITH OPEN SIDESLOPES – LOCATIONS 9 AND 10

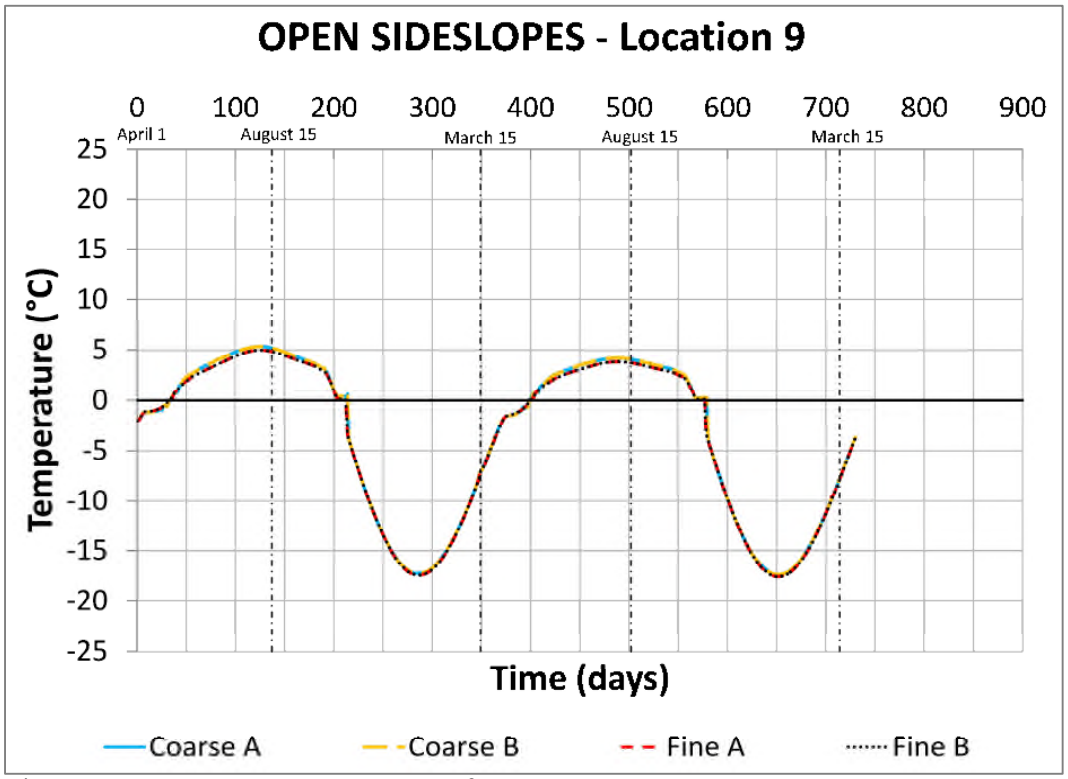

A) Time-temperature plots in Location 9

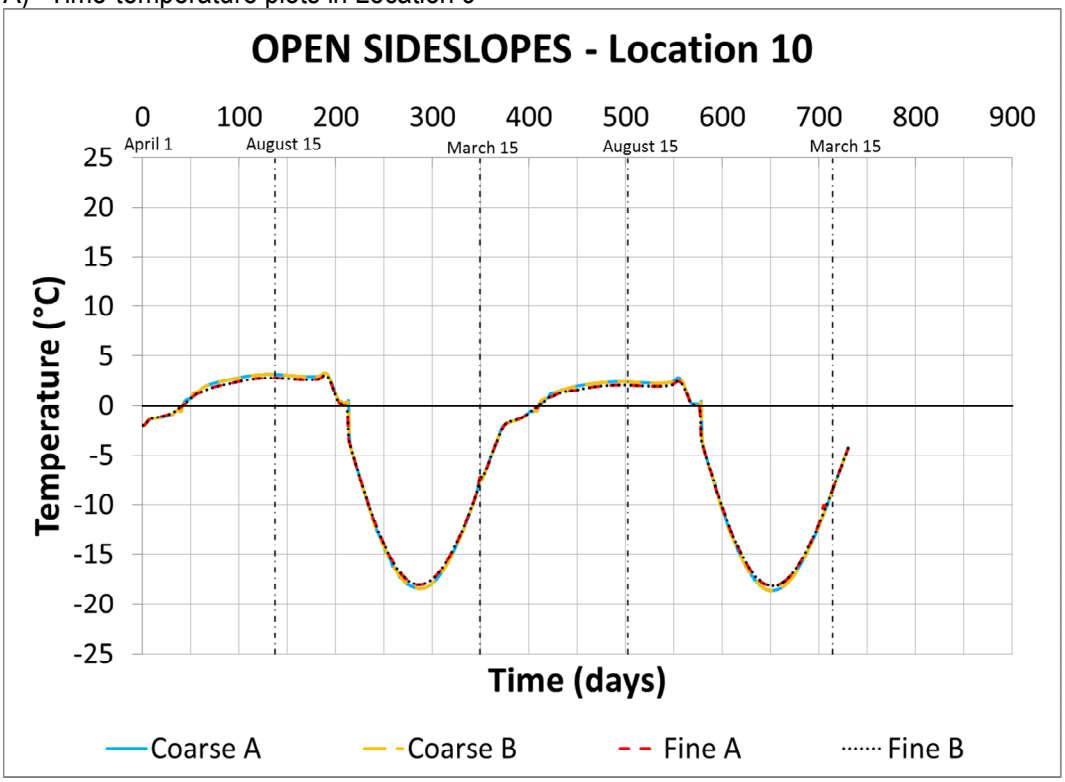

B) Time-temperature plots in Location 10

FIGURE 3.42: TRENDS IN GEOSTUDIO COARSE MESH MODEL AND FINE MESH MODEL BOTH WITH OPEN SIDESLOPES – LOCATIONS 11 AND 12

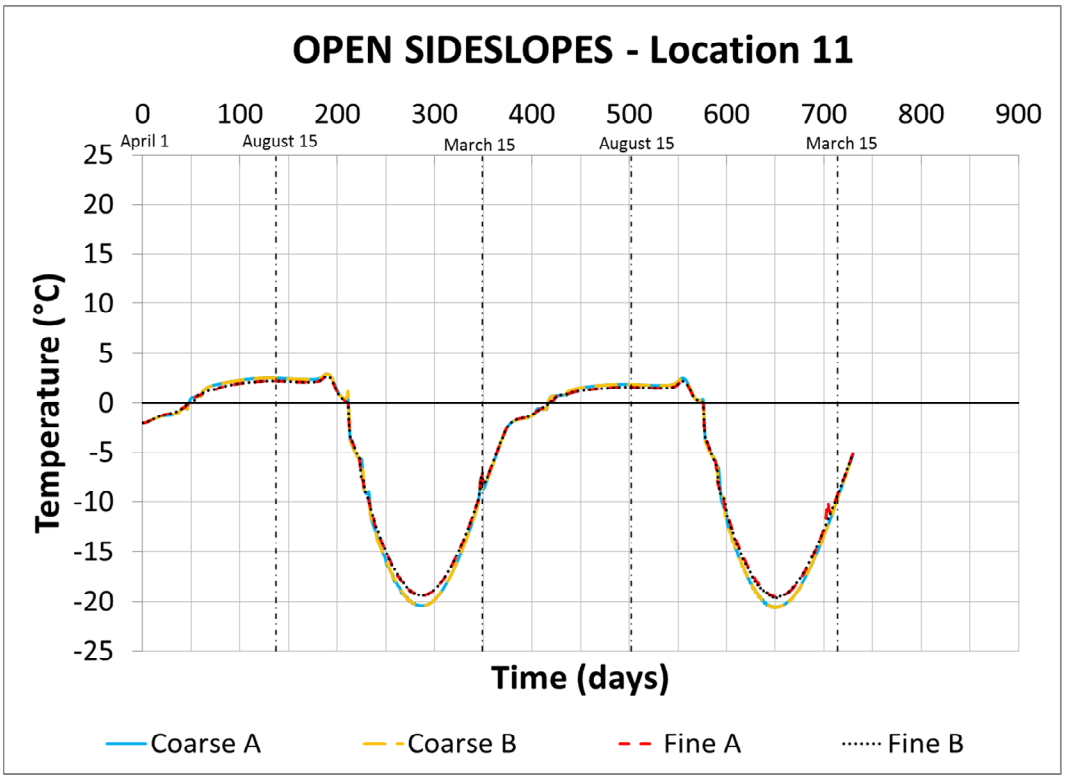

A) Time-temperature plots in Location 11

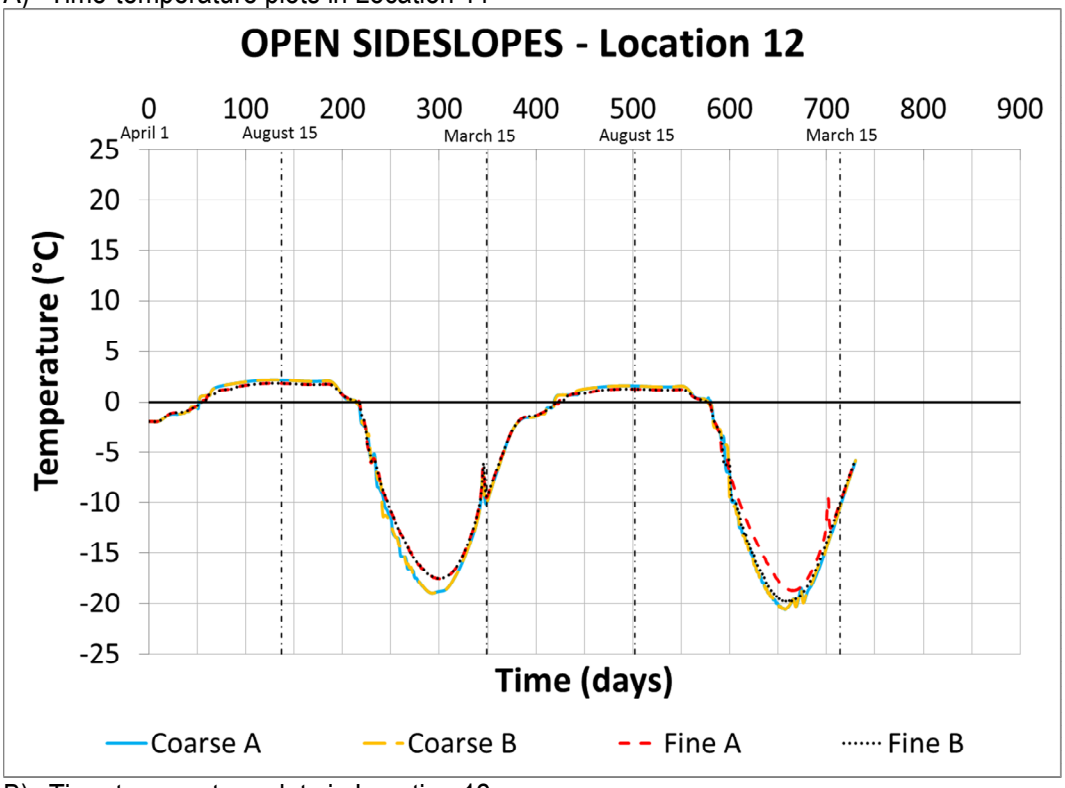

B) Time-temperature plots in Location 12

FIGURE 3.43: TRENDS IN GEOSTUDIO COARSE MESH MODEL AND FINE MESH MODEL BOTH WITH OPEN SIDESLOPES – LOCATIONS 13 AND 14

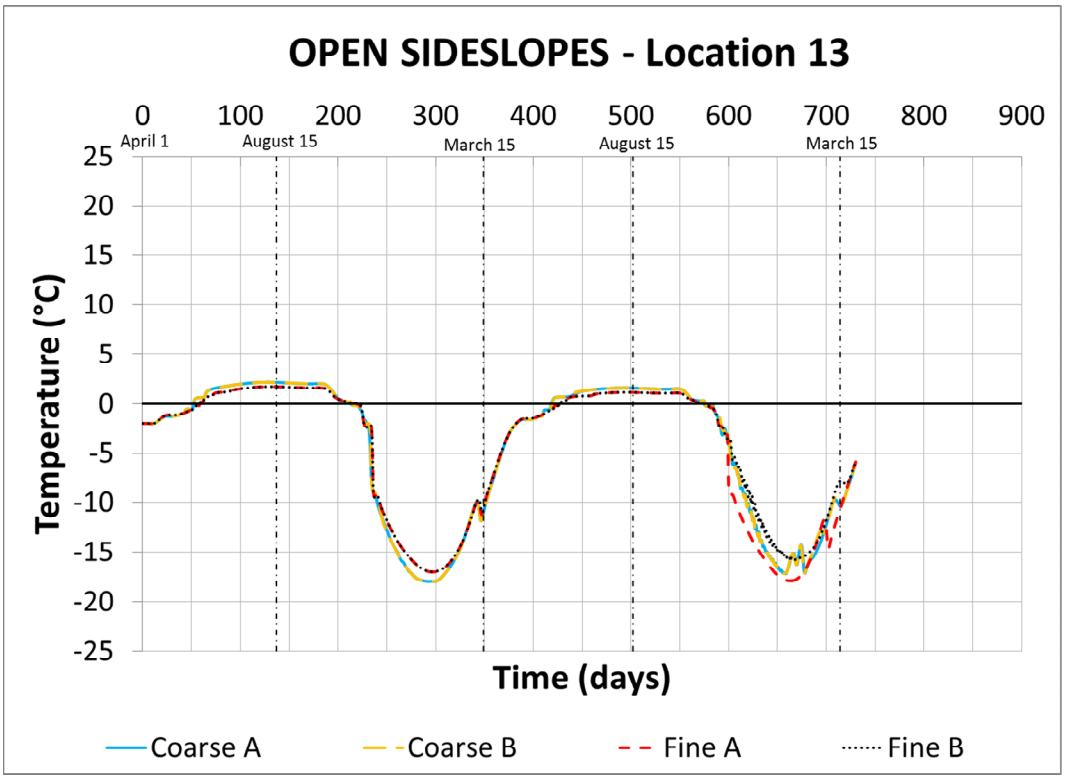

A) Time-temperature plots in Location 13

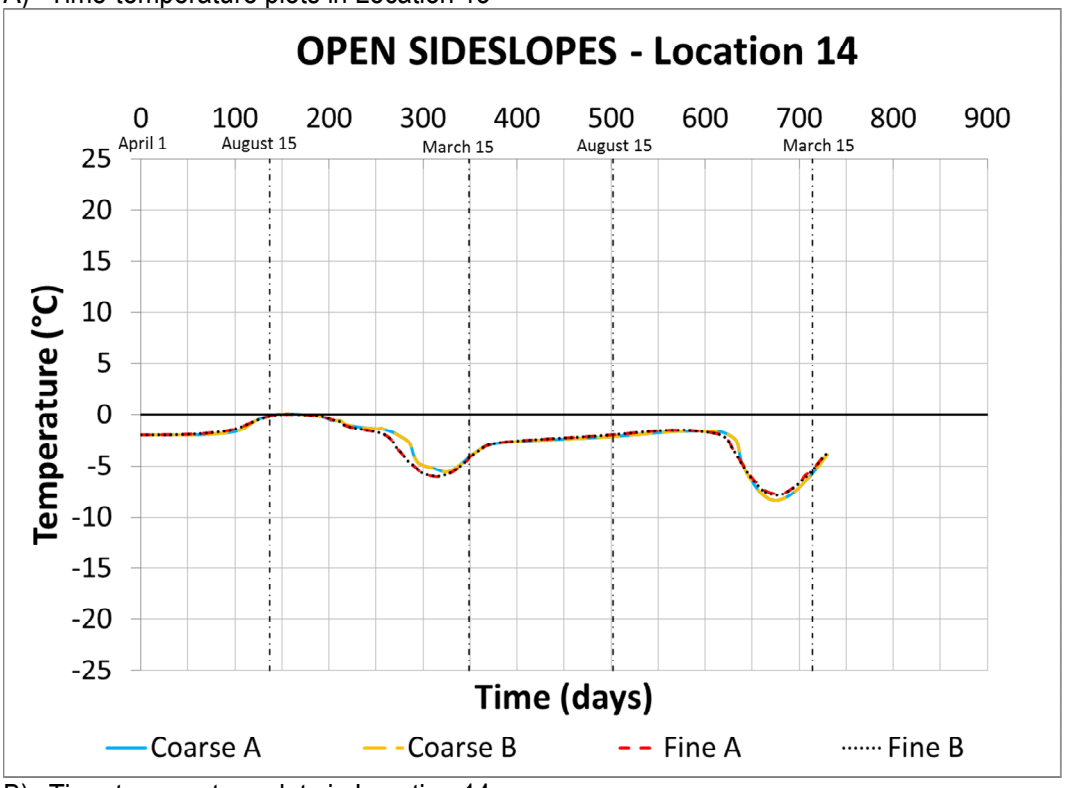

B) Time-temperature plots in Location 14

FIGURE 3.44: TRENDS IN GEOSTUDIO COARSE MESH MODEL AND FINE MESH MODEL BOTH WITH OPEN SIDESLOPES – LOCATIONS 15 AND 16

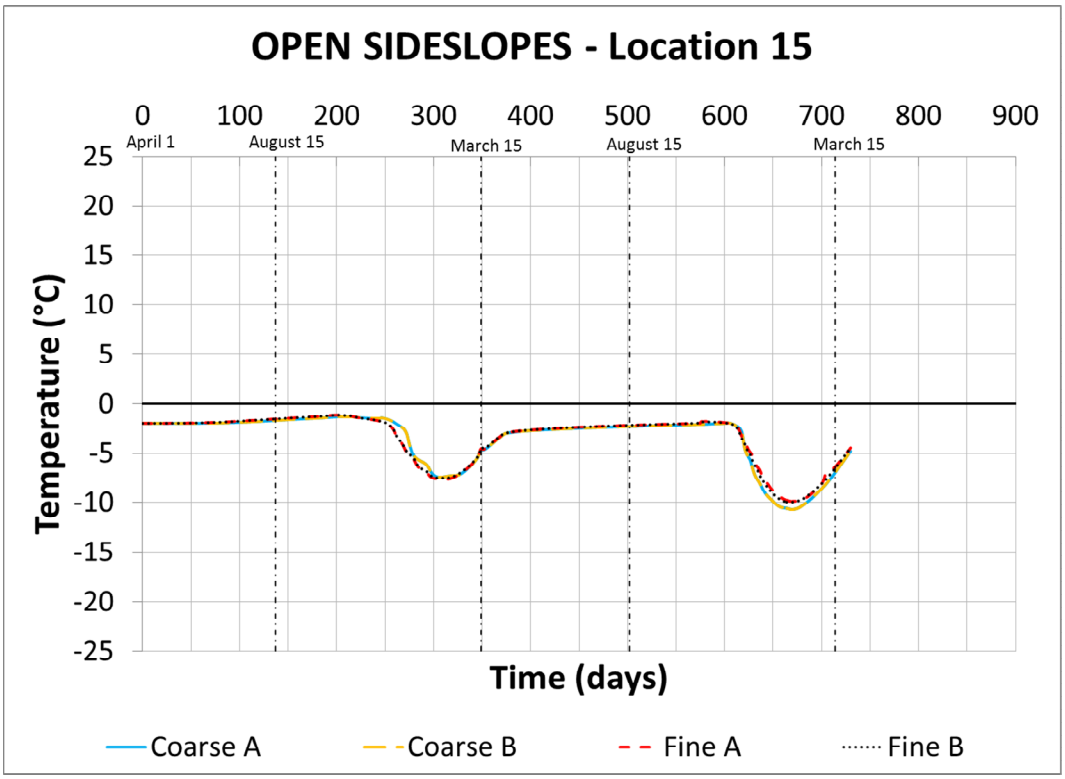

A) Time-temperature plots in Location 15

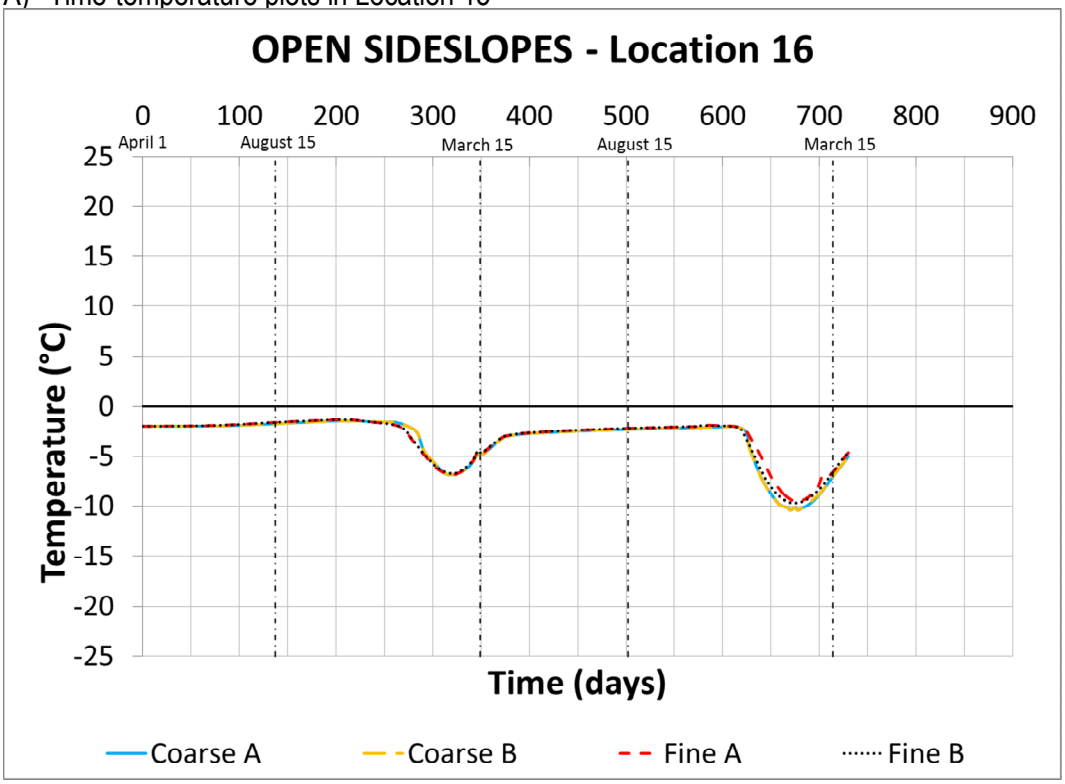

B) Time-temperature plots in Location 16

FIGURE 3.45: TRENDS IN GEOSTUDIO COARSE MESH MODEL WITH CLOSED BOUNDARIES

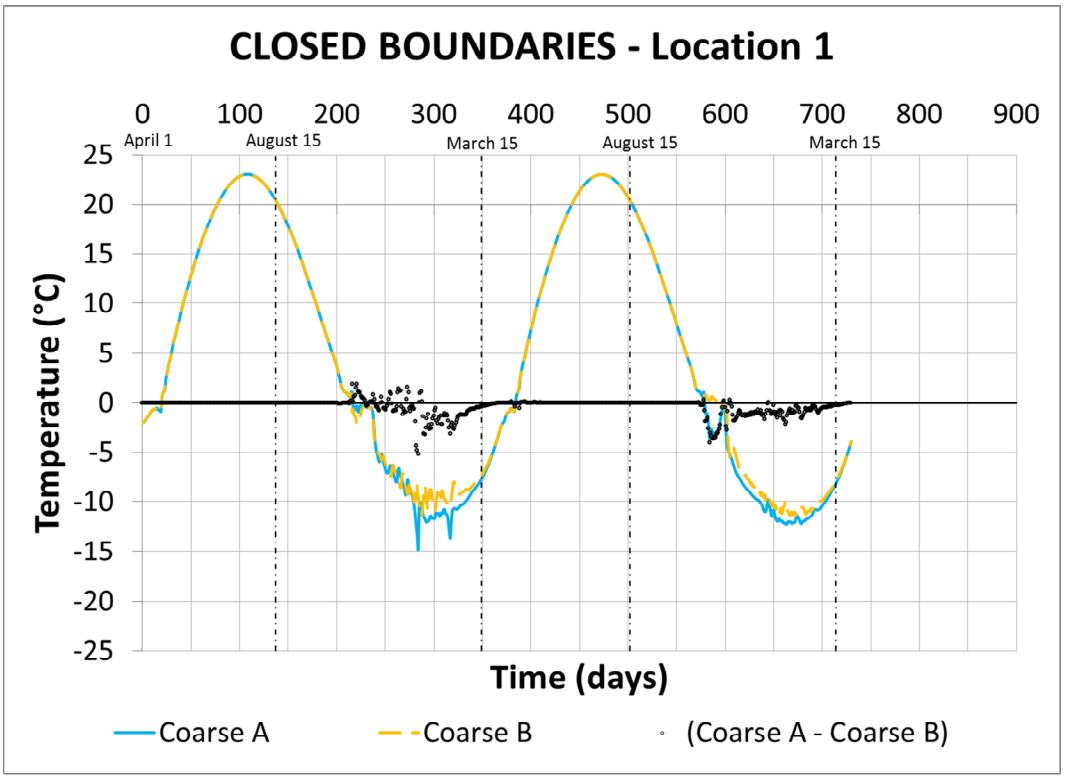

A) Time-temperature plots in Location 1A) Temperature isotherms in full model

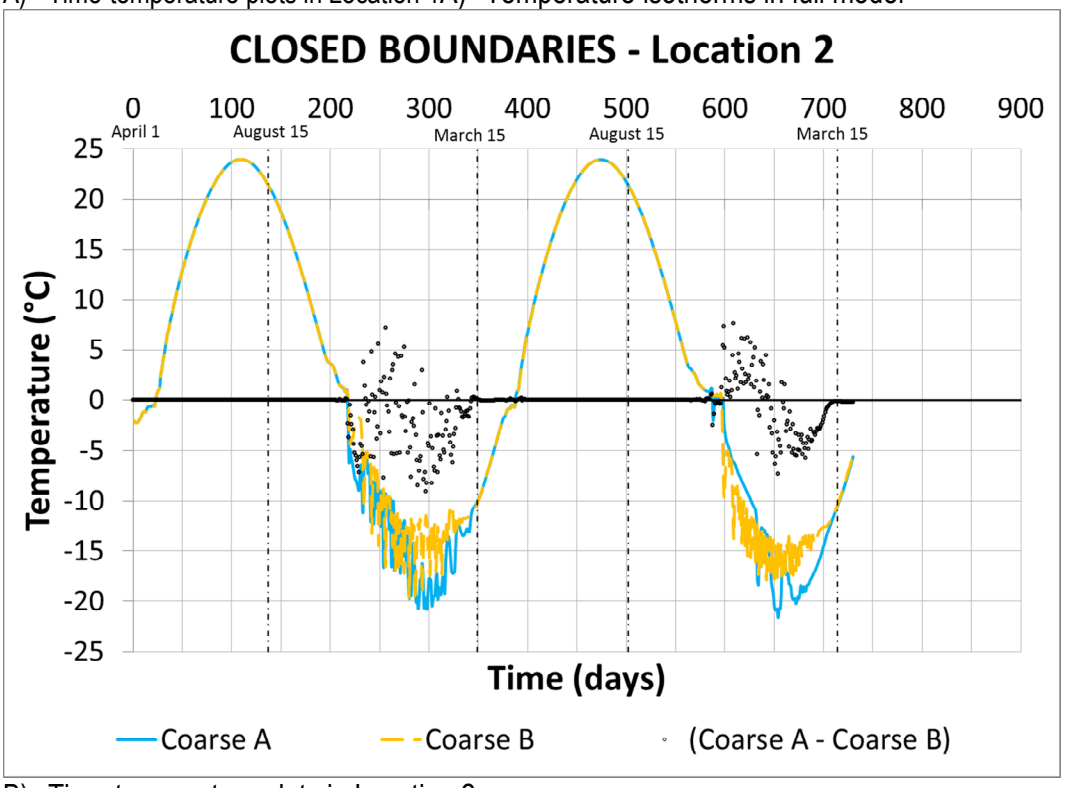

B) Time-temperature plots in Location 2

FIGURE 3.46: TRENDS IN GEOSTUDIO COARSE MESH MODEL WITH CLOSED BOUNDARIES – LOCATIONS 3 AND 4

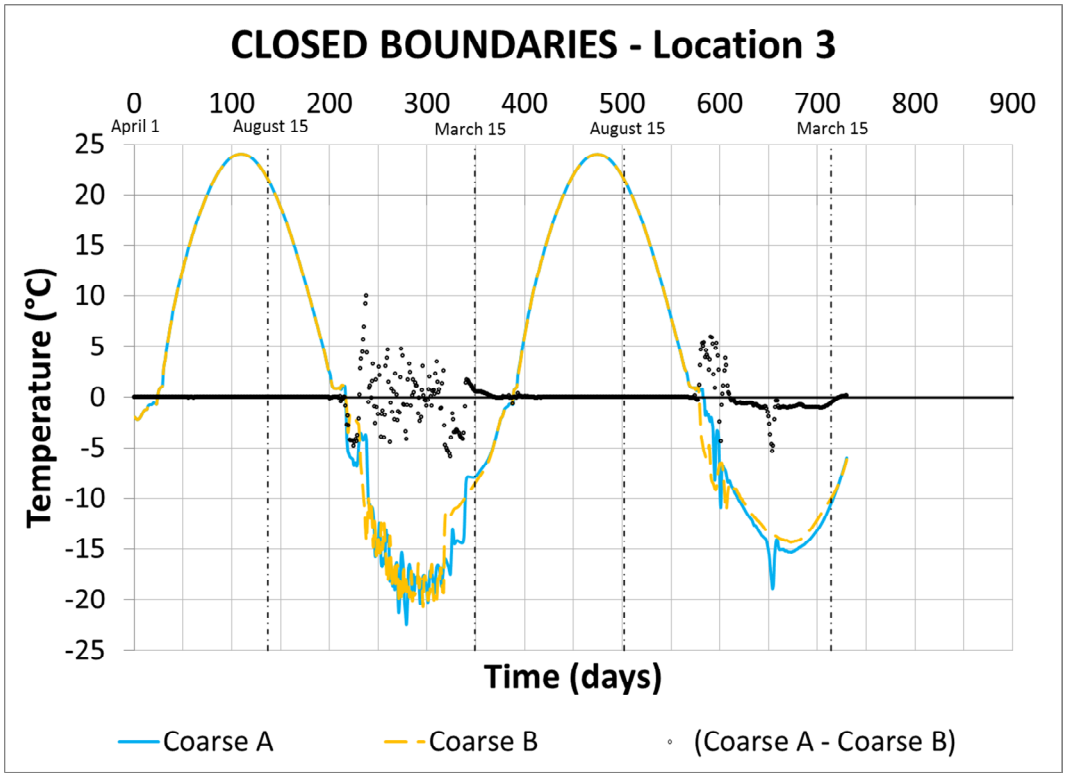

A) Time-temperature plots in Location 3

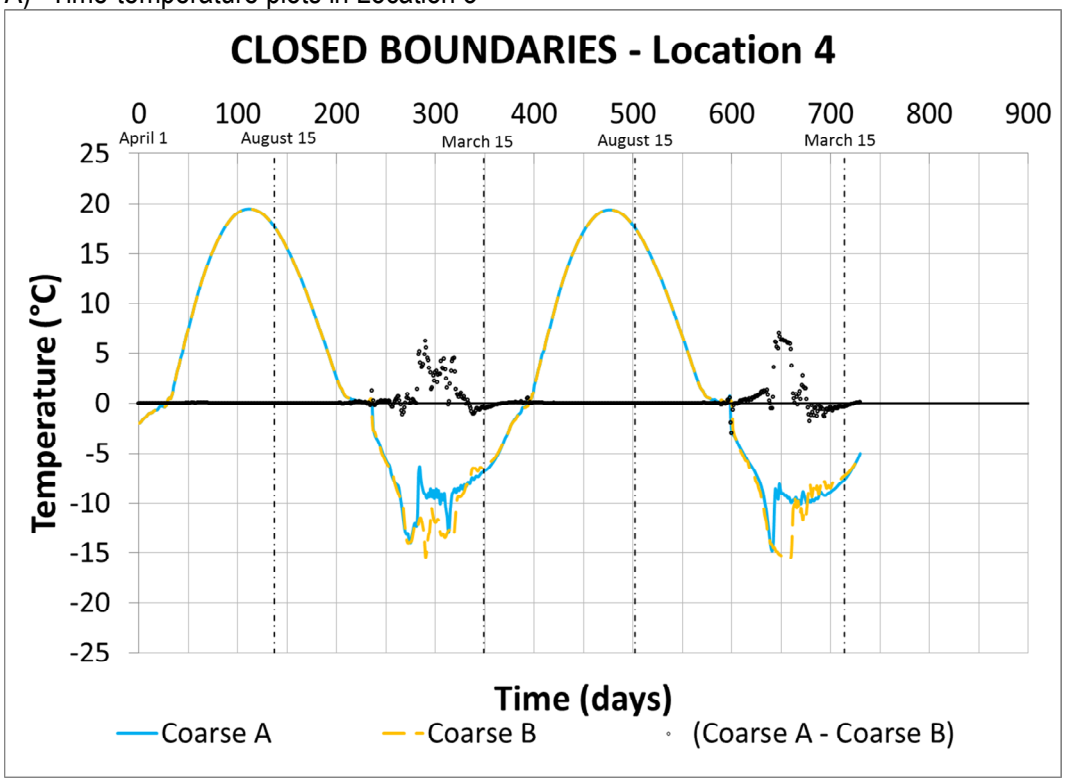

B) Time-temperature plots in Location 4

FIGURE 3.47: TRENDS IN GEOSTUDIO COARSE MESH MODEL WITH CLOSED BOUNDARIES – LOCATIONS 5 AND 6

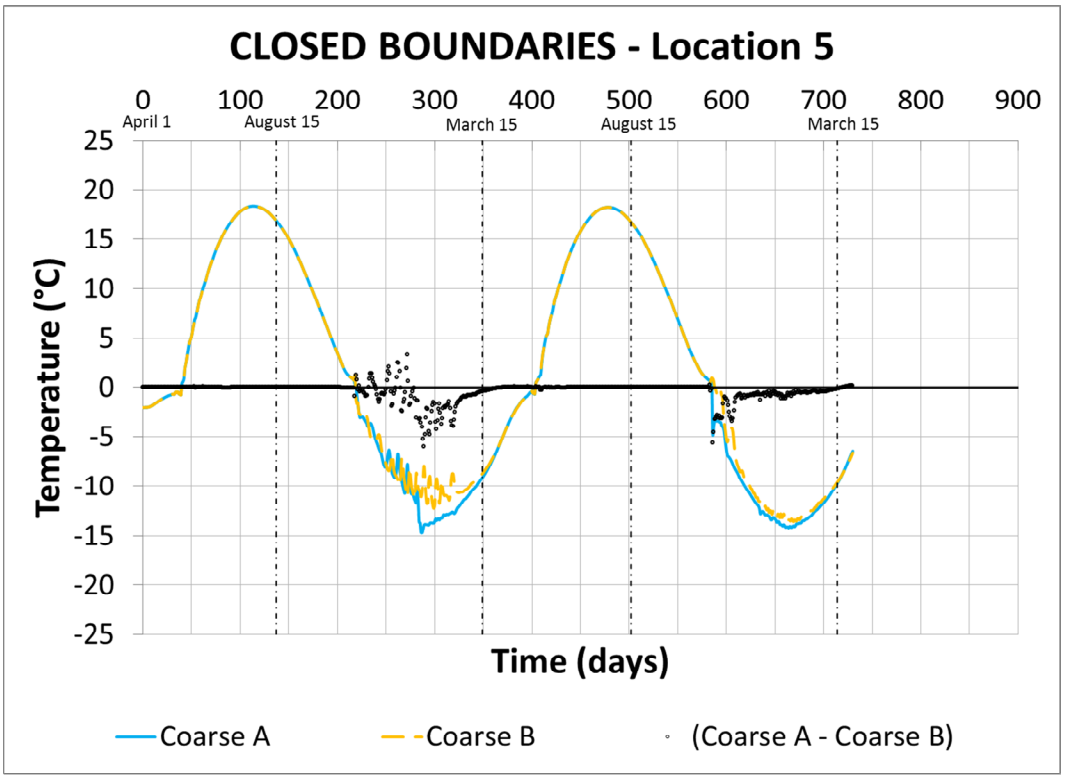

A) Time-temperature plots in Location 5

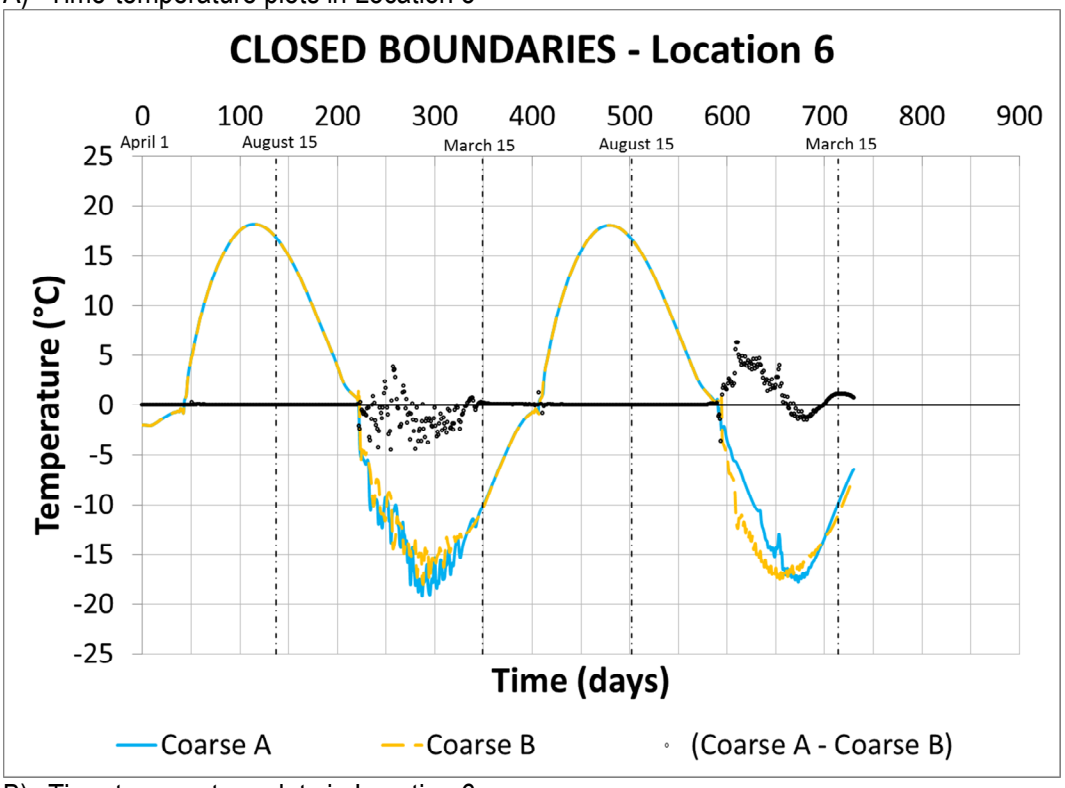

B) Time-temperature plots in Location 6

FIGURE 3.48: TRENDS IN GEOSTUDIO COARSE MESH MODEL WITH CLOSED BOUNDARIES – LOCATIONS 7 AND 8

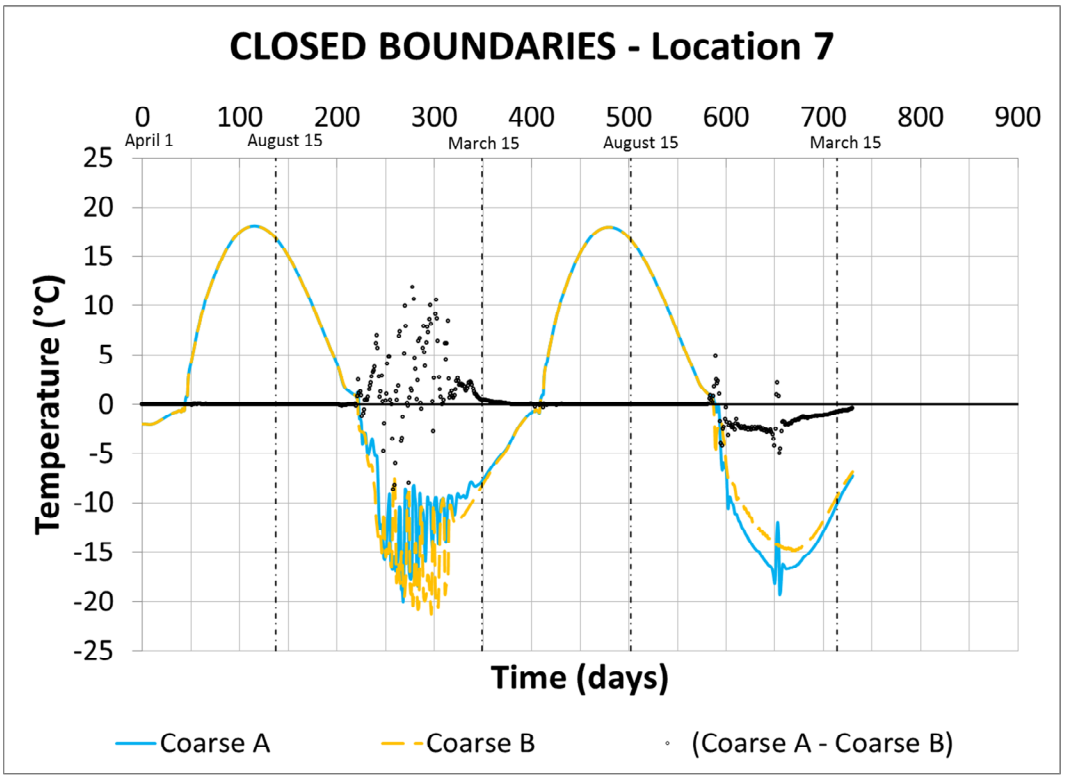

A) Time-temperature plots in Location 7

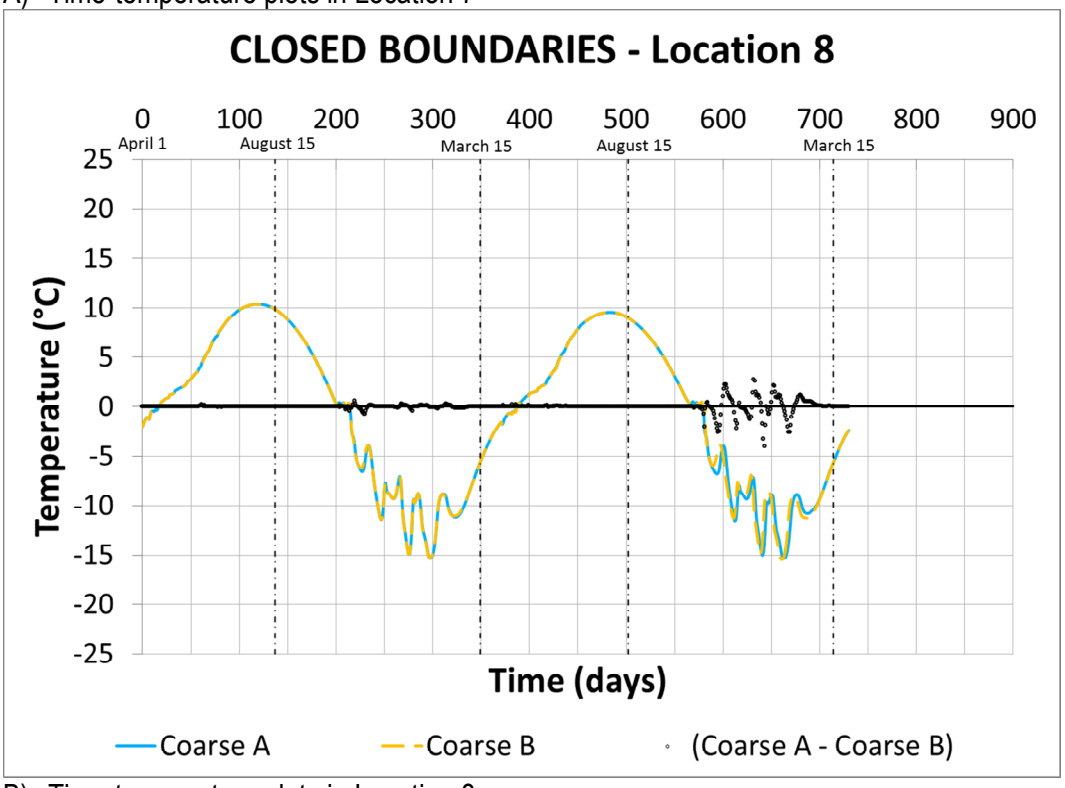

B) Time-temperature plots in Location 8

FIGURE 3.49: TRENDS IN GEOSTUDIO COARSE MESH MODEL WITH CLOSED BOUNDARIES – LOCATIONS 9 AND 10

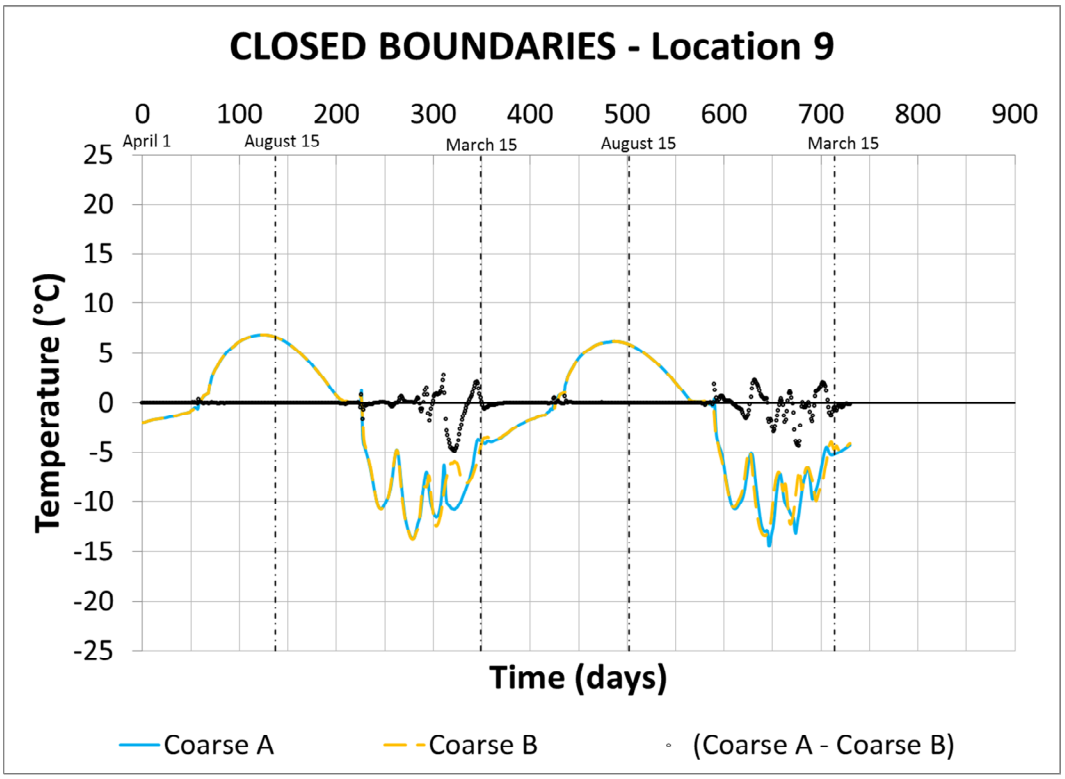

A) Time-temperature plots in Location 9

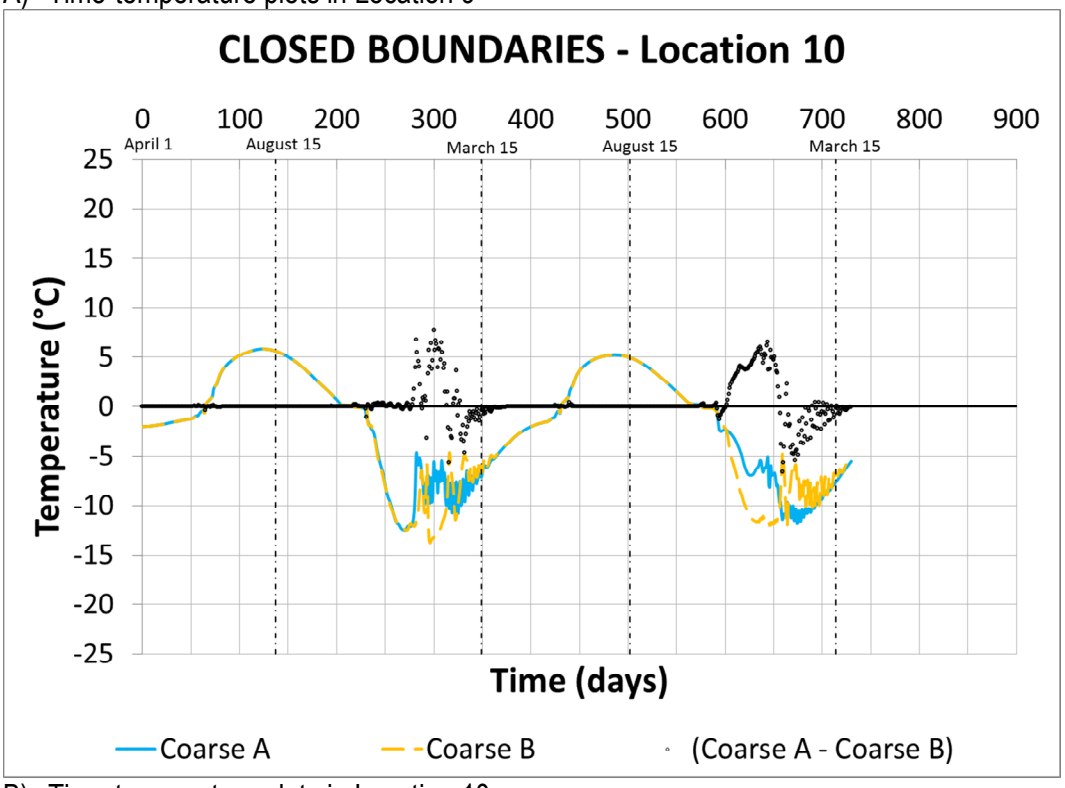

B) Time-temperature plots in Location 10

FIGURE 3.50: TRENDS IN GEOSTUDIO COARSE MESH MODEL WITH CLOSED BOUNDARIES – LOCATIONS 11 AND 12

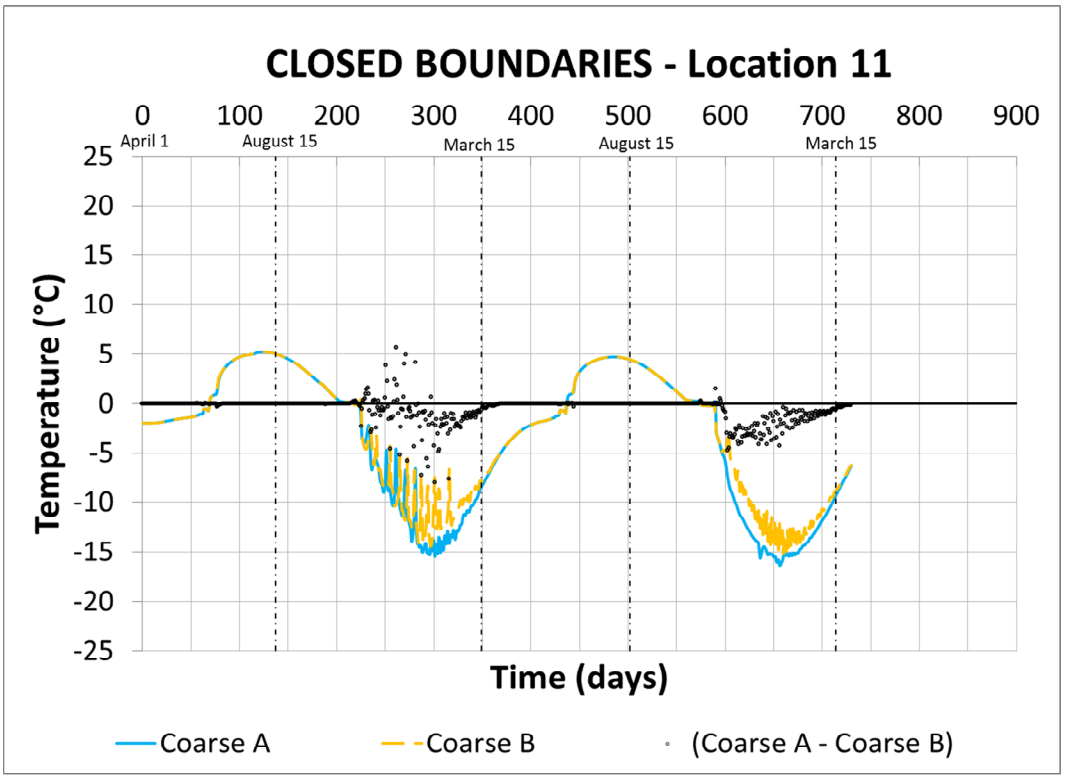

A) Time-temperature plots in Location 11

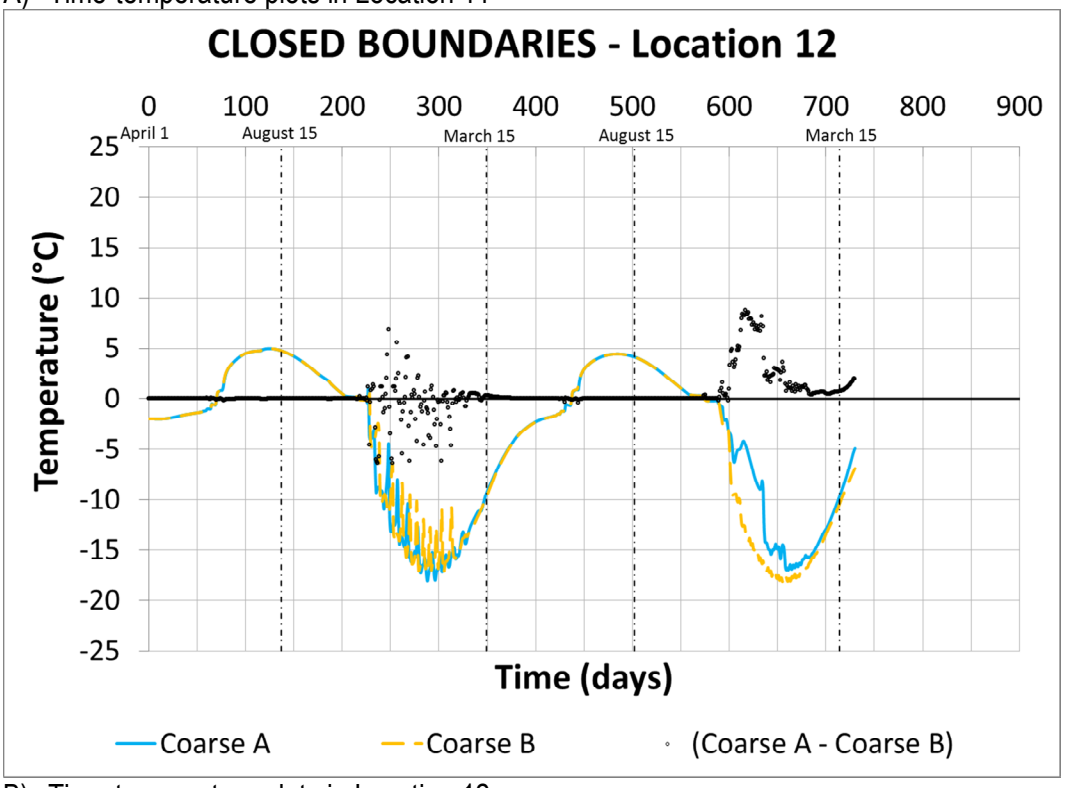

B) Time-temperature plots in Location 12

FIGURE 3.51: TRENDS IN GEOSTUDIO COARSE MESH MODEL WITH CLOSED BOUNDARIES – LOCATIONS 13 AND 14

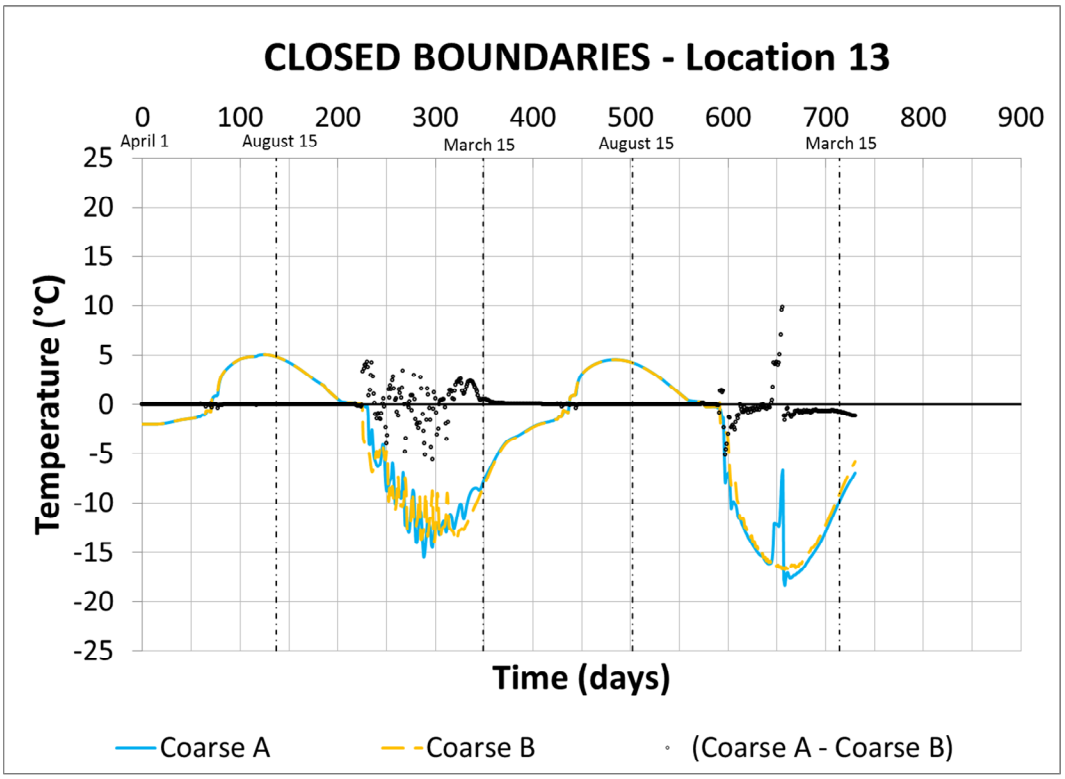

A) Time-temperature plots in Location 13

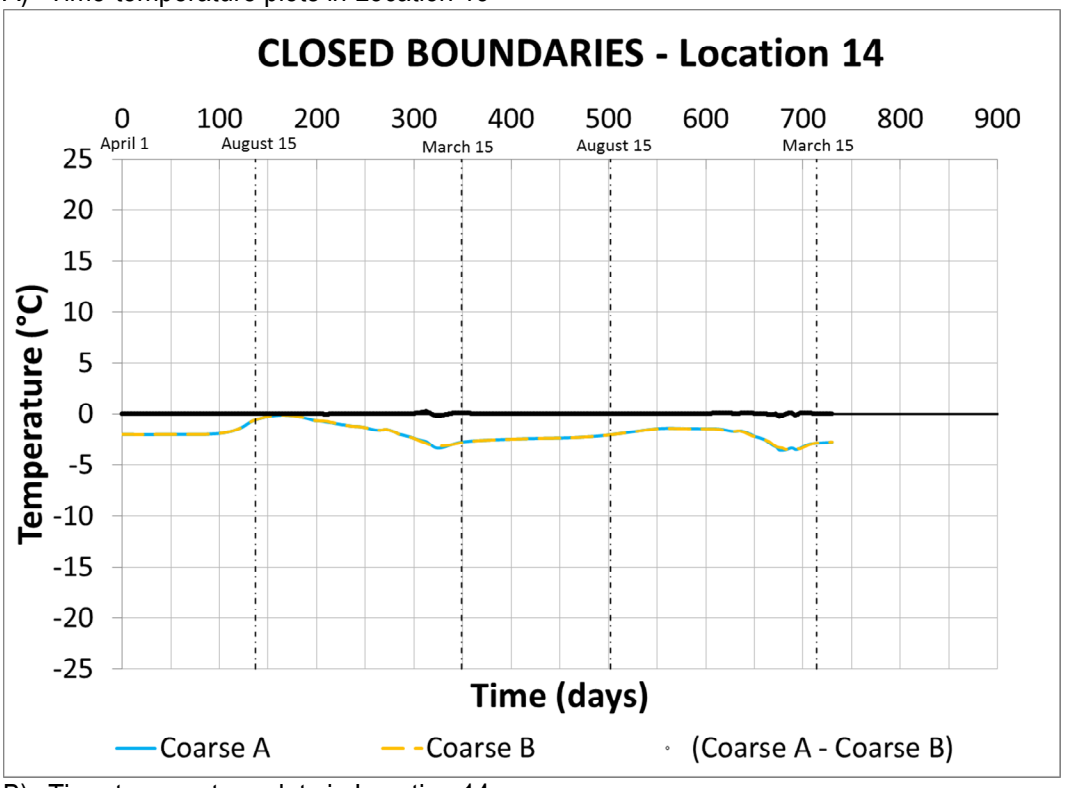

B) Time-temperature plots in Location 14

FIGURE 3.52: TRENDS IN GEOSTUDIO COARSE MESH MODEL WITH CLOSED BOUNDARIES – LOCATIONS 15 AND 16

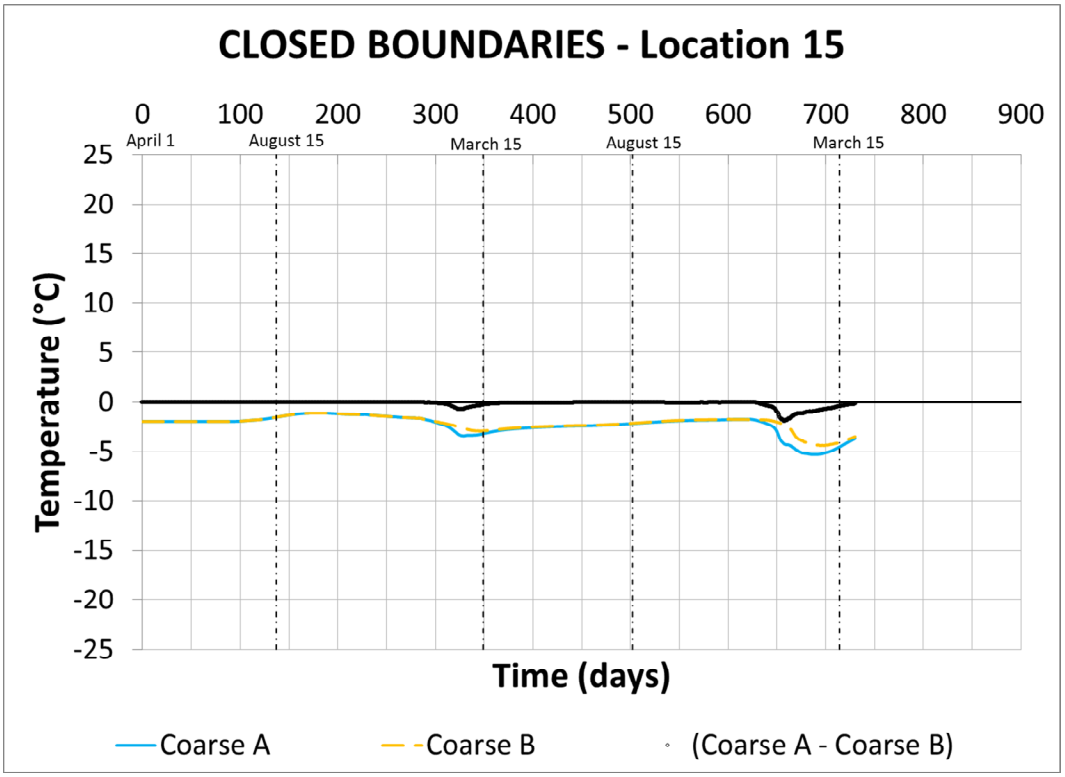

A) Time-temperature plots in Location 15

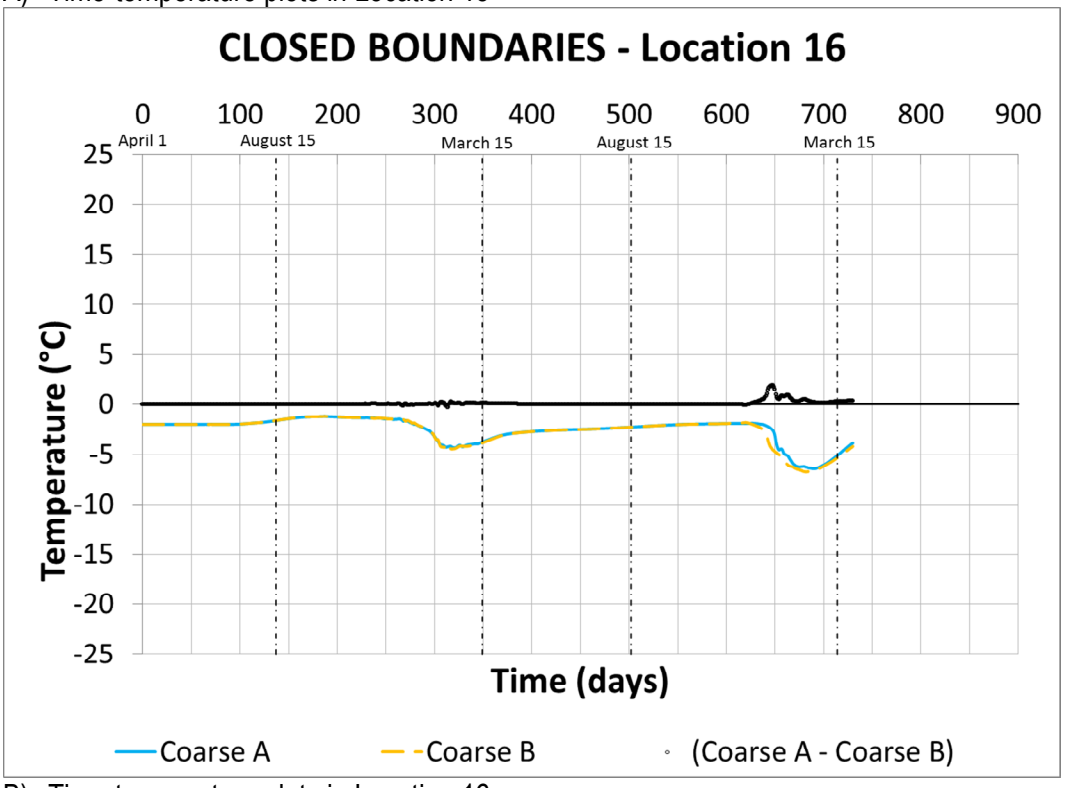

B) Time-temperature plots in Location 16

FIGURE 3.53: TRENDS IN GEOSTUDIO FINE MESH MODEL WITH CLOSED BOUNDARIES – LOCATIONS 1 AND 2

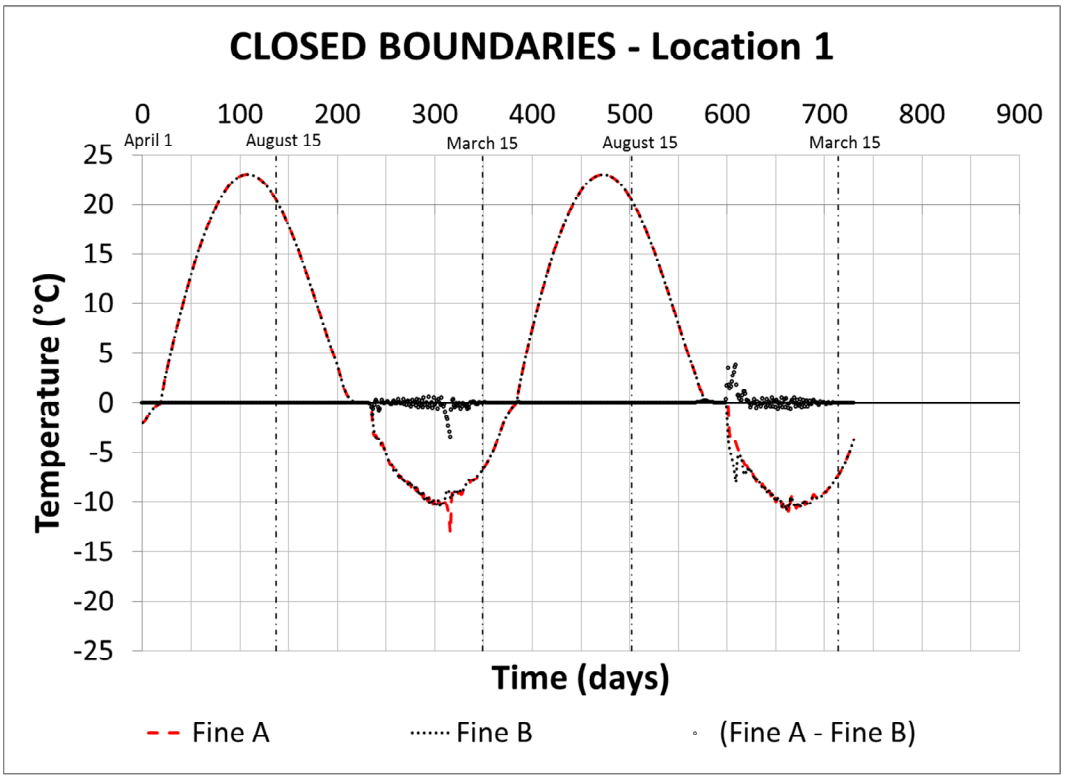

A) Time-temperature plots in Location 1

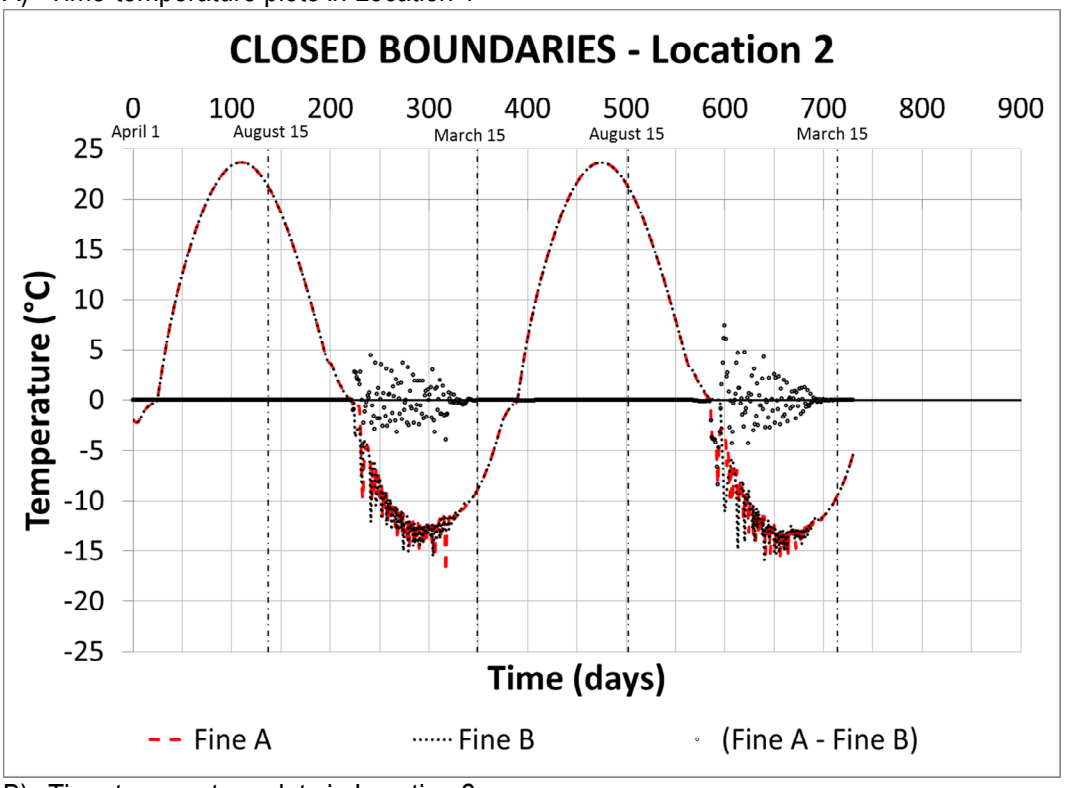

B) Time-temperature plots in Location 2

FIGURE 3.54: TRENDS IN GEOSTUDIO FINE MESH MODEL WITH CLOSED BOUNDARIES – LOCATIONS 3 AND 4

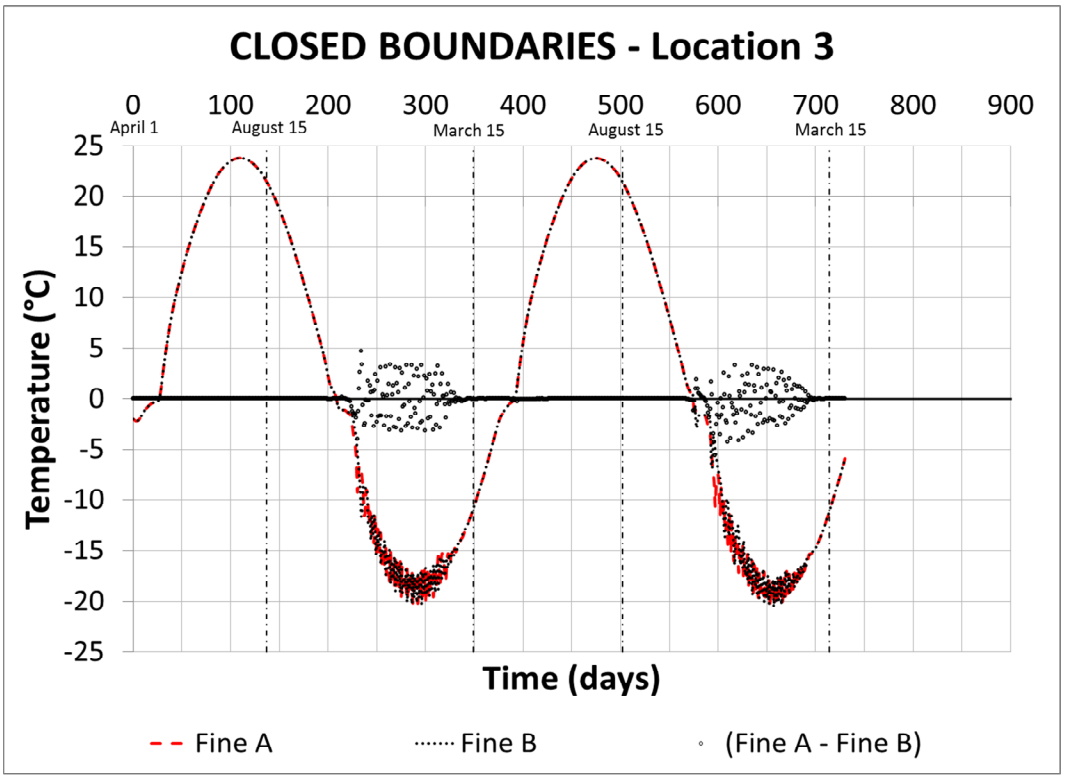

A) Time-temperature plots in Location 3

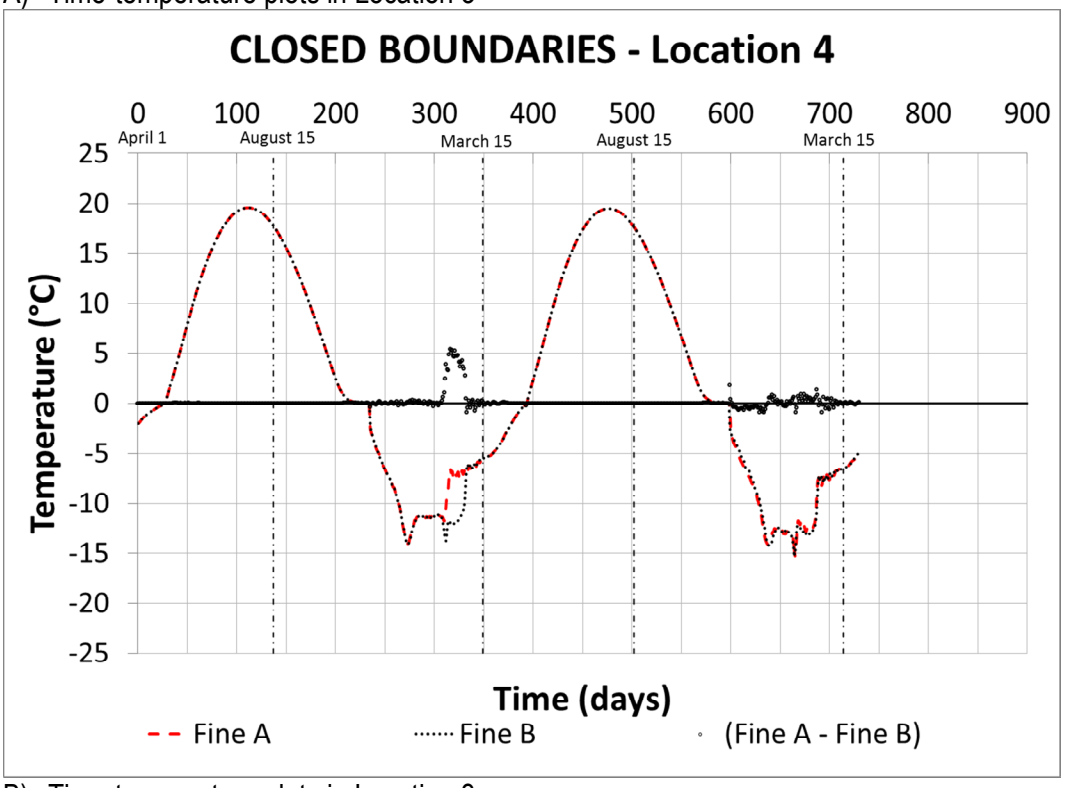

B) Time-temperature plots in Location 3

FIGURE 3.55: TRENDS IN GEOSTUDIO FINE MESH MODEL WITH CLOSED BOUNDARIES – LOCATIONS 5 AND 6

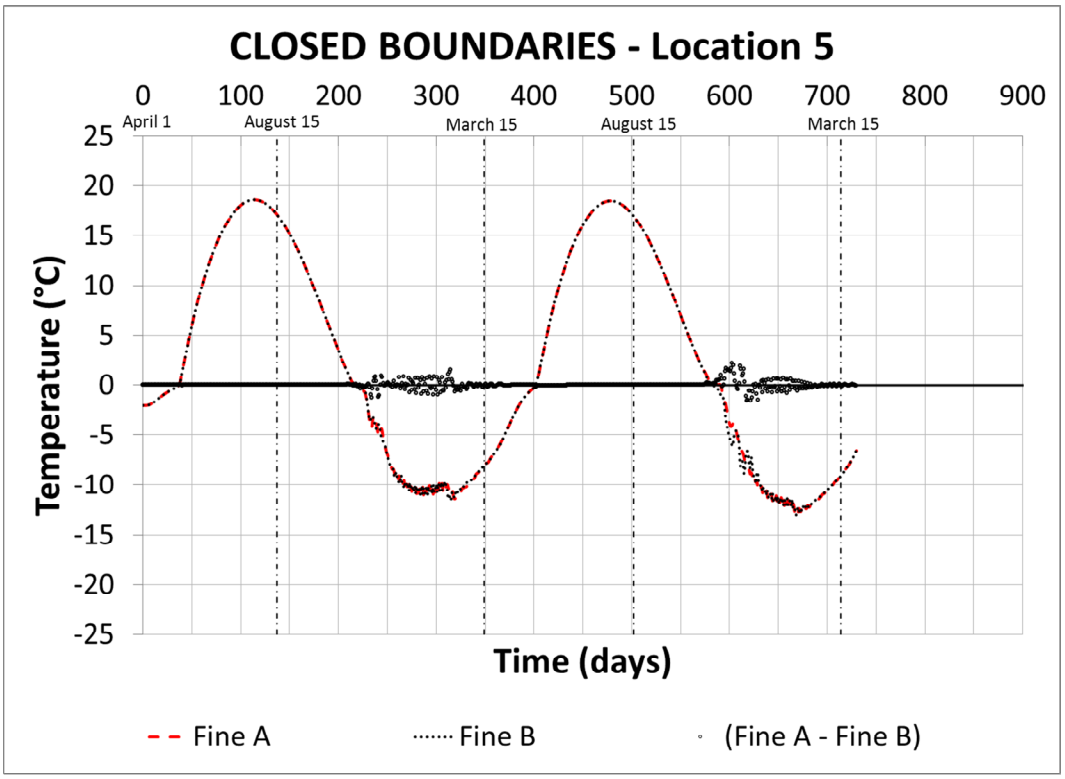

A) Time-temperature plots in Location 5

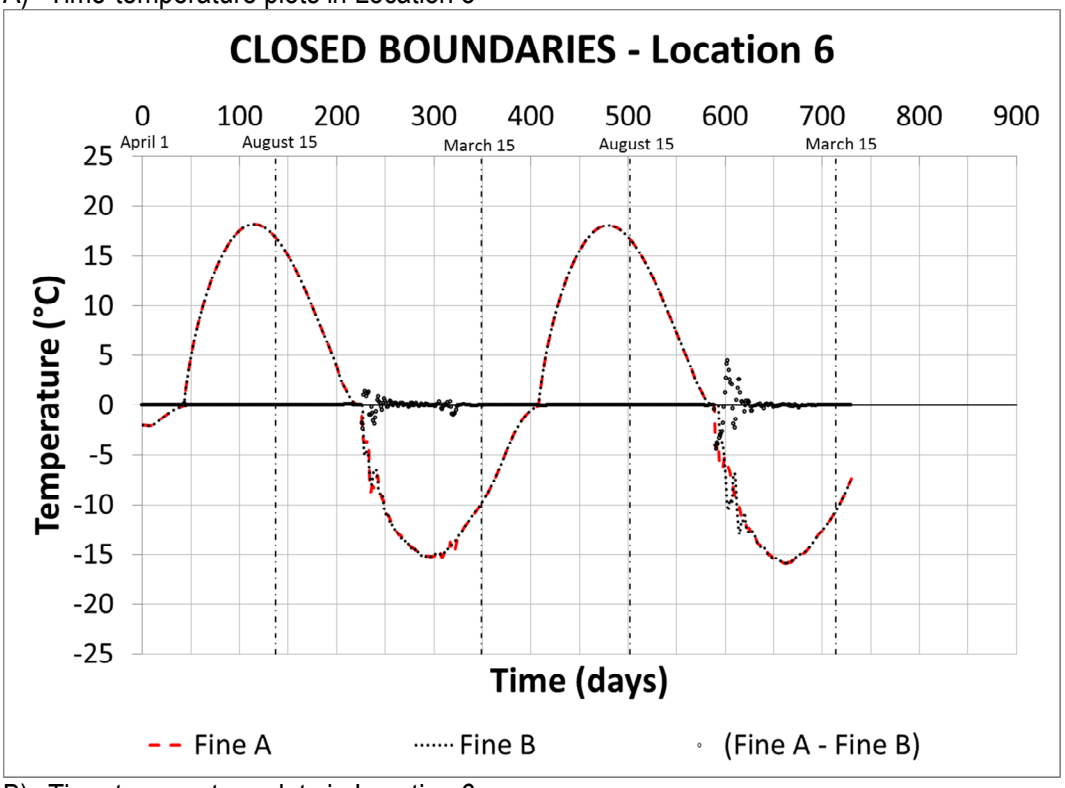

B) Time-temperature plots in Location 6

FIGURE 3.56: TRENDS IN GEOSTUDIO FINE MESH MODEL WITH CLOSED BOUNDARIES – LOCATIONS 7 AND 8

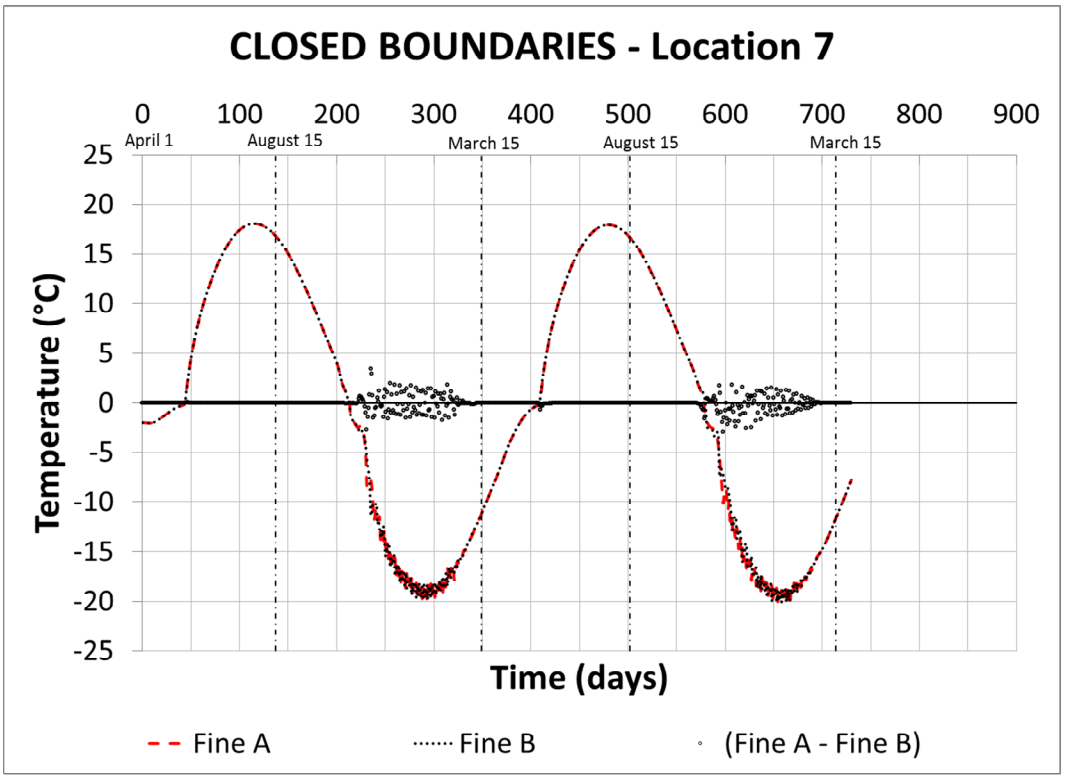

A) Time-temperature plots in Location 7

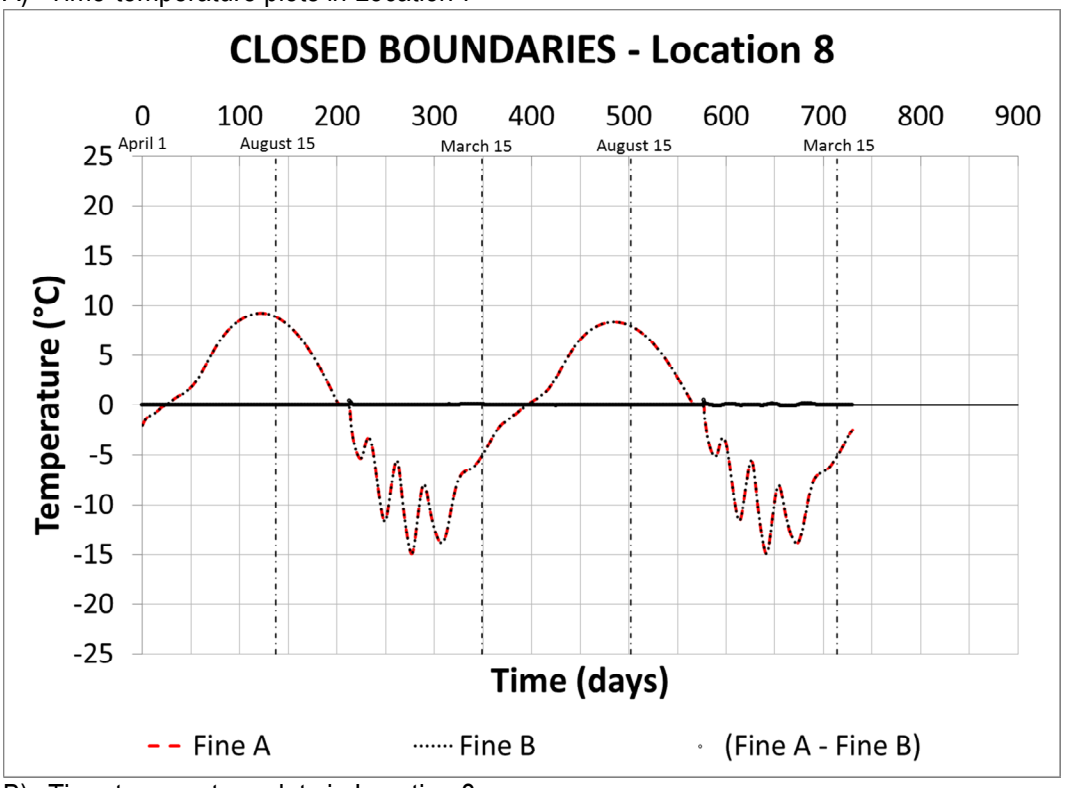

B) Time-temperature plots in Location 8

FIGURE 3.57: TRENDS IN GEOSTUDIO FINE MESH MODEL WITH CLOSED BOUNDARIES – LOCATIONS 9 AND 10

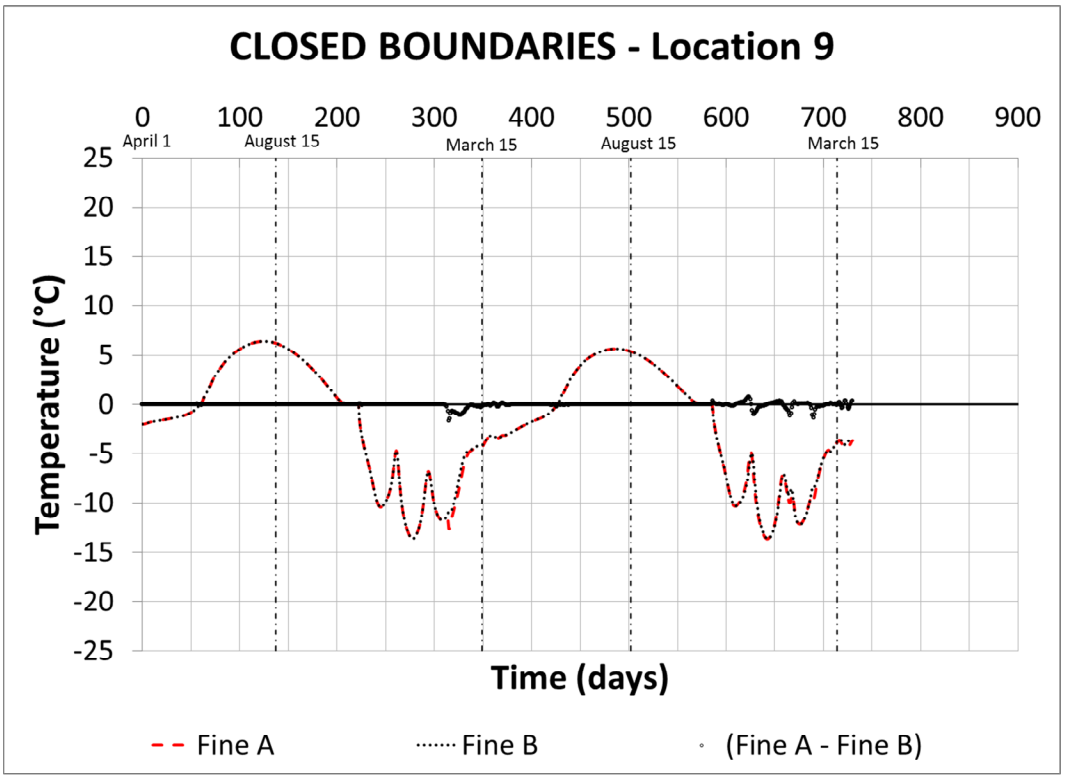

A) Time-temperature plots in Location 9

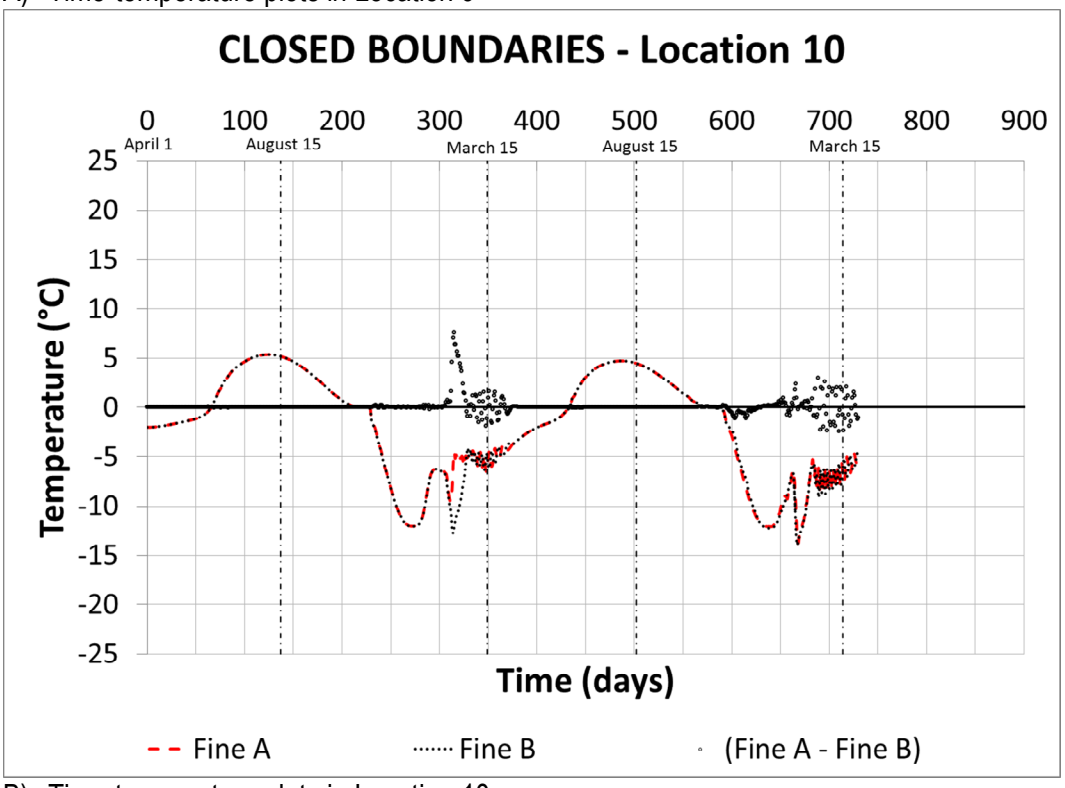

B) Time-temperature plots in Location 10

FIGURE 3.58: TRENDS IN GEOSTUDIO FINE MESH MODEL WITH CLOSED BOUNDARIES – LOCATIONS 11 AND 12

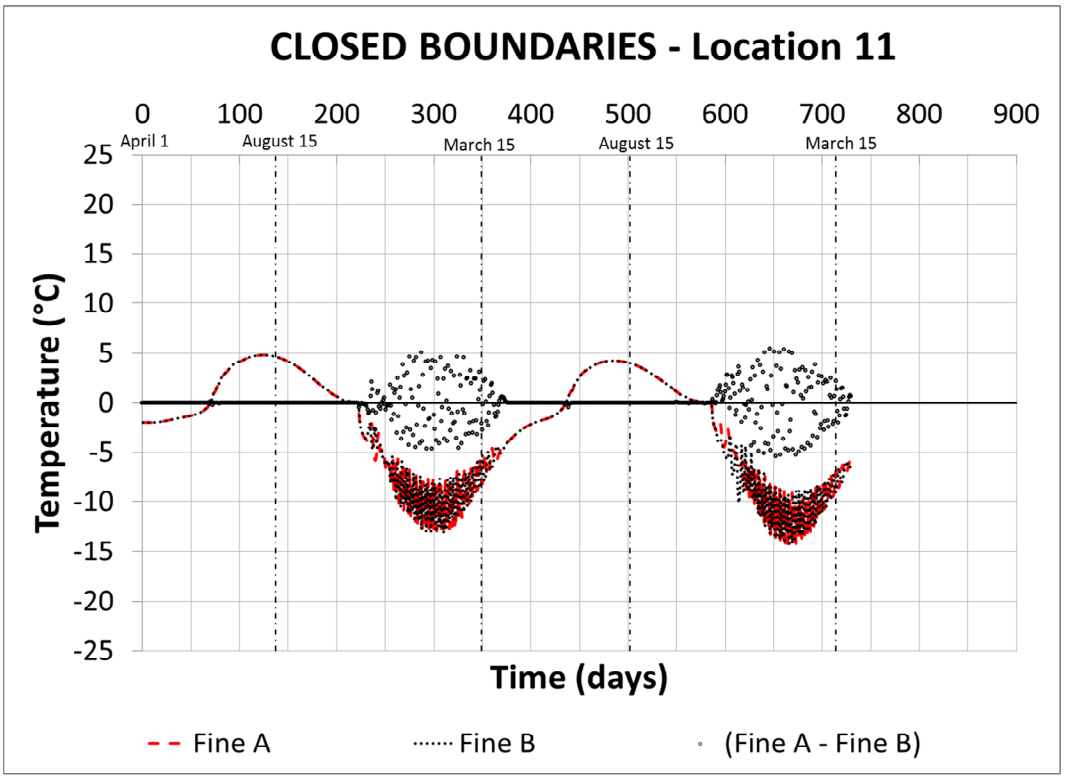

A) Time-temperature plots in Location 11

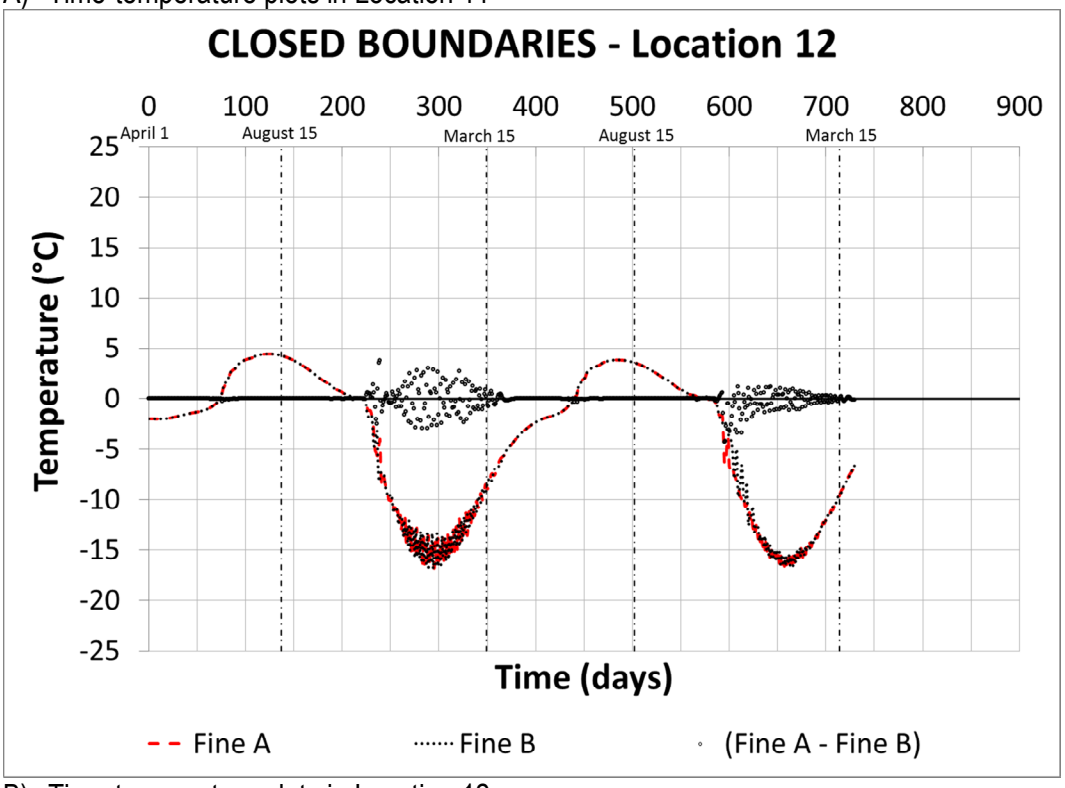

B) Time-temperature plots in Location 12

FIGURE 3.59: TRENDS IN GEOSTUDIO FINE MESH MODEL WITH CLOSED BOUNDARIES – LOCATIONS 13 AND 14

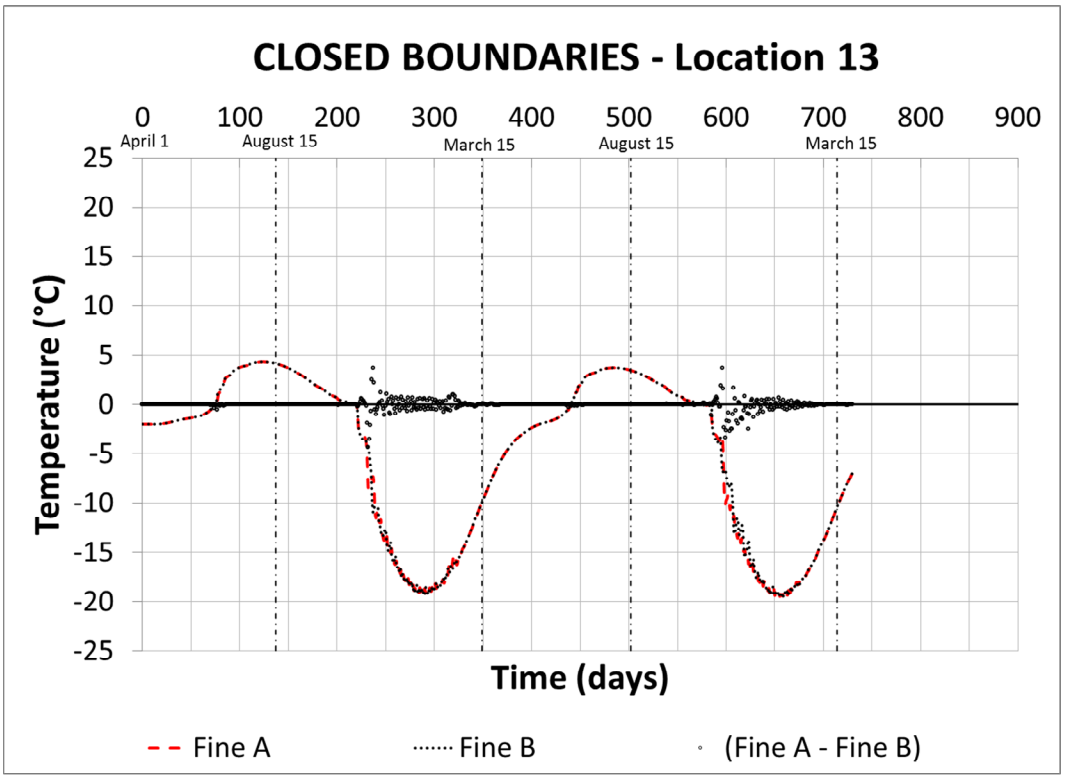

A) Time-temperature plots in Location 13

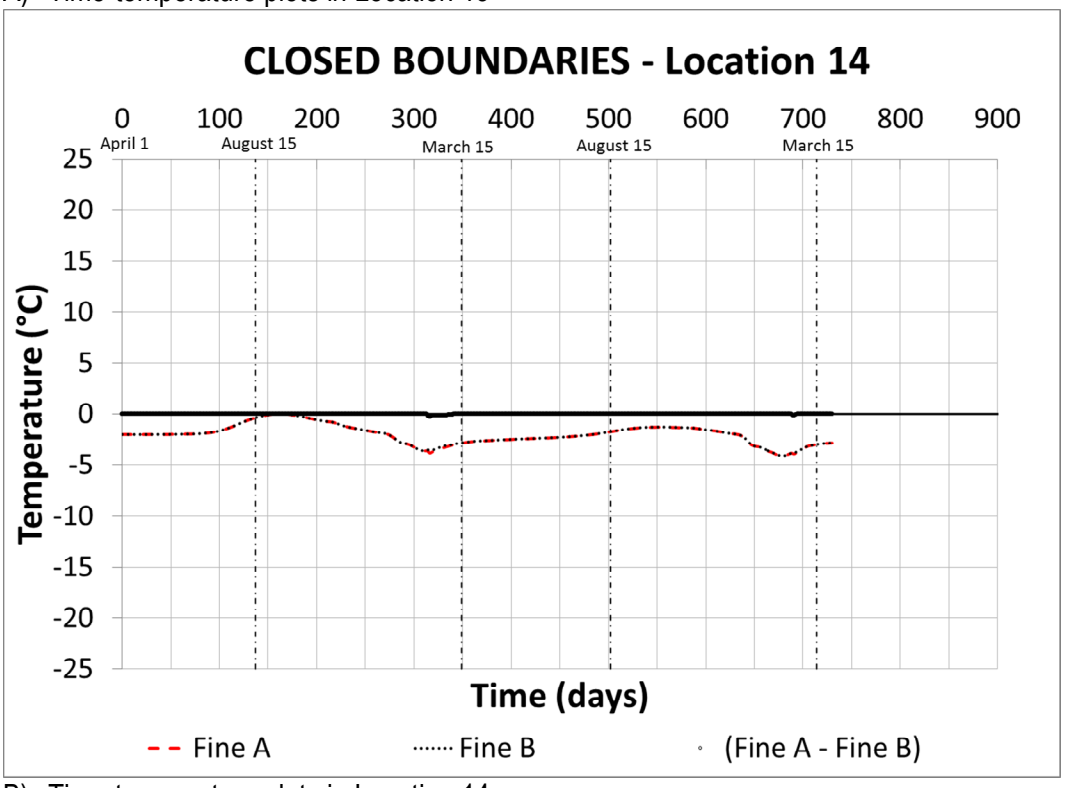

B) Time-temperature plots in Location 14

FIGURE 3.60: TRENDS IN GEOSTUDIO FINE MESH MODEL WITH CLOSED BOUNDARIES – LOCATIONS 15 AND 16

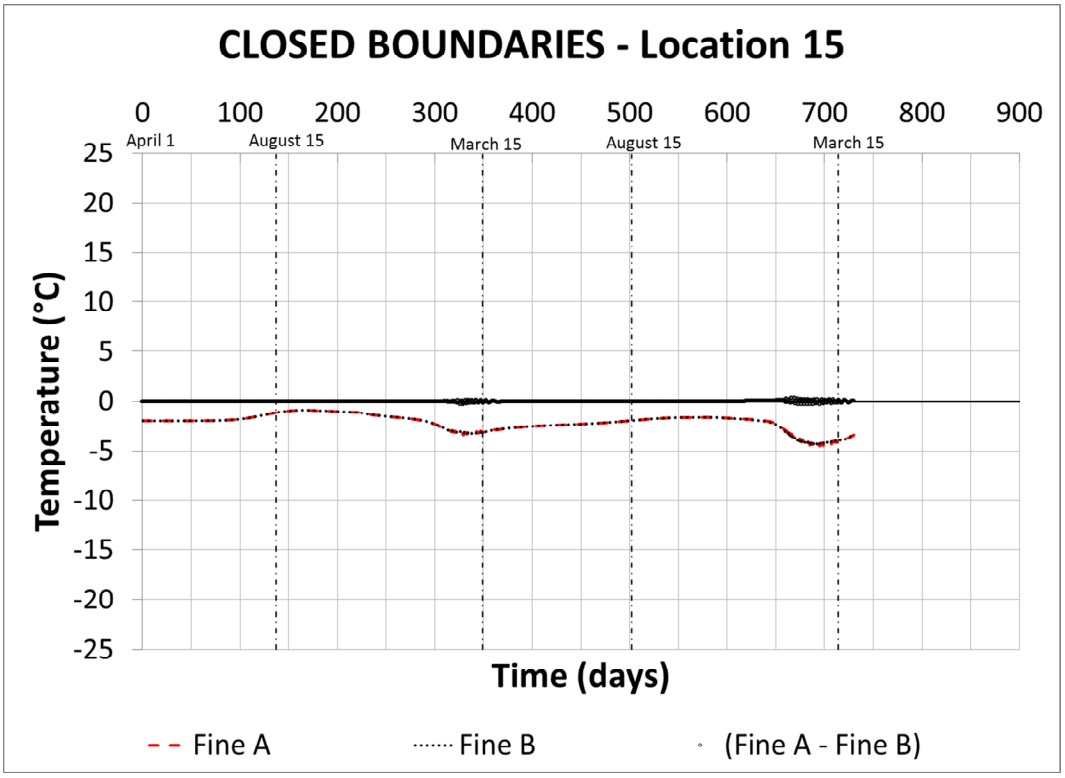

A) Time-temperature plots in Location 15

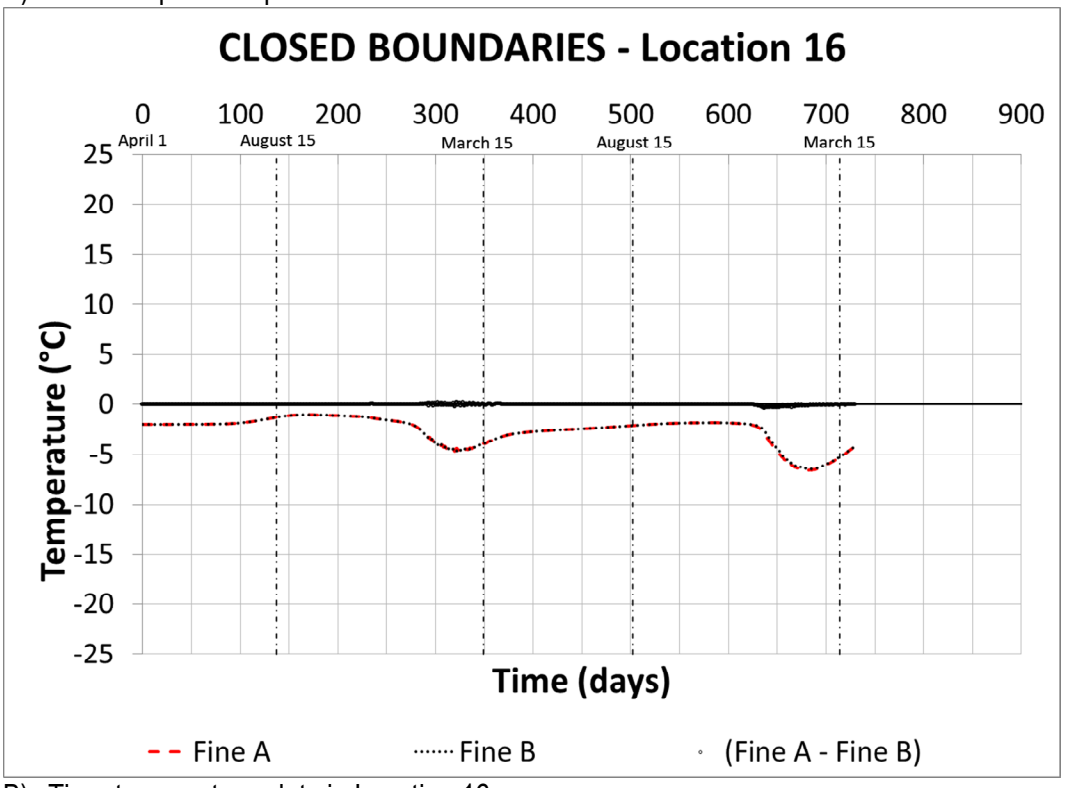

B) Time-temperature plots in Location 16

FIGURE 3.61: TRENDS IN TWO GEOSTUDIO COARSE MESH MODELS WITH EITHER CLOSED BOUNDARIES OR OPEN SIDESLOPES – LOCATIONS 1 AND 2

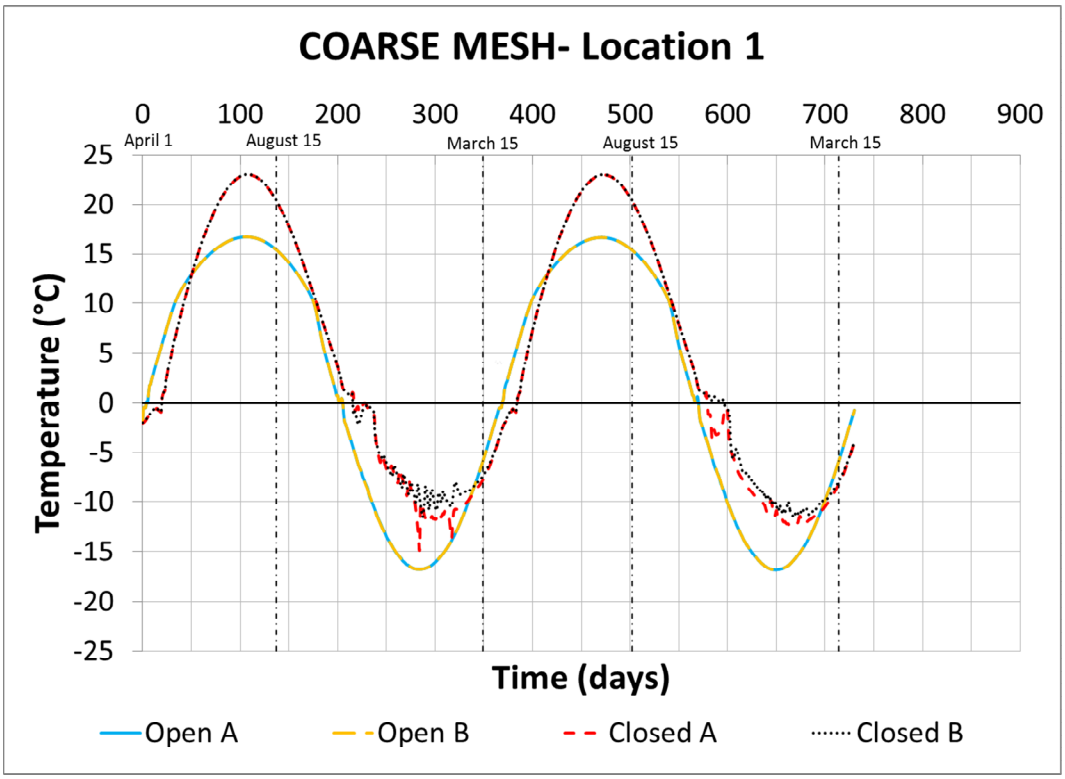

A) Time-temperature plots in Location 1

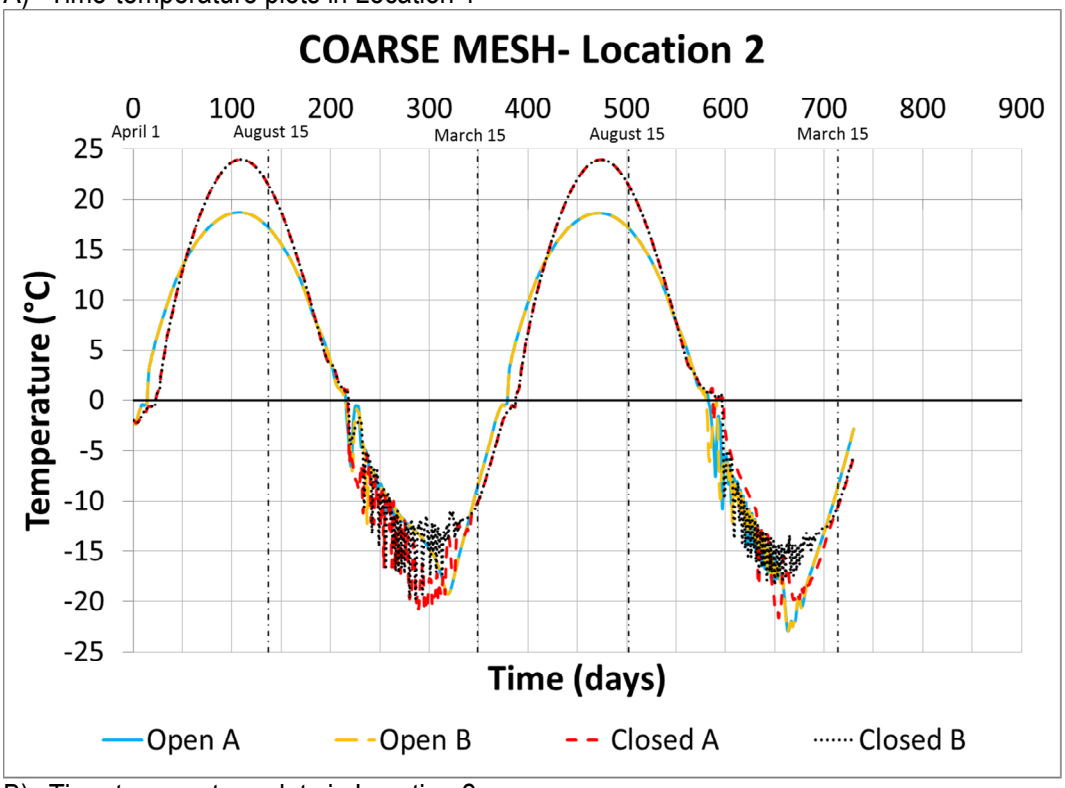

B) Time-temperature plots in Location 2

FIGURE 3.62: TRENDS IN TWO GEOSTUDIO COARSE MESH MODELS WITH EITHER CLOSED BOUNDARIES OR OPEN SIDESLOPES – LOCATIONS 3 AND 4

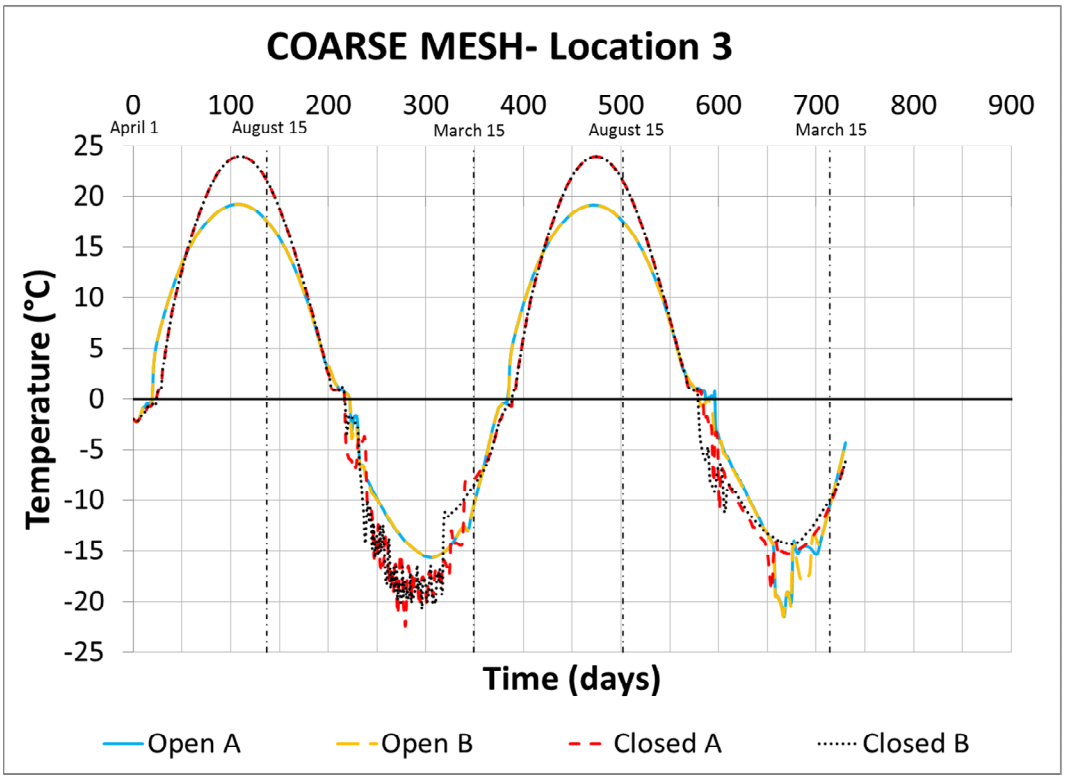

A) Time-temperature plots in Location 3

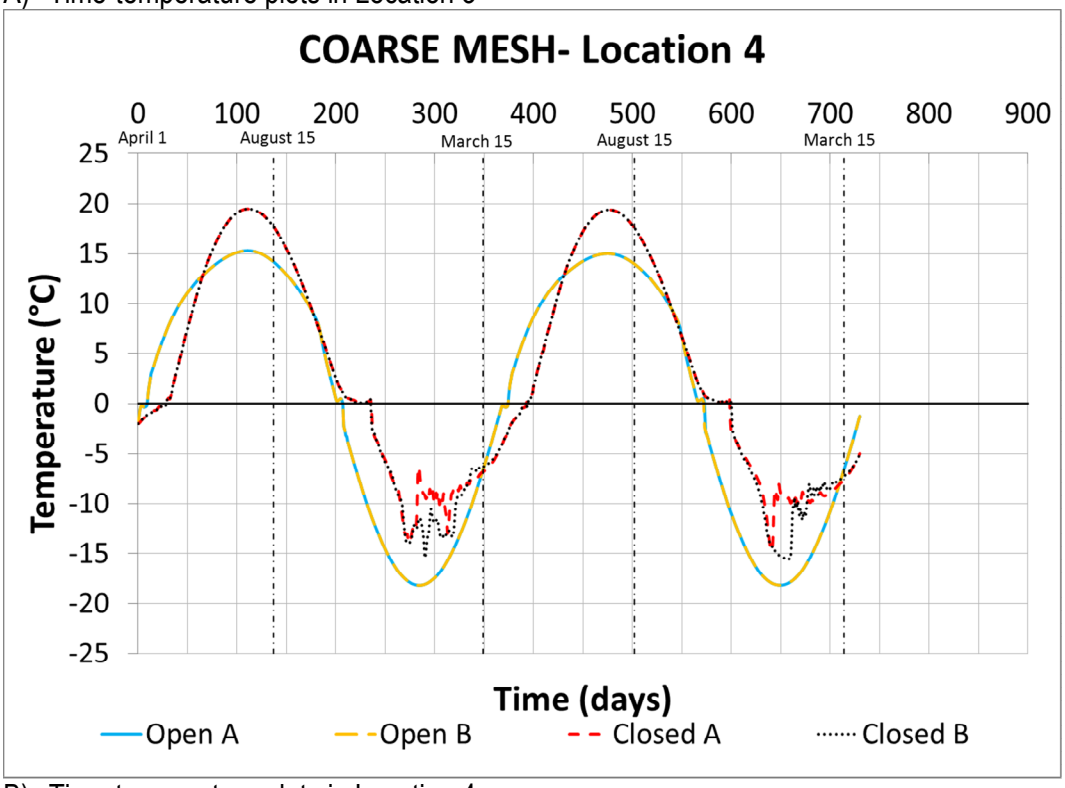

B) Time-temperature plots in Location 4

FIGURE 3.63: TRENDS IN TWO GEOSTUDIO COARSE MESH MODELS WITH EITHER CLOSED BOUNDARIES OR OPEN SIDESLOPES – LOCATIONS 5 AND 6

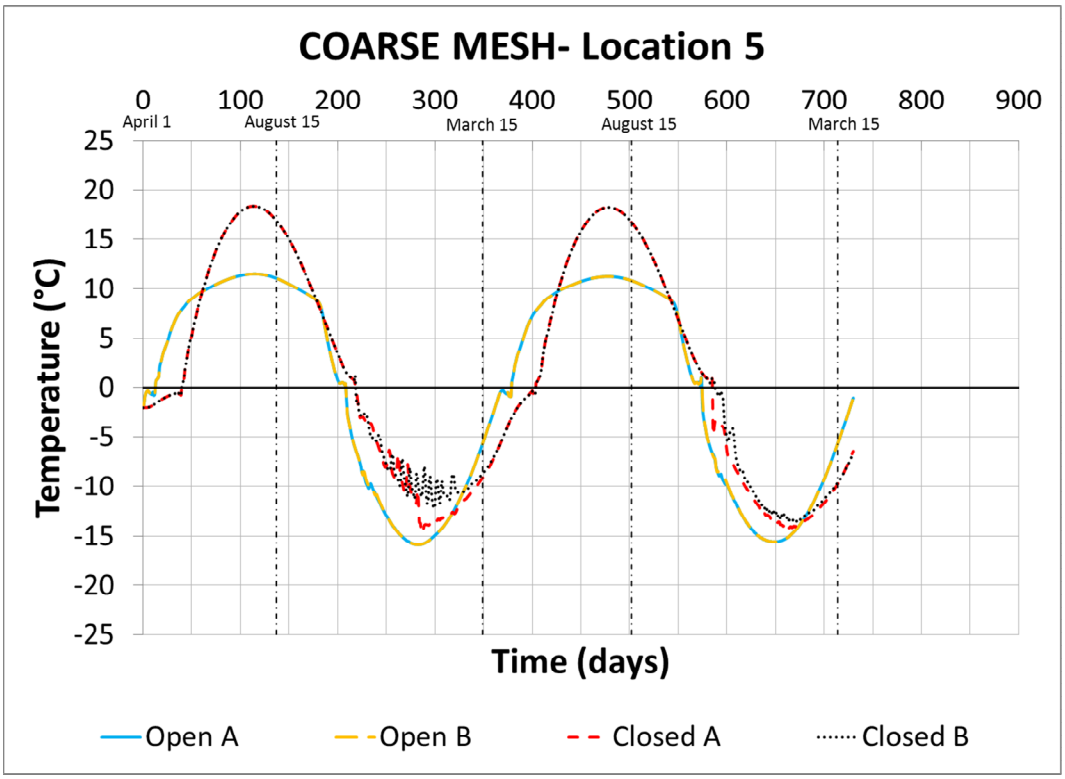

A) Time-temperature plots in Location 5

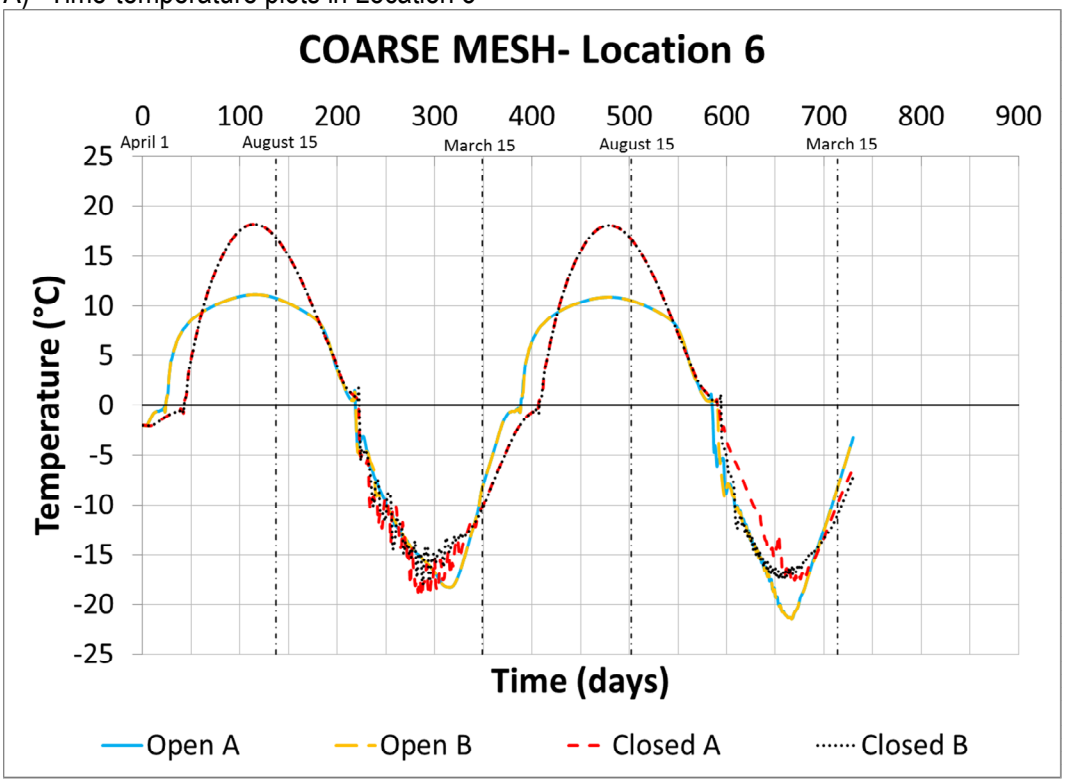

B) Time-temperature plots in Location 6

FIGURE 3.64: TRENDS IN TWO GEOSTUDIO COARSE MESH MODELS WITH EITHER CLOSED BOUNDARIES OR OPEN SIDESLOPES – LOCATIONS 7 AND 8

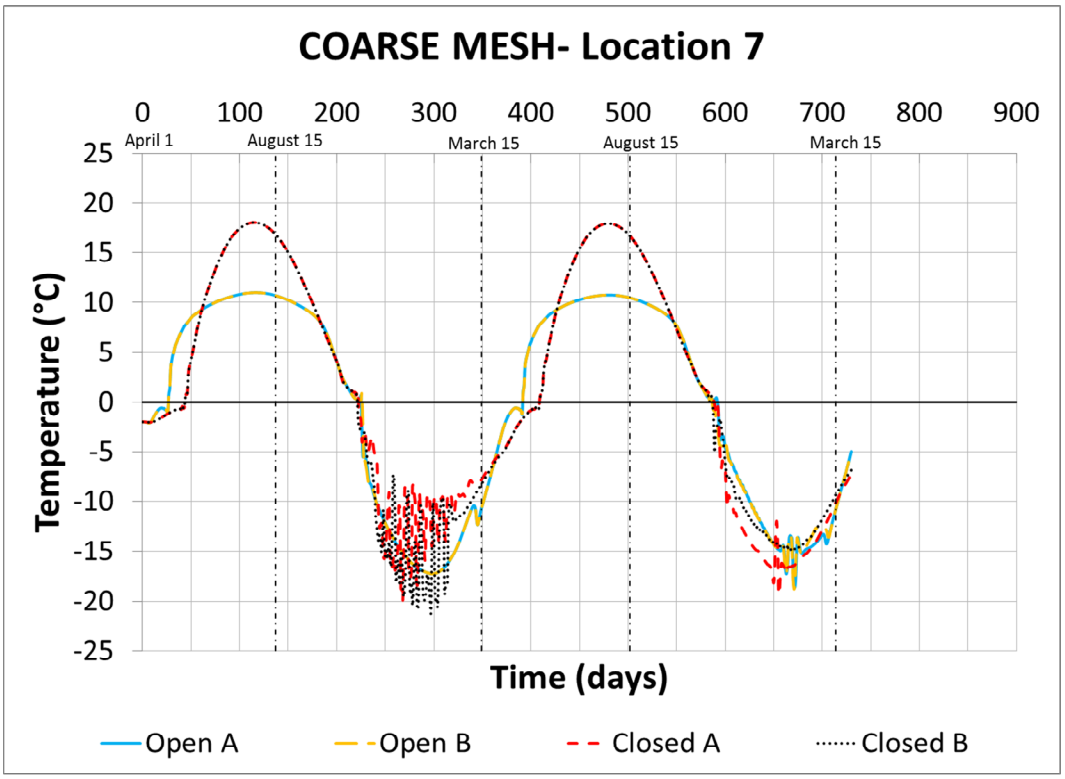

A) Time-temperature plots in Location 9

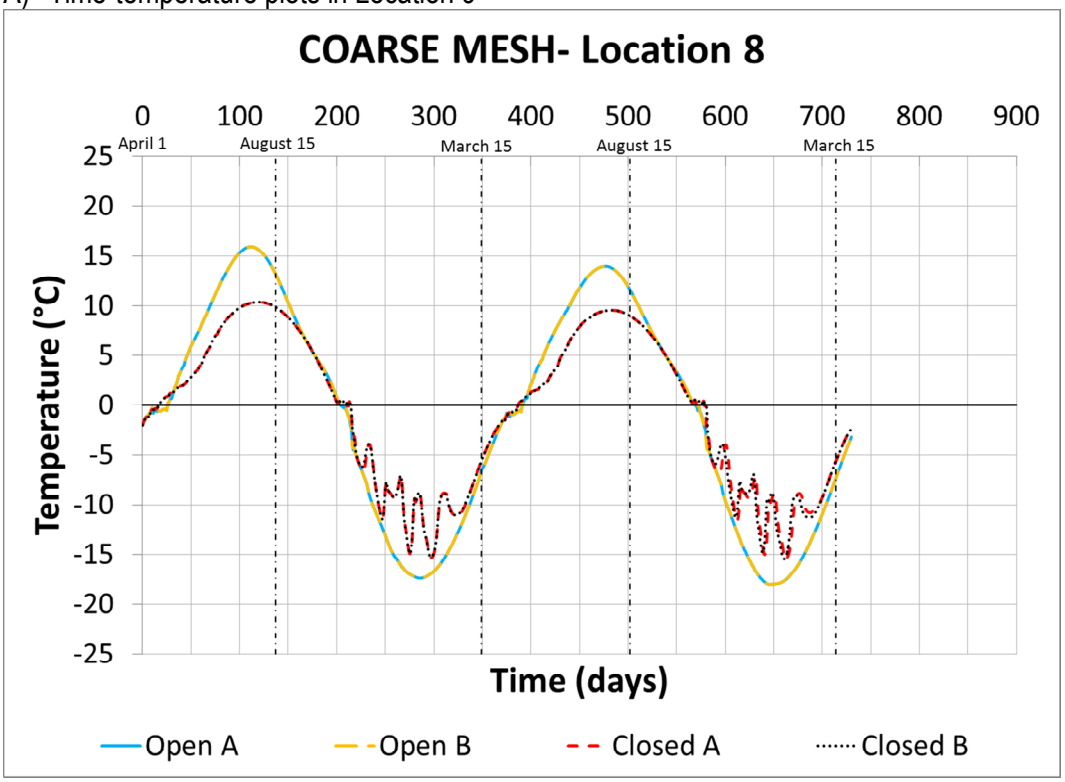

B) Time-temperature plots in Location 10

FIGURE 3.65: TRENDS IN TWO GEOSTUDIO COARSE MESH MODELS WITH EITHER CLOSED BOUNDARIES OR OPEN SIDESLOPES – LOCATIONS 9 AND 10

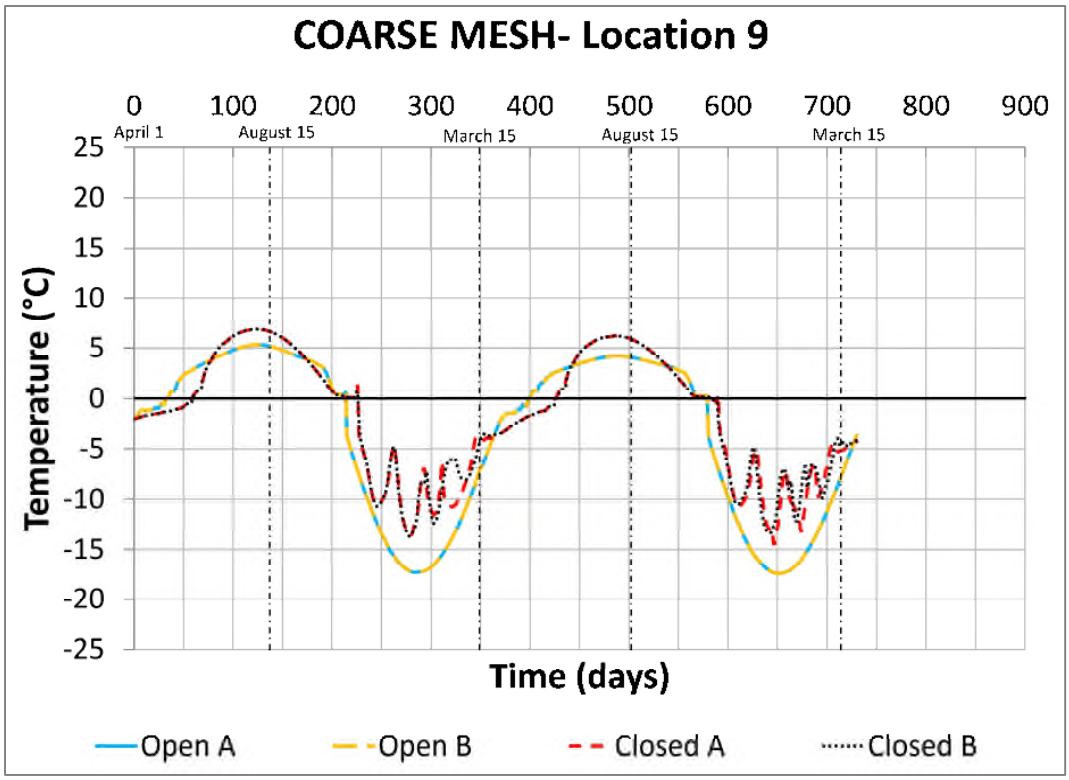

A) Time-temperature plots in Location 9

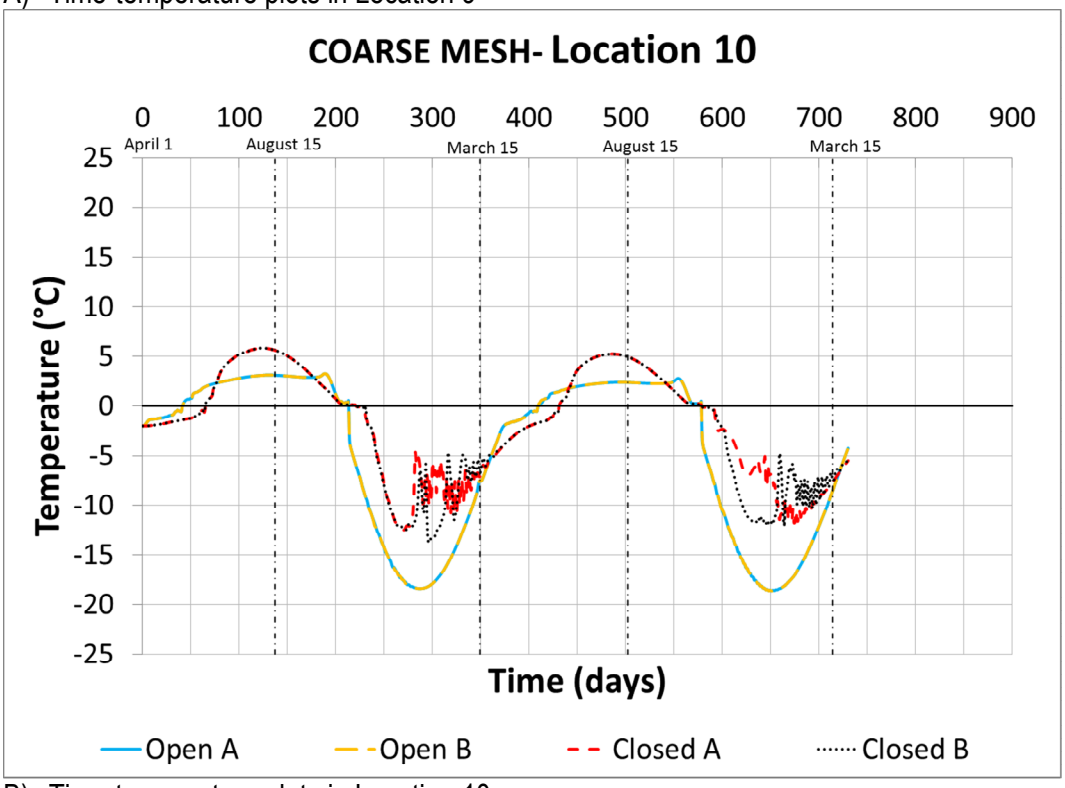

B) Time-temperature plots in Location 10

FIGURE 3.66: TRENDS IN TWO GEOSTUDIO COARSE MESH MODELS WITH EITHER CLOSED BOUNDARIES OR OPEN SIDESLOPES – LOCATIONS 11 AND 12

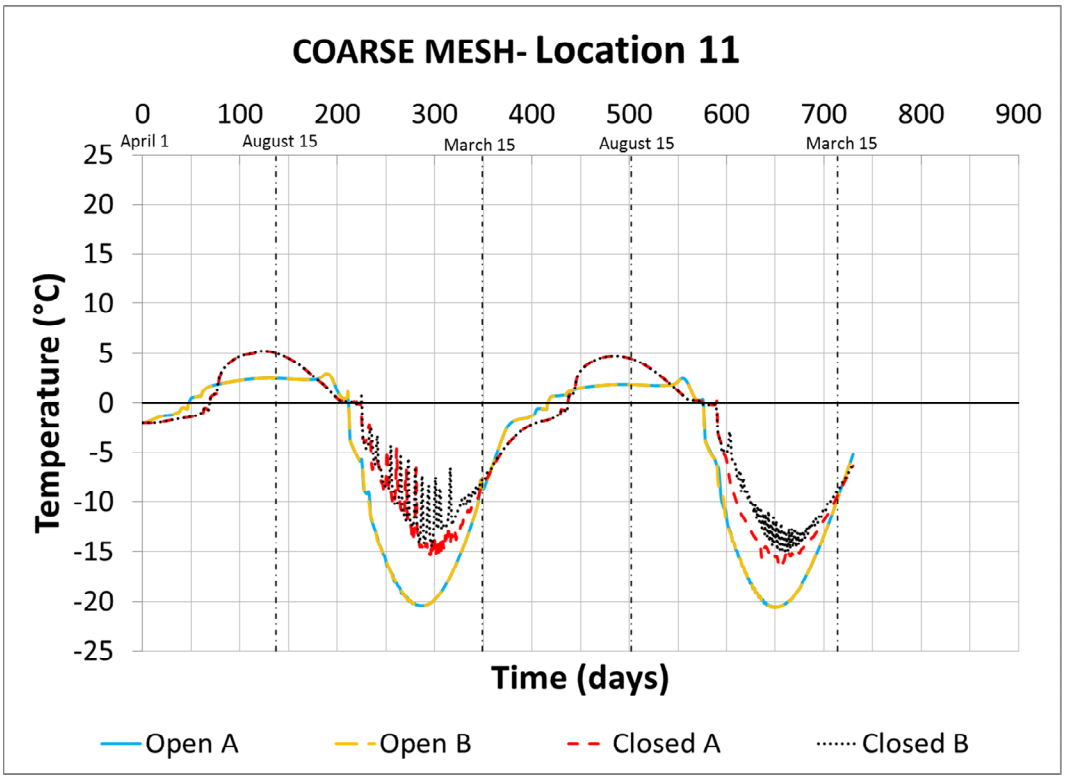

A) Time-temperature plots in Location 11

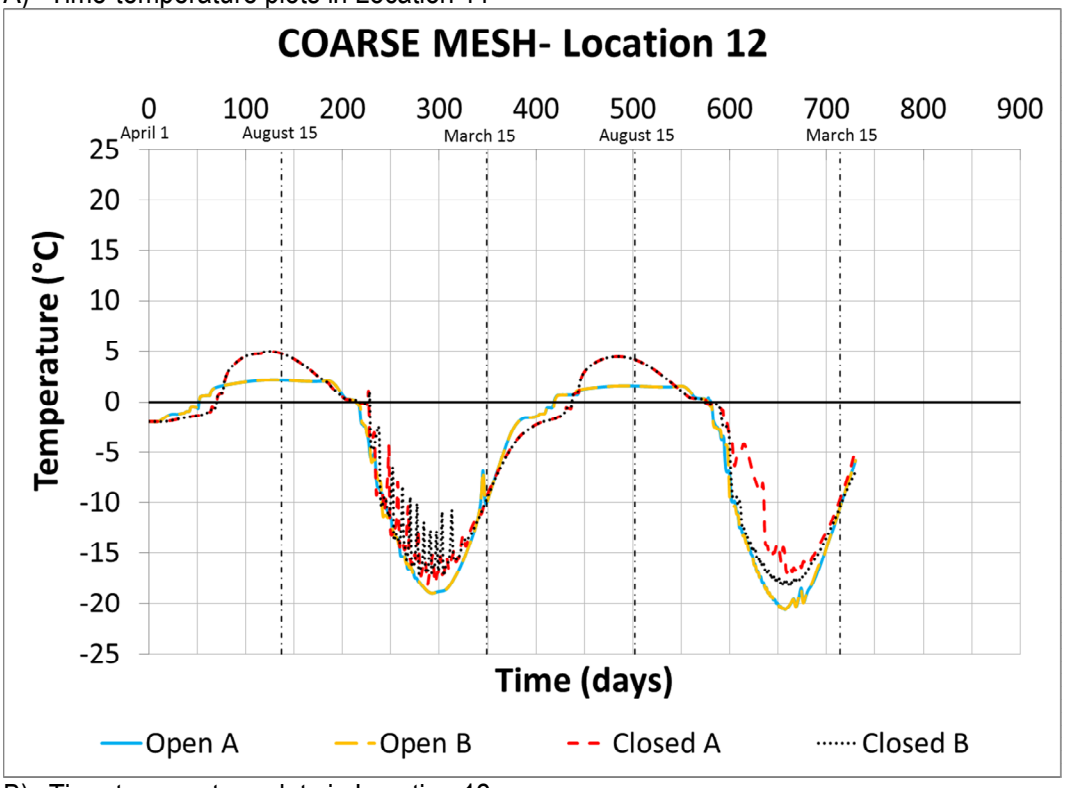

B) Time-temperature plots in Location 12

FIGURE 3.67: TRENDS IN TWO GEOSTUDIO COARSE MESH MODELS WITH EITHER CLOSED BOUNDARIES OR OPEN SIDESLOPES – LOCATIONS 13 AND 14

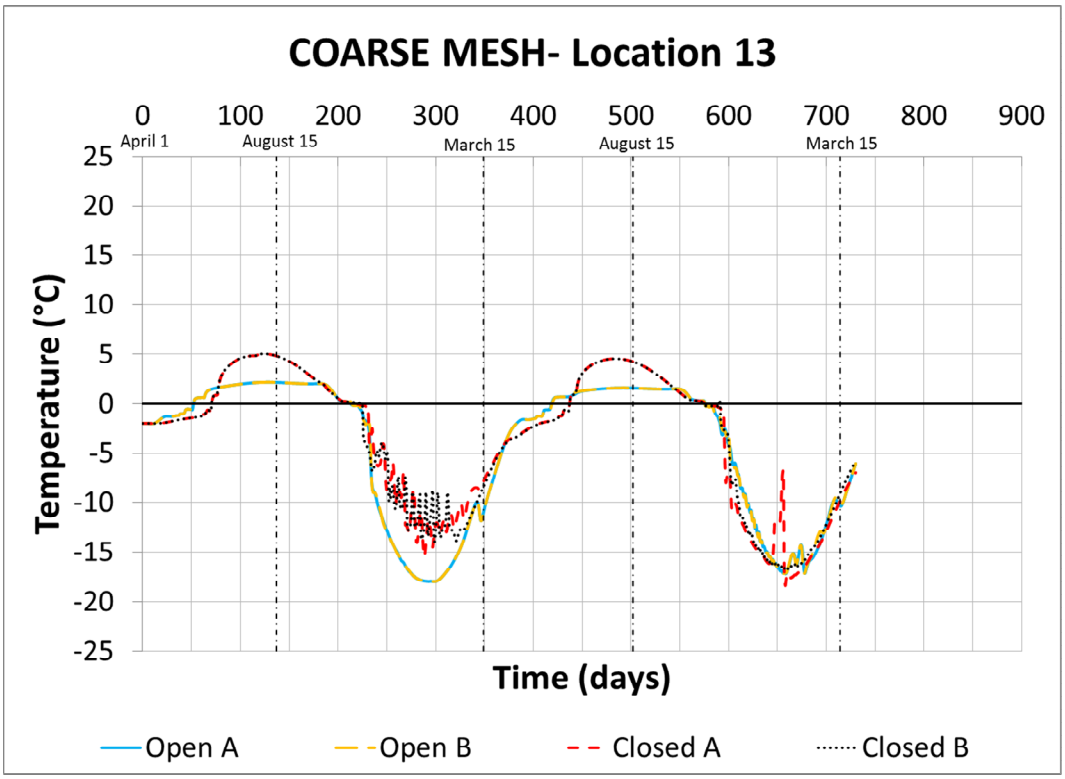

A) Time-temperature plots in Location 13

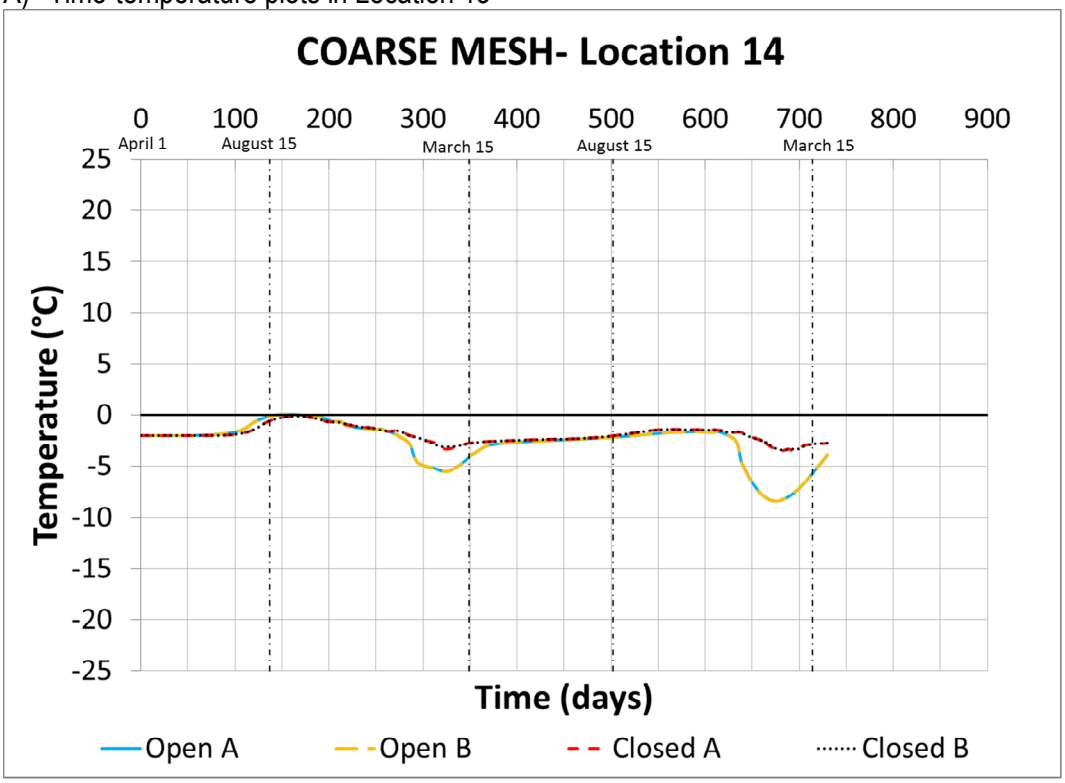

B) Time-temperature plots in Location 14

FIGURE 3.68: TRENDS IN TWO GEOSTUDIO COARSE MESH MODELS WITH EITHER CLOSED BOUNDARIES OR OPEN SIDESLOPES – LOCATIONS 15 AND 16

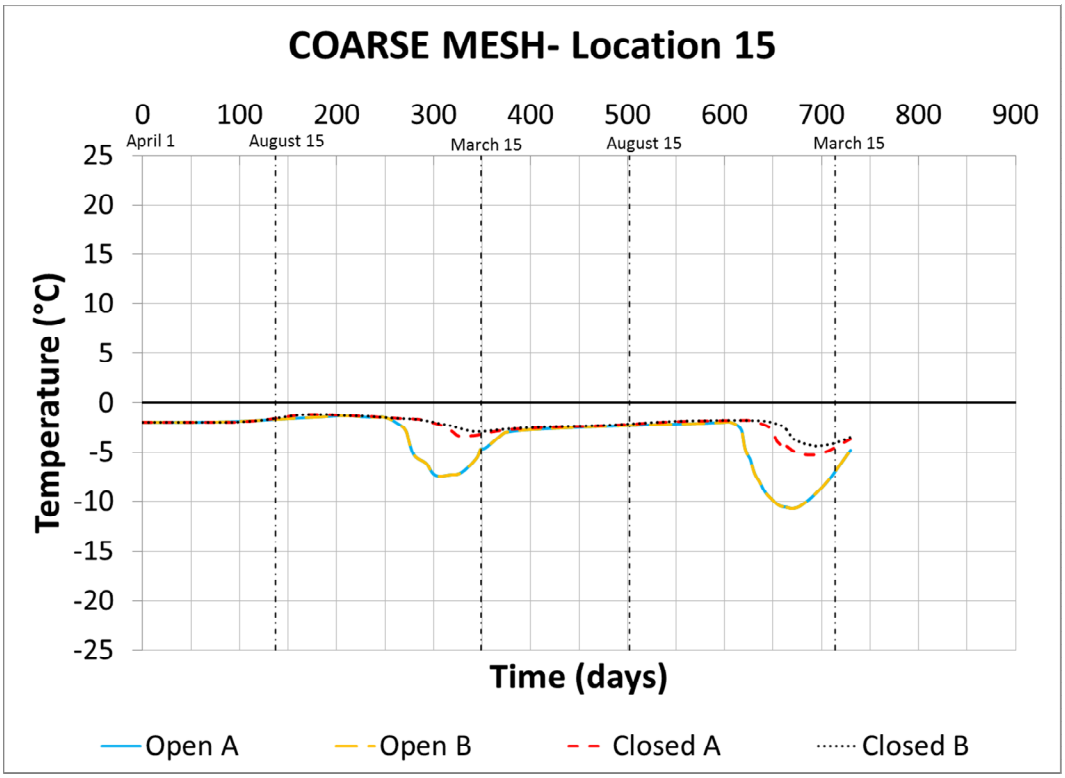

A) Time-temperature plots in Location 15

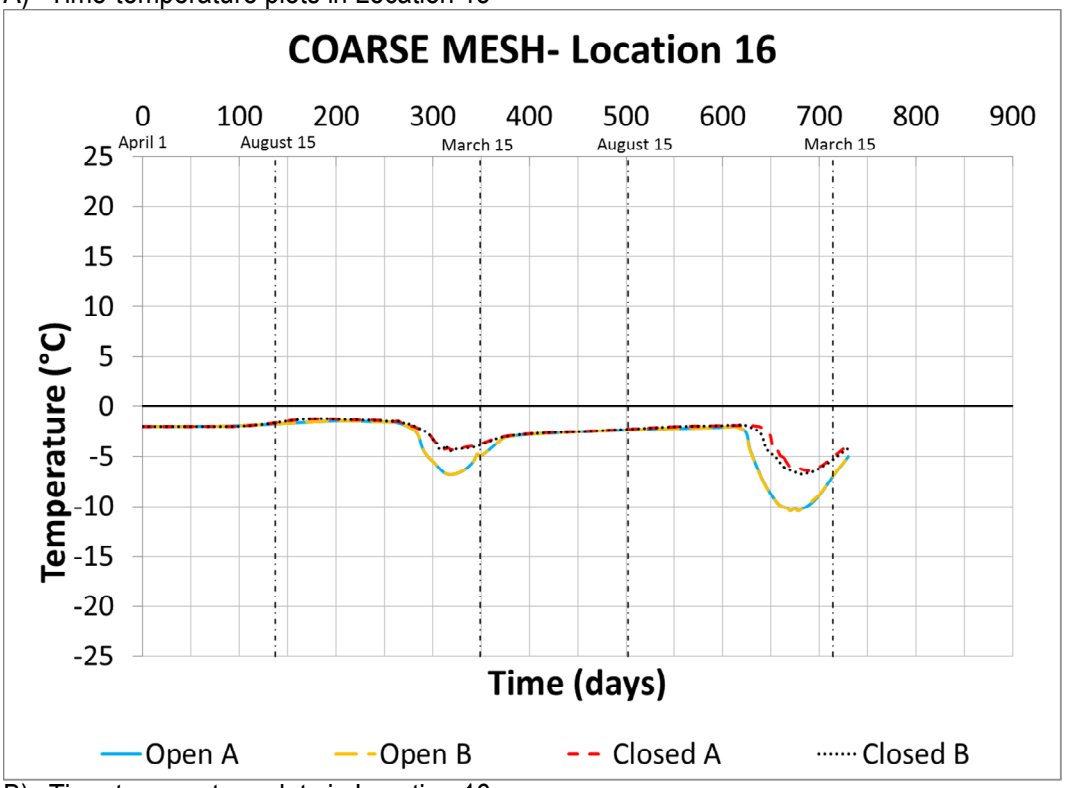

B) Time-temperature plots in Location 16

FIGURE 3.69: TWO GEOSTUDIO MODELS USED TO MODEL GOERING (2000) WITH OPEN SIDESLOPES

GEOSTUDIO SIMULATION

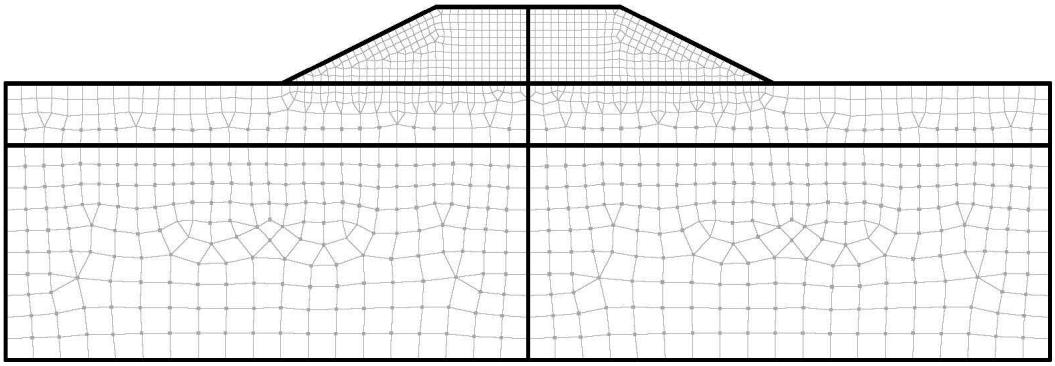

A) Coarse mesh model; 2286 nodes and 1286 elements; quads and triangles mesh

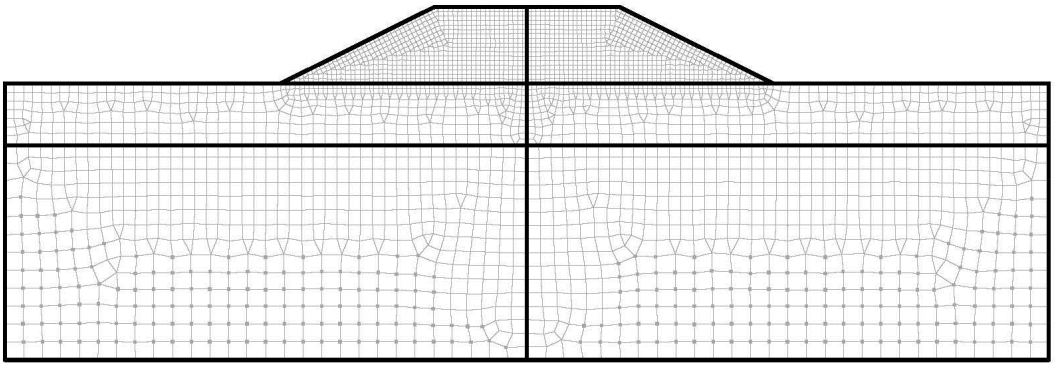

B) Fine mesh model; 5829 nodes and 3190 elements; quads and triangles mesh

FIGURE 3.70: COMPARISON OF NUMERICAL RESULTS ON FEBRUARY 1 FOR GEOSTUDIO SIMULATIONS WITH OPEN SIDESLOPES

GEOSTUDIO SIMULATION

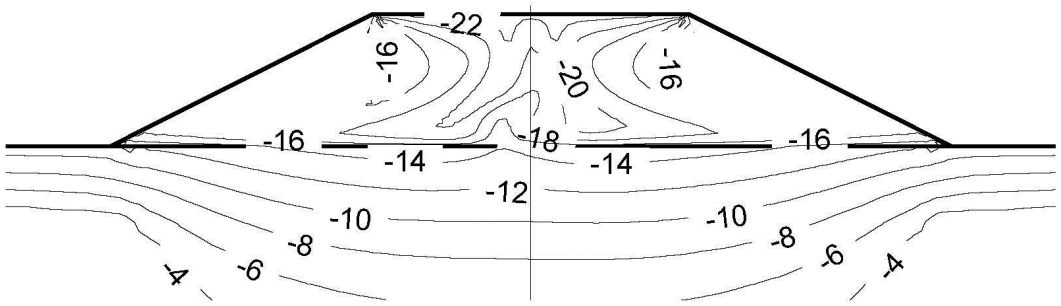

A) Isotherms – coarse mesh model; foundation porosity 0.65 (Case 1)

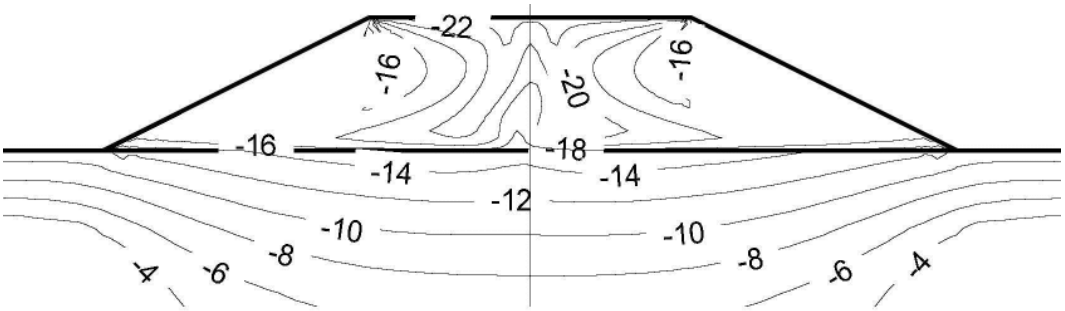

B) Isotherms – coarse mesh model; foundation porosity 0.45 (Case 2)

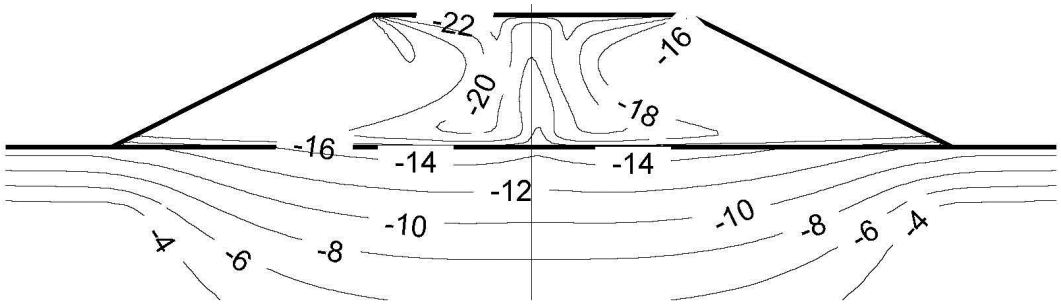

C) Isotherms – fine mesh model; foundation porosity 0.65 (Case 3)

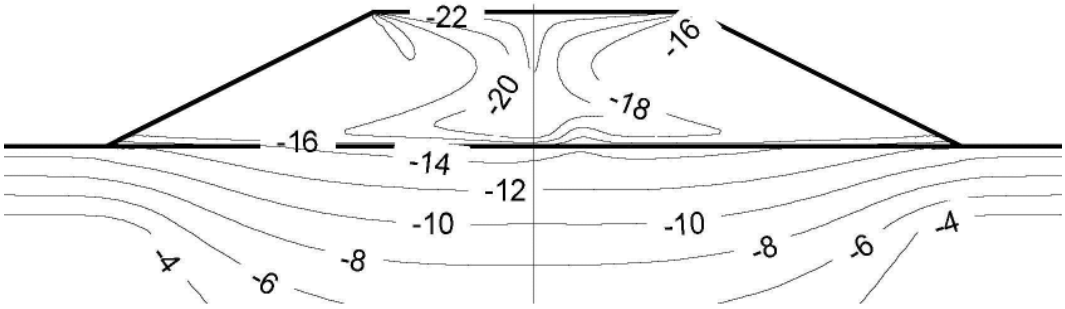

D) Isotherms – fine mesh model; foundation porosity 0.45 (Case 4)

FIGURE 3.71: TRENDS IN GEOSTUDIO MODELS AND NUMERICAL AND EXPERIMENTAL RESULTS GOERING (2000) – LOCATION 1 AND 2

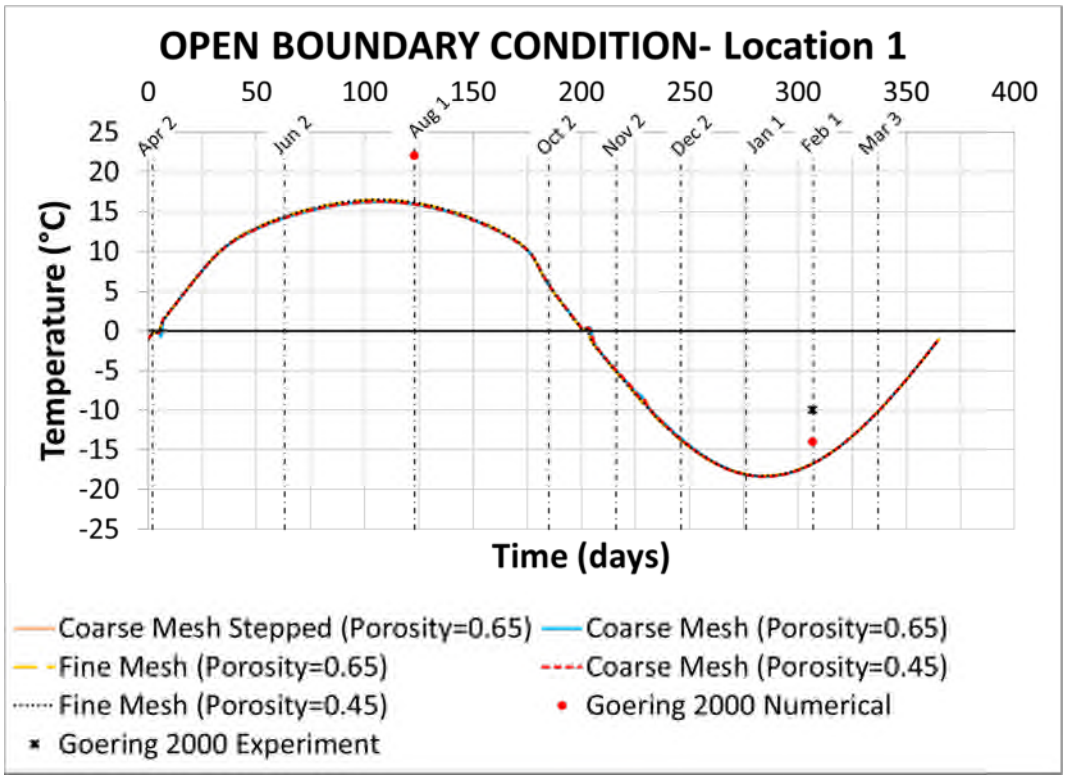

A) Time-temperature plots in Location 1

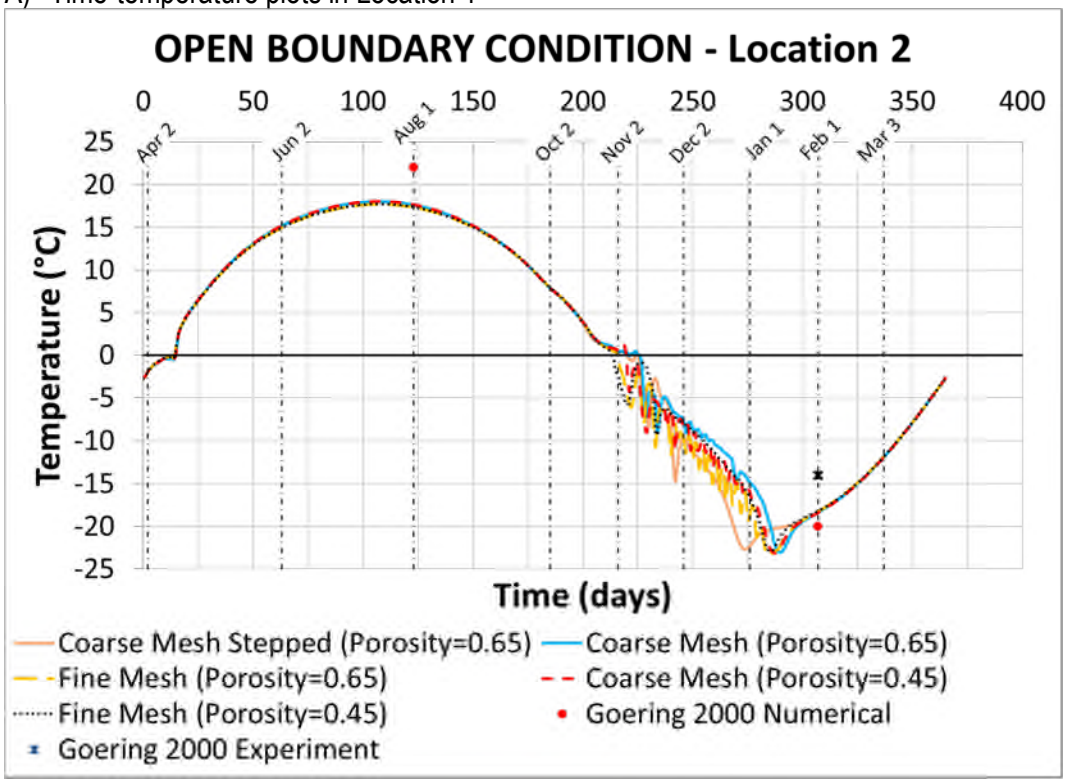

B) Time-temperature plots in Location 2

FIGURE 3.72: TRENDS IN GEOSTUDIO MODELS AND NUMERICAL AND EXPERIMENTAL RESULTS GOERING (2000) – LOCATION 3 AND 4

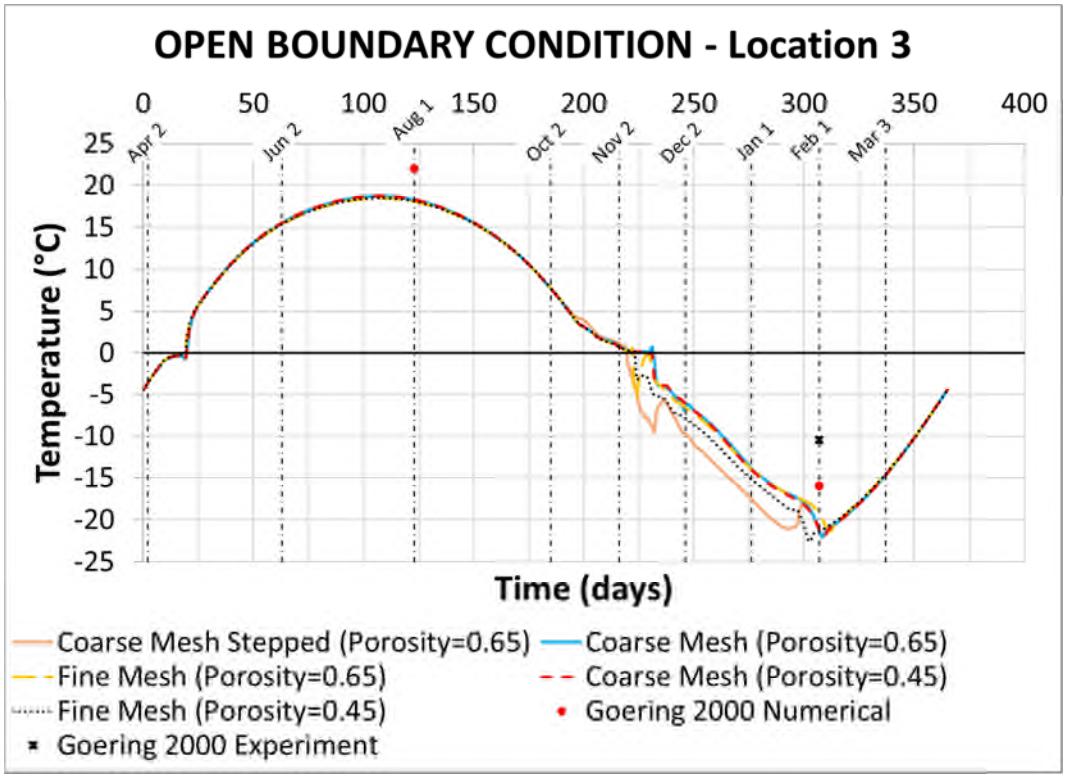

A) Time-temperature plots in Location 3

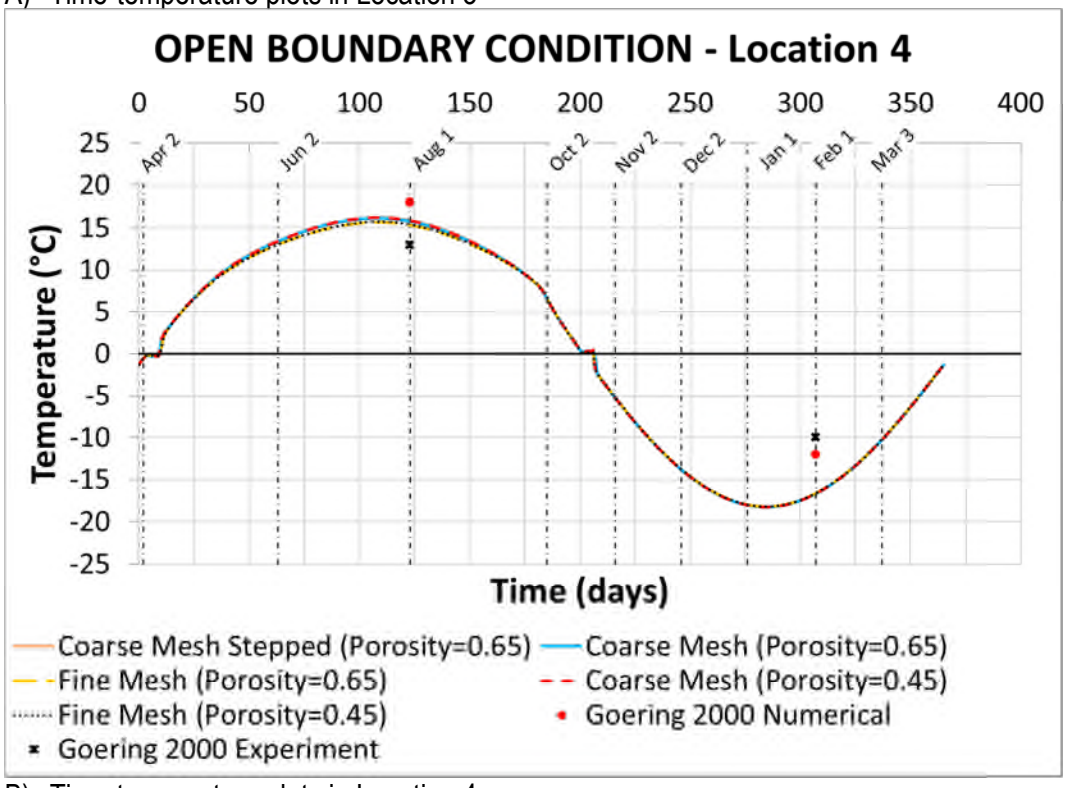

B) Time-temperature plots in Location 4

FIGURE 3.73: TRENDS IN GEOSTUDIO MODELS AND NUMERICAL AND EXPERIMENTAL RESULTS GOERING (2000) – LOCATION 5 AND 6

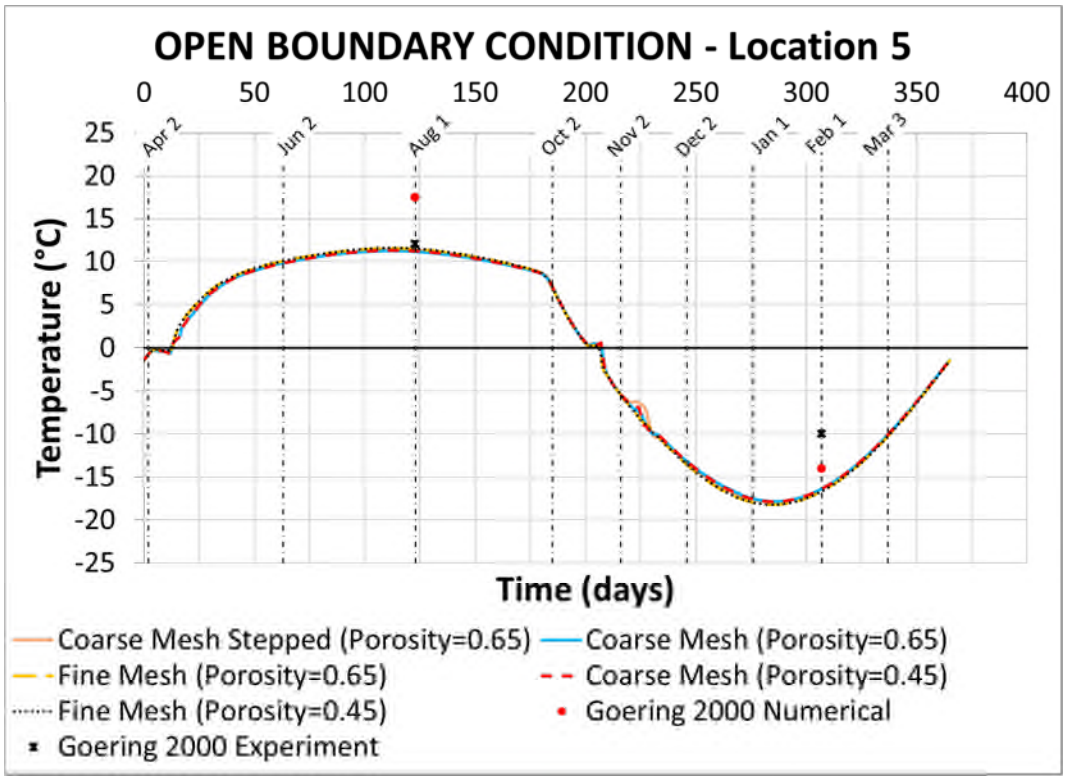

A) Time-temperature plots in Location 5

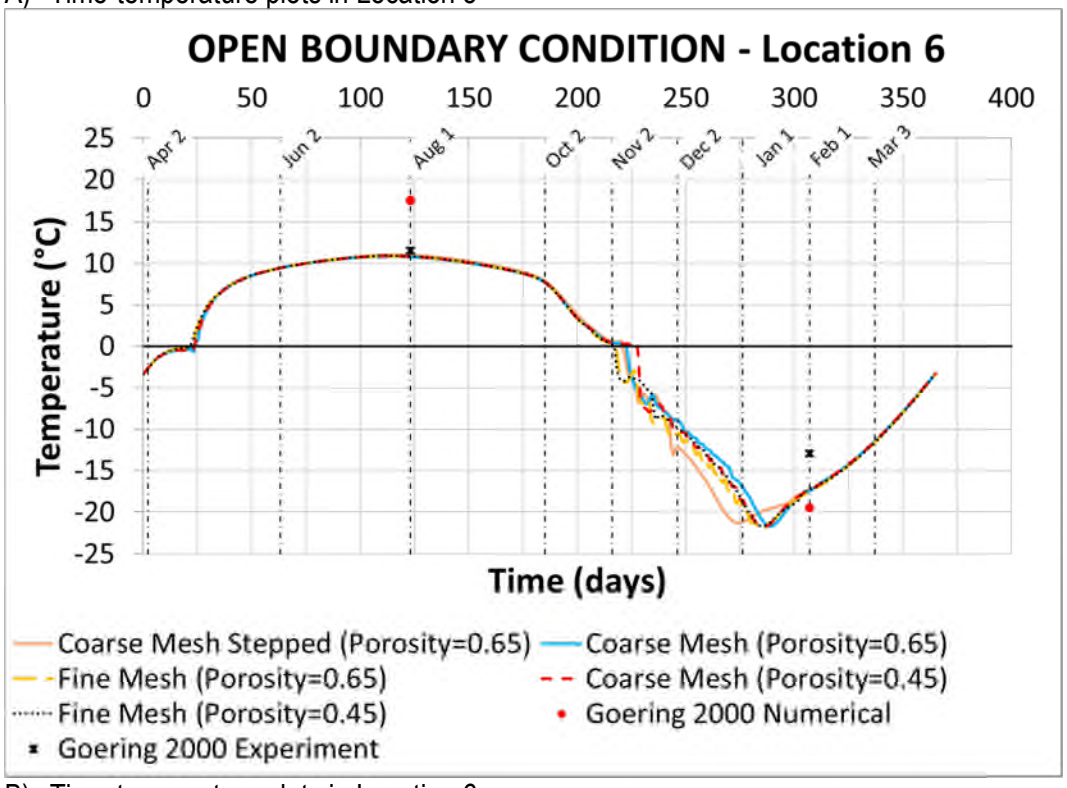

B) Time-temperature plots in Location 6

FIGURE 3.74: TRENDS IN GEOSTUDIO MODELS AND NUMERICAL AND EXPERIMENTAL RESULTS GOERING (2000) – LOCATION 7 AND 8

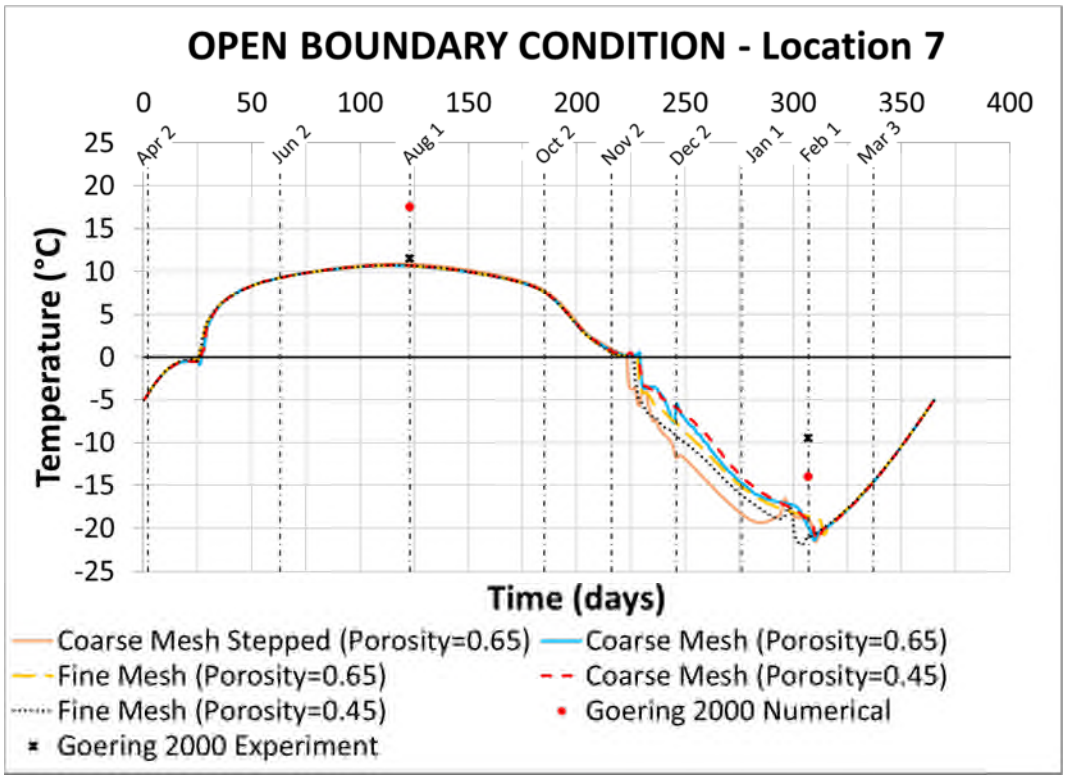

A) Time-temperature plots in Location 7

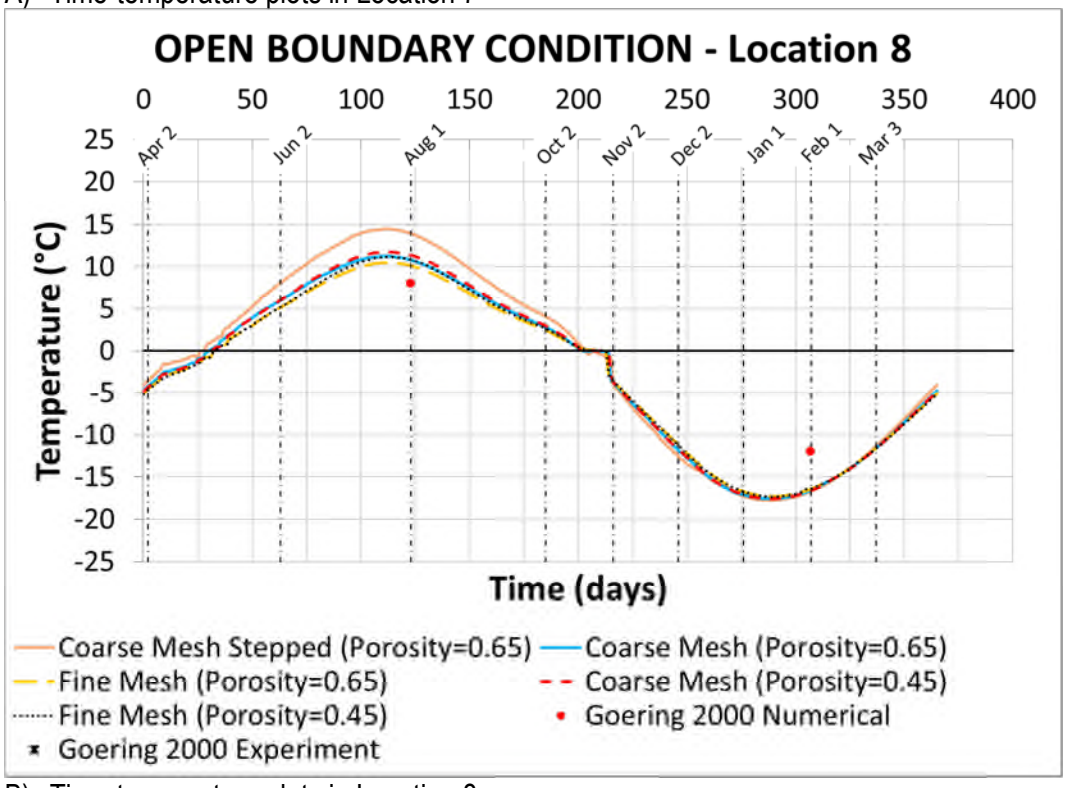

B) Time-temperature plots in Location 8

FIGURE 3.75: TRENDS IN GEOSTUDIO MODELS AND NUMERICAL AND EXPERIMENTAL RESULTS GOERING (2000) – LOCATION 9 AND 10

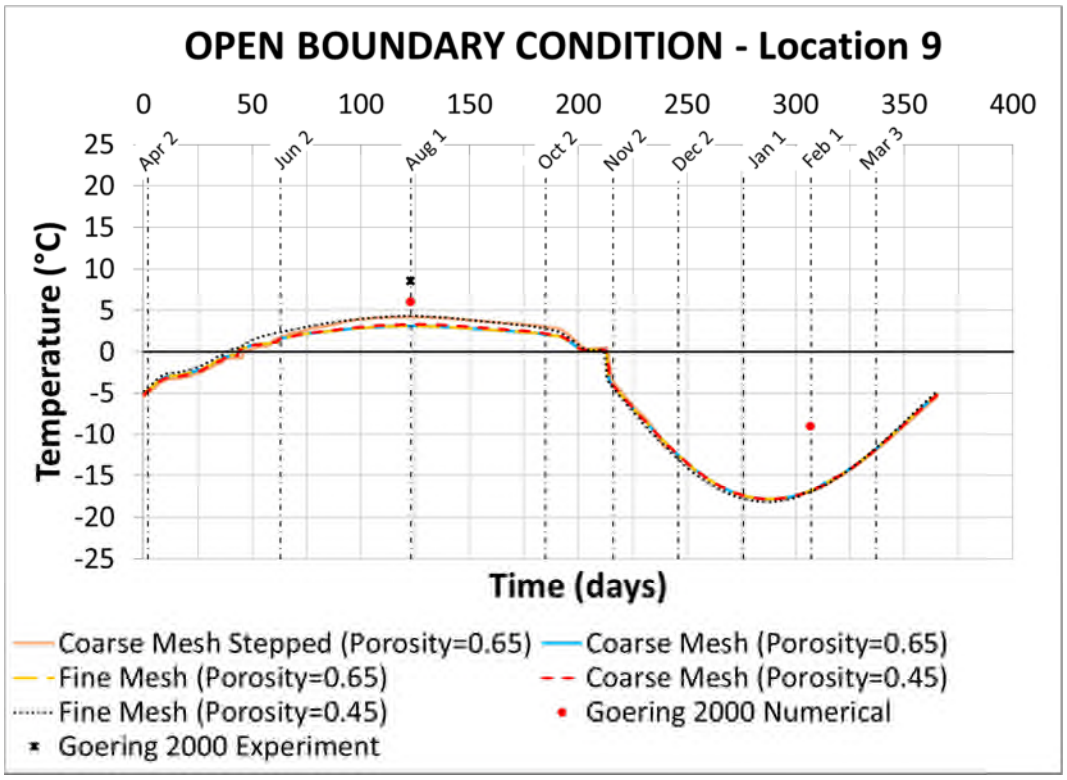

A) Time-temperature plots in Location 9

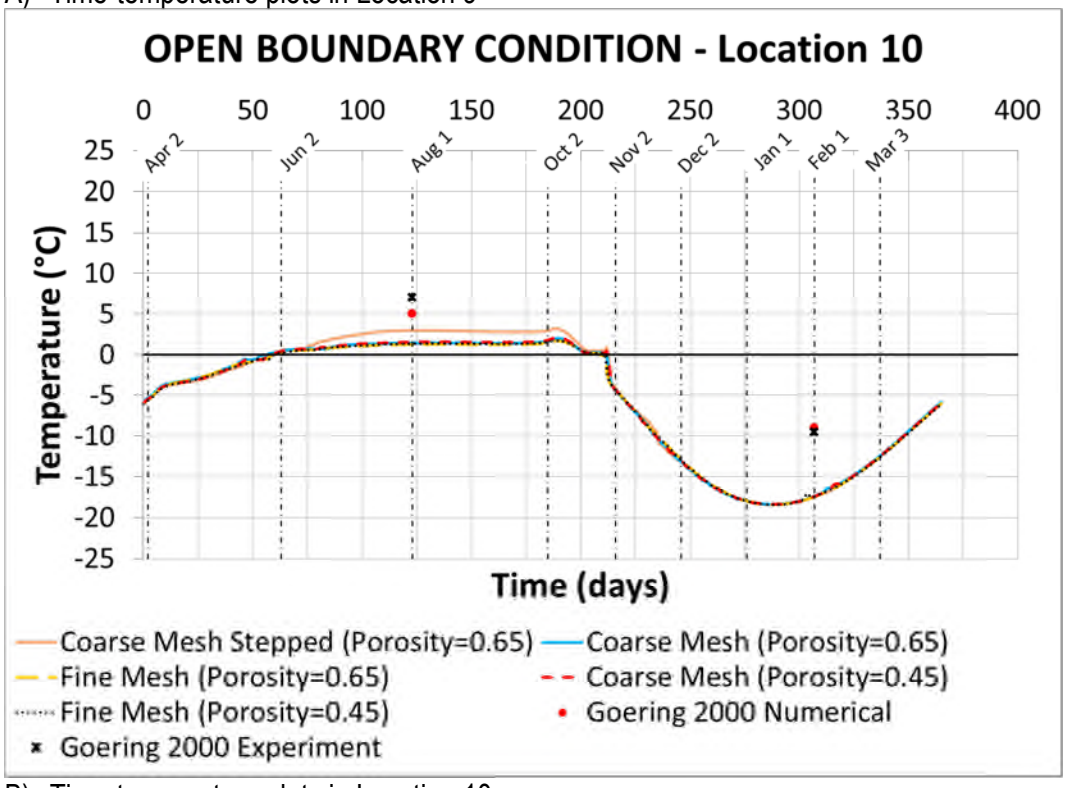

B) Time-temperature plots in Location 10

FIGURE 3.76: TRENDS IN GEOSTUDIO MODELS AND NUMERICAL AND EXPERIMENTAL RESULTS GOERING (2000) - LOCATION 11 AND 12

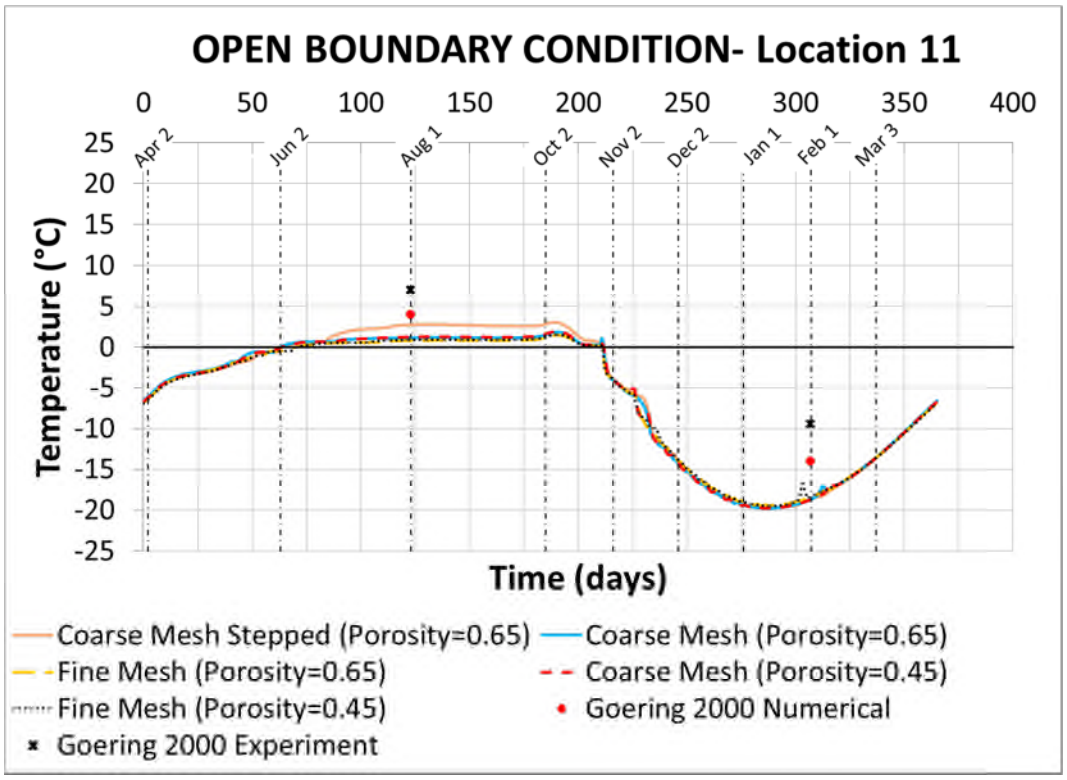

A) Time-temperature plots in Location 11

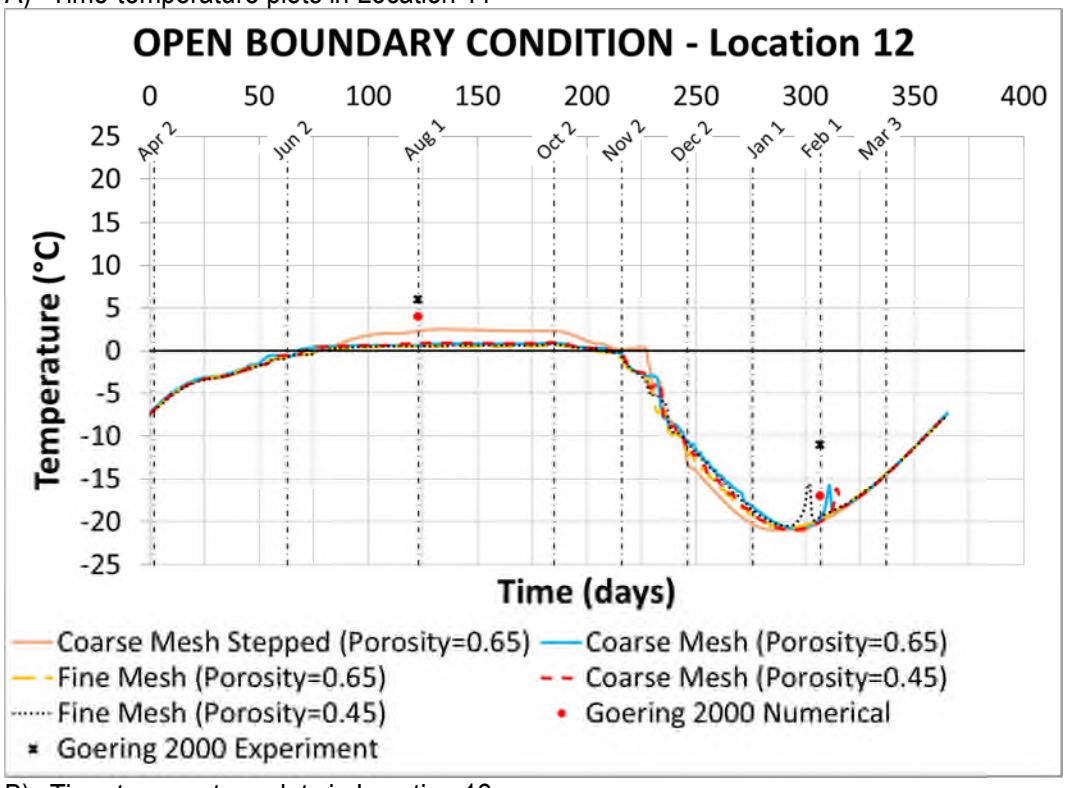

B) Time-temperature plots in Location 12

FIGURE 3.77: TRENDS IN GEOSTUDIO MODELS AND NUMERICAL AND EXPERIMENTAL RESULTS GOERING (2000) - LOCATION 13 AND 14

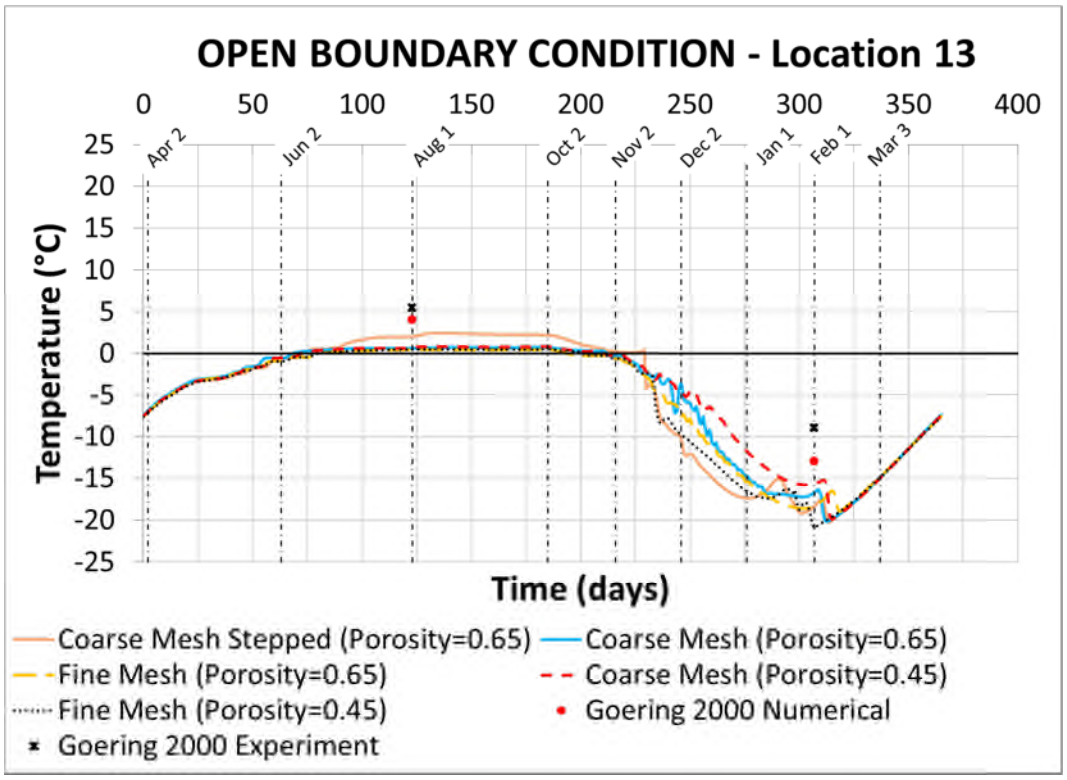

A) Time-temperature plots in Location 13

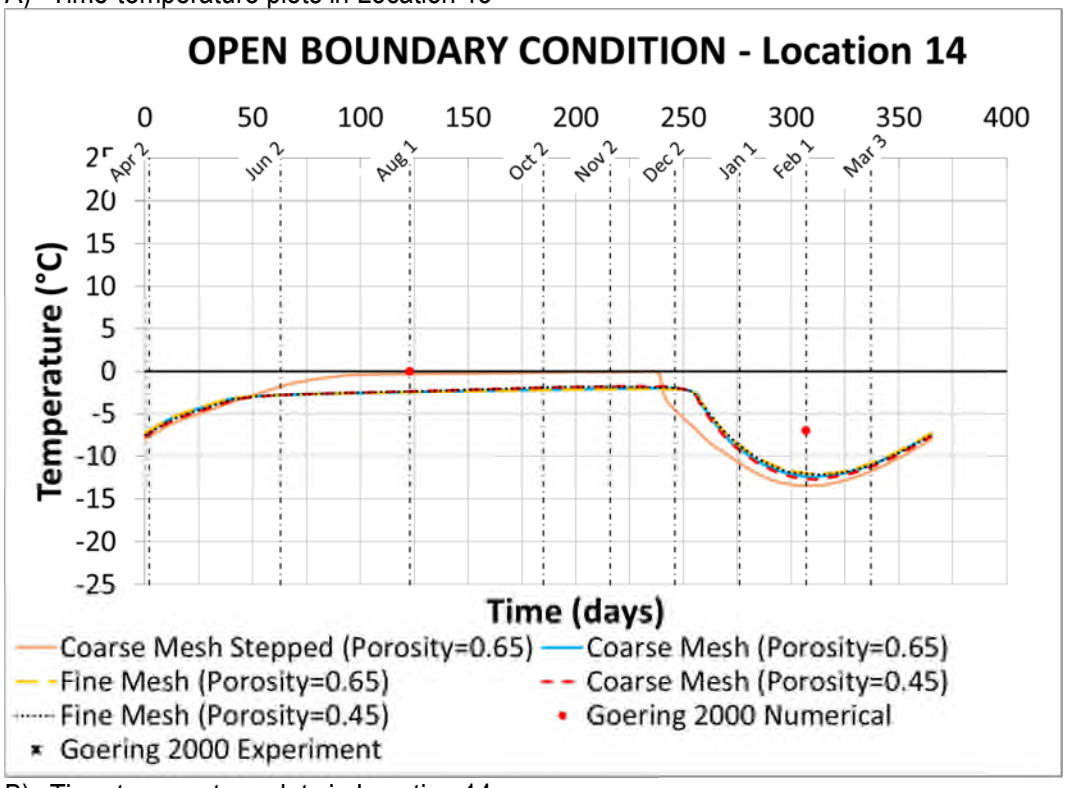

B) Time-temperature plots in Location 14

FIGURE 3.78: TRENDS IN GEOSTUDIO MODELS AND NUMERICAL AND EXPERIMENTAL RESULTS GOERING (2000) – LOCATION 15 AND 16

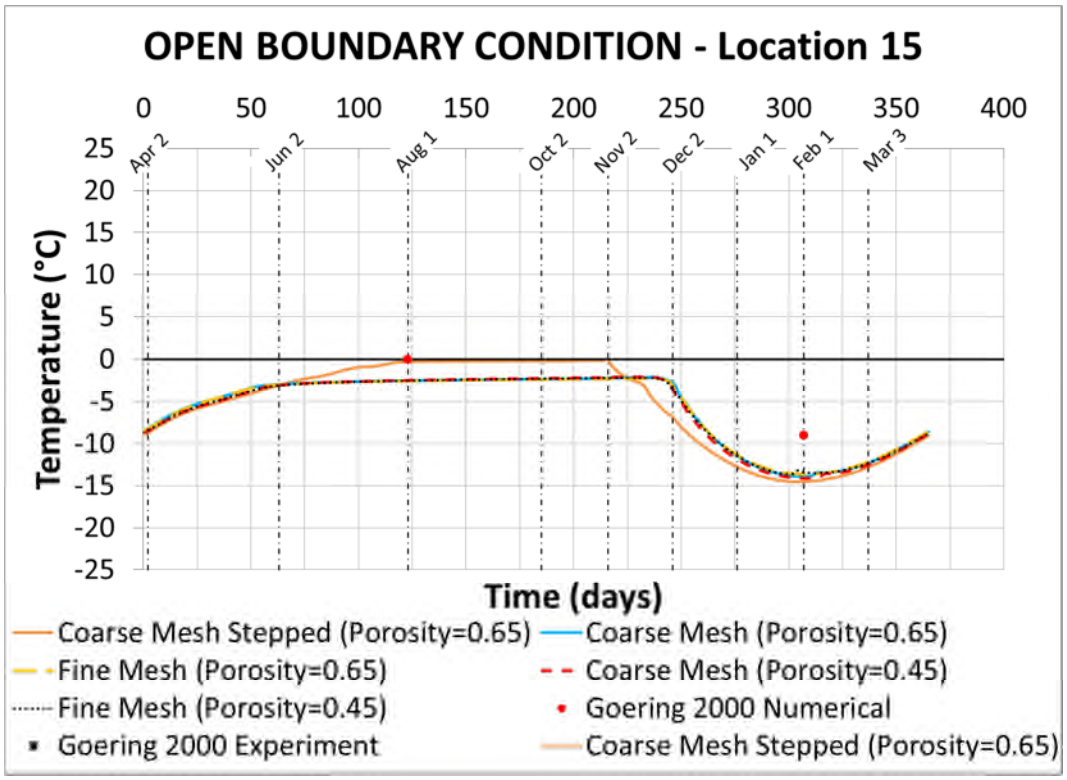

A) Time-temperature plots in Location 15

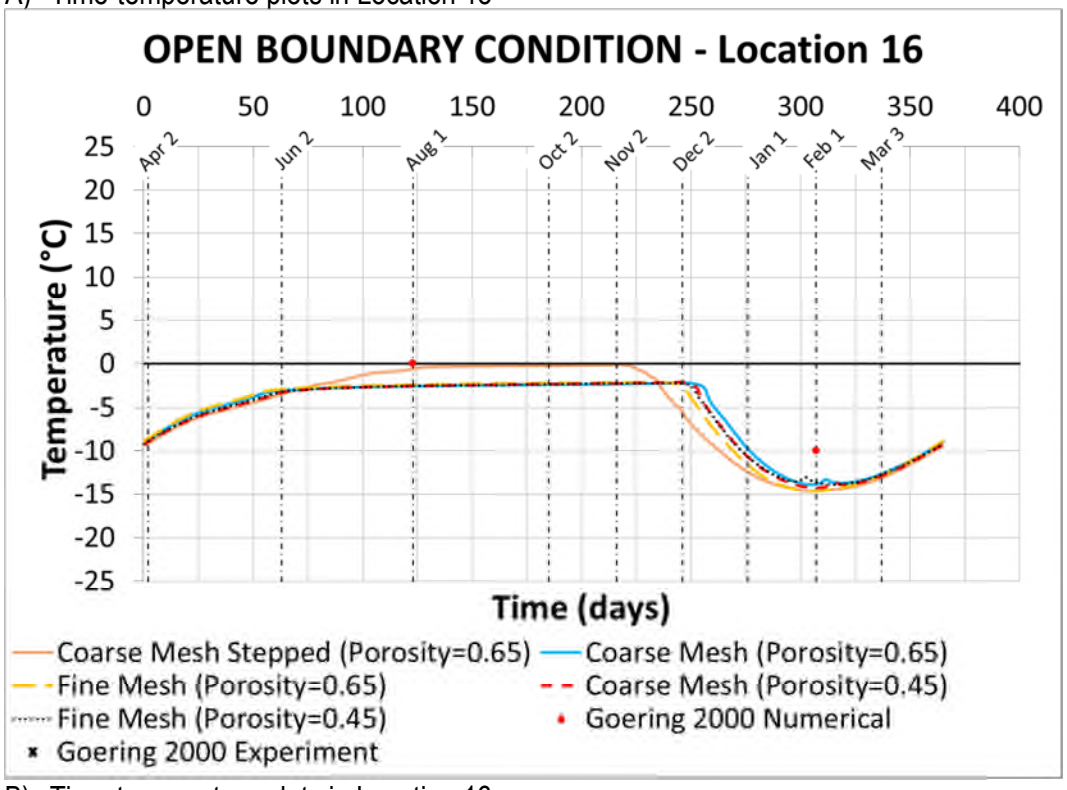

B) Time-temperature plots in Location 16

FIGURE 3.79: COMPARISON OF NUMERICAL AND EXPERIMENTAL RESULTS ON AUGUST 1 FOR GEOSTUDIO SIMULATIONS WITH OPEN SIDESLOPES AND GOERING (2000) - ISOTHERMS

GEOSTUDIO SIMULATION

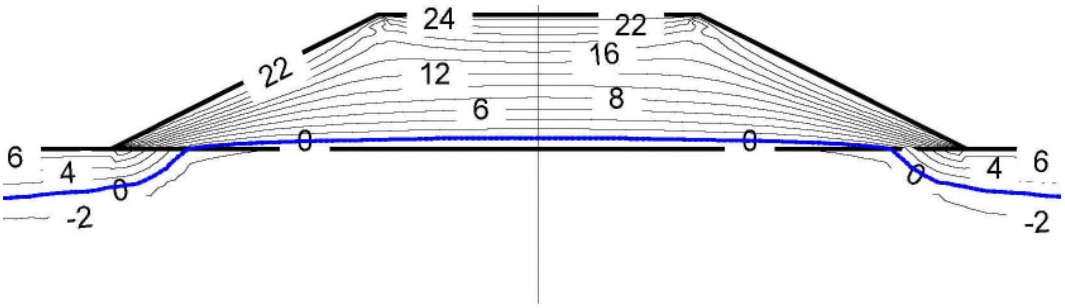

A) Isotherms - coarse mesh model; foundation porosity of 0.65 (GeoStudio) (Case 1)

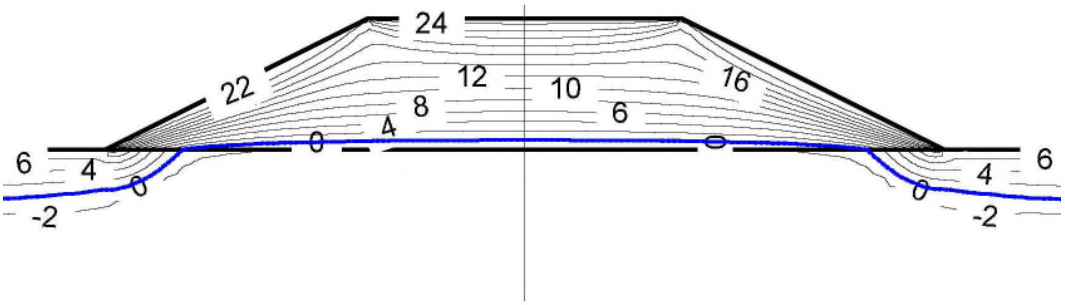

B) Isotherms - fine mesh model; foundation porosity 0.65 (GeoStudio) (Case 3)

GOERING (2000)

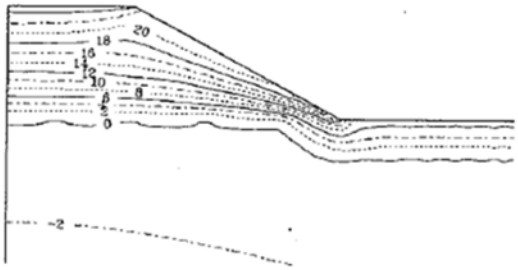

C) Isotherms – numerical (Goering, 2000)

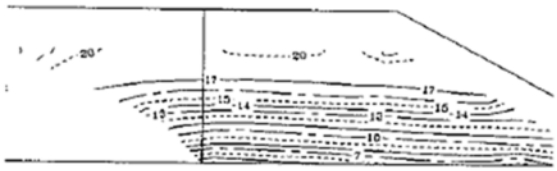

D) Isotherms – experimental (Goering, 2000)

FIGURE 3.80: COMPARISON OF NUMERICAL RESULTS ON FEBRUARY 1 FOR GEOSTUDIO SIMULATIONS WITH OPEN SIDESLOPES AND GOERING (2000) – AIR FLOW VECTORS

GEOSTUDIO SIMULATION

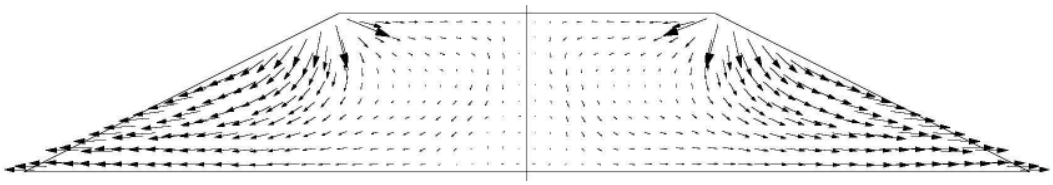

A) Air flow vectors - coarse mesh model (GeoStudio)

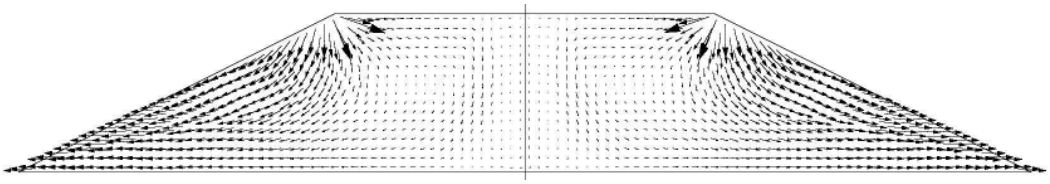

B) Air flow vectors – fine mesh model (GeoStudio)

GOERING (2000)

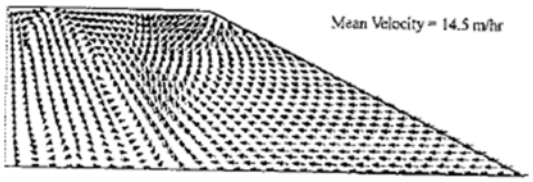

C) Air flow vectors – numerical (Goering, 2000)

FIGURE 3.81: COMPARISON OF NUMERICAL AND EXPERIMENTAL RESULTS ON FEBRUARY 1 FOR GEOSTUDIO SIMULATION WITH OPEN SIDESLOPES AND GOERING (2000)

GEOSTUDIO SIMULATION

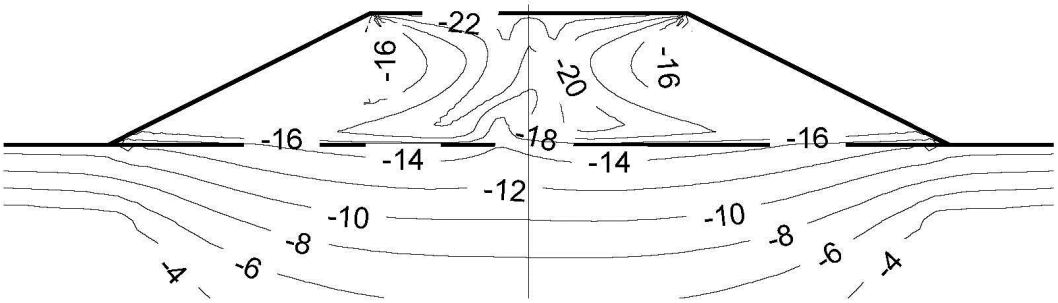

A) Isotherms - coarse mesh model; foundation porosity 0.65 (GeoStudio) (Case 1)

GOERING (2000)

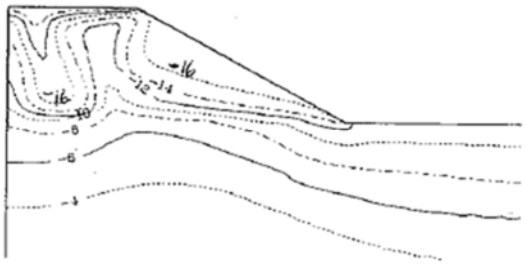

B) Isotherms – numerical (Goering, 2000)

C) Isotherms – experimental (Goering, 2000)

FIGURE 3.82: TWO GEOSTUDIO MODELS USED TO MODEL GOERING AND KUMAR (1996) AND GOERING (2000) WITH CLOSED BOUNDARIES

GEOSTUDIO SIMULATION

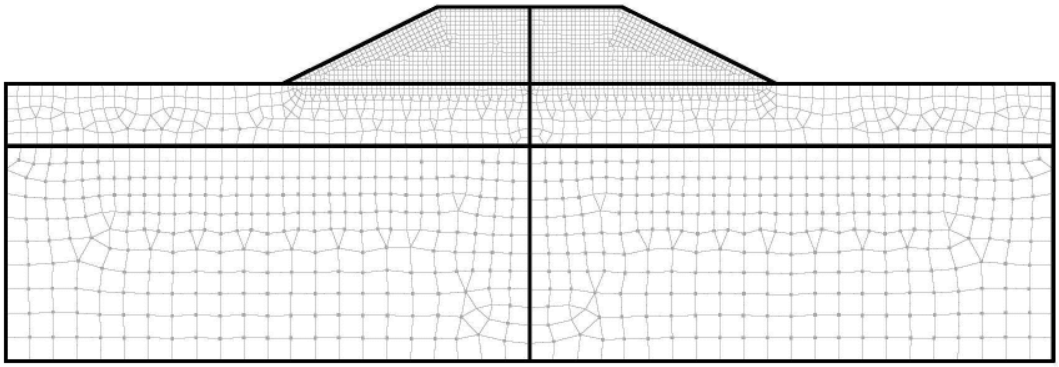

A) GeoStudio model for Goering and Kumar (1996) (GeoStudio 1996 Model); 5177 nodes and 2561 elements; quads and triangles mesh

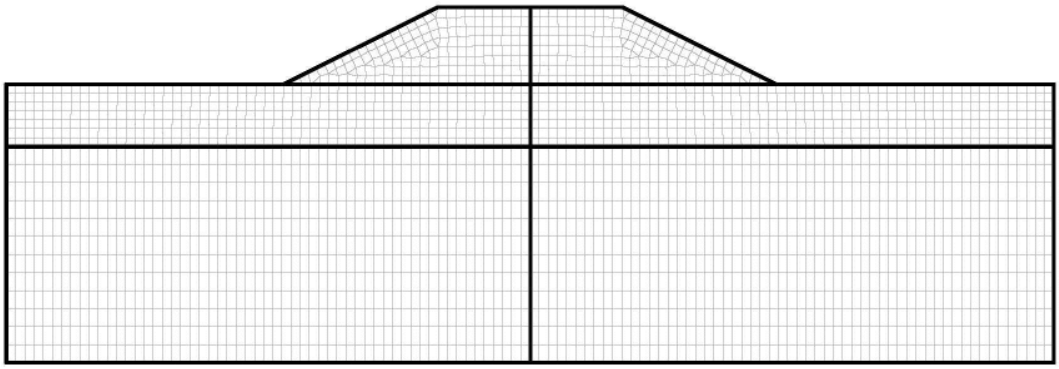

B) GeoStudio model for Goering (2000) (GeoStudio 2000 Model); 3286 nodes and 2482 elements; quads and triangles mesh

FIGURE 3.83: TRENDS IN GEOSTUDIO MODELS AND GOERING AND KUMAR (1996) AND GOERING (2000) RESULTS – LOCATION 1 AND 2

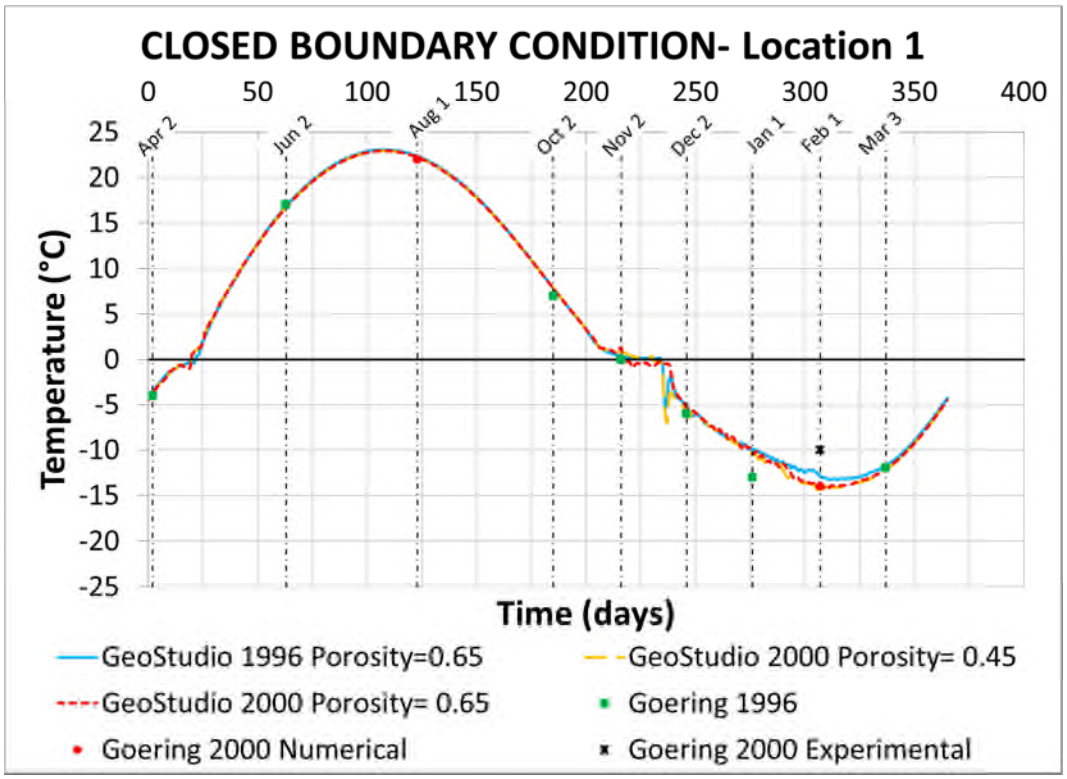

A) Time-temperature plots in Location 1

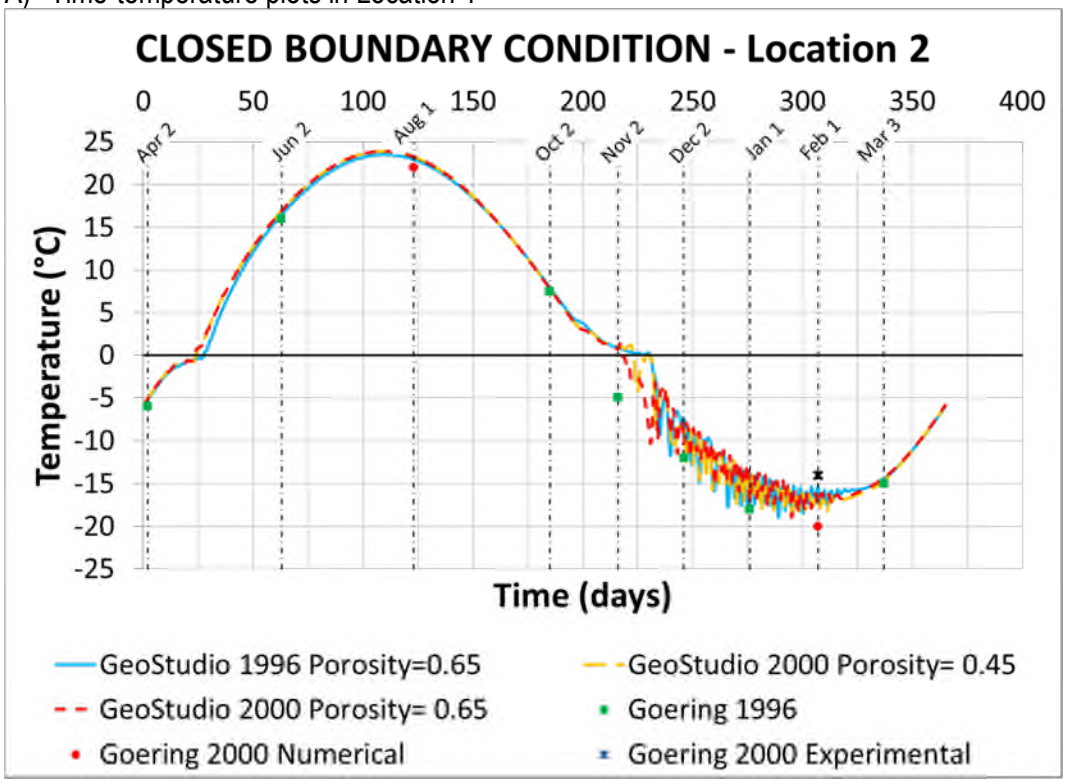

B) Time-temperature plots in Location 2

FIGURE 3.84: TRENDS IN GEOSTUDIO MODELS AND GOERING AND KUMAR (1996) AND GOERING (2000) RESULTS – LOCATION 3 AND 4

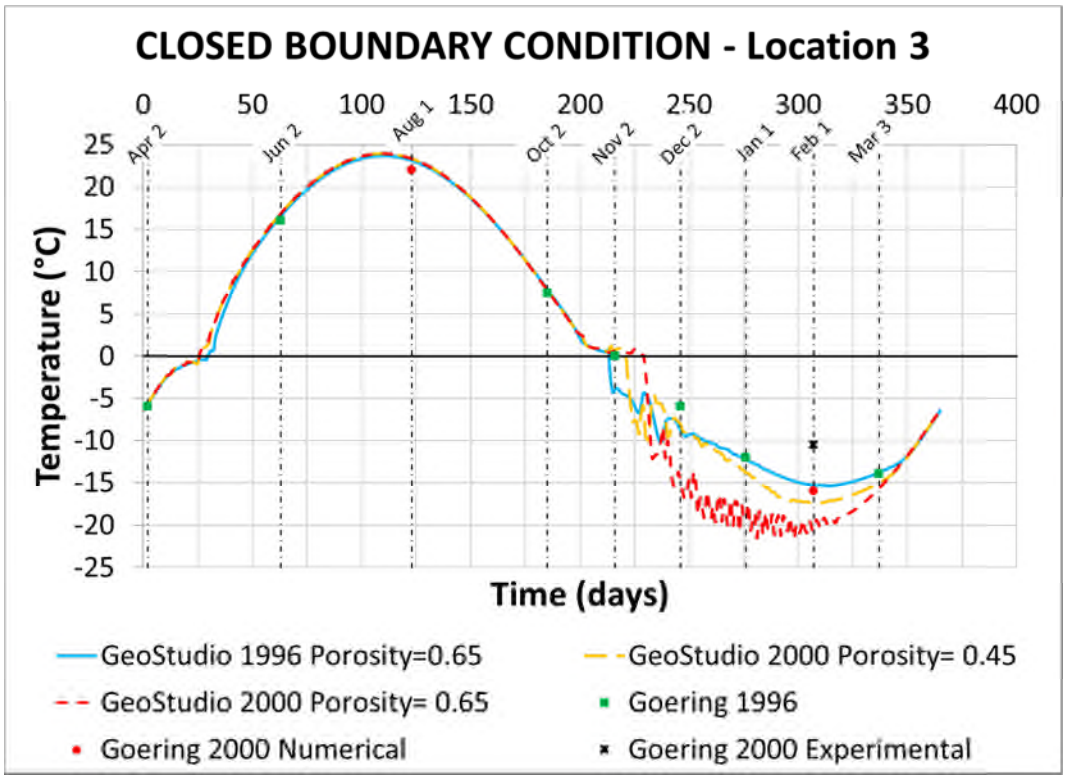

A) Time-temperature plots in Location 3

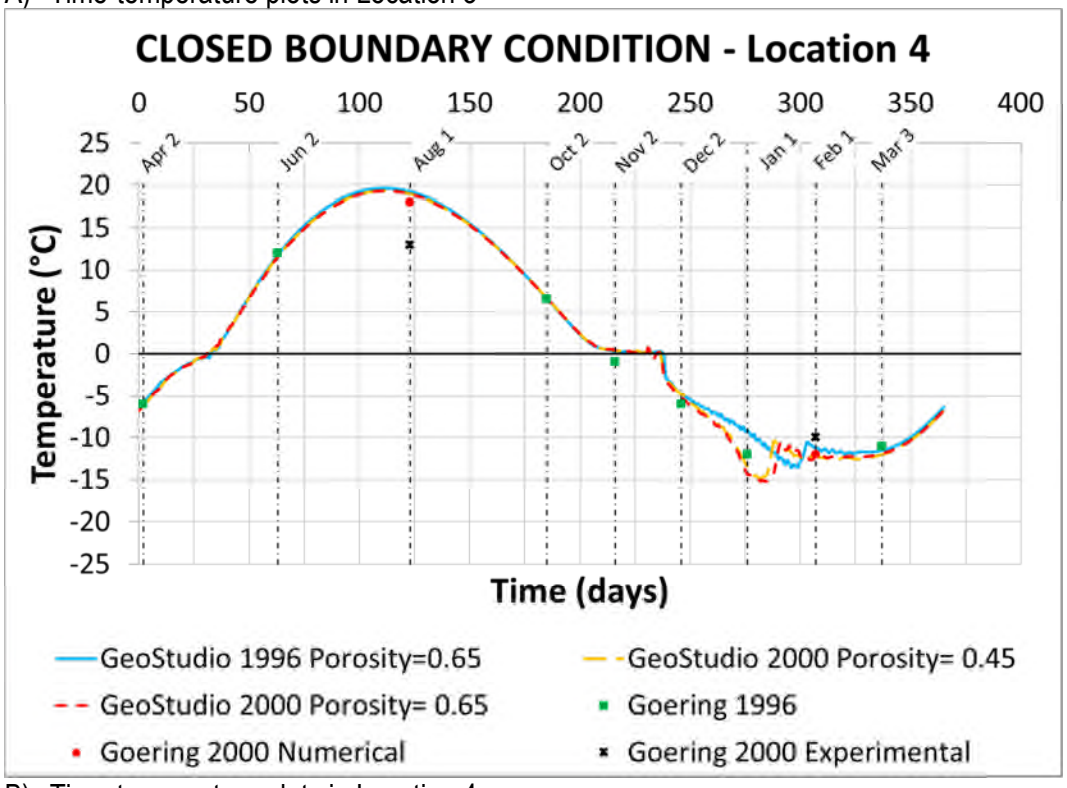

B) Time-temperature plots in Location 4

FIGURE 3.85: TRENDS IN GEOSTUDIO MODELS AND GOERING AND KUMAR (1996) AND GOERING (2000) RESULTS – LOCATION 5 AND 6

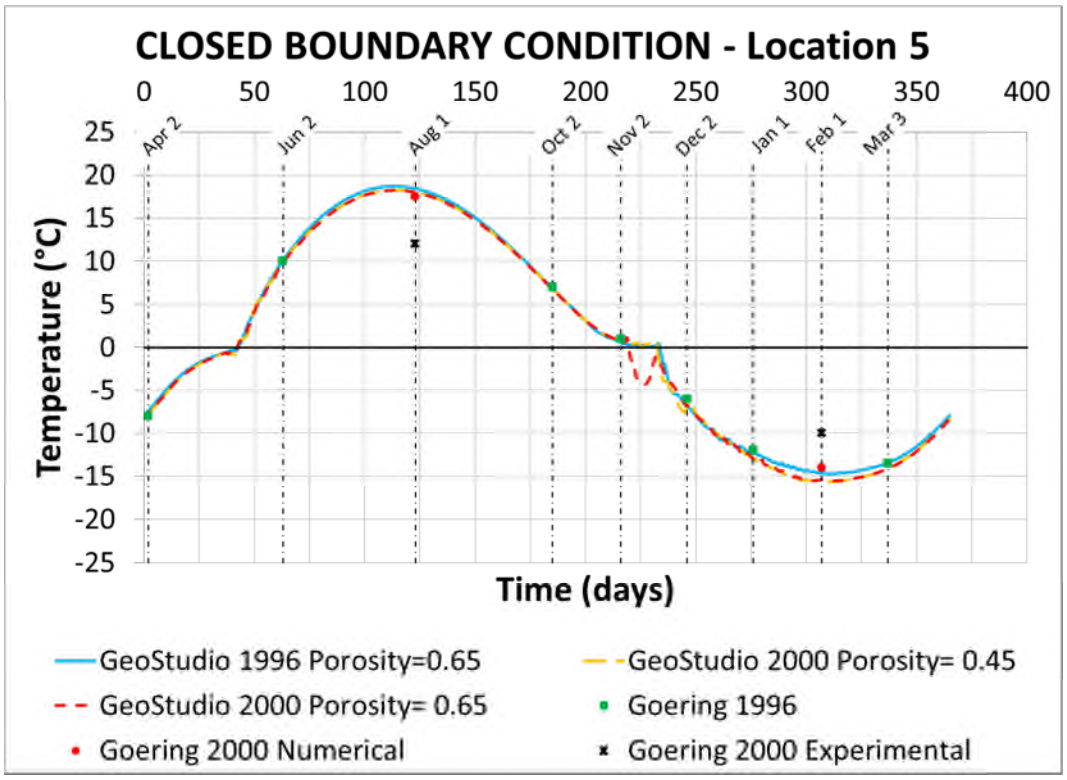

A) Time-temperature plots in Location 5

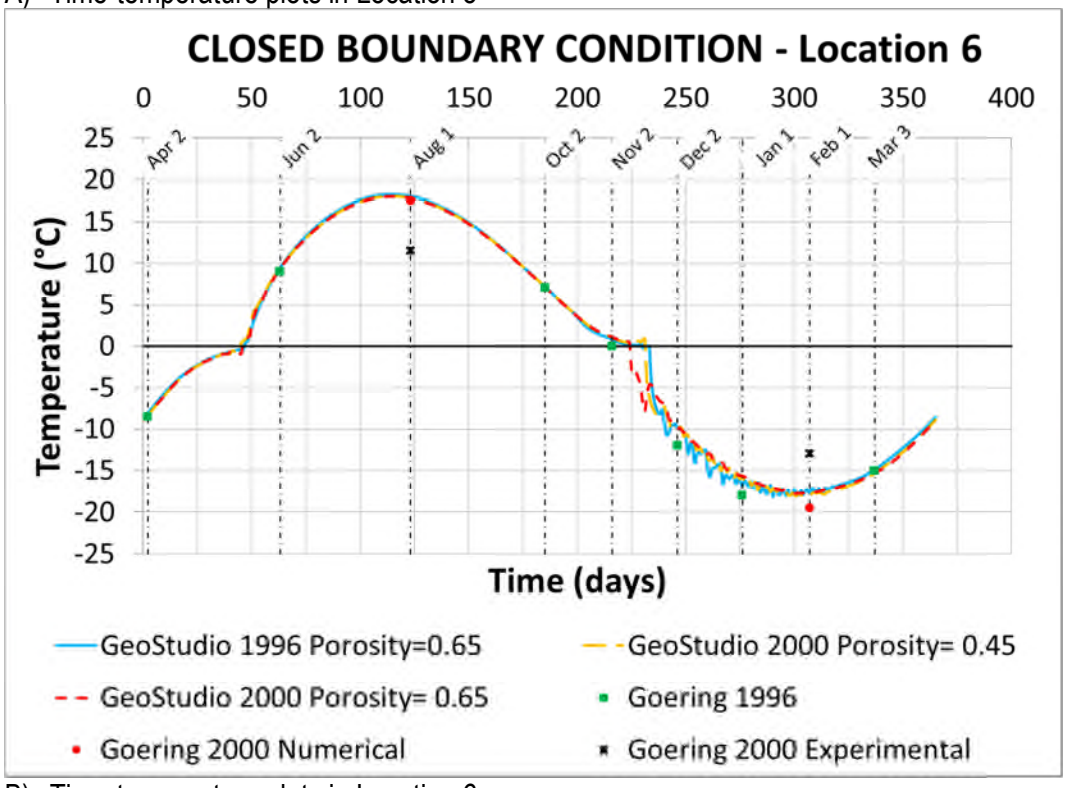

B) Time-temperature plots in Location 6

FIGURE 3.86: TRENDS IN GEOSTUDIO MODELS AND GOERING AND KUMAR (1996) AND GOERING (2000) RESULTS – LOCATION 7 AND 8

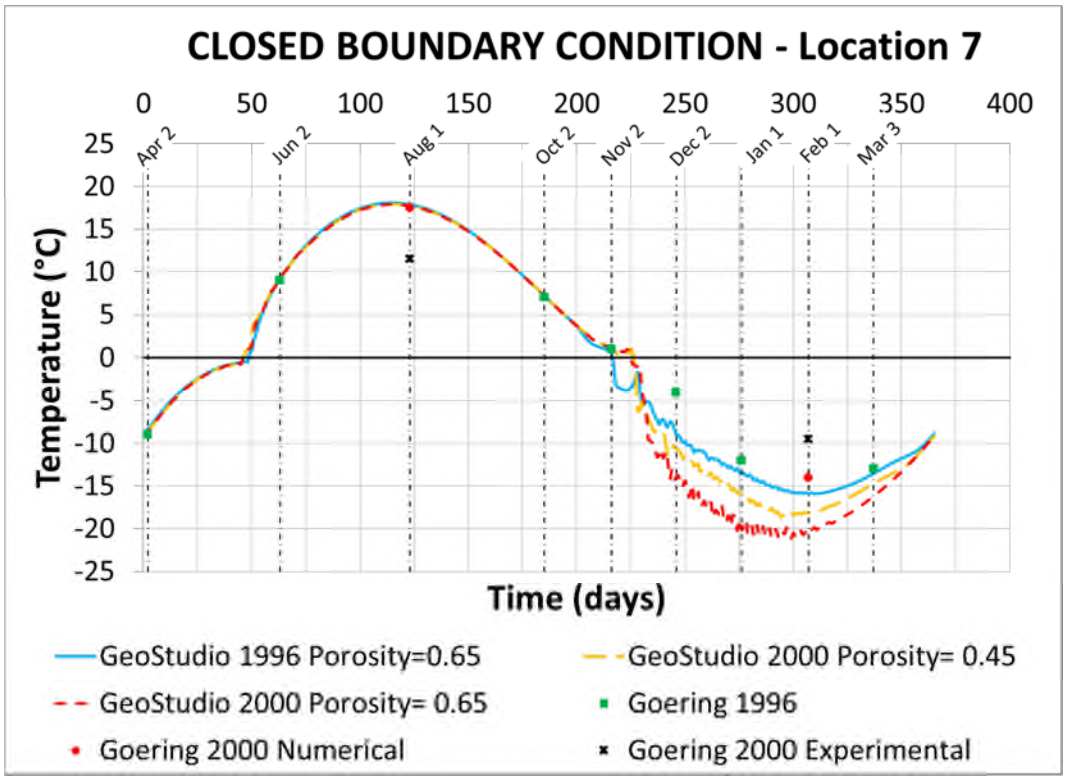

A) Time-temperature plots in Location 7

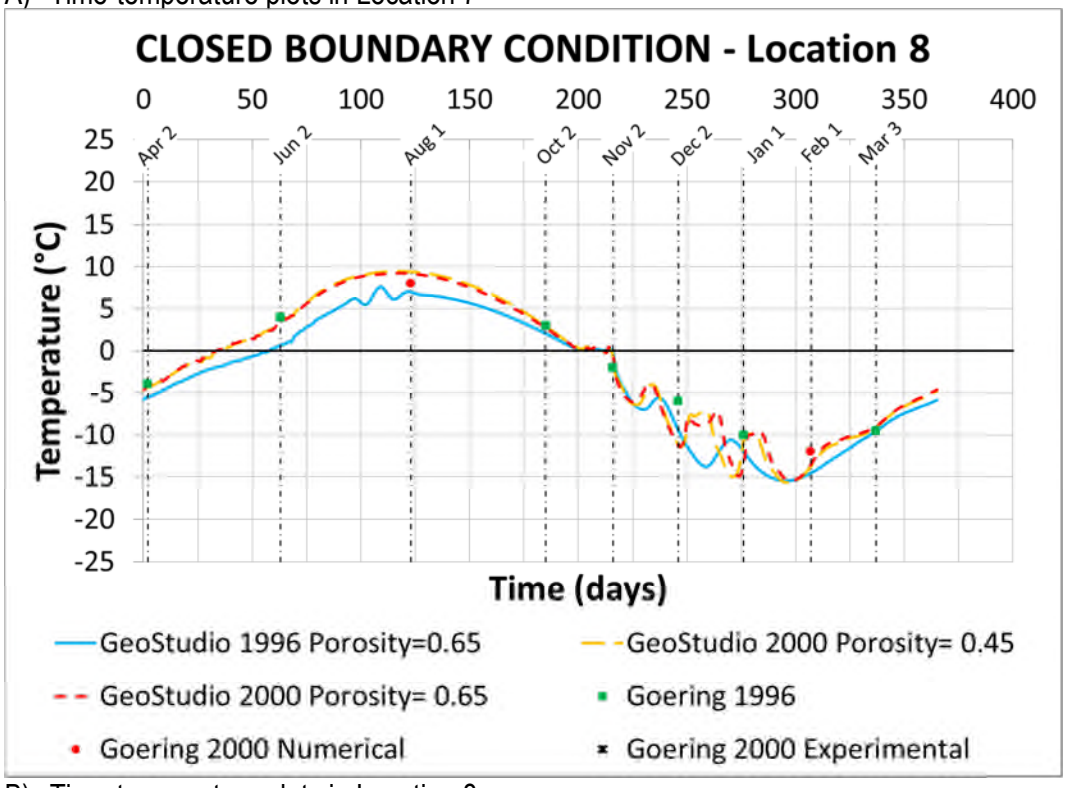

B) Time-temperature plots in Location 8

FIGURE 3.87: TRENDS IN GEOSTUDIO MODELS AND GOERING AND KUMAR (1996) AND GOERING (2000) RESULTS – LOCATION 9 AND 10

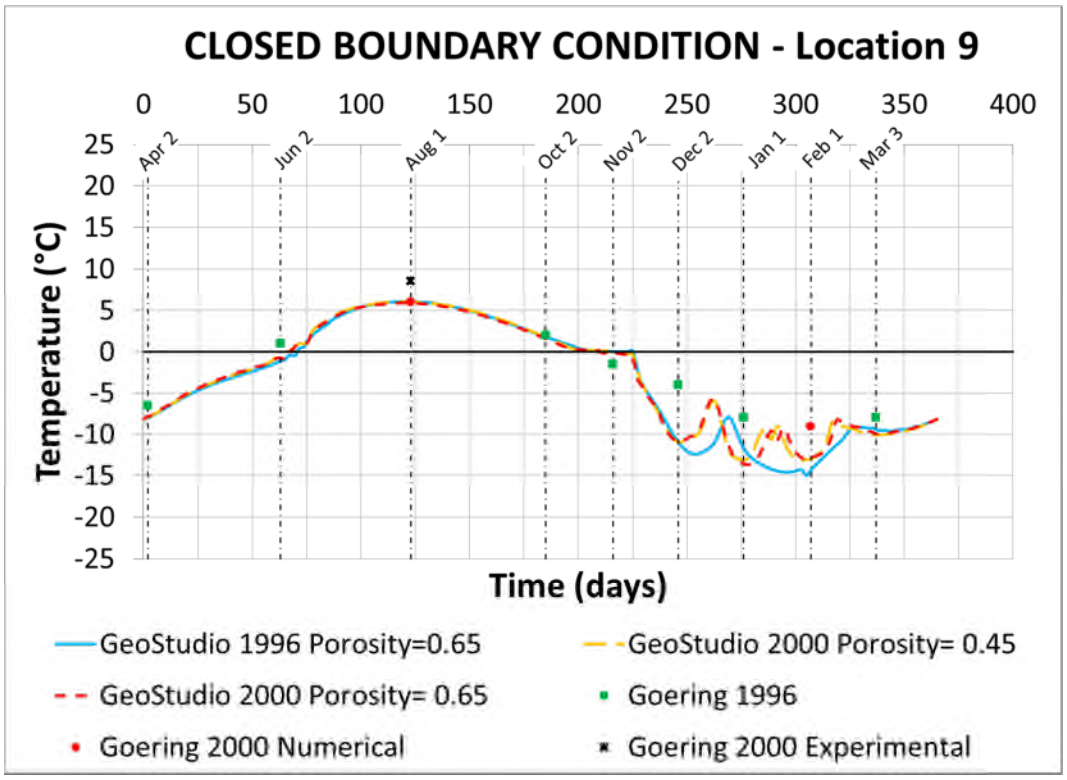

A) Time-temperature plots in Location 9

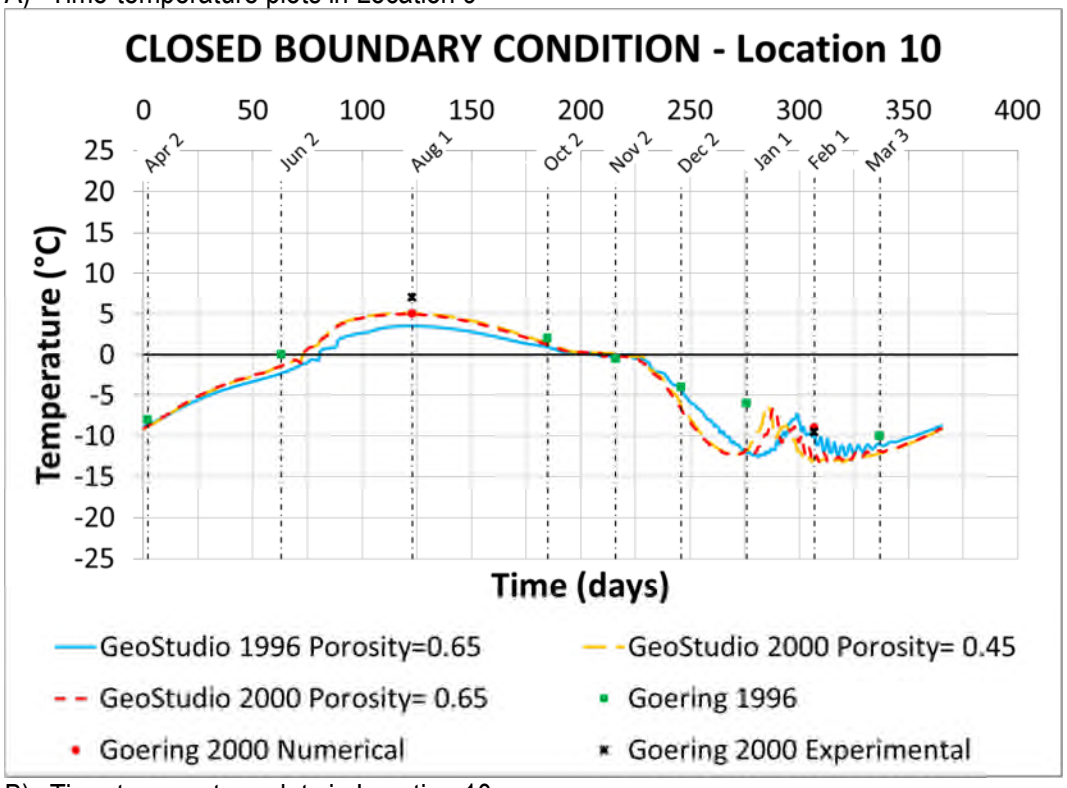

B) Time-temperature plots in Location 10

FIGURE 3.88: TRENDS IN GEOSTUDIO MODELS AND GOERING AND KUMAR (1996) AND GOERING (2000) RESULTS – LOCATION 11 AND 12

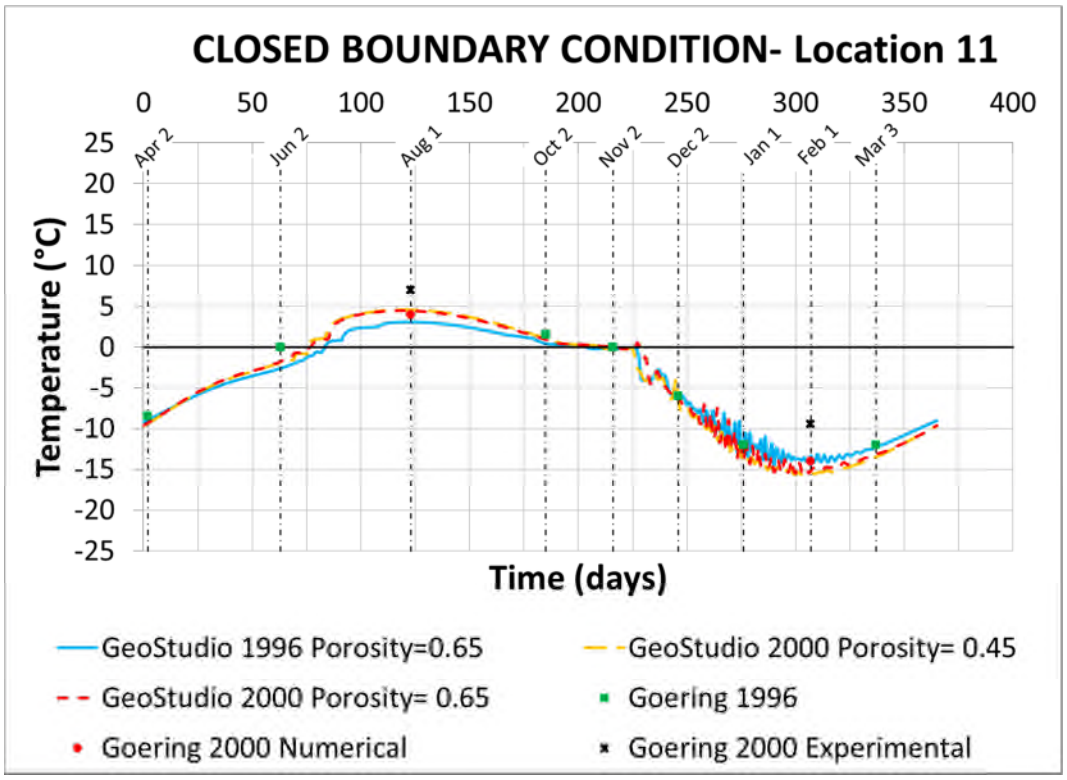

A) Time-temperature plots in Location 11

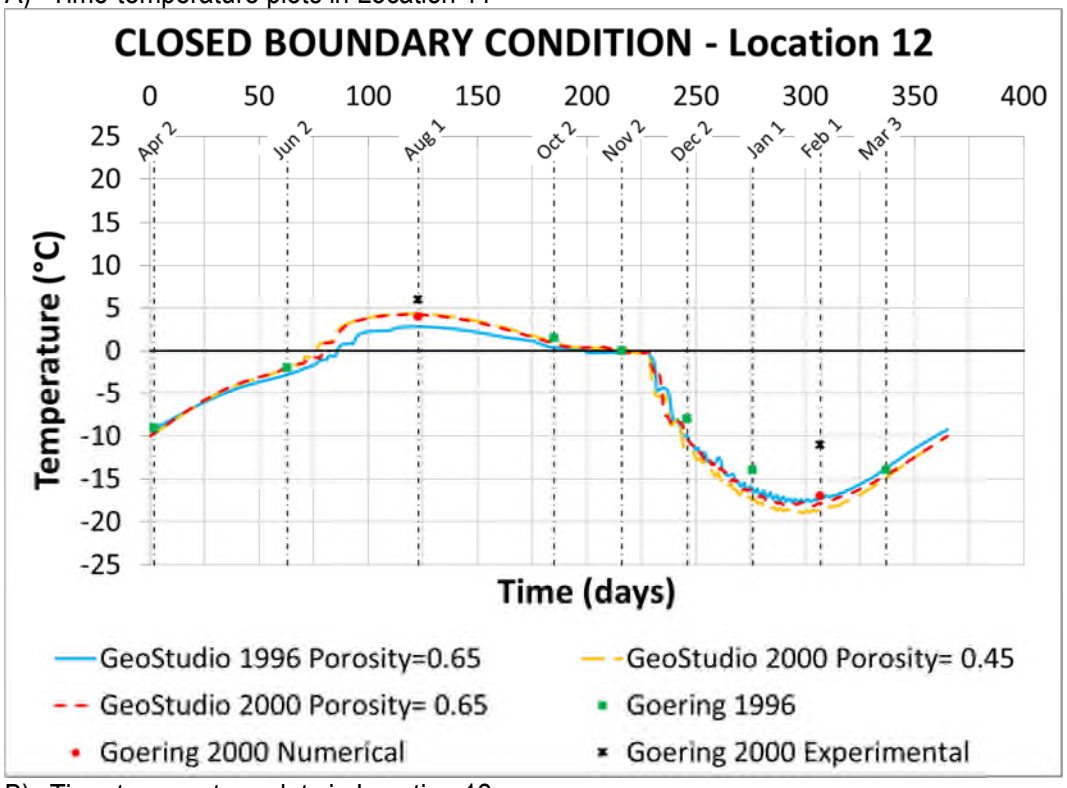

B) Time-temperature plots in Location 12

FIGURE 3.89: TRENDS IN GEOSTUDIO MODELS AND GOERING AND KUMAR (1996) AND GOERING (2000) RESULTS – LOCATION 13 AND 14

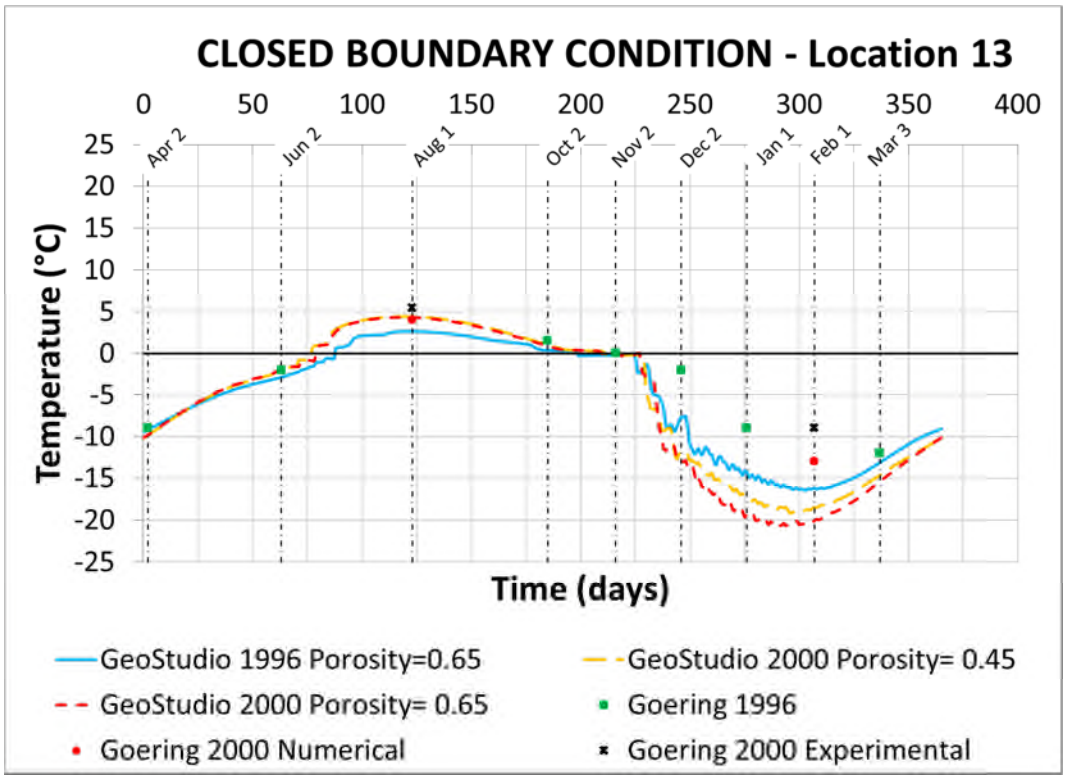

A) Time-temperature plots in Location 13

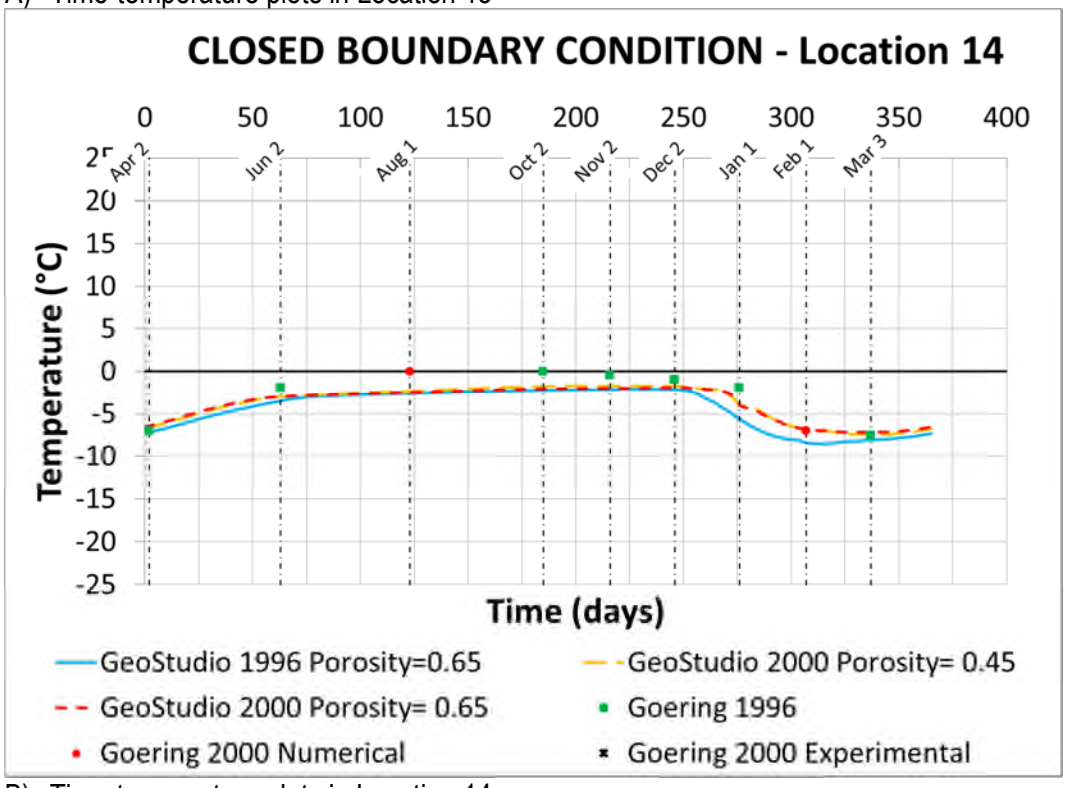

B) Time-temperature plots in Location 14

FIGURE 3.90: TRENDS IN GEOSTUDIO MODELS AND GOERING AND KUMAR (1996) AND GOERING (2000) RESULTS – LOCATION 15 AND 16

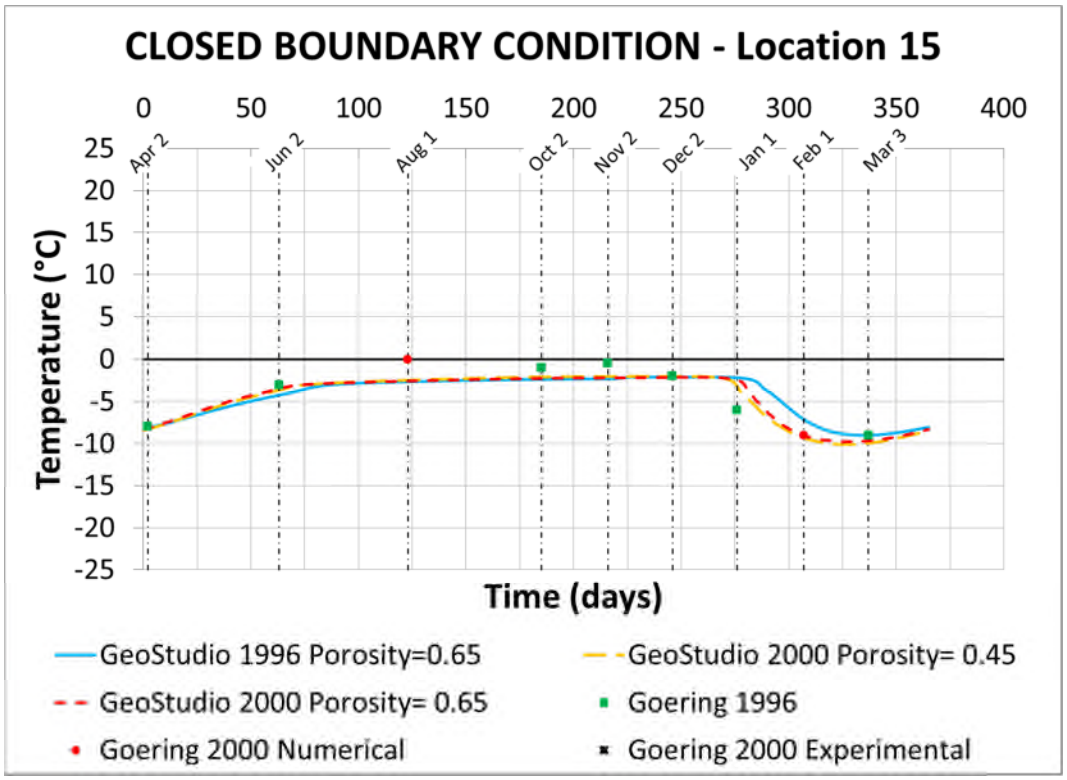

A) Time-temperature plots in Location 15

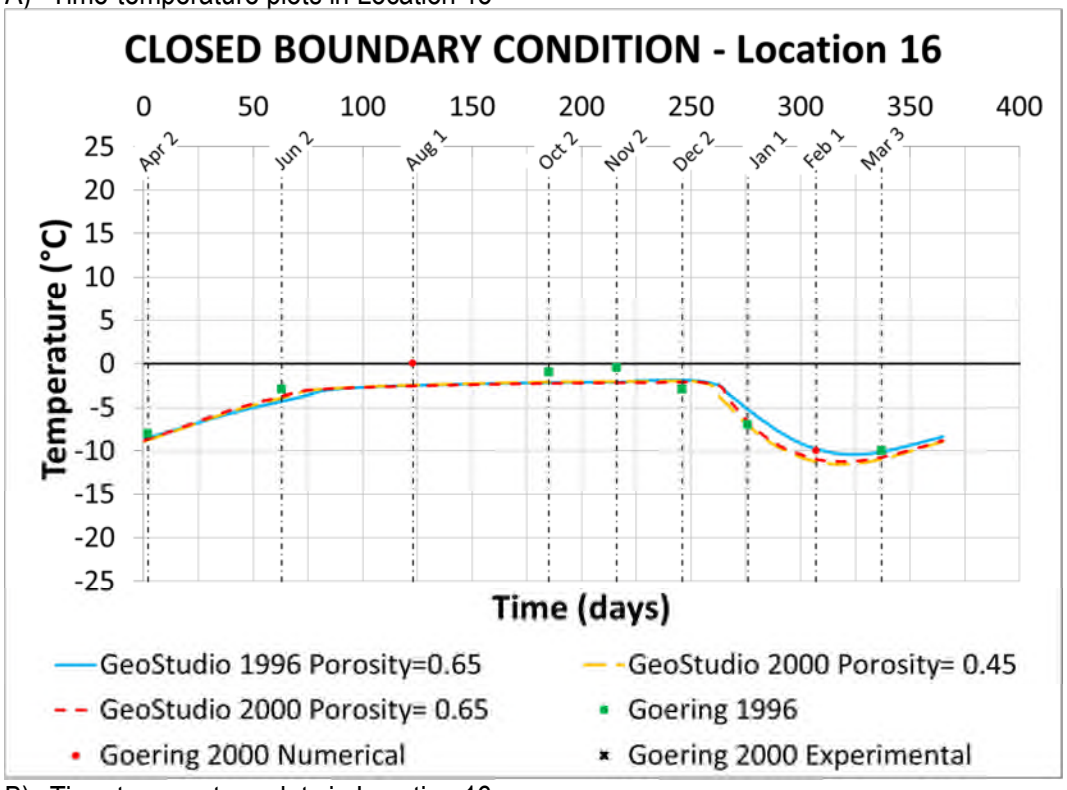

B) Time-temperature plots in Location 16

FIGURE 3.91 COMPARISON OF NUMERICAL RESULTS ON JUNE 2 FOR GOERING AND KUMAR (1996) AND GEOSTUDIO 1996 MODEL WITH CLOSED BOUNDARIES

GOERING AND KUMAR (1996)

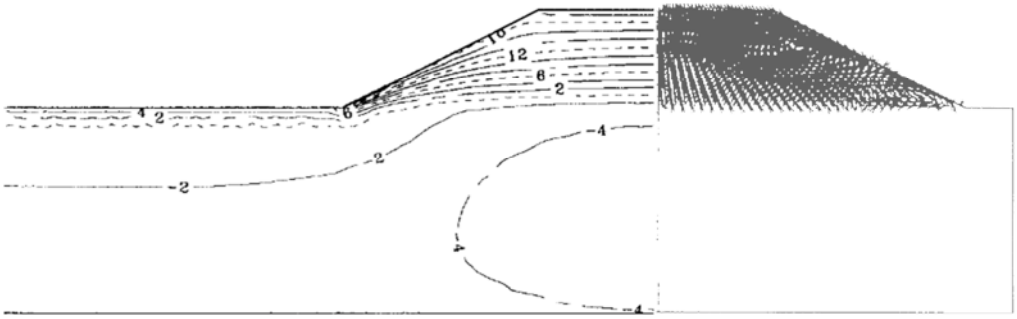

A) Isotherms (left) and air flow vectors (right) (Goering and Kumar 1996)

GEOSTUDIO SIMULATION

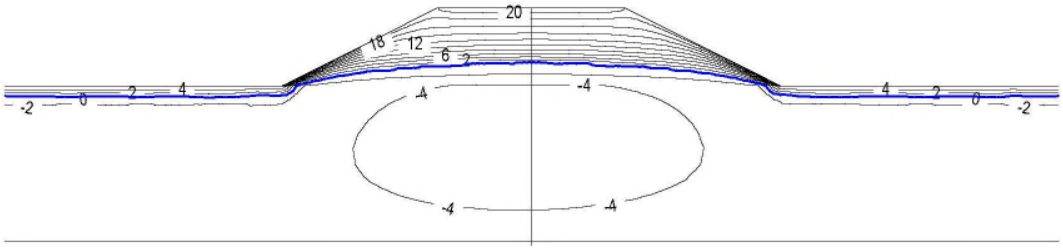

B) Isotherms (GeoStudio 1996 Model)

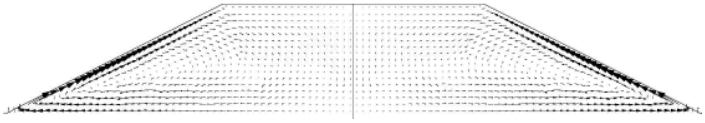

C) Air flow vectors (GeoStudio 1996 Model)

FIGURE 3.92 COMPARISON OF NUMERICAL RESULTS ON OCTOBER 2 FOR GOERING AND KUMAR (1996) AND GEOSTUDIO 1996 MODEL WITH CLOSED BOUNDARIES

GOERING AND KUMAR (1996)

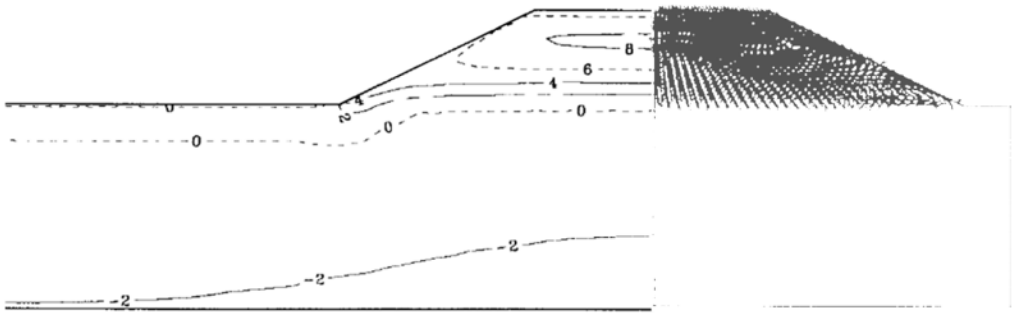

A) Isotherms (left) and air flow vectors (right) (Goering and Kumar, 1996)

GEOSTUDIO SIMULATION

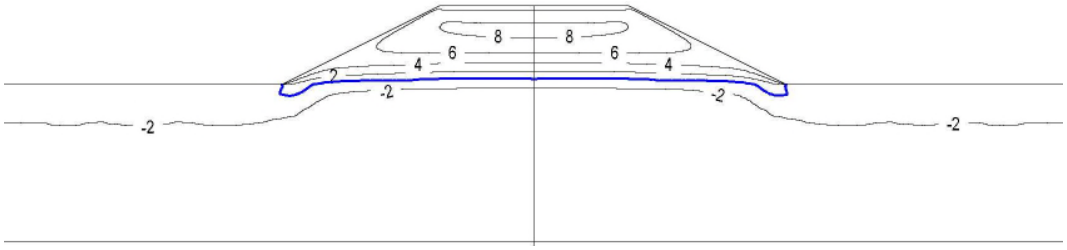

B) Isotherms (GeoStudio 1996 Model)

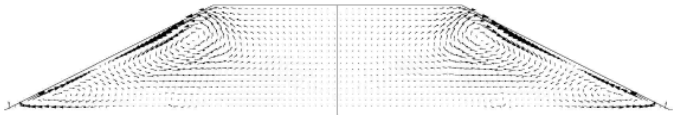

C) Air flow vectors (GeoStudio 1996 Model)

FIGURE 3.93: COMPARISON OF NUMERICAL RESULTS ON NOVEMBER 2 FOR GOERING AND KUMAR (1996) AND GEOSTUDIO 1996 MODEL WITH CLOSED BOUNDARIES

GOERING AND KUMAR (1996)

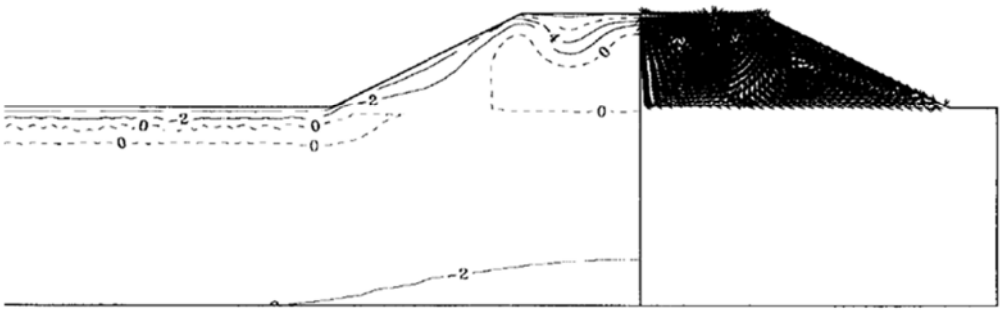

A) Isotherms (left) and air flow vectors (right) (Goering and Kumar 1996)

GEOSTUDIO SIMULATION

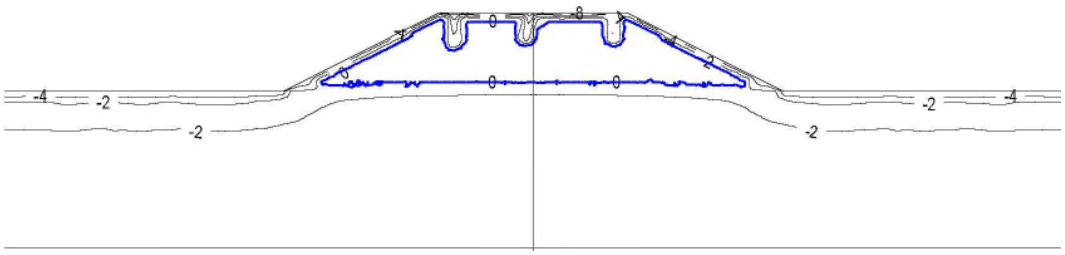

B) Isotherms (GeoStudio 1996 Model)

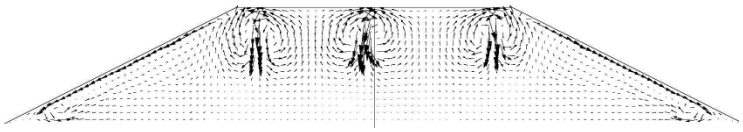

C) Air flow vectors (GeoStudio 1996 Model)

FIGURE 3.94: COMPARISON OF NUMERICAL RESULTS ON DECEMBER 2 FOR GOERING AND KUMAR (1996) AND GEOSTUDIO 1996 MODEL WITH CLOSED BOUNDARIES

GOERING AND KUMAR (1996)

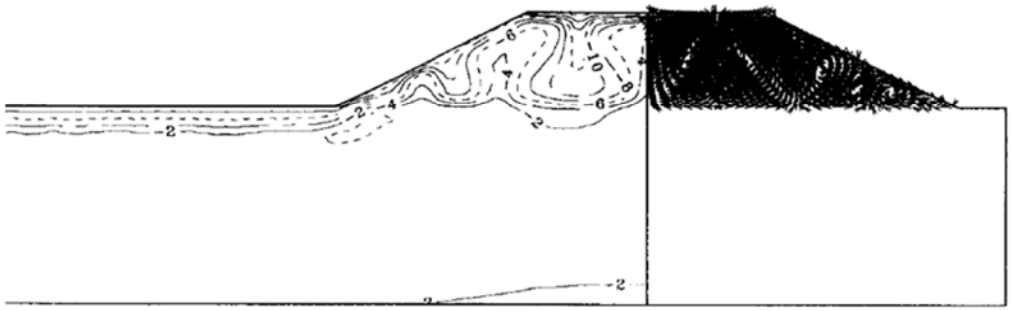

A) Isotherms (left) and air flow vectors (right) (Goering and Kumar 1996)

GEOSTUDIO SIMULATION

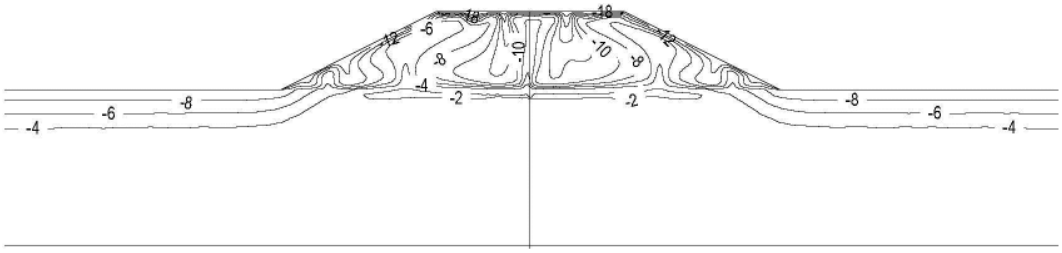

B) Isotherms (GeoStudio 1996 Model)

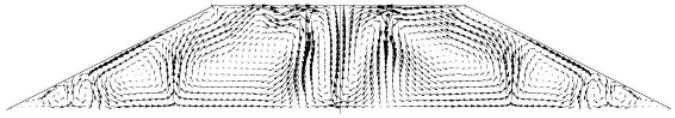

C) Air flow vectors (GeoStudio 1996 Model)

FIGURE 3.95: COMPARISON OF NUMERICAL RESULTS ON JANUARY 1 FOR GOERING AND KUMAR (1996) AND GEOSTUDIO 1996 MODEL WITH CLOSED BOUNDARIES

GOERING AND KUMAR (1996)

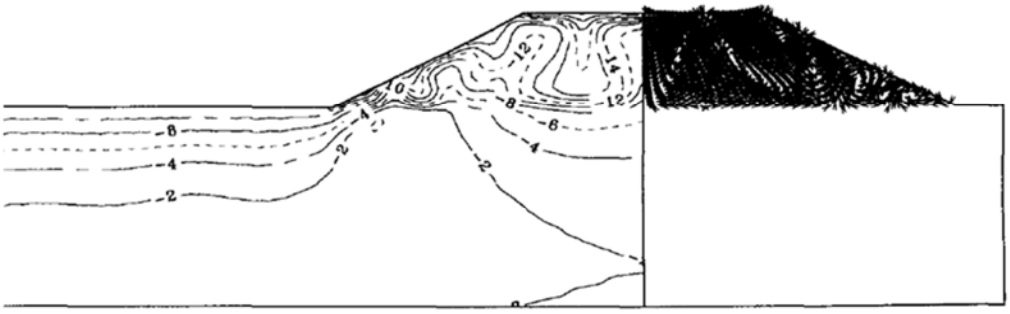

A) Isotherms (left) and air flow vectors (right) (Goering and Kumar 1996)

GEOSTUDIO SIMULATION

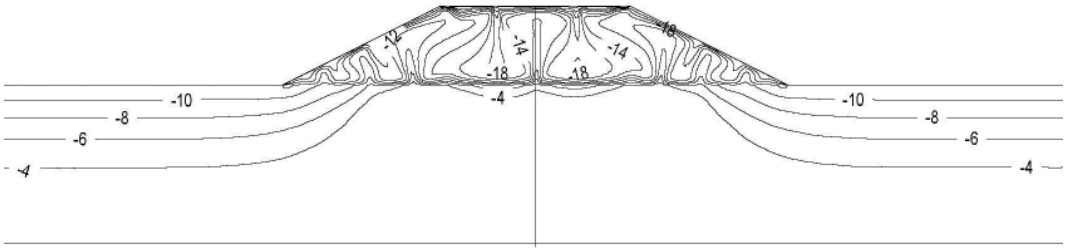

B) Isotherms (GeoStudio 1996 Model)

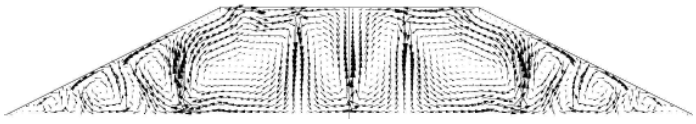

C) Air flow vectors (GeoStudio 1996 Model)

FIGURE 3.96: COMPARISON OF NUMERICAL RESULTS ON MARCH 3 FOR GOERING AND KUMAR (1996) AND GEOSTUDIO 1996 MODEL WITH CLOSED BOUNDARIES

GOERING AND KUMAR (1996)

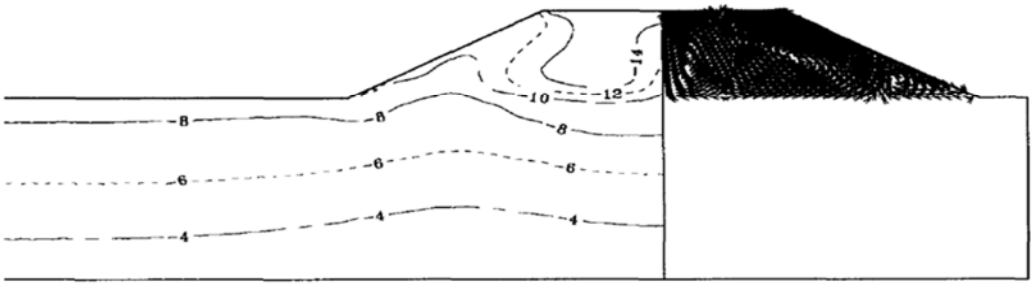

A) Isotherms (left) and air flow vectors (right) (Goering and Kumar 1996)

GEOSTUDIO SIMULATION

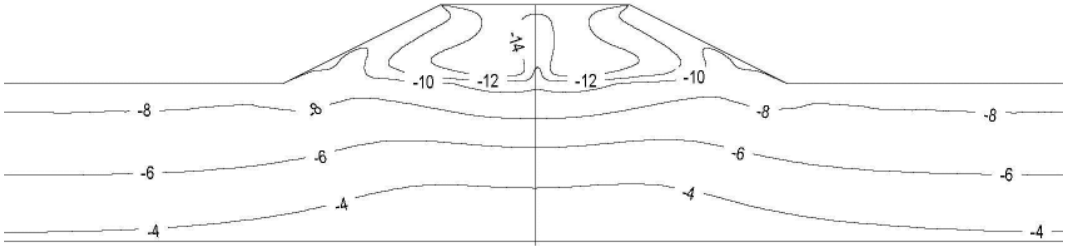

B) Isotherms (GeoStudio 1996 Model)

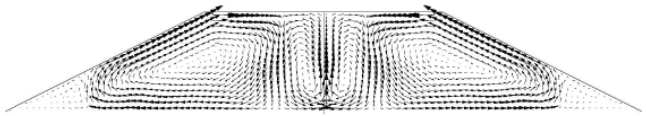

C) Air flow vectors (GeoStudio 1996 Model)

FIGURE 3.97: COMPARISON OF NUMERICAL RESULTS ON APRIL 2 FOR GOERING AND KUMAR (1996) AND GEOSTUDIO 1996 MODEL WITH CLOSED BOUNDARIES

GOERING AND KUMAR (1996)

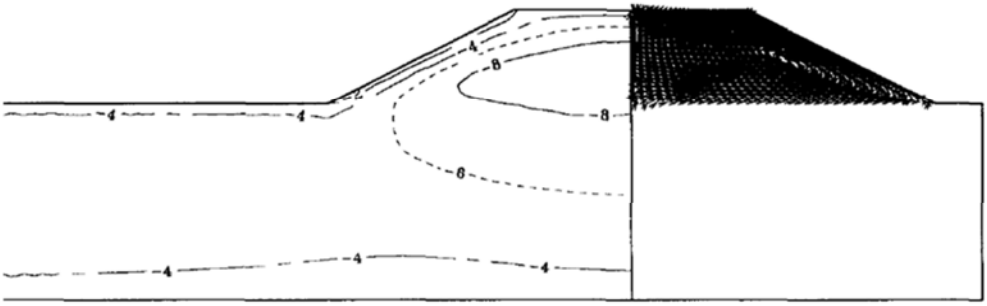

A) Isotherms (left) and air flow vectors (right) (Goering and Kumar 1996)

GEOSTUDIO SIMULATION

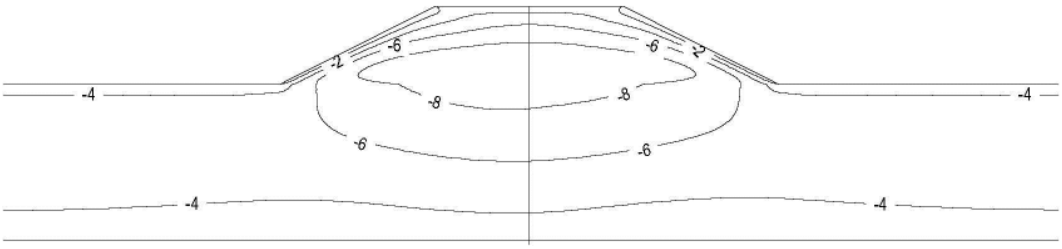

B) Isotherms (GeoStudio 1996 Model)

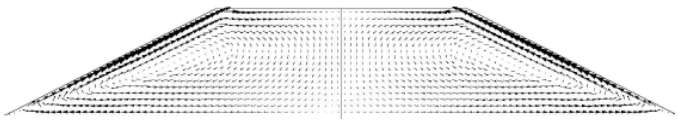

C) Air flow vectors (GeoStudio 1996 Model)

FIGURE 3.98: COMPARISON OF NUMERICAL RESULTS FOR GOERING AND KUMAR (1996) AND GEOSTUDIO 1996 MODEL WITH CLOSED BOUNDARIES

GOERING AND KUMAR (1996)

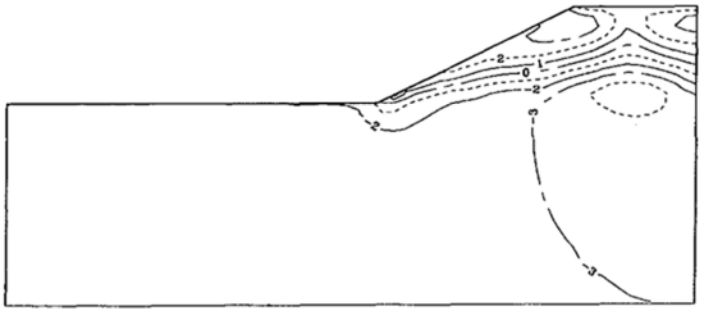

A) Average annual temperatures (Goering and Kumar 1996)

GEOSTUDIO SIMULATION

B) Average annual temperatures (GeoStudio 1996 Model)

FIGURE 3.99: COMPARISON OF NUMERICAL RESULTS FOR GOERING AND KUMAR (1996) AND GEOSTUDIO 1996 MODEL WITH CLOSED BOUNDARIES

GOERING AND KUMAR (1996)

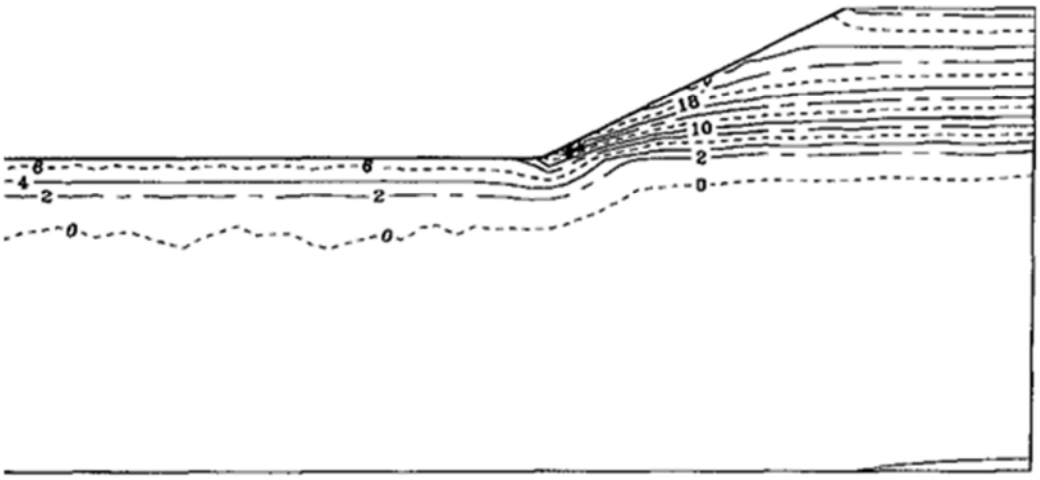

A) Yearly maximum temperature extremes (Goering and Kumar, 1996)

GEOSTUDIO SIMULATION

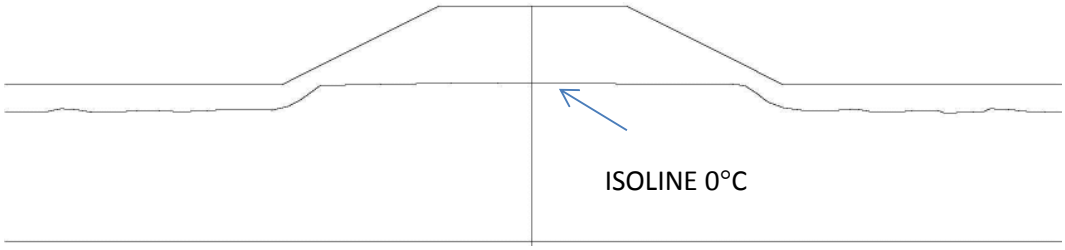

B) Isoline 0°C (GeoStudio 1996 Model)

FIGURE 3.100: COMPARISON OF NUMERICAL RESULTS FOR GOERING AND KUMAR (1996) AND GEOSTUDIO 1996 MODEL WITH CLOSED BOUNDARIES

GOERING AND KUMAR (1996)

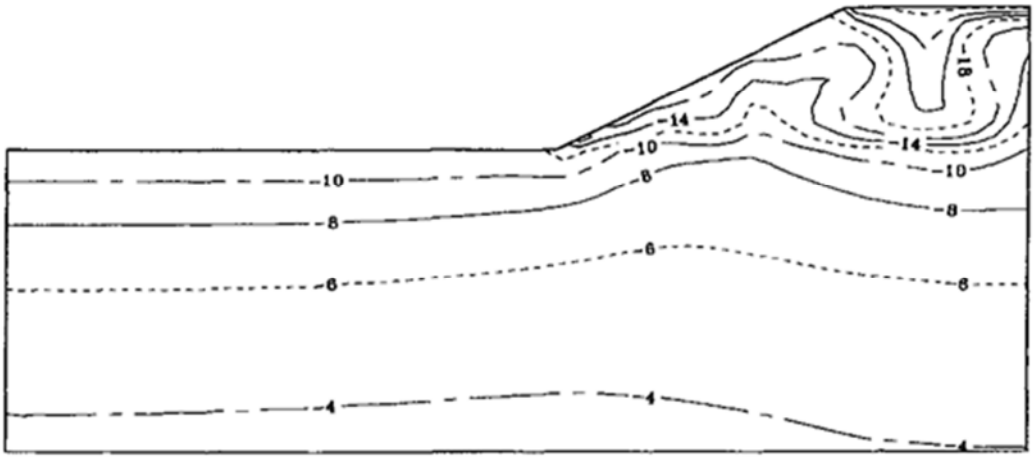

A) Yearly minimum temperature extremes (Goering and Kumar, 1996)

GEOSTUDIO SIMULATION

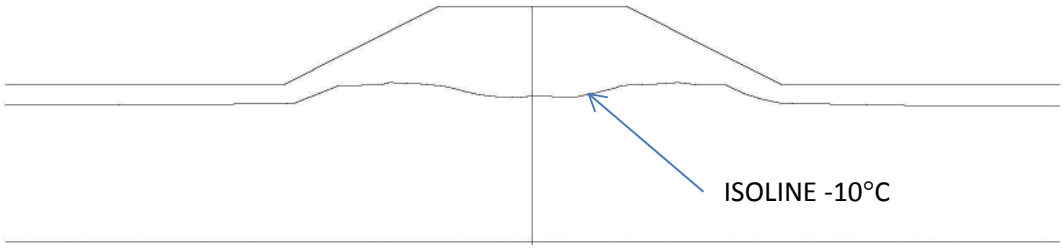

B) Isoline -10°C (GeoStudio 1996 Model)

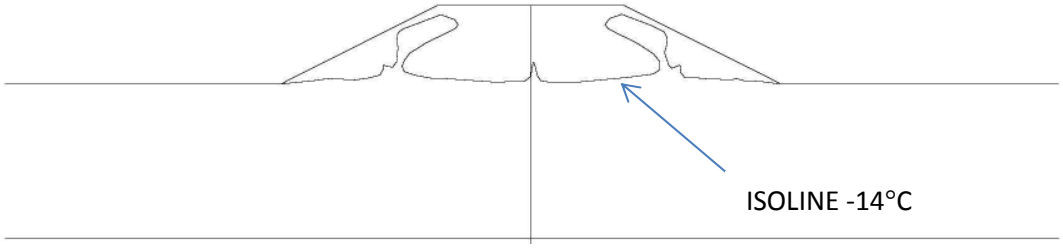

C) Isoline -14°C (GeoStudio 1996 Model)

FIGURE 3.101: COMPARISON OF NUMERICAL RESULTS ON FEBRUARY 1 FOR GOERING (2000) AND GEOSTUDIO 2000 MODEL WITH CLOSED BOUNDARIES

GOERING (2000)

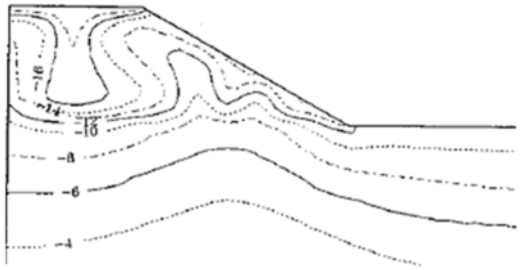

A) Isotherms (Goering, 2000)

GEOSTUDIO SIMULATION

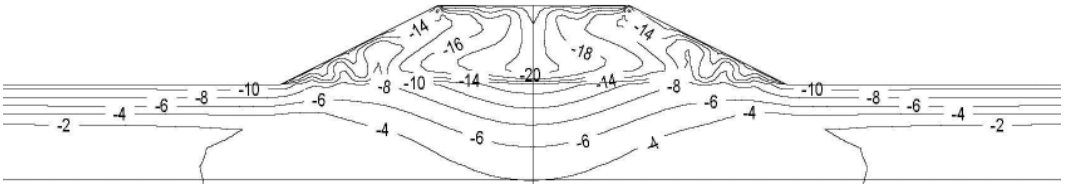

B) Isotherms (GeoStudio 2000 Model)

GOERING (2000)

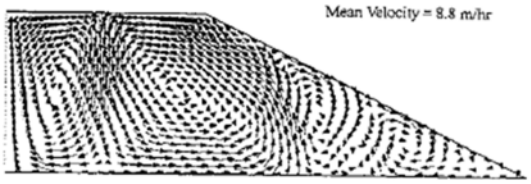

C) Air flow vectors (Goering, 2000)

GEOSTUDIO SIMULATION

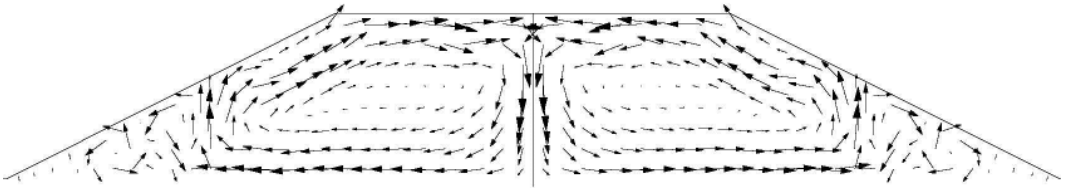

D) Air flow vectors (GeoStudio 2000 Model)

FIGURE 3.102: COMPARISON OF NUMERICAL AND EXPERIMENTAL RESULTS ON FEBRUARY 1 FOR GOERING (2000) AND GEOSTUDIO 2000 MODEL WITH CLOSED BOUNDARIES

GOERING (2000)

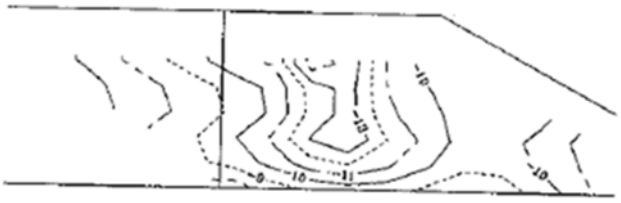

A) Experimental isotherms (Goering, 2000)

B) Numerical isotherms (Goering, 2000)

GEOSTUDIO SIMULATION

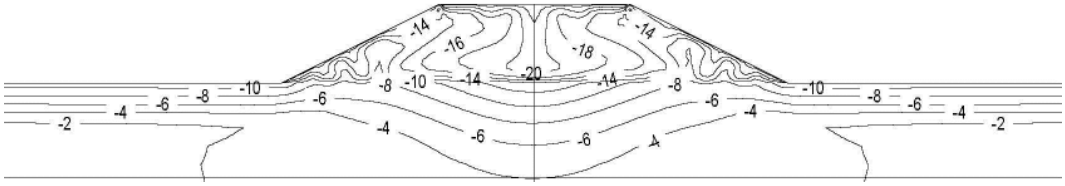

C) Isotherms (GeoStudio 2000 Model)

FIGURE 3.103: COMPARISON OF EXPERIMENTAL AND NUMERICAL RESULTS ON AUGUST 1 FOR GOERING (2000) AND GEOSTUDIO 2000 MODEL WITH CLOSED BOUNDARIES

GOERING (2000)

A) Experimental isotherms (Goering, 2000)

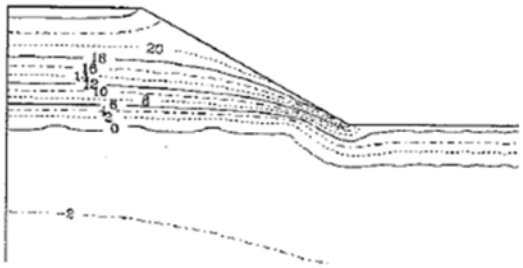

B) Numerical isotherms (Goering, 2000)

GEOSTUDIO SIMULATION

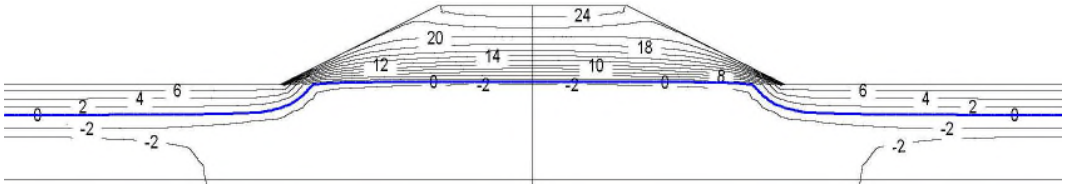

C) Isotherms (GeoStudio 2000 Model)

FIGURE 3.104: GROUND TEMPERATURE PROFILE; SITE 4 (30 M BENCH); PANDA WRSA (SRK, 2003)

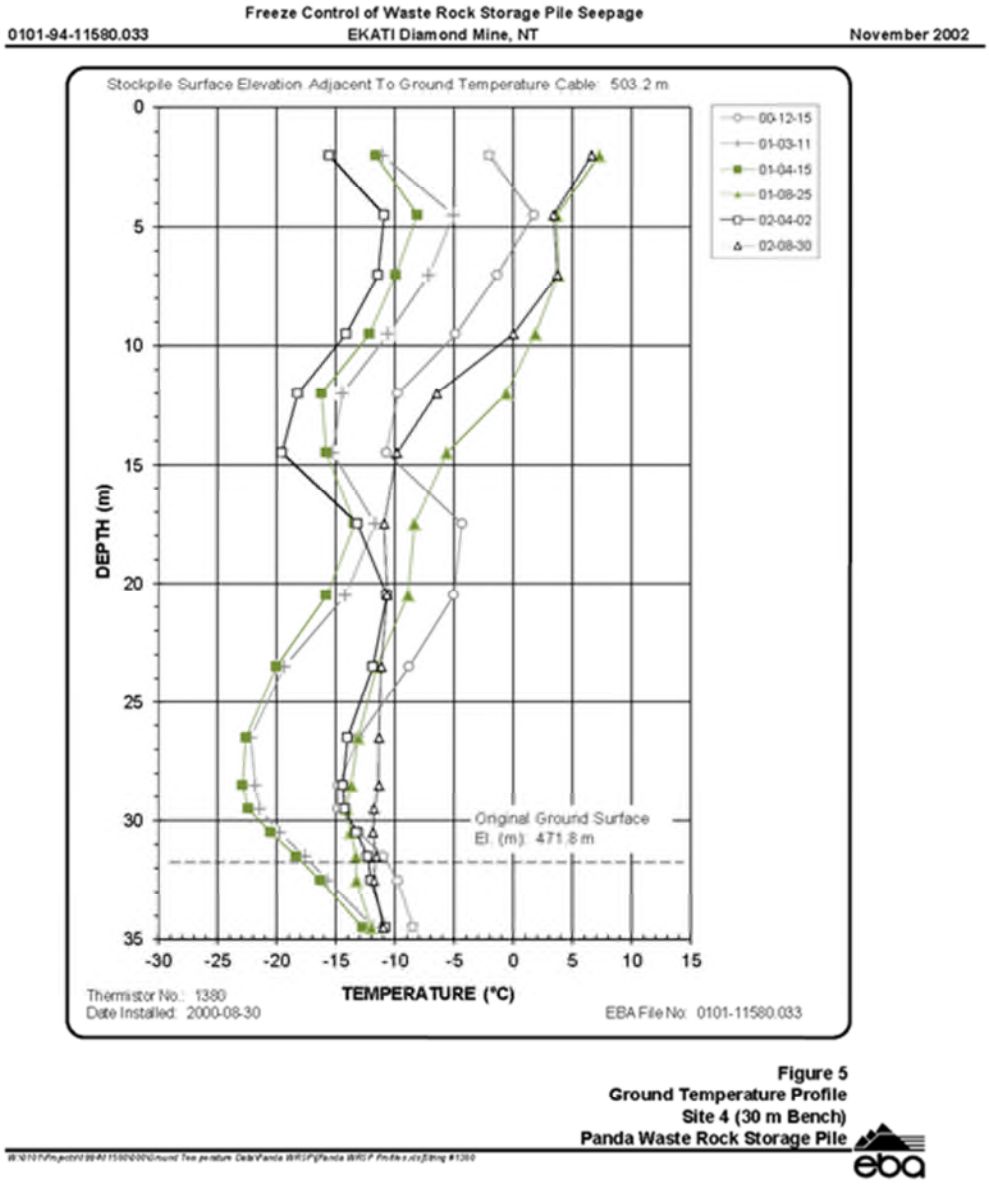

Figure 5
Ground Temperature Profile
Site 4 (30 m Bench)
Panda Waste Rock Storage Pile

FIGURE 3.105: PANDA WRSA PLAN INCLUDING SITE 4 LOCATION (SRK, 2003)

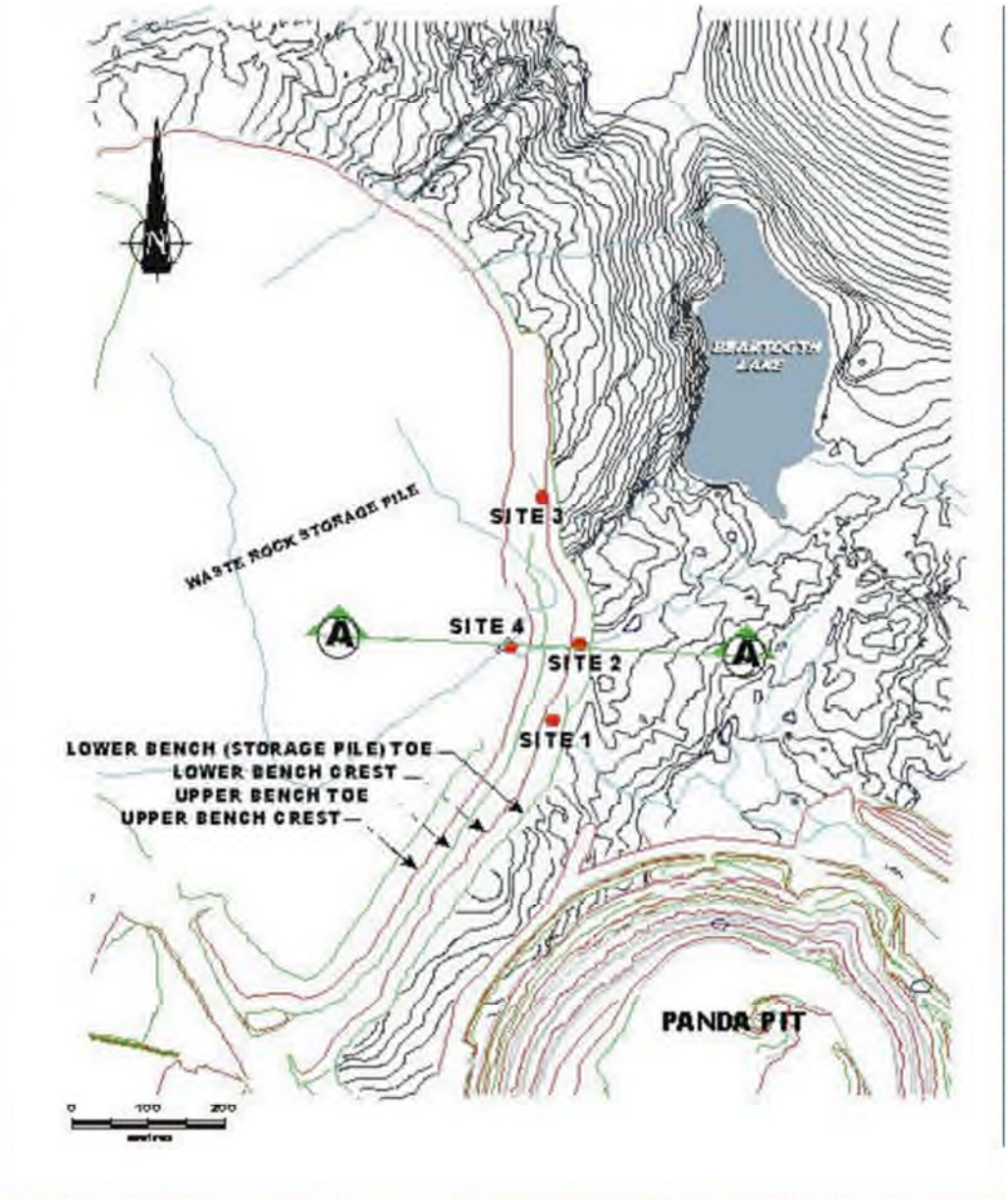

FIGURE 3.106 GEOSTUDIO MODEL USED TO MODEL EKATI PANDA WRSA AND LOCATIONS WHERE TEMPERATURES WERE EXTRACTED

GEOSTUDIO SIMULATION

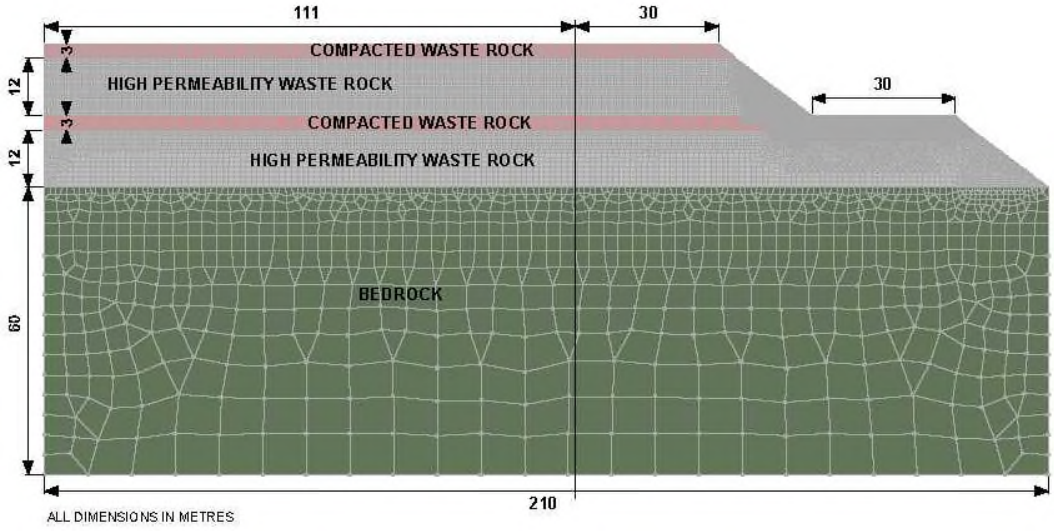

A) Ekati model (GeoStudio); 27,670 nodes and 27,750 elements; quads and triangles mesh

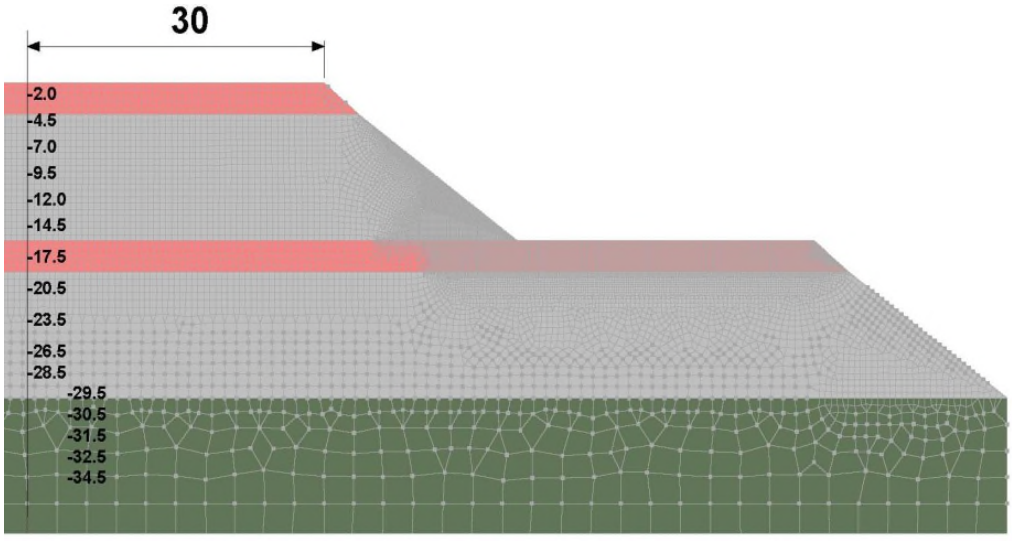

B) Locations identified by their depths in the pile selected to extract temperatures from Ekati model (close-up)

FIGURE 3.107: TRUMPET CURVES FOR CASE 1

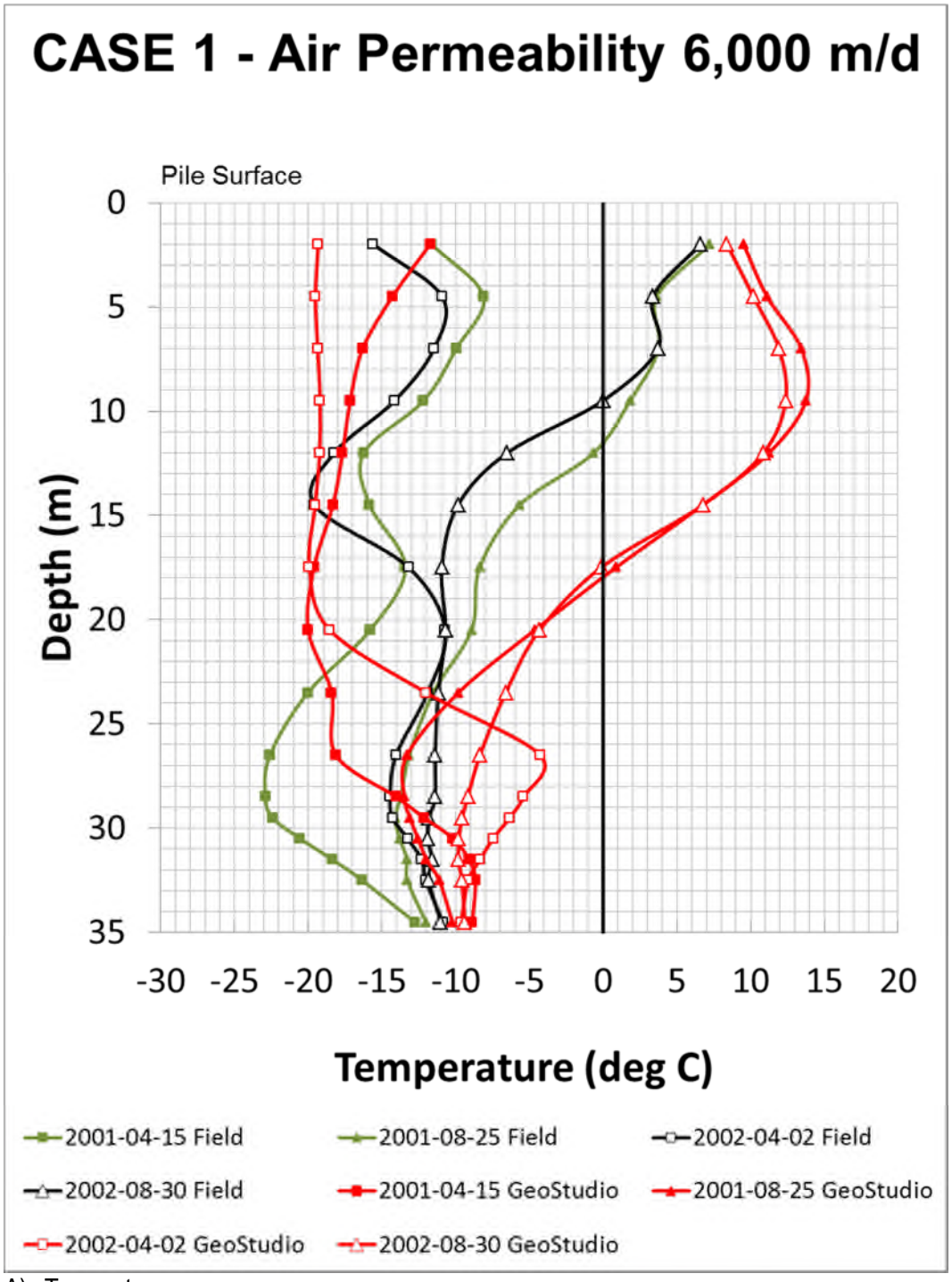

A) Trumpet curves

FIGURE 3.108: TRUMPET CURVES FOR CASE 2

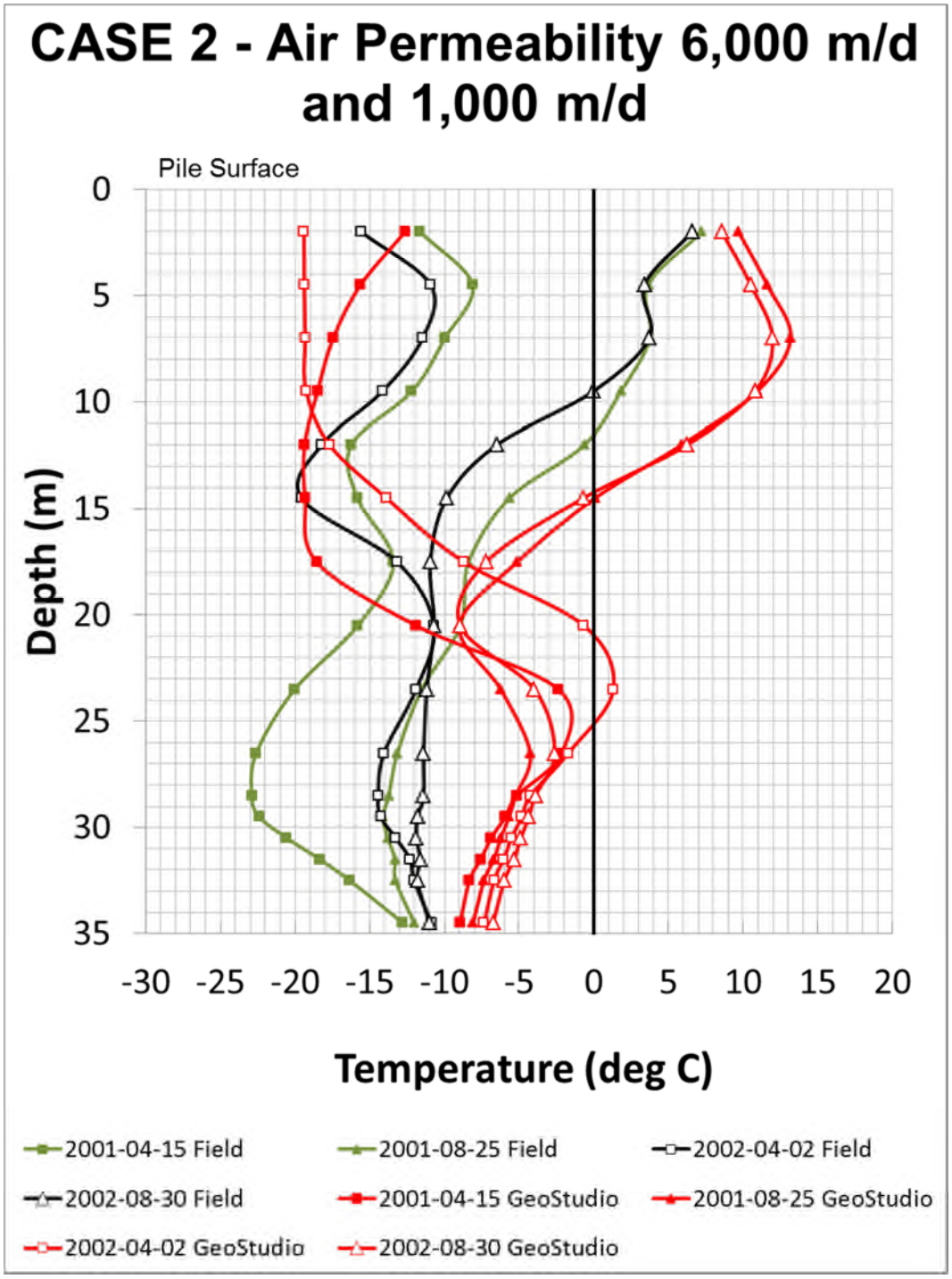

A) Trumpet curves

FIGURE 3.109: TRUMPET CURVES FOR CASE 3

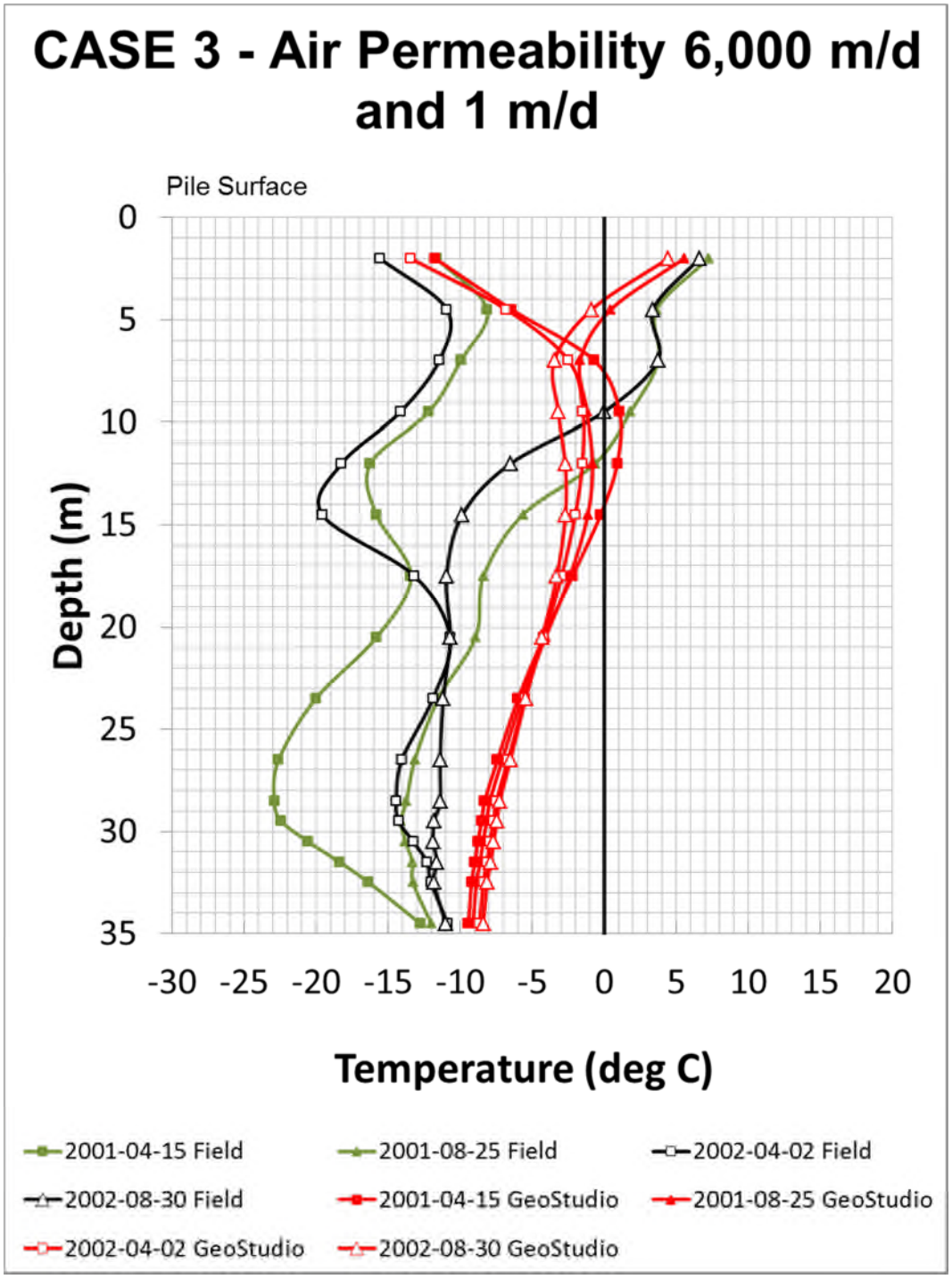

A) Trumpet curves

FIGURE 3.110: TRUMPET CURVES FOR CASE 4

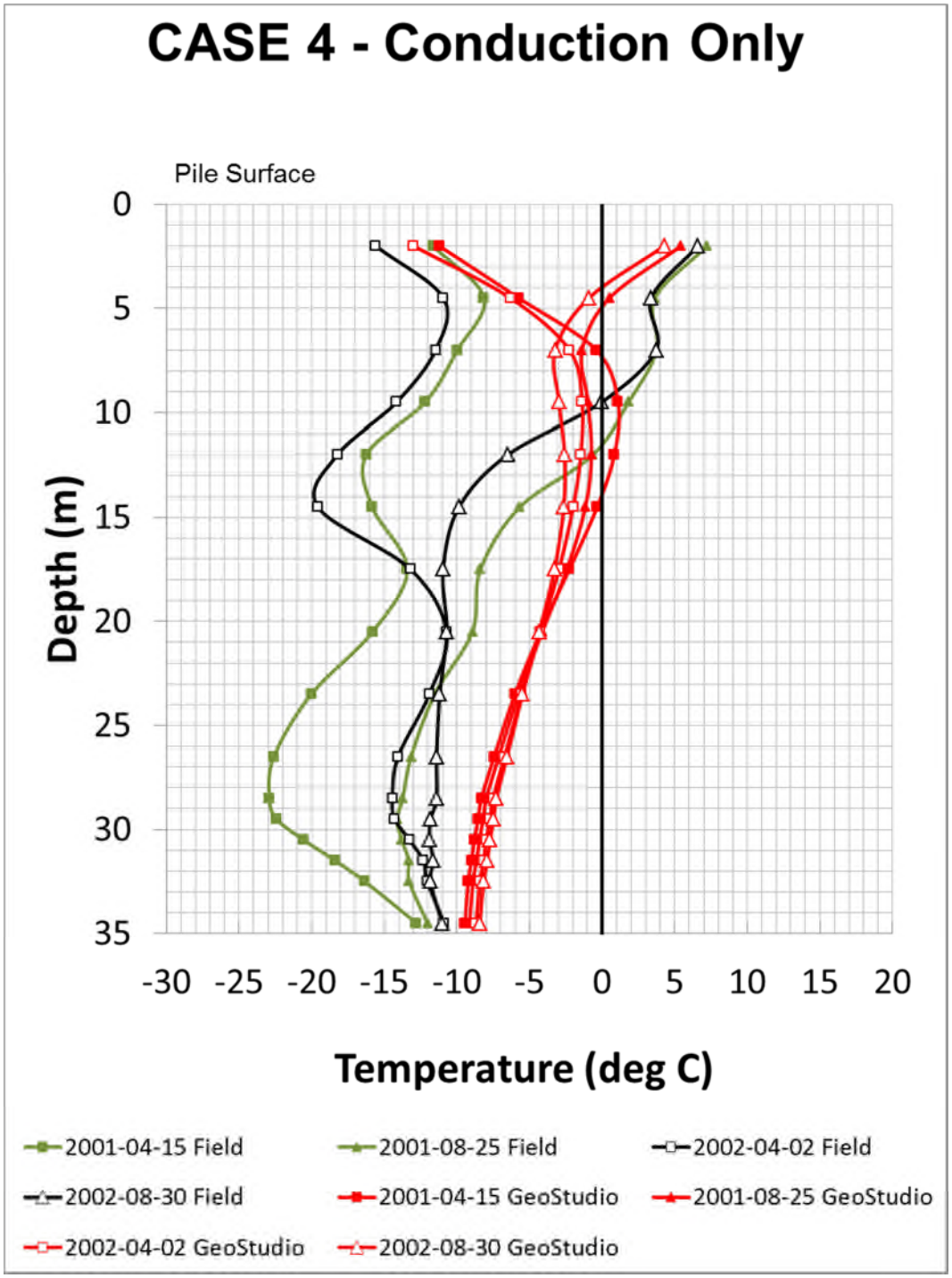

A) Trumpet curves

FIGURE 3.111: EMBANKMENT GEOMETRY (SUN ET AL., 2005) USED TO MODEL SUN ET AL. (2005) CASES 1 THROUGH 5

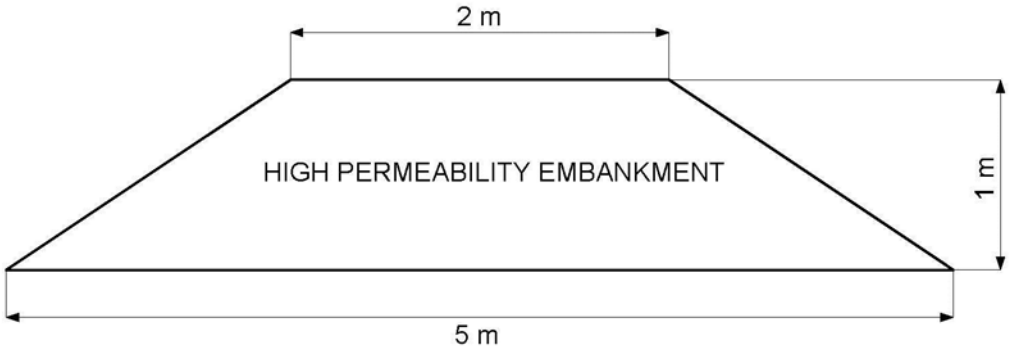

A) Embankment dimensions

FIGURE 3.112: COMPARISON OF NUMERICAL RESULTS FOR SUN ET AL. (2005) AT RA=50 AND GEOSTUDIO SIMULATION AT RA=25; CASE 1 (SUN ET AL., 2005) – ALL BOUNDARIES CLOSED

SUN ET AL. CASE 1

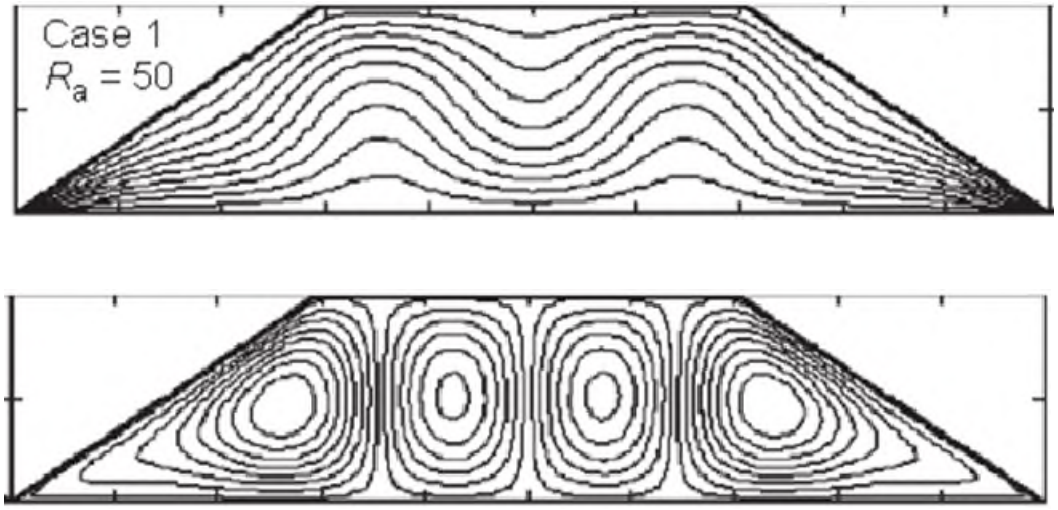

A) Sun et al. Case 1 (Ra=50); isotherms (top) and air flow vectors (bottom) (Sun et al., 2005)

GEOSTUDIO SIMULATION

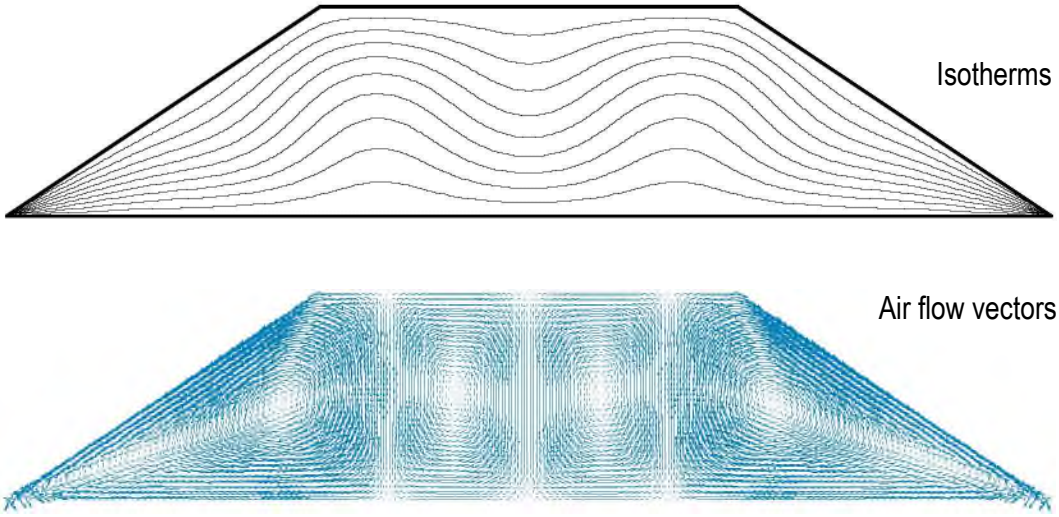

B) GeoStudio simulation at GeoStudio default temperature of 10°C (Ra=25); isotherms (top) and air flow vectors (bottom); solution stable within 500 days

FIGURE 3.113: COMPARISON OF NUMERICAL RESULTS FOR SUN ET AL. (2005) AT RA=50 AND GEOSTUDIO SIMULATION AT RA=50; CASE 1 (SUN ET AL., 2005) – ALL BOUNDARIES CLOSED

SUN ET AL. CASE 1

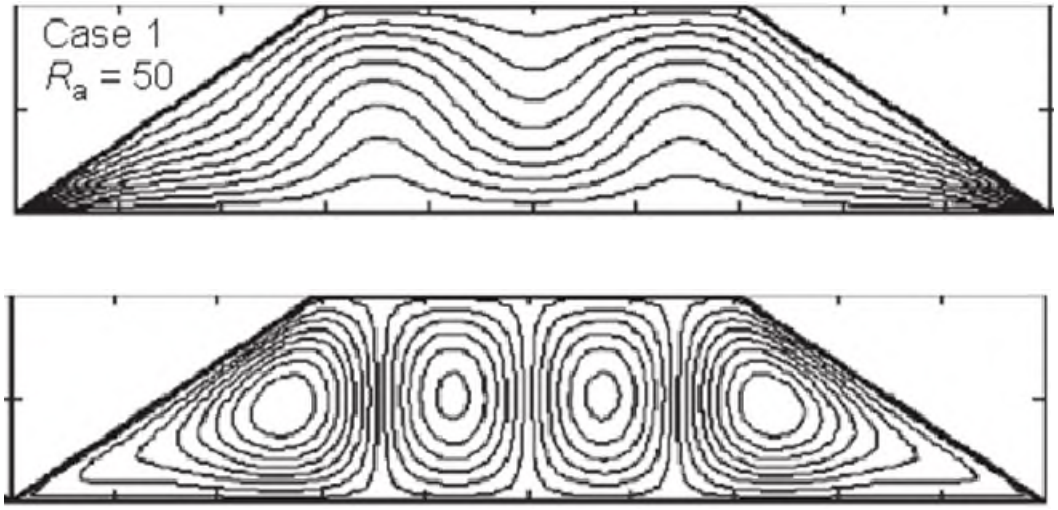

A) Sun et al. Case 1 (Ra=50); isotherms (top) and air flow vectors (bottom) (Sun et al., 2005)

GEOSTUDIO SIMULATION

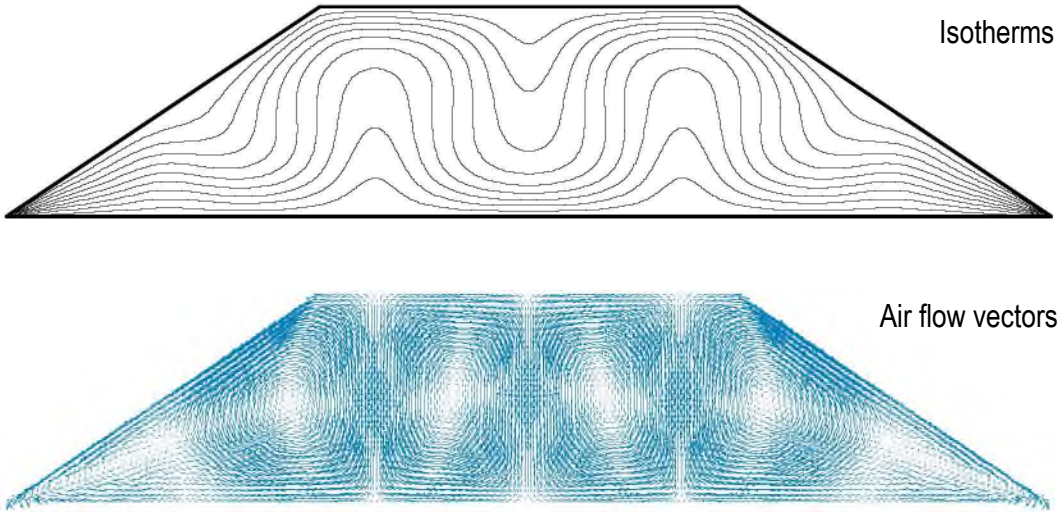

B) GeoStudio simulation at GeoStudio default temperature of 10°C (Ra=50); isotherms (top) and air flow vectors (bottom); solution stable within 500 days

FIGURE 3.114: COMPARISON OF NUMERICAL RESULTS FOR SUN ET AL. (2005) AT RA=80 AND GEOSTUDIO SIMULATION AT RA=50; CASE 1 (SUN ET AL., 2005) – ALL BOUNDARIES CLOSED

SUN ET AL. CASE 1

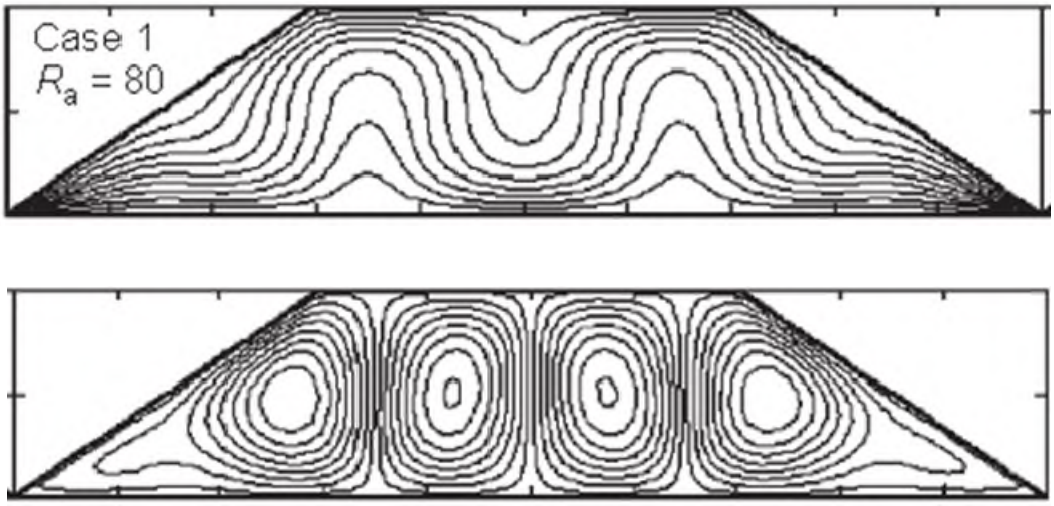

A) Sun et al. Case 1 (Ra=50); isotherms (top) and air flow vectors (bottom) (Sun et al., 2005)

GEOSTUDIO SIMULATION

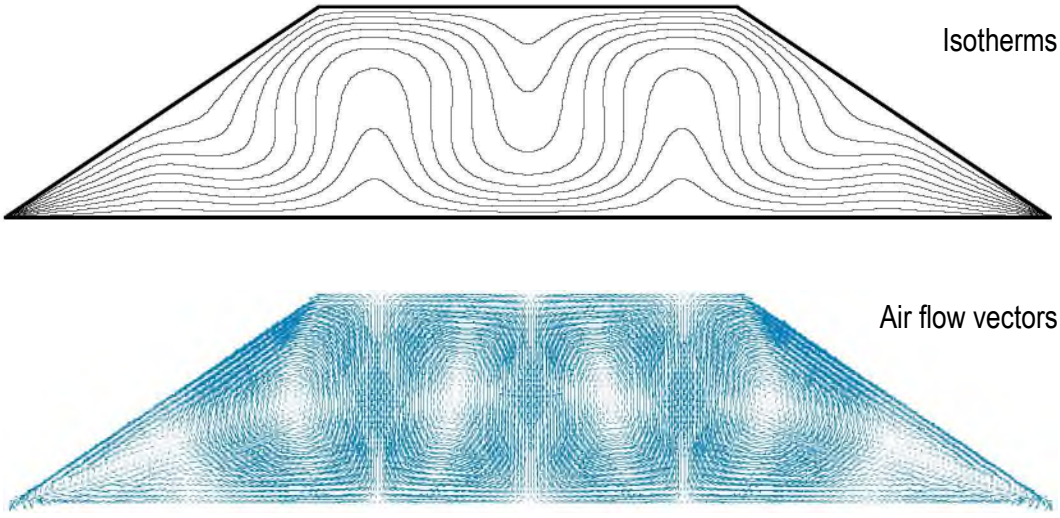

B) GeoStudio simulation at GeoStudio default temperature of 10°C (Ra=50); isotherms (top) and air flow vectors (bottom); solution stable within 500 days

FIGURE 3.115: COMPARISON OF NUMERICAL RESULTS FOR SUN ET AL. (2005) AT RA=80 AND GEOSTUDIO SIMULATION AT RA=80; CASE 1 (SUN ET AL., 2005) – ALL BOUNDARIES CLOSED

SUN ET AL. CASE 1

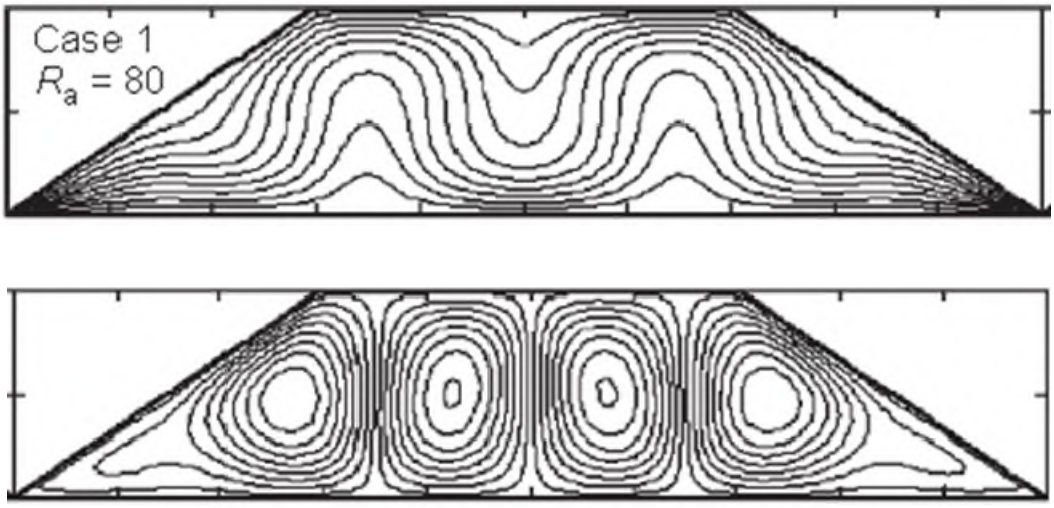

A) Sun et al. Case 1 (Ra=80); isotherms (top) and air flow vectors (bottom) (Sun et al., 2005)

GEOSTUDIO SIMULATION

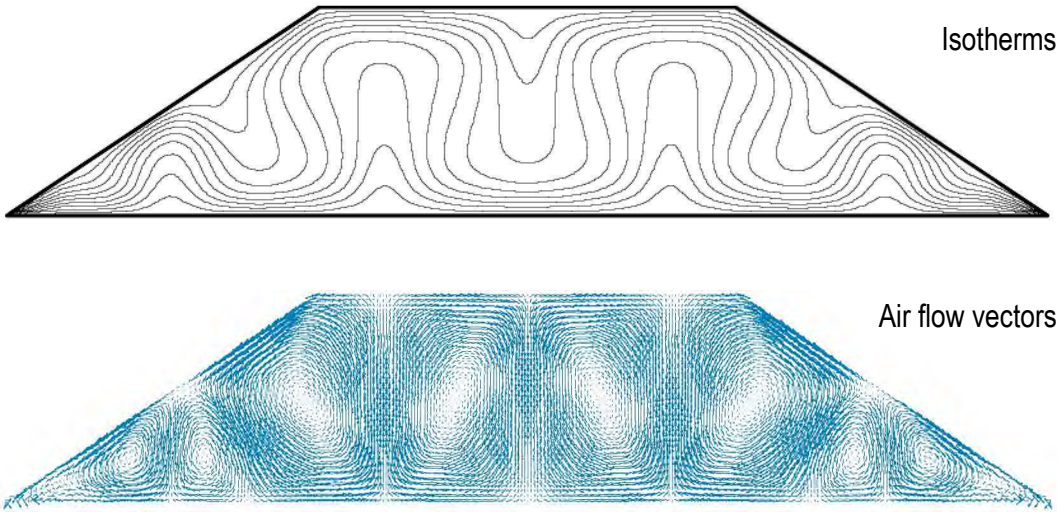

B) GeoStudio simulation at GeoStudio default temperature of 10°C (Ra=80); isotherms (top) and air flow vectors (bottom); solution did not stabilize within 500 days

FIGURE 3.116: COMPARISON OF NUMERICAL RESULTS FOR GEOSTUDIO SIMULATIONS AT RA=50 AT TWO TEMPERATURES; CASE 1 (SUN ET AL., 2005) – ALL BOUNDARIES CLOSED

GEOSTUDIO SIMULATION 1

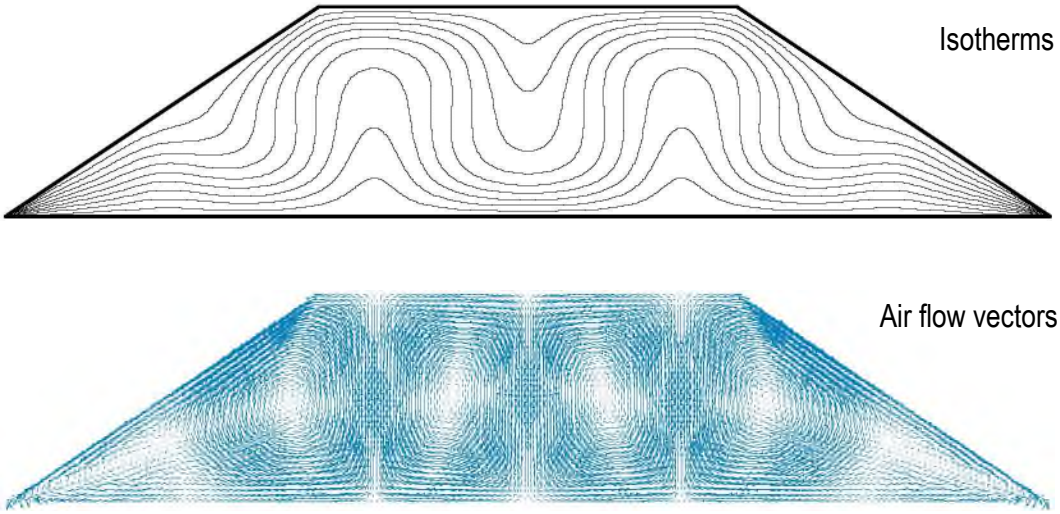

A) GeoStudio simulation at GeoStudio default temperature of 10°C (Ra=50); isotherms (top) and air flow vectors (bottom); solution stable within 500 days

GEOSTUDIO SIMULATION 2

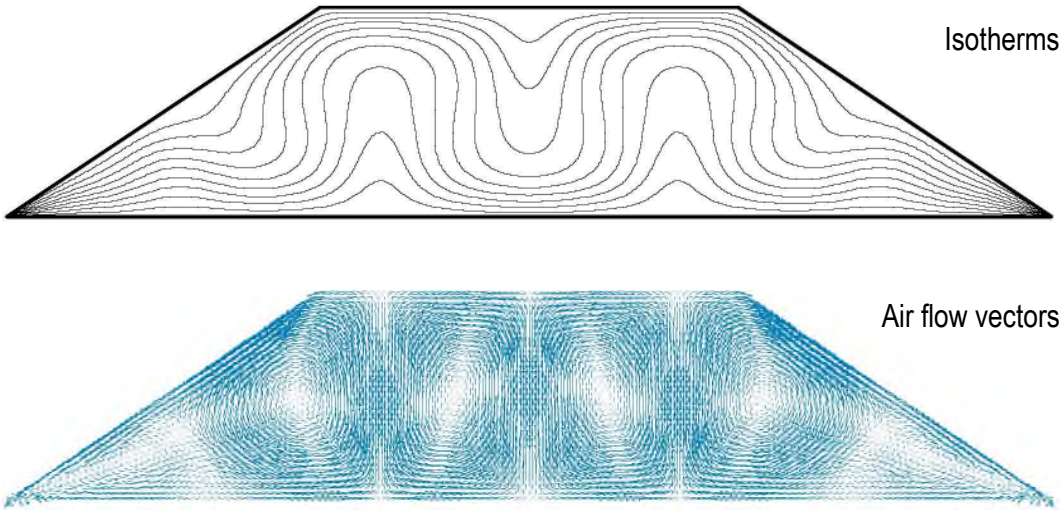

B) GeoStudio simulation at near 0°C (Ra=50); isotherms (top) and air flow vectors (bottom); solution stable within 500 days

FIGURE 3.117: COMPARISON OF NUMERICAL RESULTS FOR GEOSTUDIO SIMULATIONS AT RA=80 AT VARIOUS TEMPERATURES; CASE 1 (SUN ET AL., 2005) – ALL BOUNDARIES CLOSED

GEOSTUDIO SIMULATION 1

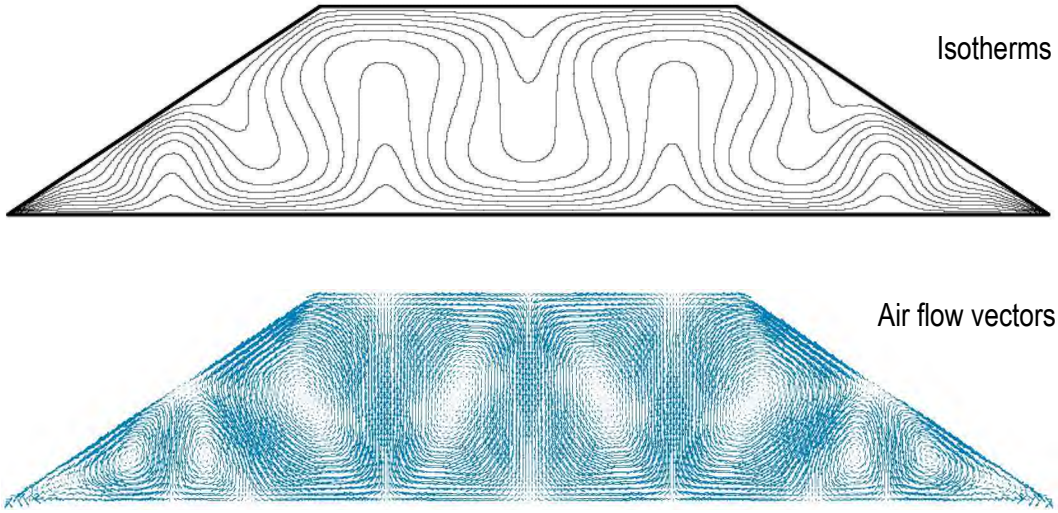

A) GeoStudio simulation at GeoStudio default temperature of 10°C (Ra=80); isotherms (top) and air flow vectors (bottom); solution did not stabilize within 500 days

GEOSTUDIO SIMULATION 2

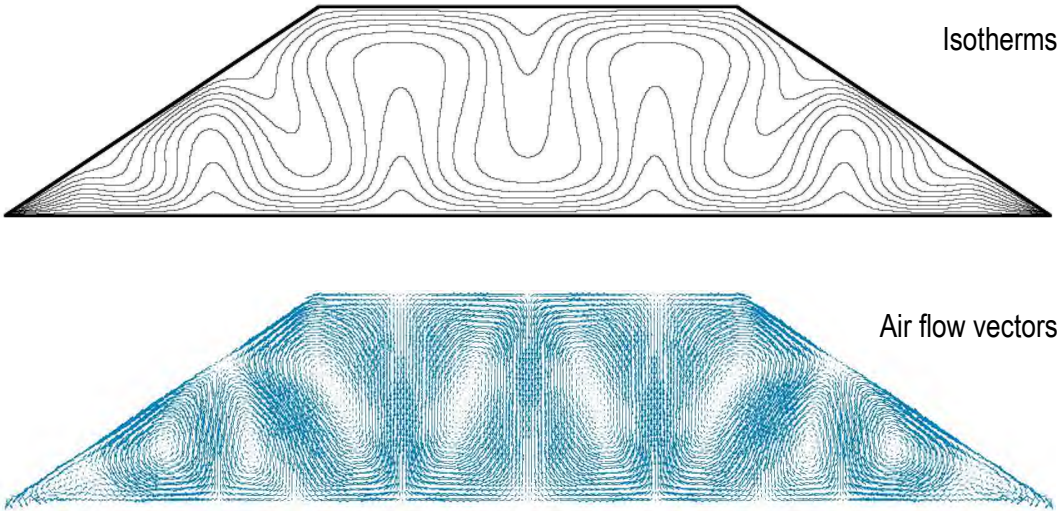

B) GeoStudio simulation at near 0°C (Ra=80); isotherms (top) and air flow vectors (bottom); solution did not stabilize within 500 days

FIGURE 3.118: COMPARISON OF NUMERICAL RESULTS FOR SUN ET AL. (2005) AT RA=50 AND GEOSTUDIO SIMULATION AT RA=25; CASE 2 (SUN ET AL., 2005) – SIDESLOPES OPEN

SUN ET AL. CASE 2

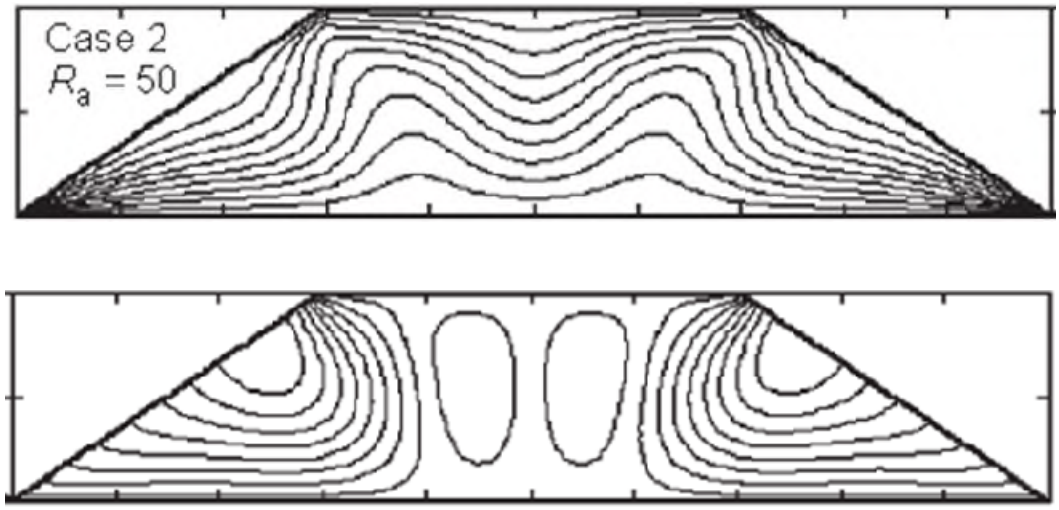

A) Sun et al. Case 2 (Ra=50); isotherms (top) and air flow vectors (bottom) (Sun et al., 2005)

GEOSTUDIO SIMULATION

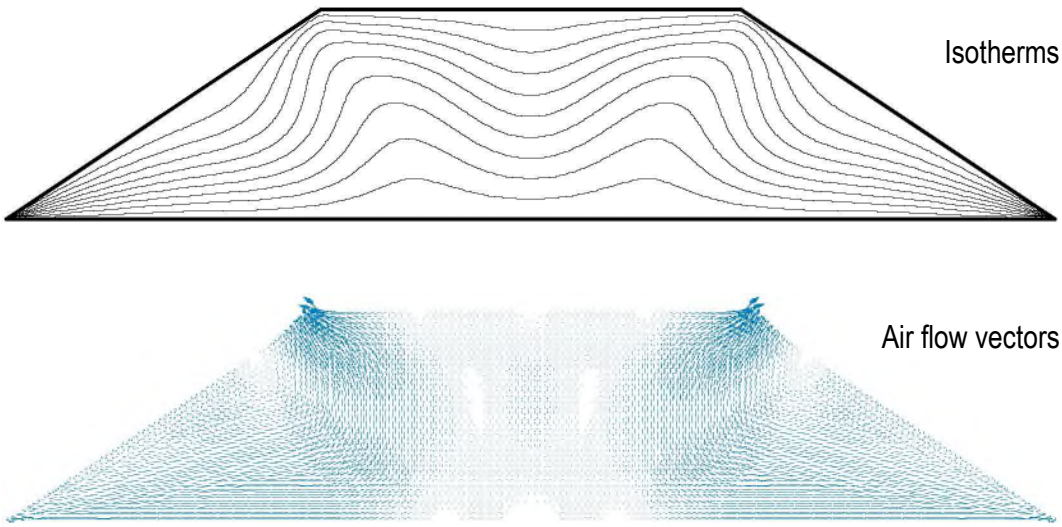

B) GeoStudio simulation at GeoStudio default temperature of 10°C (Ra=25); isotherms (top) and air flow vectors (bottom); solution stable within 500 days

FIGURE 3.119: COMPARISON OF NUMERICAL RESULTS FOR SUN ET AL. (2005) AT RA=50 AND GEOSTUDIO SIMULATION AT RA=50; CASE 2 (SUN ET AL., 2005) – SIDESLOPES OPEN

SUN ET AL. CASE 2

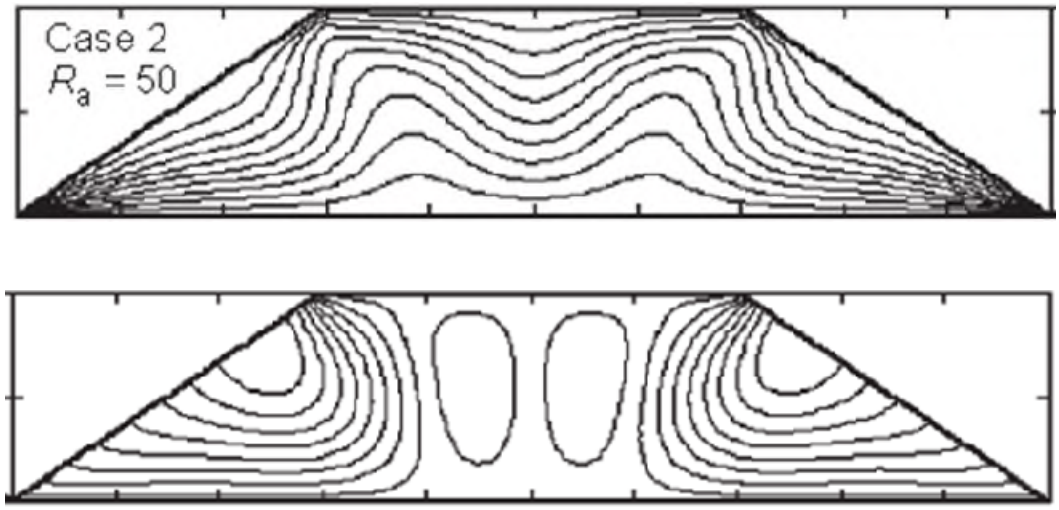

A) Sun et al. Case 2 (Ra=50); isotherms (top) and air flow vectors (bottom) (Sun et al., 2005)

GEOSTUDIO SIMULATION

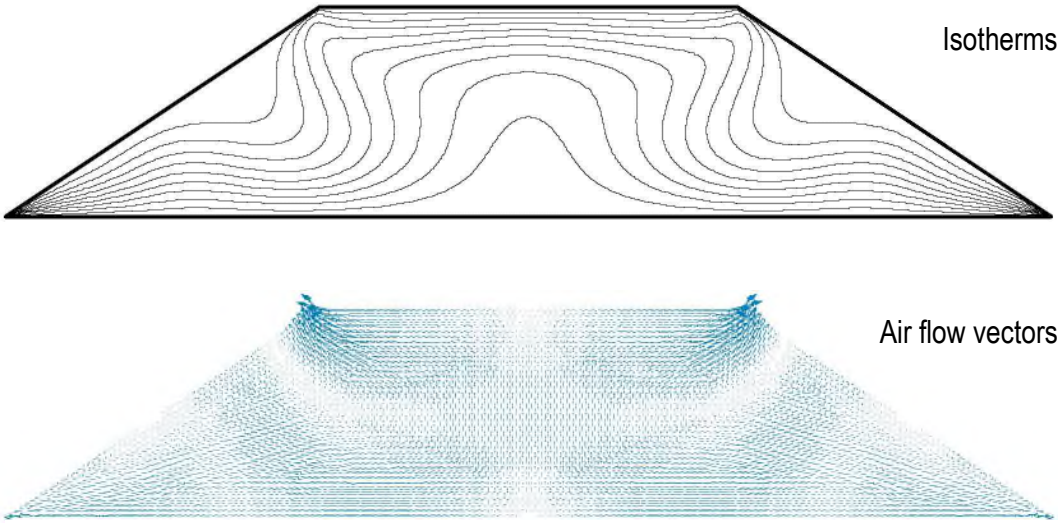

B) GeoStudio simulation at GeoStudio default temperature of 10°C (Ra=50); isotherms (top) and air flow vectors (bottom); solution did not stabilize within 500 days

FIGURE 3.120: COMPARISON OF NUMERICAL RESULTS FOR SUN ET AL. (2005) AT RA=80 AND GEOSTUDIO SIMULATION AT RA=50; CASE 2 (SUN ET AL., 2005) – SIDESLOPES OPEN

SUN ET AL. CASE 2

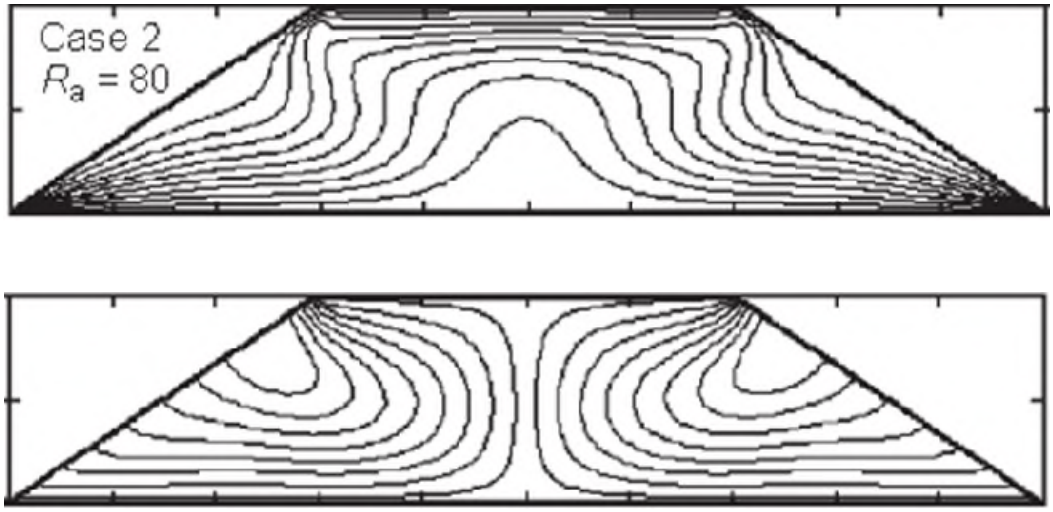

A) Sun et al. Case 2 (Ra=50); isotherms (top) and air flow vectors (bottom) (Sun et al., 2005)

GEOSTUDIO SIMULATION

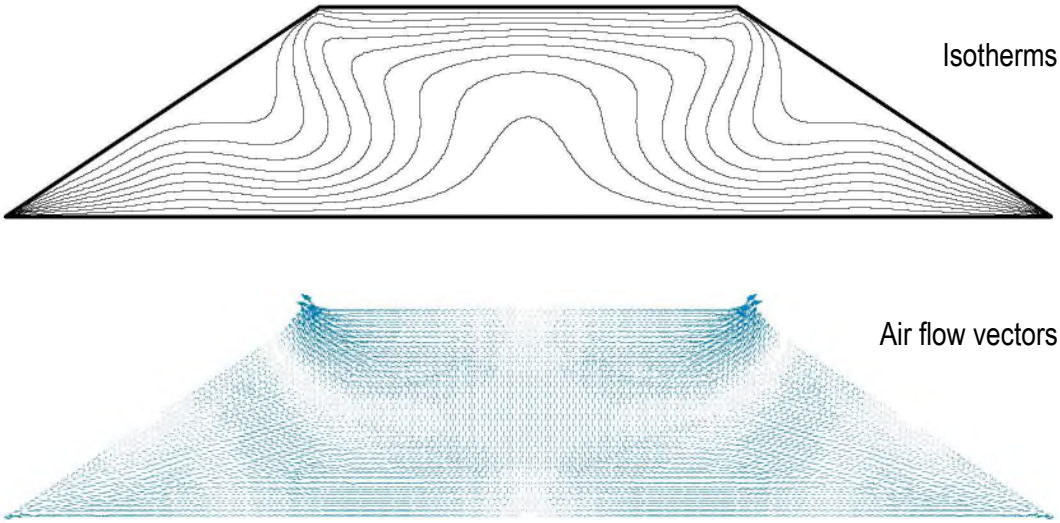

B) GeoStudio simulation at GeoStudio default temperature of 10°C (Ra=50); isotherms (top) and air flow vectors (bottom); solution did not stabilize within 500 days

FIGURE 3.121: COMPARISON OF NUMERICAL RESULTS FOR SUN ET AL. (2005) AT RA=80 AND GEOSTUDIO SIMULATION AT RA=80; CASE 2 (SUN ET AL., 2005) – SIDESLOPES OPEN

SUN ET AL. CASE 2

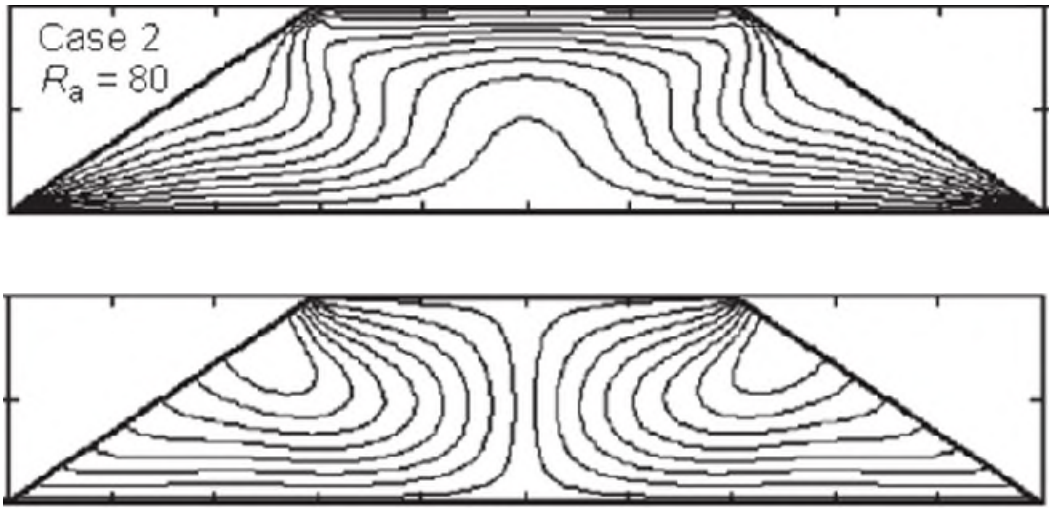

A) Sun et al. Case 2 (Ra=80); isotherms (top) and air flow vectors (bottom) (Sun et al., 2005)

GEOSTUDIO SIMULATION

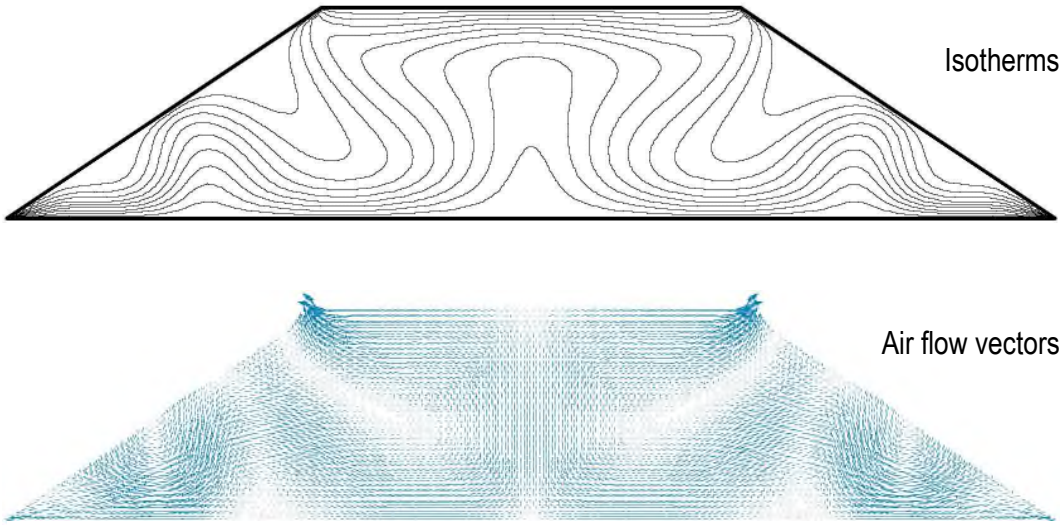

B) GeoStudio simulation at GeoStudio default temperature of 10°C (Ra=80); isotherms (top) and air flow vectors (bottom); solution did not stabilize within 500 days

FIGURE 3.122: COMPARISON OF NUMERICAL RESULTS FOR GEOSTUDIO SIMULATIONS AT RA=50 AT VARIOUS TEMPERATURES; CASE 2 (SUN ET AL., 2005) – SIDESLOPES OPEN

GEOSTUDIO SIMULATION 1

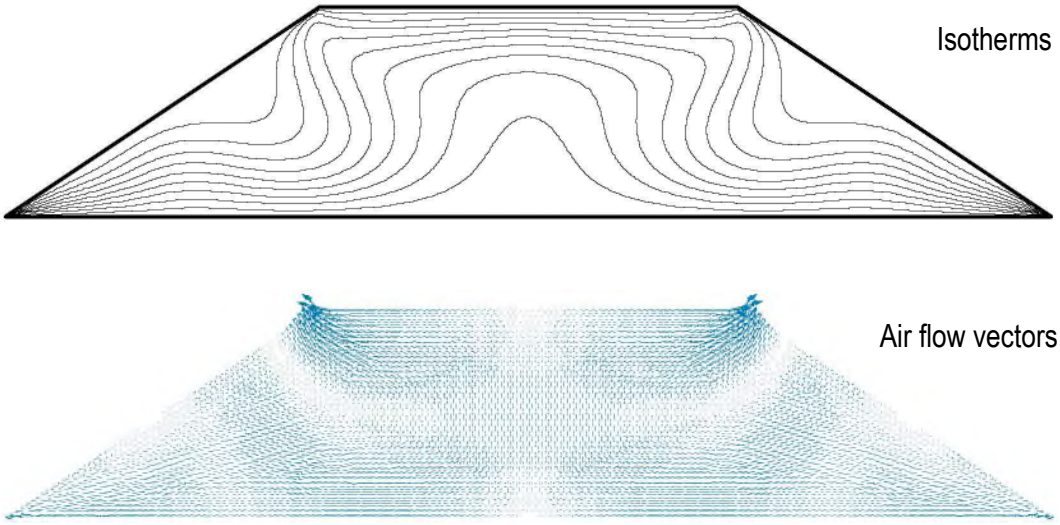

A) GeoStudio simulation at GeoStudio default temperature of 10°C (Ra=50); isotherms (top) and air flow vectors (bottom); solution did not stabilize within 500 days

GEOSTUDIO SIMULATION 2

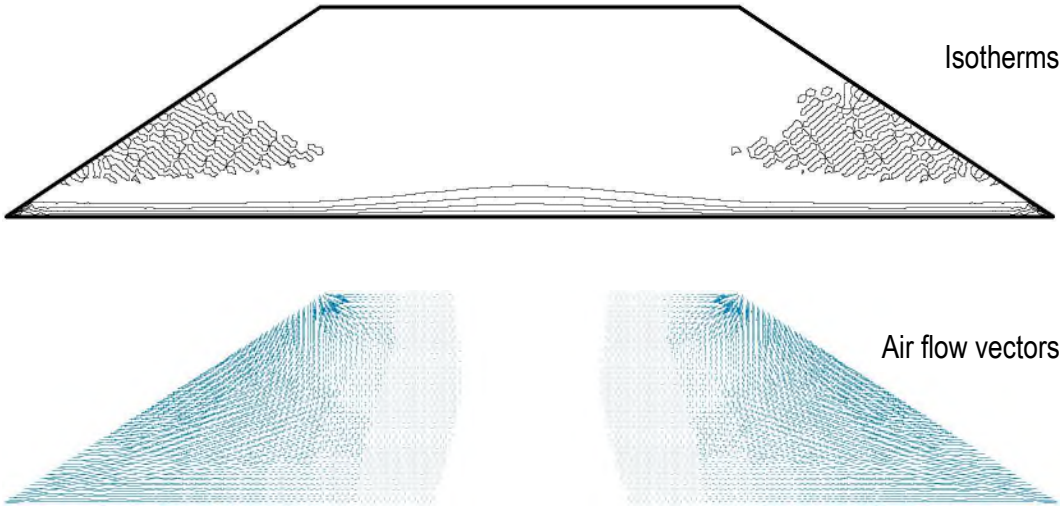

B) GeoStudio simulation at near 0°C (Ra=50); isotherms (top) and air flow vectors (bottom); numerical instabilities

FIGURE 3.123: COMPARISON OF NUMERICAL RESULTS FOR GEOSTUDIO SIMULATIONS AT RA=80 AT VARIOUS TEMPERATURES; CASE 2 (SUN ET AL., 2005) – SIDESLOPES OPEN

GEOSTUDIO SIMULATION 1

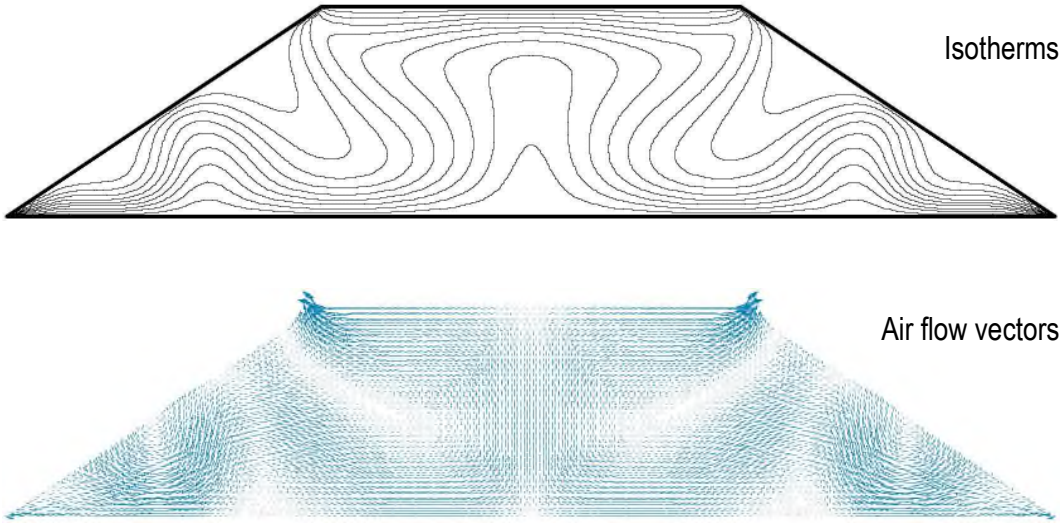

A) GeoStudio simulation at GeoStudio default temperature of 10°C (Ra=80); isotherms (top) and air flow vectors (bottom); solution did not stabilize within 500 days

GEOSTUDIO SIMULATION 2

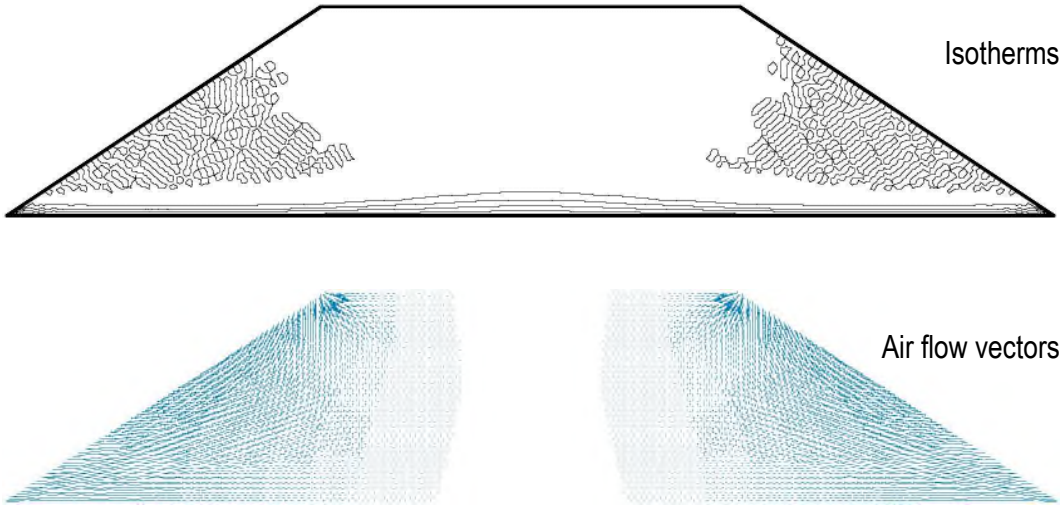

B) GeoStudio simulation at near 0°C (Ra=80); isotherms (top) and air flow vectors (bottom); numerical instabilities

FIGURE 3.124: COMPARISON OF NUMERICAL RESULTS FOR SUN ET AL. (2005) AT RA=50 AND GEOSTUDIO SIMULATION AT RA=25; CASE 3 (SUN ET AL., 2005) – SIDESLOPES AND TOP OPEN

SUN ET AL. CASE 3

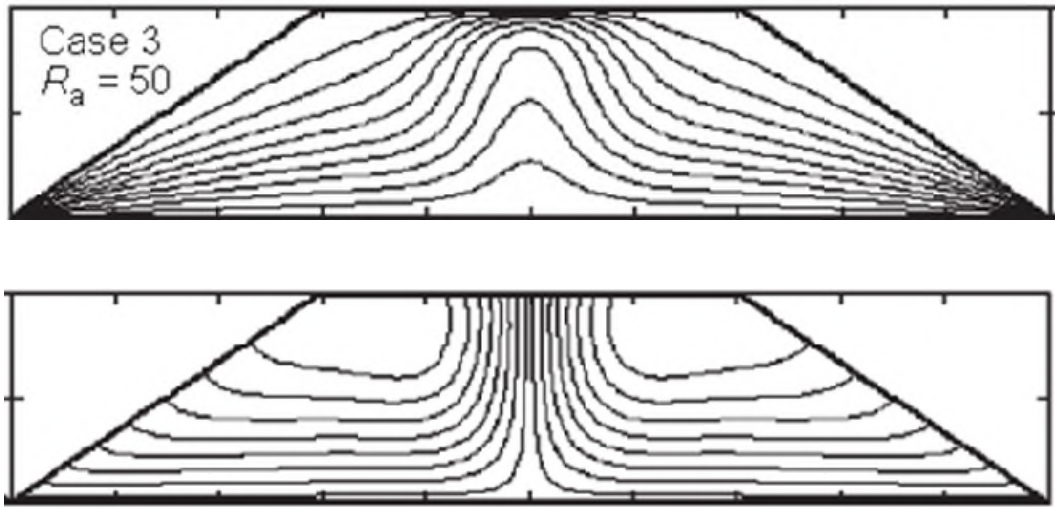

A) Sun et al. Case 3 (Ra=50); isotherms (top) and air flow vectors (bottom) (Sun et al., 2005)

GEOSTUDIO SIMULATION

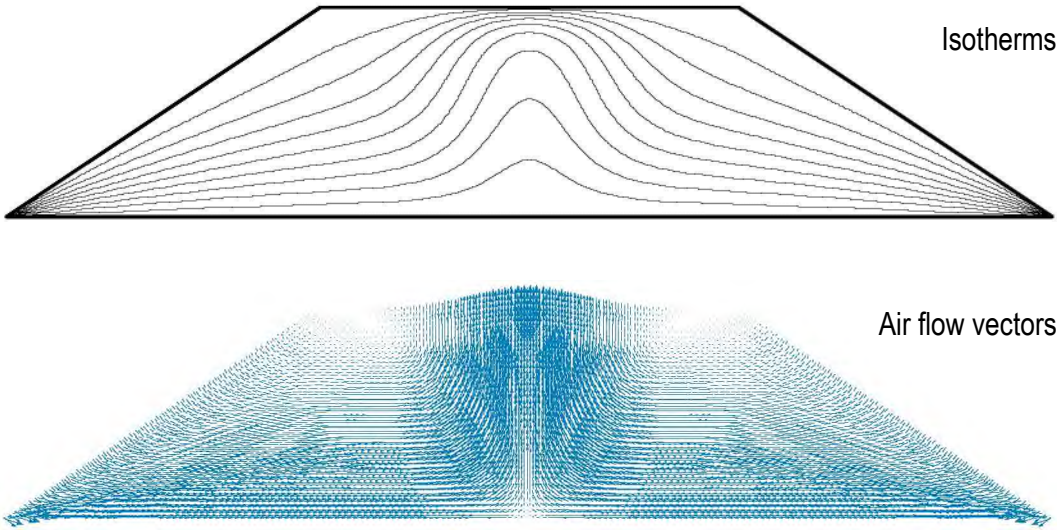

B) GeoStudio simulation at GeoStudio default temperature of 10°C (open; Ra=25); isotherms (top) and air flow vectors (bottom); solution stable within 500 days

FIGURE 3.125: COMPARISON OF NUMERICAL RESULTS FOR SUN ET AL. (2005) AT RA=50 AND GEOSTUDIO SIMULATION AT RA=50; CASE 3 (SUN ET AL., 2005) – SIDESLOPES AND TOP OPEN

SUN ET AL. CASE 3

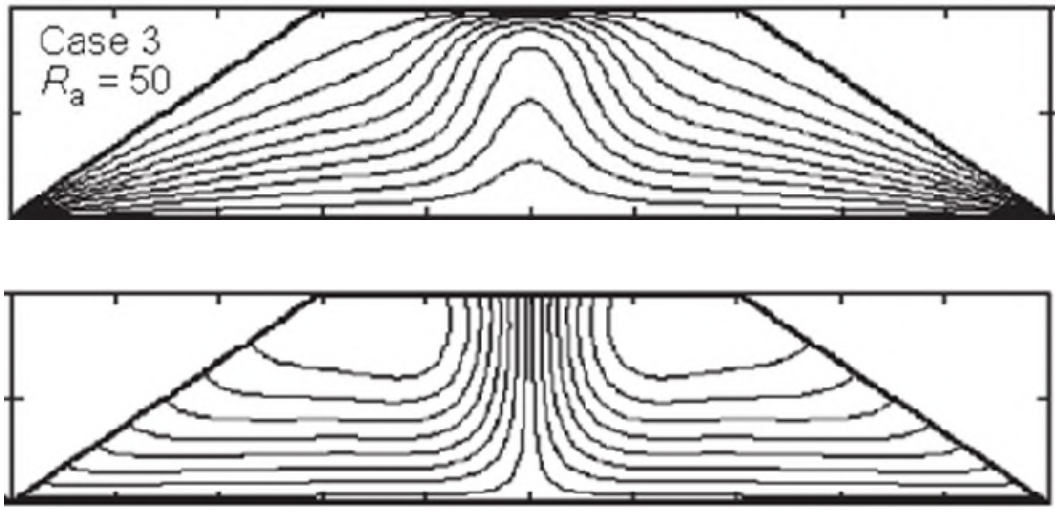

A) Sun et al. Case 3 (Ra=50); isotherms (top) and air flow vectors (bottom) (Sun et al., 2005)

GEOSTUDIO SIMULATION

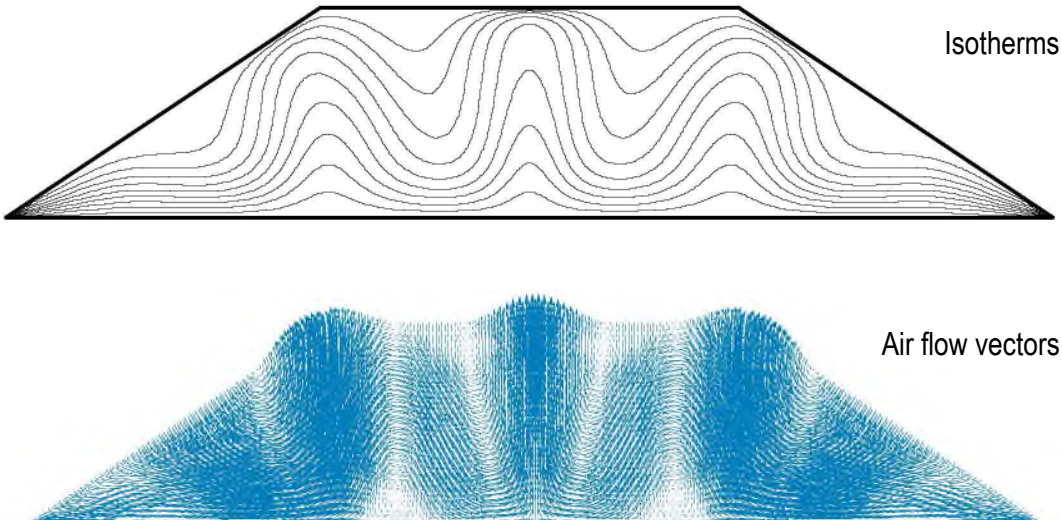

B) GeoStudio simulation at GeoStudio default temperature of 10°C (Ra=50); isotherms (top) and air flow vectors (bottom); solution did not stabilize within 500 days

FIGURE 3.126: COMPARISON OF NUMERICAL RESULTS FOR SUN ET AL. (2005) AT RA=80 AND GEOSTUDIO SIMULATION AT RA=50; CASE 3 (SUN ET AL., 2005) – SIDESLOPES AND TOP OPEN

SUN ET AL. CASE 3

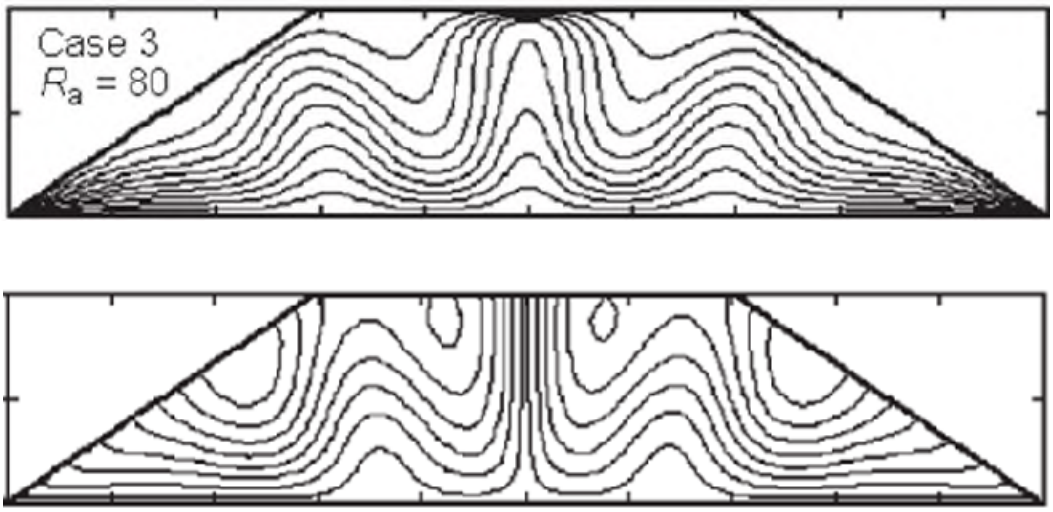

A) Sun et al. Case 3 (Ra=50); isotherms (top) and air flow vectors (bottom) (Sun et al., 2005)

GEOSTUDIO SIMULATION

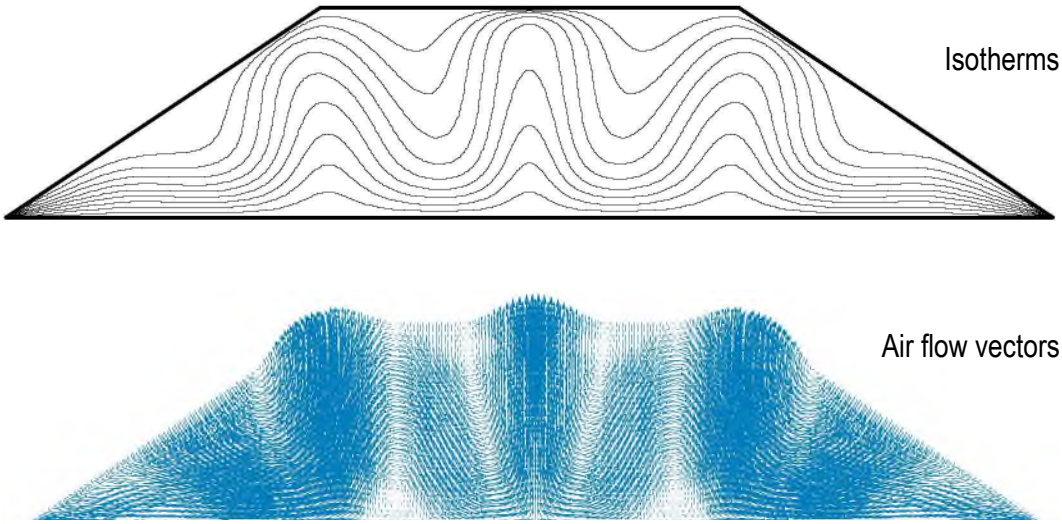

B) GeoStudio simulation at GeoStudio default temperature of 10°C (Ra=50); isotherms (top) and air flow vectors (bottom); solution did not stabilize within 500 days

FIGURE 3.127: COMPARISON OF NUMERICAL RESULTS FOR SUN ET AL. (2005) AT RA=80 AND GEOSTUDIO SIMULATION AT RA=80; CASE 3 (SUN ET AL., 2005) – SIDESLOPES AND TOP OPEN

SUN ET AL. CASE 3

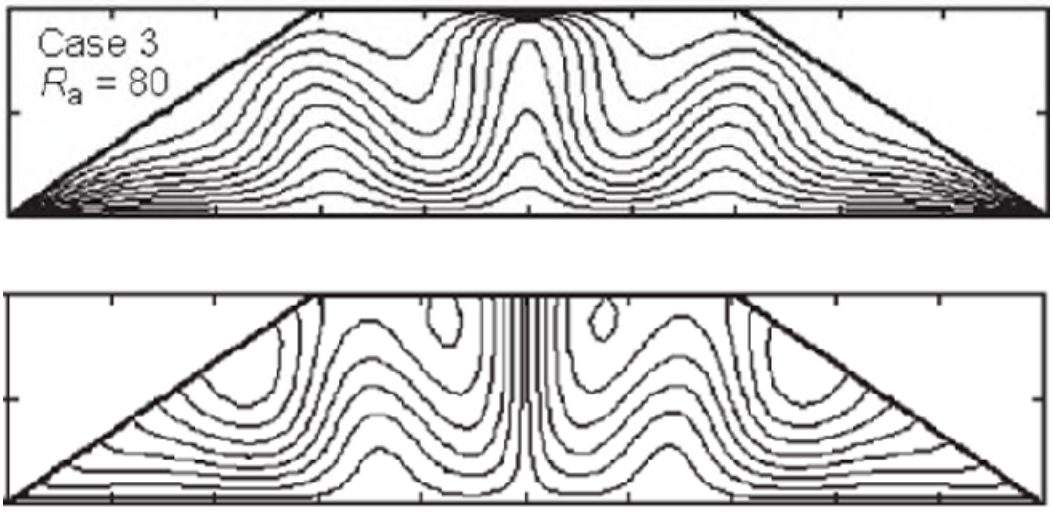

A) Sun et al. Case 3 (Ra=50); isotherms (top) and air flow vectors (bottom) (Sun et al., 2005)

GEOSTUDIO SIMULATION

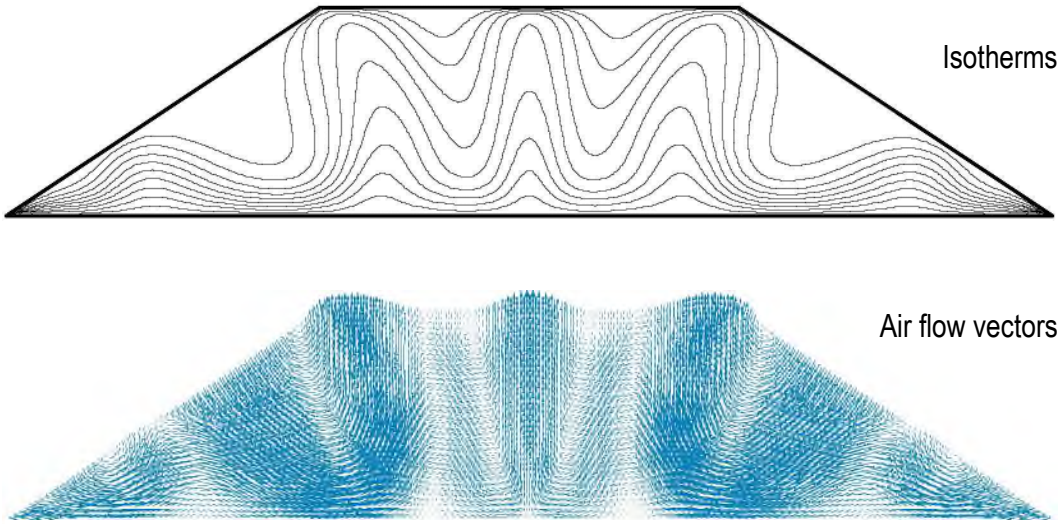

B) GeoStudio simulation at GeoStudio default temperature of 10°C (Ra=80); isotherms (top) and air flow vectors (bottom); solution did not stabilize within 500 days

FIGURE 3.128: COMPARISON OF NUMERICAL RESULTS FOR GEOSTUDIO SIMULATIONS AT RA=50 AT VARIOUS TEMPERATURES; CASE 3 (SUN ET AL., 2005) – SIDESLOPES AND TOP OPEN

GEOSTUDIO SIMULATION 1

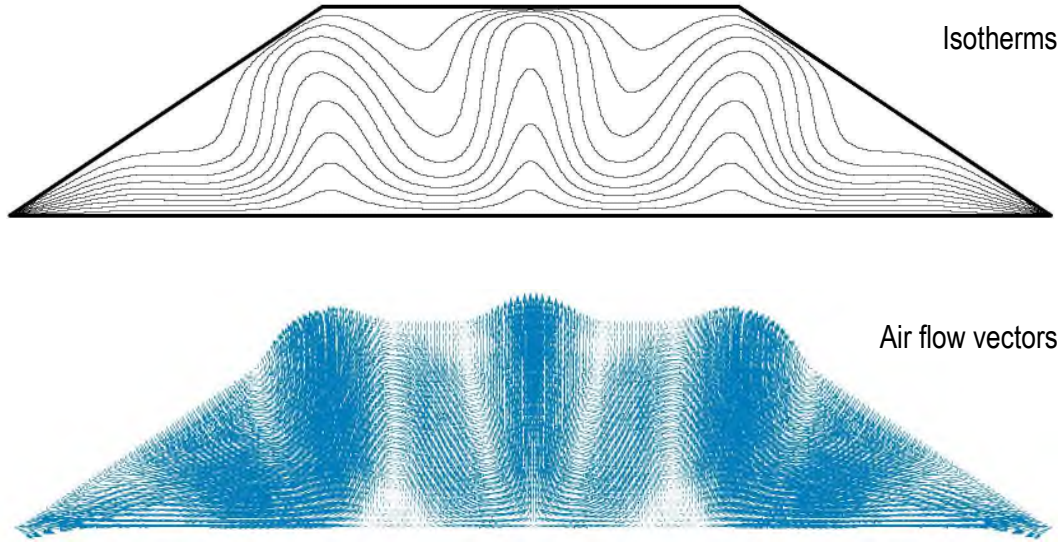

A) GeoStudio simulation at GeoStudio default temperature of 10°C (Ra=50); isotherms (top) and air flow vectors (bottom); solution did not stabilize within 500 days

GEOSTUDIO SIMULATION 2

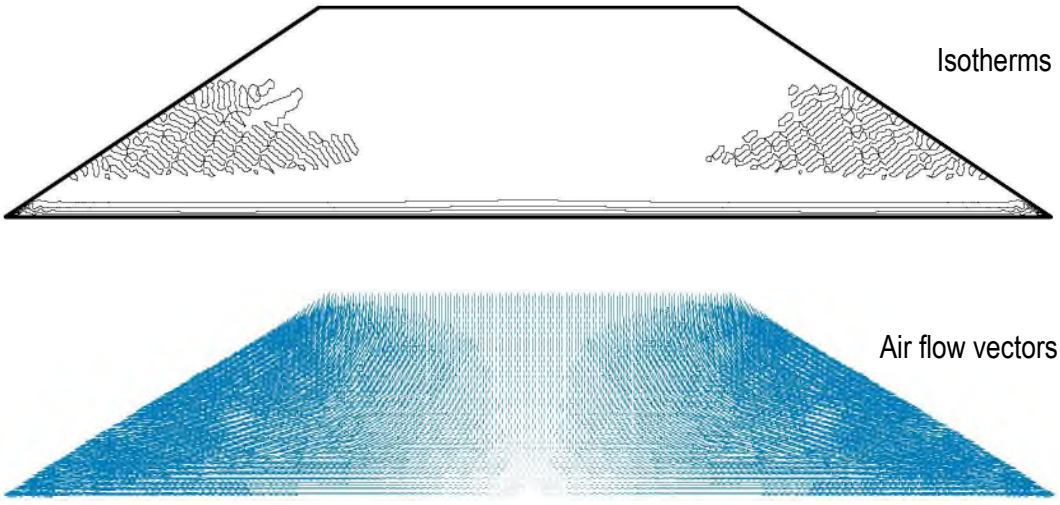

B) GeoStudio simulation at near 0°C (Ra=50); isotherms (top) and air flow vectors (bottom); numerical instabilities

FIGURE 3.129: COMPARISON OF NUMERICAL RESULTS FOR GEOSTUDIO SIMULATIONS AT RA=80 AT VARIOUS TEMPERATURES; CASE 3 (SUN ET AL., 2005) – SIDESLOPES AND TOP OPEN

GEOSTUDIO SIMULATION 1

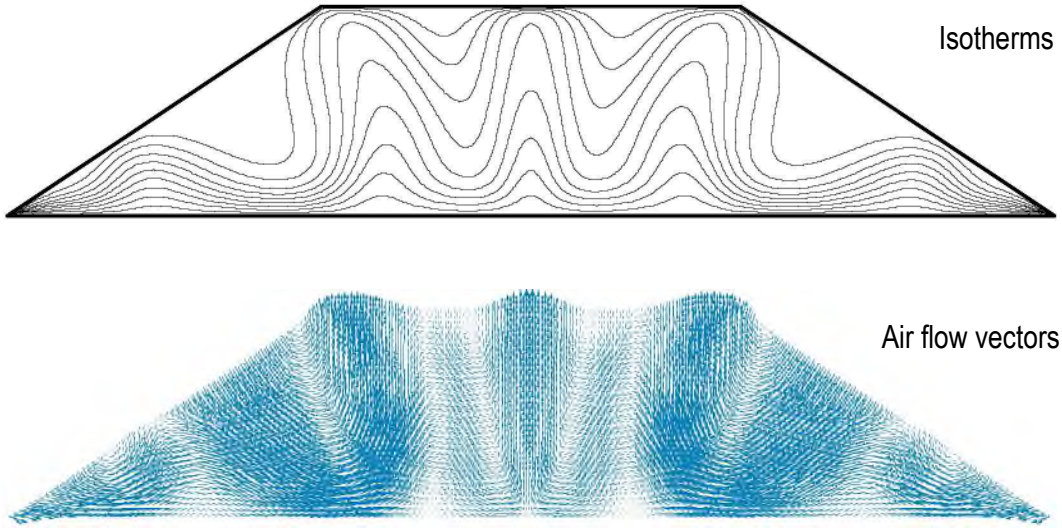

A) GeoStudio simulation at GeoStudio default temperature of 10°C (Ra=80); isotherms (top) and air flow vectors (bottom); solution did not stabilize within 500 days

GEOSTUDIO SIMULATION 2

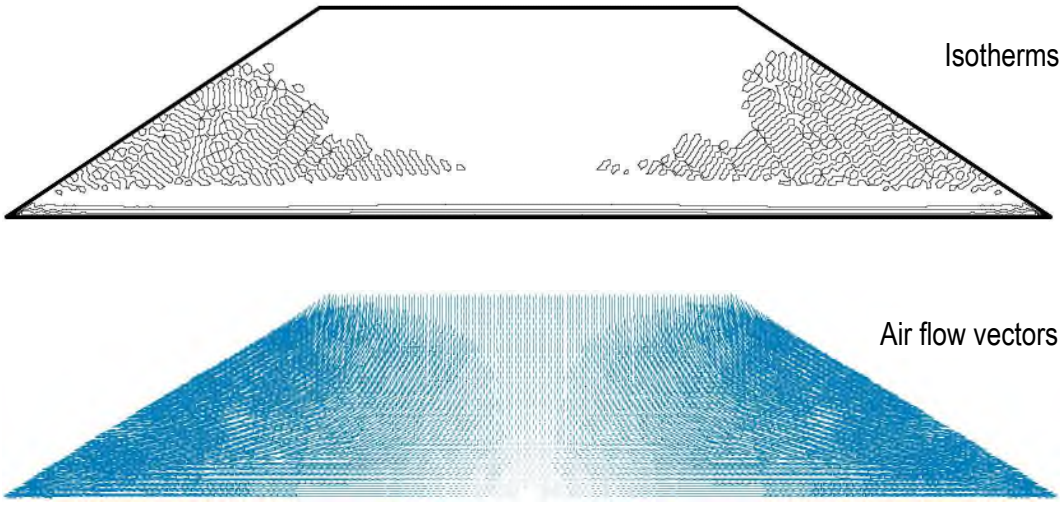

B) GeoStudio simulation at near 0°C (Ra=80); isotherms (top) and air flow vectors (bottom); numerical instabilities

FIGURE 3.130: COMPARISON OF NUMERICAL RESULTS FOR SUN ET AL. (2005) AT RA=50 AND GEOSTUDIO SIMULATION AT RA=25; CASE 4 (SUN ET AL., 2005) – TOP OPEN

SUN ET AL. CASE 4

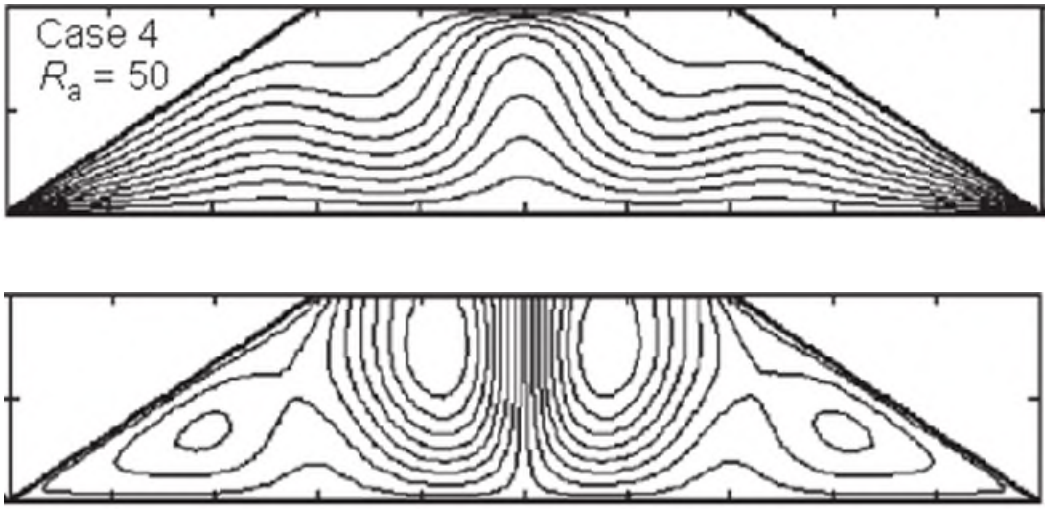

A) Sun et al. Case 4 (Ra=50); isotherms (top) and air flow vectors (bottom) (Sun et al., 2005)

GEOSTUDIO SIMULATION

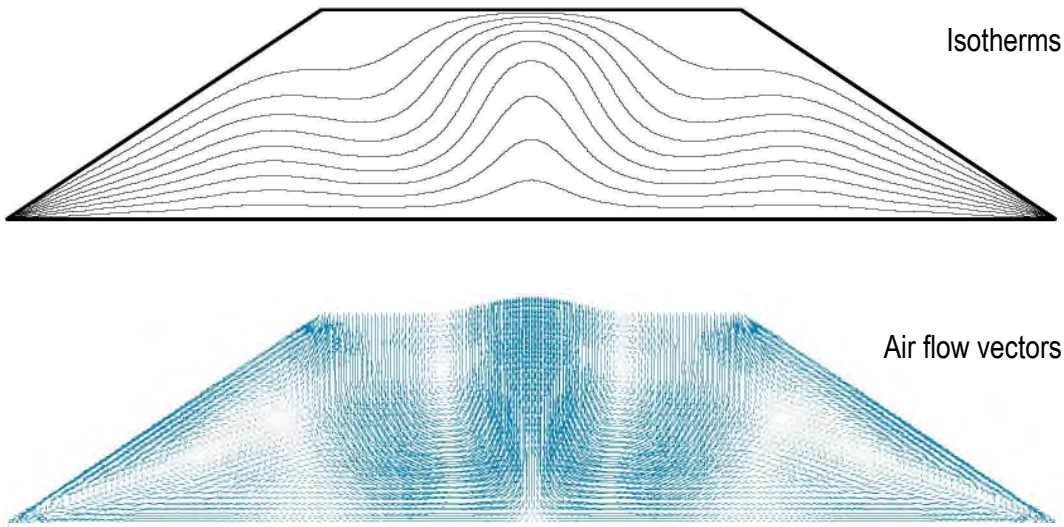

B) GeoStudio simulation at GeoStudio default temperature of 10°C (Ra=25); isotherms (top) and air flow vectors (bottom); solution stable within 500 days

FIGURE 3.131: COMPARISON OF NUMERICAL RESULTS FOR SUN ET AL. (2005) AT RA=50 AND GEOSTUDIO SIMULATION AT RA=50; CASE 4 (SUN ET AL., 2005) – TOP OPEN

SUN ET AL. CASE 4

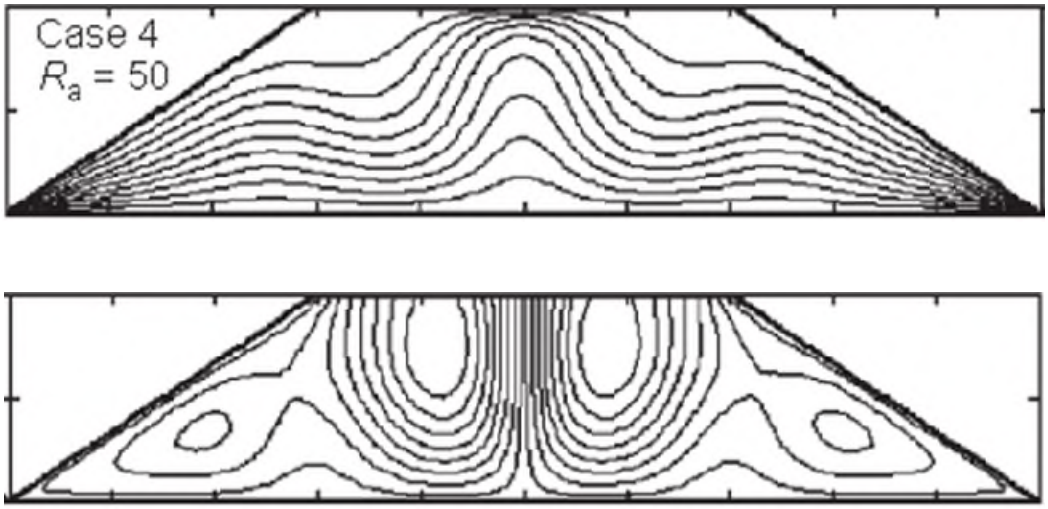

A) Sun et al. Case 4 (Ra=50); isotherms (top) and air flow vectors (bottom) (Sun et al., 2005)

GEOSTUDIO SIMULATION

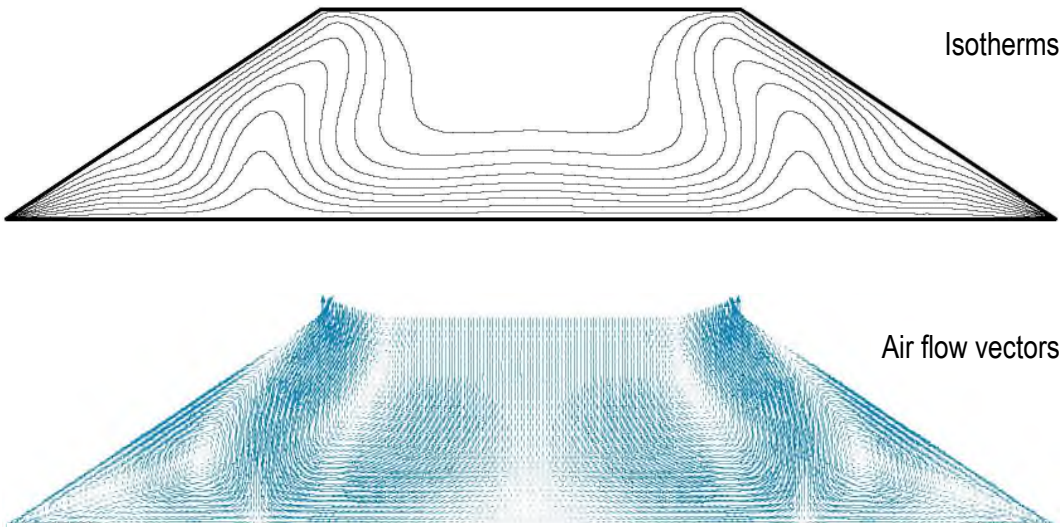

B) GeoStudio simulation at GeoStudio default temperature of 10°C (Ra=50); isotherms (top) and air flow vectors (bottom); solution stable within 500 days

FIGURE 3.132: COMPARISON OF NUMERICAL RESULTS FOR SUN ET AL. (2005) AT RA=80 AND GEOSTUDIO SIMULATION AT RA=50; CASE 4 (SUN ET AL., 2005) – TOP OPEN

SUN ET AL. CASE 4

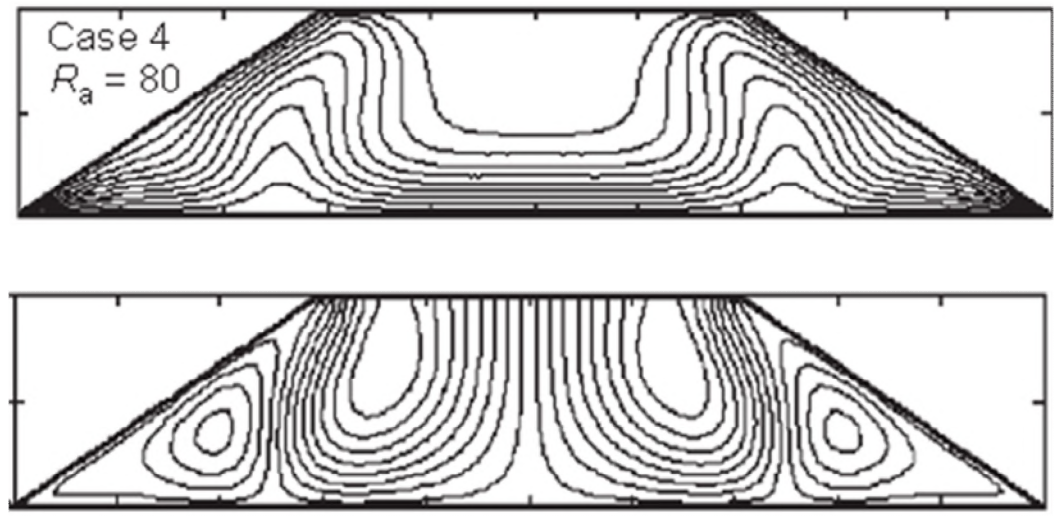

A) Sun et al. Case 4 (Ra=80); isotherms (top) and air flow vectors (bottom) (Sun et al., 2005)

GEOSTUDIO SIMULATION

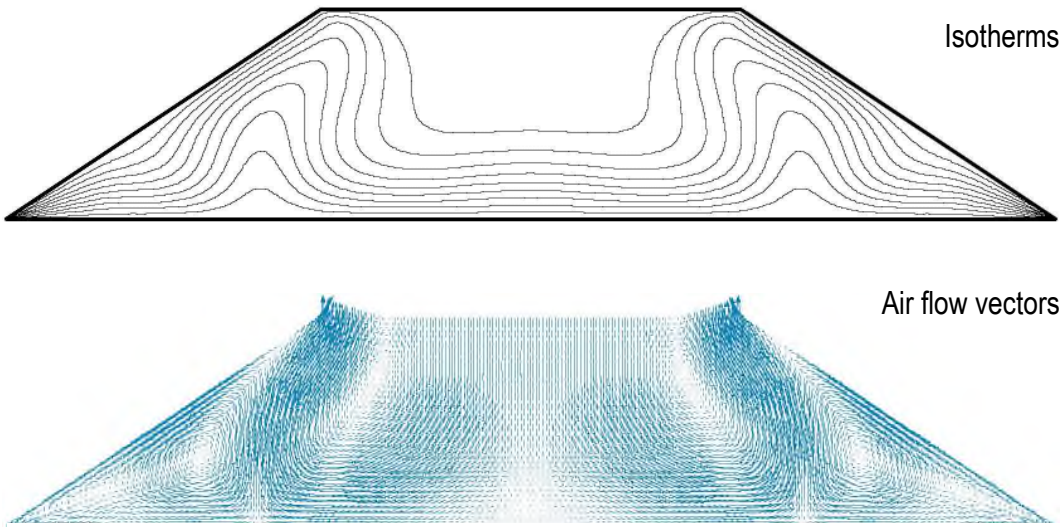

B) GeoStudio simulation at GeoStudio default temperature of 10°C (Ra=50); isotherms (top) and air flow vectors (bottom); solution stable within 500 days

FIGURE 3.133: COMPARISON OF NUMERICAL RESULTS FOR SUN ET AL. (2005) AT RA=80 AND GEOSTUDIO SIMULATION AT RA=80; CASE 4 (SUN ET AL., 2005) – TOP OPEN

SUN ET AL. CASE 4

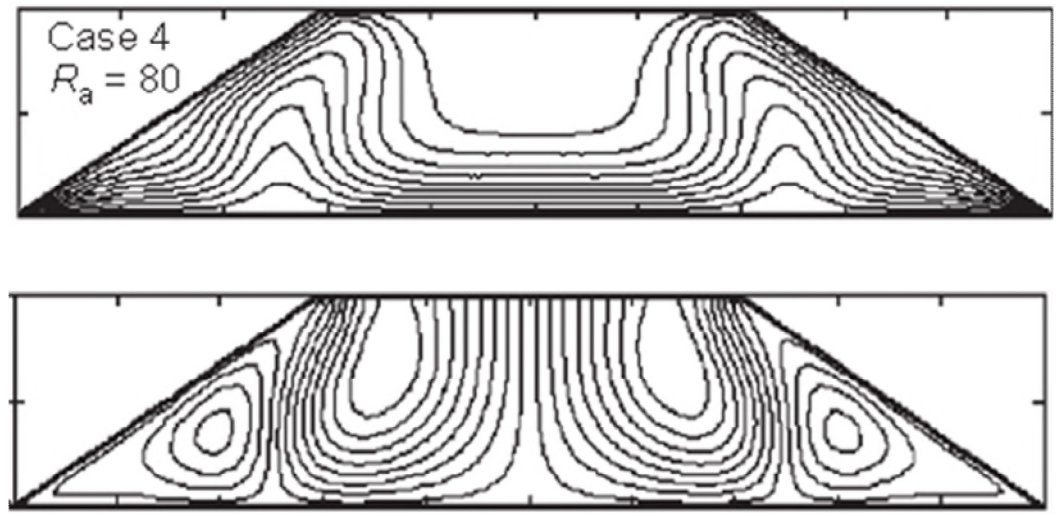

A) Sun et al. Case 4 (Ra=80); isotherms (top) and air flow vectors (bottom) (Sun et al., 2005)

GEOSTUDIO SIMULATION

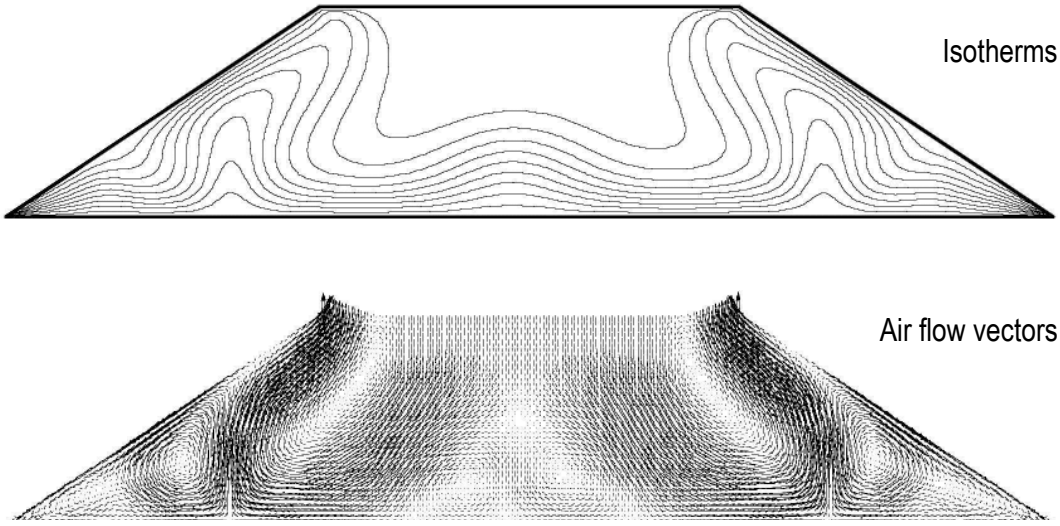

B) GeoStudio simulation at GeoStudio default temperature of 10°C (Ra=80); isotherms (top) and air flow vectors (bottom); solution did not stabilize within 500 days

FIGURE 3.134: COMPARISON OF NUMERICAL RESULTS FOR GEOSTUDIO SIMULATIONS AT RA=50 AT VARIOUS TEMPERATURES; CASE 4 (SUN ET AL., 2005) – TOP OPEN

GEOSTUDIO SIMULATION 1

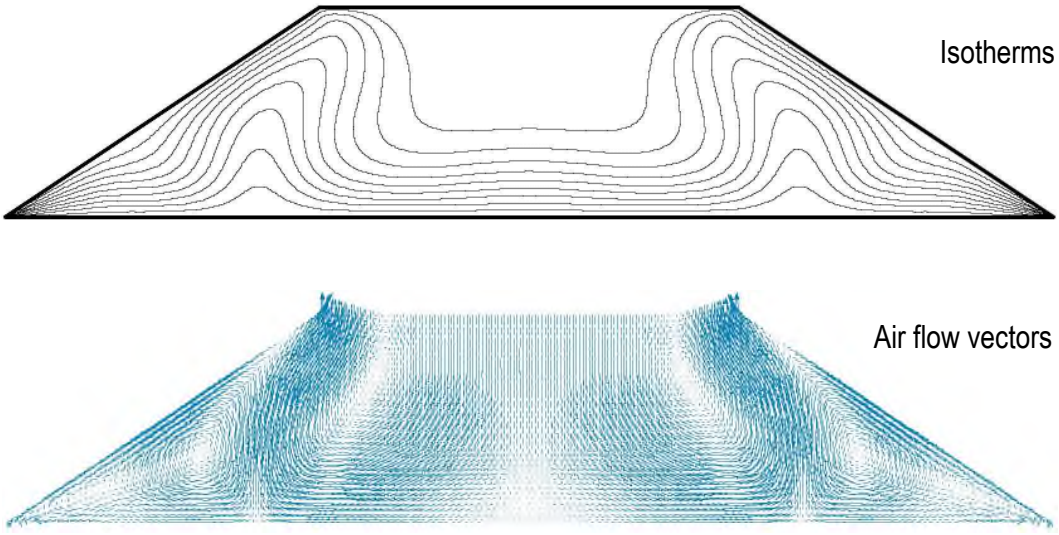

A) GeoStudio simulation at GeoStudio default temperature of 10°C (Ra=50); isotherms (top) and air flow vectors (bottom); solution stable within 500 days

GEOSTUDIO SIMULATION 2

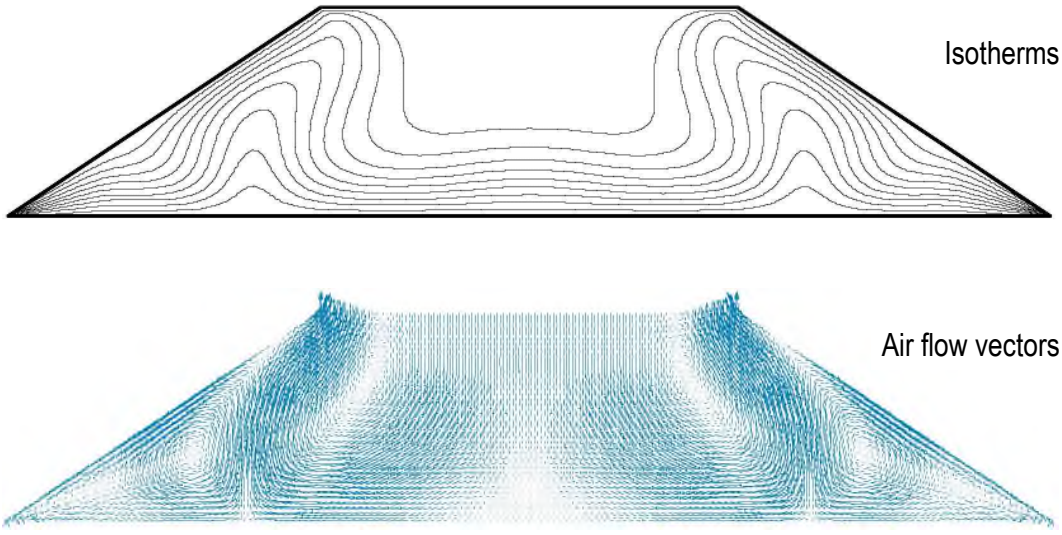

B) GeoStudio simulation at near 0°C (Ra=50); isotherms (top) and air flow vectors (bottom); solution stable within 500 days

FIGURE 3.135: COMPARISON OF NUMERICAL RESULTS FOR GEOSTUDIO SIMULATIONS AT RA=80 AT VARIOUS TEMPERATURES; CASE 4 (SUN ET AL., 2005) – TOP OPEN

GEOSTUDIO SIMULATION 1

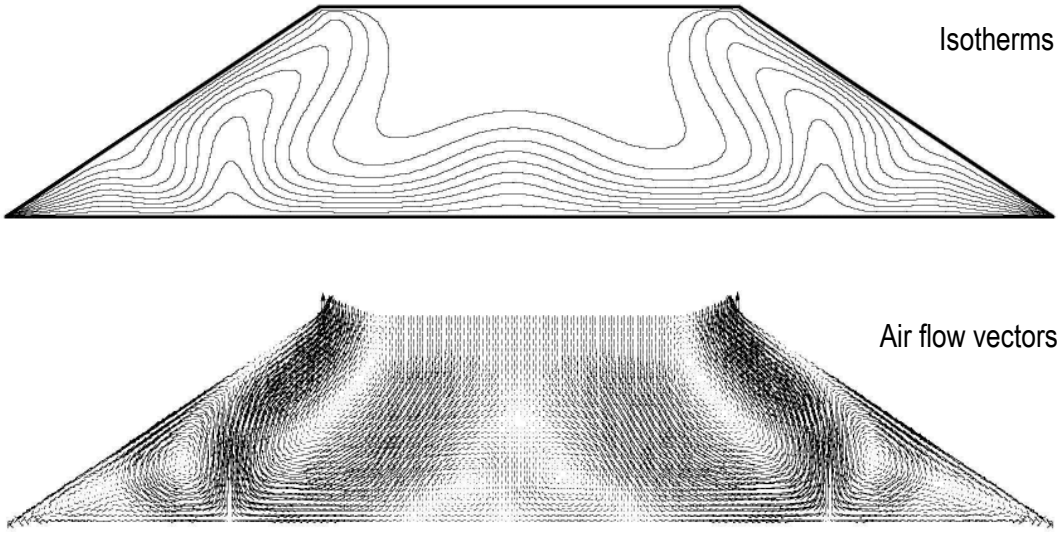

A) GeoStudio simulation at GeoStudio default temperature of 10°C (Ra=80); isotherms (top) and air flow vectors (bottom); solution did not stabilize within 500 days

GEOSTUDIO SIMULATION 2

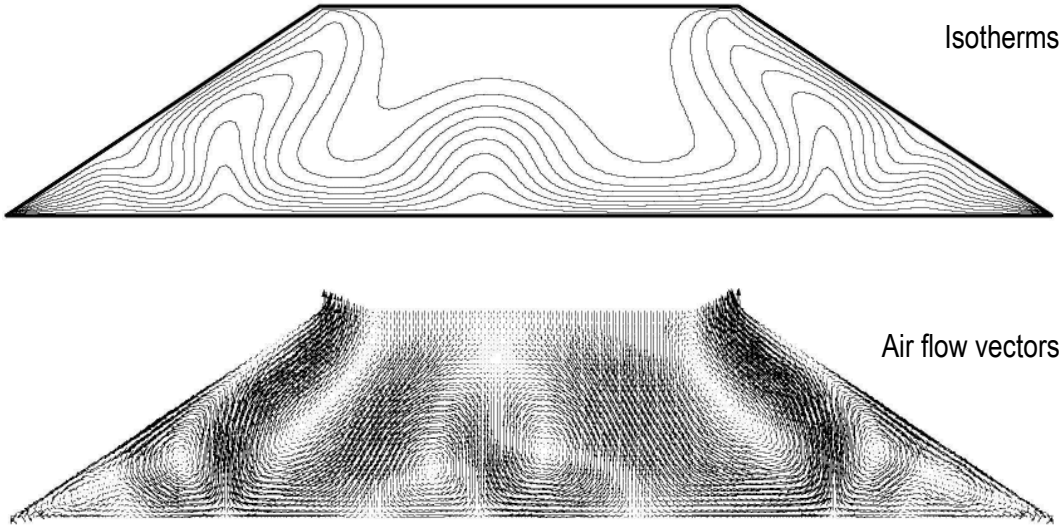

B) GeoStudio simulation at near 0°C (Ra=80); isotherms (top) and air flow vectors (bottom); solution did not stabilize within 500 days

FIGURE 3.136: COMPARISON OF NUMERICAL RESULTS FOR SUN ET AL. (2005) AT RA=50 AND GEOSTUDIO SIMULATION AT RA=25; CASE 5 (SUN ET AL., 2005) – ALL BOUNDARIES CLOSED AND SIDESLOPES ADIABATIC

SUN ET AL. CASE 5

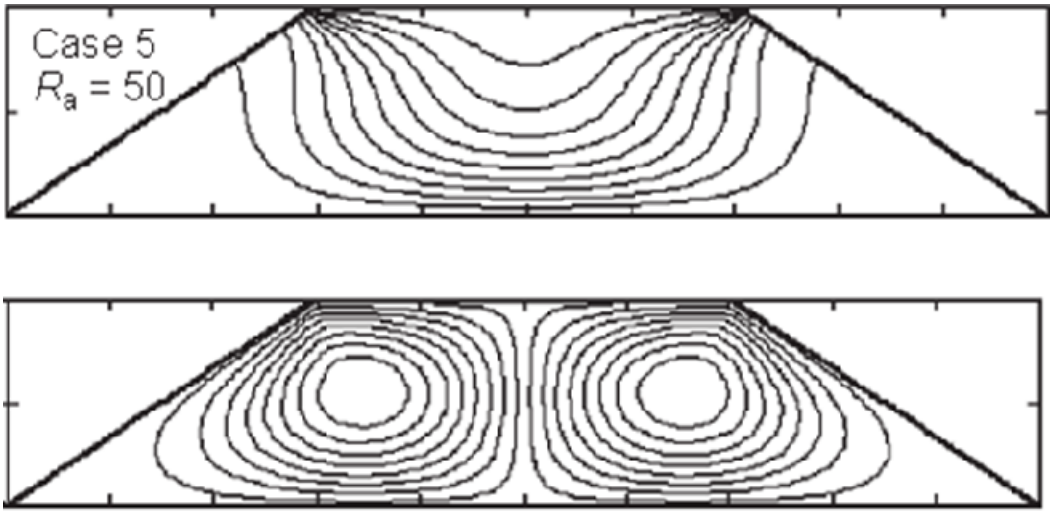

A) Sun et al. Case 5 (Ra=50); isotherms (top) and air flow vectors (bottom) (Sun et al., 2005)

GEOSTUDIO SIMULATION

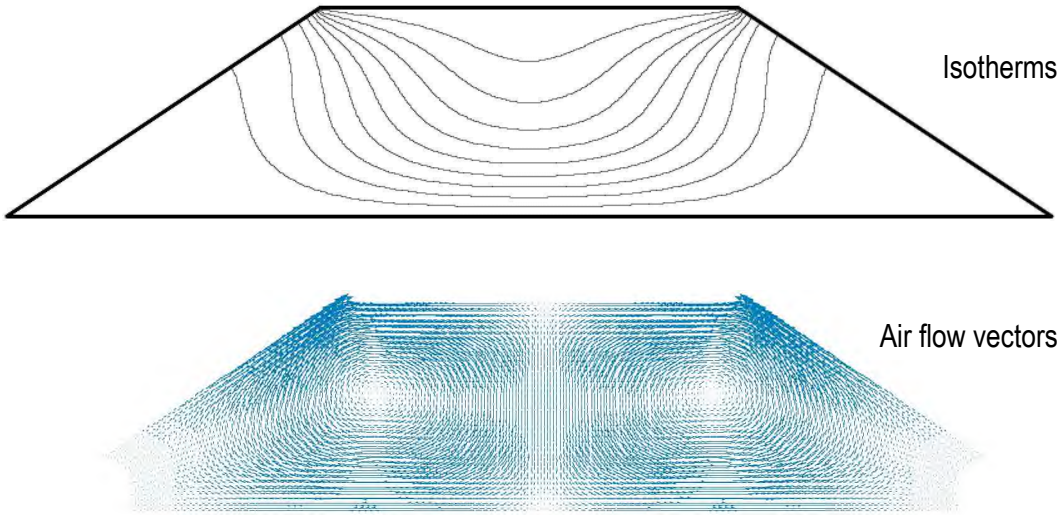

B) GeoStudio simulation at GeoStudio default temperature of 10°C (Ra=25); isotherms (top) and air flow vectors (bottom); solution stabilized within 500 days

FIGURE 3.137: COMPARISON OF NUMERICAL RESULTS FOR SUN ET AL. (2005) AT RA=50 AND GEOSTUDIO SIMULATION AT RA=50; CASE 5 (SUN ET AL., 2005) – ALL BOUNDARIES CLOSED AND SIDESLOPES ADIABATIC

SUN ET AL. CASE 5

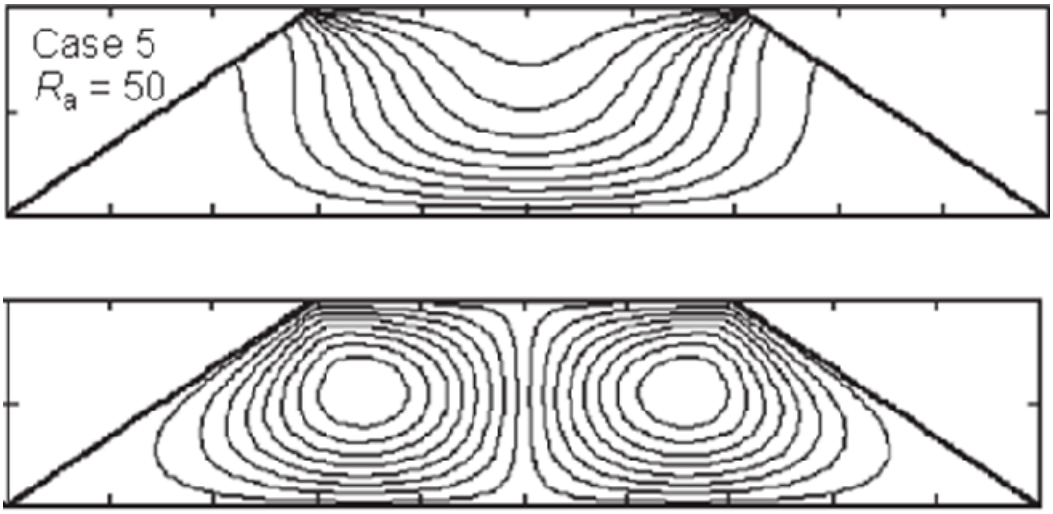

A) Sun et al. Case 5 (Ra=50); isotherms (top) and air flow vectors (bottom) (Sun et al., 2005)

GEOSTUDIO SIMULATION

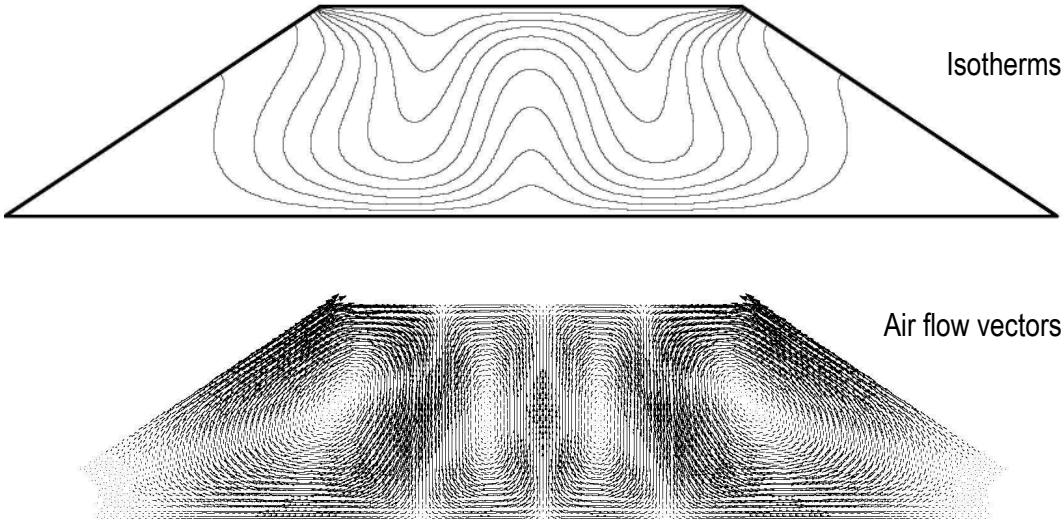

B) GeoStudio simulation at GeoStudio default temperature of 10°C (Ra=50); isotherms (top) and air flow vectors (bottom); solution stabilized within 500 days

FIGURE 3.138: COMPARISON OF NUMERICAL RESULTS FOR SUN ET AL. (2005) AT RA=80 AND GEOSTUDIO SIMULATION AT RA=50; CASE 5 (SUN ET AL., 2005) – ALL BOUNDARIES CLOSED AND SIDESLOPES ADIABATIC

SUN ET AL. CASE 5

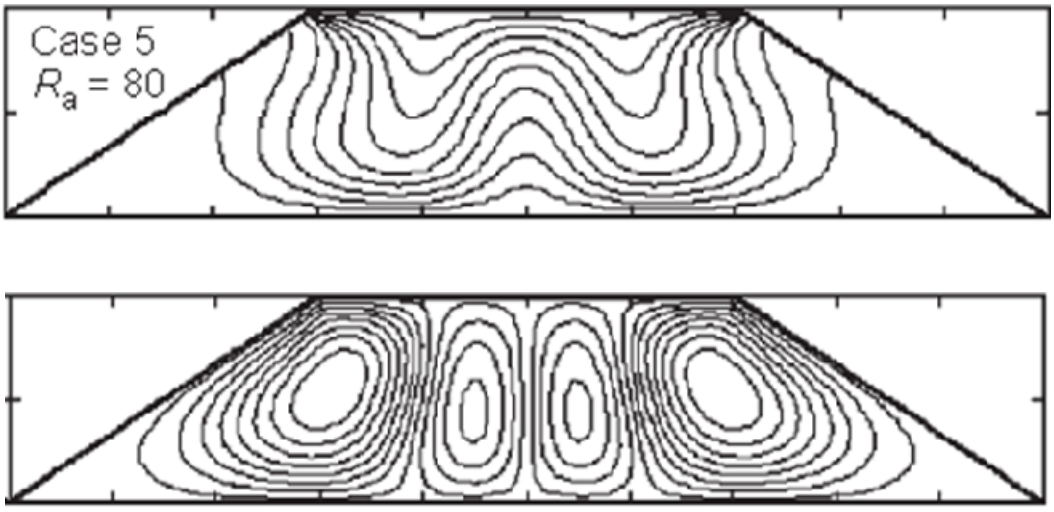

A) Sun et al. Case 5 (Ra=80); isotherms (top) and air flow vectors (bottom) (Sun et al., 2005)

GEOSTUDIO SIMULATION

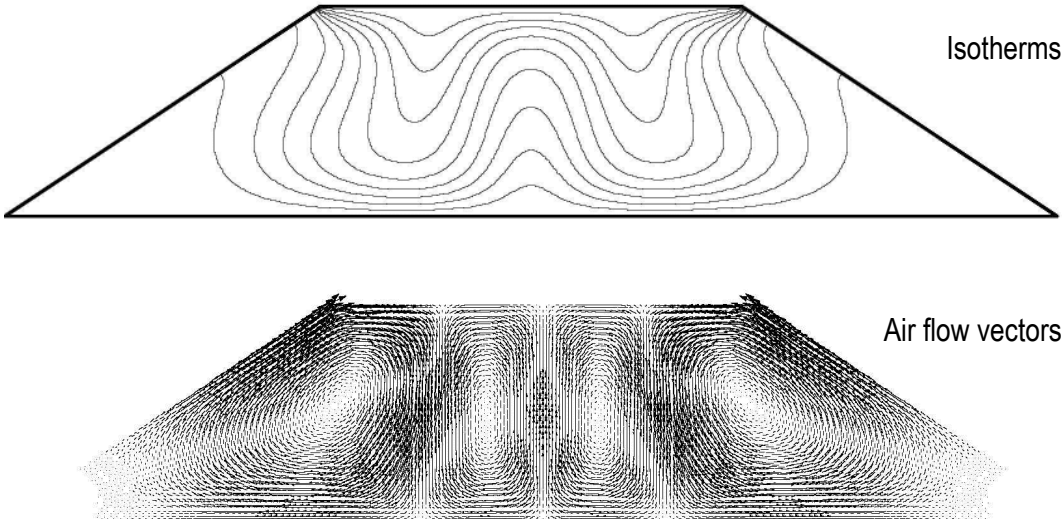

B) GeoStudio simulation at GeoStudio default temperature of 10°C (Ra=50); isotherms (top) and air flow vectors (bottom); solution stable within 500 days

FIGURE 3.139: COMPARISON OF NUMERICAL RESULTS FOR SUN ET AL. (2005) AT RA=80 AND GEOSTUDIO SIMULATION AT RA=80; CASE 5 (SUN ET AL., 2005) – ALL BOUNDARIES CLOSED AND SIDESLOPES ADIABATIC

SUN ET AL. CASE 5

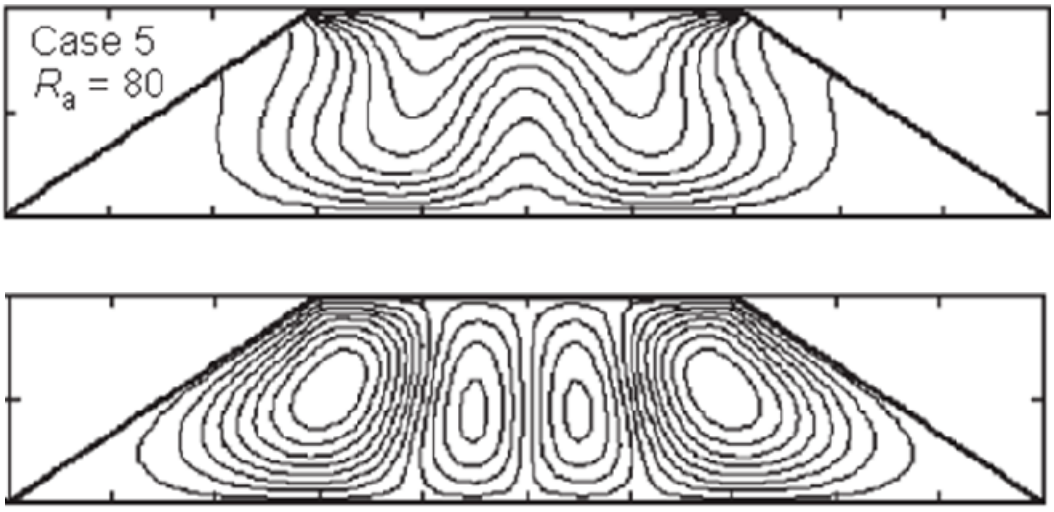

A) Sun et al. Case 5 (Ra=80); isotherms (top) and air flow vectors (bottom) (Sun et al., 2005)

GEOSTUDIO SIMULATION

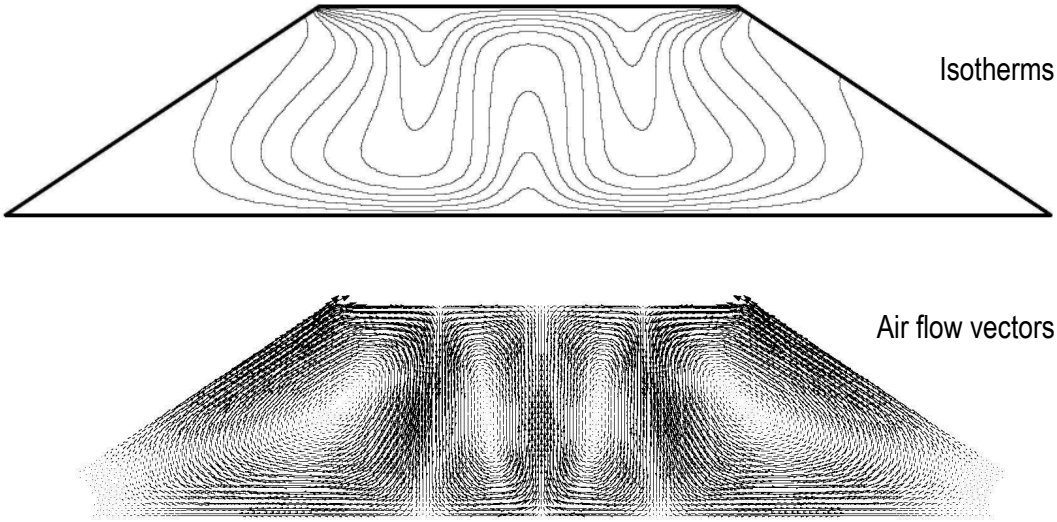

B) GeoStudio simulation at GeoStudio default temperature of 10°C (Ra=80); isotherms (top) and air flow vectors (bottom); solution stable within 500 days

FIGURE 3.140: COMPARISON OF NUMERICAL RESULTS FOR GEOSTUDIO SIMULATIONS AT RA=50 AT VARIOUS TEMPERATURES; CASE 5 (SUN ET AL., 2005) – ALL BOUNDARIES CLOSED AND SIDESLOPES ADIABATIC

GEOSTUDIO SIMULATION 1

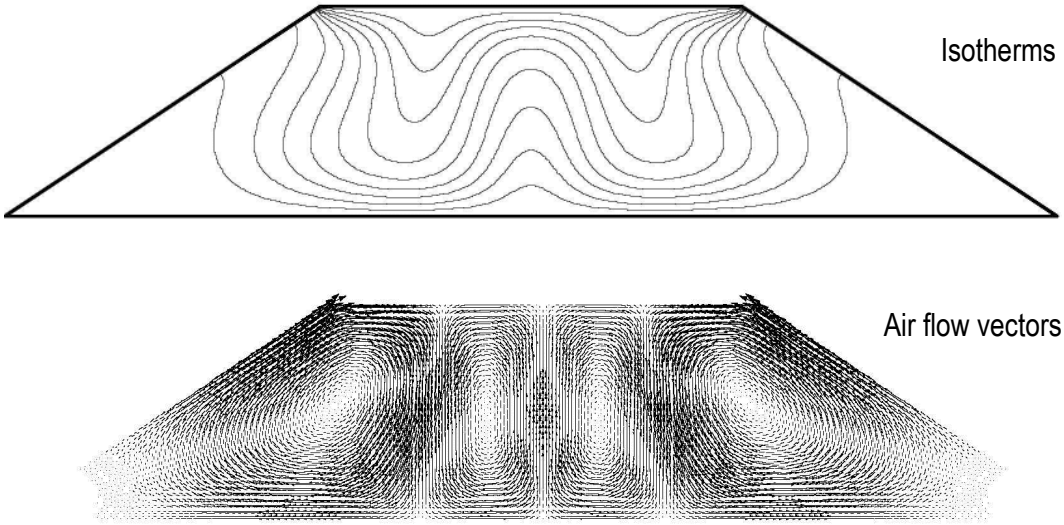

A) GeoStudio simulation at GeoStudio default temperature of 10°C (Ra=50); isotherms (top) and air flow vectors (bottom); solution stable within 500 days

GEOSTUDIO SIMULATION 2

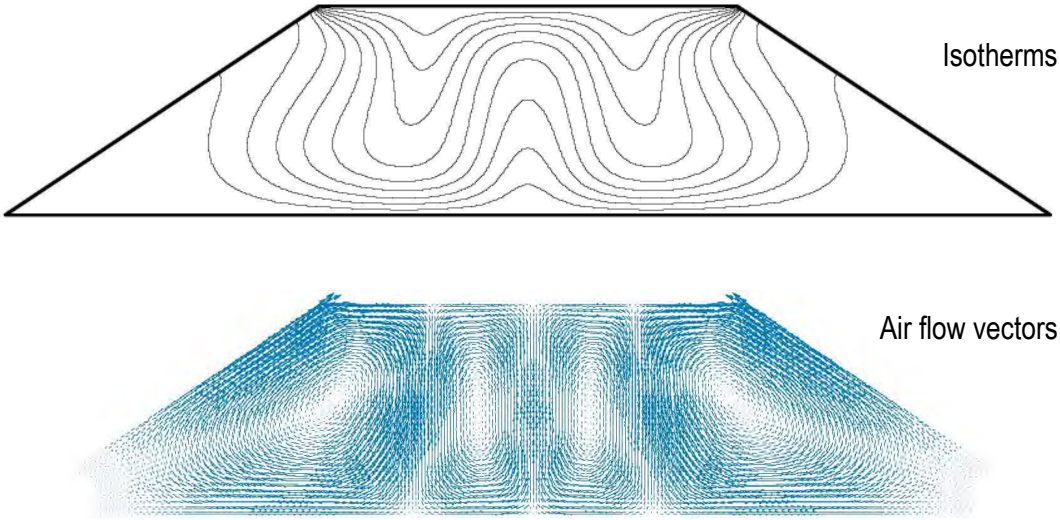

B) GeoStudio simulation at near 0°C (Ra=50); isotherms (top) and air flow vectors (bottom); solution stable within 500 days

FIGURE 3.141: COMPARISON OF NUMERICAL RESULTS FOR GEOSTUDIO SIMULATIONS AT RA=80 AT VARIOUS TEMPERATURES; CASE 5 (SUN ET AL., 2005) – ALL BOUNDARIES CLOSED AND SIDESLOPES ADIABATIC

GEOSTUDIO SIMULATION 1

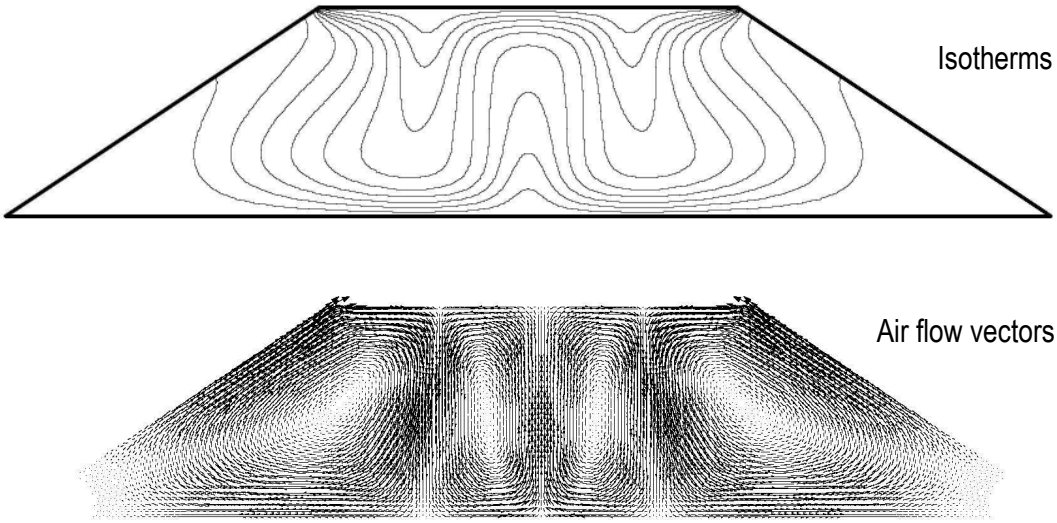

A) GeoStudio simulation at GeoStudio default temperature of 10°C (Ra=80); isotherms (top) and air flow vectors (bottom); solution stable within 500 days

GEOSTUDIO SIMULATION 2

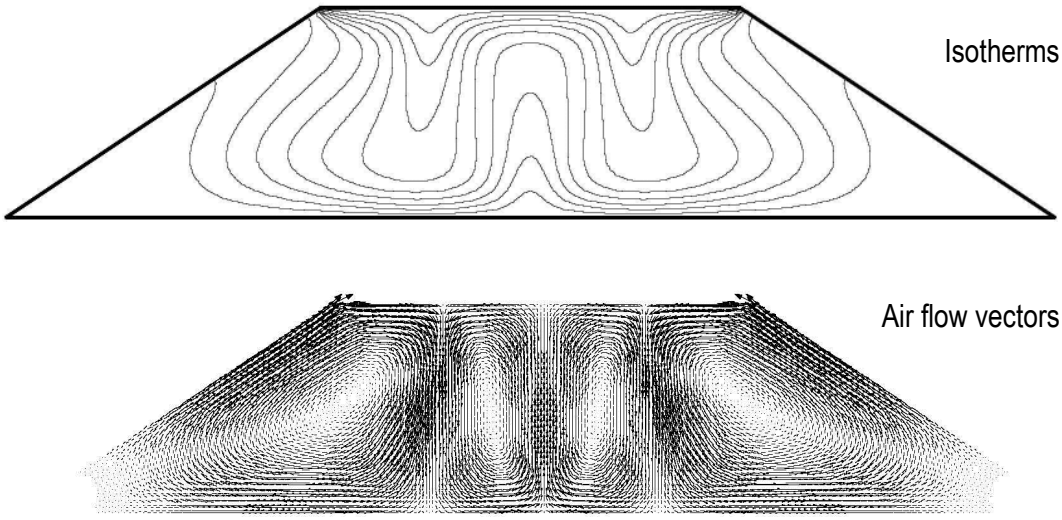

B) GeoStudio simulation at near 0°C (Ra=80); isotherms (top) and air flow vectors (bottom); solution stable within 500 days

FIGURE 3.142: AIR DENSITY AND AIR PRESSURE IN GEOSTUDIO SIMULATIONS AT RA=50 AT SUN'S AND MODIFIED ISOTHERMAL CONDITIONS; CASE 2 (SUN ET AL., 2005) – SIDESLOPES OPEN

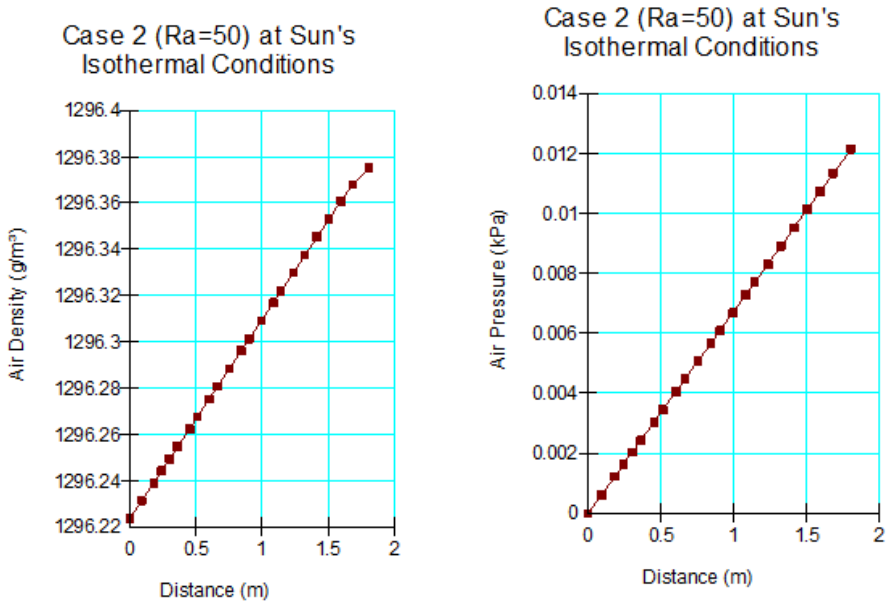

A) GeoStudio results along the sideslope from top (distance=0) to bottom (distance=2) at Sun's isothermal conditions (graphs drawn by GeoStudio)

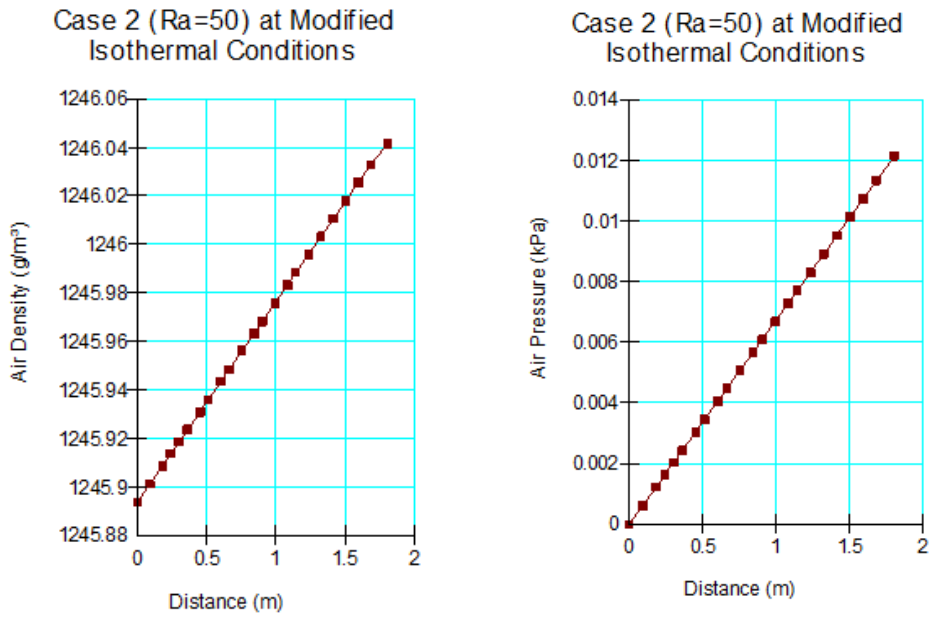

B) GeoStudio results along the sideslope from top (distance=0) to bottom (distance=2) at modified isothermal conditions (graphs drawn by GeoStudio)

FIGURE 3.143: AIR DENSITY AND AIR PRESSURE IN GEOSTUDIO SIMULATIONS AT RA=50 AT SUN'S AND MODIFIED ISOTHERMAL CONDITIONS; CASE 3 (SUN ET AL., 2005) – SIDESLOPES AND TOP OPEN

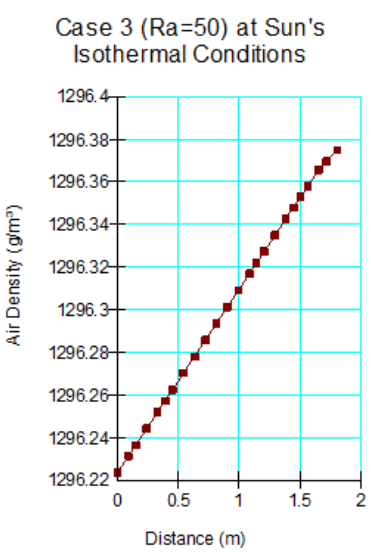

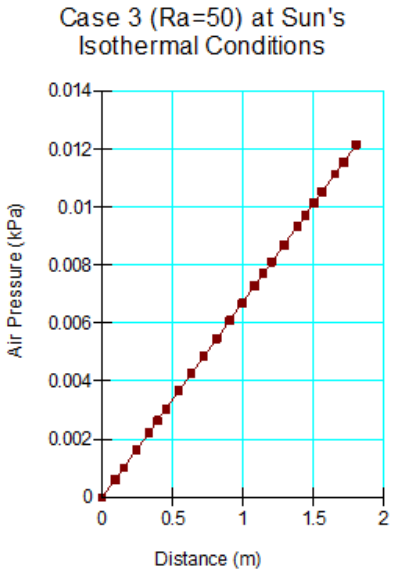

A) GeoStudio results along the sideslope from top (distance=0) to bottom (distance=2) at Sun's isothermal conditions (graphs drawn by GeoStudio)

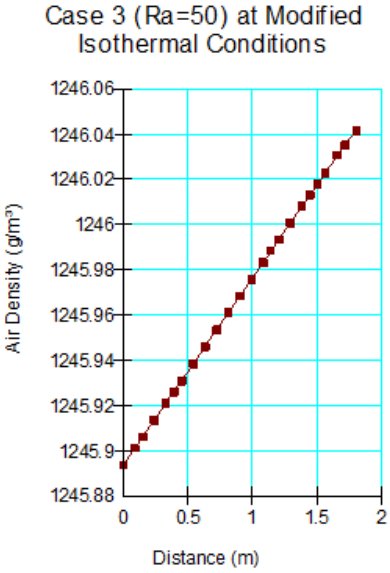

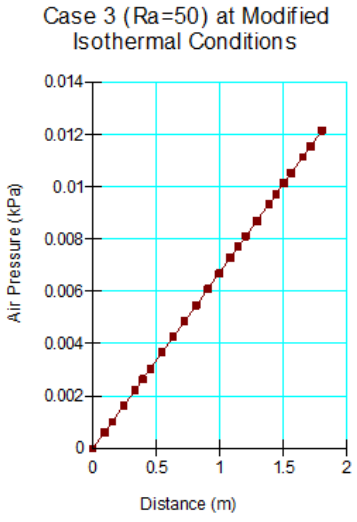

B) GeoStudio results along the sideslope from top (distance=0) to bottom (distance=2) at modified isothermal conditions (graphs drawn by GeoStudio)

FIGURE 3.144: AIR DENSITY AND AIR PRESSURE IN GEOSTUDIO SIMULATIONS AT RA=50 AT SUN'S AND MODIFIED ISOTHERMAL CONDITIONS; CASE 4 (SUN ET AL., 2005) – SIDESLOPES AND TOP OPEN

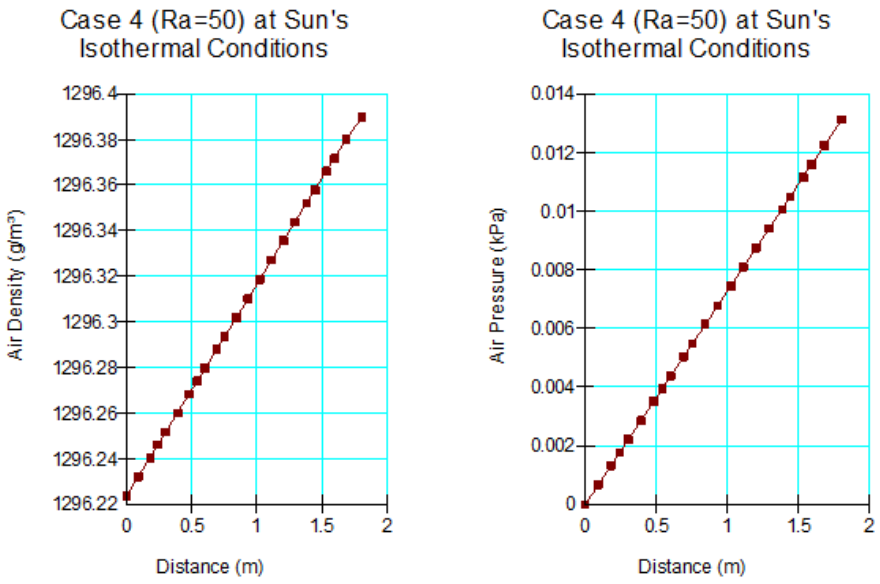

A) GeoStudio results along the sideslope from top (distance=0) to bottom (distance=2) at Sun's isothermal conditions (graphs drawn by GeoStudio)

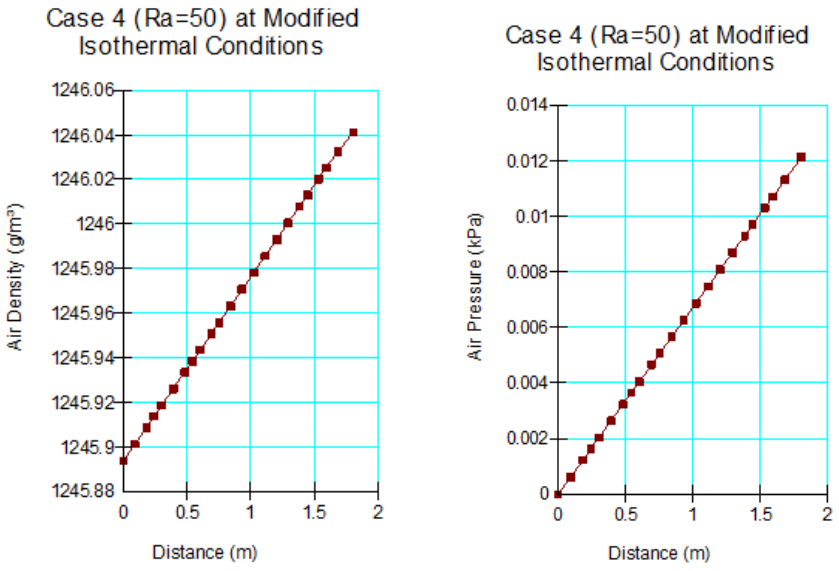

B) GeoStudio results along the sideslope from top (distance=0) to bottom (distance=2) at modified isothermal conditions (graphs drawn by GeoStudio)

FIGURE 4.1: DIAVIK DIAMOND MINE LOCATION PLAN AND OPEN PIT A154

A) Diavik Diamond Mine (Google Earth Image)

B) Diavik Open Pit A154 from air; July 28, 2005

FIGURE 4.2: DIAVIK WASTE ROCK AND WASTE ROCK TEST PILES

A) Waste rock pile at Diavik Diamond Mine; June 15, 2005

B) Diavik waste rock test piles; April 26, 2008

FIGURE 4.3: TYPE 1 PILE PLAN VIEWS AND CROSS SECTION

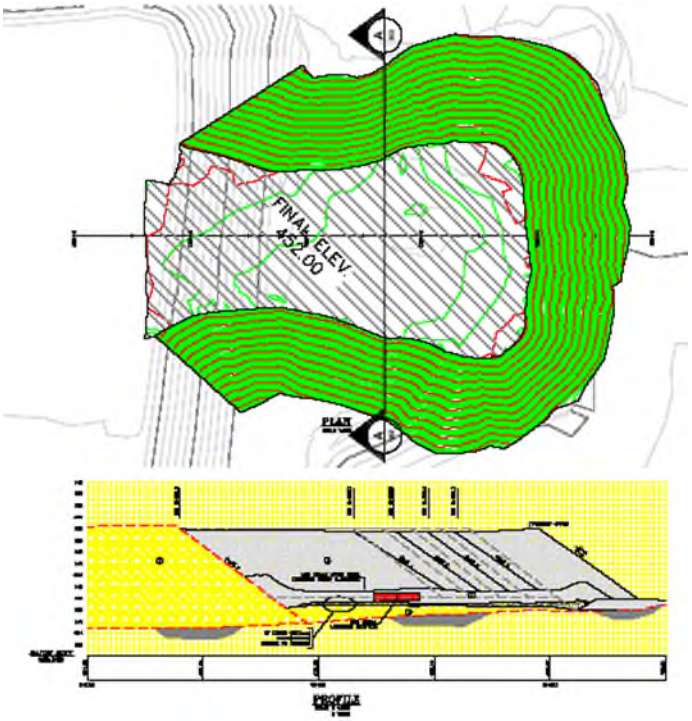

A) Type 1 Pile as-built plan view and cross section (FDA, 2006; Drawing 8000-2400-301 RevF).

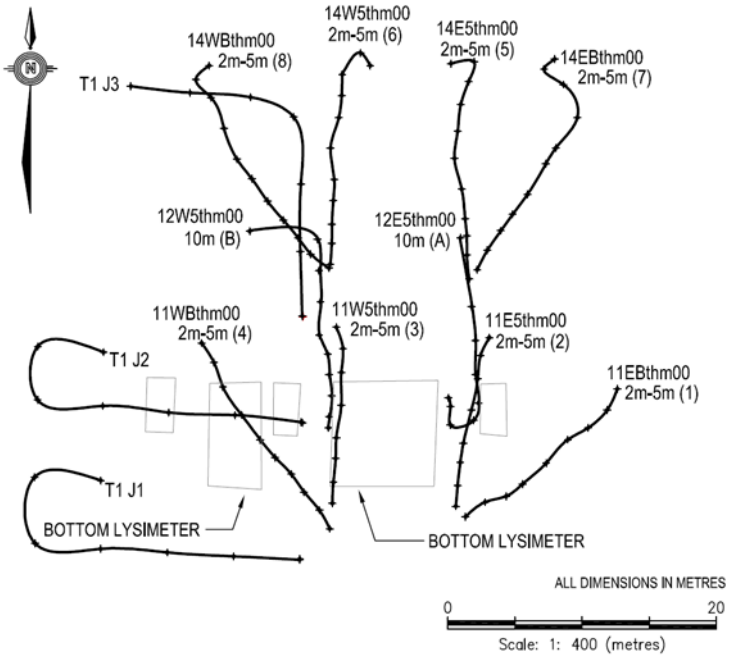

B) Ground temperature cables in Type 1 Pile (plan view)

FIGURE 4.4: TYPE 3 PILE PLAN VIEWS AND CROSS SECTION

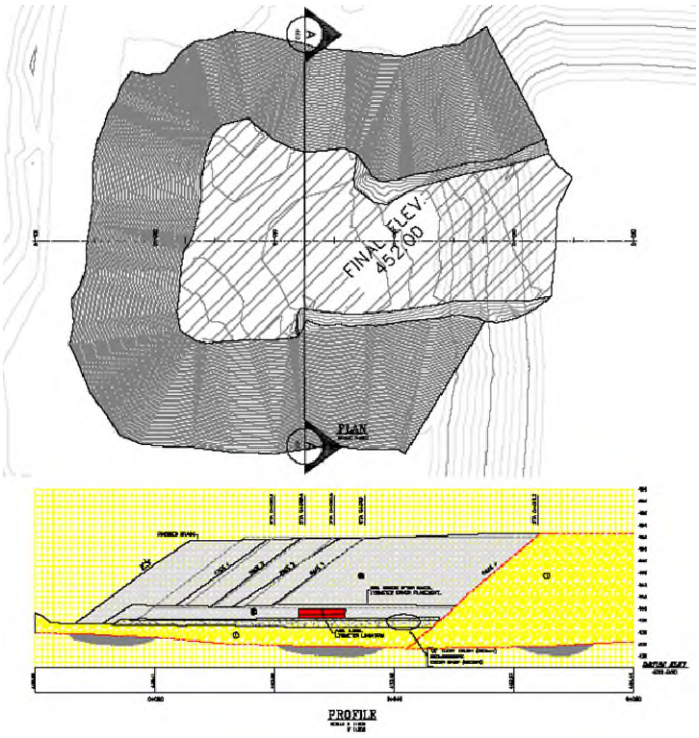

A) Type 3 Pile as-built plan view and cross section (FDA, 2006; Drawing 8000-2400-401 RevF)

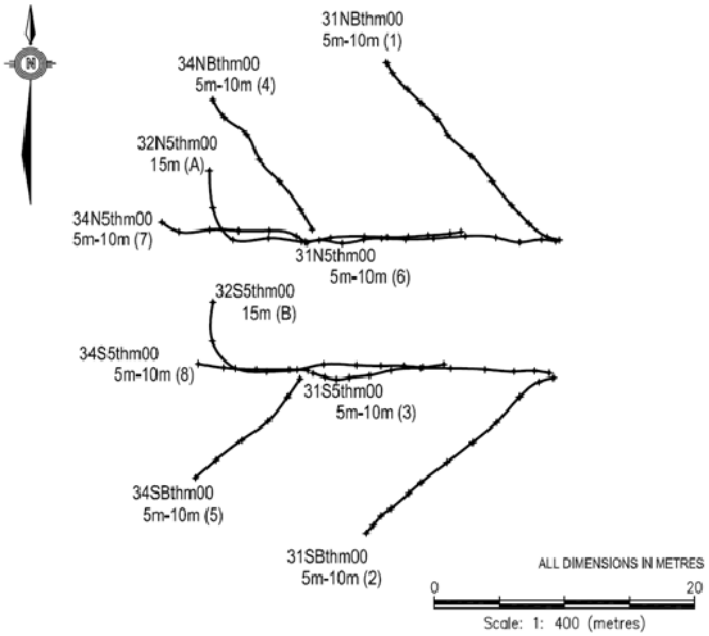

B) Ground temperature cables in Type 3 Pile (plan view)

FIGURE 4.5: COMPONENTS OF TYPE 3 PILE

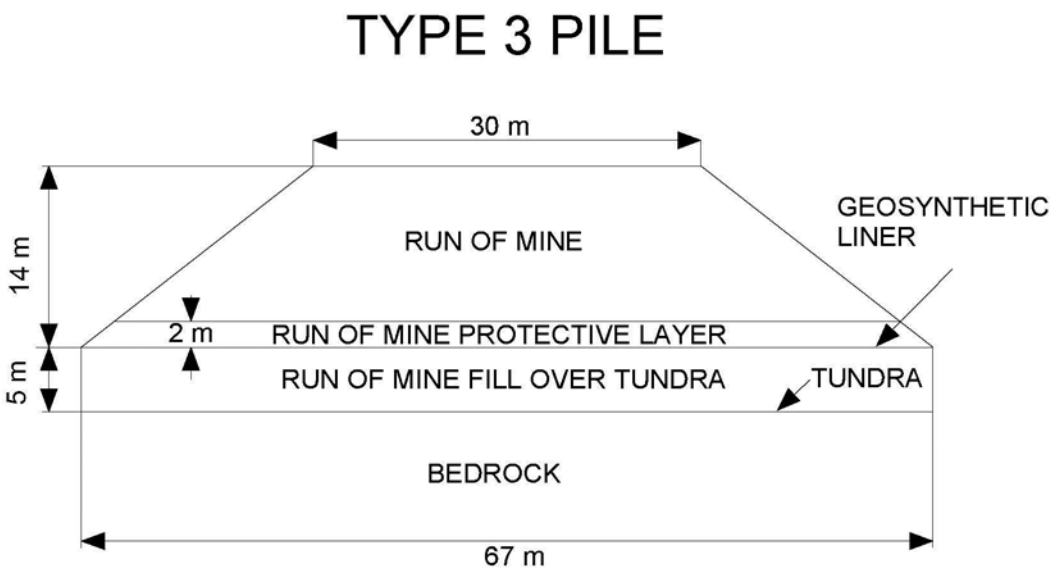

Explanatory Notes:

1. Run of mine is another name for waste rock
2. Run of mine protective layer is a lift of waste rock placed from the ground level over the base instrumentation to protect base instrumentation
3. Run of mine fill over tundra is a pad built over the tundra to provide solid base for the pile construction

FIGURE 4.6: 3-DIMENSIONAL REPRESENTATION OF BEDROCK GROUND TEMPERATURE CABLES UNDER TYPE 1 AND TYPE 3 PILES

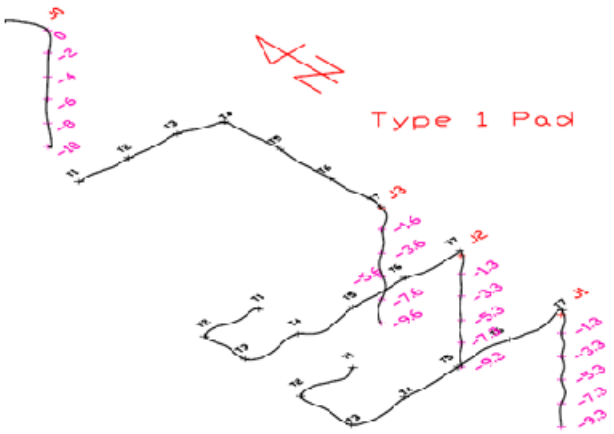

ALL DIMENSIONS IN METRES

A) Ground temperature cables under Type 1 Pile are J1 (or T1J1), J2 (or T1J2) and J3 (or T1J3); pink numbers identify depths below Type 1 Pile base; Ground Temperature Cable J0 (or T1J0) is beside the Type 1 Pile to provide background temperatures

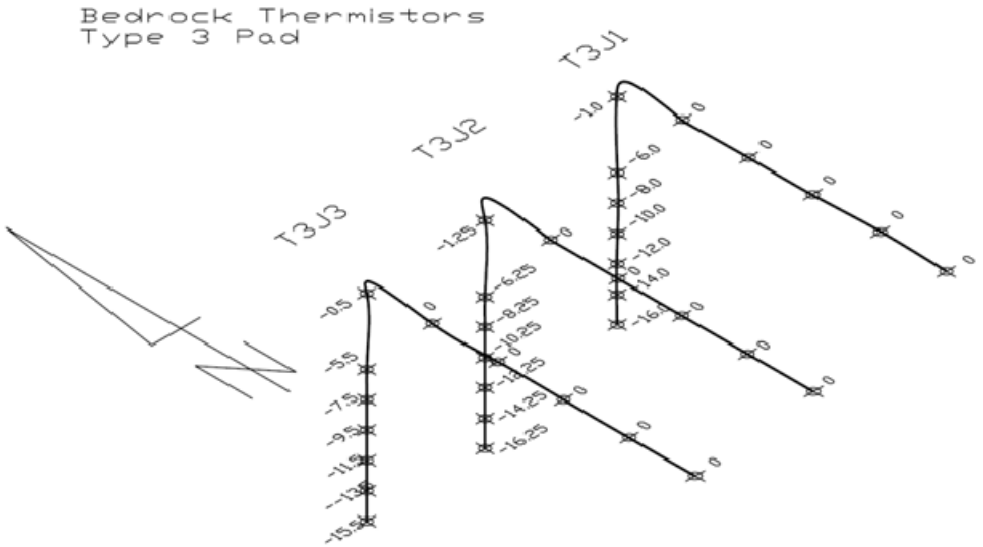

B) Ground temperature cables under Type 3 Pile are JT3J1, T3J2, and T3J3; numbers identify depths below Type 3 Pile base; zero identifies pile base elevation

FIGURE 4.7: BEDROCK GROUND TEMPERATURE CABLE INSTALLATION INTO BEDROCK WITH AIR TRACK DRILL RIG

A) Installing Ground Temperature Cable T1J1; September 22, 2004

B) Ground temperature cable before installation; September 23, 2004

FIGURE 4.8: BEDROCK GROUND TEMPERATURE CABLE STRETCHING ON PAD SURFACE

A) Ground Temperature Cable T1J3 after installation; the cable will be stretched in the adjacent trench; September 24, 2004

B) Stretching Ground Temperature Cable T1J0 in a protective conduit; September 24, 2004

FIGURE 4.9: BEDROCK GROUND TEMPERATURE CABLE BACKFILLING ON PAD SURFACE

A) Backfilling Ground Temperature Cable T1J0 with processed kimberlite; September 24, 2004

B) Stretched ground temperature cables before backfilling; September 27, 2004

FIGURE 4.10: BEDROCK GROUND TEMPERATURE CABLE STRETCHING THROUGH PROTECTIVE CONDUIT AND CONNECTING TO DATALOGGERS

A) Feeding ground temperature cable through protective conduit; September 26, 2004

B) Two NEMA containers with dataloggers; September 27, 2004

FIGURE 4.11: STRINGING GROUND TEMPERATURE CABLES TO BE INSTALLED IN WASTE ROCK TEST PILES

A) Ground temperature cables strung through flexible tubing; September 28, 2005

B) Holes drilled around thermistor beads to inject insulation; September 28, 2005

FIGURE 4.12: NEAR-SURFACE TEMPERATURES IN TYPE 1 AND TYPE 3 PILES

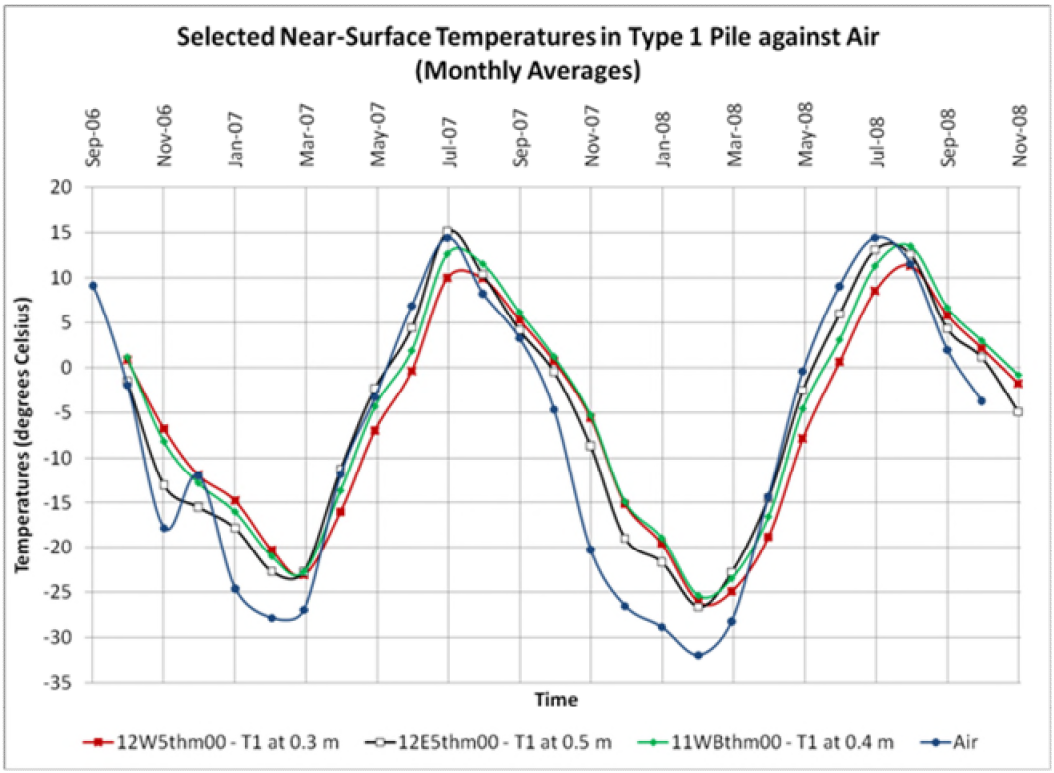

A) Selected near-surface temperatures in Type 1 Pile

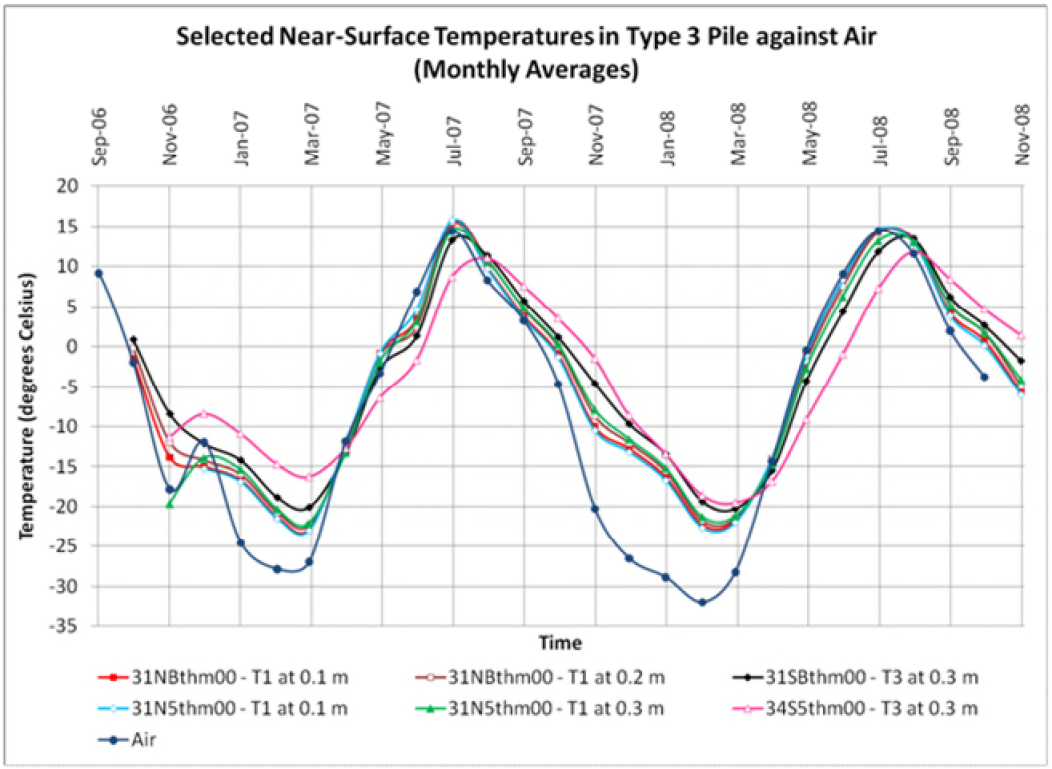

B) Selected near-surface temperatures in Type 3 Pile

FIGURE 4.13: NEAR-SURFACE TEMPERATURES IN TC (COVERED) PILE

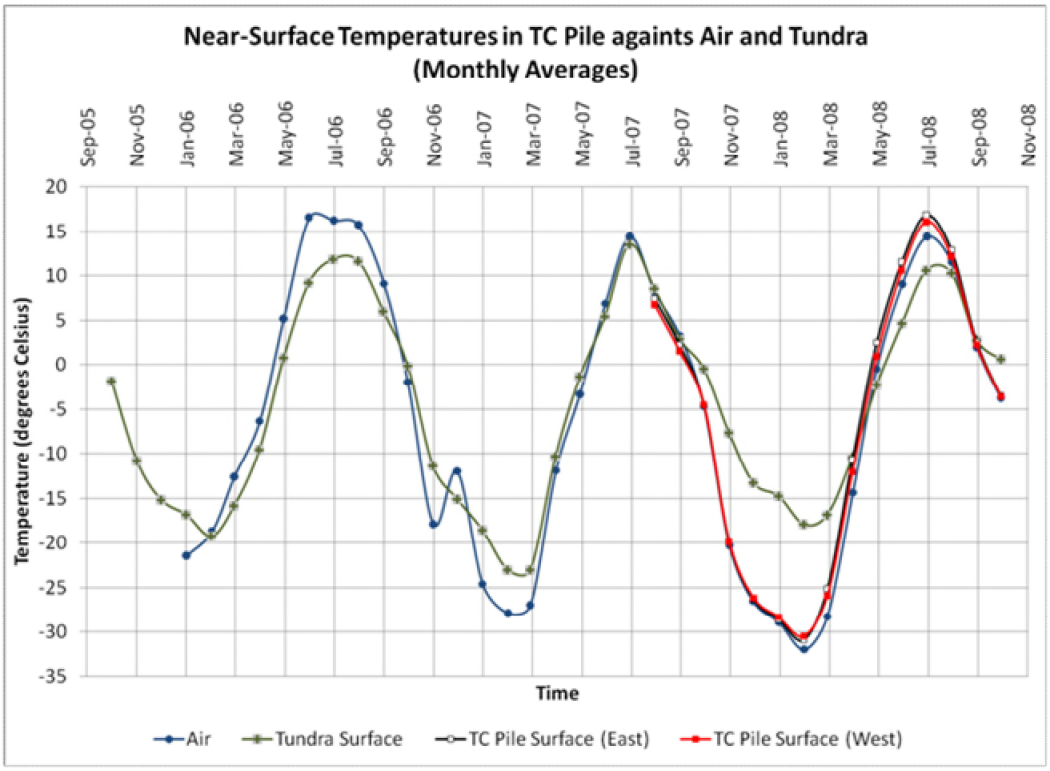

A) Selected near-surface temperatures in TC (Covered) Pile

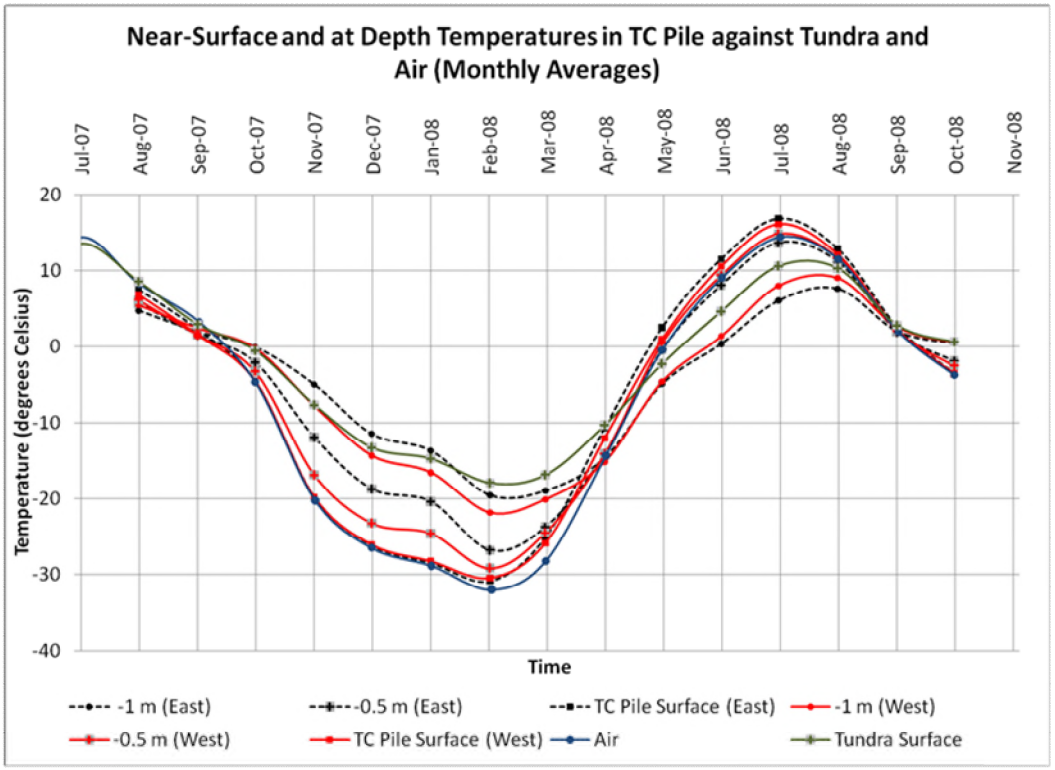

B) Selected near-surface and below-surface temperatures in TC (Covered) Pile

FIGURE 4.14: INNER WASTE ROCK TEMPERATURES IN TYPE 3 PILE ON FACE 2

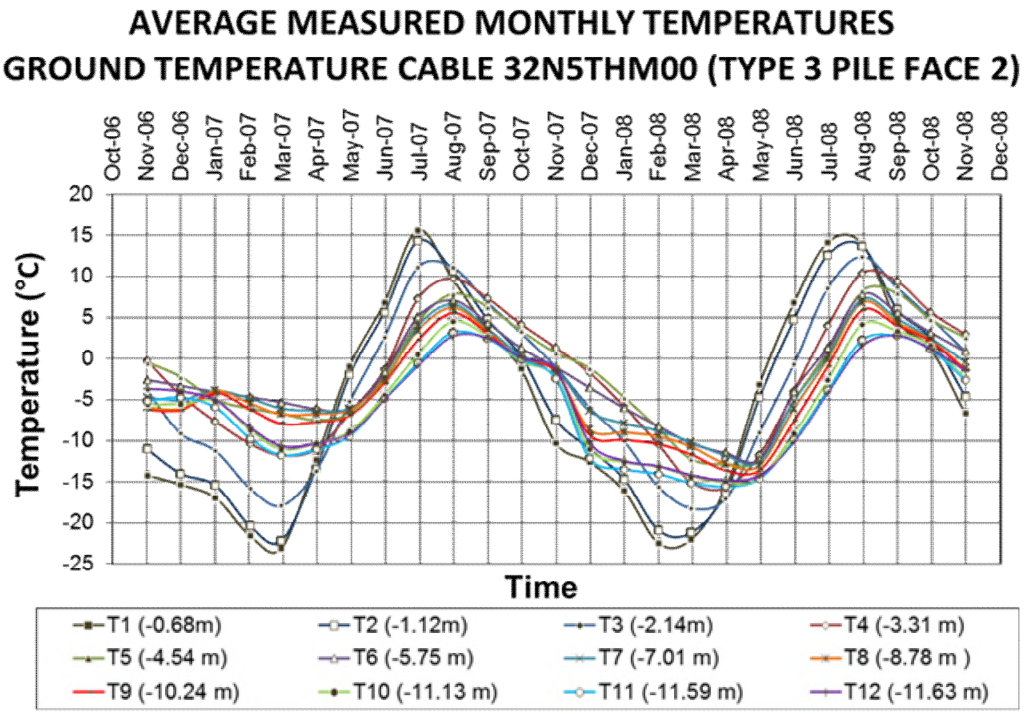

A) Average measured monthly temperatures in Ground Temperature Cable 32N5thm00

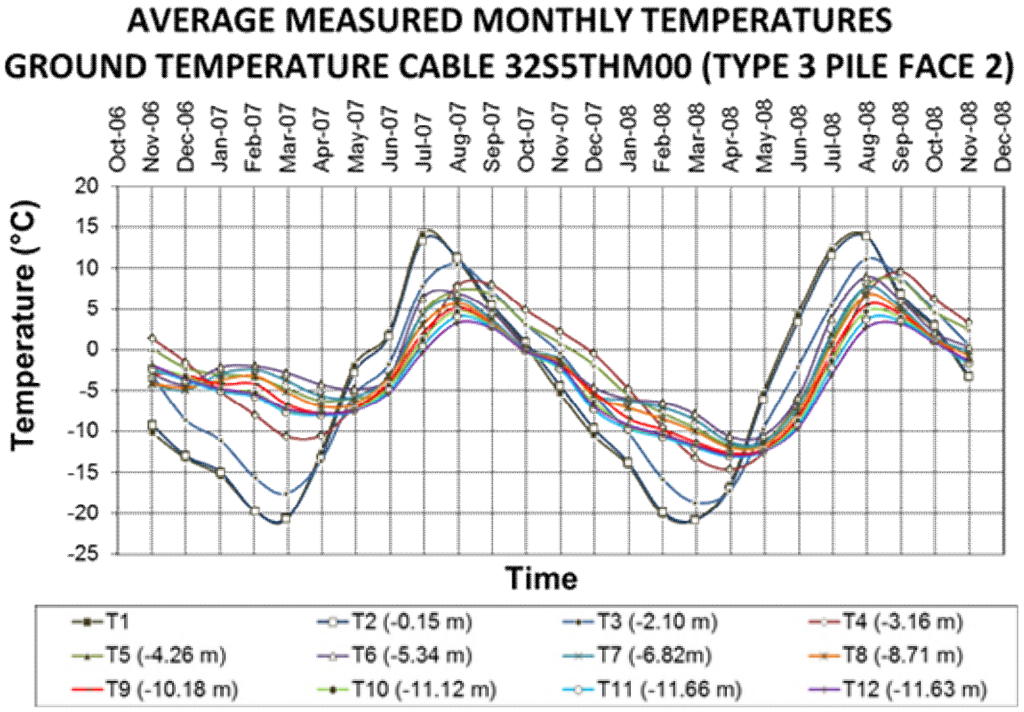

B) Average measured monthly temperatures in Ground Temperature Cable 32S5thm00

FIGURE 4.15: BEDROCK TEMPERATURES UNDER TYPE 3 PILE

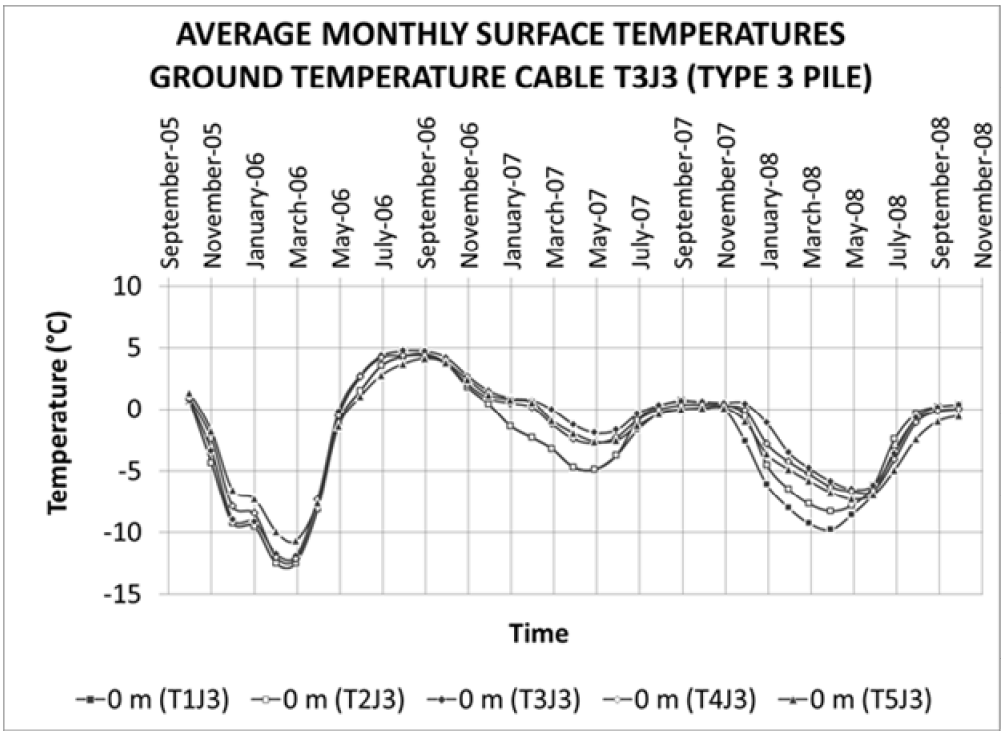

A) Average measured monthly temperatures in surface thermistor beads on Ground Temperature Cable T3J3

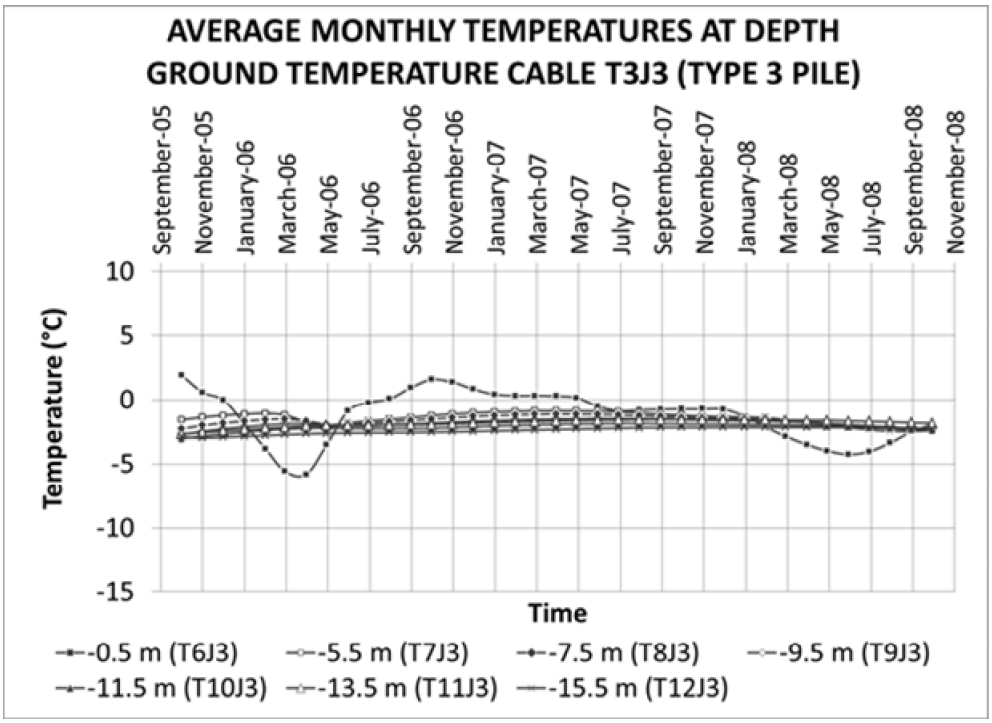

B) Average measured monthly temperatures in deep thermistor beads on Ground Temperature Cable T3J3

FIGURE 5.1: 11WBthm00 (2m-5m (4)) - AS MANUFACTURED, PLAN, AND SECTION

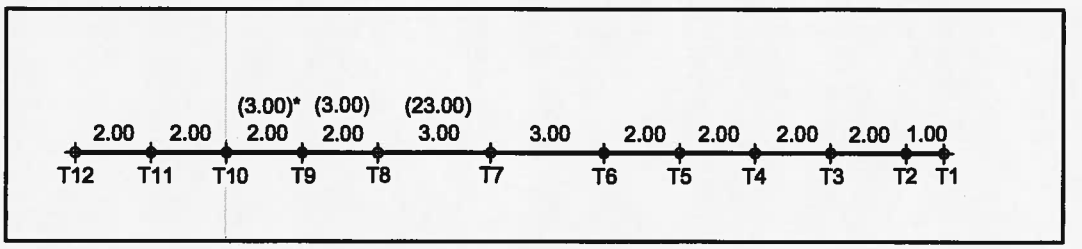

AS MANUFACTURED - GTC 2m-5m (4)

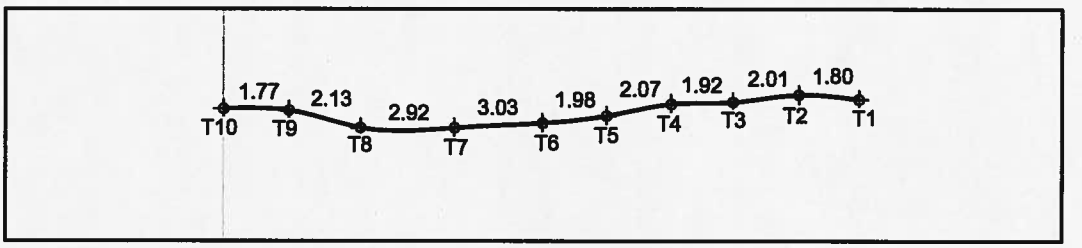

PLAN - GTC 11WBthm00

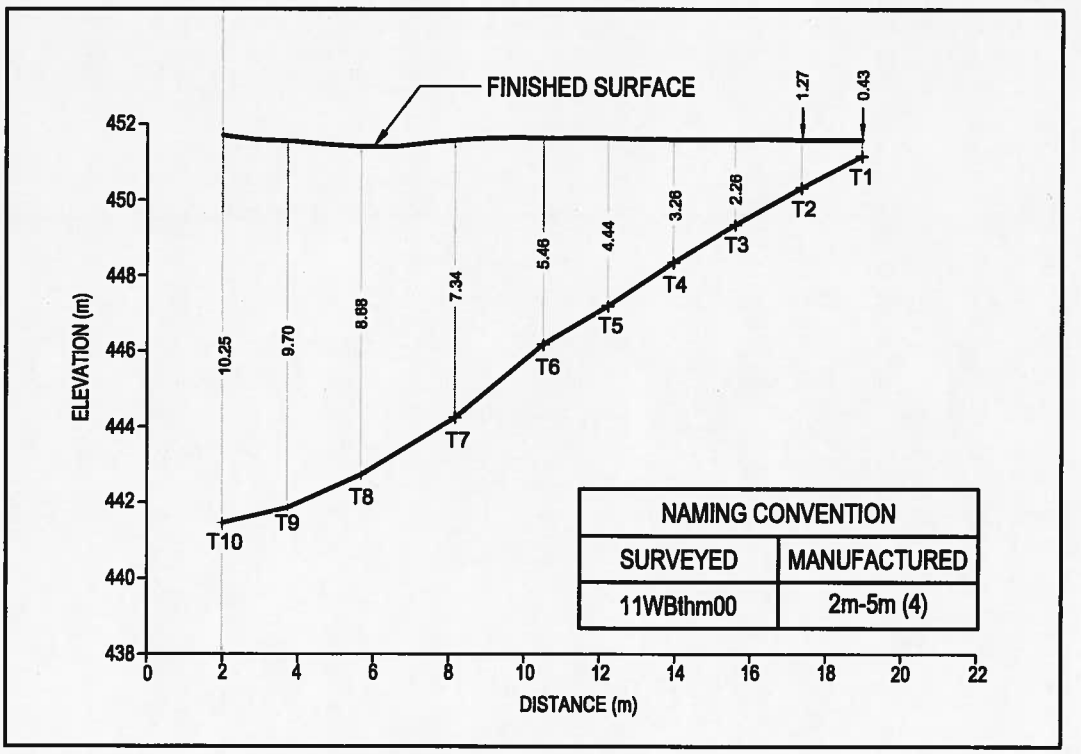

SECTION - GTC 11WBthm00

* MANUFACTURED LENGTH 3.00 M, INSTALLED LENGTH 2.00 M
ALL DIMENSIONS IN METRES

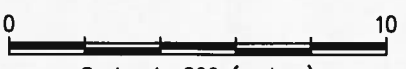

Scale: 1: 200 (metres)

FIGURE 5.2: 11W5thm00 (2m-5m (3)) - AS MANUFACTURED, PLAN, AND SECTION

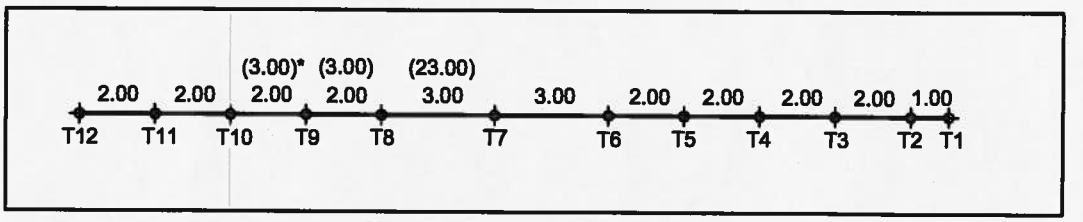

AS MANUFACTURED - 2m-5m (3)

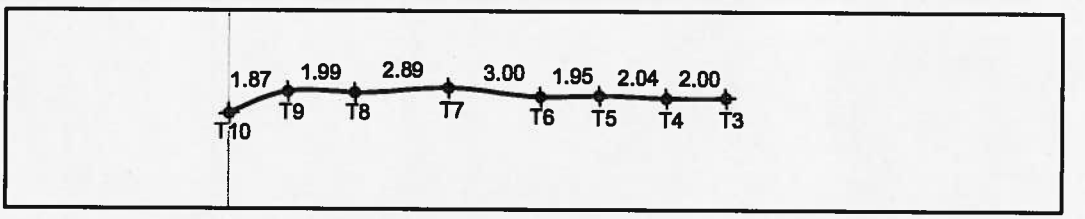

PLAN - 11W5thm00

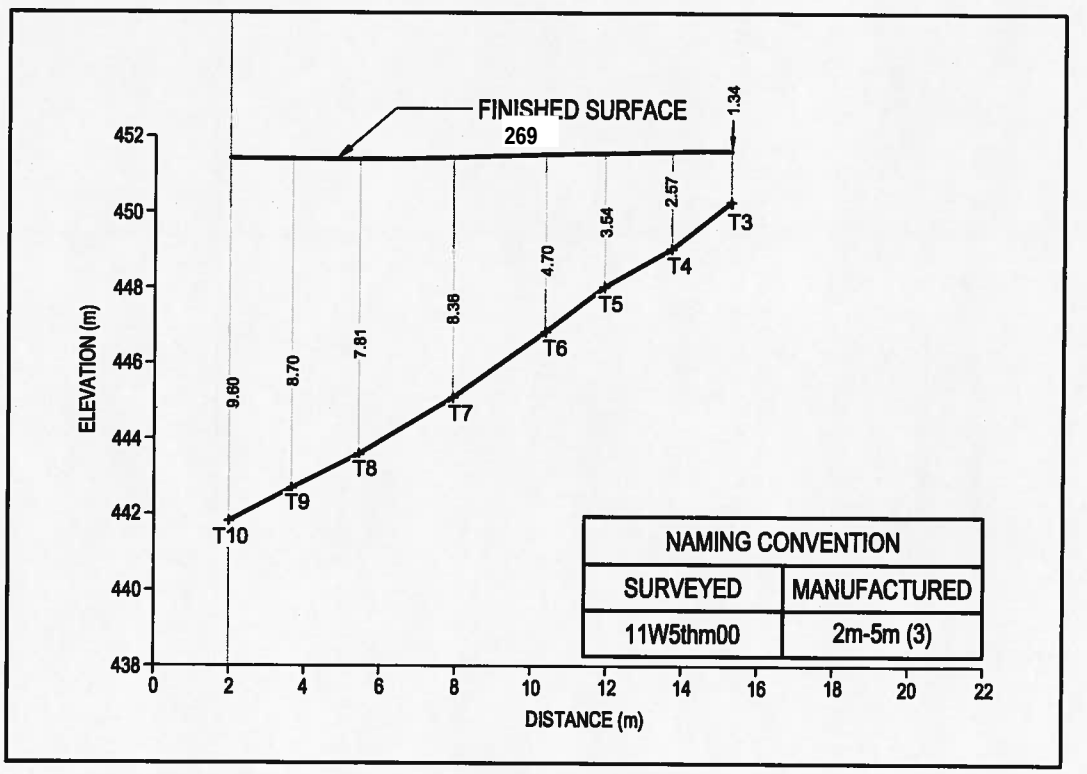

SECTION - 11W5thm00

* MANUFACTURED LENGTH 3.00 M, INSTALLED LENGTH 2.00 M
ALL DIMENSIONS IN METRES

Scale: 1: 200 (metres)

FIGURE 5.3: 11E5thm00 (2m-5m (2)) - AS MANUFACTURED, PLAN, AND SECTION

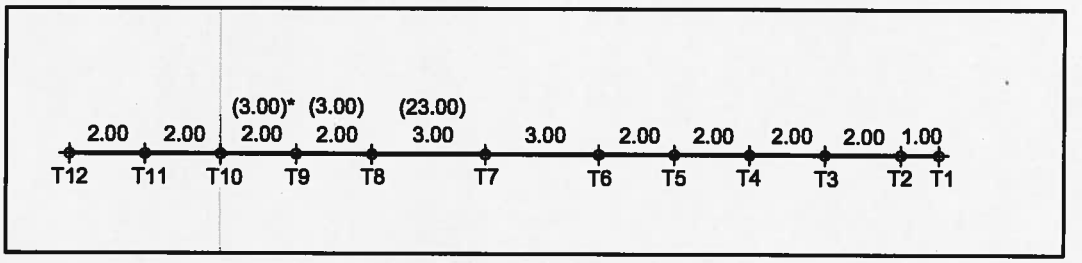

AS MANUFACTURED - 2m-5m (2)

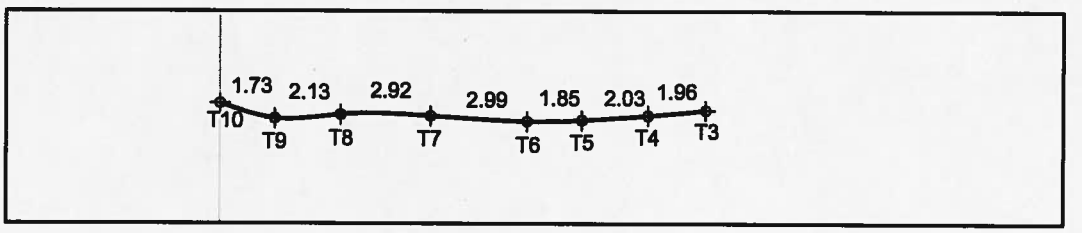

PLAN - 11E5thm00

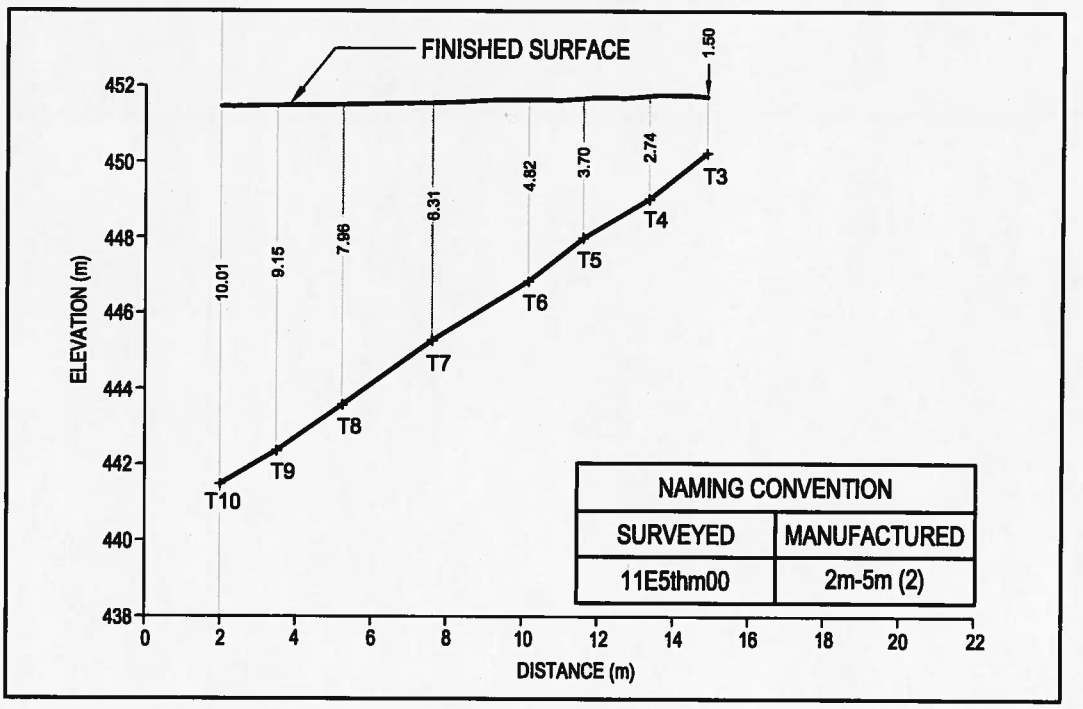

SECTION - 11E5thm00

* MANUFACTURED LENGTH 3.00 M, INSTALLED LENGTH 2.00 M
ALL DIMENSIONS IN METRES

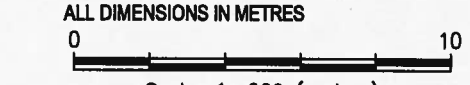

Scale: 1: 200 (metres)

FIGURE 5.4: 11EBthm00 (2m-5m (1)) - AS MANUFACTURED, PLAN, AND SECTION

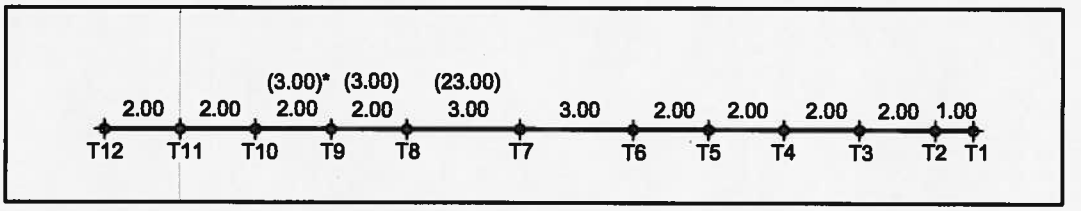

AS MANUFACTURED - 2m-5m (1)

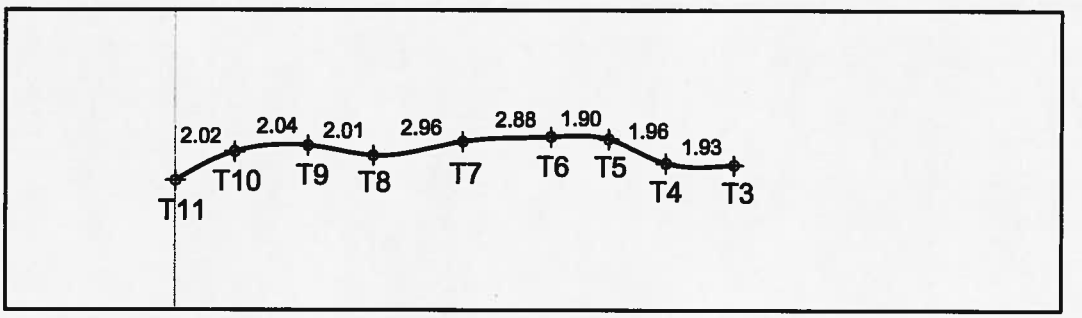

PLAN - 11EBthm00

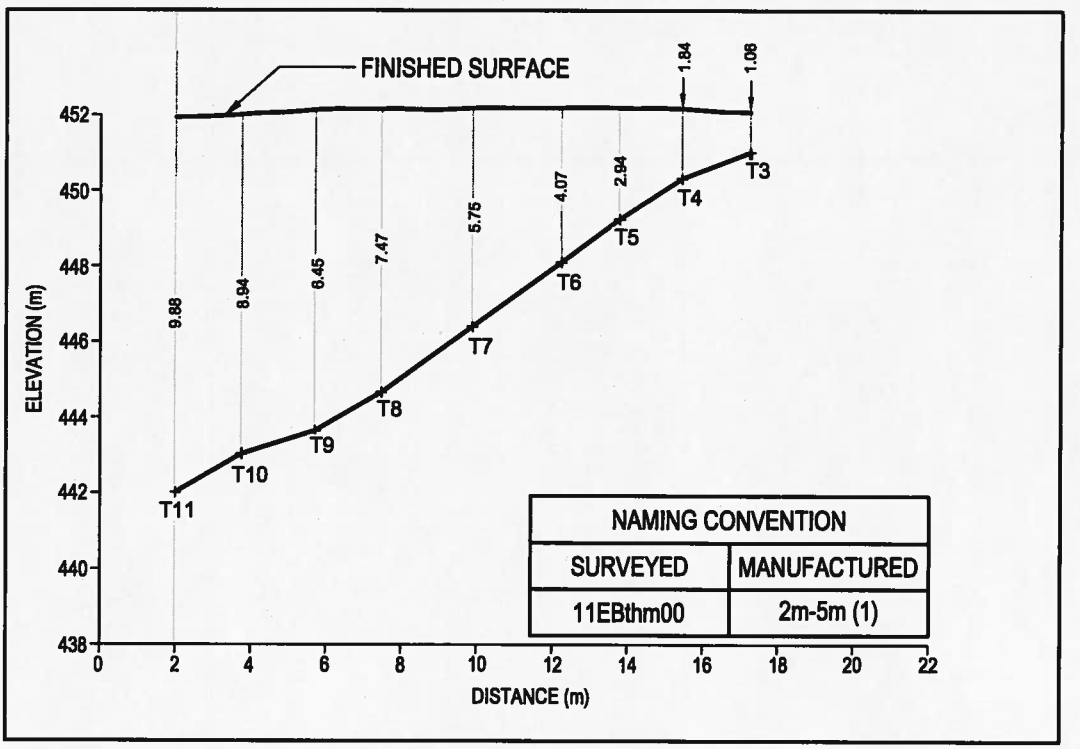

SECTION - 11EBthm00

* MANUFACTURED LENGTH 3.00 M, INSTALLED LENGTH 2.00 M
ALL DIMENSIONS IN METRES

Scale: 1: 200 (metres)

FIGURE 5.5: 12W5thm00 (10m (B)) - AS MANUFACTURED, PLAN, AND SECTION

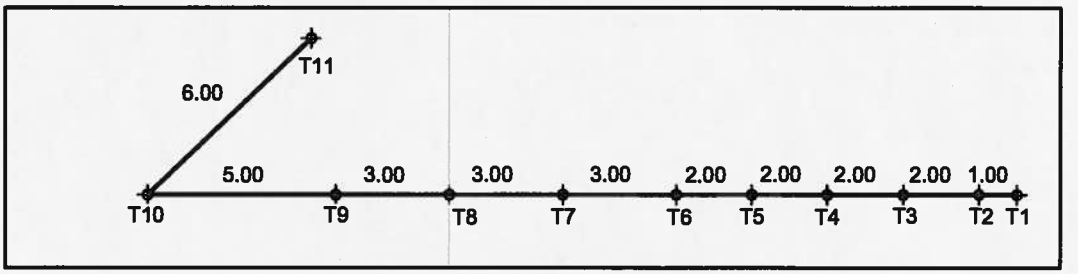

AS MANUFACTURED - 10m (B)

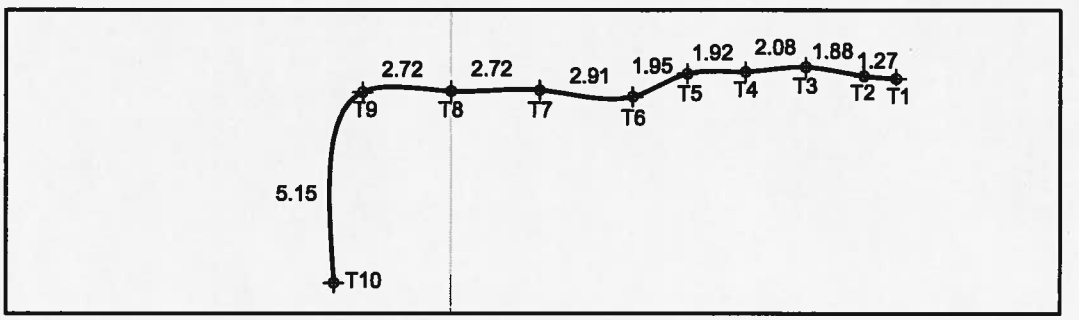

PLAN - 12W5thm00

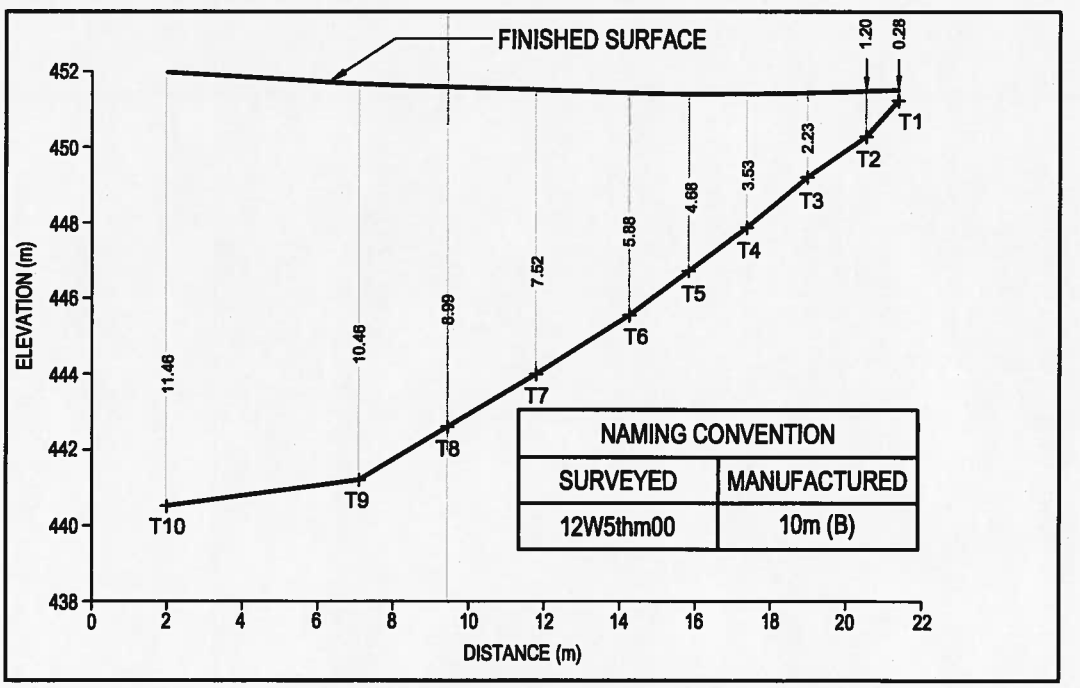

SECTION - 12W5thm00

ALL DIMENSIONS IN METRES

0 10

Scale: 1: 200 (metres)

FIGURE 5.6: 12E5thm00 (10m (A)) - AS MANUFACTURED, PLAN, AND SECTION

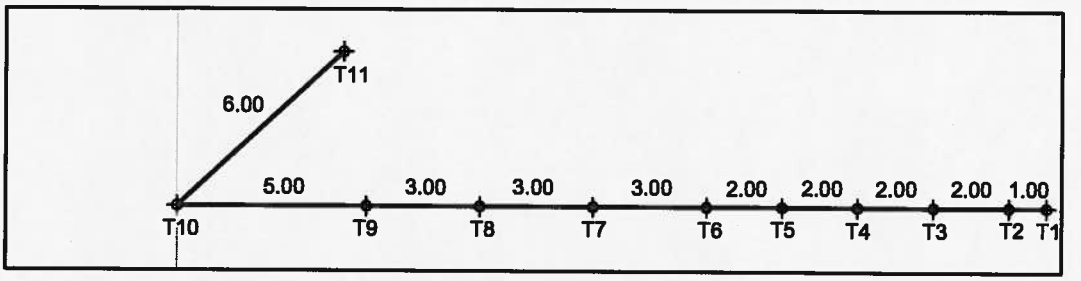

AS MANUFACTURED - 10m (A)

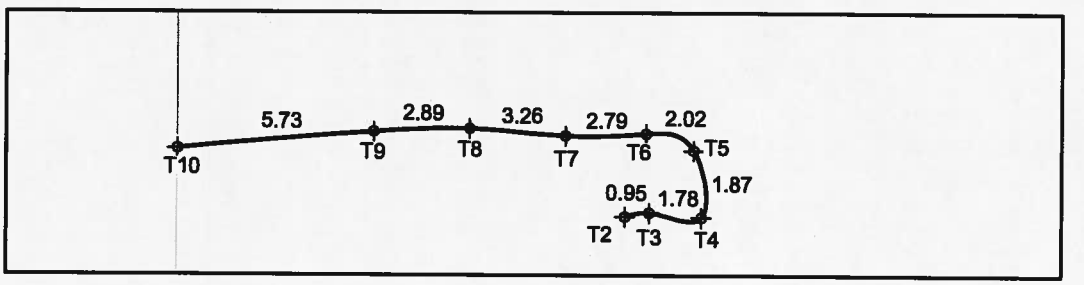

PLAN - 12E5thm00

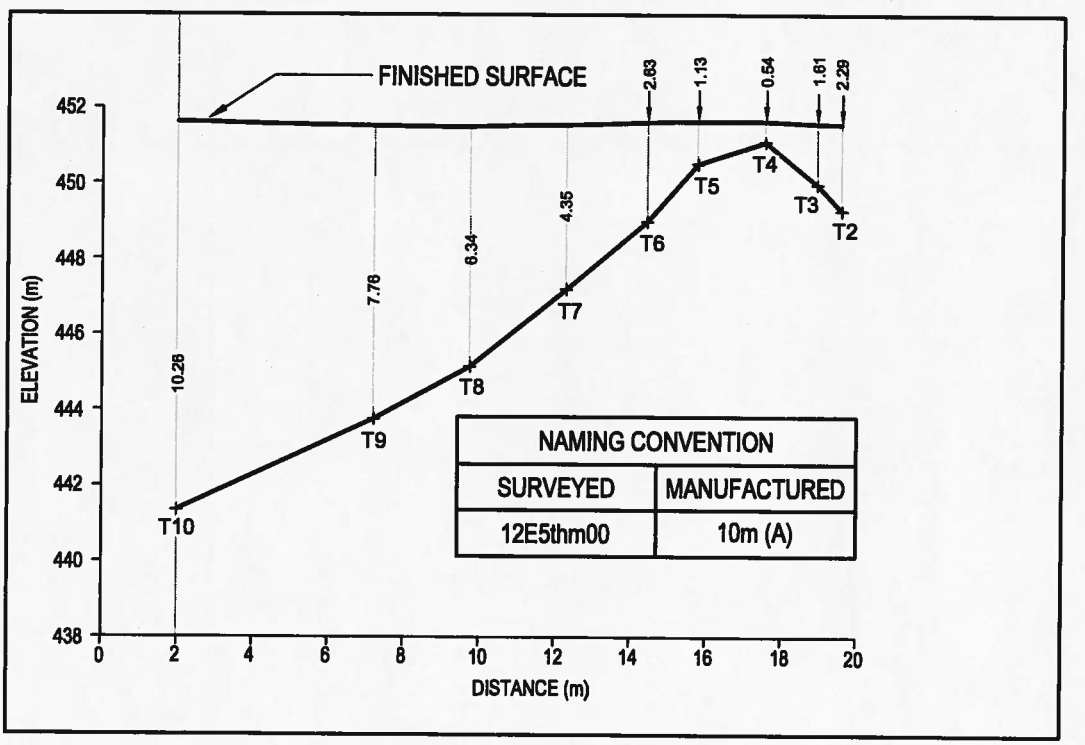

SECTION - 12E5thm00

ALL DIMENSIONS IN METRES

0 10

Scale: 1: 200 (metres)

FIGURE 5.6a: 12E5thm00 (10m (A)) - AS MANUFACTURED, PLAN, AND SECTION

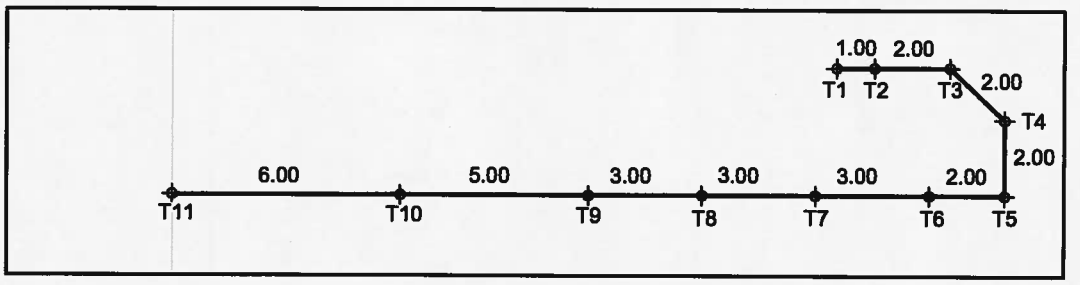

AS MANUFACTURED - 10m (A)

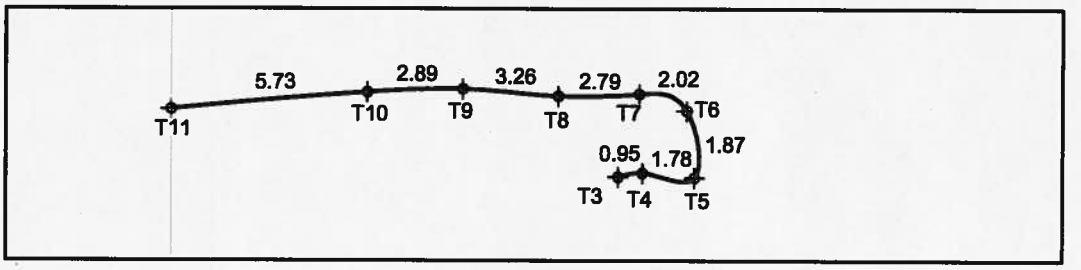

PLAN - 12E5thm00

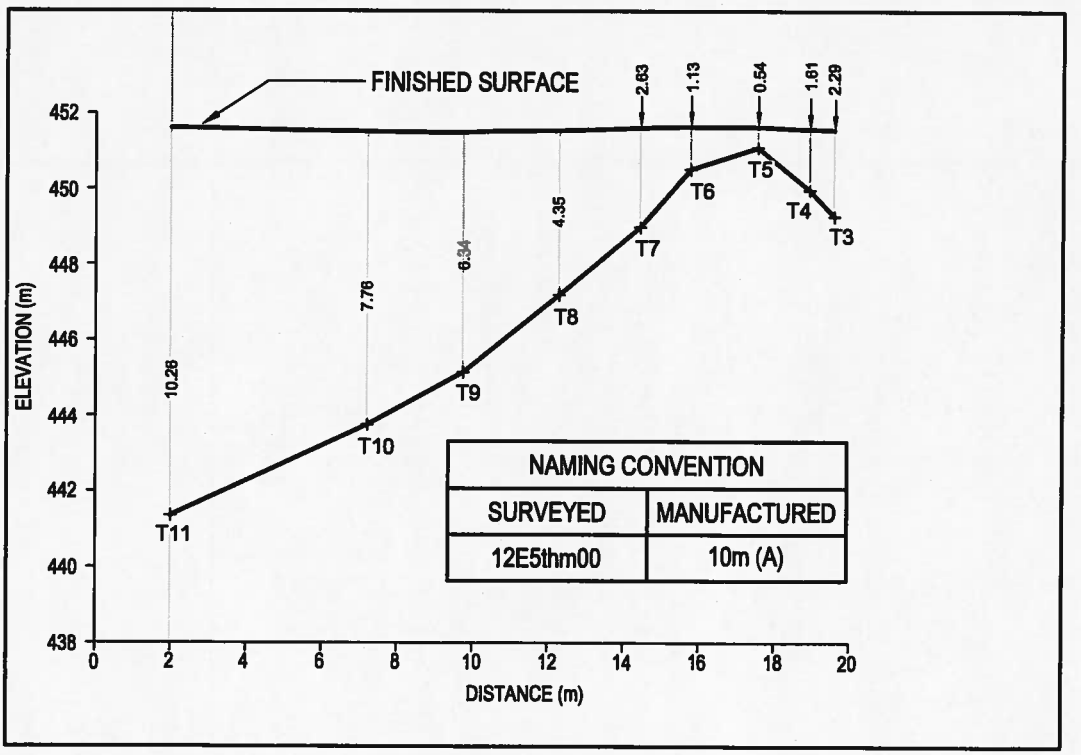

SECTION - 12E5thm00

ALL DIMENSIONS IN METRES

0 10

Scale: 1: 200 (metres)

FIGURE 5.6b: 12E5thm00 (10m (A)) - AS MANUFACTURED, PLAN, AND SECTION

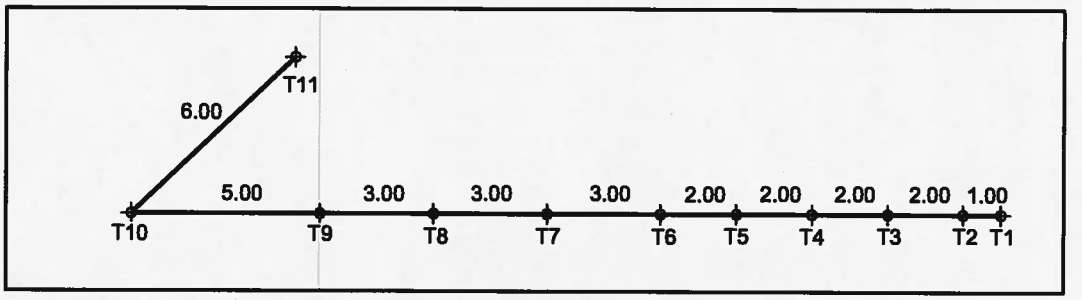

AS MANUFACTURED - 10m (A)

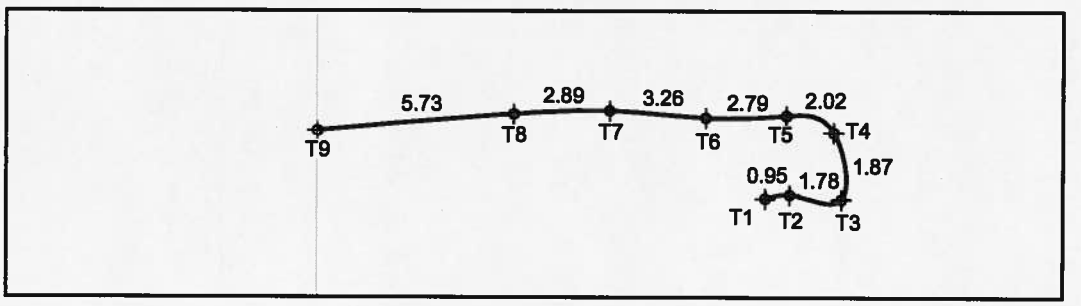

PLAN - 12E5thm00

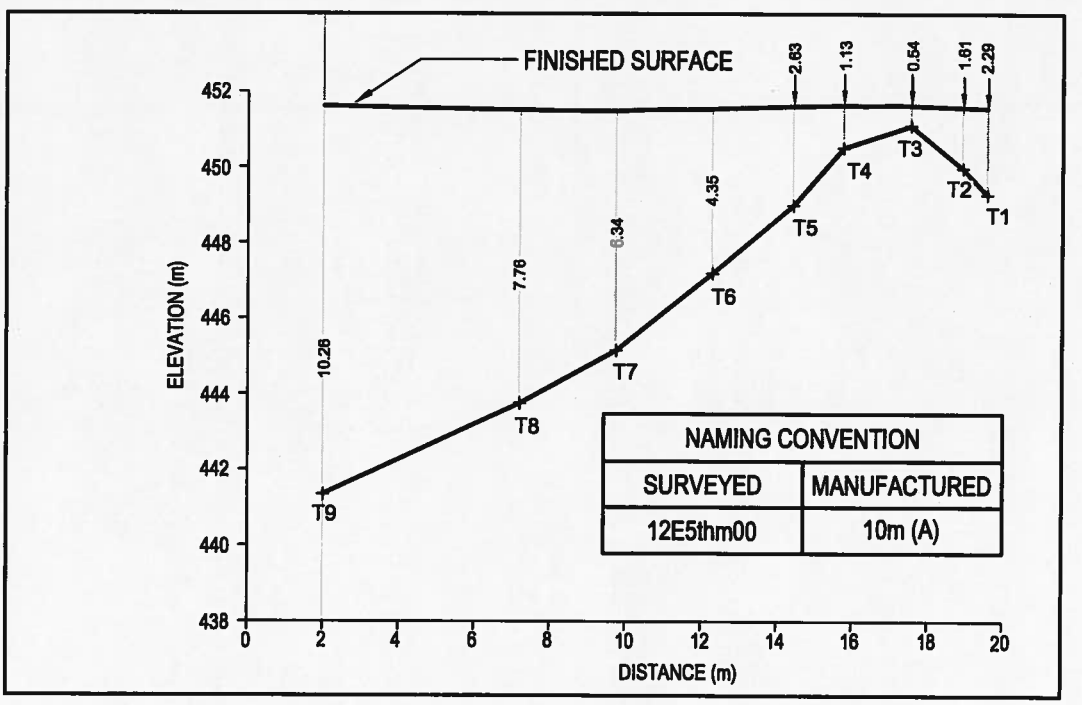

SECTION - 12E5thm00

ALL DIMENSIONS IN METRES

0 10

Scale: 1: 200 (metres)

FIGURE 5.7: 14WBthm00 (2m-5m (8)) - AS MANUFACTURED, PLAN, AND SECTION

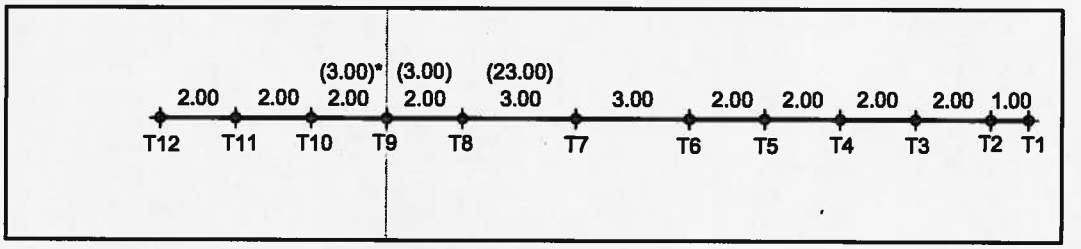

AS MANUFACTURED - 2m-5m (8)

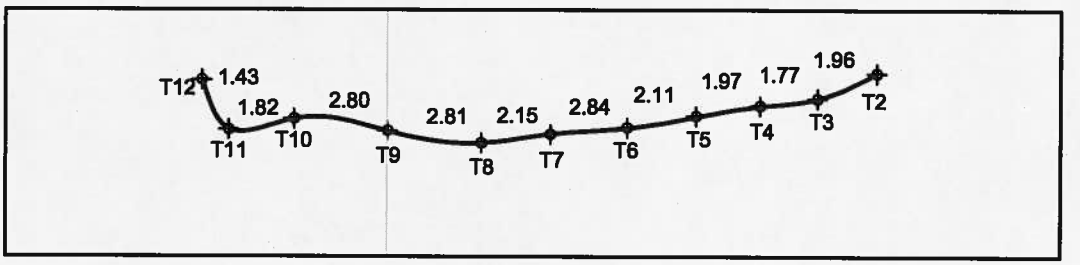

PLAN - 14WBthm00

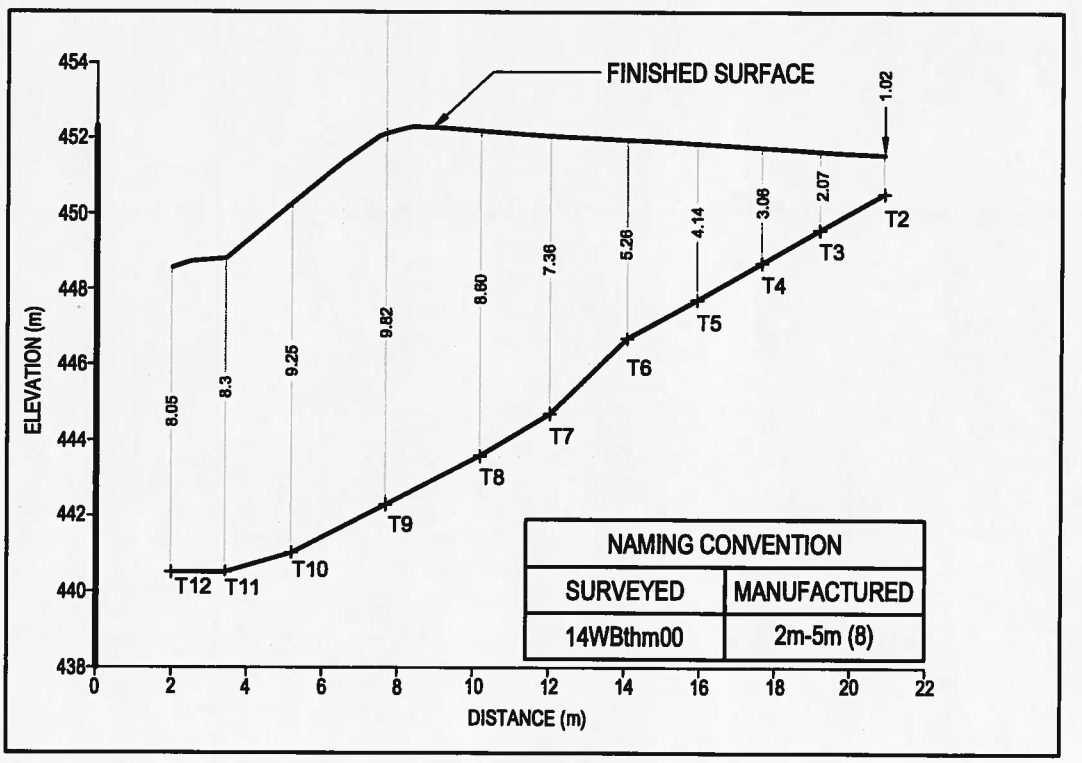

SECTION - 14WBthm00

* MANUFACTURED LENGTH 3.00 M, INSTALLED LENGTH 2.00 M
ALL DIMENSIONS IN METRES

Scale: 1: 200 (metres)

FIGURE 5.8: 14W5thm00 (2m-5m (6)) - AS MANUFACTURED, PLAN, AND SECTION

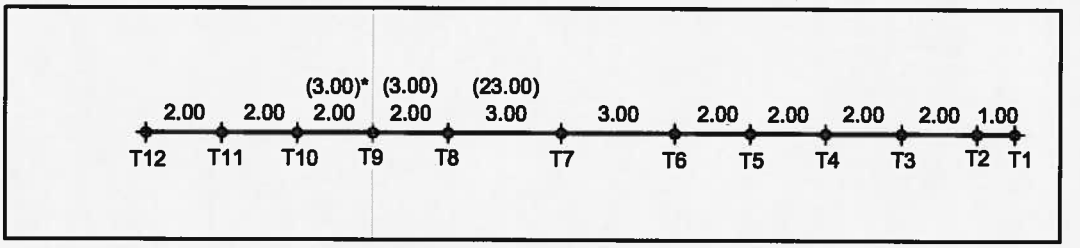

AS MANUFACTURED - 2m-5m (6)

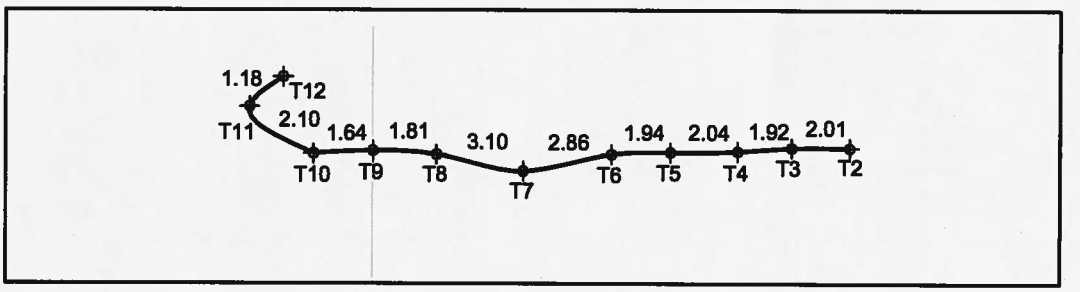

PLAN - 14W5thm00

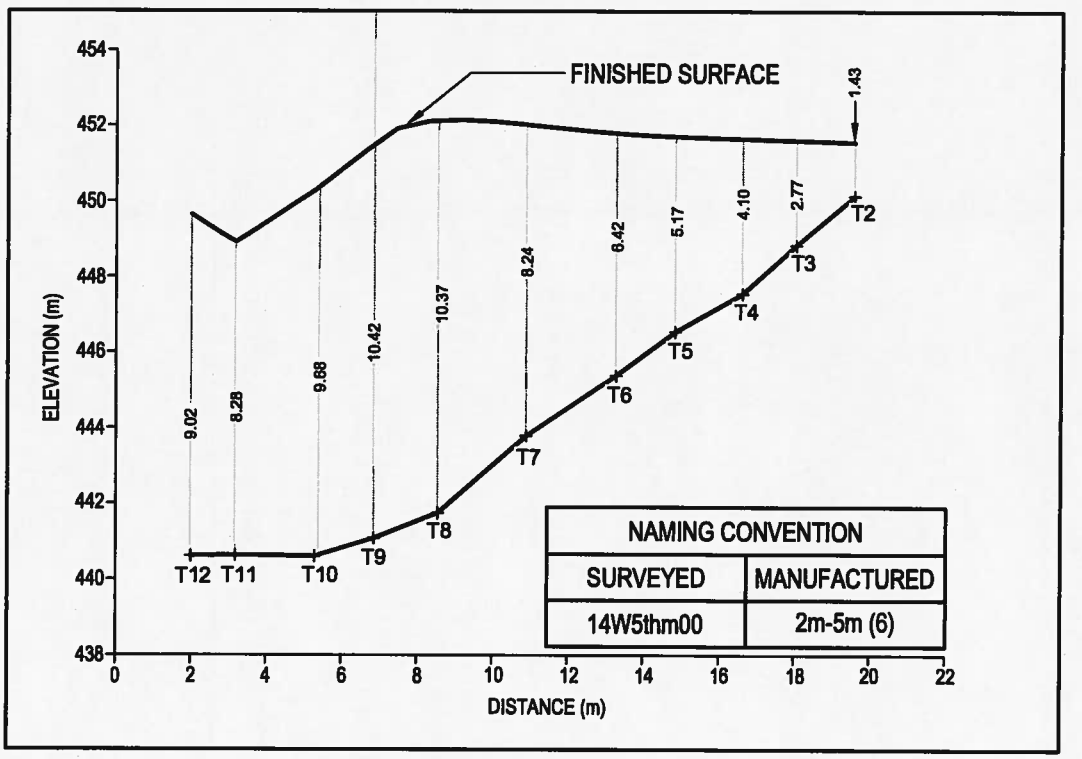

SECTION - 14W5thm00

* MANUFACTURED LENGTH 3.00 M, INSTALLED LENGTH 2.00 M
ALL DIMENSIONS IN METRES

Scale: 1: 200 (metres)

FIGURE 5.9: 14E5thm00 (2m-5m (5)) - AS MANUFACTURED, PLAN, AND SECTION

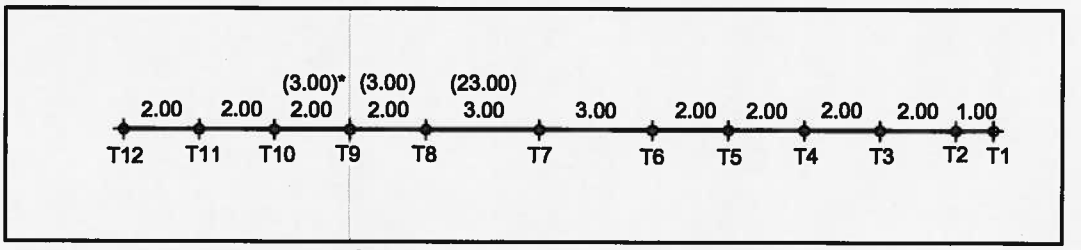

AS MANUFACTURED - 2m-5m (5)

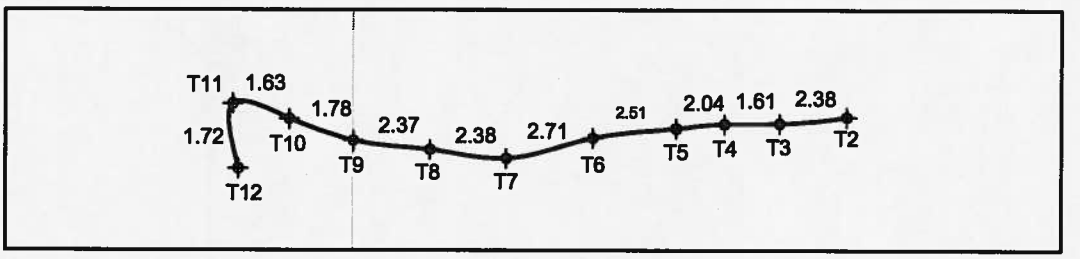

PLAN - 14E5thm00

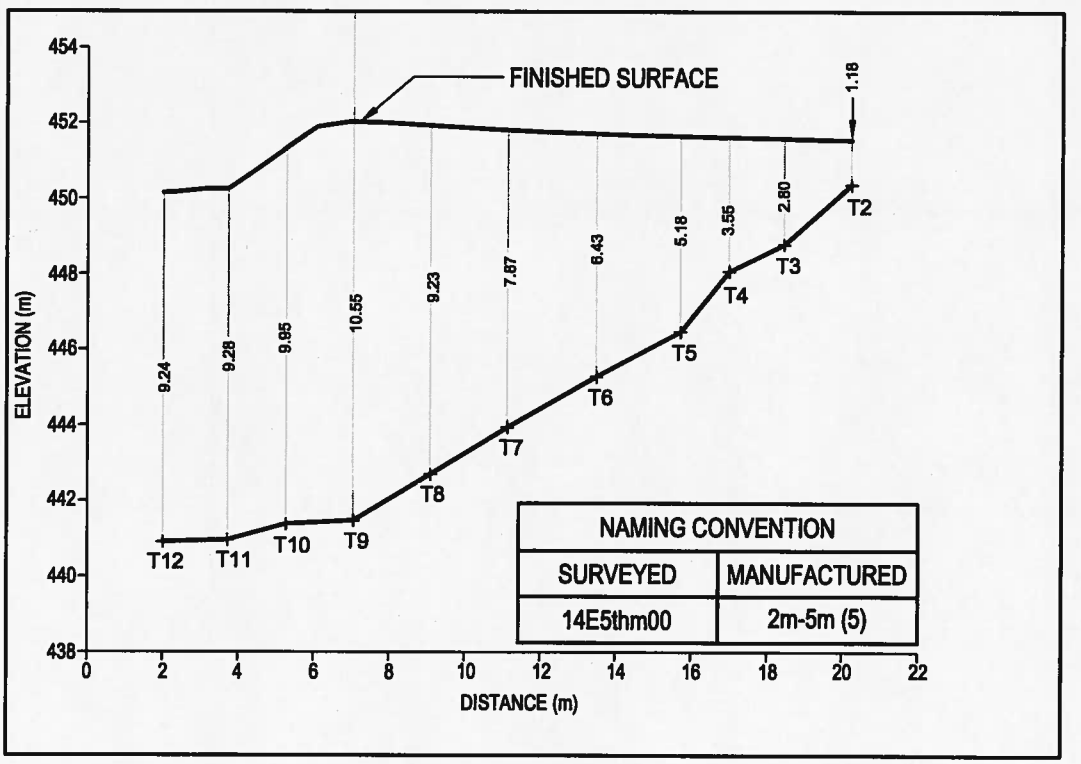

SECTION - 14E5thm00

* MANUFACTURED LENGTH 3.00 M, INSTALLED LENGTH 2.00 M
ALL DIMENSIONS IN METRES

Scale: 1: 200 (metres)

FIGURE 5.10: 14EBthm00 (2m-5m (7)) - AS MANUFACTURED, PLAN, AND SECTION

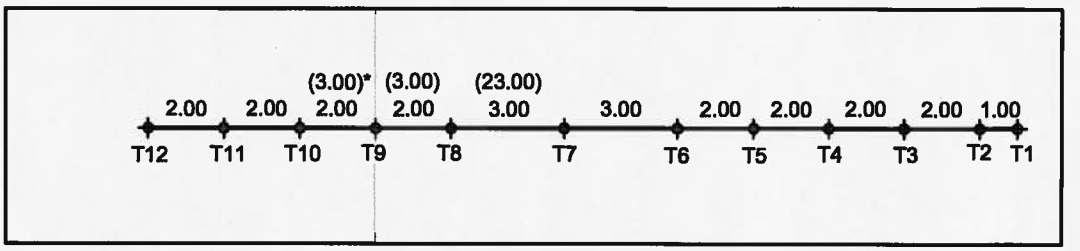

AS MANUFACTURED - 2m-5m (7)

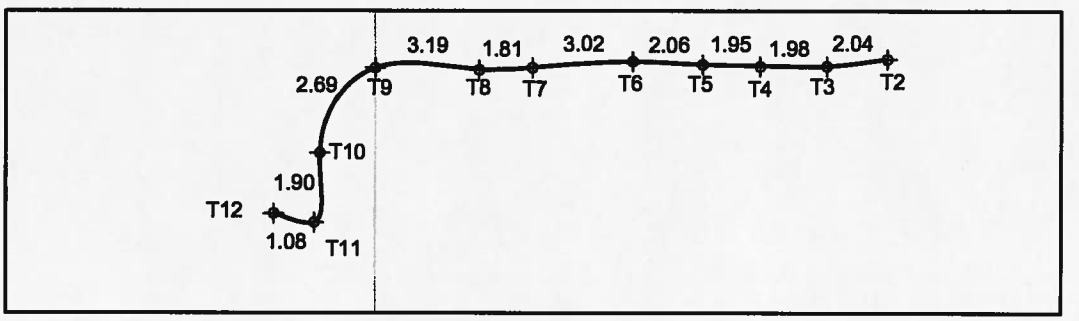

PLAN -14EBthm00

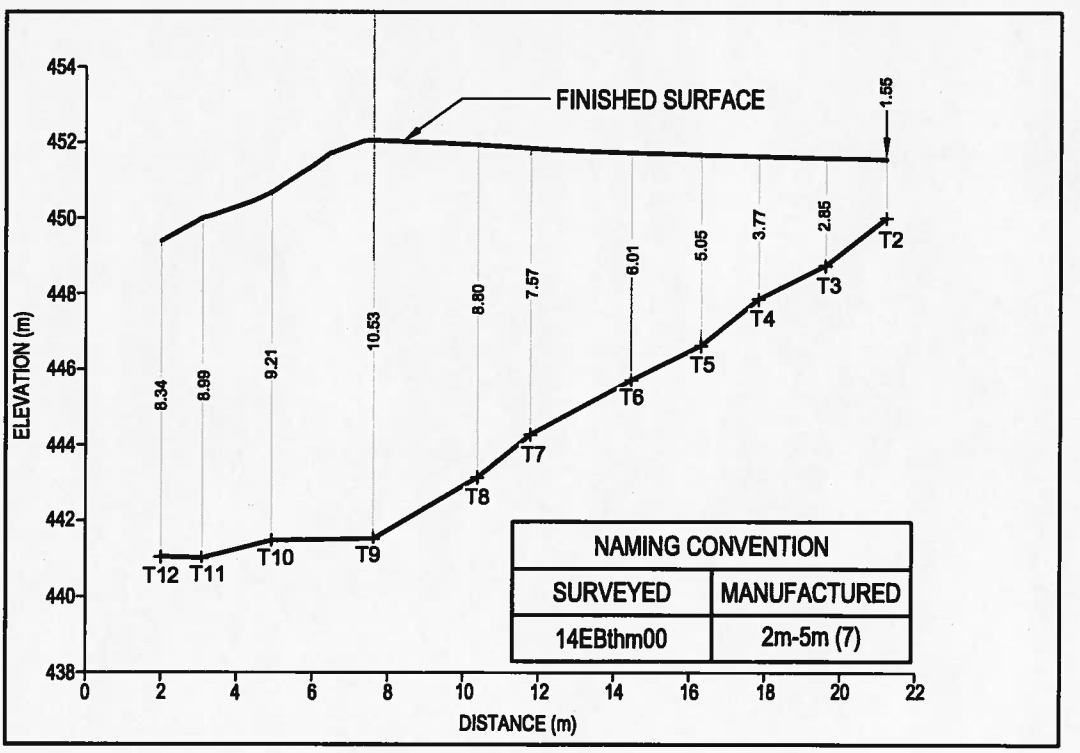

SECTION - 14EBthm00

* MANUFACTURED LENGTH 3.00 M, INSTALLED LENGTH 2.00 M
ALL DIMENSIONS IN METRES

0 10

Scale: 1: 200 (metres)

FIGURE 5.11: 31NBthm00 (5m-10m (1)) - AS MANUFACTURED, PLAN, AND SECTION

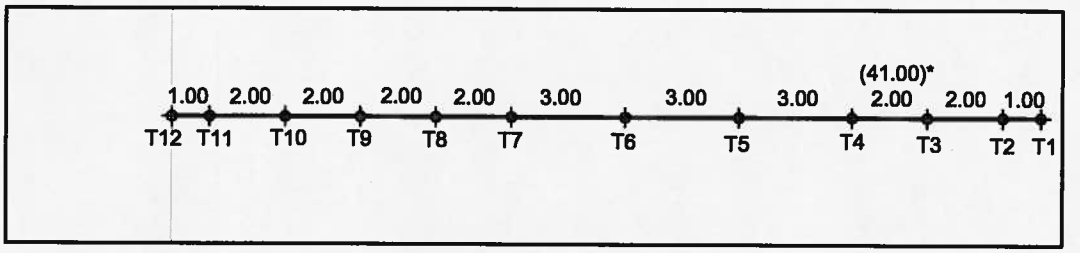

AS MANUFACTURED - 5m-10m (1)

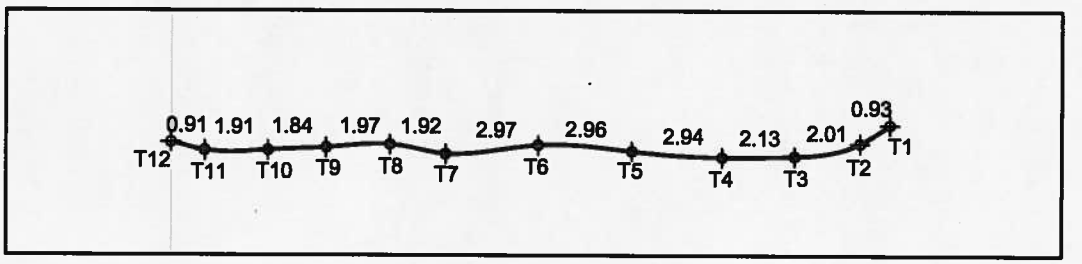

PLAN - 31NBthm00

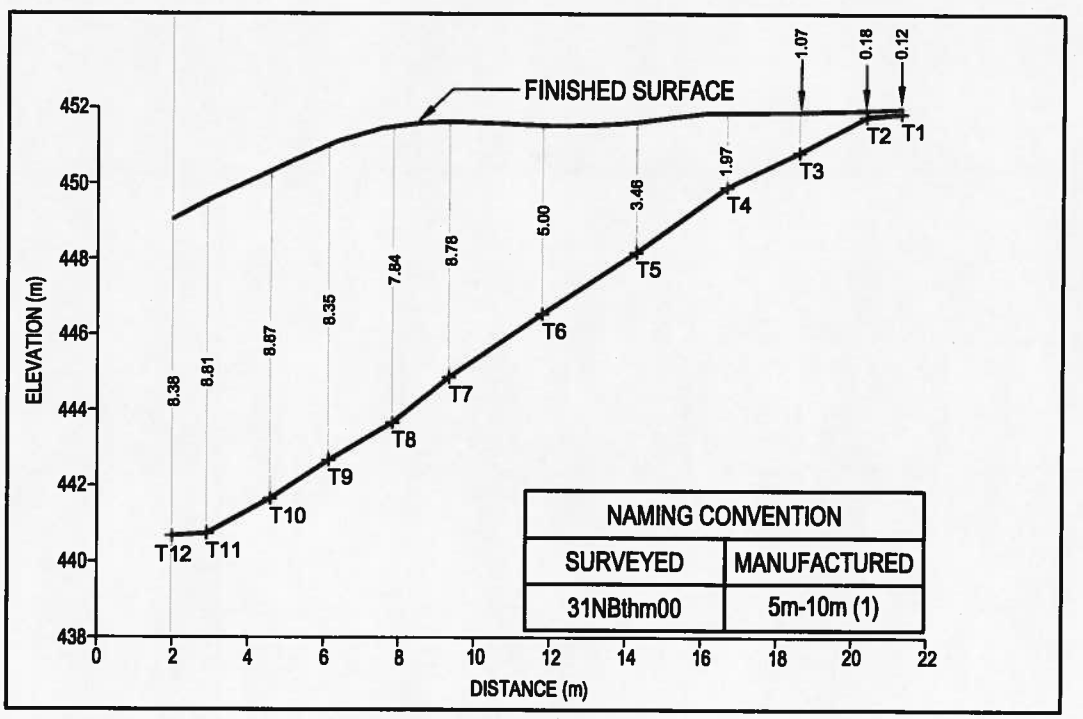

SECTION - 31NBthm00

* MANUFACTURED LENGTH 41.00 M, INSTALLED LENGTH 2.00 M
ALL DIMENSIONS IN METRES

0 10

Scale: 1: 200 (metres)

FIGURE 5.12: 31N5thm00 (5m-10m (6)) - AS MANUFACTURED, PLAN, AND SECTION

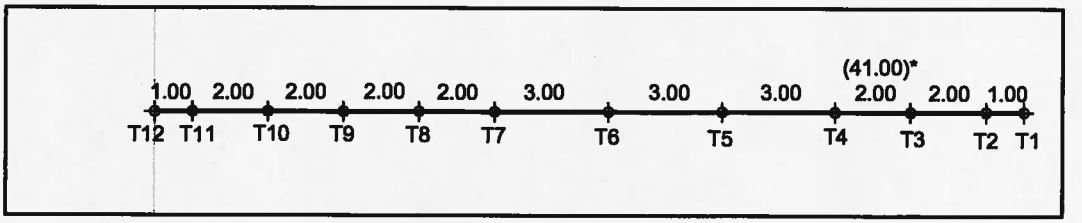

AS MANUFACTURED - 5m-10m (6)

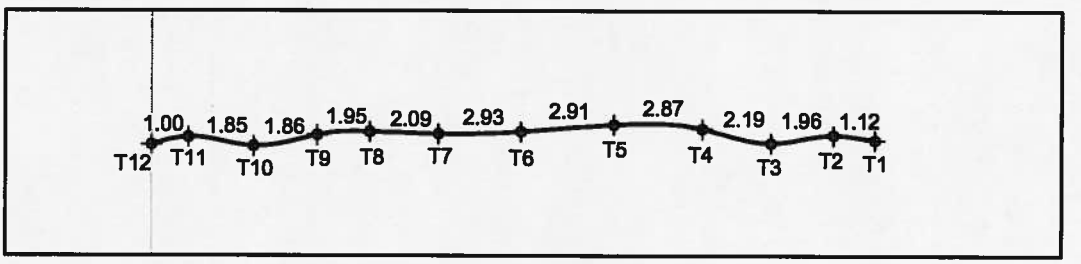

PLAN - 31N5thm00

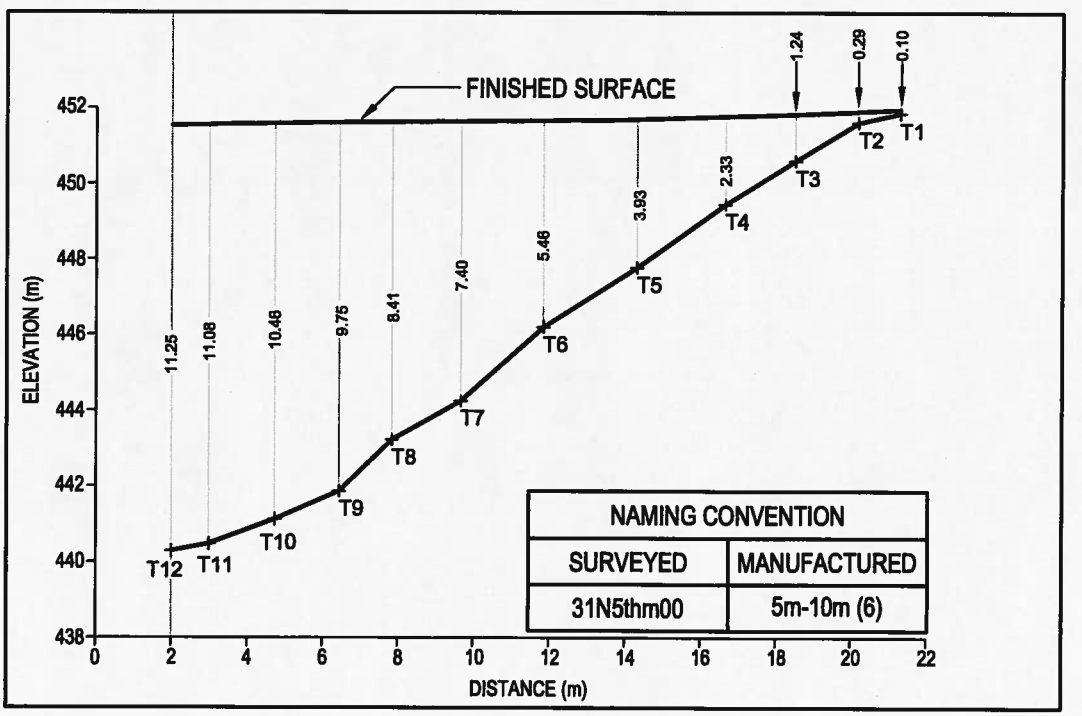

SECTION - 31N5thm00

* MANUFACTURED LENGTH 41.00 M, INSTALLED LENGTH 2.00 M
ALL DIMENSIONS IN METRES

0 10

Scale: 1: 200 (metres)

FIGURE 5.13: 31S5thm00 (5m-10m (3)) - AS MANUFACTURED, PLAN, AND SECTION

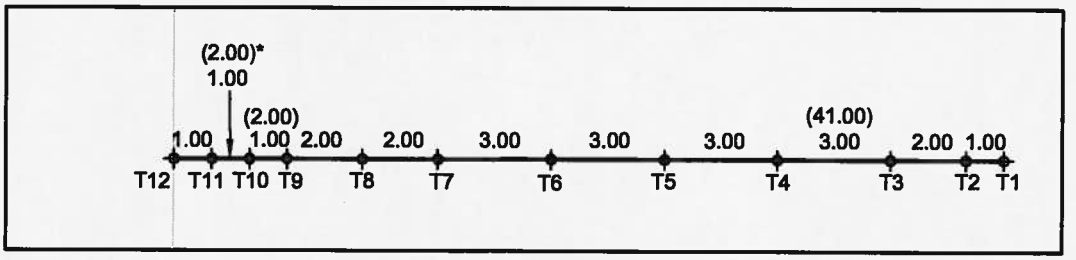

AS MANUFACTURED - 5m-10m (3)

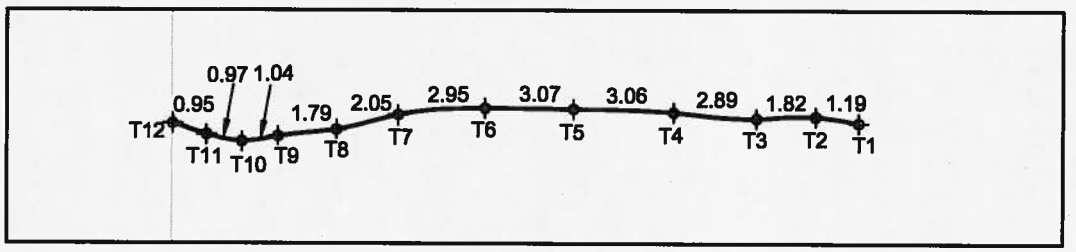

PLAN - 31S5thm00

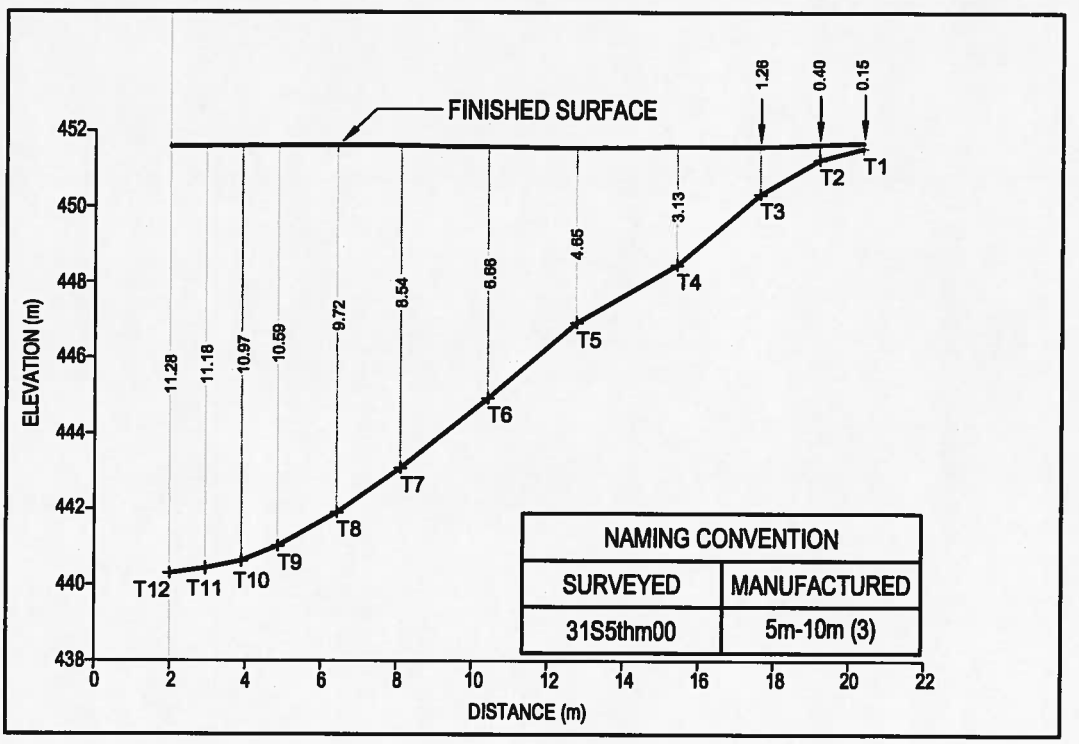

SECTION - 31S5thm00

* MANUFACTURED LENGTH 2.00 M, INSTALLED LENGTH 1.00 M
ALL DIMENSIONS IN METRES

Scale: 1: 200 (metres)

FIGURE 5.14: 31SBthm00 (5m-10m (2)) - AS MANUFACTURED, PLAN, AND SECTION

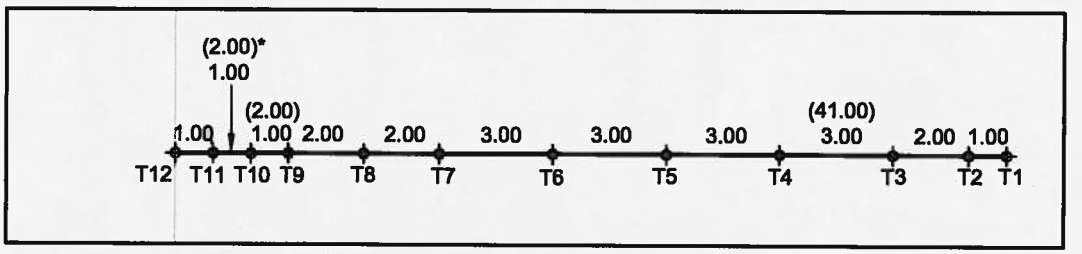

AS MANUFACTURED - 5m-10m (2)

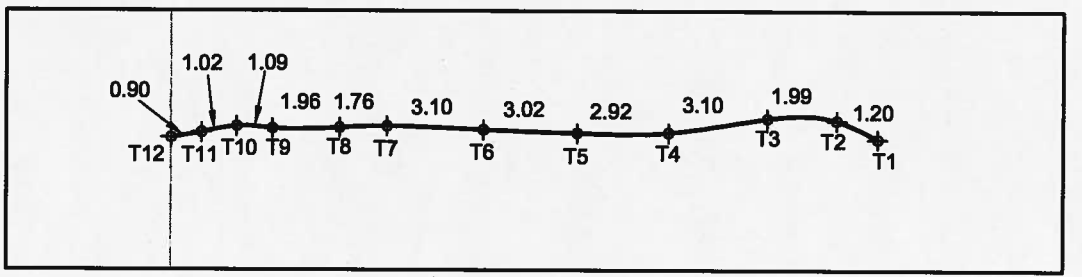

PLAN - 31SBthm00

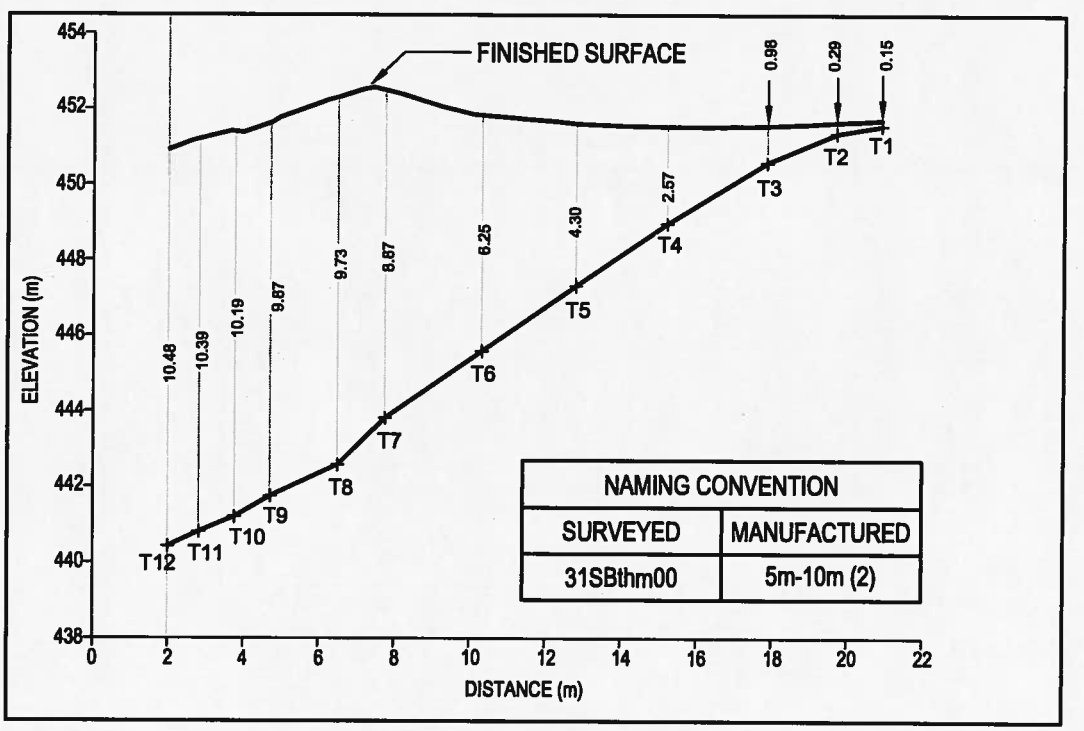

SECTION - 31SBthm00

* MANUFACTURED LENGTH 2.00 M, INSTALLED LENGTH 1.00 M
ALL DIMENSIONS IN METRES

Scale: 1: 200 (metres)

FIGURE 5.15: 32N5thm00 (15m (A)) - AS MANUFACTURED, PLAN, AND SECTION

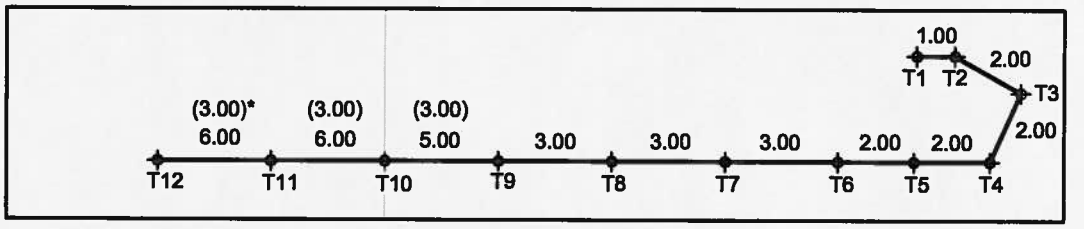

AS MANUFACTURED - 15m (A)

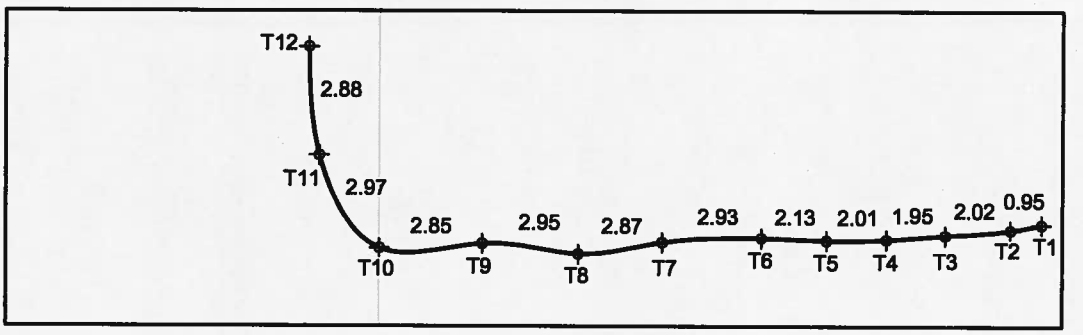

PLAN - 32N5thm00

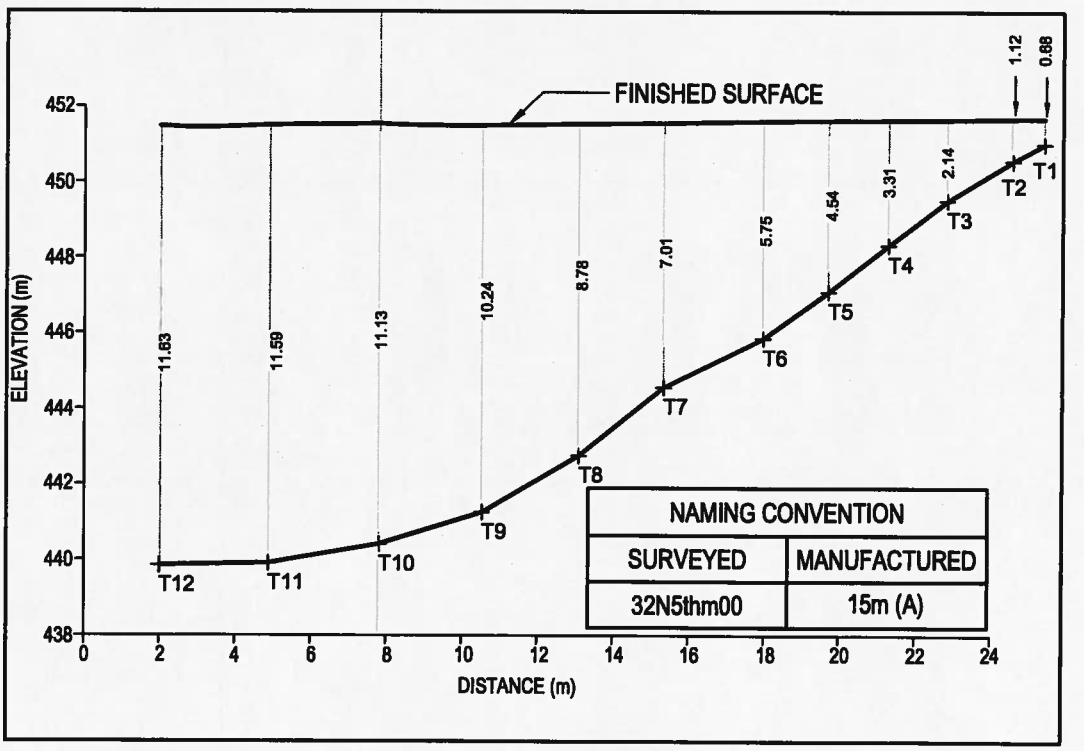

SECTION - 32N5thm00

* MANUFACTURED LENGTH 3.00 M, INSTALLED LENGTH 6.00 M
ALL DIMENSIONS IN METRES

0 10

Scale: 1: 200 (metres)

FIGURE 5.16: 32S5thm00 (15m (B)) - AS MANUFACTURED, PLAN, AND SECTION

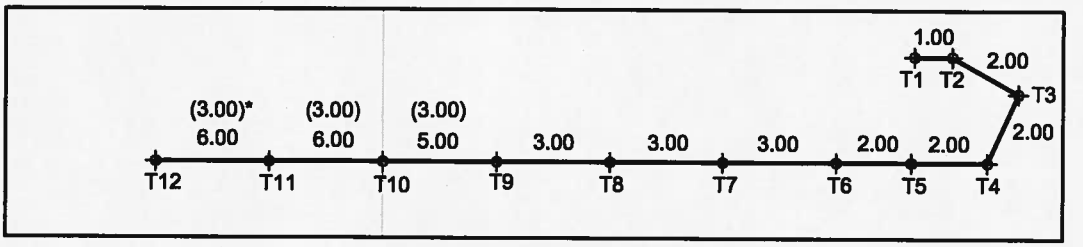

AS MANUFACTURED - 15m (B)

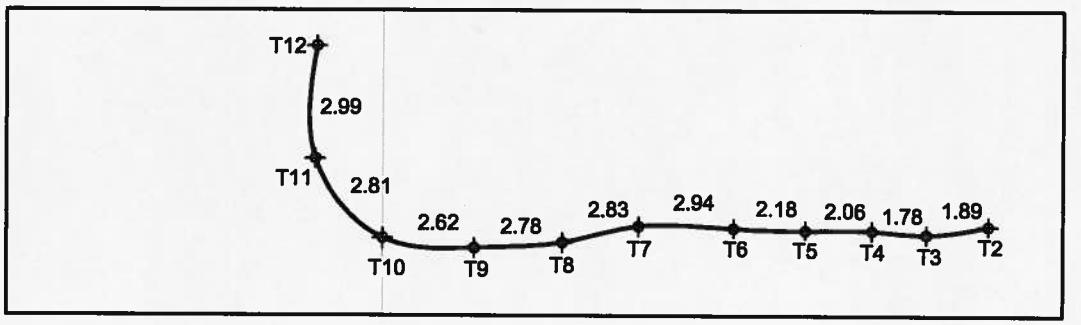

PLAN - 32S5thm00

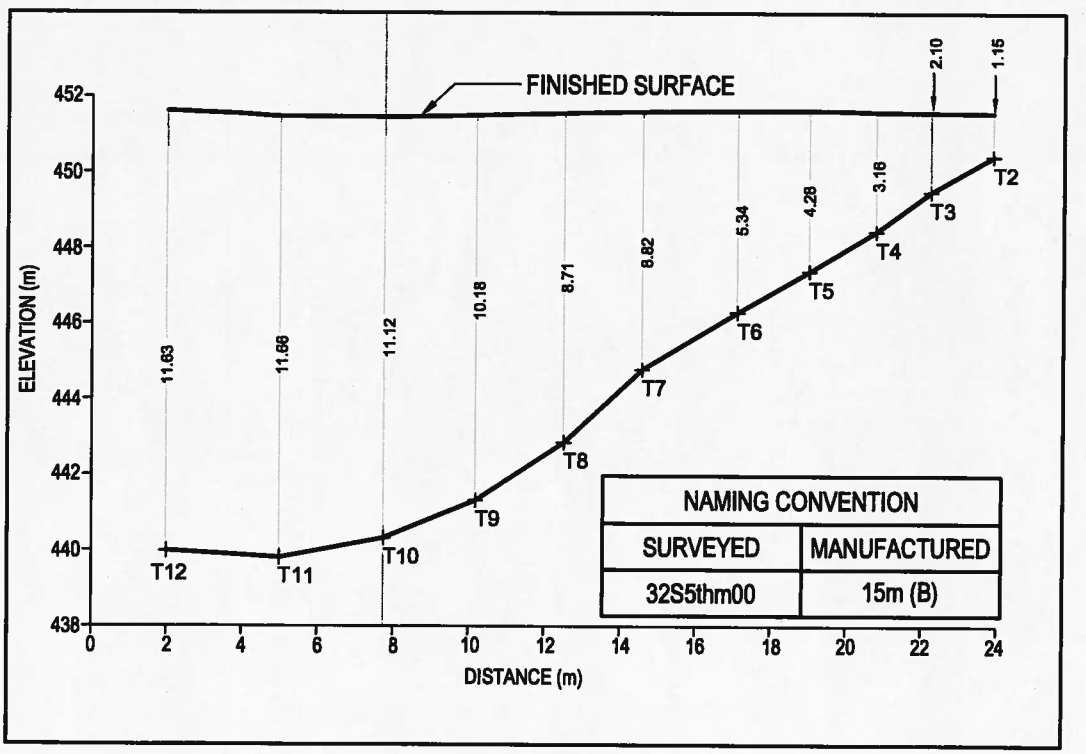

SECTION - 32S5thm00

* MANUFACTURED LENGTH 3.00 M, INSTALLED LENGTH 6.00 M

ALL DIMENSIONS IN METRES

0 10

Scale: 1: 200 (metres)

FIGURE 5.17: 34NBthm00 (5m-10m (4)) - AS MANUFACTURED, PLAN, AND SECTION

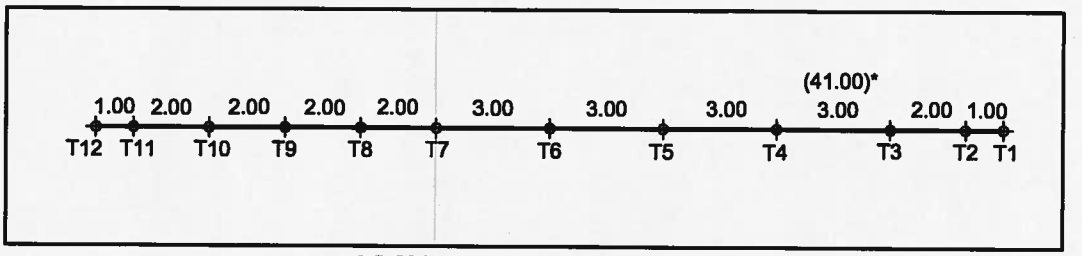

AS MANUFACTURED - 5m-10m (4)

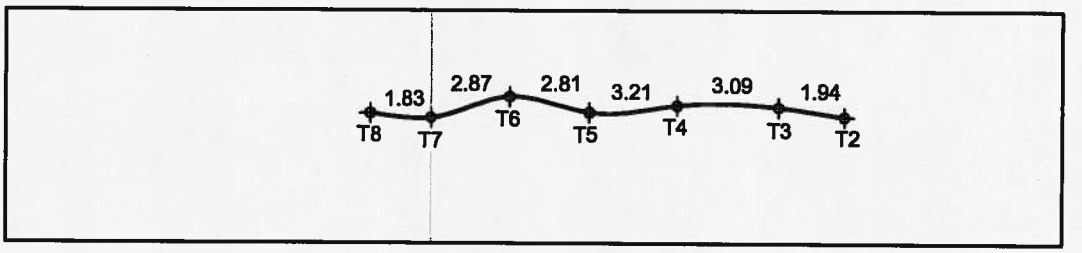

PLAN - 34NBthm00

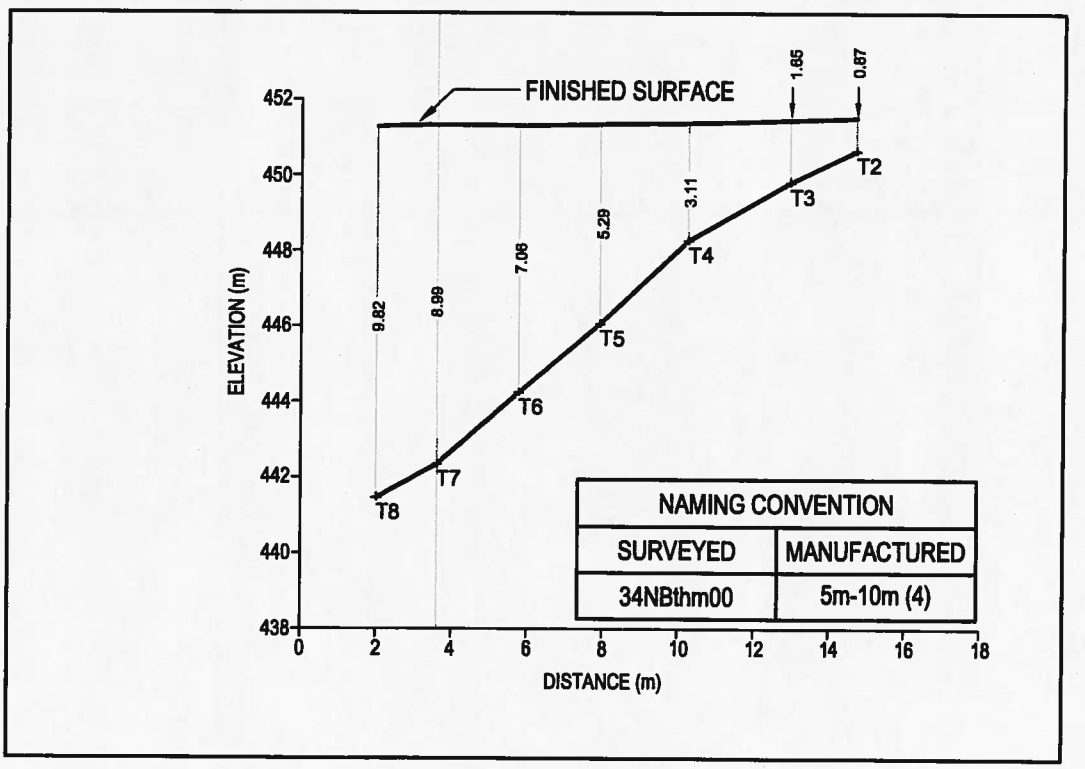

SECTION - 34NBthm00

* MANUFACTURED LENGTH 41.00 M, INSTALLED LENGTH 3.00 M

ALL DIMENSIONS IN METRES

0 10

Scale: 1: 200 (metres)

FIGURE 5.18: 34N5thm00 (5m-10m (7)) - AS MANUFACTURED, PLAN, AND SECTION

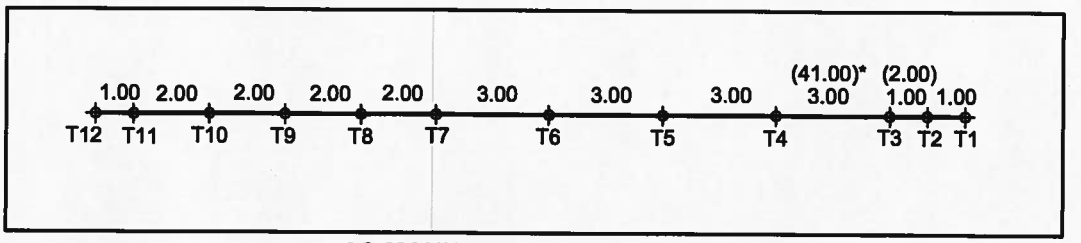

AS MANUFACTURED - 5m-10m (7)

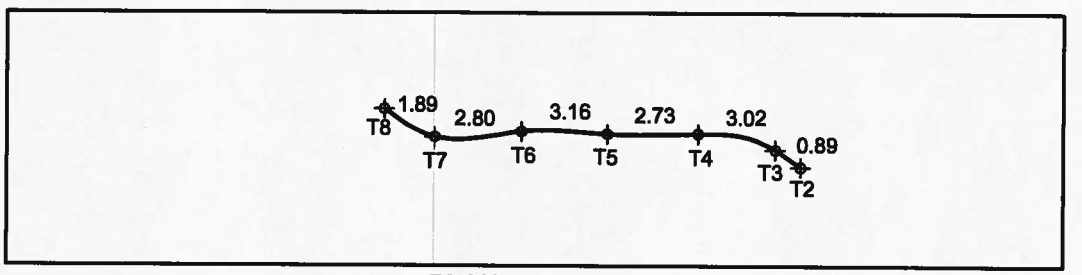

PLAN - 34N5thm00

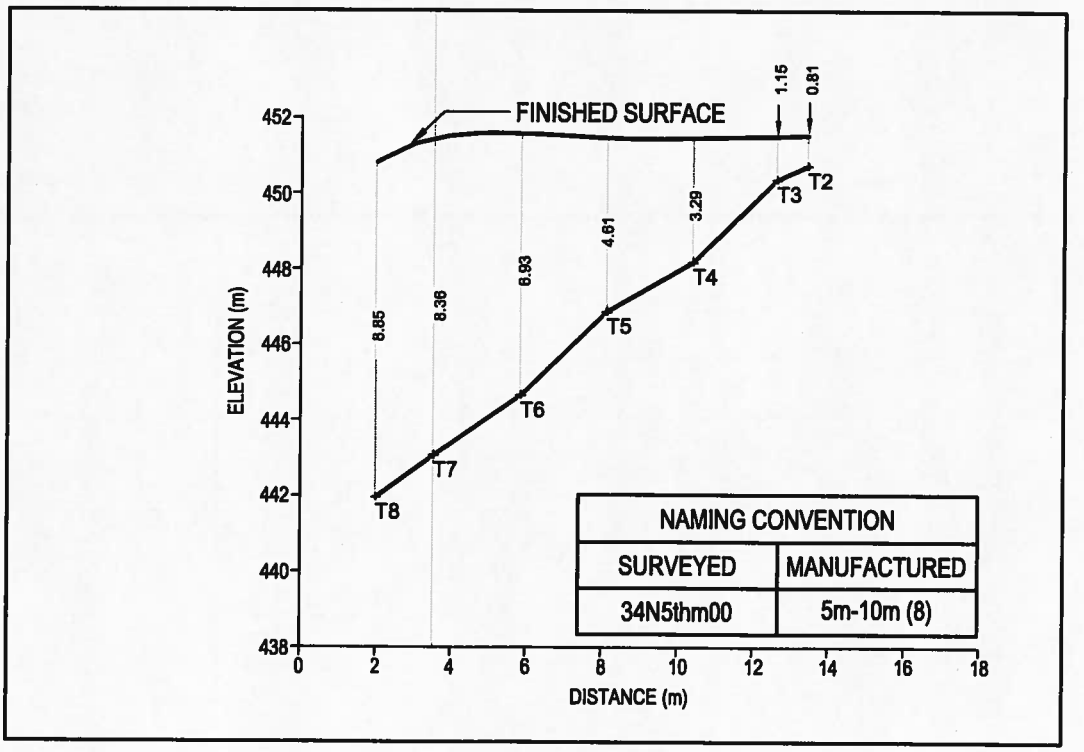

SECTION - 34N5thm00

* MANUFACTURED LENGTH 41.00 M, INSTALLED LENGTH 3.00 M
ALL DIMENSIONS IN METRES

Scale: 1: 200 (metres)

FIGURE 5.19: 34S5thm00 (5m-10m (8)) - AS MANUFACTURED, PLAN, AND SECTION

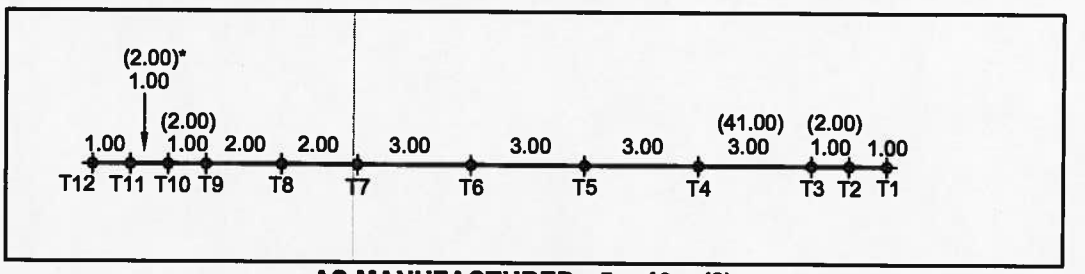

AS MANUFACTURED - 5m-10m (8)

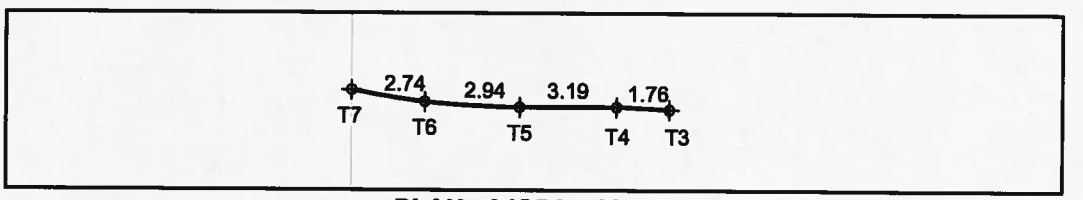

PLAN - 34S5thm00

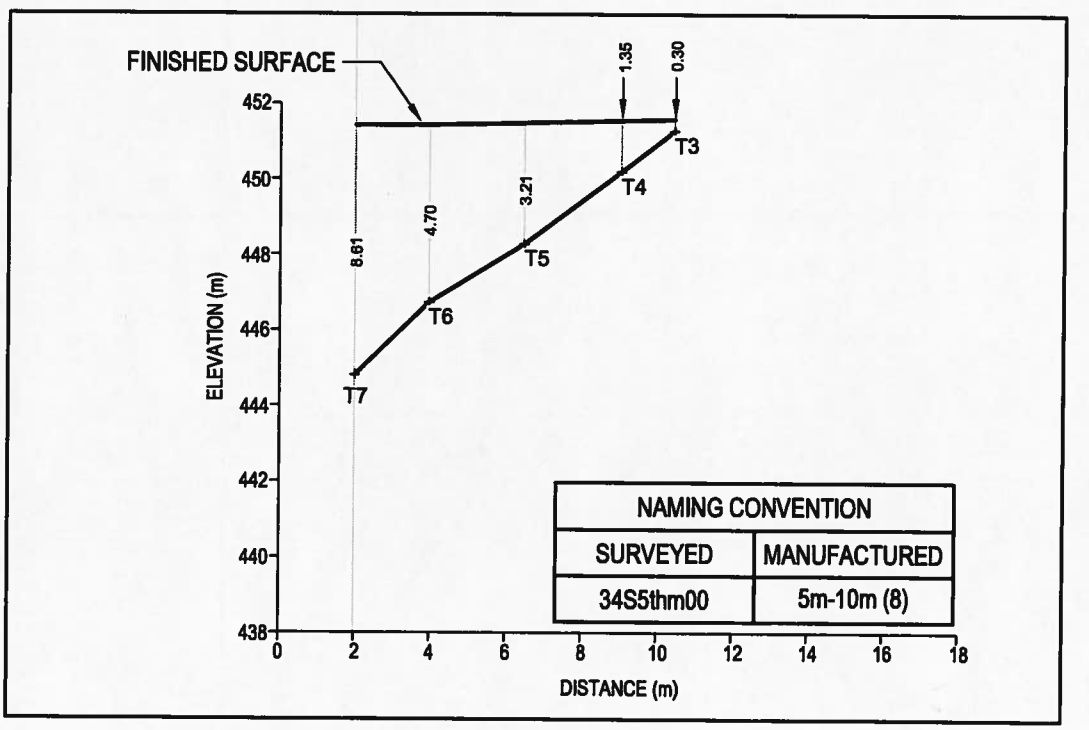

SECTION - 34S5thm00

* MANUFACTURED LENGTH 2.00 M, INSTALLED LENGTH 1.00 M

ALL DIMENSIONS IN METRES

Scale: 1: 200 (metres)

FIGURE 5.20: 34SBthm00 (5m-10m (5)) - AS MANUFACTURED, PLAN, AND SECTION

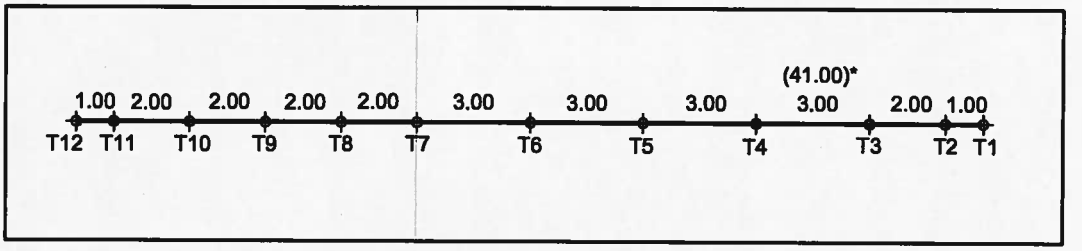

AS MANUFACTURED - 5m-10m (5)

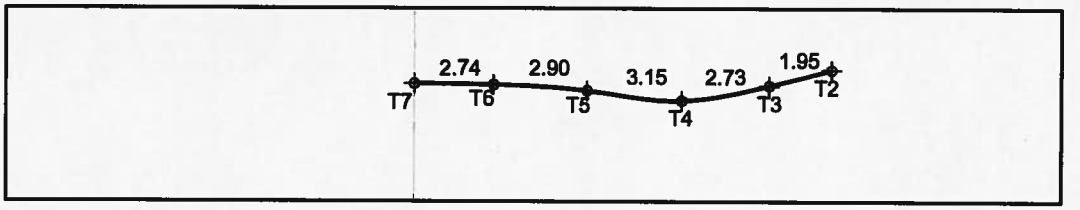

PLAN - 34SBthm00

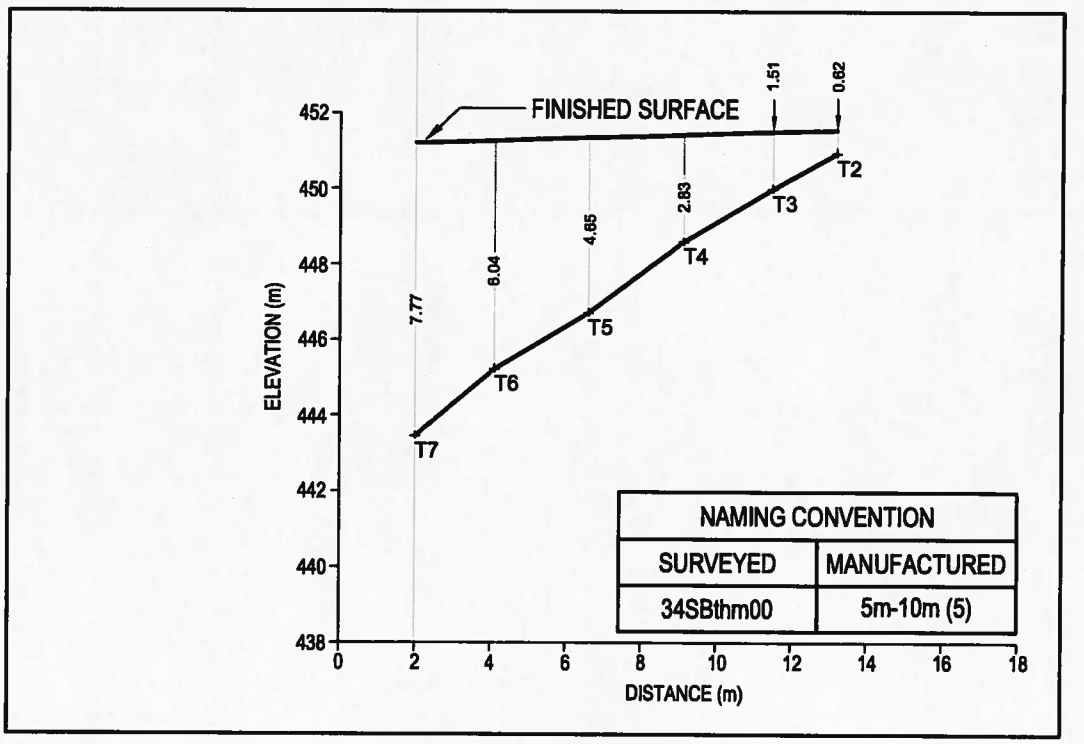

SECTION - 34SBthm00

* MANUFACTURED LENGTH 41.00 M, INSTALLED LENGTH 3.00 M
ALL DIMENSIONS IN METRES

0 10

Scale: 1: 200 (metres)

FIGURE 5.21: TI PILE SURFACE AND TIII PILE SURFACE

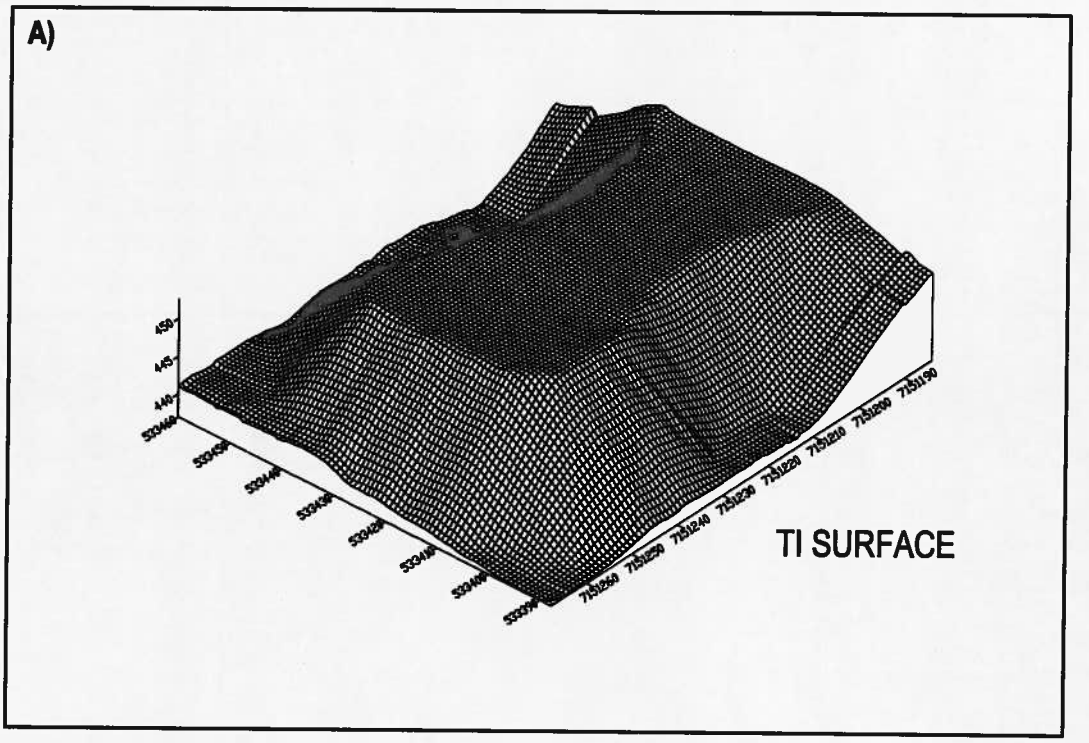

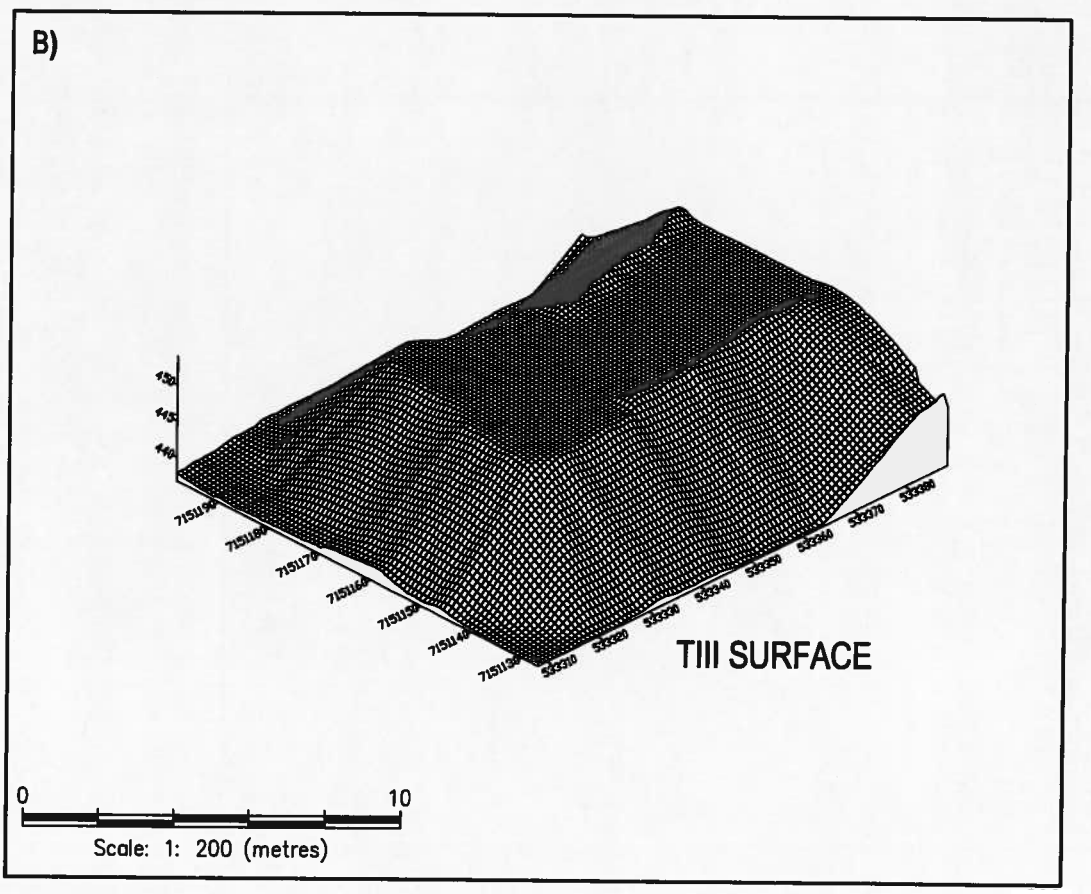

FIGURE 6.1: ONE-DIMENSIONAL GEOSTUDIO MODEL USED IN CALIBRATION ANALYSIS

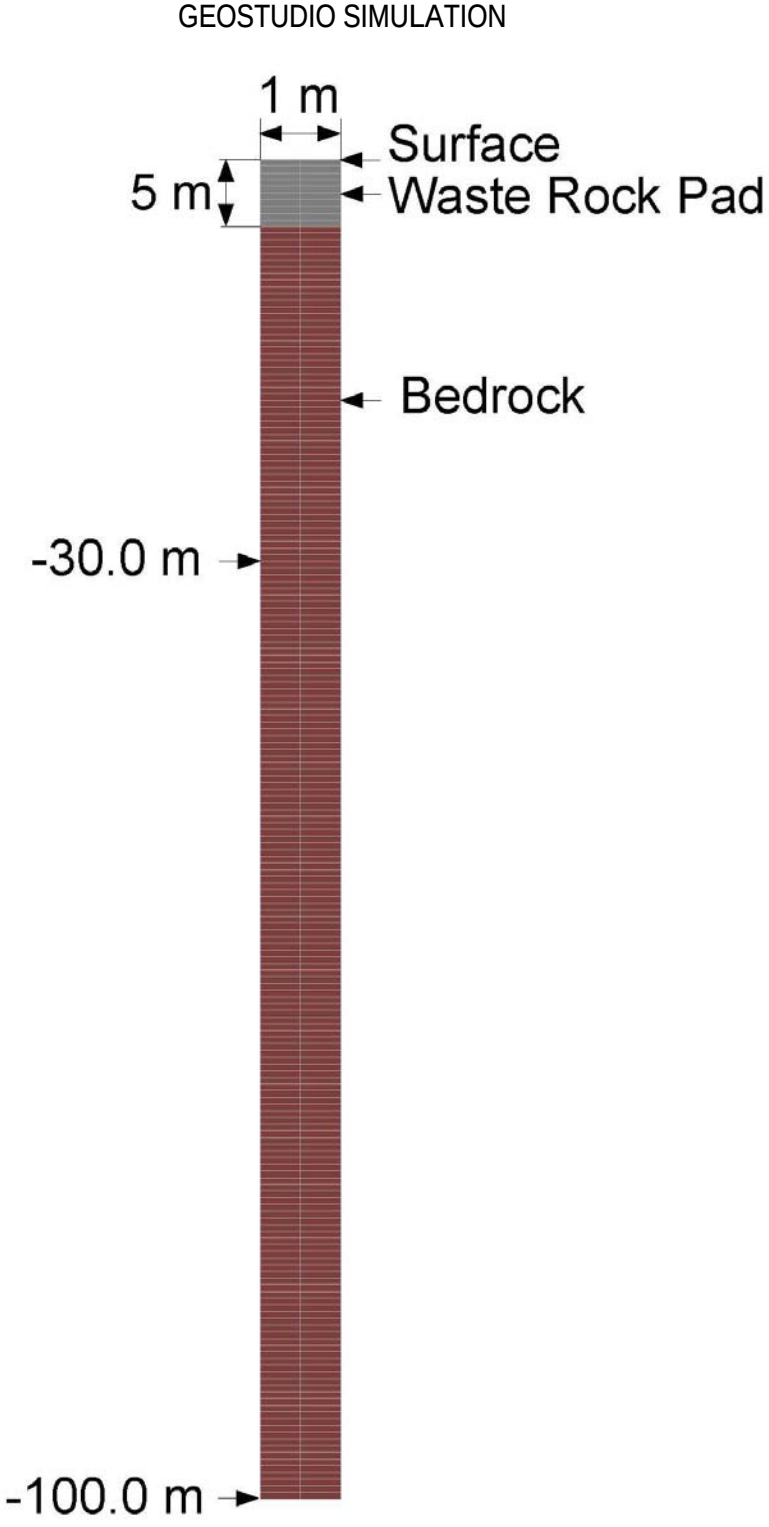

FIGURE 6.2: STEADY STATE BOUNDARY CONDITIONS APPLIED TO ONE-DIMENSIONAL GEOSTUDIO MODEL USED IN CALIBRATION ANALYSIS

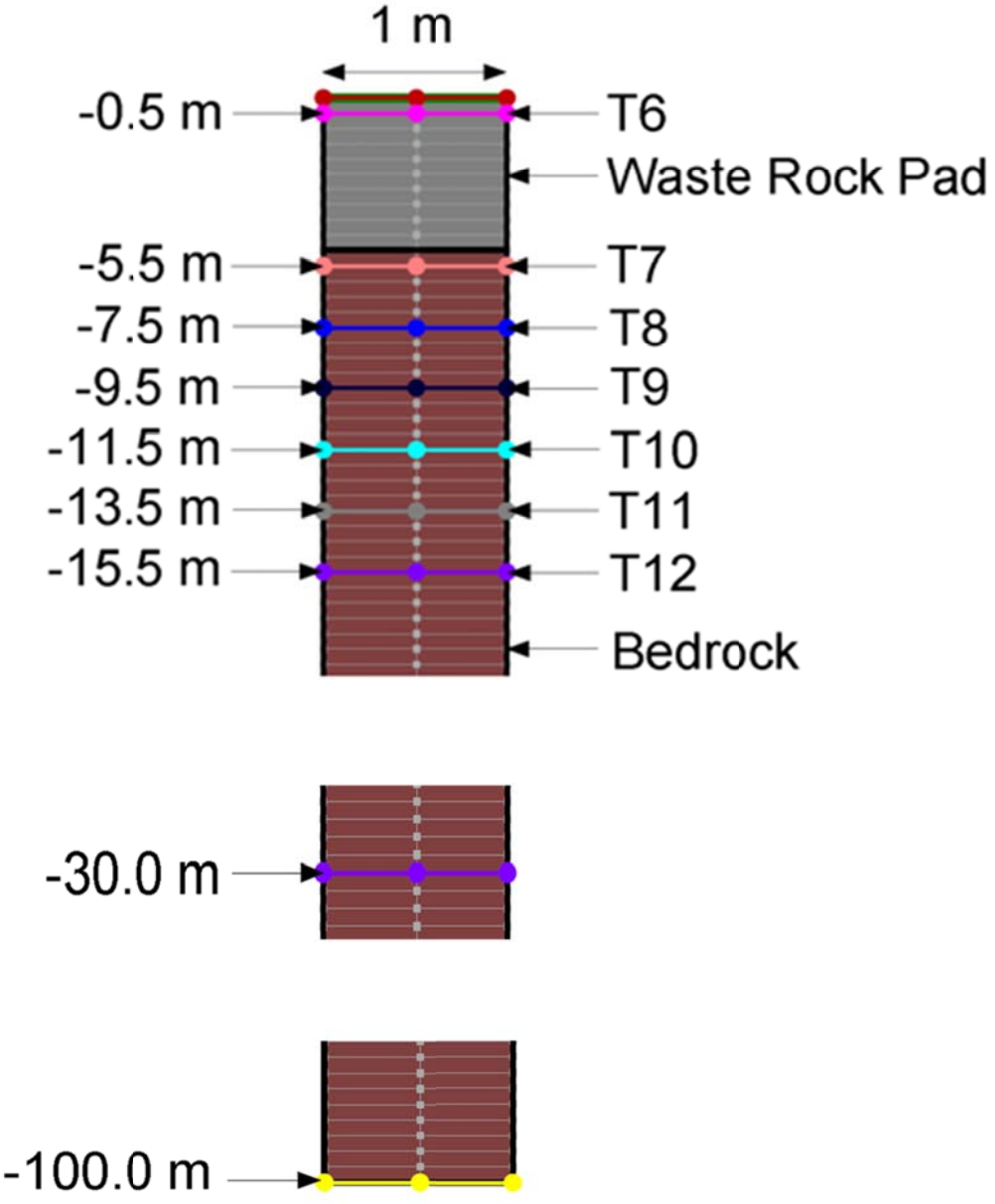

FIGURE 6.3: TRANSIENT STATE BOUNDARY CONDITIONS APPLIED TO GEOSTUDIO MODEL USED IN CALIBRATION ANALYSIS

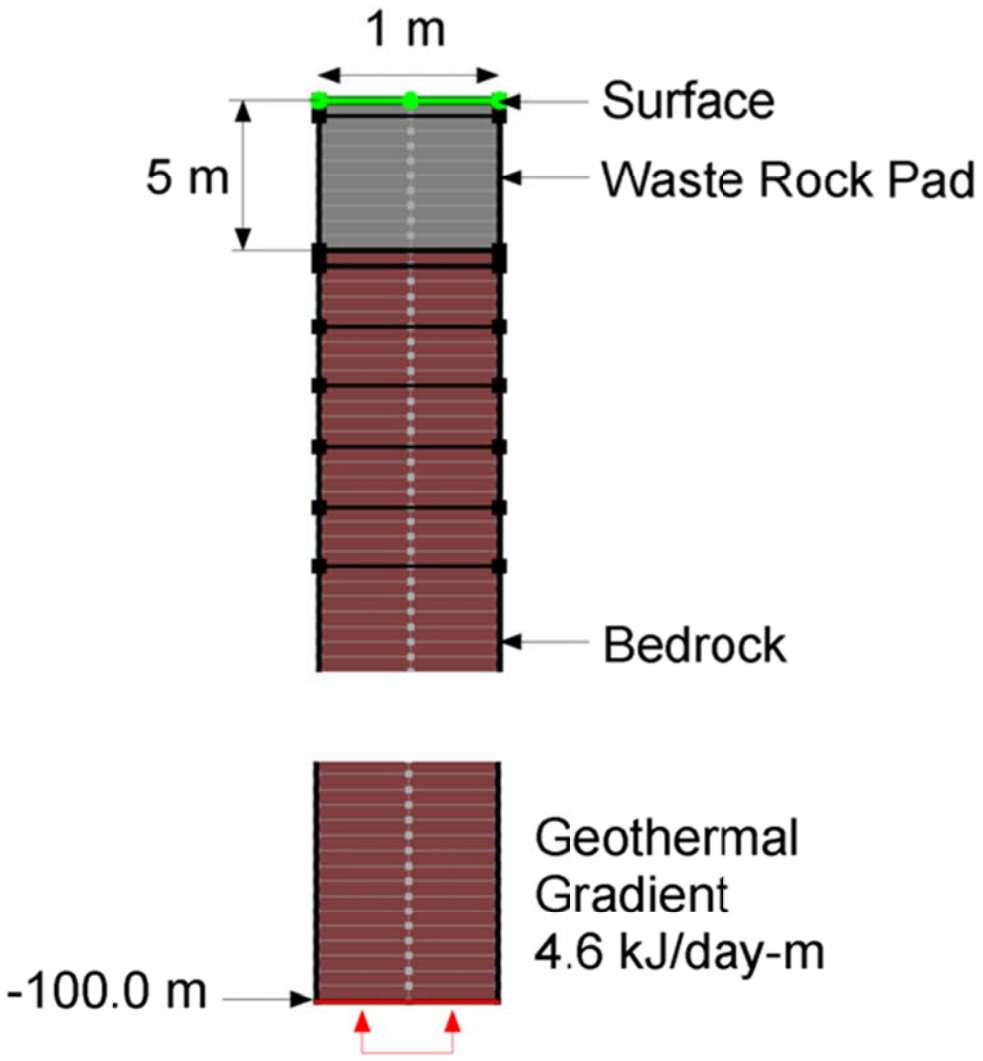

FIGURE 6.4: RESULTS OF CALIBRATION ANALYSIS; COMPARISON BETWEEN TEMPERATURES MEASURED IN JUNE, JULY AND AUGUST 2006 AND MODELED TEMPERATURES IN JUNE 2006

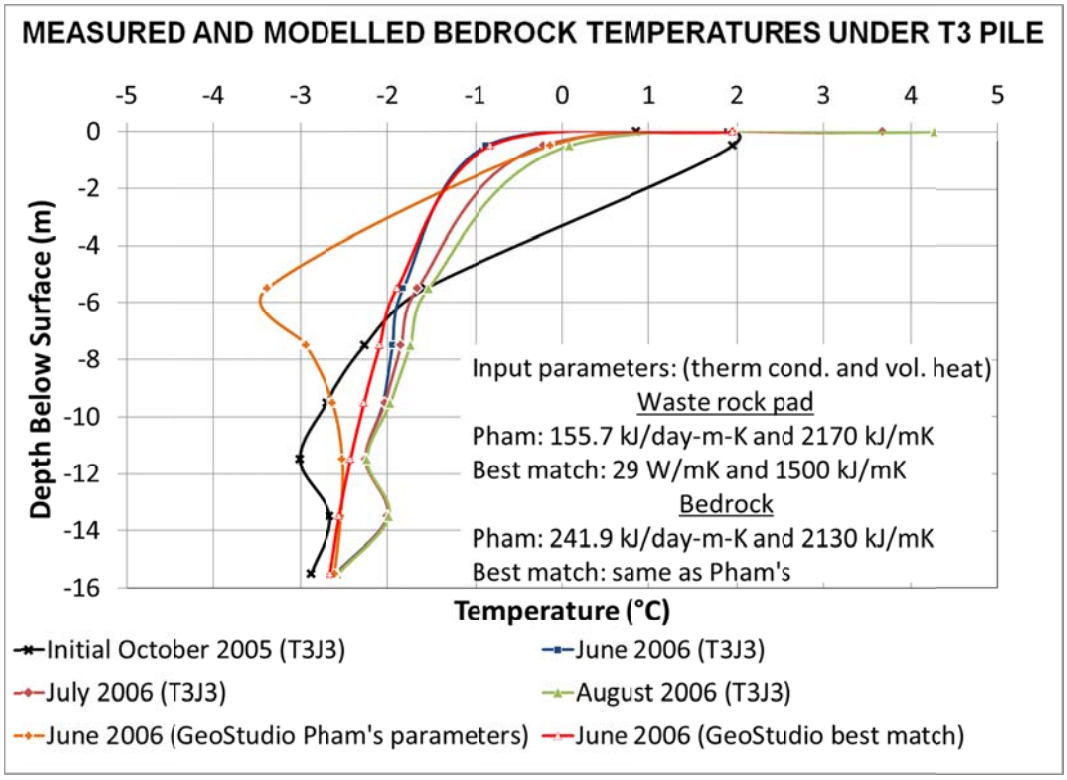

A) Results of GeoStudio modeling with Pham's parameters and with best match parameters

FIGURE 6.5: GEOSTUDIO MODEL USED TO MODEL DIAVIK WASTE ROCK TEST PILE

GEOSTUDIO SIMULATION

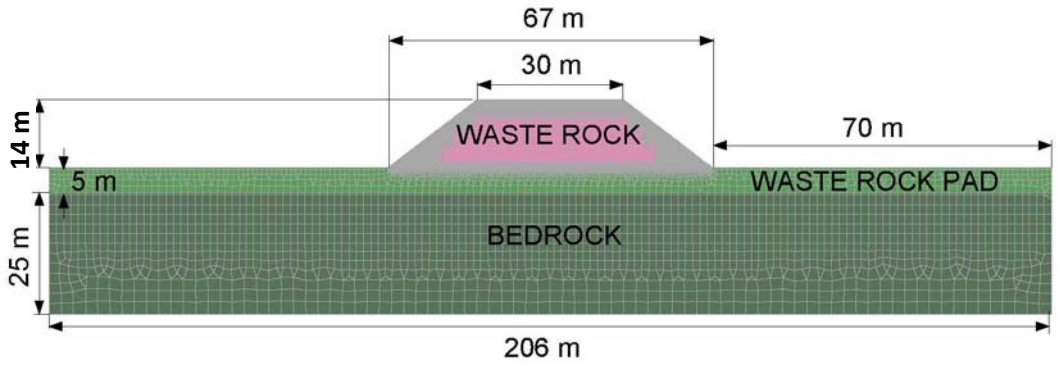

A) Model dimensions; 32,332 nodes and 32,840 elements

FIGURE 6.6: TEMPERATURE MEASURING LOCATIONS IN AND UNDER DIAVIK WASTE ROCK TEST PILE

GEOSTUDIO SIMULATION

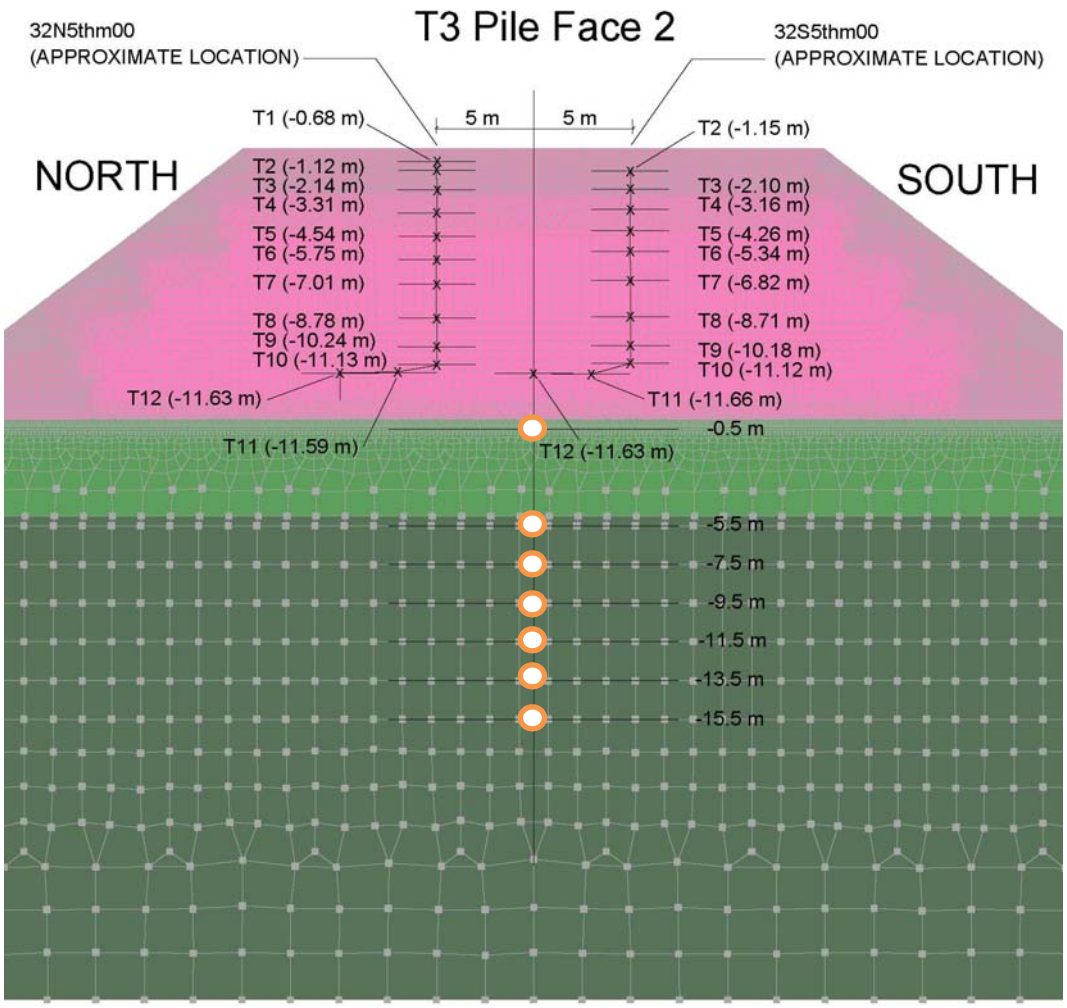

A) Face 2 of the Type 3 Pile

FIGURE 6.7: TYPE 3 PILE IN PLAN VIEW SHOWING GROUND TEMPERATURE CABLES 32N5THM00, 32S5THM00, AND T3J3

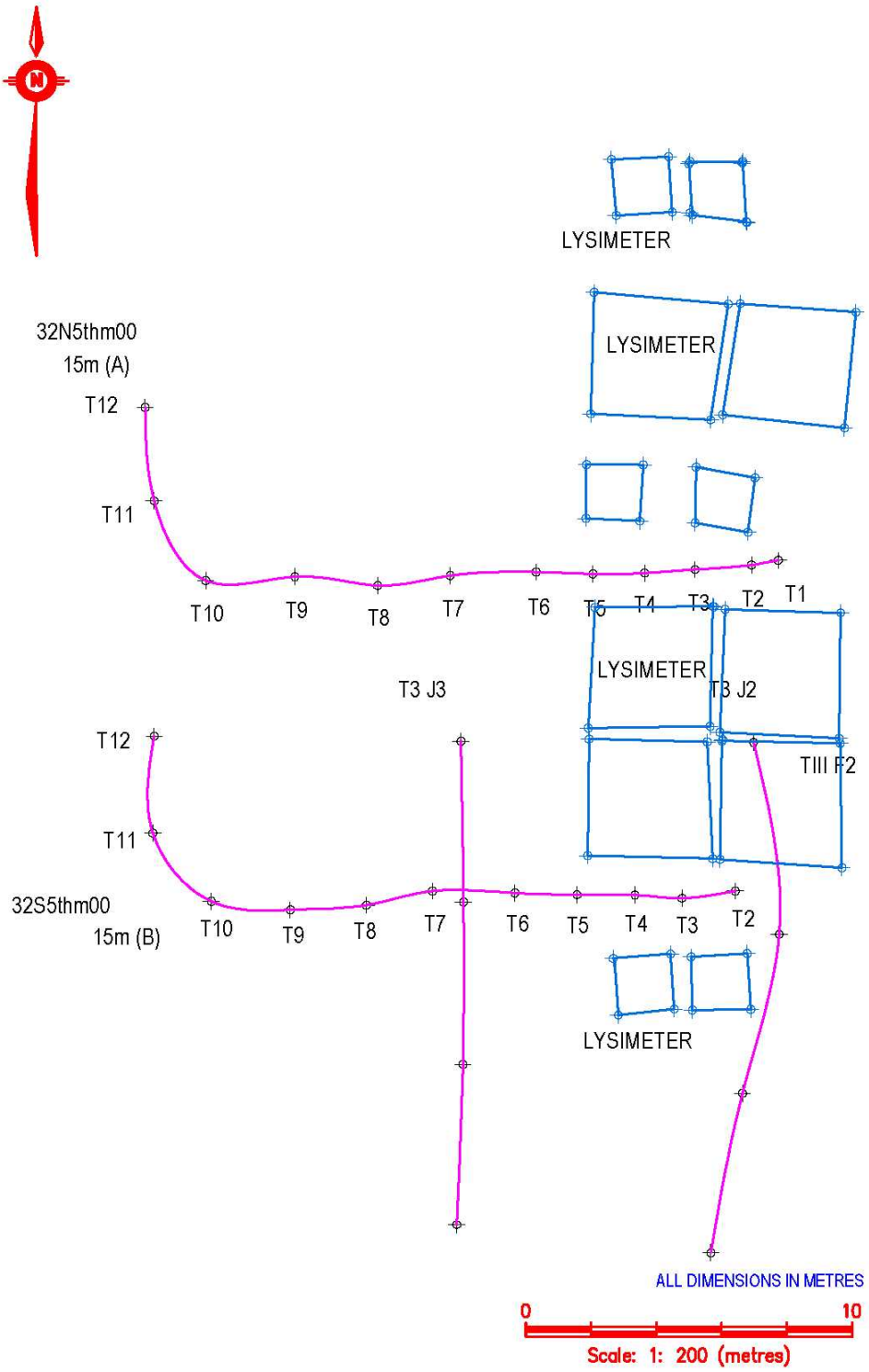

FIGURE 6.8: SURFACE TEMPERATURES IN TYPE 3 PILE

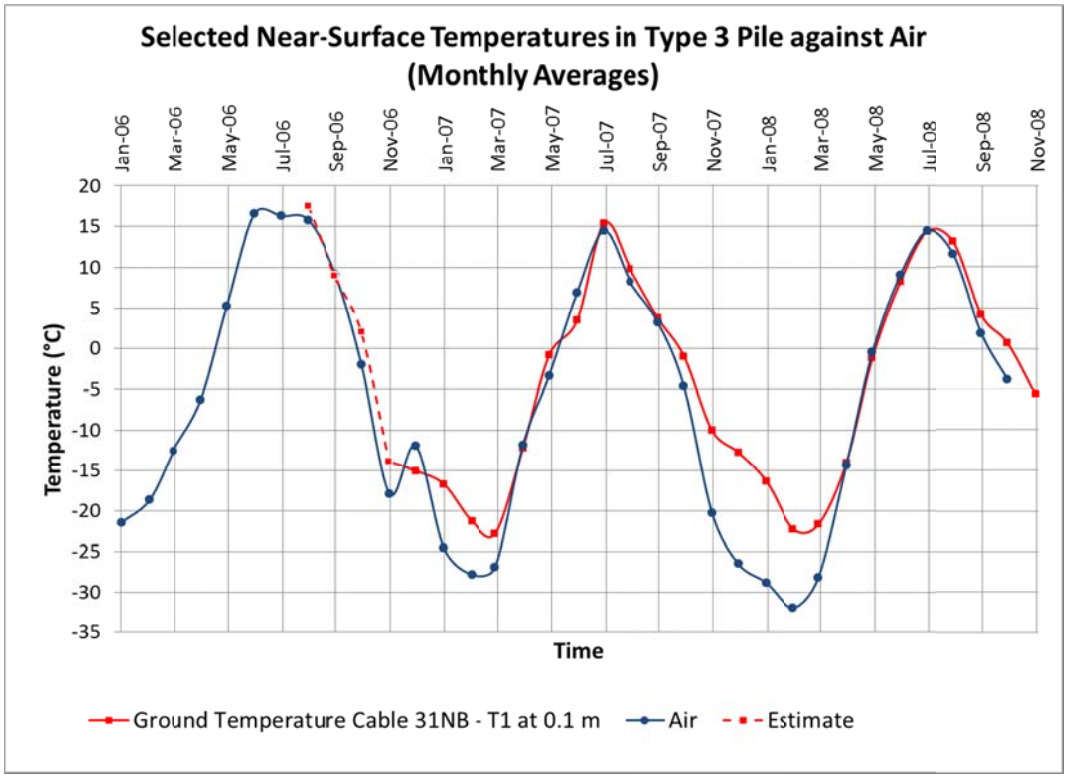

A) Thermistor bead T1 on Ground Temperature Cable 31NBthm000

FIGURE 6.9: ISOTHERMS AND AIR FLOW VECTORS ON MARCH 18, 2007 AND MARCH 19, 2008 IN DIAVIK WASTE ROCK TEST PILE MODEL

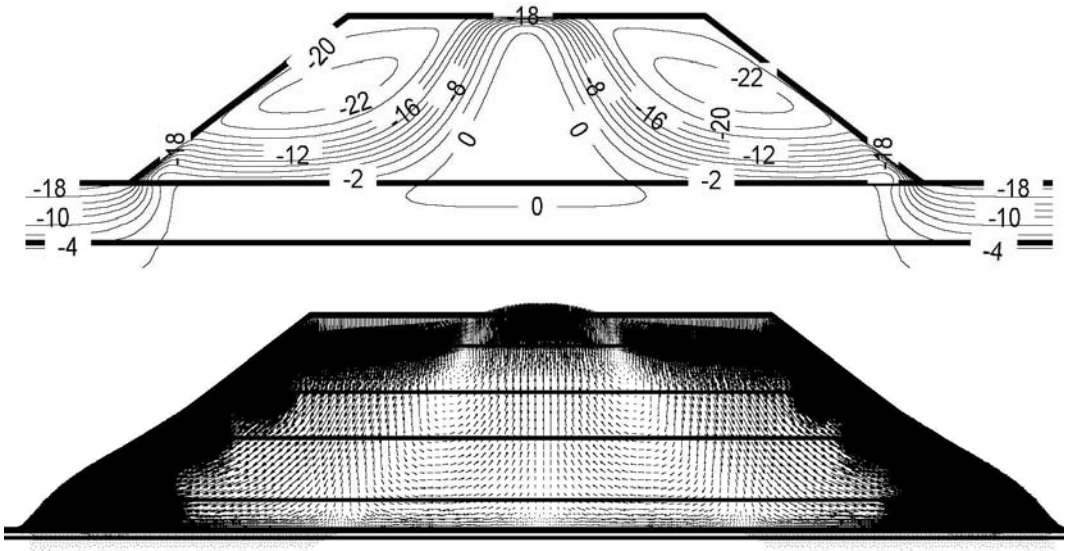

A) Isotherms (top) and air flow vectors (bottom) on March 18, 2007 (GeoStudio Diavik model)

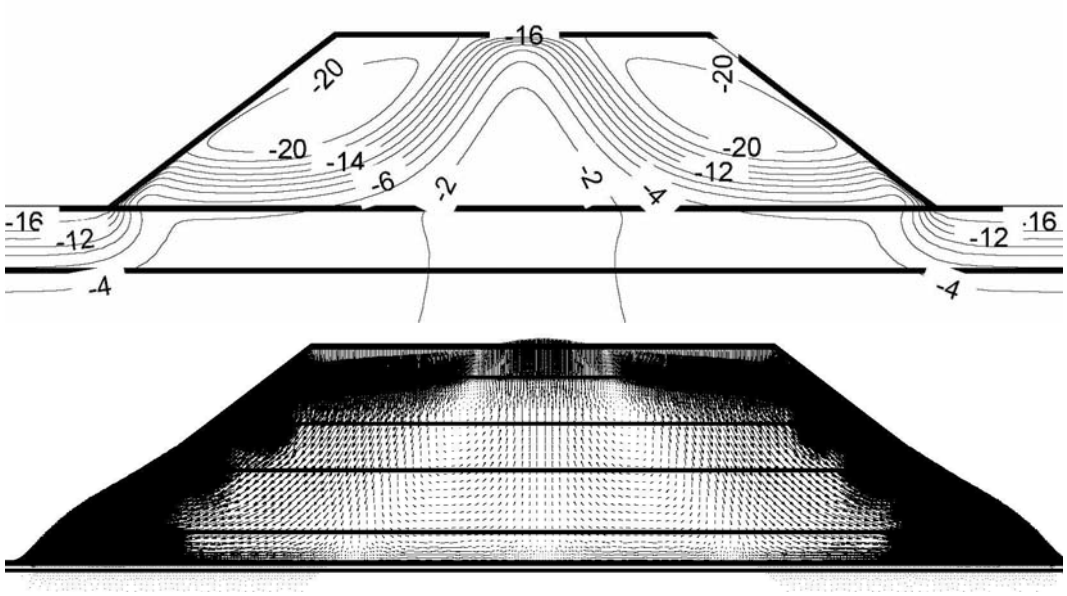

B) Isotherms (top) and air flow vectors (bottom) on March 19, 2008 (GeoStudio Diavik model)

FIGURE 6.10: COMPARISON OF MODELLED AND MEASURED TEMPERATURES IN LOCATION OF GROUND TEMPERATURE CABLES 32N5THM00 AND 32S5THM00; THERMISTOR BEAD T1

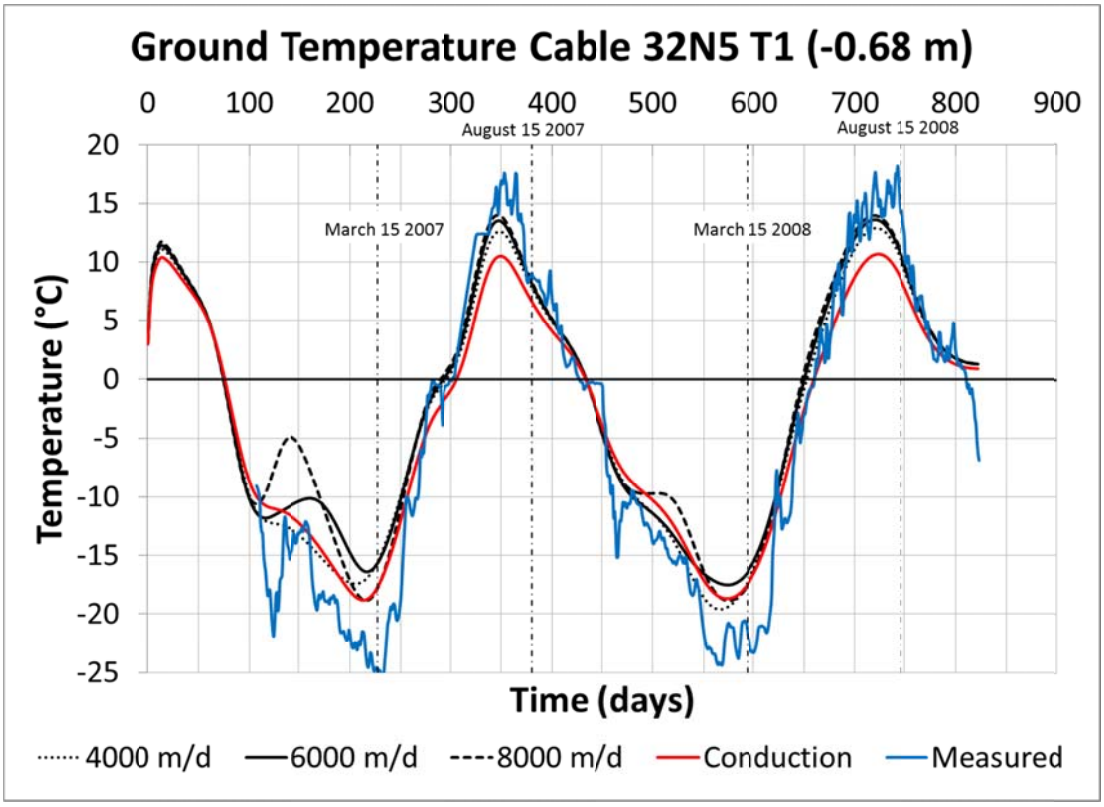

FIGURE 6.11: COMPARISON OF MODELLED AND MEASURED TEMPERATURES IN LOCATION OF GROUND TEMPERATURE CABLES 32N5THM00 AND 32S5THM00; THERMISTOR BEAD T2

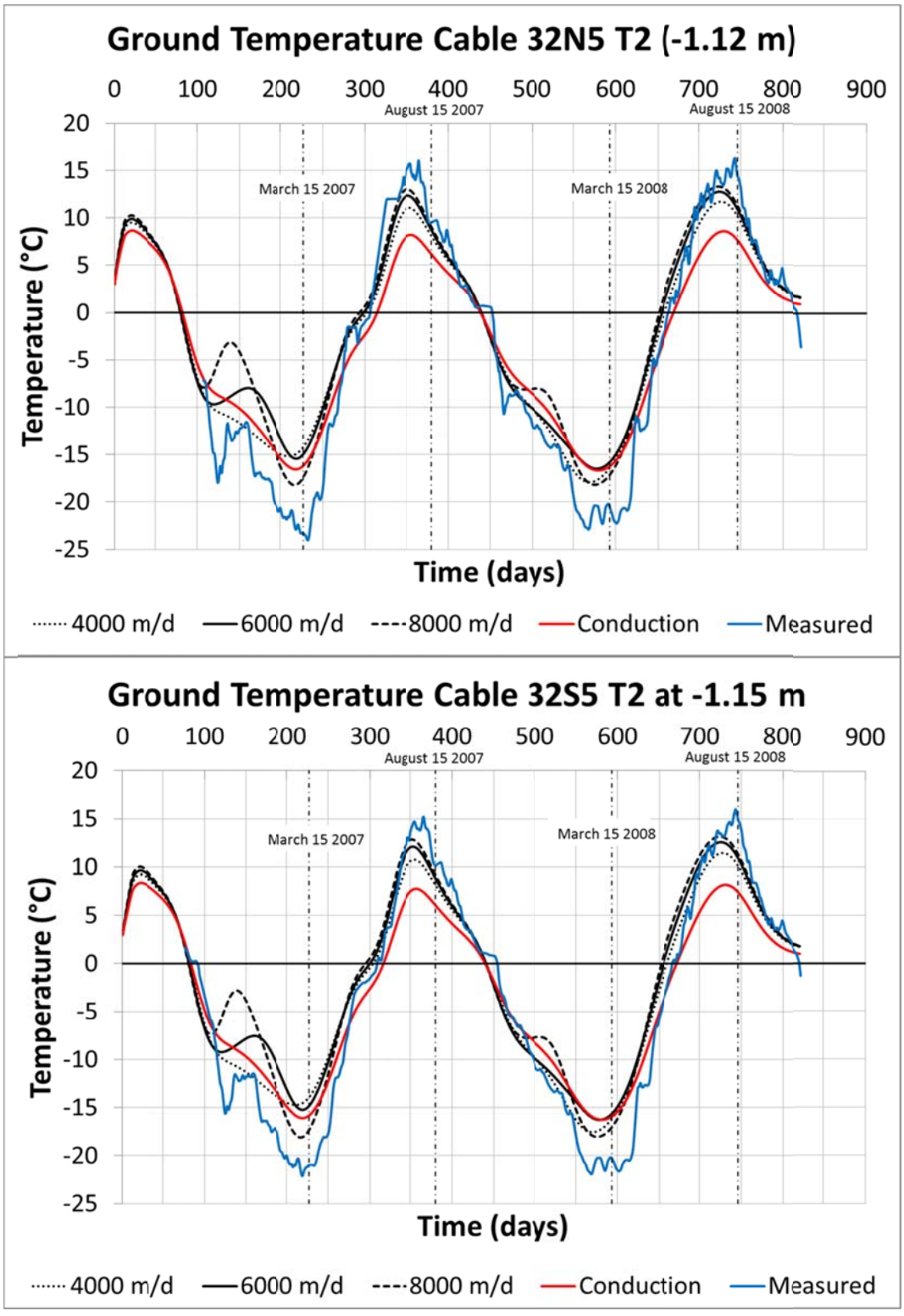

FIGURE 6.12: COMPARISON OF MODELLED AND MEASURED TEMPERATURES IN LOCATION OF GROUND TEMPERATURE CABLES 32N5THM00 AND 32S5THM00; THERMISTOR BEAD T3

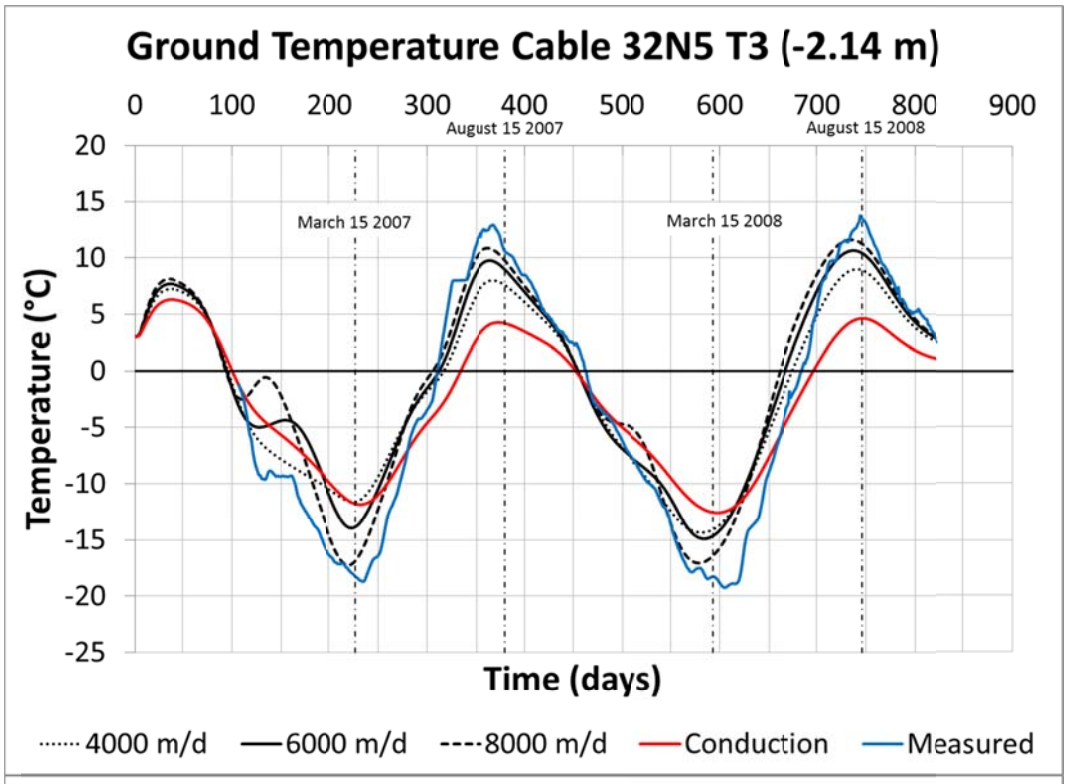

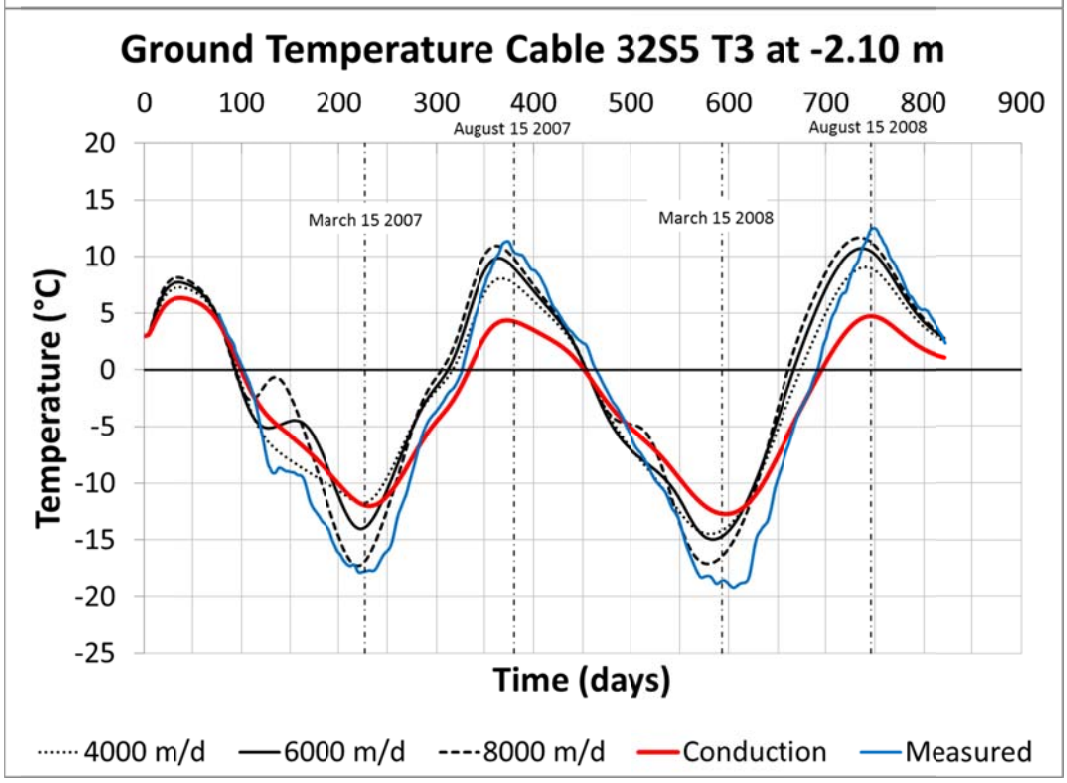

FIGURE 6.13: COMPARISON OF MODELLED AND MEASURED TEMPERATURES IN LOCATION OF GROUND TEMPERATURE CABLES 32N5THM00 AND 32S5THM00; THERMISTOR BEAD T4

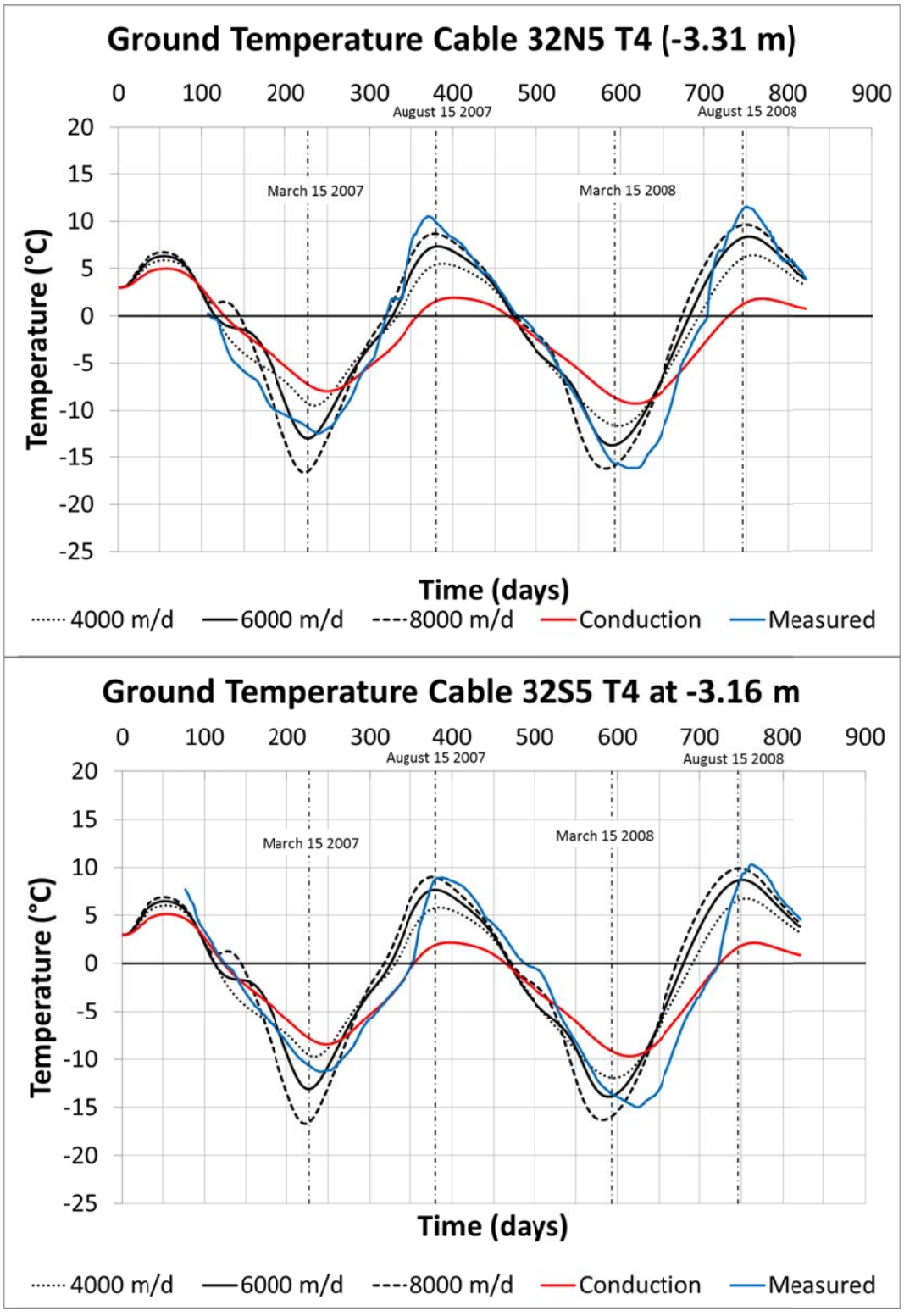

FIGURE 6.14: COMPARISON OF MODELLED AND MEASURED TEMPERATURES IN LOCATION OF GROUND TEMPERATURE CABLES 32N5THM00 AND 32S5THM00; THERMISTOR BEAD T5

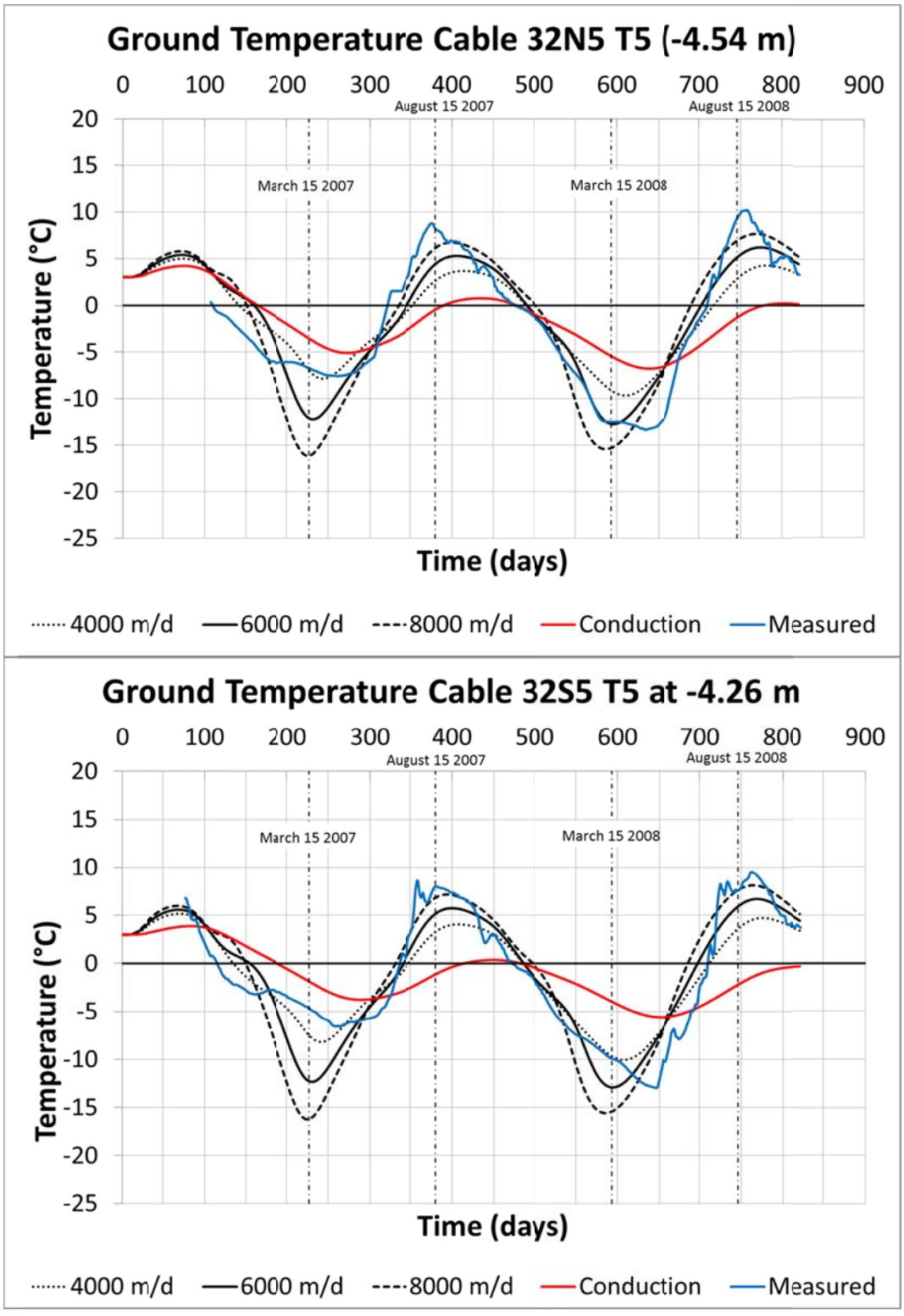

FIGURE 6.15: COMPARISON OF MODELLED AND MEASURED TEMPERATURES IN LOCATION OF GROUND TEMPERATURE CABLES 32N5THM00 AND 32S5THM00; THERMISTOR BEAD T6

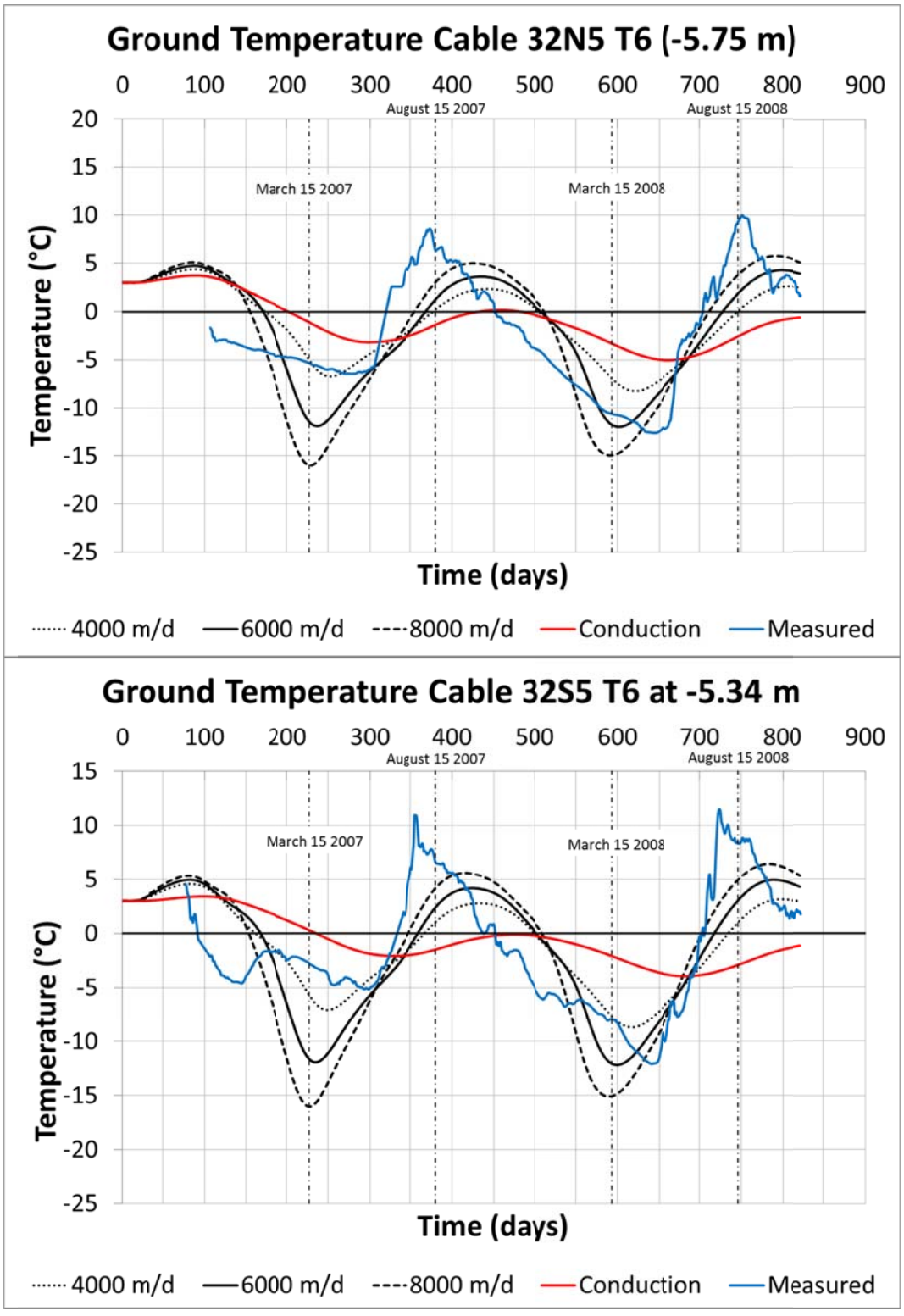

FIGURE 6.16: COMPARISON OF MODELLED AND MEASURED TEMPERATURES IN LOCATION OF GROUND TEMPERATURE CABLES 32N5THM00 AND 32S5THM00; THERMISTOR BEAD T7

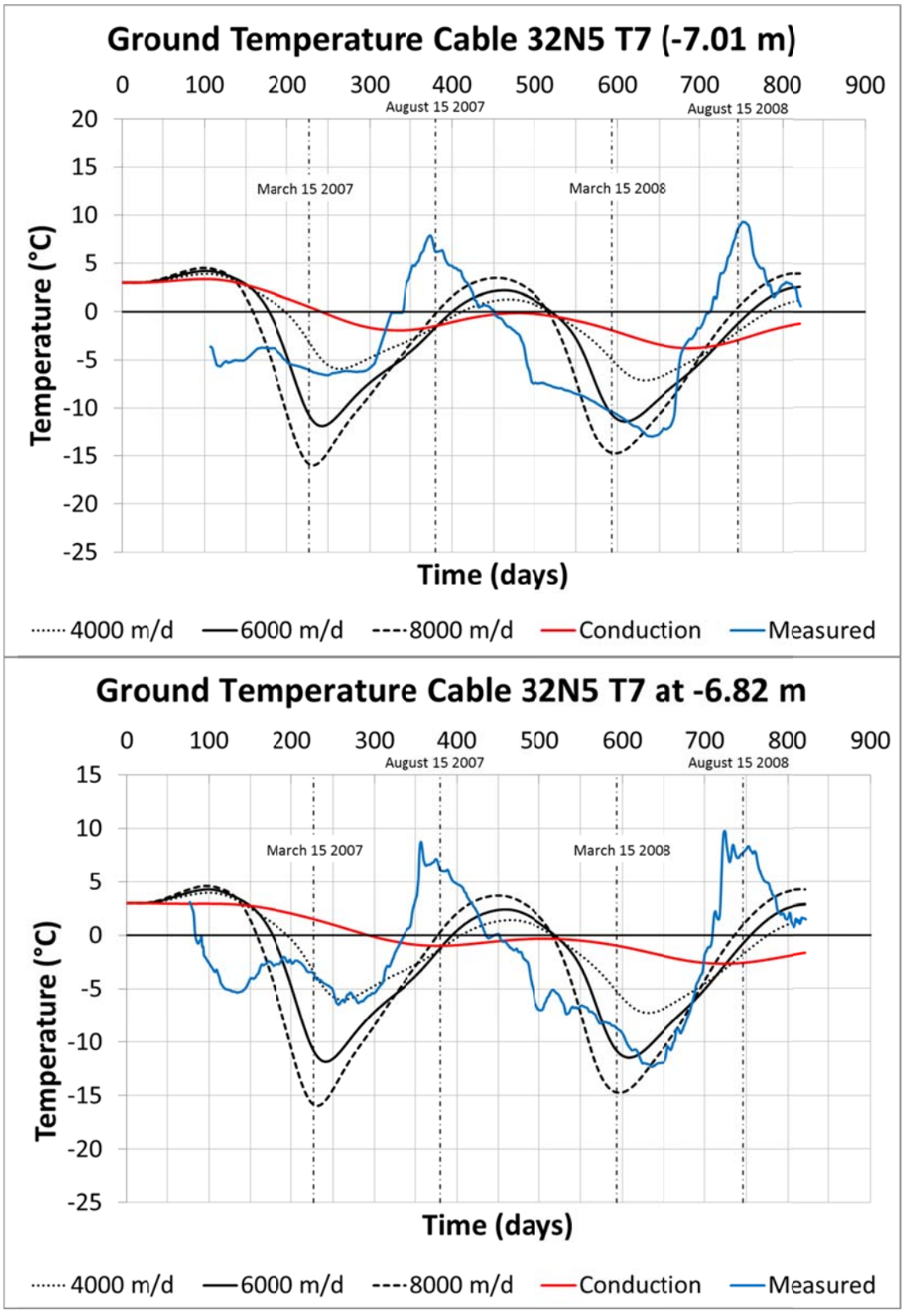

FIGURE 6.17: COMPARISON OF MODELLED AND MEASURED TEMPERATURES IN LOCATION OF GROUND TEMPERATURE CABLES 32N5THM00 AND 32S5THM00; THERMISTOR BEAD T8

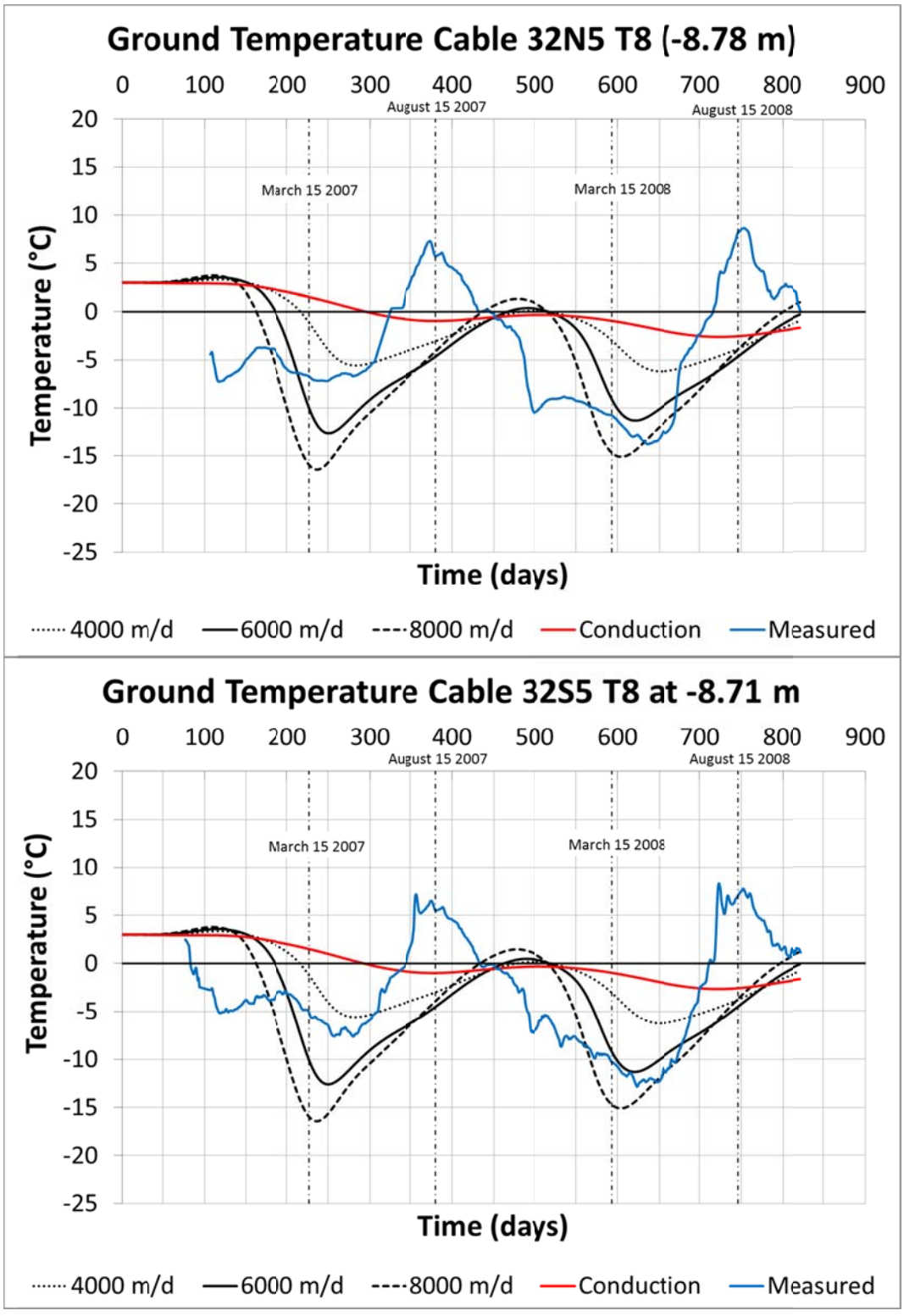

FIGURE 6.18: COMPARISON OF MODELLED AND MEASURED TEMPERATURES IN LOCATION OF GROUND TEMPERATURE CABLES 32N5THM00 AND 32S5THM00; THERMISTOR BEAD T9

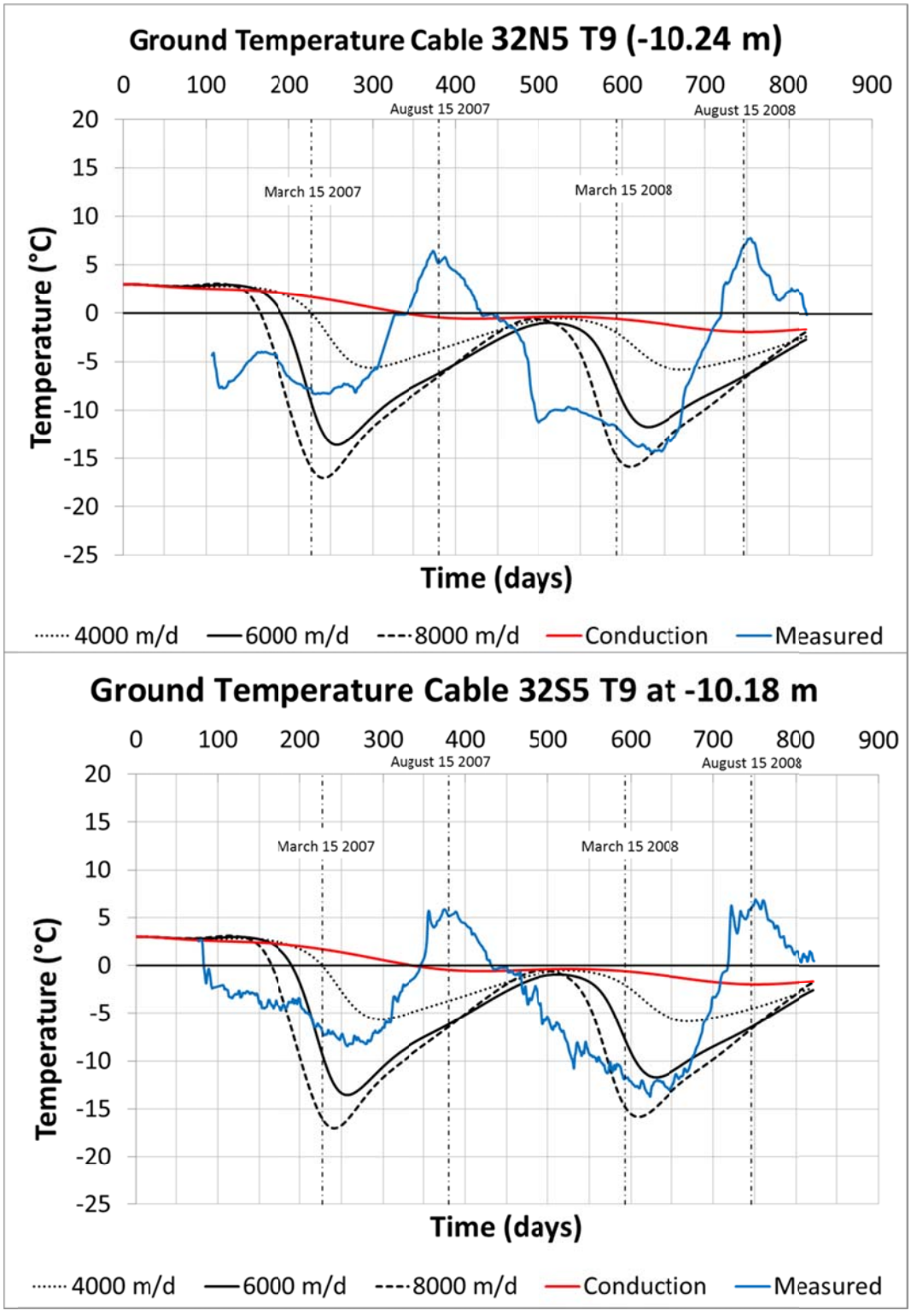

FIGURE 6.19: COMPARISON OF MODELLED AND MEASURED TEMPERATURES IN LOCATION OF GROUND TEMPERATURE CABLES 32N5THM00 AND 32S5THM00; THERMISTOR BEAD T10

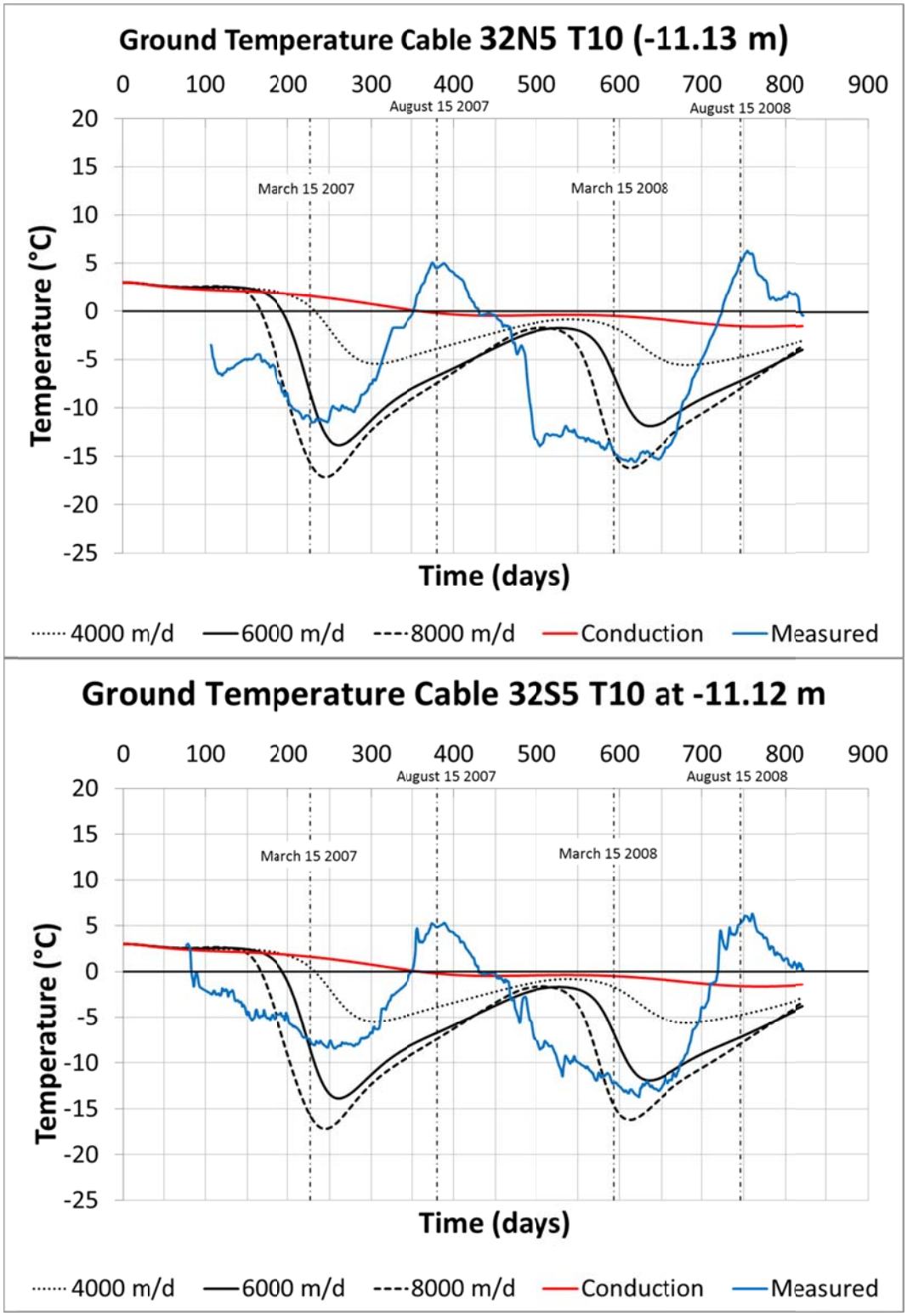

FIGURE 6.20: COMPARISON OF MODELLED AND MEASURED TEMPERATURES IN LOCATION OF GROUND TEMPERATURE CABLES 32N5THM00 AND 32S5THM00; THERMISTOR BEAD T11

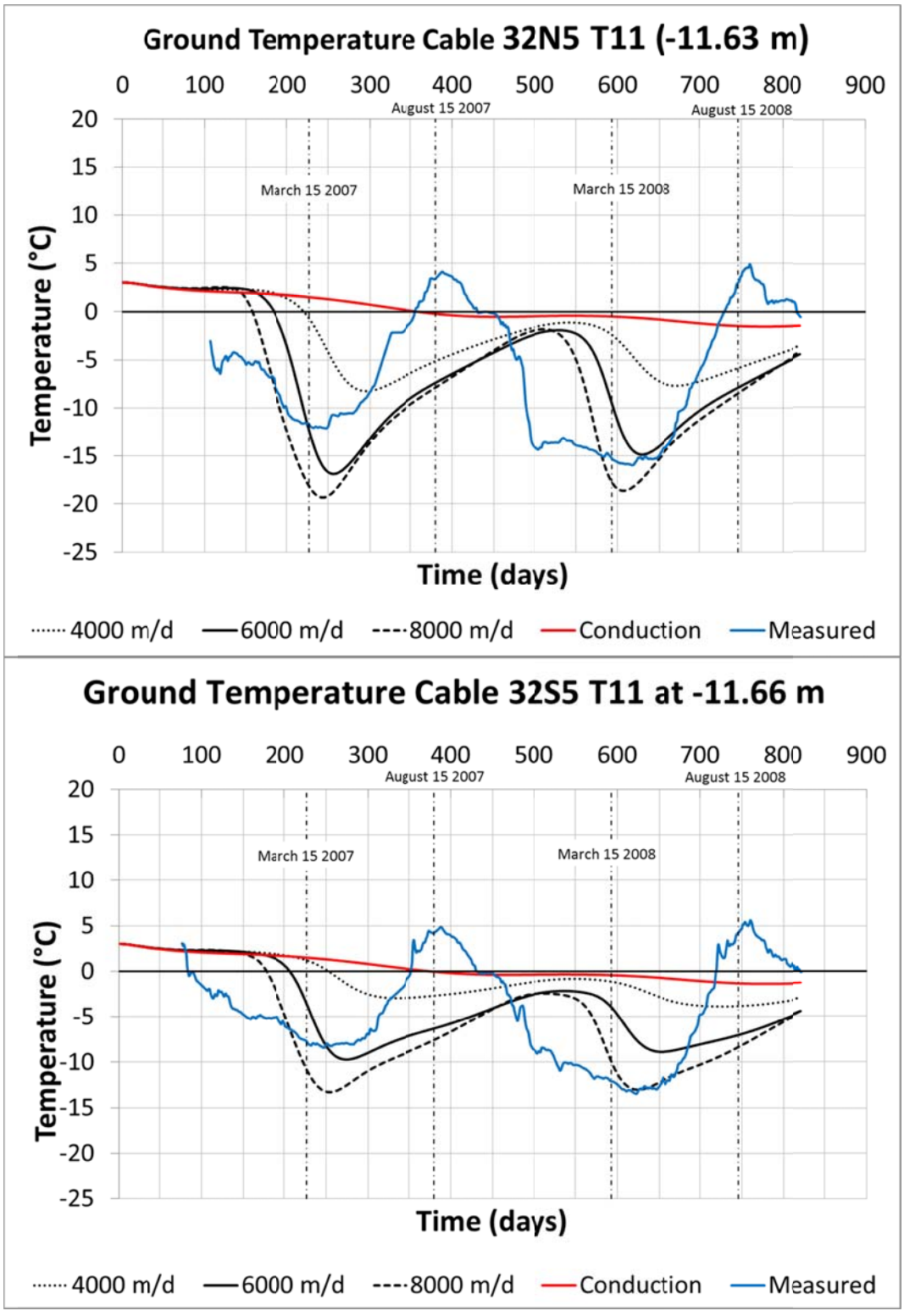

FIGURE 6.21: COMPARISON OF MODELLED AND MEASURED TEMPERATURES IN LOCATION OF GROUND TEMPERATURE CABLES 32N5THM00 AND 32S5THM00; THERMISTOR BEAD T12

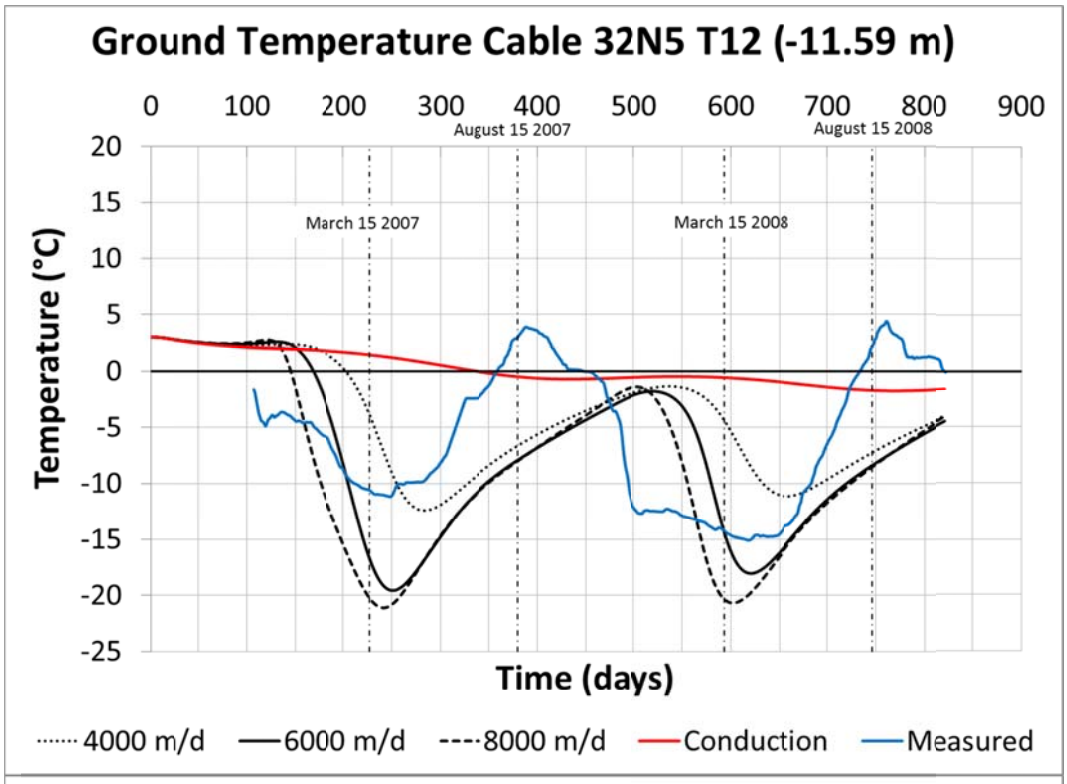

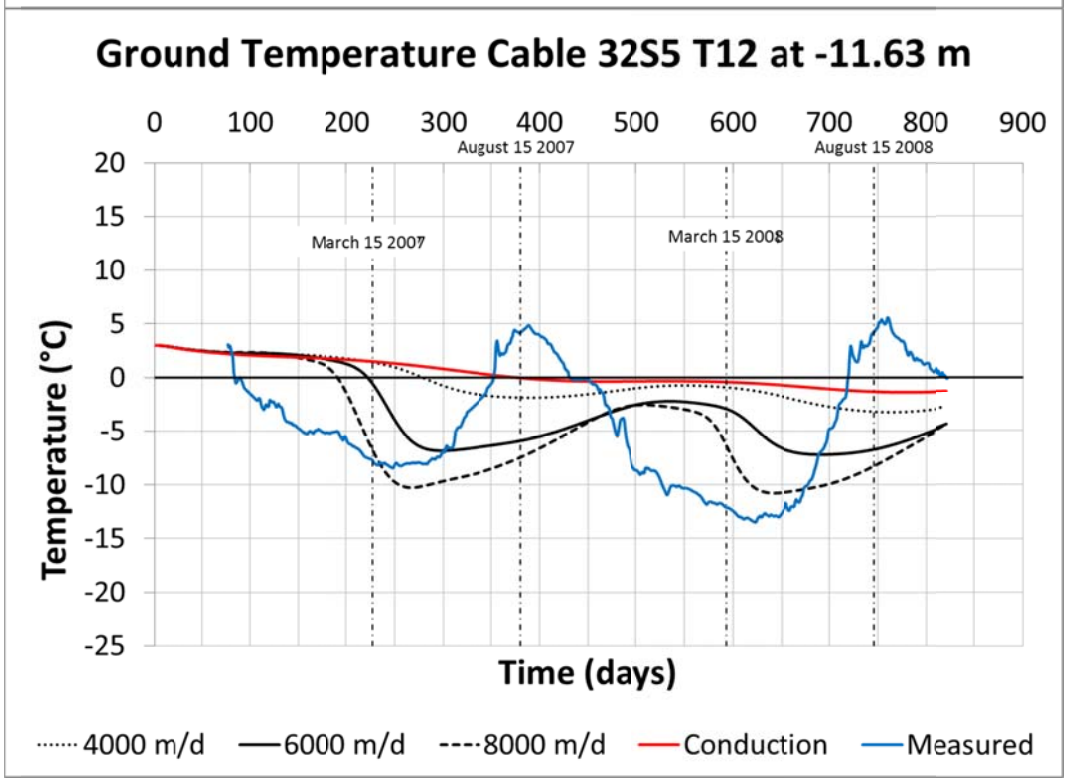

FIGURE 6.22: COMPARISON OF MODELLED AND MEASURED TEMPERATURES IN LOCATION OF GROUND TEMPERATURE CABLE T3J3; THERMISTOR BEADS T6 AND T7

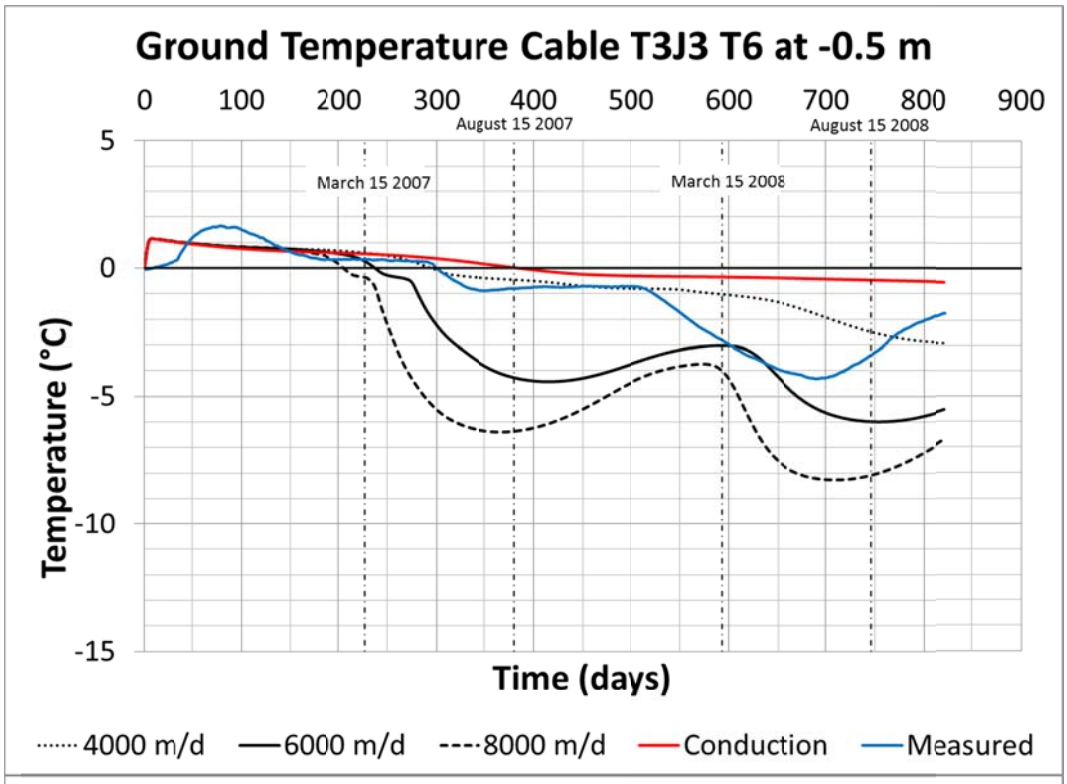

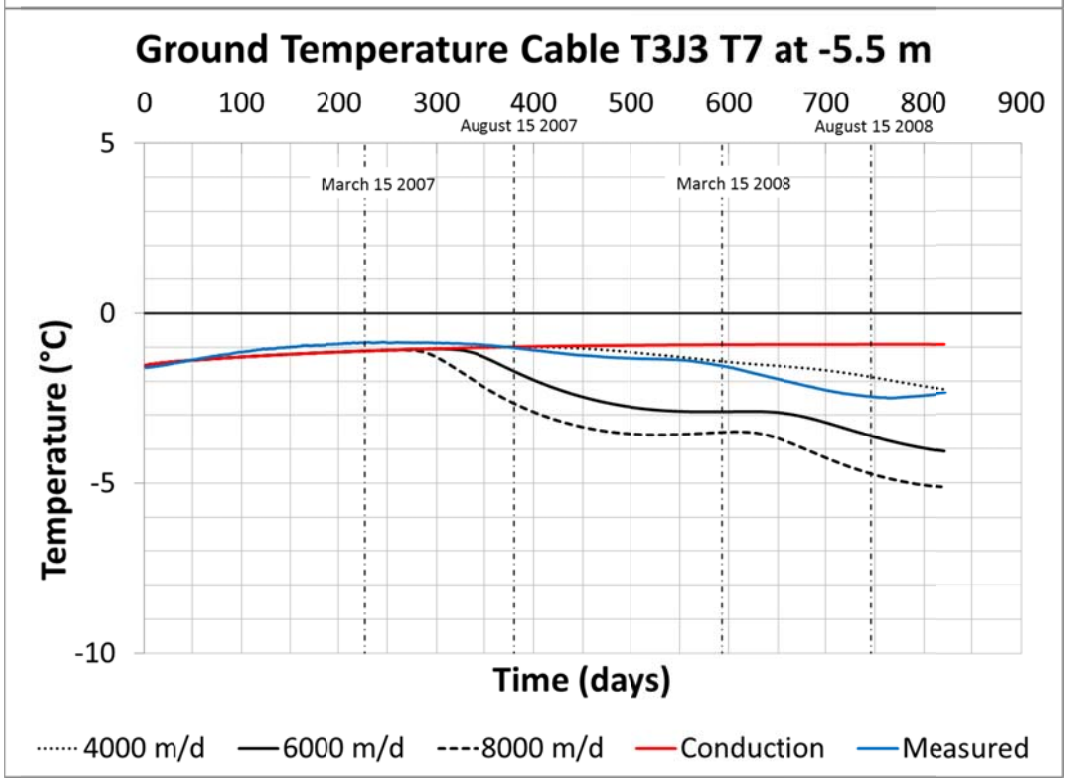

FIGURE 6.23: COMPARISON OF MODELLED AND MEASURED TEMPERATURES IN LOCATION OF GROUND TEMPERATURE CABLE T3J3; THERMISTOR BEAD T8 AND T9

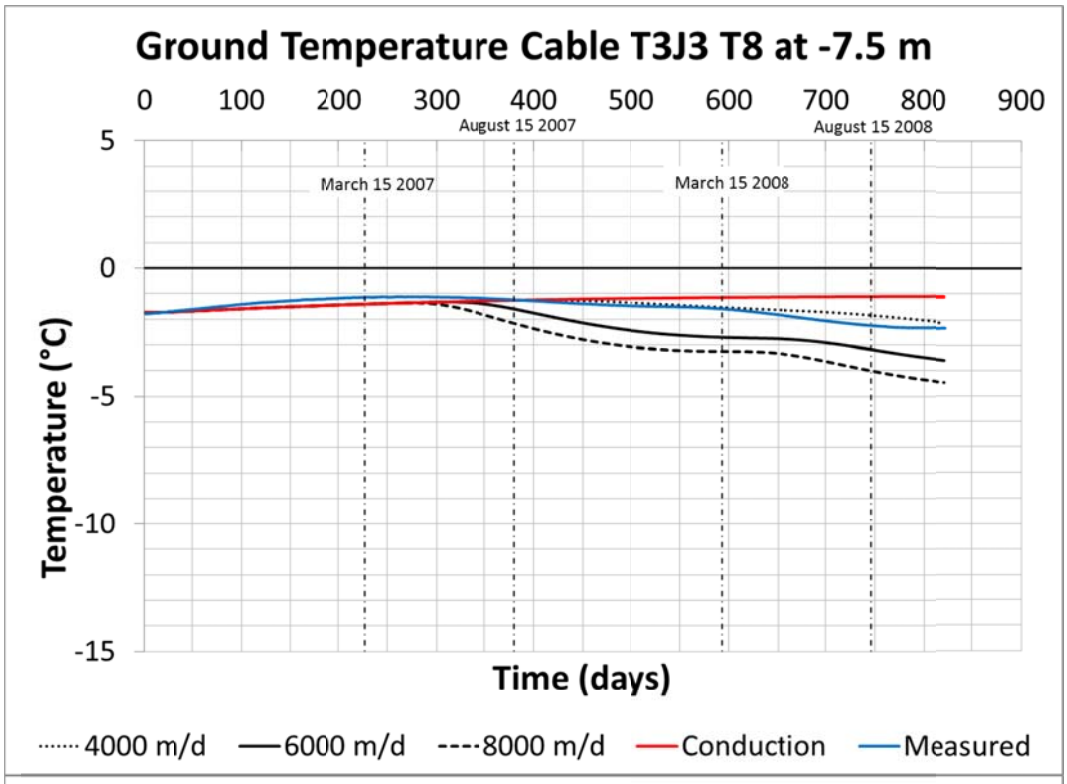

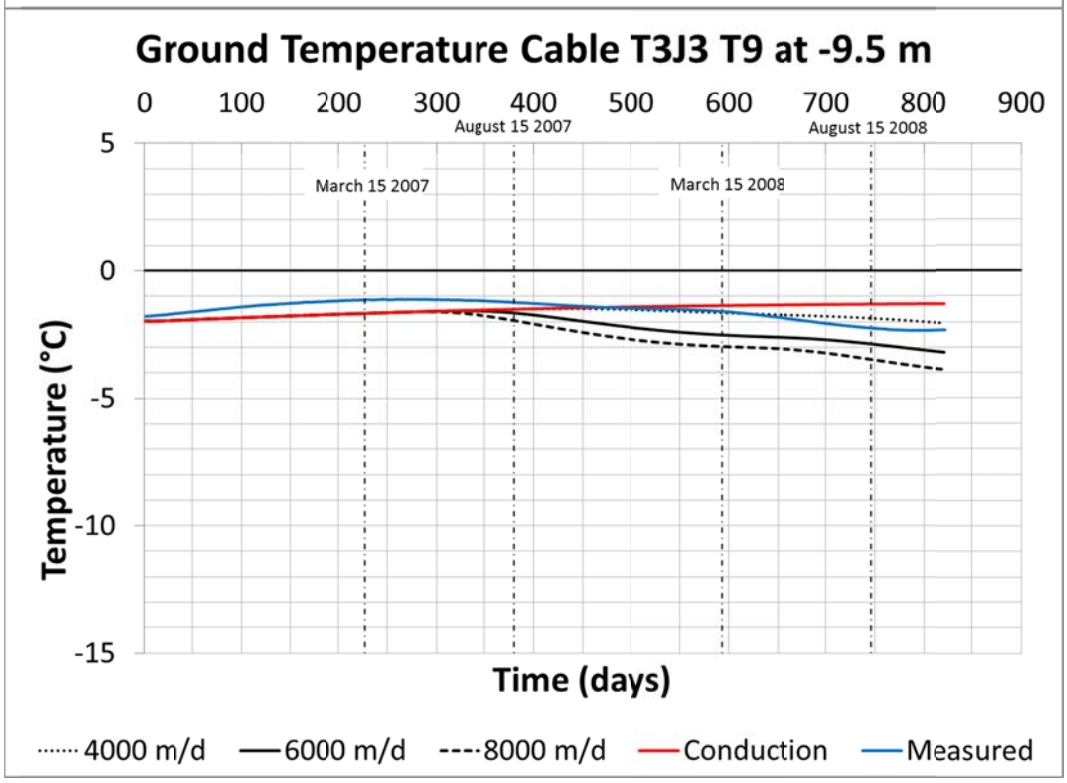

FIGURE 6.24: COMPARISON OF MODELLED AND MEASURED TEMPERATURES IN LOCATION OF GROUND TEMPERATURE CABLE T3J3; THERMISTOR BEAD T10 AND T11

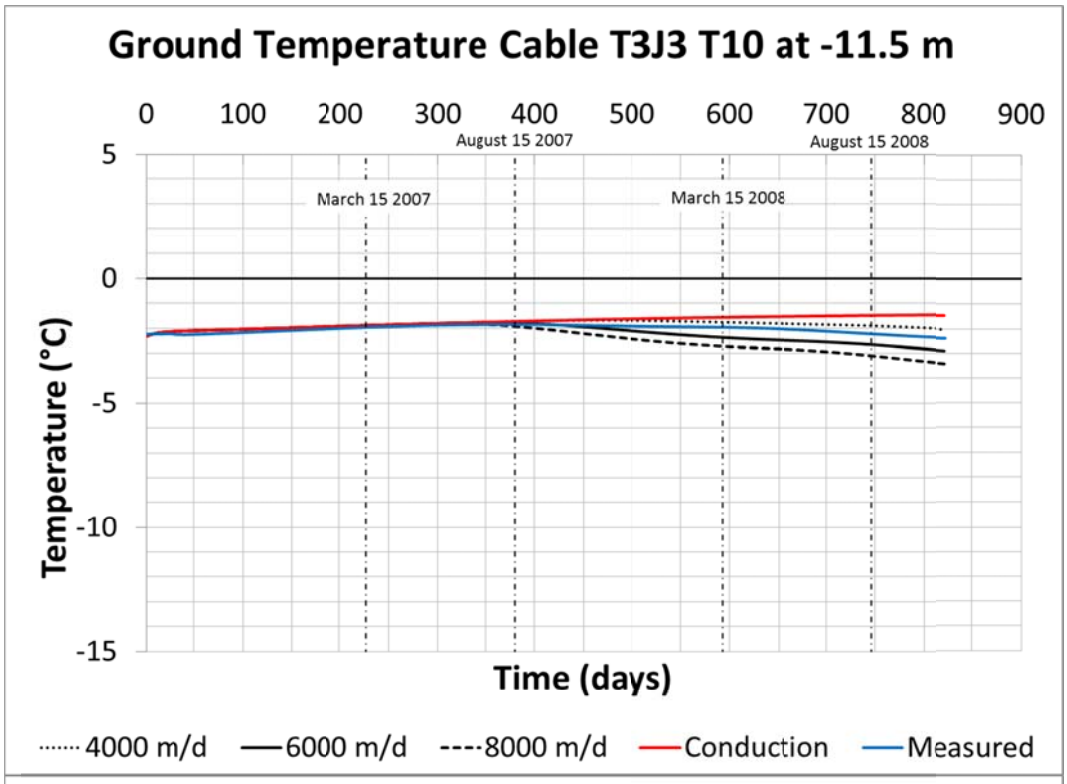

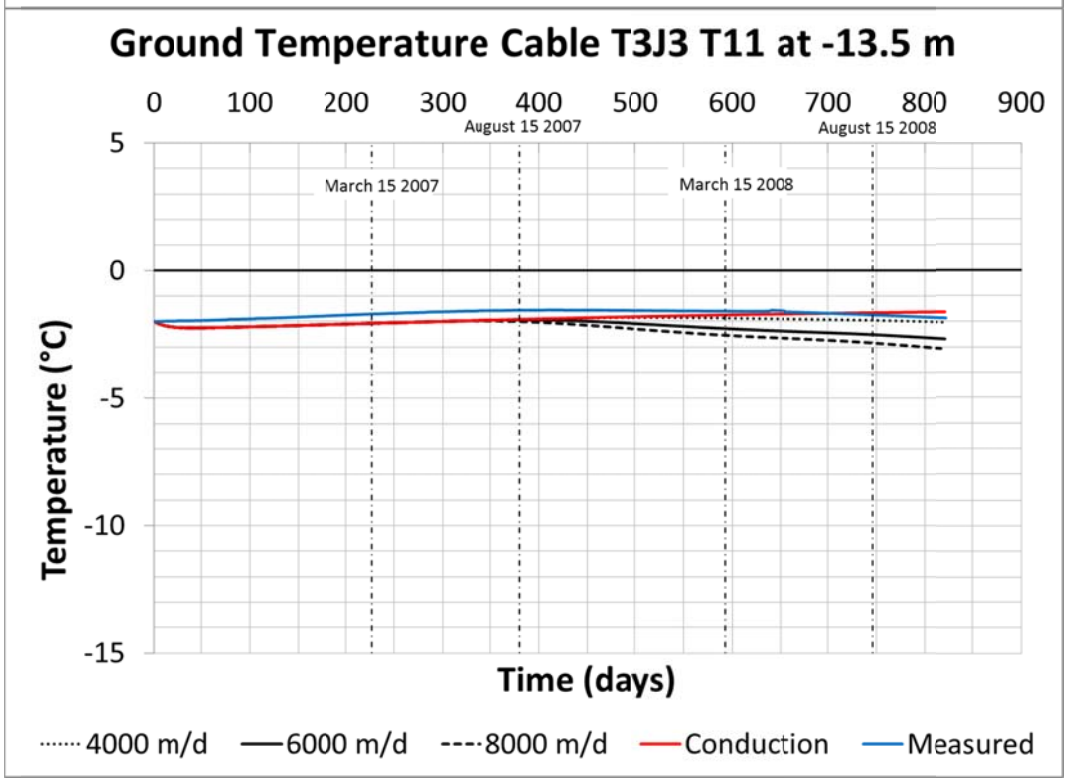

FIGURE 6.25: COMPARISON OF MODELLED AND MEASURED TEMPERATURES IN LOCATION OF GROUND TEMPERATURE CABLE T3J3; THERMISTOR BEAD T12

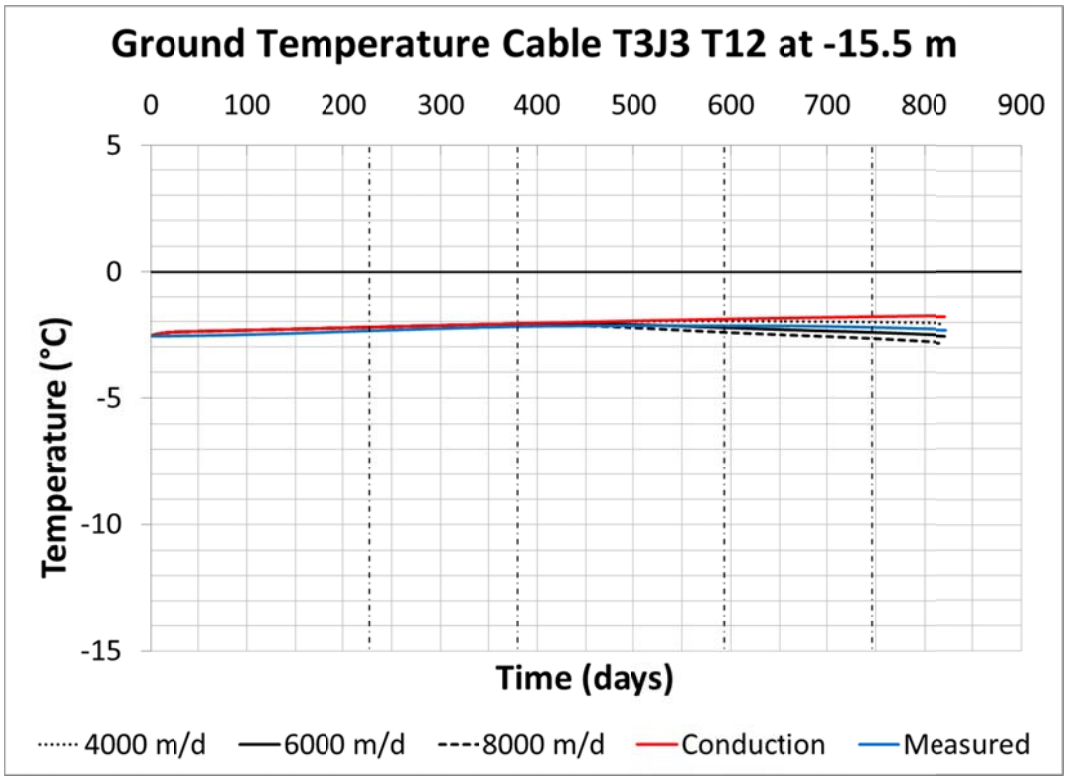

APPENDIX A

APPENDIX A – GEOSTUDIO 2007 THEORY

CONSERVATION OF MASS

One dimensional conservation of mass equation for compressible flow

$$\frac{\partial(\rho_f \theta_f)}{\partial t} = \frac{\partial}{\partial y}\left[-\left(\rho_f K_f\right)\frac{\partial H_f}{\partial y}\right] + Q_f$$

Where H is a total energy potential (pressure and elevation) expressed as a column of water

$$H_f = \left(\frac{P_f}{\gamma_w} + \frac{\rho_f}{\rho_w} y\right)$$

and f means any fluid.

Conservation of Mass for Water

Conservation of mass for water can be obtained by simplifying general conservation of mass equation.

After expansion with a chain rule the left hand side becomes

$$\frac{\partial\left(\rho_w \theta_w\right)}{\partial t} = \theta_w \frac{\partial \rho_w}{\partial t} + \rho_w \frac{\partial \theta_w}{\partial t}$$

and the right hand side becomes

$$\frac{\partial}{\partial y}\left[\left(\rho_w K_w\right)\frac{\partial H_w}{\partial y}\right] = K_w \frac{\partial H_w}{\partial y}\frac{\partial \rho_w}{\partial y} + \rho_w \frac{\partial}{\partial y}\left[K_w \frac{\partial H_w}{\partial y}\right].$$

Because water is incompressible, time and space derivatives of density are zero. The remaining density terms can be cancelled out from the equation and the balance equation for water becomes

$$\frac{\partial\left(\theta_w\right)}{\partial t} = \frac{\partial}{\partial y}\left[K_w \frac{\partial\left(H_w\right)}{\partial y}\right] + Q_w$$

A matric suction term can be introduced as a difference in capillary pressure between air and water as follows

$$\psi = -\left(P_a - P_w\right) = \left[\gamma_w H_w - P_a\right]$$

and its time derivative

$$\frac{\partial \psi}{\partial t} = -\frac{\partial (P_a - P_w)}{\partial t} = \frac{\partial [\gamma_w H_w - P_a]}{\partial t}$$

The left hand side of the conservation of mass for water equation can be expressed as a time derivative of total head using the slope of the water content versus matric suction relationship

$$\frac{\partial \theta_w}{\partial t} = \frac{\partial \theta_w}{\partial \psi}\frac{\partial \psi}{\partial t} = m_w \frac{\partial \psi}{\partial t} = m_w \frac{\partial [\gamma_w H_w - P_a]}{\partial t}$$

The elevation term in the time derivative of matric suction can be excluded as elevation is constant with time, and the final equation of conservation of mass for water becomes

$$m_w \gamma_w \frac{\partial H_w}{\partial t} = \frac{\partial}{\partial y}\left[K_w \frac{\partial H_w}{\partial y} \right] + m_w \frac{\partial P_a}{\partial t} + Q_w$$

Conservation of Mass for Air

The general one dimensional conservation of mass equation for compressible flow can be rewritten as follows for air

$$\frac{\partial (\rho_a \theta_a)}{\partial t} = \theta_a \frac{\partial \rho_a}{\partial t} + \rho_a \frac{\partial \theta_a}{\partial t} = \frac{\partial}{\partial y}\left[(\rho_a K_a) \frac{\partial H_a}{\partial y} \right] + Q_a$$

The time derivative of density can be expanded using the chain rule and the law for idea gas

$$\theta_a \frac{\partial \rho_a}{\partial t} = \frac{\theta_a}{RT}\frac{\partial P_a}{\partial t} + \frac{\theta_a P_a}{R}\frac{\partial \left(\frac{1}{T}\right)}{\partial t}$$

Where R=287.1 J/(kg-K) for dry air.

The change in air volume over time is the negative of the change in water volume over time and can be expressed by the change in matric suction

$$\rho_a \frac{\partial \theta_a}{\partial t} = -\rho_a \frac{\partial \theta_w}{\partial t} = \rho_a m_w \frac{\partial \psi}{\partial t}$$

Thus, the general conservation of mass for air equation becomes

$$\frac{\theta_a}{RT}\frac{\partial P_a}{\partial t}+\frac{\theta_a P_a}{R}\frac{\partial\left(\frac{1}{T}\right)}{\partial t}+\rho_a m_w\frac{\partial \psi}{\partial t}=\frac{\partial}{\partial y}\left[\left(\rho_a K_a\right)\frac{\partial\left(\frac{P_a}{\gamma_{oa}}+\frac{\rho_a}{\rho_{oa}}y\right)}{\partial y}\right]$$

The air source/sink has been removed as it is difficult to inject a known mass into the soil.

The equation can be rearranged as follows

$$\frac{\theta_a}{RT}\frac{\partial P_a}{\partial t}=\frac{\partial}{\partial y}\left[\frac{\rho_a K_a}{\gamma_{oa}}\frac{\partial P_a}{\partial y}+\frac{\rho_a^2 K_a}{\rho_{oa}}\right]-\frac{\theta_a P_a}{R}\frac{\partial\left(\frac{1}{T}\right)}{\partial t}-\rho_a m_w\frac{\partial \psi}{\partial t}$$

And the change in matric suction on the right can be expanded into air and water pressure as follows

$$\frac{\theta_a}{RT}\frac{\partial P_a}{\partial t}=\frac{\partial}{\partial y}\left[\frac{\rho_a K_a}{\gamma_{oa}}\frac{\partial P_a}{\partial y}+\frac{\rho_a^2 K_a}{\rho_{oa}}\right]-\frac{\theta_a P_a}{R}\frac{\partial\left(\frac{1}{T}\right)}{\partial t}-\rho_a m_w\frac{\partial\left(P_a-P_w\right)}{\partial t}$$

The Pa terms can be combined and Pw can be expressed as hydraulic head

$$\left(\frac{\theta_a}{RT}+\rho_a m_w\right)\frac{\partial P_a}{\partial t}=\frac{\partial}{\partial y}\left[\frac{\rho_a K_a}{\gamma_{oa}}\frac{\partial P_a}{\partial y}+\frac{\rho_a^2 K_a}{\rho_{oa}}\right]-\frac{\theta_a P_a}{R}\frac{\partial\left(\frac{1}{T}\right)}{\partial t}-\rho_a\gamma_w m_w\frac{\partial H_w}{\partial t}$$

THERMAL ENERGY BALANCE

Air density is a function of temperature and thermal energy has to be balanced. The energy balance equation with phase change in the water phase is

$$\left(\rho_s c_{ps}+L\theta_w\frac{\partial\theta_u}{\partial T}\right)\frac{\partial T}{\partial t}=\frac{\partial}{\partial y}\left[K_t\frac{\partial T}{\partial y}\right]+c_{pa}\frac{\partial\left(m_a T\right)}{\partial y}+\theta_w\rho_w c_{pw}\frac{\partial\left(q_w T\right)}{\partial y}+Q$$

SYMBOLS

H	total energy potential
K	permeability
L	latent heat of water
P	pressure
Q	external energy flux (source/sink)
R	gas constant for air = 287.1 J/(kg-K)
T	absolute temperature
m_v	slope of water content versus matric suction relationship
ρ	density
θ	volume
ψ	matric suction
v	specific discharge
$\rho_s c_{ps}$	volumetric heat capacity of soil
$c_{pa/w}$	mass specific heat of air or water
$\dot{m}_a$	mass flow rate
$\frac{\partial \theta_u}{\partial T}$	slope of the unfrozen water content function
q_w	specific discharge (Darcy velocity) of water

Subscripts

a	air
w	water
f	fluid

SOLUTION SCHEME

There are two equations and two unknowns of total water head H_w and air pressure Pa. Both equations can have time derivative of the depend variable isolated as follows

for water

$$m_w \gamma_w \frac{\partial H_w}{\partial t} = \frac{\partial}{\partial y}\left[K_w \frac{\partial H_w}{\partial y} \right] + m_w \frac{\partial P_a}{\partial t} + Q_w$$

On the first iteration the air pressure is not known. For all other iterations, it can be obtained from the solution at the previous iteration.

and for air

$$\left(\frac{\theta_a}{RT} + \rho_a m_w \right) \frac{\partial P_a}{\partial t} = \frac{\partial}{\partial y}\left[\frac{\rho_a K_a}{\gamma_{oa}} \frac{\partial P_a}{\partial y} + \frac{\rho_a^2 K_a}{\rho_{oa}} \right] - \left[\frac{\theta_a P_a}{R} \frac{\partial\left(\frac{1}{T}\right)}{\partial t} \right] + \left[\rho_a \gamma_w m_w \frac{\partial H_w}{\partial t} \right]$$

The terms on the right hand side can be expressed as sinks or sources as follows:

If SEEP/W is coupled with TEMP/W, the second term on the right can be obtained which represents flow in response to thermally induced density changes. The actual temperatures values can also be used in all terms where T appears.

If SEEP/W is not coupled with TEMP/W, the second term will be zero and will assume room temperatures for all T terms.

The last term on the right hand side of the equation is known from previously solved seepage equation at each iteration.

APPENDIX B

FIGURE B1: STEADY STATE PRESSURE BOUNDARY CONDITIONS APPLIED TO GEOSTUDIO COARSE MESH FULL MODEL WITH CLOSED BOUNDARIES AND CORRESPONDING HALF MODEL USED TO EXAMINE SNAPSHOTS

GEOSTUDIO SIMULATION

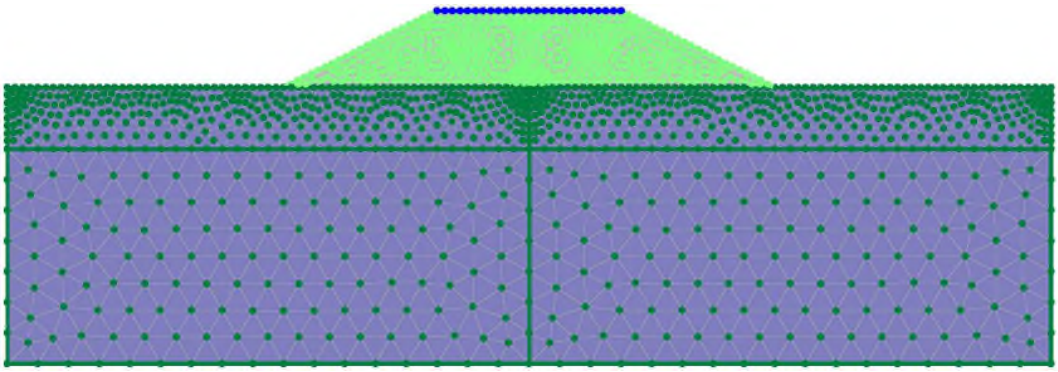

A) Coarse mesh full model; 1574 nodes and 1138 elements

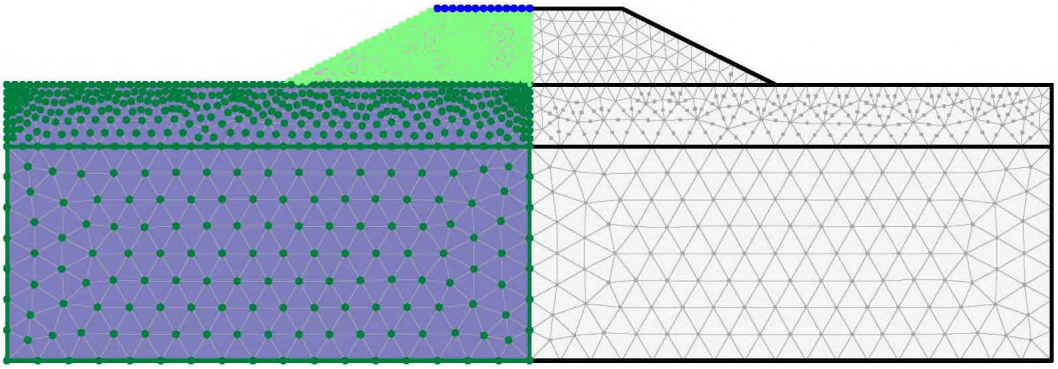

B) Corresponding half model

FIGURE B2: TRANSIENT STATE PRESSURE BOUNDARY CONDITIONS APPLIED TO GEOSTUDIO COARSE MESH FULL MODEL WITH CLOSED BOUNDARIES AND CORRESPONDING HALF MODEL USED TO EXAMINE SNAPSHOTS

GEOSTUDIO SIMULATION

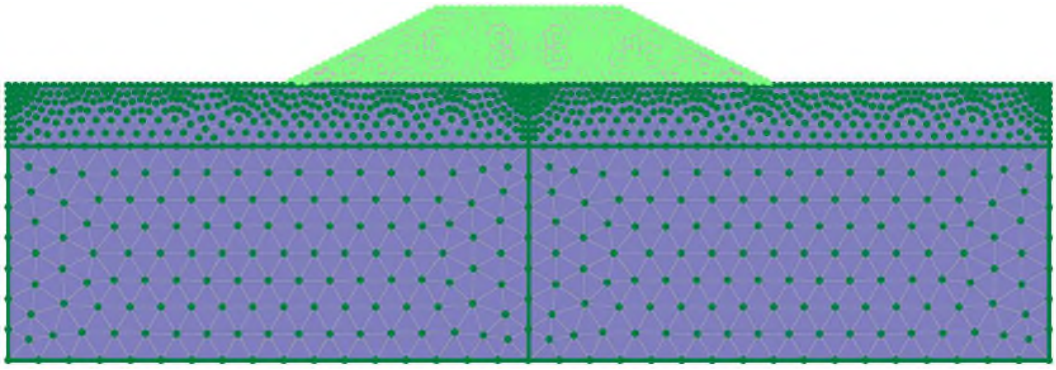

A) Coarse mesh full model; 1574 nodes and 1138 elements

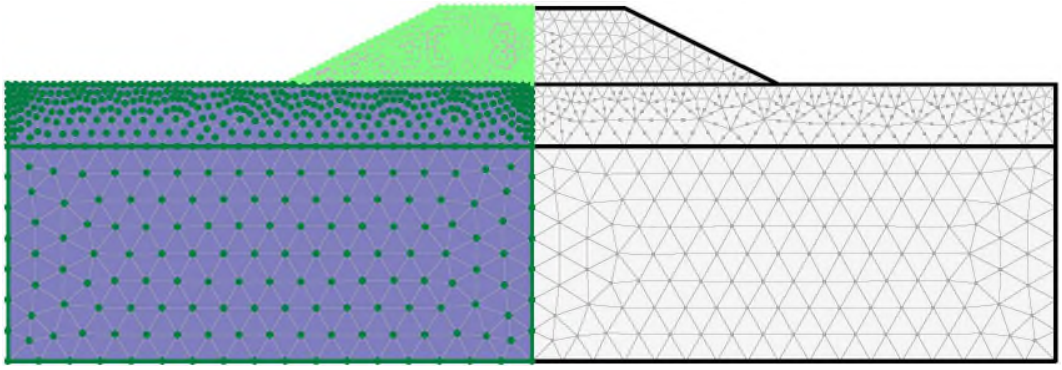

B) Corresponding half model

FIGURE B3: TRANSIENT STATE PRESSURE BOUNDARY CONDITIONS APPLIED TO GEOSTUDIO FULL MODEL WITH OPEN SIDESLOPES AND CORRESPONDING HALF MODEL USED TO EXAMINE SNAPSHOTS

GEOSTUDIO SIMULATION

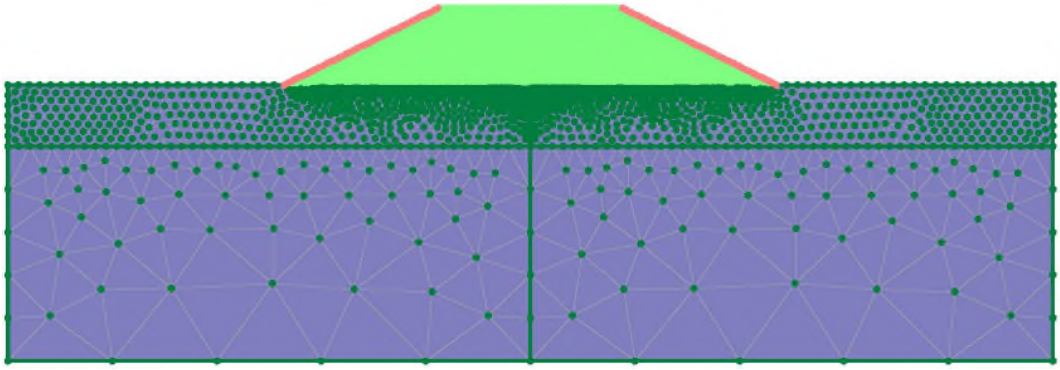

A) Full model; 3124 nodes and 1712 elements

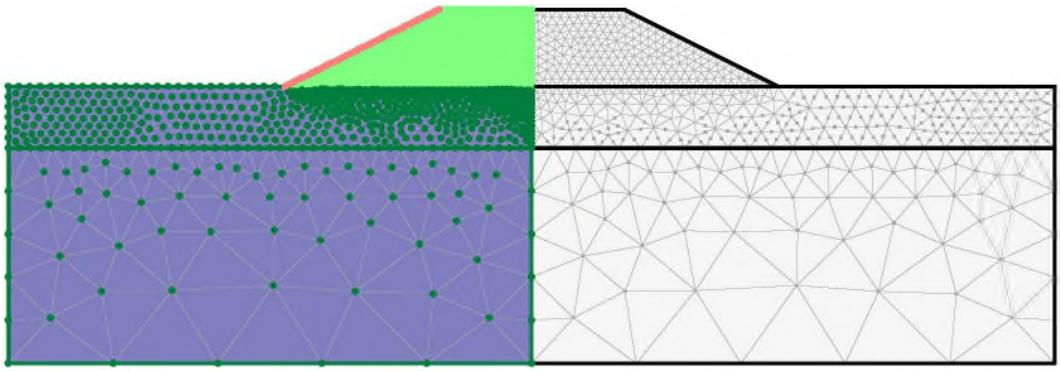

B) Corresponding half model

FIGURE B4: STEADY STATE TEMPERATURE BOUNDARY CONDITION APPLIED TO GEOSTUDIO COARSE MESH FULL MODEL WITH CLOSED BOUNDARIES AND CORRESPONDING HALF MODEL USED TO EXAMINE SNAPSHOTS

GEOSTUDIO SIMULATION

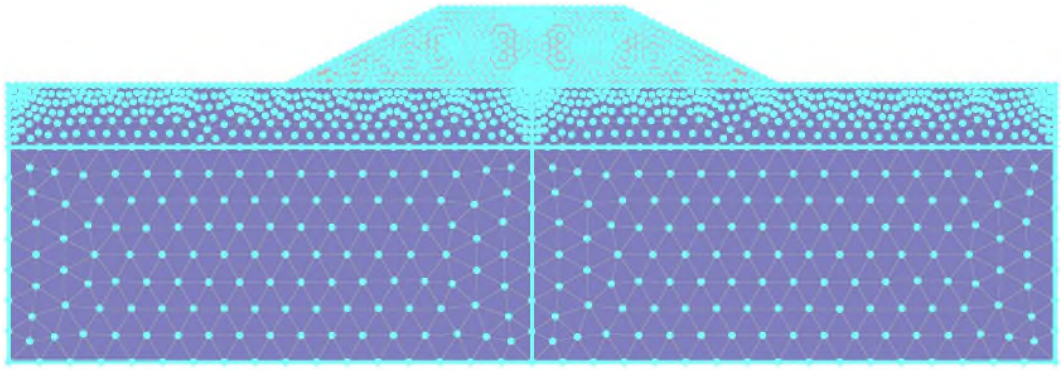

A) Coarse mesh full model; 1574 nodes and 1138 elements

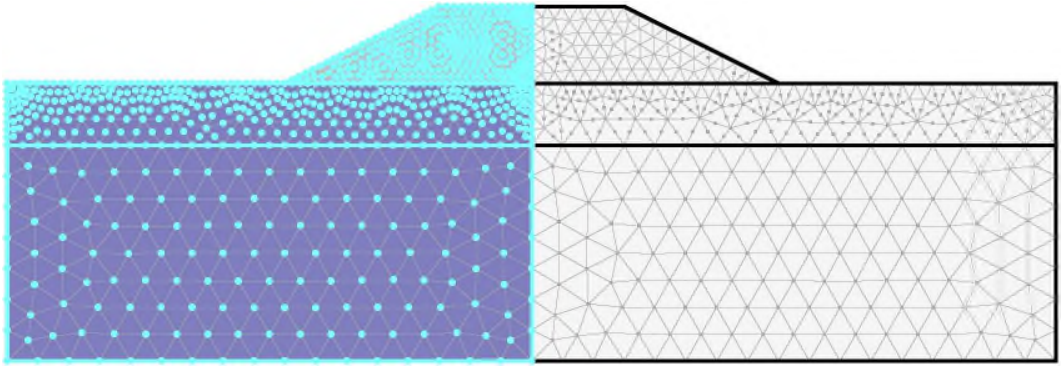

B) Corresponding half model

APPENDIX C

FIGURE C1: STEADY STATE PRESSURE BOUNDARY CONDITIONS APPLIED TO GEOSTUDIO HALF MODEL WITH CLOSED BOUNDARIES AND CORRESPONDING FULL MODEL USED TO EXAMINE TRENDS

GEOSTUDIO SIMULATION

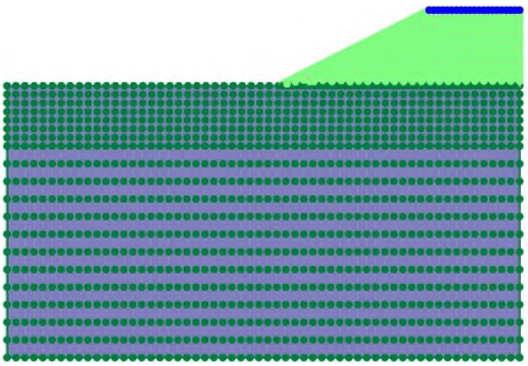

A) Half model; 1661 nodes and 1241 elements

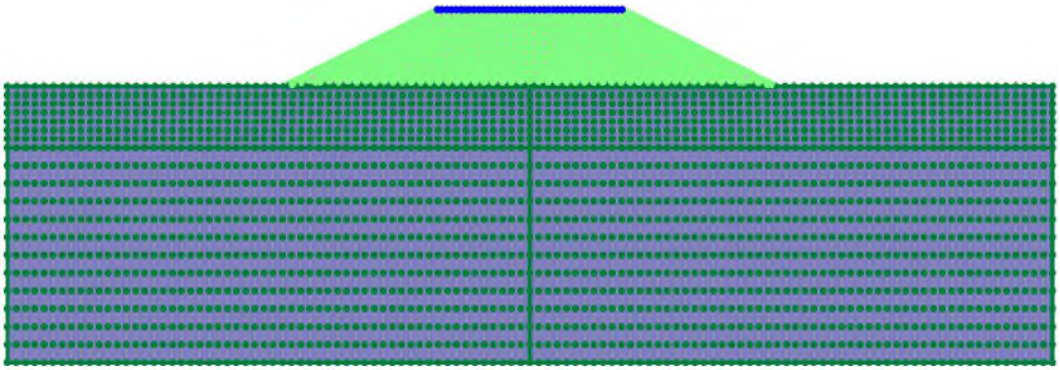

B) Corresponding full model; 3286 nodes and 2482 elements

FIGURE C2: TRANSIENT STATE PRESSURE BOUNDARY CONDITIONS APPLIED TO GEOSTUDIO HALF MODEL WITH CLOSED BOUNDARIES AND CORRESPONDING FULL MODEL USED TO EXAMINE TRENDS

GEOSTUDIO SIMULATION

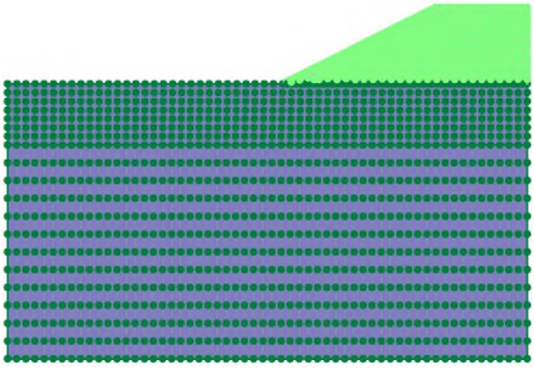

A) Half model; 1661 nodes and 1241 elements

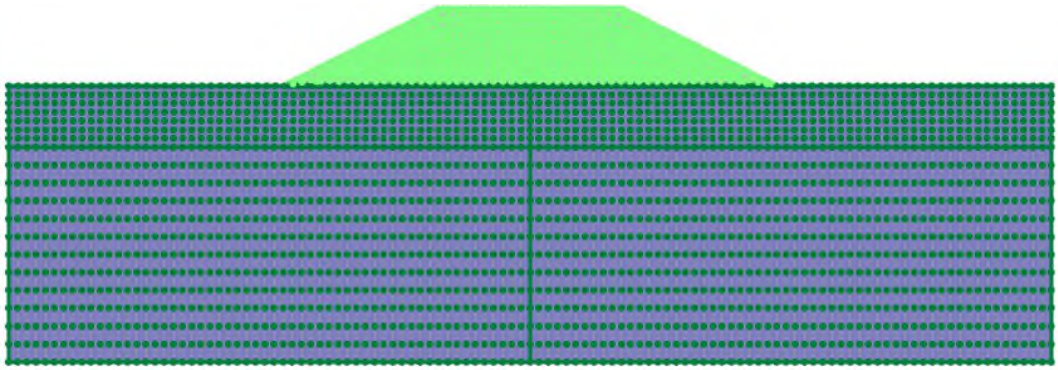

B) Corresponding full model; 3286 nodes and 2482 elements

FIGURE C3: STEADY STATE TEMPERATURE BOUNDARY CONDITIONS APPLIED TO GEOSTUDIO HALF MODEL WITH CLOSED BOUNDARIES AND CORRESPONDING FULL MODEL USED TO EXAMINE TRENDS

GEOSTUDIO SIMULATION

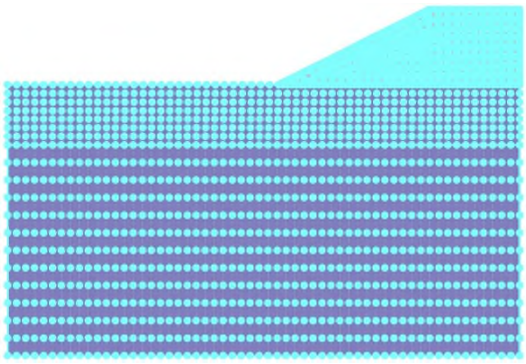

A) Half model; 1661 nodes and 1241 elements

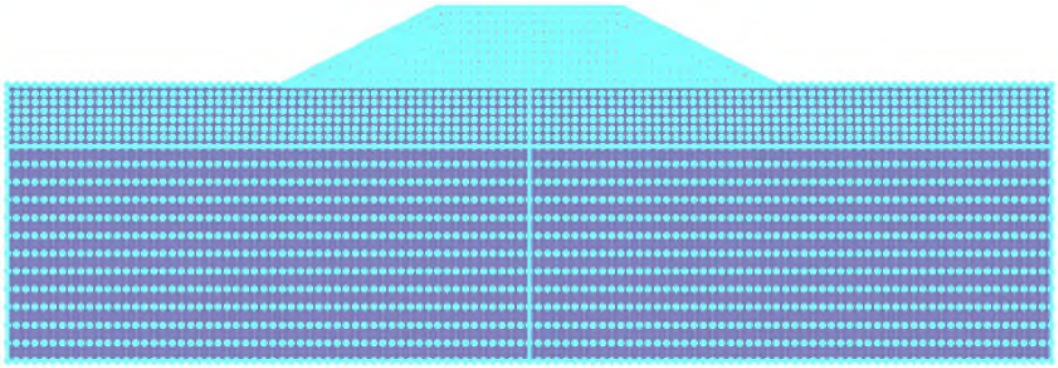

B) Corresponding full model; 3286 nodes and 2482 elements

FIGURE C4: TRANSIENT STATE TEMPERATURE BOUNDARY CONDITIONS APPLIED TO GEOSTUDIO HALF MODEL WITH CLOSED BOUNDARIES AND CORRESPONDING FULL MODEL USED TO EXAMINE TRENDS

GEOSTUDIO SIMULATION

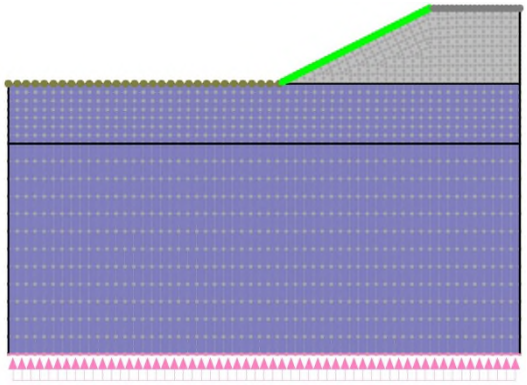

A) Half model; 1661 nodes and 1241 elements

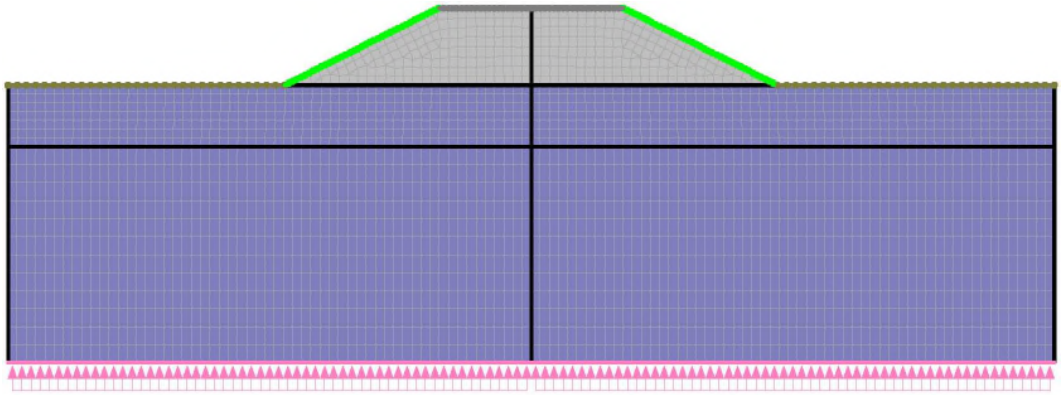

B) Corresponding full model; 3286 nodes and 2482 elements

FIGURE C5: TRENDS IN GEOSTUDIO HALF MODEL WITH CLOSED BOUNDARIES AND CORRESPONDING FULL MODEL – LOCATION 1 AND 2

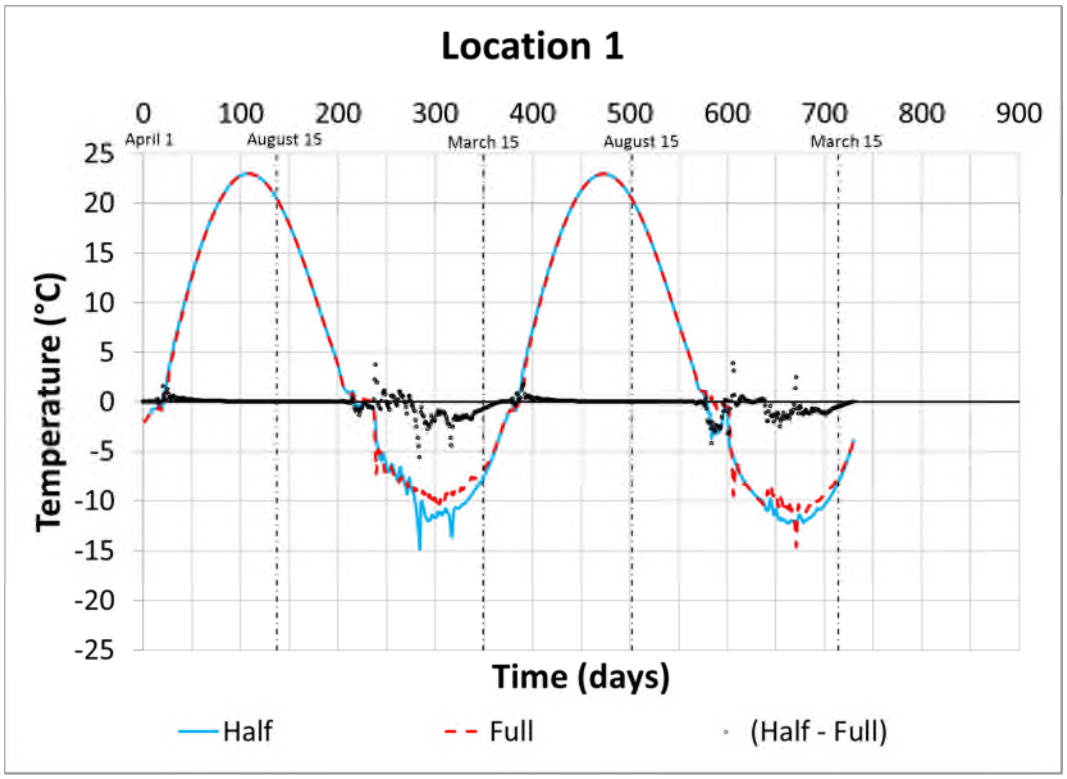

A) Time-temperature plots in Location 1

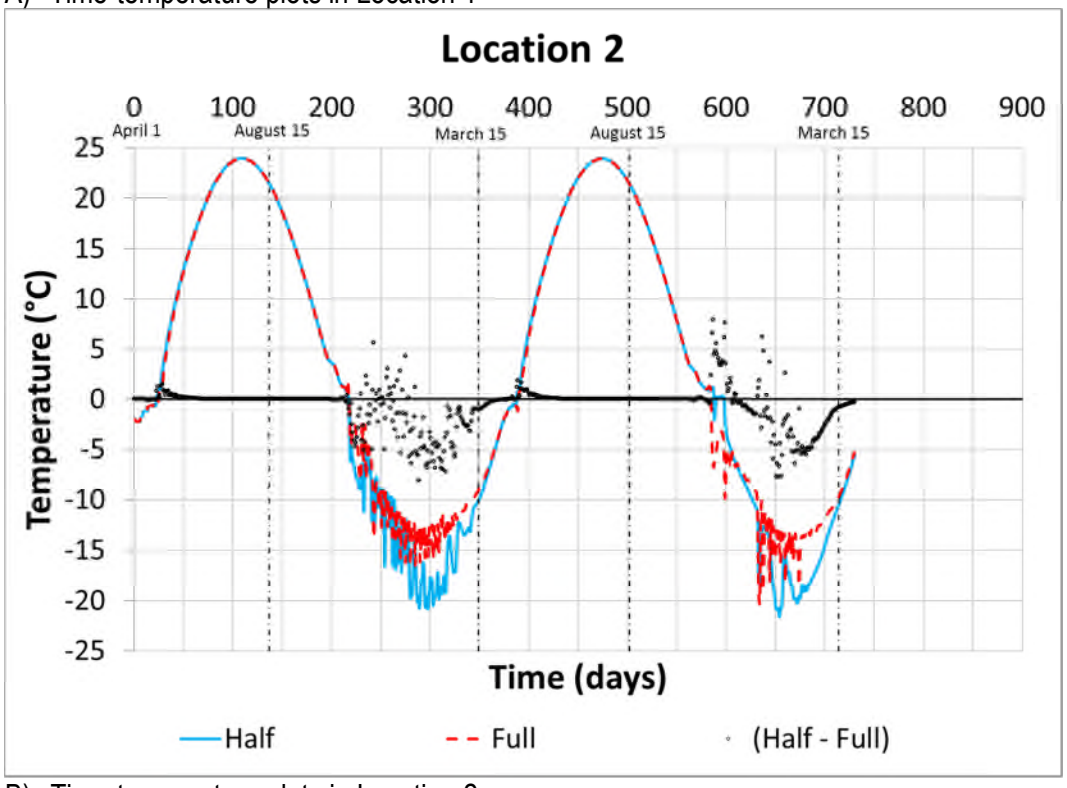

B) Time-temperature plots in Location 2

FIGURE C6: TRENDS IN GEOSTUDIO HALF MODEL WITH CLOSED BOUNDARIES AND CORRESPONDING FULL MODEL - LOCATION 3 AND 4

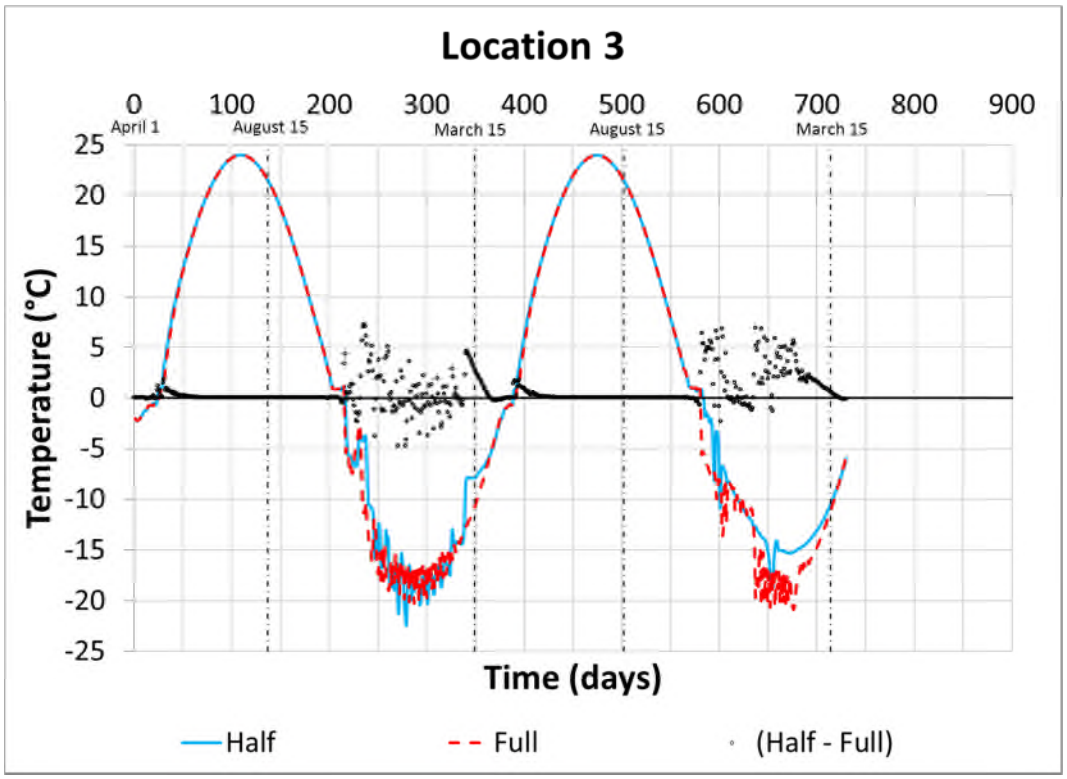

A) Time-temperature plots in Location 3

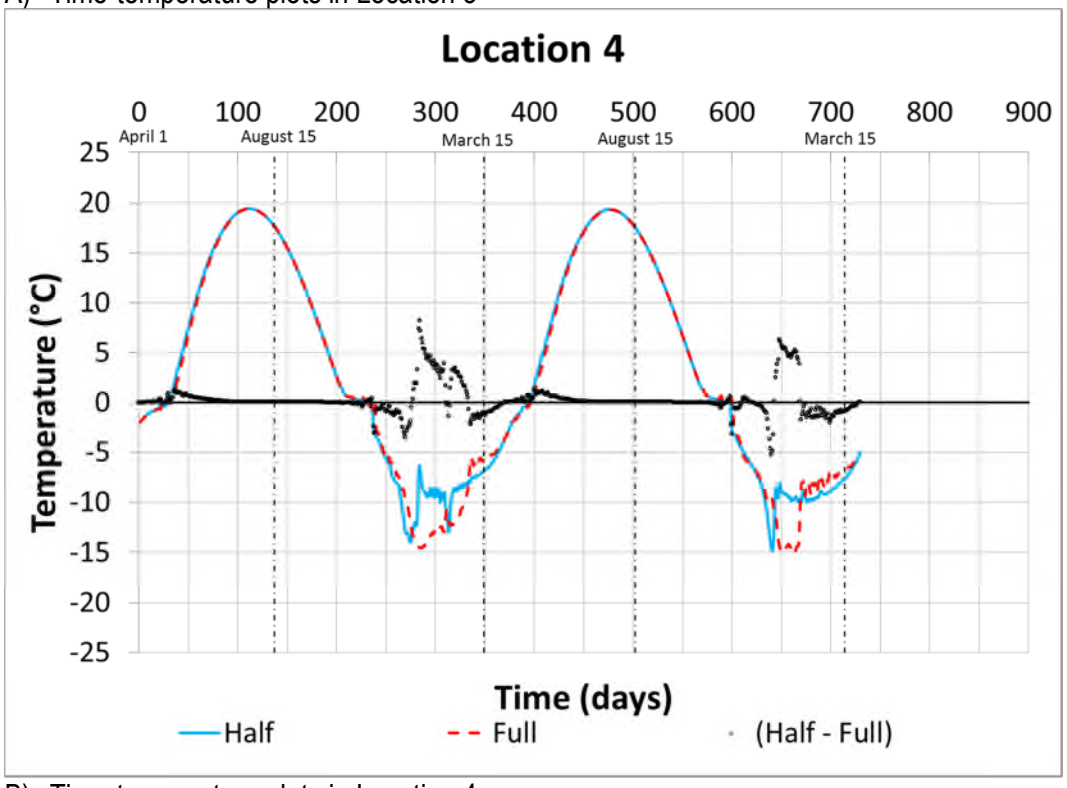

B) Time-temperature plots in Location 4

FIGURE C7: TRENDS IN GEOSTUDIO HALF MODEL WITH CLOSED BOUNDARIES AND CORRESPONDING FULL MODEL – LOCATIONS 5 AND 6

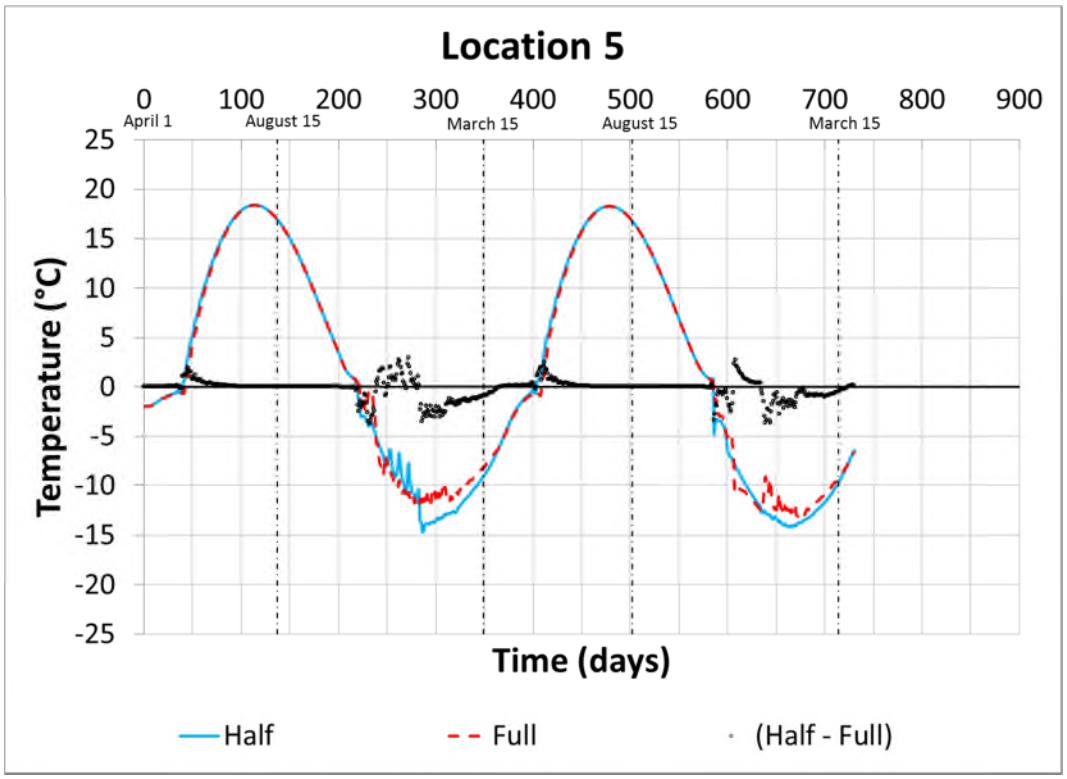

A) Time-temperature plots in Location 5

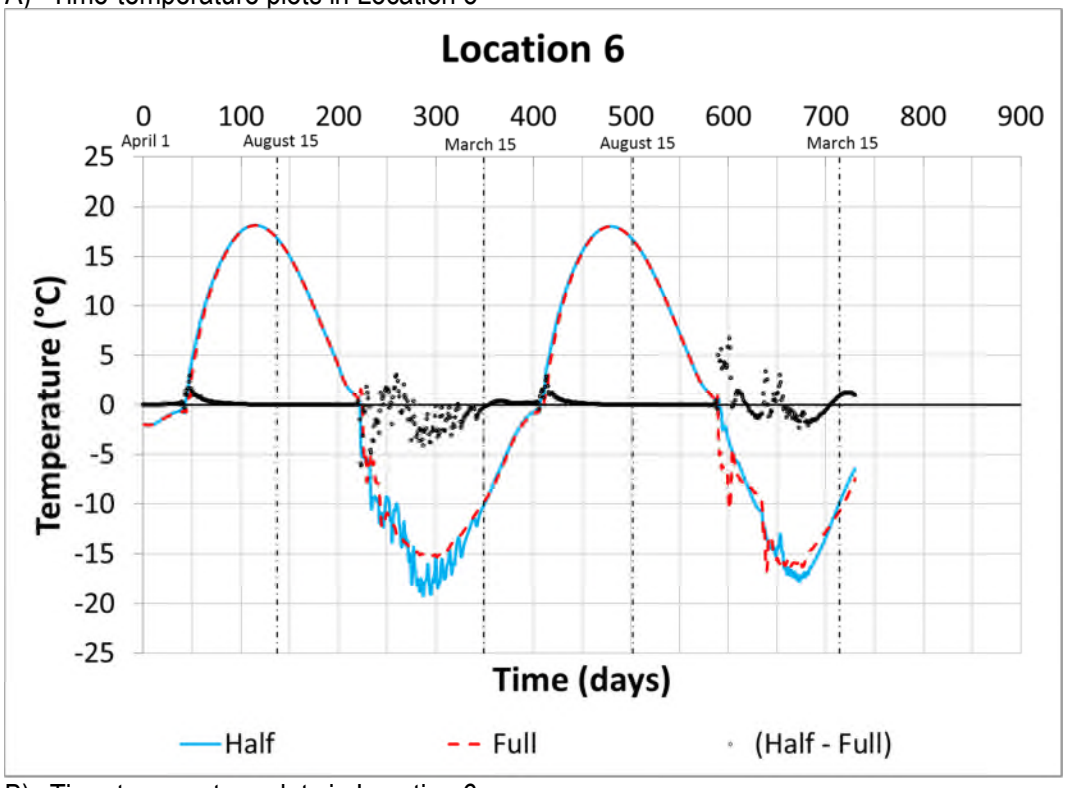

B) Time-temperature plots in Location 6

FIGURE C8: TRENDS IN GEOSTUDIO HALF MODEL WITH CLOSED BOUNDARIES AND CORRESPONDING FULL MODEL – LOCATIONS 7 AND 8

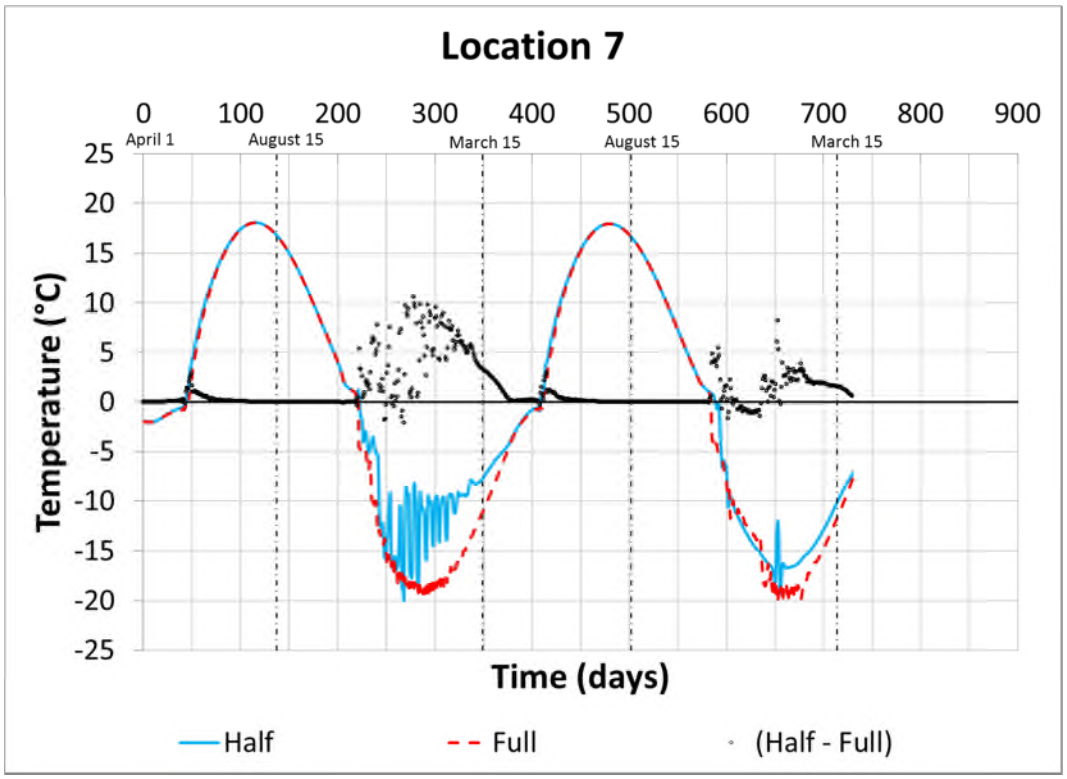

A) Time-temperature plots in Location 7

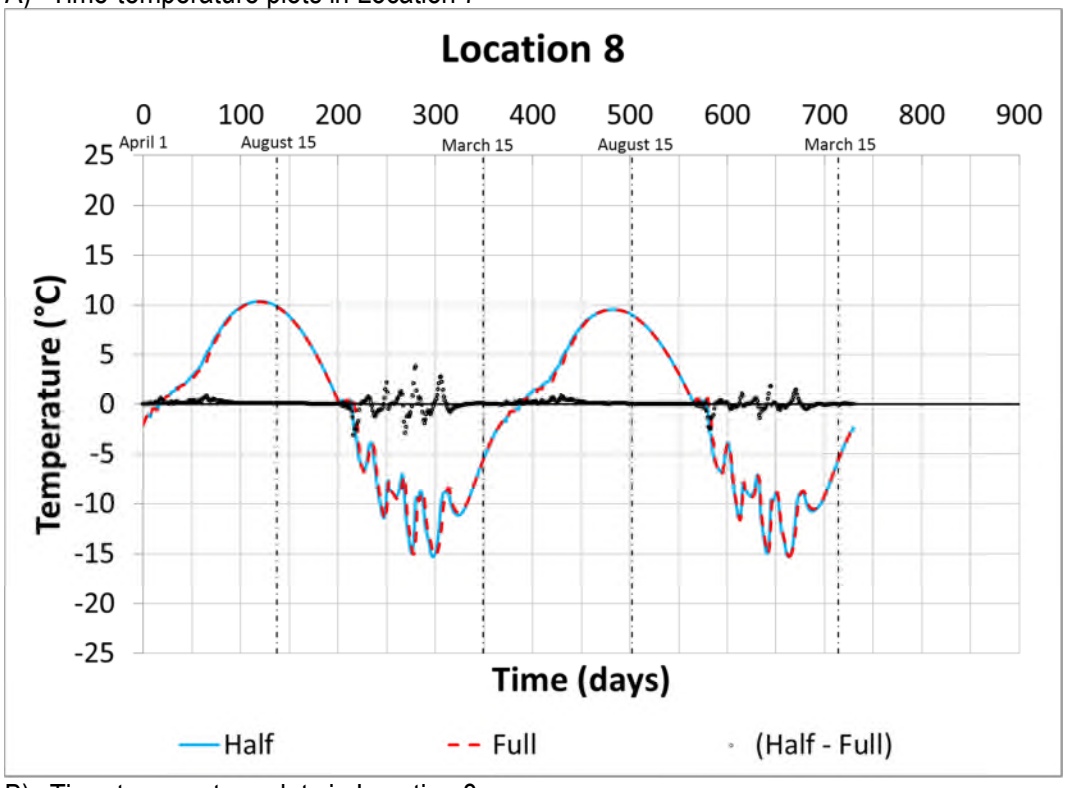

B) Time-temperature plots in Location 8

FIGURE C9: TRENDS IN GEOSTUDIO HALF MODEL WITH CLOSED BOUNDARIES AND CORRESPONDING FULL MODEL – LOCATIONS 9 AND 10

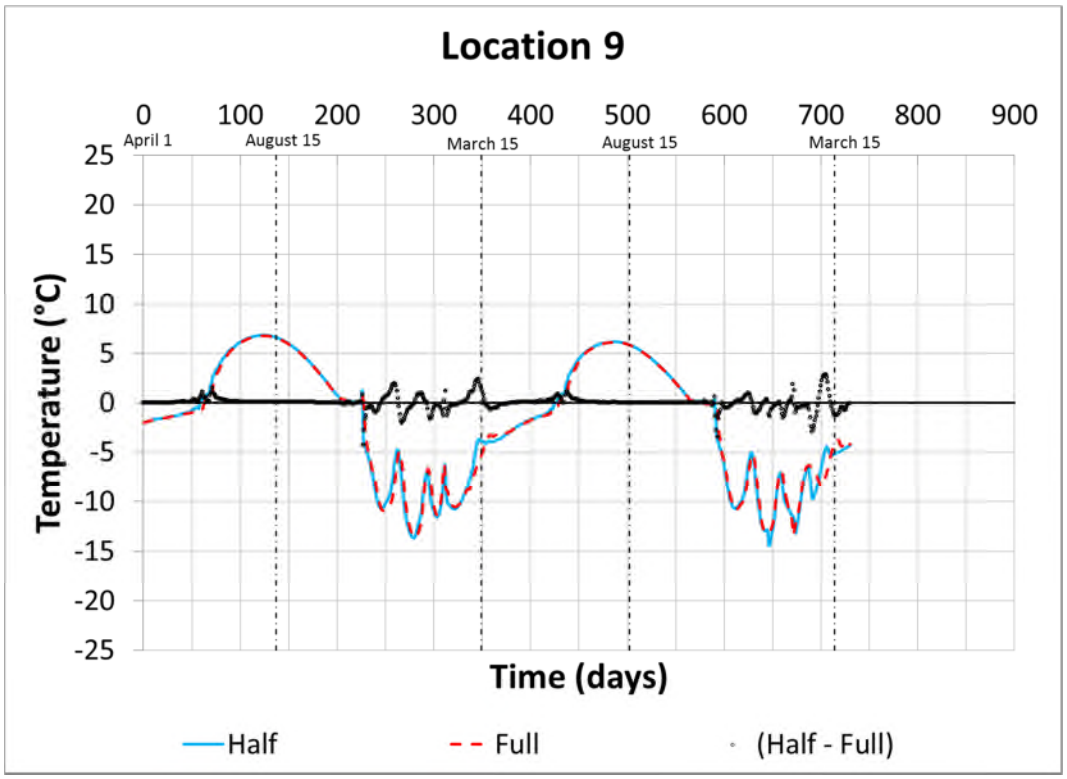

A) Time-temperature plots in Location 9

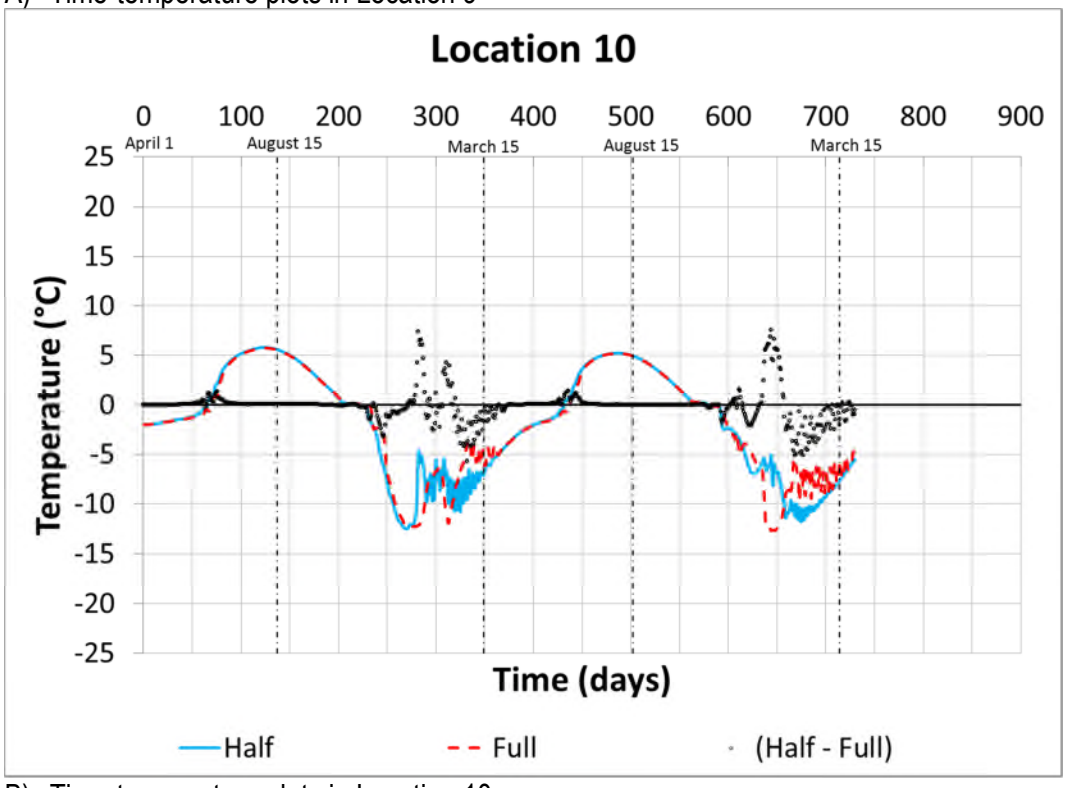

B) Time-temperature plots in Location 10

FIGURE C10: TRENDS IN GEOSTUDIO HALF MODEL WITH CLOSED BOUNDARIES AND CORRESPONDING FULL MODEL – LOCATIONS 11 AND 12

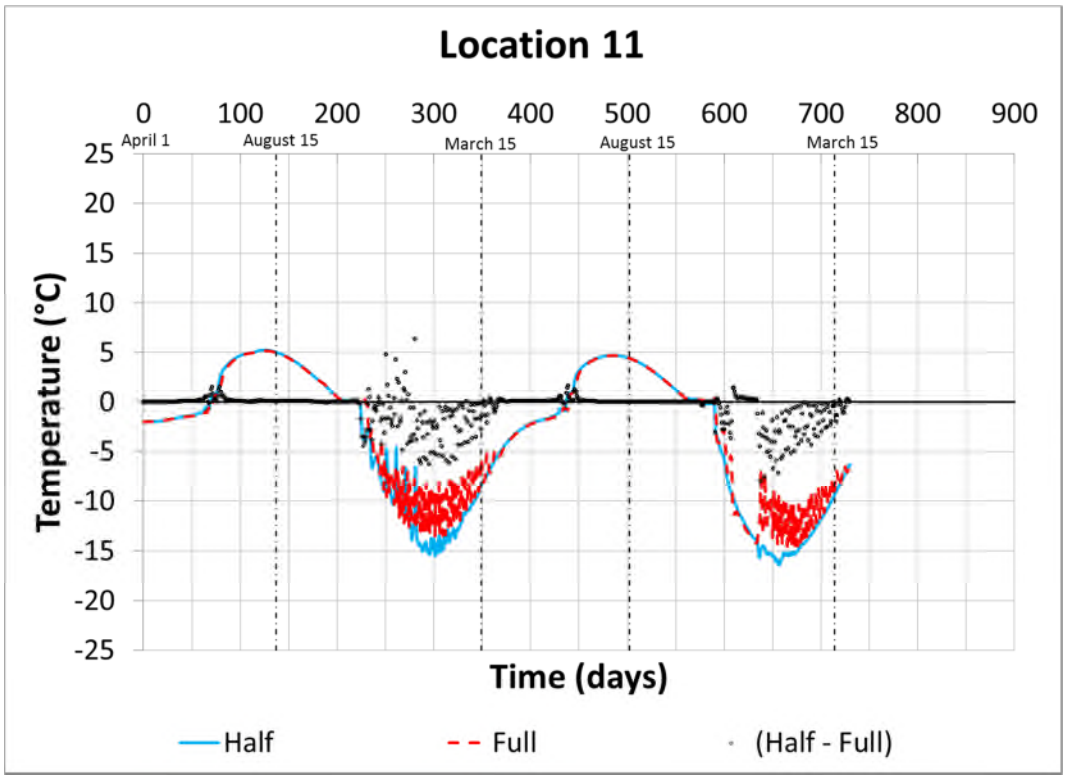

A) Time-temperature plots in Location 11

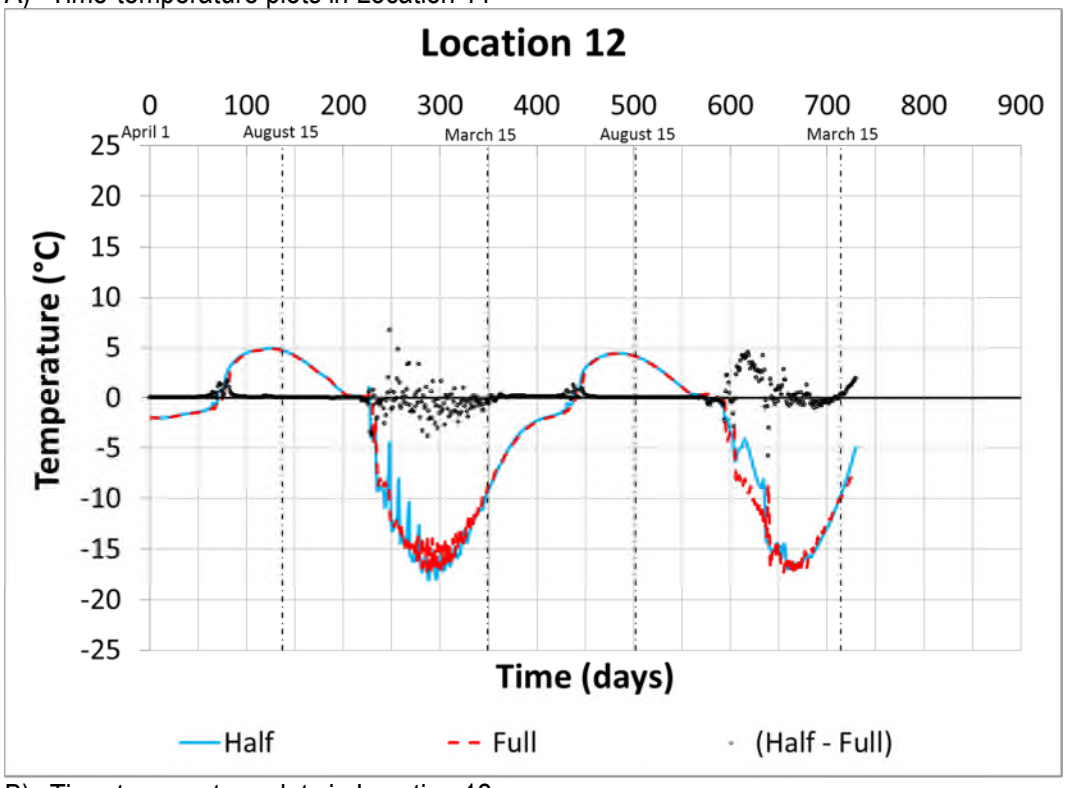

B) Time-temperature plots in Location 12

FIGURE C11: TRENDS IN GEOSTUDIO HALF MODEL WITH CLOSED BOUNDARIES AND CORRESPONDING FULL MODEL – LOCATIONS 13 AND 14

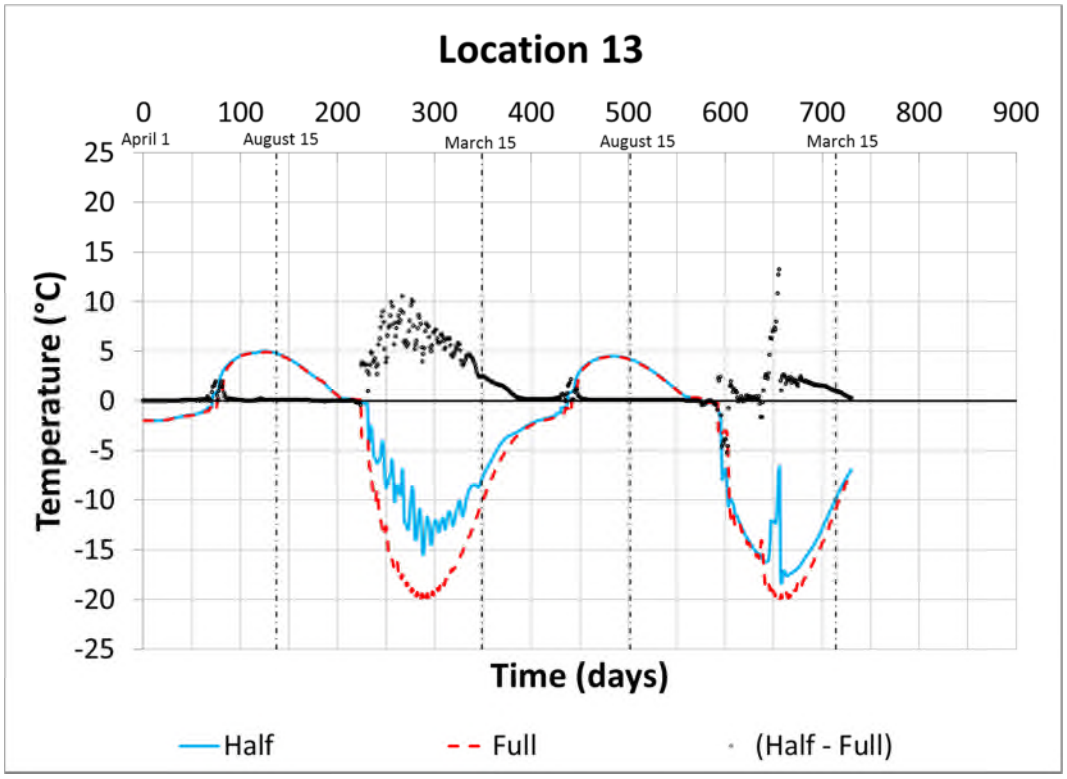

A) Time-temperature plots in Location 13

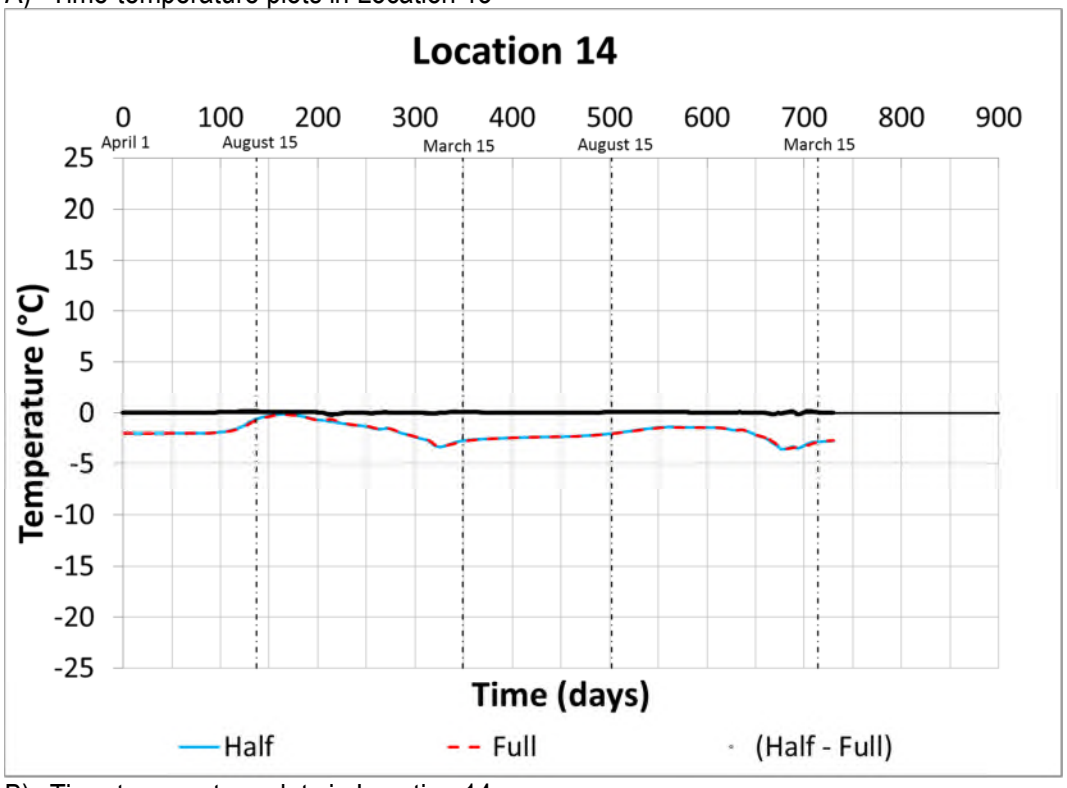

B) Time-temperature plots in Location 14

FIGURE C12: TRENDS IN GEOSTUDIO HALF MODEL WITH CLOSED BOUNDARIES AND CORRESPONDING FULL MODEL – LOCATIONS 15 AND 16

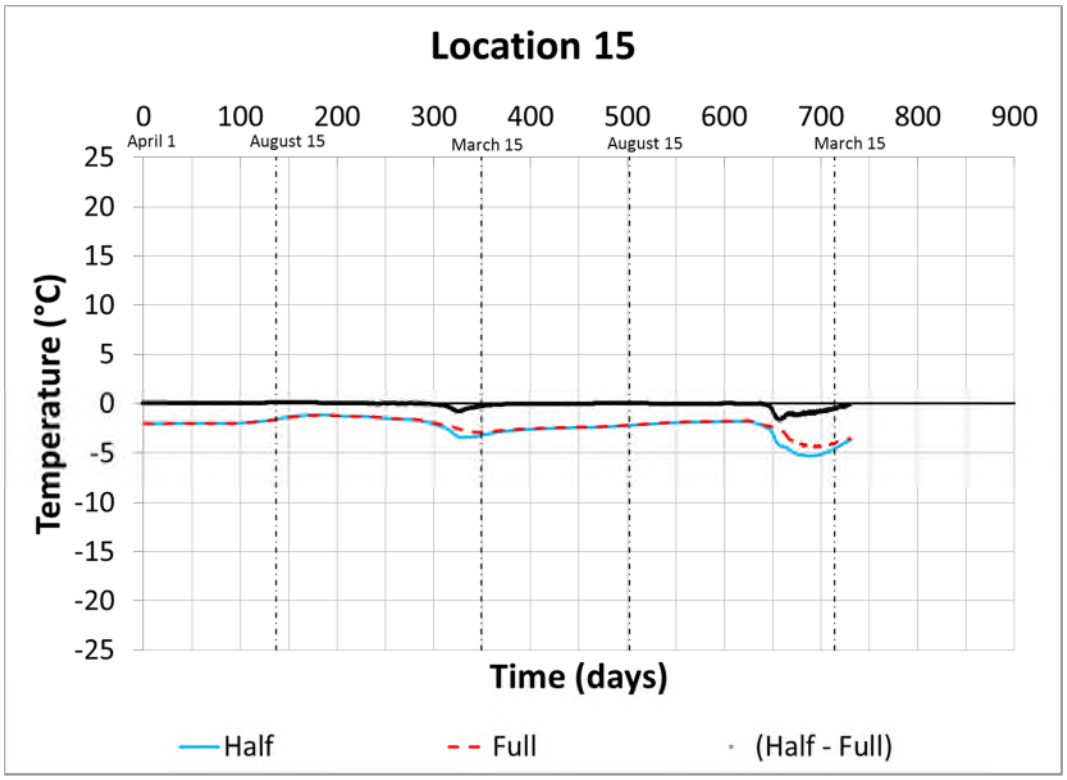

A) Time-temperature plots in Location 15

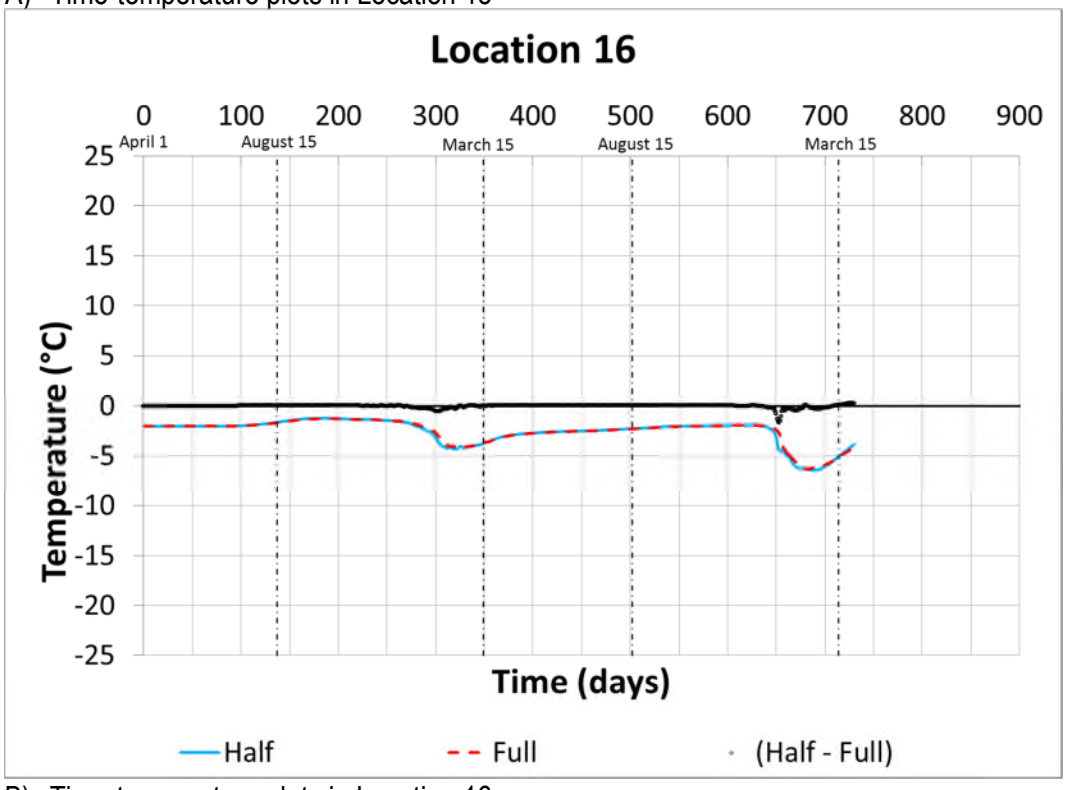

B) Time-temperature plots in Location 16

FIGURE C13: COMPARISON OF NUMERICAL RESULTS ON AUGUST 4 REPRESENTING SUMMER CONDITION FOR GEOSTUDIO HALF MODEL WITH CLOSED BOUNDARIES AND CORRESPONDING FULL MODEL

GEOSTUDIO SIMULATION

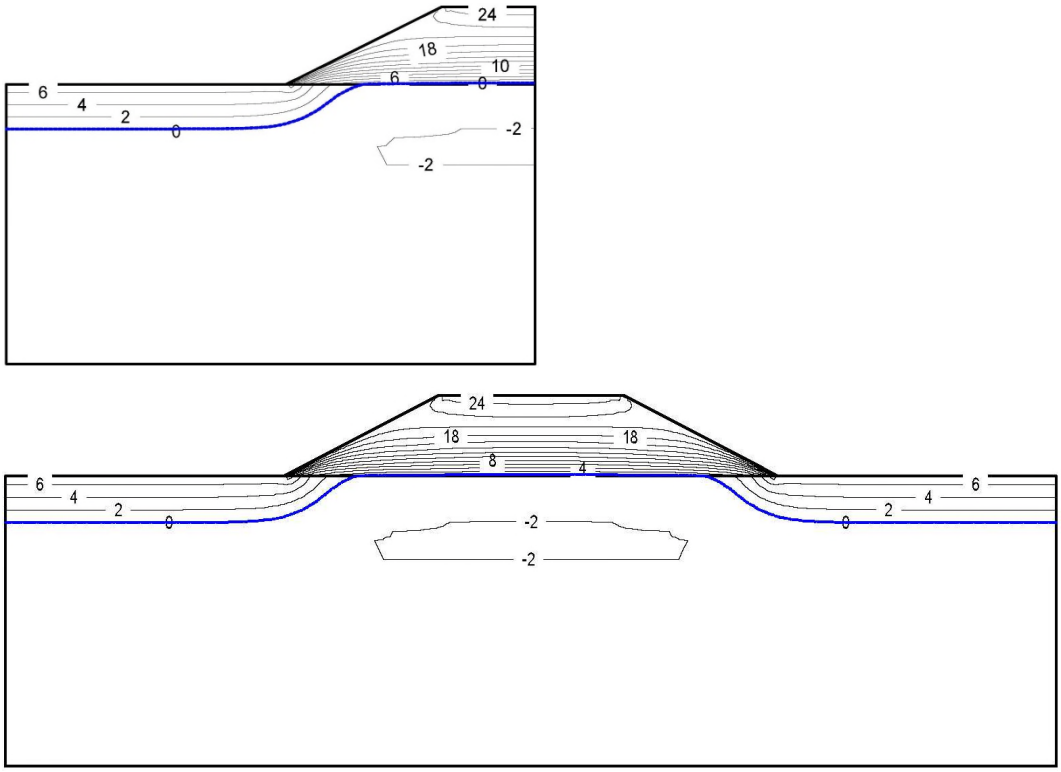

A) Temperature isotherms in half model (top) and corresponding full model (bottom)

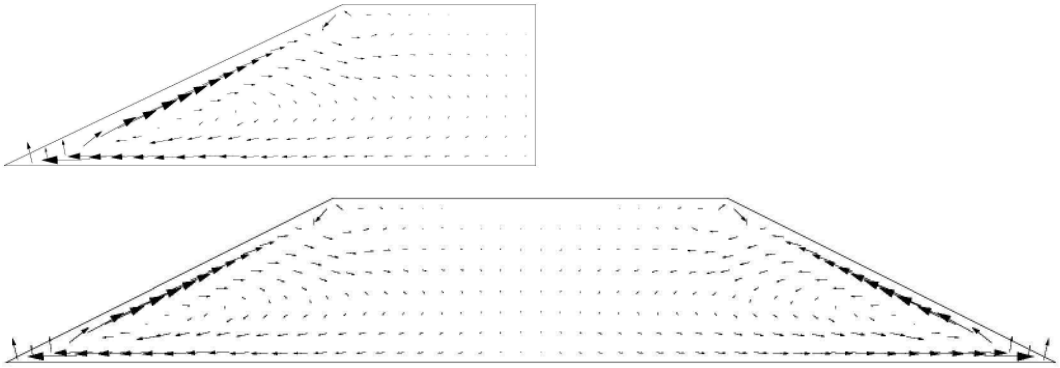

B) Air flow vectors in half model (top) and corresponding full model (bottom)

FIGURE C14: COMPARISON OF NUMERICAL RESULTS ON NOVEMBER 14 REPRESENTING FALL CONDITION FOR GEOSTUDIO HALF MODEL WITH CLOSED BOUNDARIES AND CORRESPONDING FULL MODEL

GEOSTUDIO SIMULATION

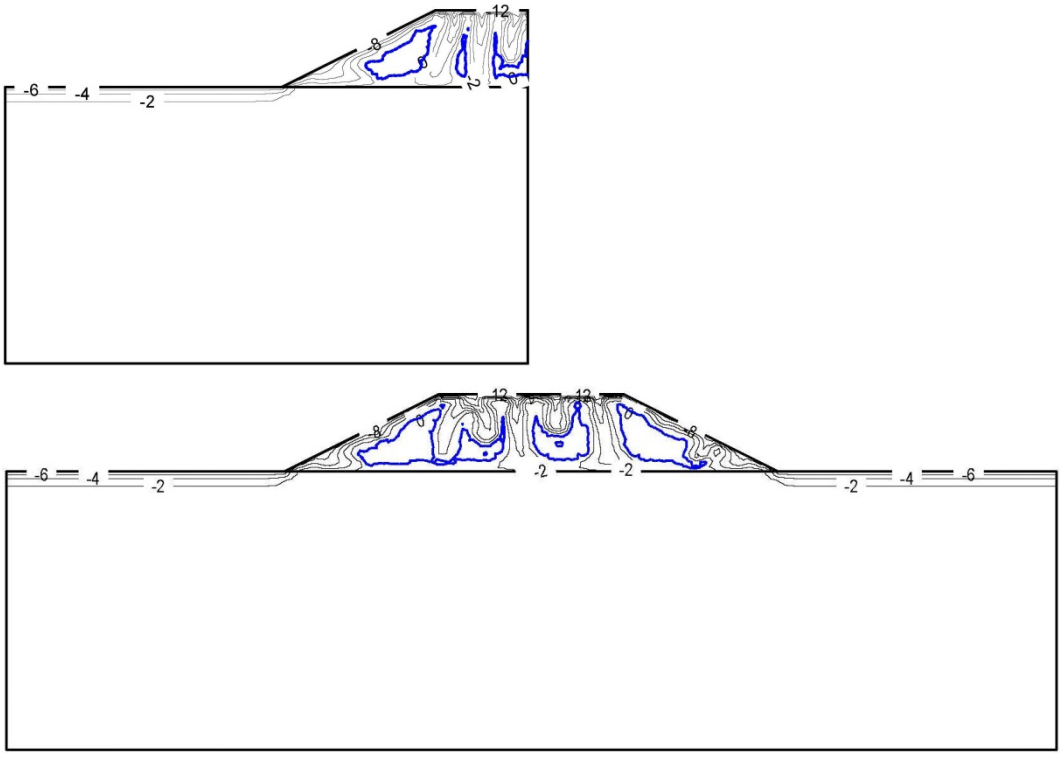

A) Temperature isotherms in half model (top) and corresponding full model (bottom)

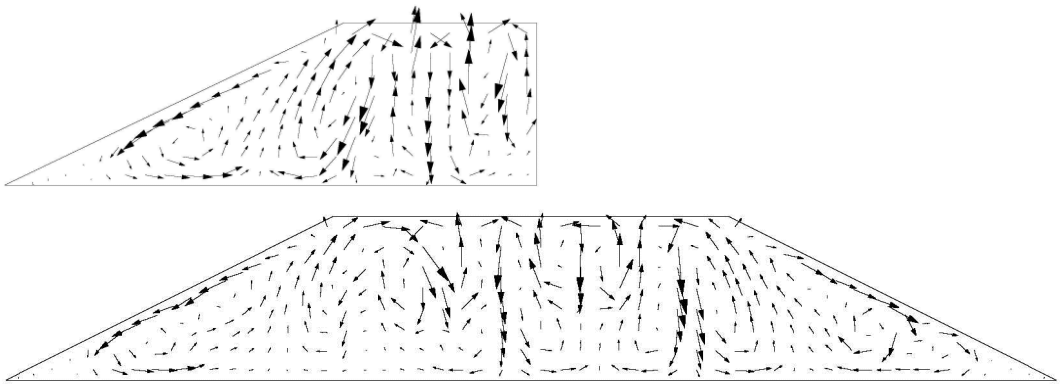

B) Air flow vectors in half model (top) and corresponding full model (bottom)

FIGURE C15: COMPARISON OF NUMERICAL RESULTS ON JANUARY 31 REPRESENTING WINTER CONDITION FOR GEOSTUDIO HALF MODEL WITH CLOSED BOUNDARIES AND CORRESPONDING FULL MODEL

GEOSTUDIO SIMULATION

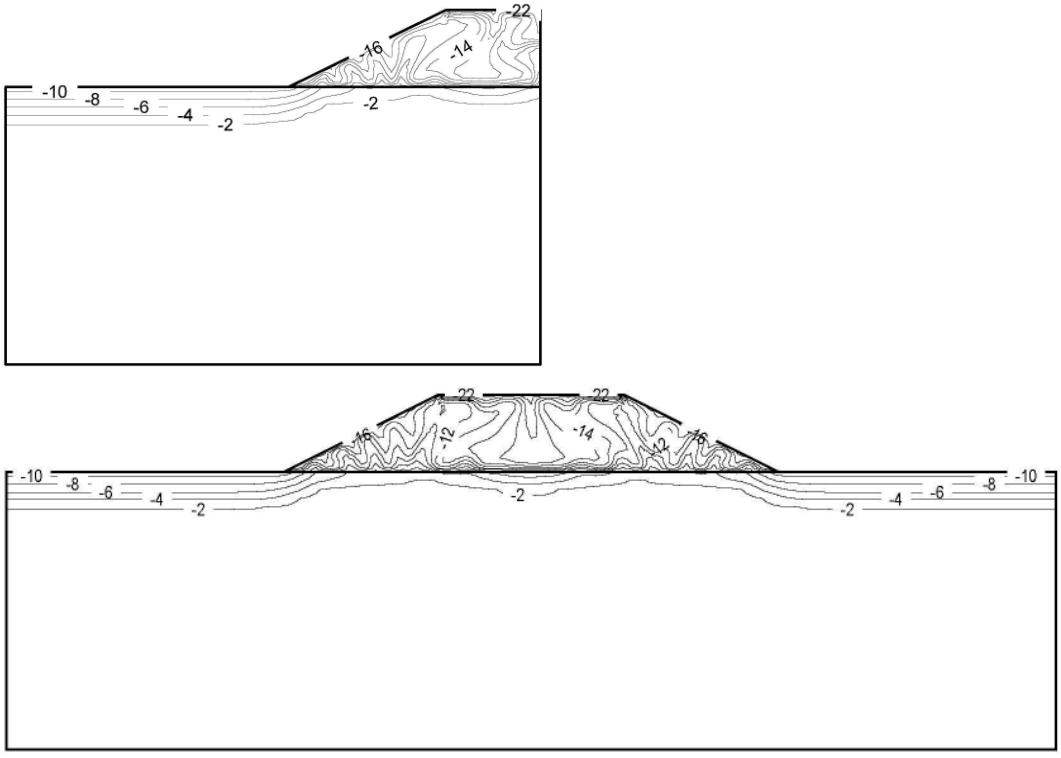

A) Temperature isotherms in half model (top) and corresponding full model (bottom)

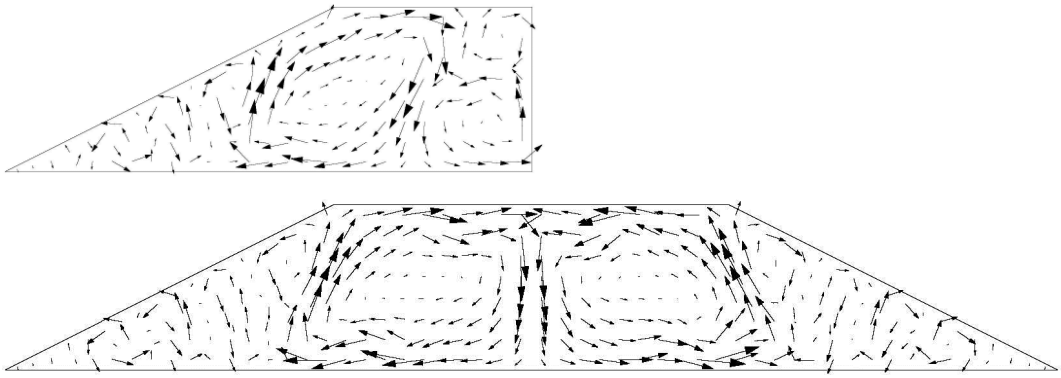

B) Air flow vectors in half model (top) and corresponding full model (bottom)

FIGURE C16: COMPARISON OF NUMERICAL RESULTS ON MAY 1 REPRESENTING SPRING CONDITION FOR GEOSTUDIO HALF MODEL WITH CLOSED BOUNDARIES AND CORRESPONDING FULL MODEL

GEOSTUDIO SIMULATION

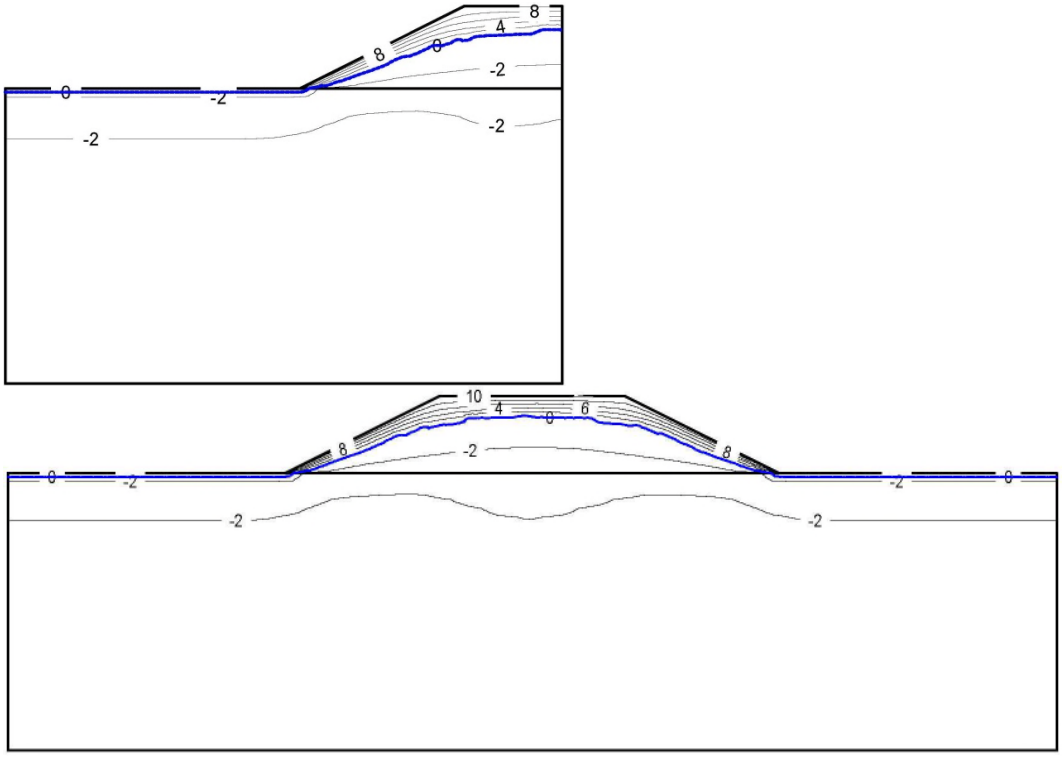

A) Temperature isotherms in half model (top) and corresponding full model (bottom)

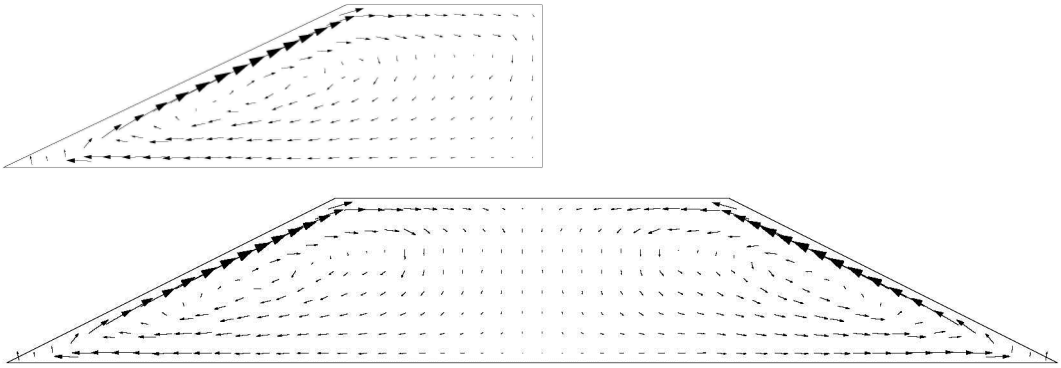

B) Air flow vectors in half model (top) and corresponding full model (bottom)

APPENDIX D

FIGURE D1: STEADY STATE PRESSURE BOUNDARY CONDITIONS APPLIED TO THREE GEOSTUDIO MODELS WITH CLOSED BOUNDARIES USED TO EXAMINE IN TERMS OF SNAPSHOTS REPEATABILITY OF MODELLING RESULTS

GEOSTUDIO SIMULATION

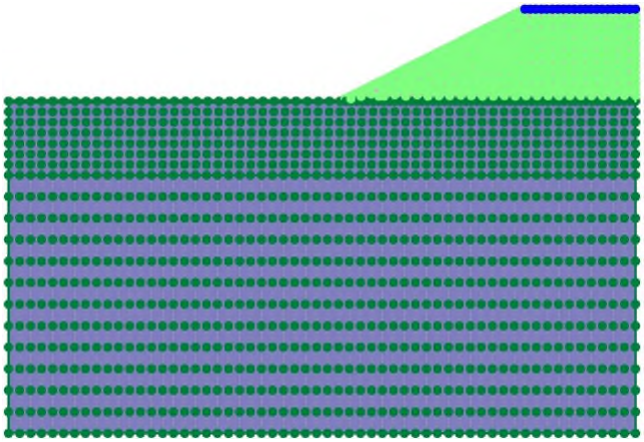

A) Coarse mesh model; 1661 nodes and 1241 elements

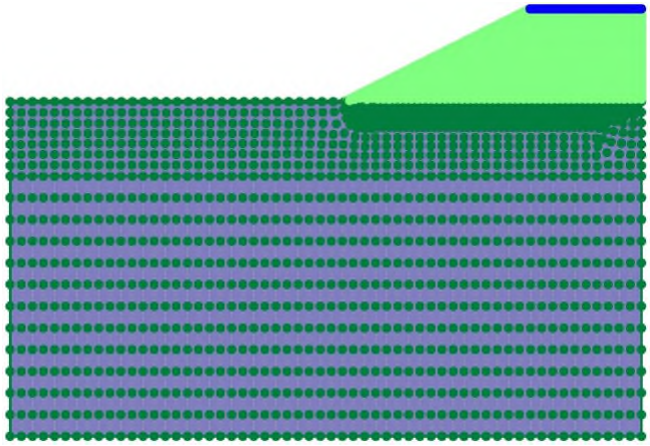

B) Medium mesh model; 3250 nodes and 1876 elements

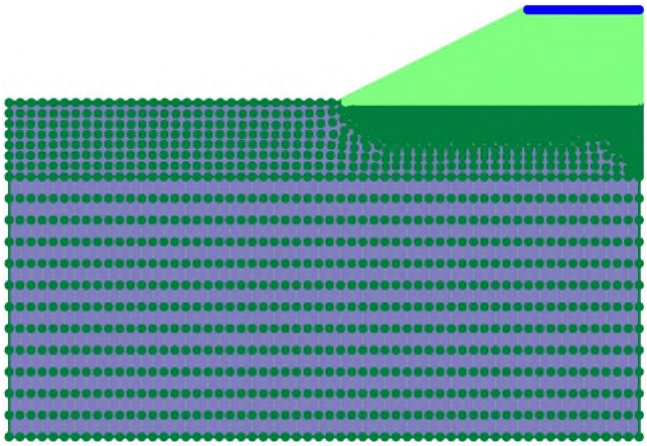

C) Fine mesh model; 6907 nodes and 3323 elements

FIGURE D2: TRANSIENT PRESSURE BOUNDARY CONDITIONS APPLIED TO THREE GEOSTUDIO MODELS WITH CLOSED BOUNDARIES USED TO EXAMINE IN TERMS OF SNAPSHOTS REPEATABILITY OF MODELLING RESULTS

GEOSTUDIO SIMULATION

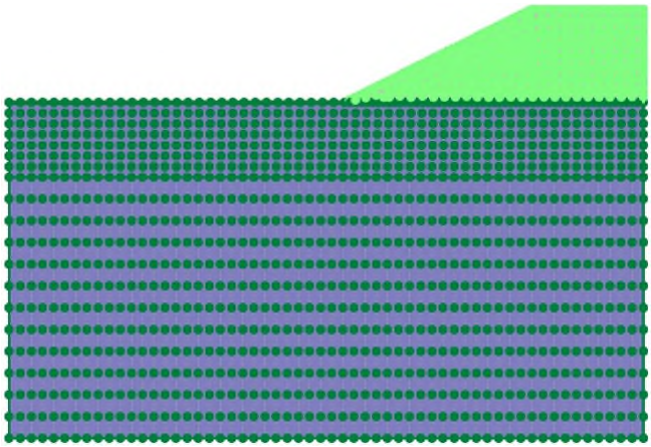

A) Coarse mesh model; 1661 nodes and 1241 elements

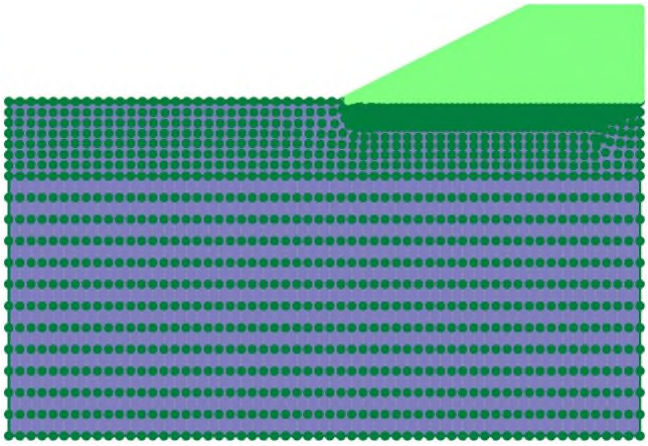

B) Medium mesh model; 3250 nodes and 1876 elements

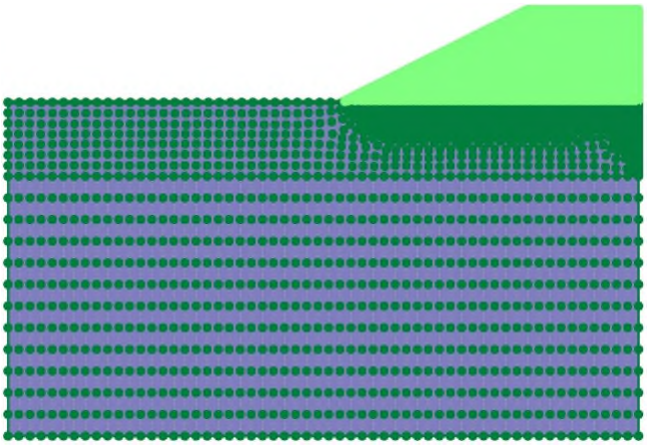

C) Fine mesh model; 6907 nodes and 3323 elements

FIGURE D3: STEADY STATE TEMPERATURE BOUNDARY CONDITION APPLIED TO THREE GEOSTUDIO MODELS WITH CLOSED BOUNDARIES USED TO EXAMINE IN TERMS OF SNAPSHOTS REPEATABILITY OF MODELLING RESULTS

GEOSTUDIO SIMULATION

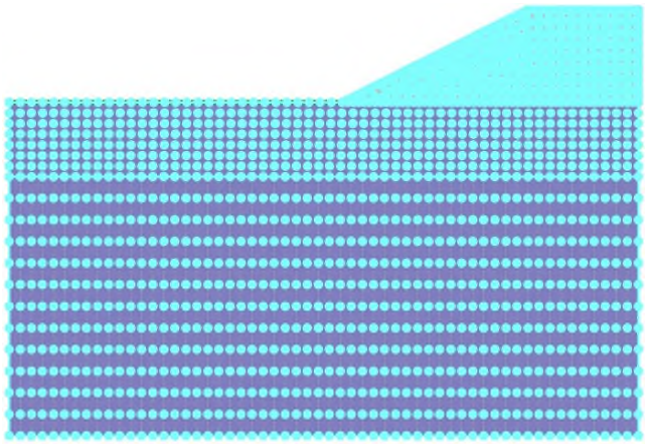

A) Coarse mesh model; 1661 nodes and 1241 elements

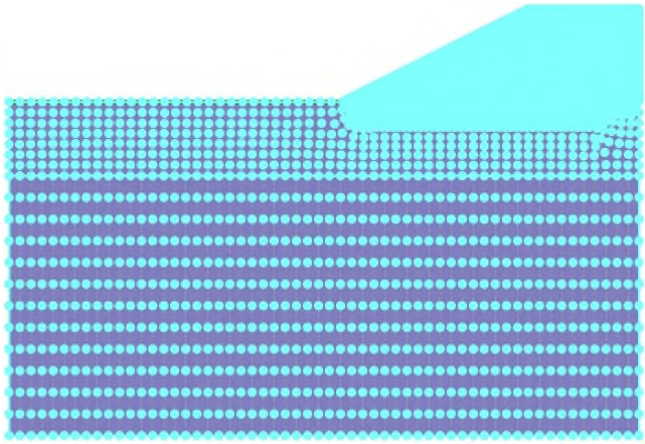

B) Medium mesh model; 3250 nodes and 1876 elements

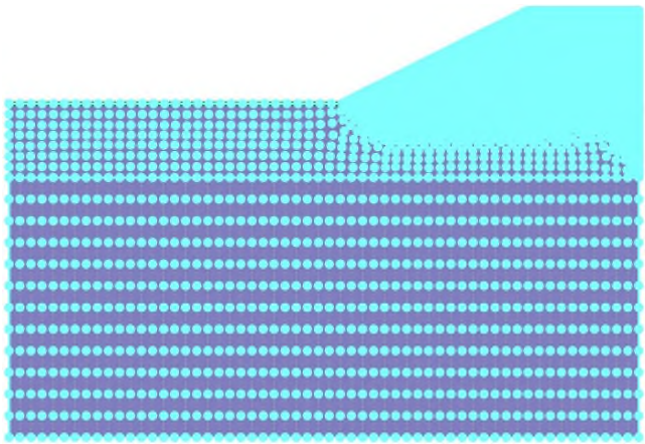

C) Fine mesh model; 6907 nodes and 3323 elements

FIGURE D4: TRANSIENT STATE TEMPERATURE BOUNDARY CONDITIONS APPLIED TO THREE GEOSTUDIO MODELS WITH CLOSED BOUNDARIES USED TO EXAMINE IN TERMS OF SNAPSHOTS REPEATABILITY OF MODELLING RESULTS

GEOSTUDIO SIMULATION

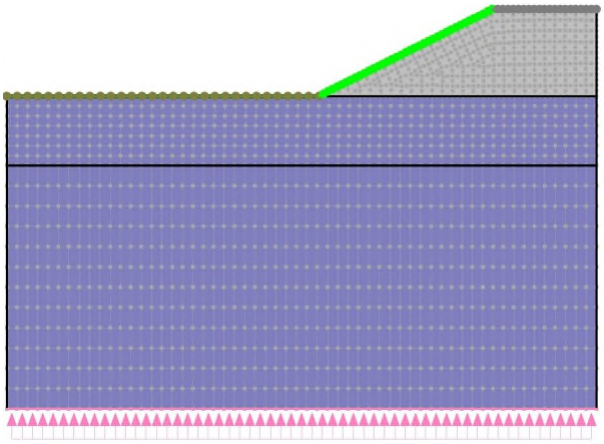

A) Coarse mesh model; 1661 nodes and 1241 elements

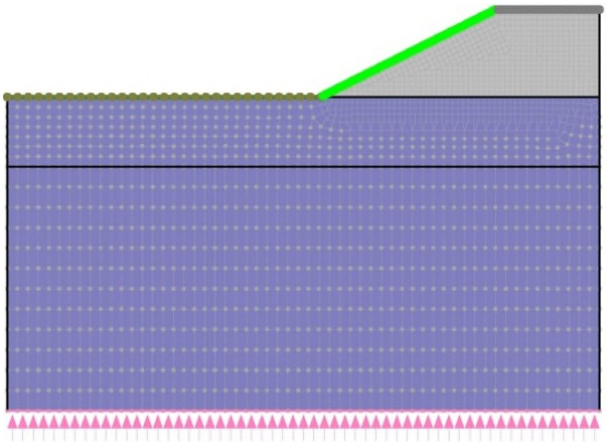

B) Medium mesh model; 3250 nodes and 1876 elements

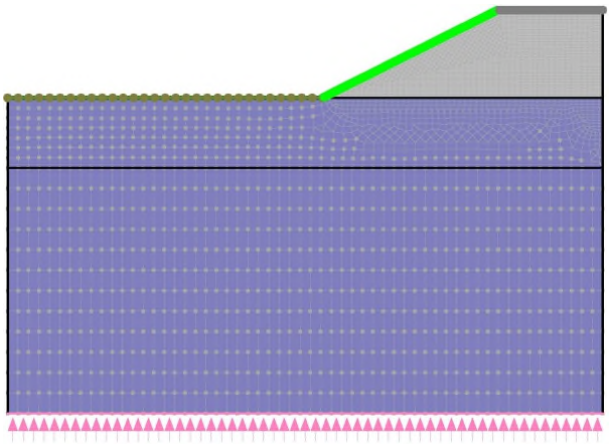

C) Fine mesh model; 6907 nodes and 3323 elements

FIGURE D5: COMPARISON OF NUMERICAL RESULTS ON AUGUST 4 REPRESENTING SUMMER CONDITION FOR GEOSTUDIO COARSE MESH MODEL WITH CLOSED BOUNDARIES

GEOSTUDIO SIMULATION

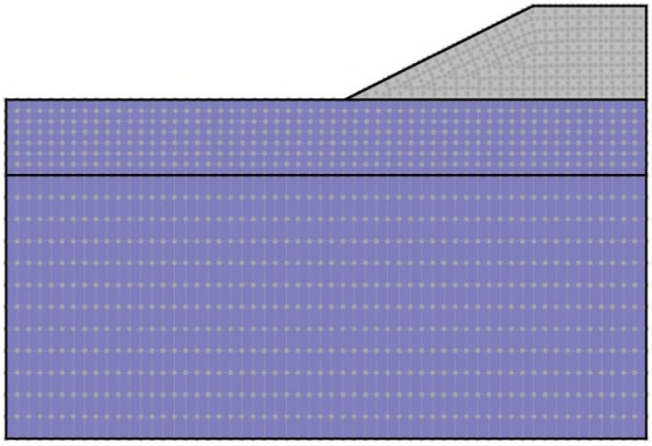

A) Coarse mesh model; 1661 nodes and 1241 elements

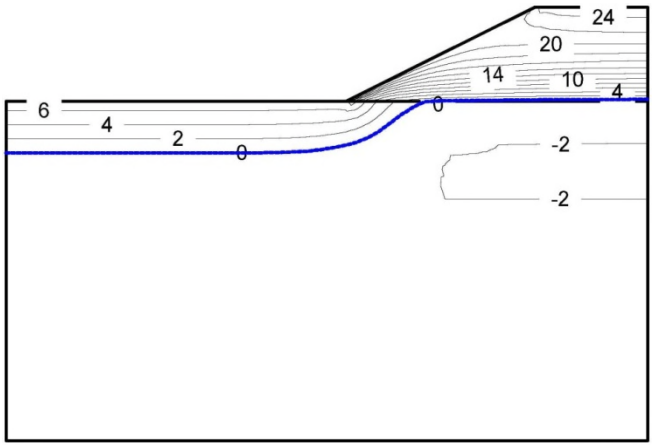

B) Temperature isotherms for run A

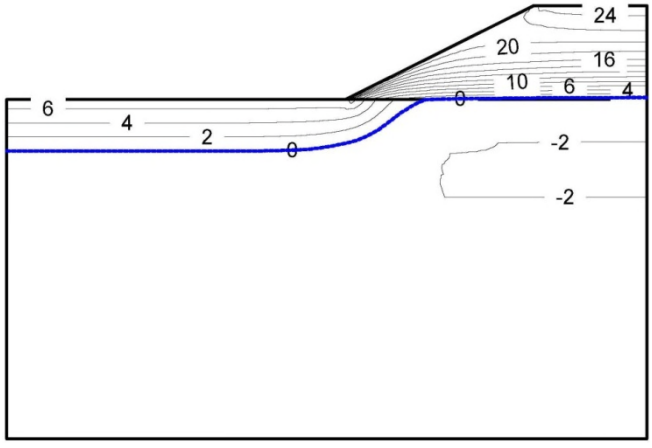

C) Temperature isotherms for run B

FIGURE D6: COMPARISON OF NUMERICAL RESULTS ON AUGUST 4 REPRESENTING SUMMER CONDITION FOR GEOSTUDIO MEDIUM MESH MODEL WITH CLOSED BOUNDARIES

GEOSTUDIO SIMULATION

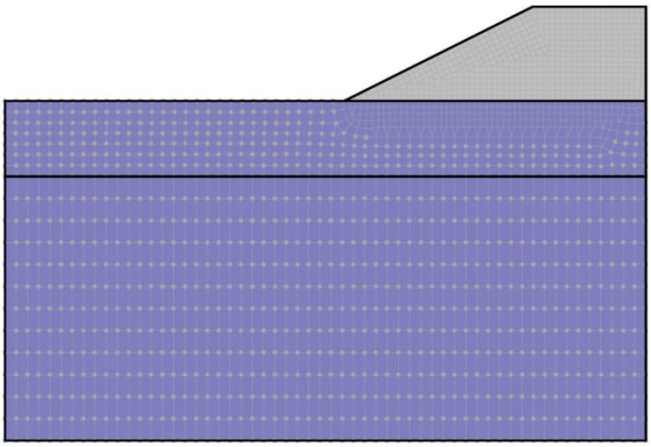

A) Medium mesh model; 3250 nodes and 1876 elements

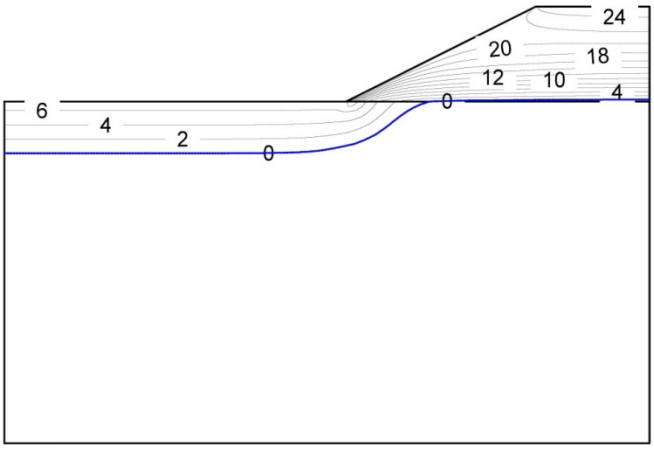

B) Temperature isotherms for run A

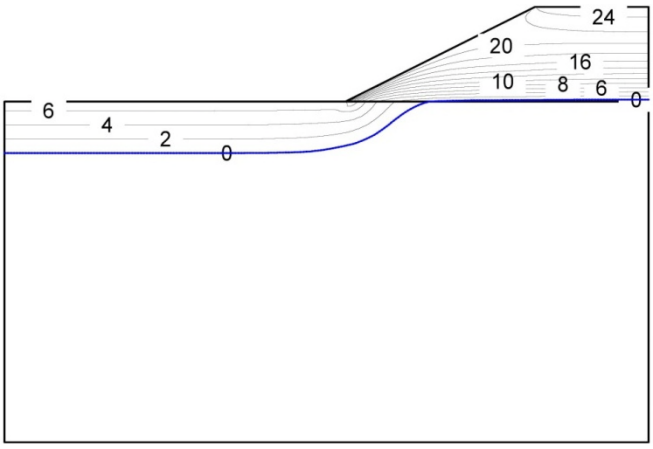

C) Temperature isotherms for run B

FIGURE D7: COMPARISON OF NUMERICAL RESULTS ON AUGUST 4 REPRESENTING SUMMER CONDITION FOR GEOSTUDIO FINE MESH MODEL WITH CLOSED BOUNDARIES

GEOSTUDIO SIMULATION

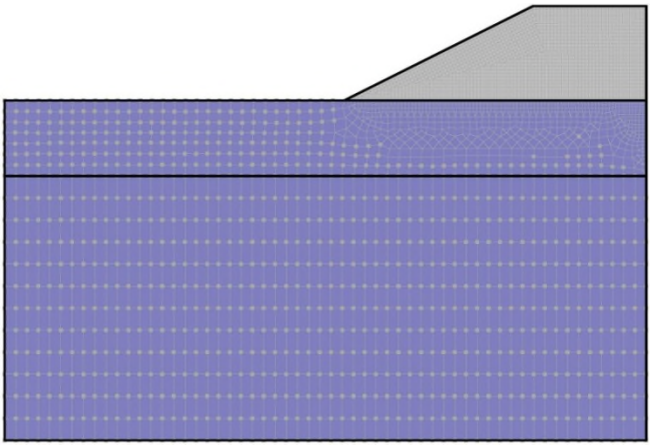

A) Fine mesh model; 6907 nodes and 3323 elements

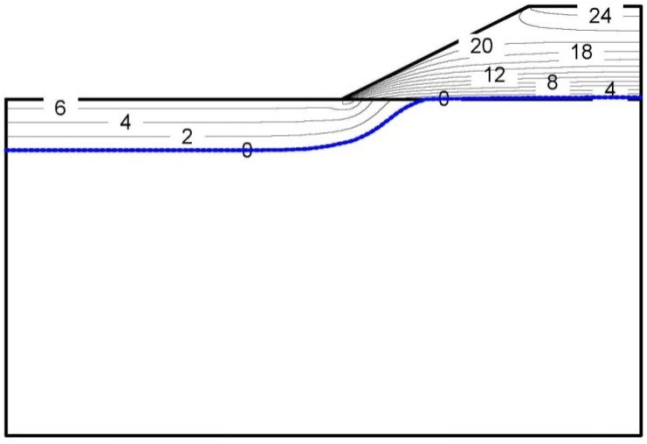

B) Temperature isotherms for run A

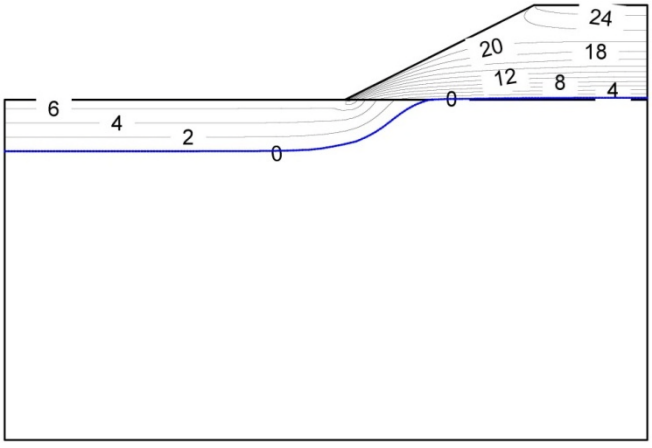

C) Temperature isotherms for run B

FIGURE D8: COMPARISON OF NUMERICAL RESULTS ON MAY 1 REPRESENTING SPRING CONDITION FOR GEOSTUDIO COARSE MESH MODEL WITH CLOSED BOUNDARIES

GEOSTUDIO SIMULATION

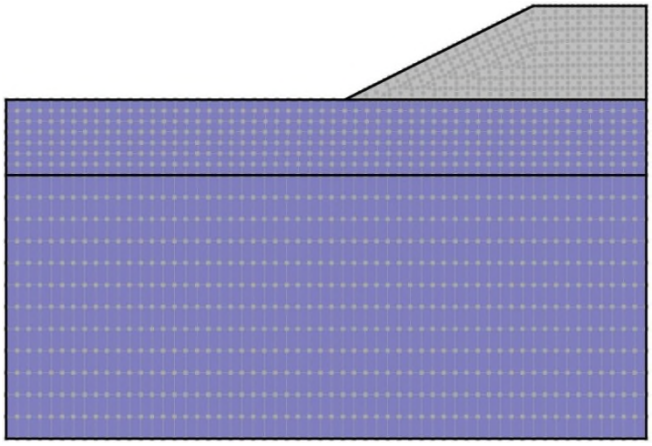

A) Coarse mesh model; 1661 nodes and 1241 elements

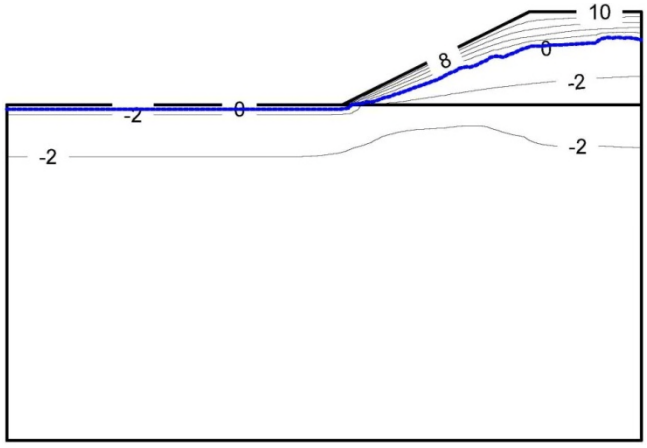

B) Temperature isotherms for run A

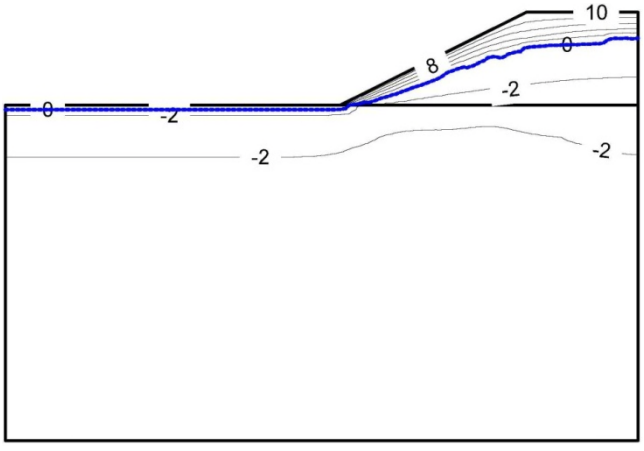

C) Temperature isotherms for run B

FIGURE D9: COMPARISON OF NUMERICAL RESULTS ON MAY 1 REPRESENTING SPRING CONDITION FOR GEOSTUDIO MEDIUM MESH MODEL WITH CLOSED BOUNDARIES

GEOSTUDIO SIMULATION

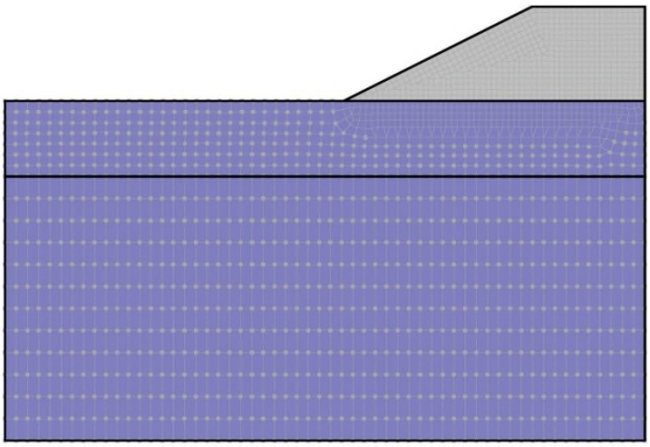

A) Medium mesh model; 3250 nodes and 1876 elements

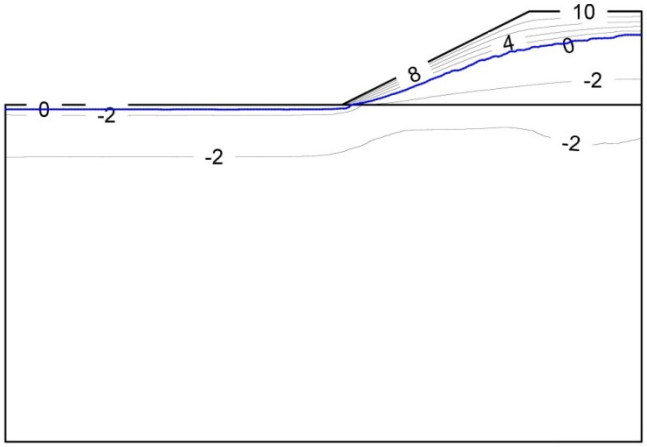

B) Temperature isotherms for run A

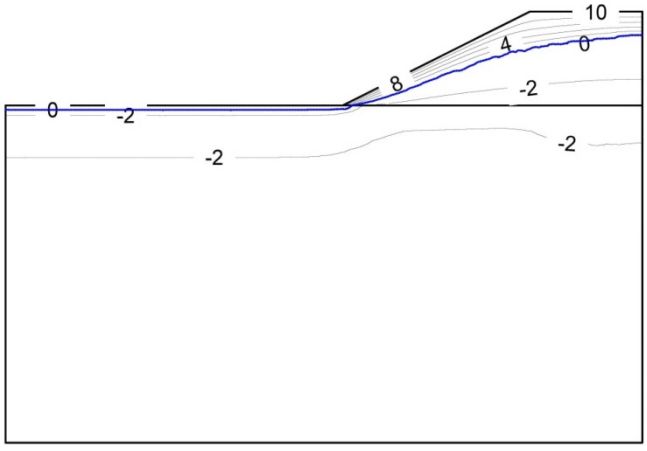

C) Temperature isotherms for run B

FIGURE D10: COMPARISON OF NUMERICAL RESULTS ON MAY 1 REPRESENTING SPRING CONDITION FOR GEOSTUDIO FINE MESH MODEL WITH CLOSED BOUNDARIES

GEOSTUDIO SIMULATION

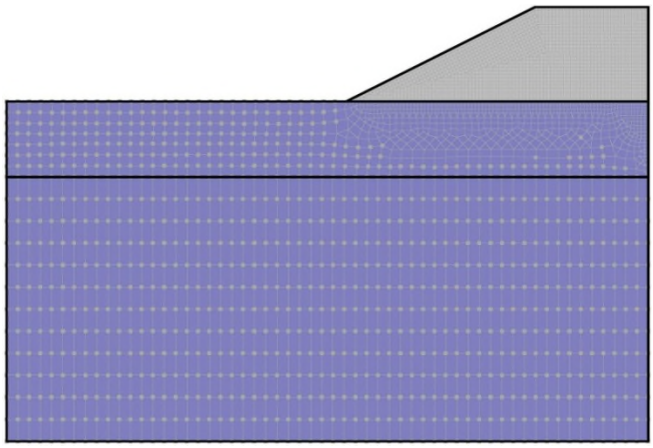

A) Fine mesh model; 6907 nodes and 3323 elements

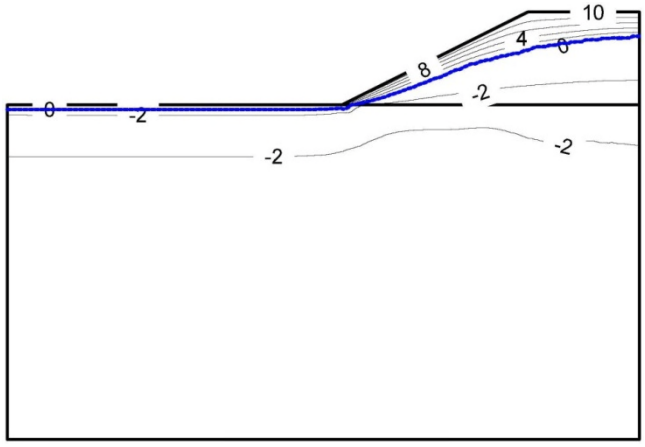

B) Temperature isotherms for run A

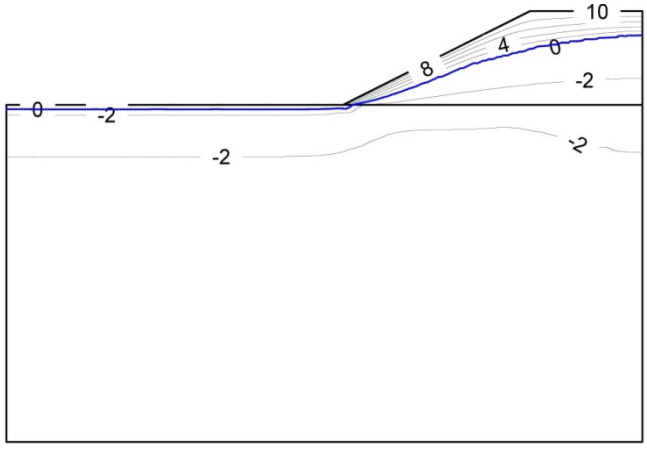

C) Temperature isotherms for run B

APPENDIX E

FIGURE E1: STEADY STATE PRESSURE BOUNDARY CONDITIONS APPLIED TO GEOSTUDIO COARSE AND FINE MESH MODELS WITH CLOSED BOUNDARIES USED TO EXAMINE IN TERMS OF TRENDS REPEATABILITY OF MODELLING RESULTS

GEOSTUDIO SIMULATION

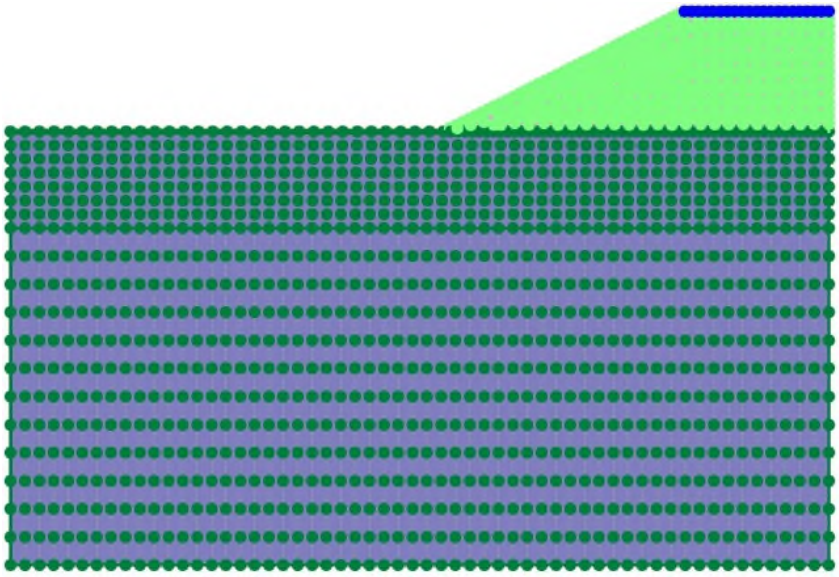

A) Coarse mesh model; 1661 nodes and 1241 elements

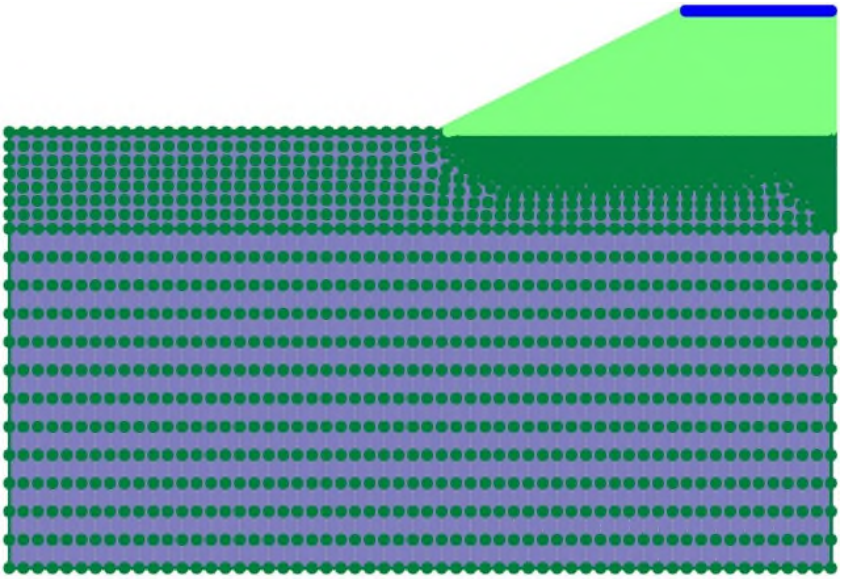

B) Fine mesh model; 6907 nodes and 3323 elements

FIGURE E2: TRANSIENT STATE PRESSURE BOUNDARY CONDITIONS APPLIED TO GEOSTUDIO COARSE AND FINE MESH MODELS WITH CLOSED BOUNDARIES USED TO EXAMINE IN TERMS OF TRENDS REPEATABILITY OF MODELLING RESULTS

GEOSTUDIO SIMULATION

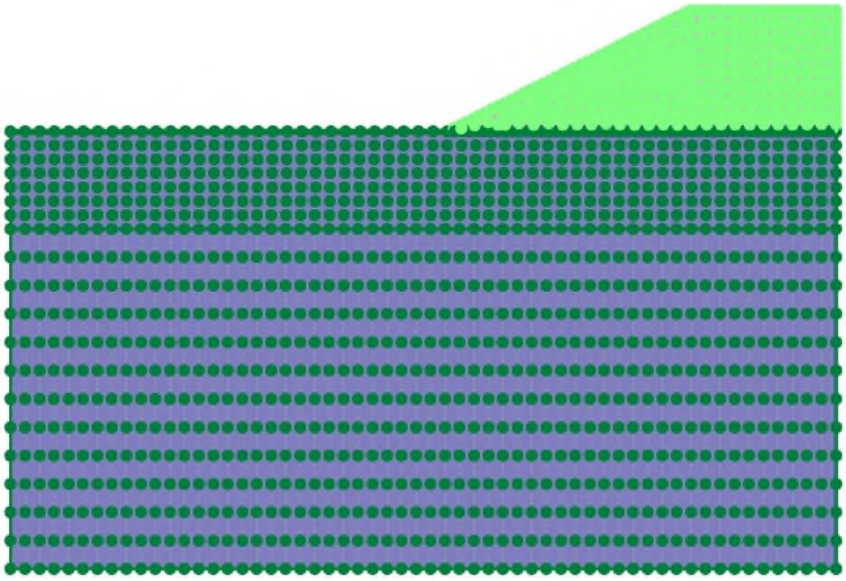

A) Coarse mesh model; 1661 nodes and 1241 elements

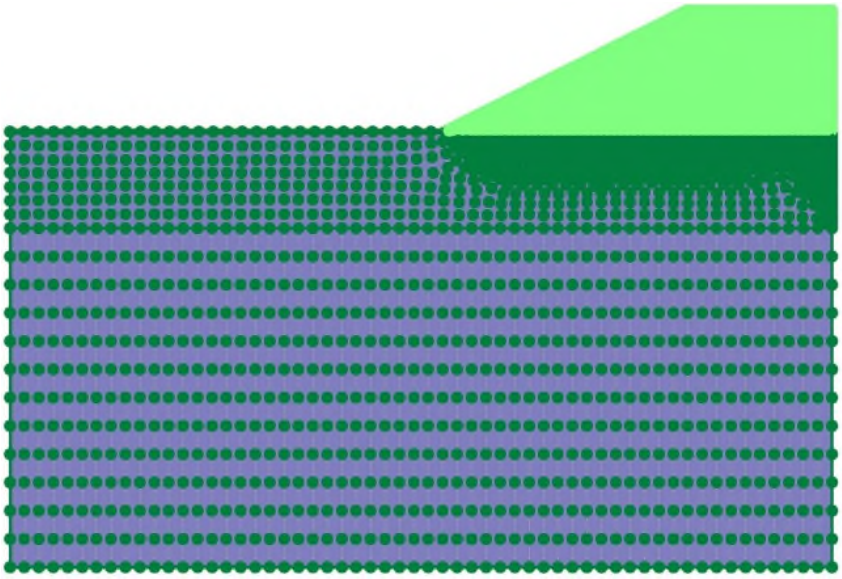

B) Fine mesh model; 6907 nodes and 3323 elements

FIGURE E3: TRANSIENT STATE PRESSURE BOUNDARY CONDITIONS APPLIED TO GEOSTUDIO COARSE AND FINE MESH MODELS WITH OPEN SIDESLOPES USED TO EXAMINE IN TERMS OF TRENDS REPEATABILITY OF MODELLING RESULTS

GEOSTUDIO SIMULATION

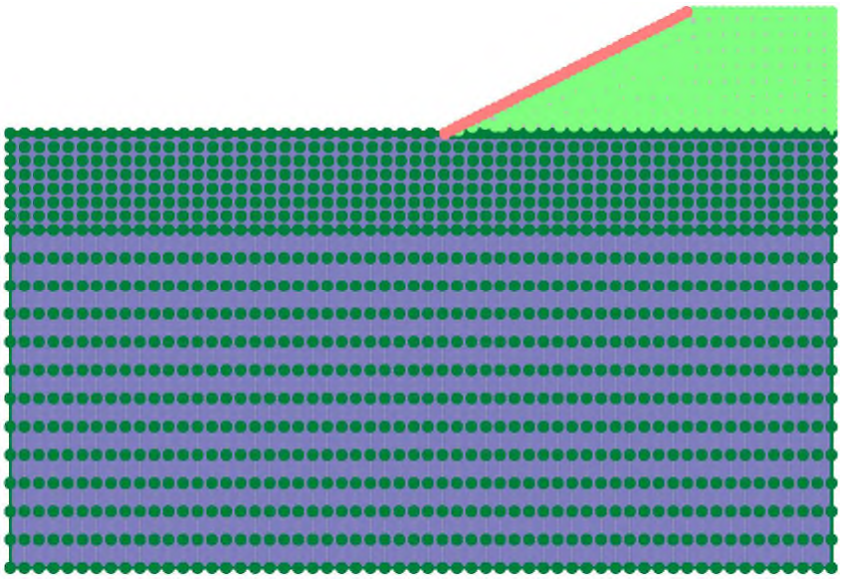

A) Coarse mesh model; 1661 nodes and 1241 elements

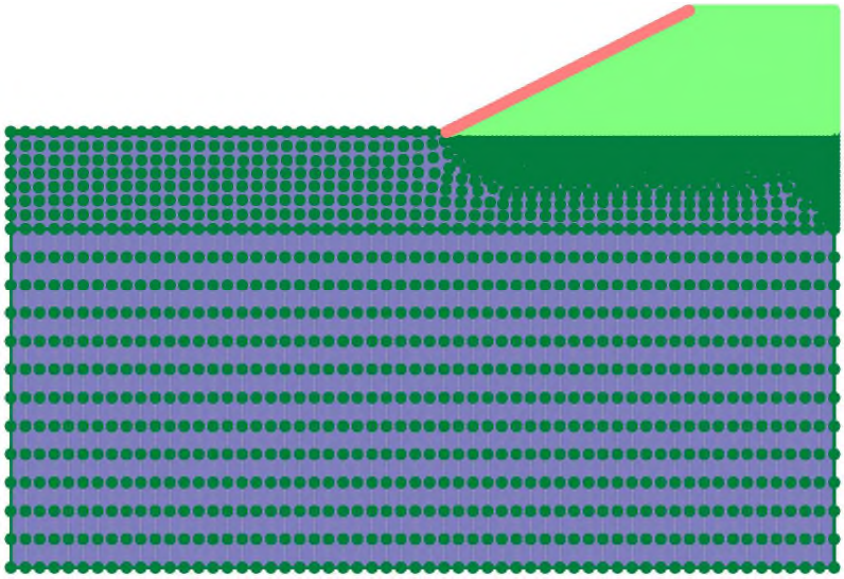

B) Fine mesh model; 6907 nodes and 3323 elements

FIGURE E4: STEADY STATE TEMPERATURE BOUNDARY CONDITION APPLIED TO GEOSTUDIO COARSE AND FINE MESH MODELS USED TO EXAMINE IN TERMS OF TRENDS REPEATABILITY OF MODELLING RESULTS

GEOSTUDIO SIMULATION

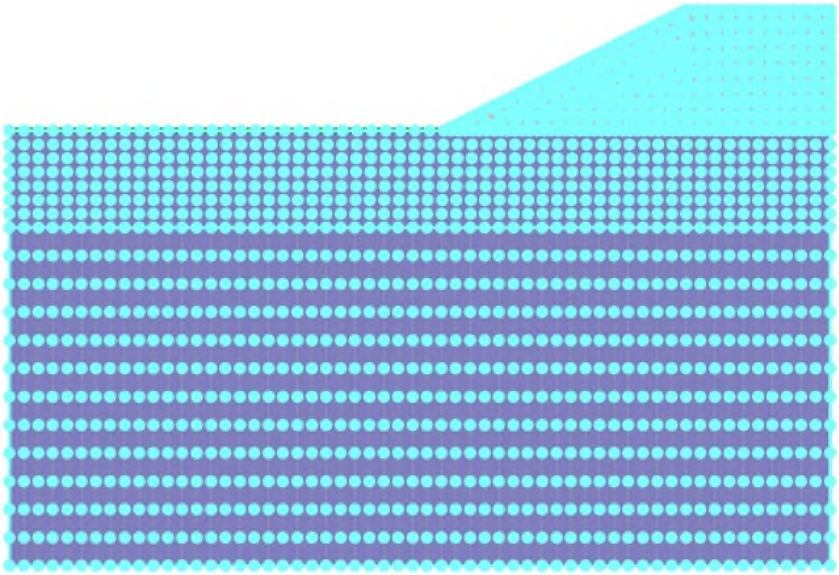

A) Coarse mesh model; 1661 nodes and 1241 elements

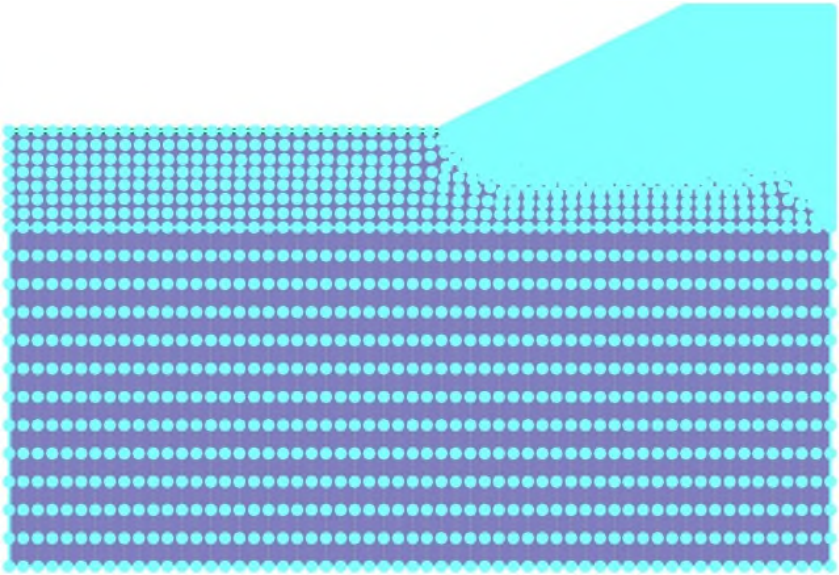

B) Fine mesh model; 6907 nodes and 3323 elements

FIGURE E5: TRANSIENT STATE TEMPERATURE BOUNDARY CONDITION APPLIED TO GEOSTUDIO COARSE AND FINE MESH MODELS USED TO EXAMINE IN TERMS OF TRENDS REPEATABILITY OF MODELLING RESULTS

GEOSTUDIO SIMULATION

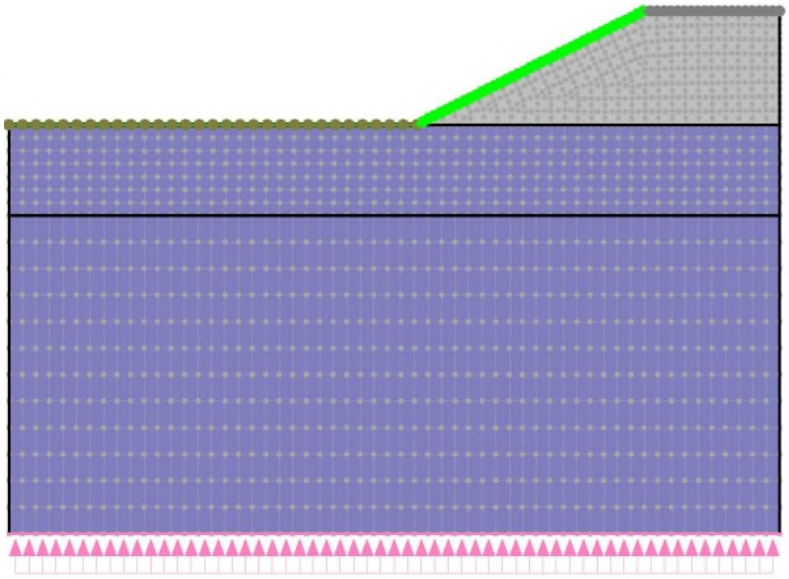

A) Coarse mesh model; 1661 nodes and 1241 elements

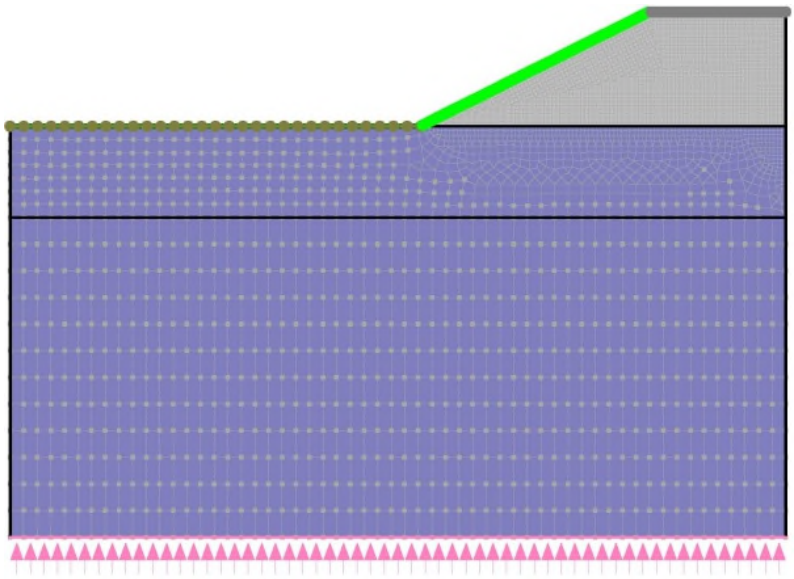

B) Fine mesh model; 6907 nodes and 3323 elements

APPENDIX F

FIGURE F1: STEADY STATE PRESSURE BOUNDARY CONDITIONS APPLIED TO GEOSTUDIO COARSE AND FINE MESH MODELS USED TO MODEL GOERING (2000) WITH OPEN SIDESLOPES

GEOSTUDIO SIMULATION

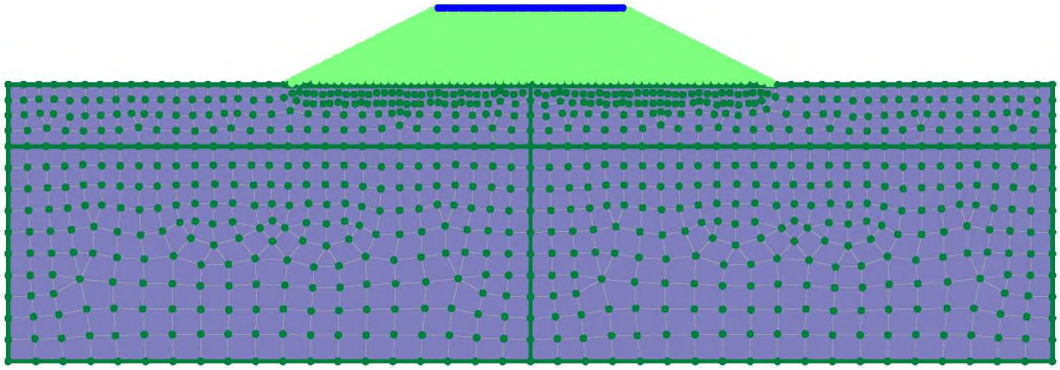

A) Coarse mesh model; 2286 nodes and 1286 elements

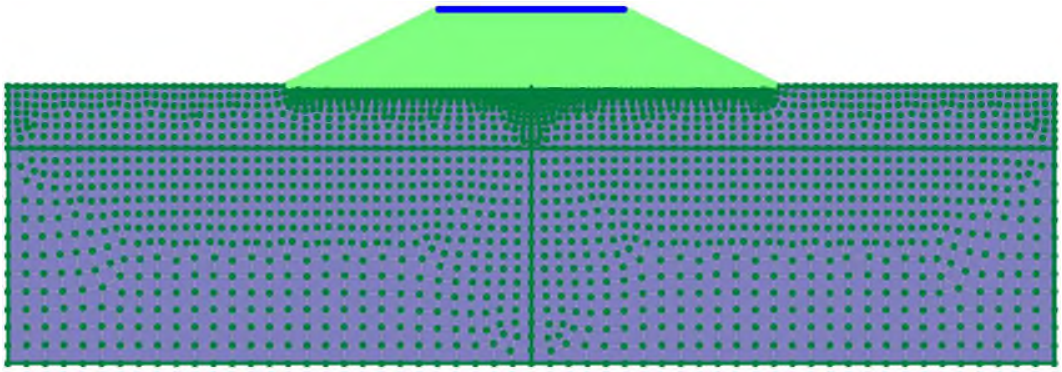

B) Fine mesh model; 5829 nodes and 3190 elements

FIGURE F2: TRANSIENT STATE PRESSURE BOUNDARY CONDITIONS APPLIED TO GEOSTUDIO COARSE AND FINE MESH MODELS USED TO MODEL GOERING (2000) WITH OPEN SIDESLOPES

GEOSTUDIO SIMULATION

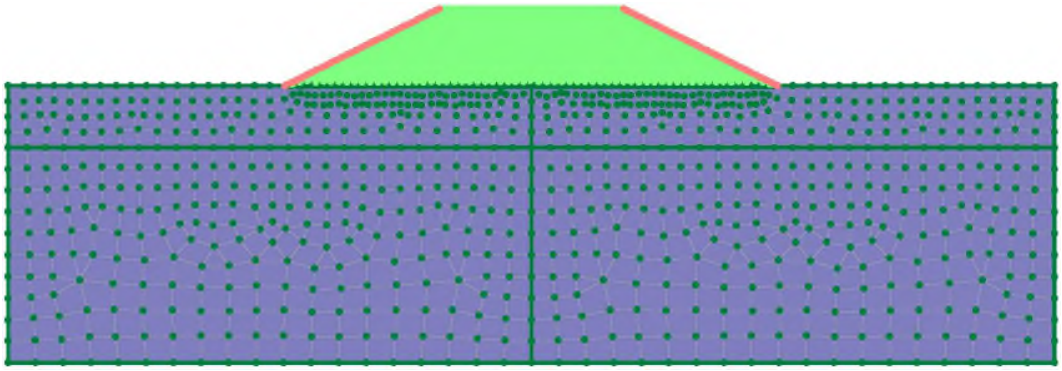

A) Coarse mesh model; 2286 nodes and 1286 elements

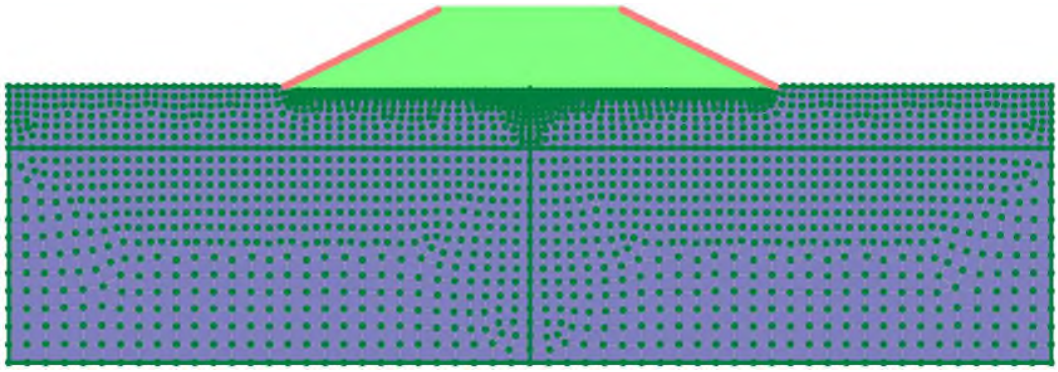

B) Fine mesh model; 5829 nodes and 3190 elements

FIGURE F3: STEADY STATE TEMPERATURE BOUNDARY CONDITION APPLIED TO GEOSTUDIO COARSE AND FINE MESH MODELS USED TO MODEL GOERING (2000) WITH OPEN SIDESLOPES

GEOSTUDIO SIMULATION

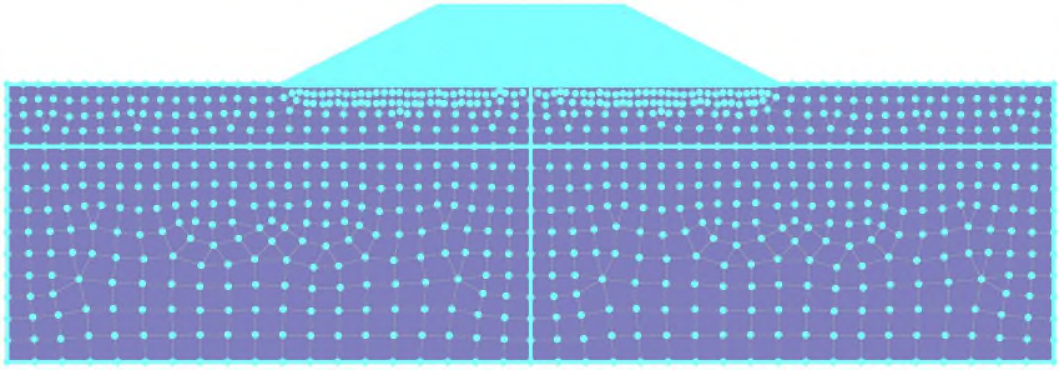

A) Coarse mesh model; 2286 nodes and 1286 elements

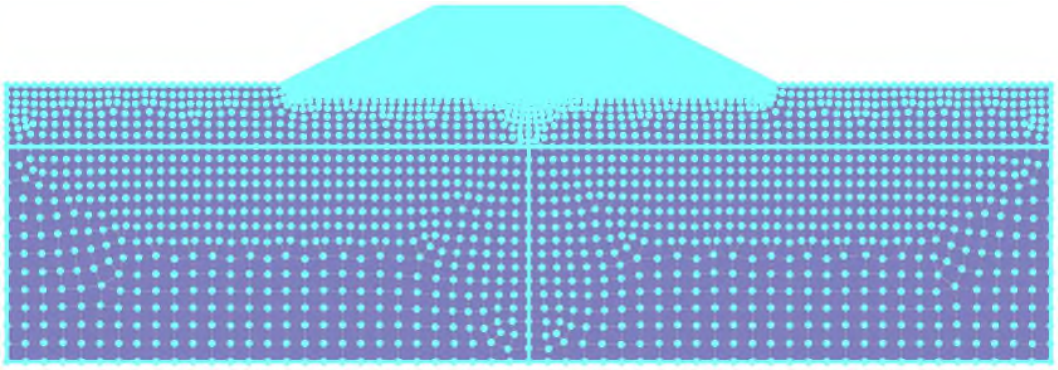

B) Fine mesh model; 5829 nodes and 3190 elements

FIGURE F4: TRANSIENT STATE TEMPERATURE BOUNDARY CONDITIONS APPLIED TO GEOSTUDIO COARSE AND FINE MESH MODELS USED TO MODEL GOERING (2000) WITH OPEN SIDESLOPES

GEOSTUDIO SIMULATION

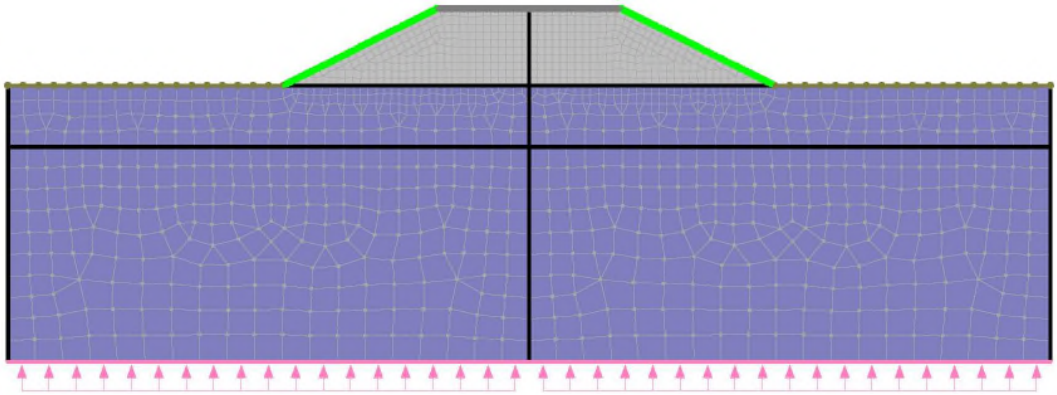

A) Coarse mesh model; 2286 nodes and 1286 elements

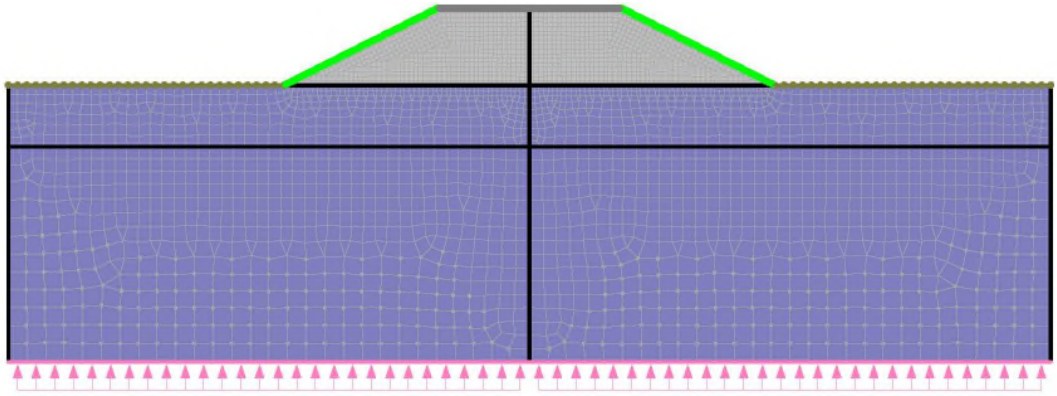

B) Fine mesh model; 5829 nodes and 3190 elements

FIGURE F5: STEADY STATE PRESSURE BOUNDARY CONDITIONS APPLIED TO GEOSTUDIO MODELS USED TO MODEL GOERING AND KUMAR (1996) AND GOERING (2000) WITH CLOSED BOUNDARIES

GEOSTUDIO SIMULATION

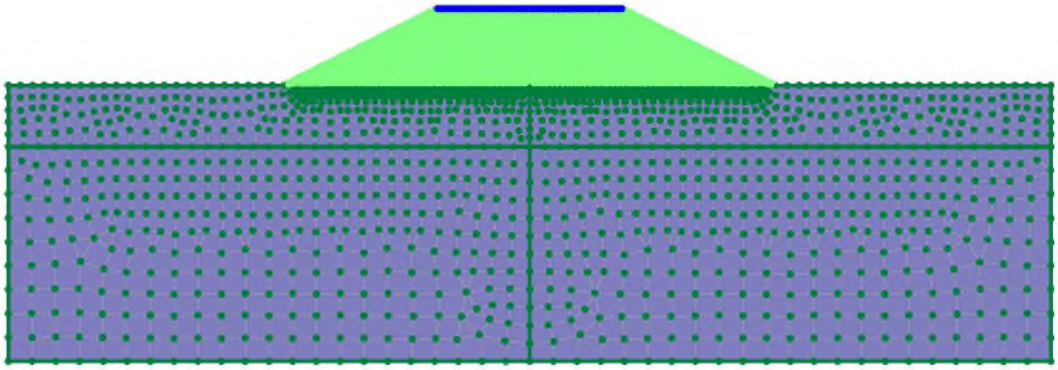

A) GeoStudio model for Goering and Kumar (1996); 5177 nodes and 2561 elements

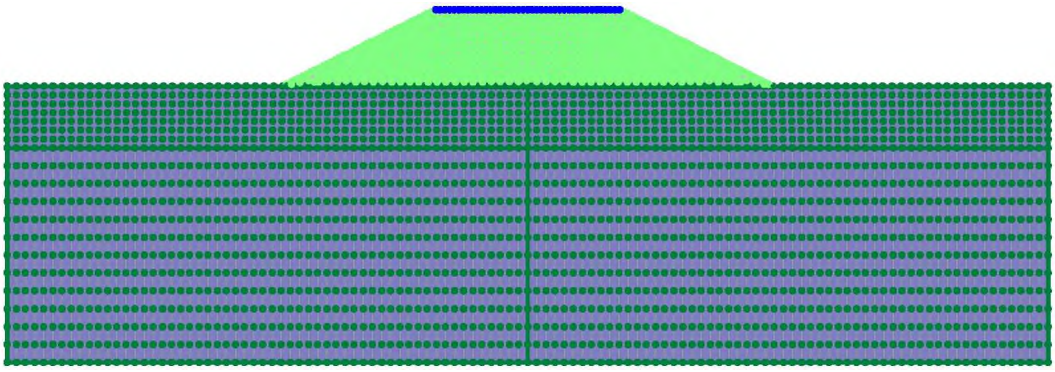

B) GeoStudio model for Goering (2000); 3286 nodes and 2482 elements

FIGURE F6: TRANSIENT STATE PRESSURE BOUNDARY CONDITIONS APPLIED TO GEOSTUDIO MODELS USED TO MODEL GOERING AND KUMAR (1996) AND GOERING (2000) WITH CLOSED BOUNDARIES

GEOSTUDIO SIMULATION

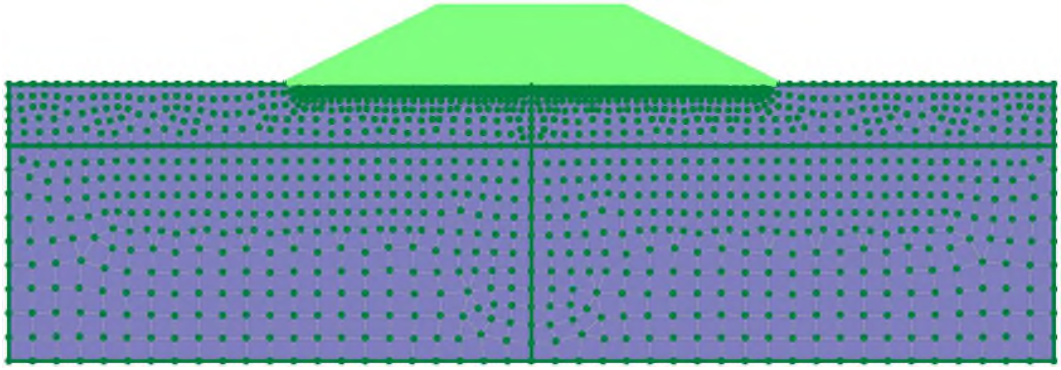

A) GeoStudio model for Goering and Kumar (1996); 5177 nodes and 2561 elements

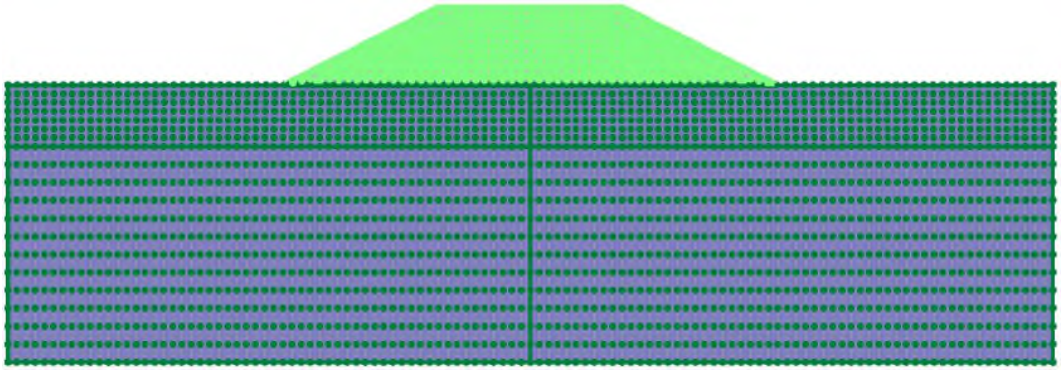

B) GeoStudio model for Goering (2000); 3286 nodes and 2482 elements

FIGURE F7: STEADY STATE TEMPERATURE BOUNDARY CONDITION APPLIED TO GEOSTUDIO MODELS USED TO MODEL GOERING AND KUMAR (1996) AND GOERING (2000) WITH CLOSED BOUNDARIES

GEOSTUDIO SIMULATION

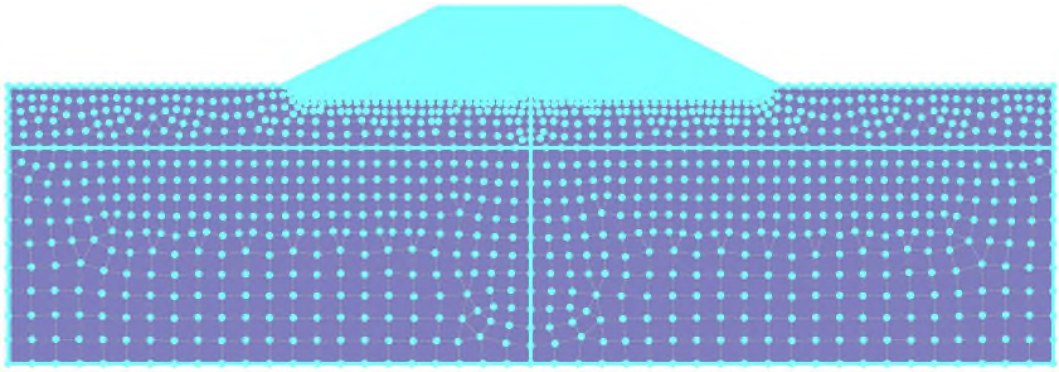

A) GeoStudio model for Goering and Kumar (1996); 5177 nodes and 2561 elements

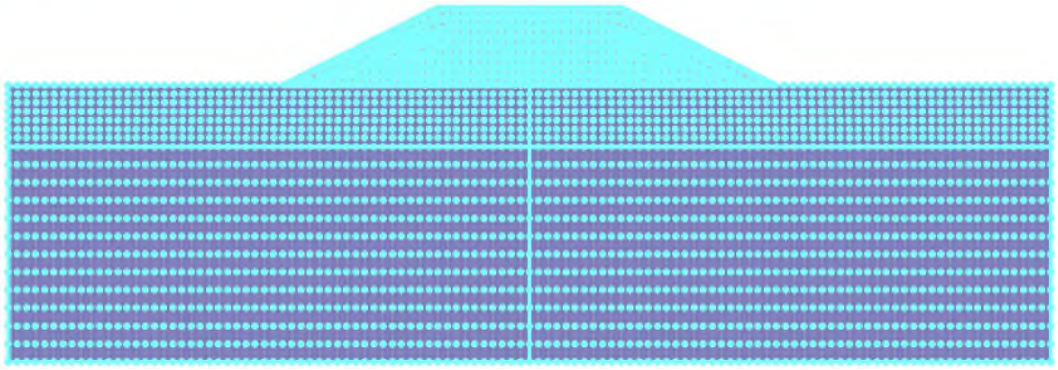

B) GeoStudio model for Goering (2000); 3286 nodes and 2482 elements

FIGURE F8: TRANSIENT STATE TEMPERATURE BOUNDARY CONDITIONS APPLIED TO GEOSTUDIO MODELS USED TO MODEL GOERING AND KUMAR (1996) AND GOERING (2000) WITH CLOSED BOUNDARIES

GEOSTUDIO SIMULATION

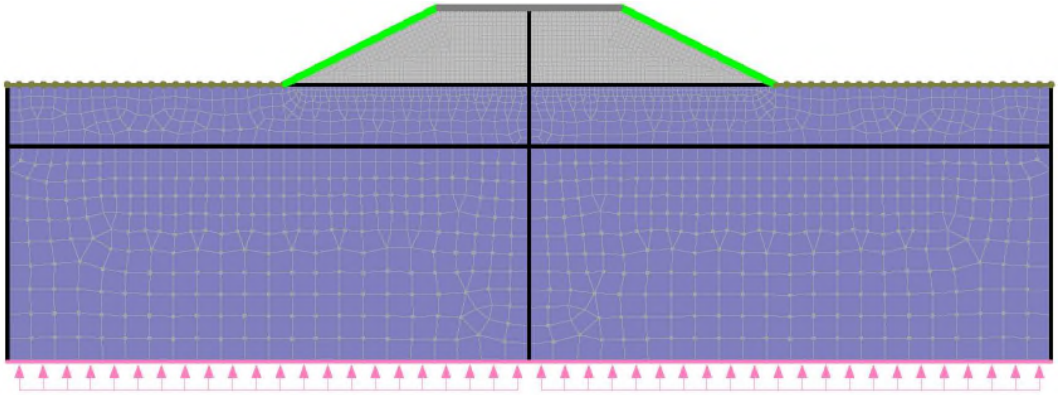

A) GeoStudio model for Goering and Kumar (1996); 5177 nodes and 2561 elements

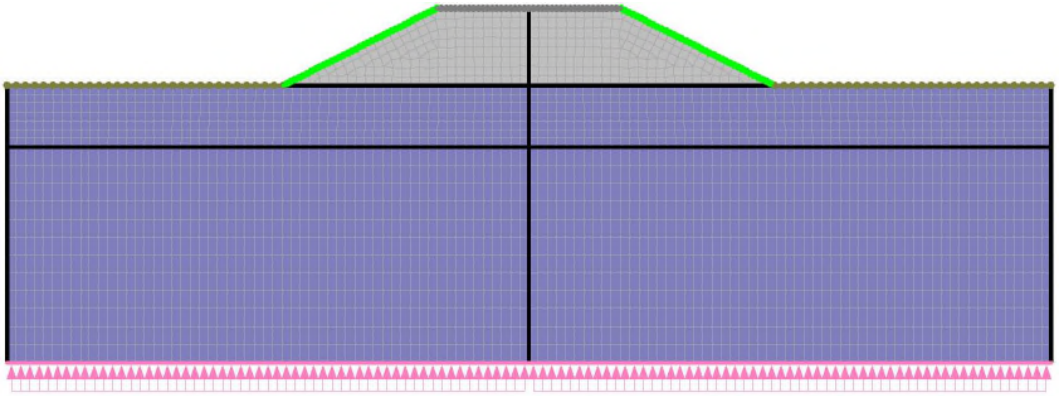

B) GeoStudio model for Goering (2000); 3286 nodes and 2482 elements

APPENDIX G

FIGURE G1: STEADY STATE AND TRANSIENT STATE PRESSURE BOUNDARY CONDITIONS APPLIED TO GEOSTUDIO MODEL USED TO MODEL EKATI EXPERIMENTAL EXAMPLE

GEOSTUDIO SIMULATION

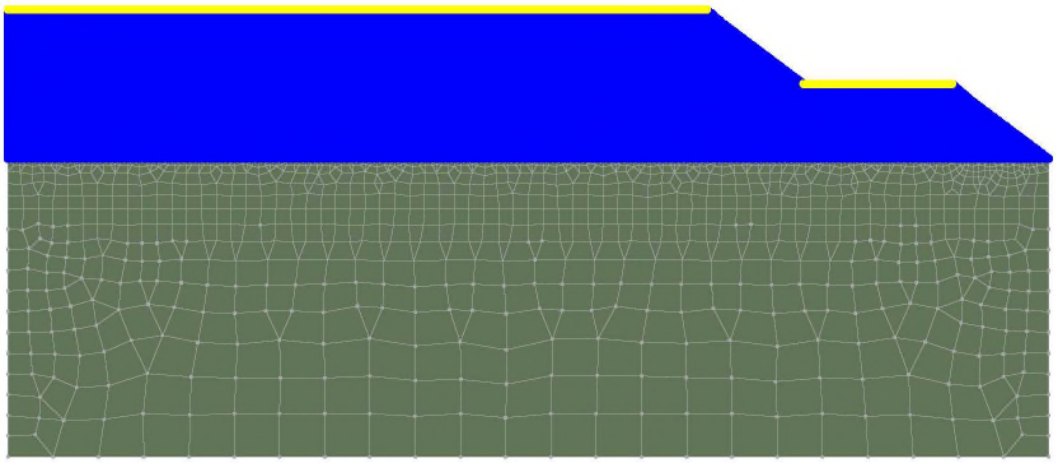

A) Steady state; 27,670 nodes and 27,750 elements

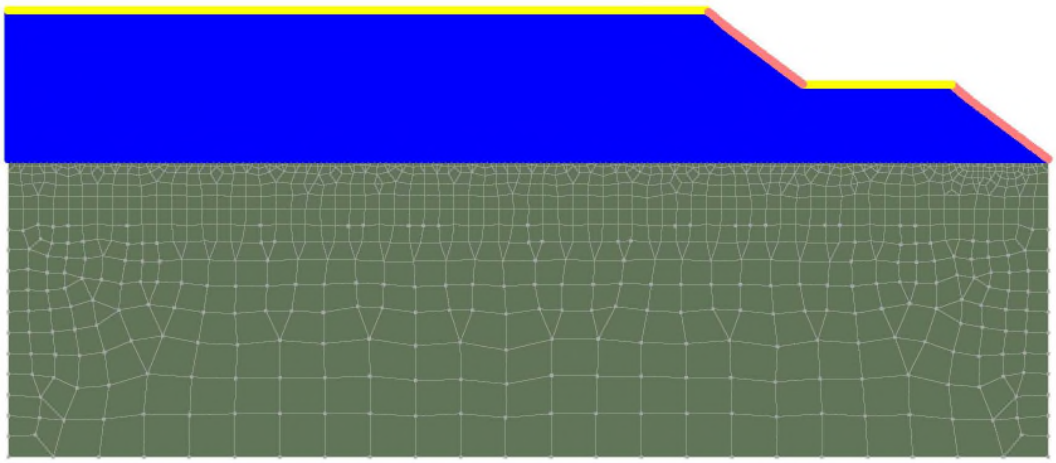

B) Transient state; 27,670 nodes and 27,750 elements

FIGURE G2: STEADY STATE AND TRANSIENT STATE TEMPERATURE BOUNDARY CONDITIONS APPLIED TO GEOSTUDIO MODEL USED TO MODEL EKATI EXPERIMENTAL EXAMPLE

GEOSTUDIO SIMULATION

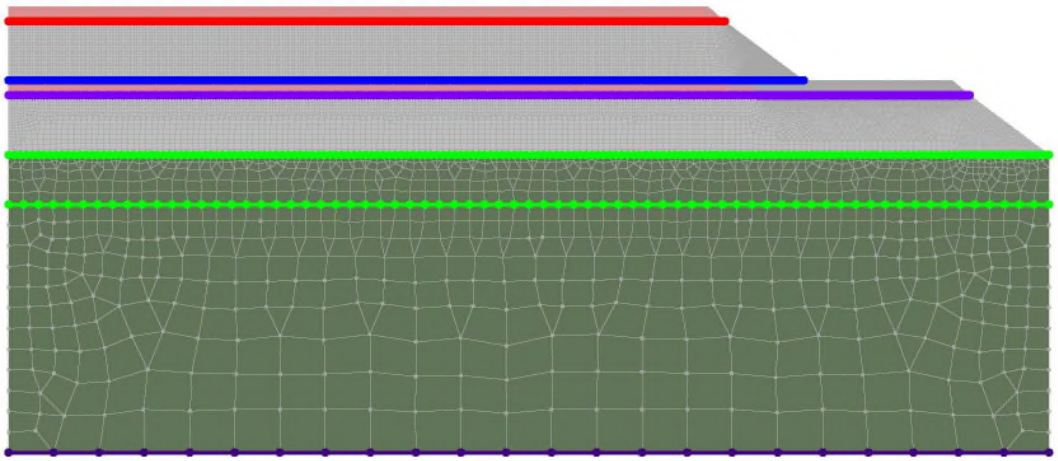

A) Steady state; 27,670 nodes and 27,750 elements

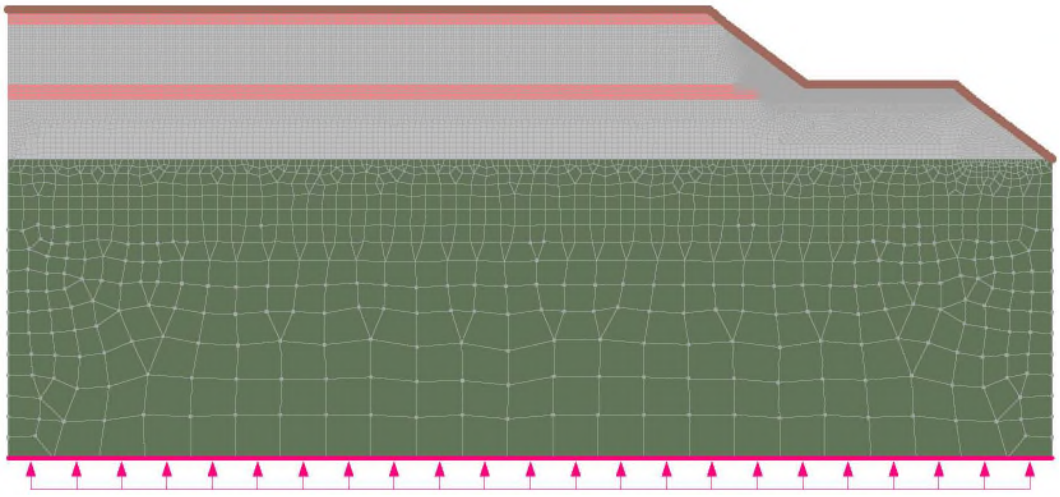

B) Transient state; 27,670 nodes and 27,750 elements

FIGURE G3: NUMERICAL RESULTS FROM GEOSTUDIO EKATI MODEL; CASE 1 – AIR PERMEABILITY 6,000 M/D IN ALL WASTE ROCK; (LACK OF COMPACTED LAYERS)

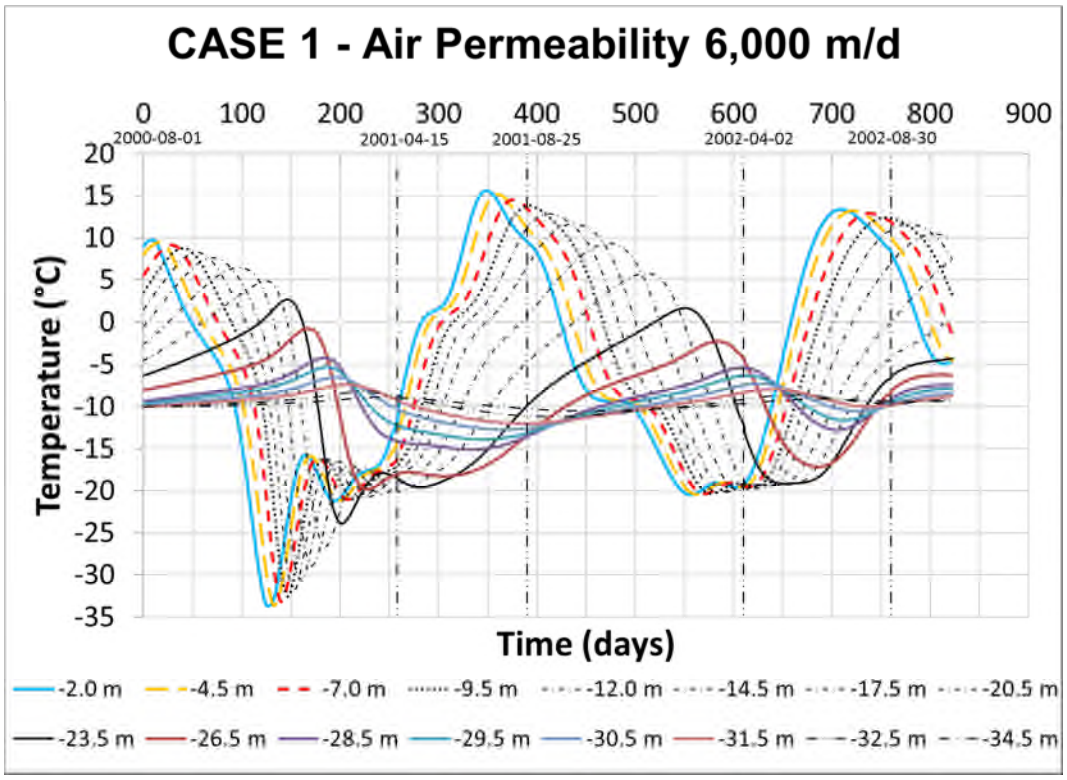

A) Time-temperature plot for Case 1

FIGURE G4: NUMERICAL RESULTS FROM GEOSTUDIO EKATI MODEL; CASE 2 – AIR PERMEABILITY 6,000 M/D IN WASTE ROCK; AIR PERMEABILITY 1,000 M/D IN COMPACTED LAYERS; (LAYERS SLIGHTLY COMPACTED)

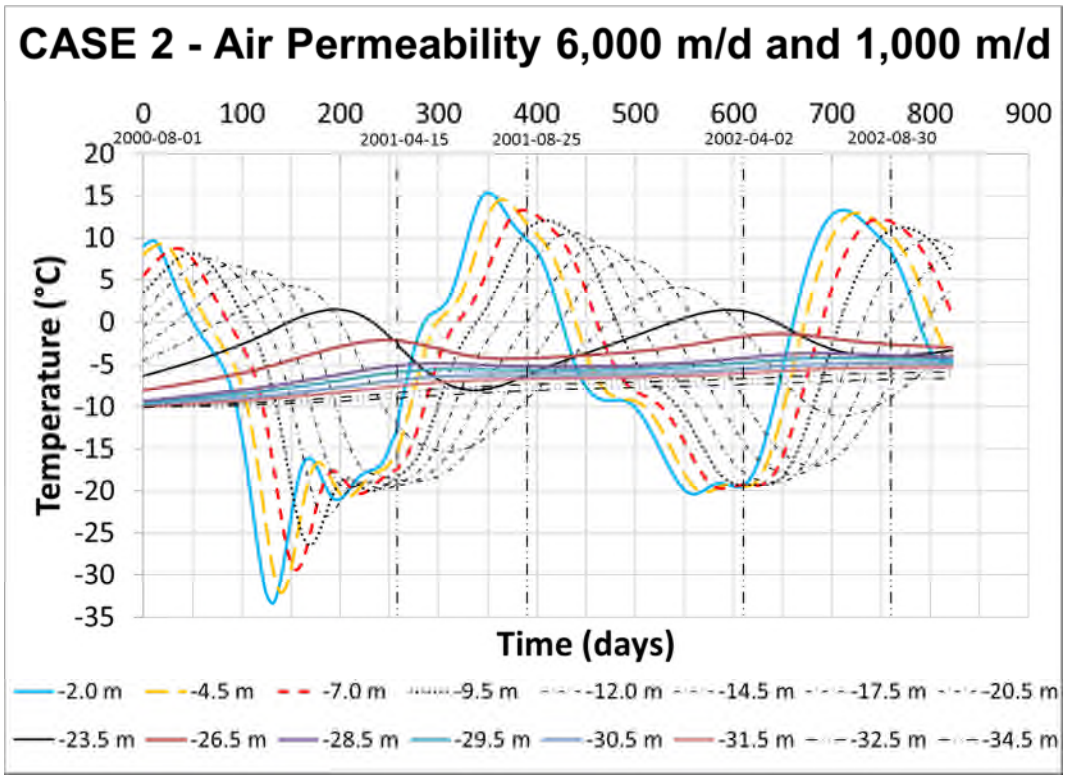

A) Time-temperature plot for Case 2

FIGURE G5: NUMERICAL RESULTS FROM GEOSTUDIO EKATI MODEL; CASE 3 – AIR PERMEABILITY 6,000 M/D IN WASTE ROCK; AIR PERMEABILITY 1 M/D IN COMPACTED LAYERS; (LAYERS MUCH COMPACTED)

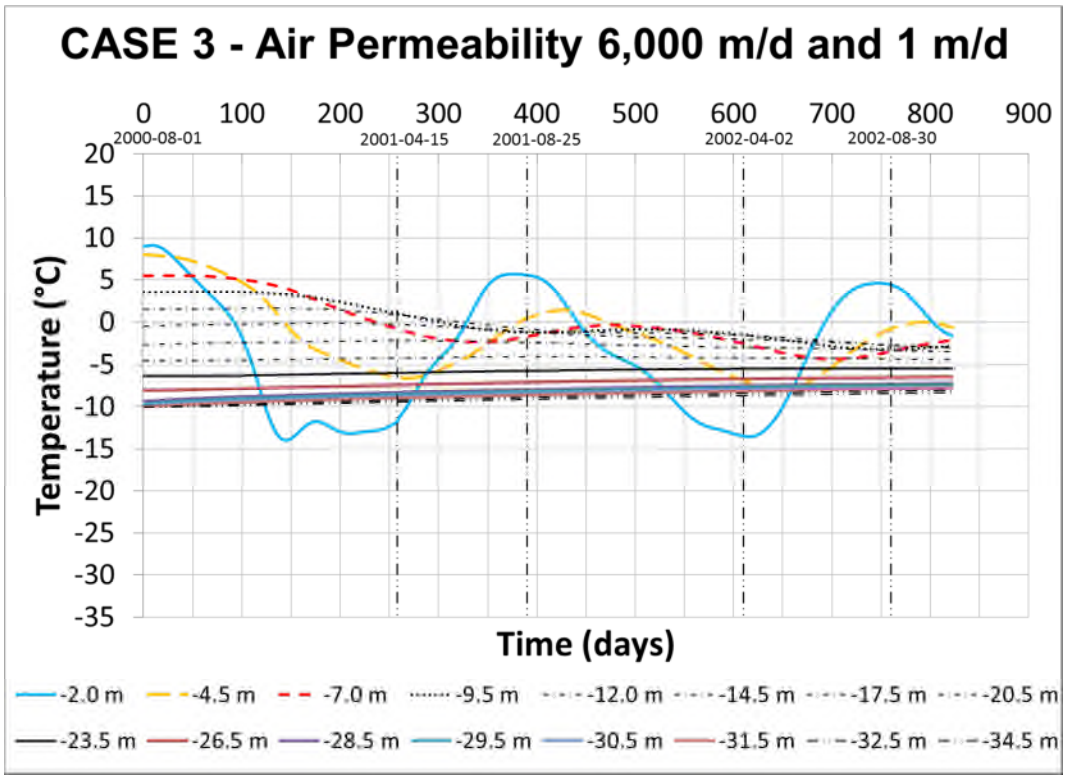

A) Time-temperature plot for Case 3

FIGURE G6: NUMERICAL RESULTS FROM GEOSTUDIO EKATI MODEL; CASE 4 – CONDUCTION ONLY; (NO CONVECTION OCCURS)

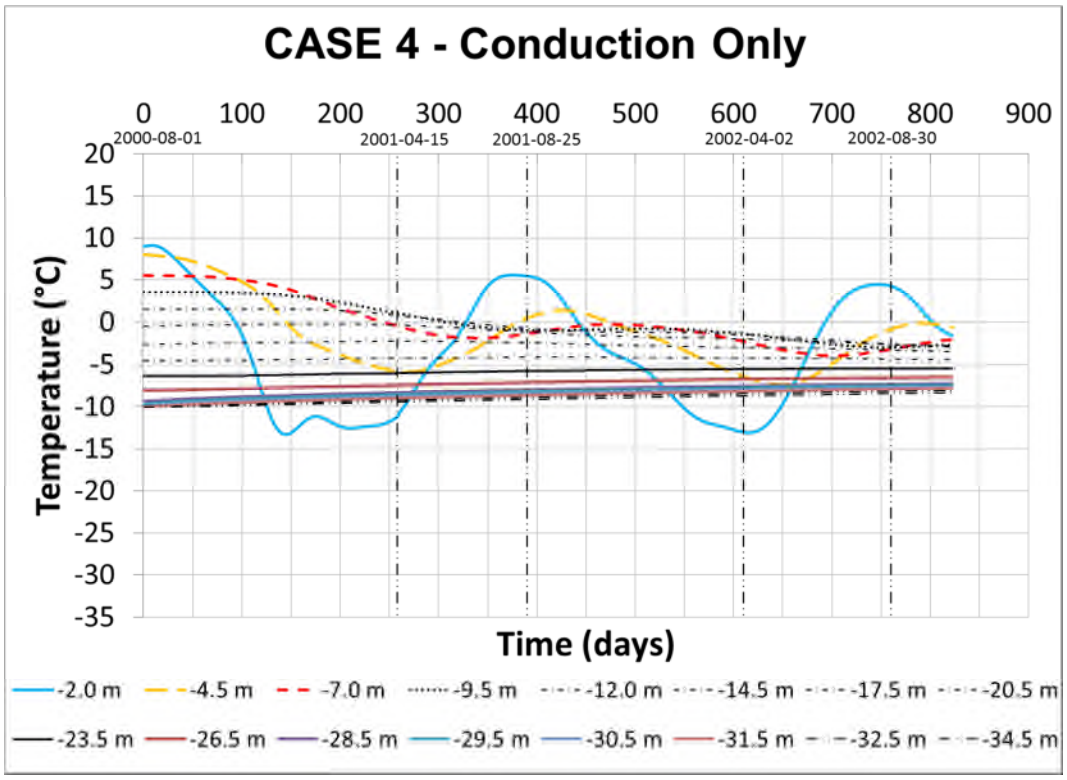

A) Time-temperature plot for Case 4

APPENDIX H

FIGURE H1. STEADY STATE AND TRANSIENT STATE TEMPERATURE BOUNDARY CONDITIONS APPLIED TO GEOSTUDIO MODELS USED TO MODEL SUN ET AL. (2005) CASE 1 THROUGH CASE 5

GEOSTUDIO SIMULATION

A) Steady state; applied is temperature 11°C; 4812 nodes and 9268 elements

B) Corresponding to A) transient state; temperature 11°C continues being applied at base; temperature 10°C is applied over top surface

C) Steady state; applied is temperature 0°C; 4812 nodes and 9268 elements

D) Corresponding to C) transient state; temperature 0°C continues being applied at base; temperature -1°C is applied over top surface

FIGURE H2: STEADY STATE AND TRANSIENT STATE PRESSURE BOUNDARY CONDITIONS APPLIED TO GEOSTUDIO MODEL USED TO MODEL SUN ET AL. (2005); CASE 1 (SUN ET AL., 2005) – ALL BOUNDARIES CLOSED

GEOSTUDIO SIMULATION

A) Steady state; 4812 nodes and 9268 elements

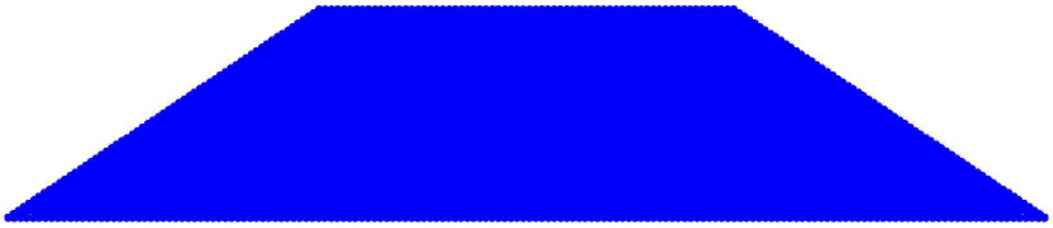

B) Transient state

FIGURE H3: STEADY STATE AND TRANSIENT STATE PRESSURE BOUNDARY CONDITIONS APPLIED TO GEOSTUDIO MODEL USED TO MODEL SUN ET AL. (2005); CASE 2 (SUN ET AL., 2005) – SIDESLOPES OPEN

GEOSTUDIO SIMULATION

A) Steady state; 4812 nodes and 9268 elements

B) Transient state

FIGURE H4: STEADY STATE AND TRANSIENT STATE PRESSURE BOUNDARY CONDITIONS APPLIED TO GEOSTUDIO MODEL USED TO MODEL SUN ET AL. (2005); CASE 3 (SUN ET AL., 2005) – SIDESLOPES AND TOP OPEN

GEOSTUDIO SIMULATION

A) Steady state; 4812 nodes and 9268 elements

B) Transient state

FIGURE H5: STEADY STATE AND TRANSIENT STATE PRESSURE BOUNDARY CONDITIONS APPLIED TO GEOSTUDIO MODEL USED TO MODEL SUN ET AL. (2005); CASE 4 (SUN ET AL., 2005) – TOP OPEN

GEOSTUDIO SIMULATION

A) Steady state; 4812 nodes and 9268 elements

B) Transient state

FIGURE H6: STEADY STATE AND TRANSIENT STATE PRESSURE BOUNDARY CONDITIONS APPLIED TO GEOSTUDIO MODEL USED TO MODEL SUN ET AL. (2005); CASE 5 (SUN ET AL., 2005) – ALL BOUNDARIES CLOSED AND SIDESLOPES ADIABATIC

GEOSTUDIO SIMULATION

A) Steady state; 4812 nodes and 9268 elements

B) Transient state

APPENDIX I

FIGURE I1: STEADY STATE AND TRANSIENT STATE PRESSURE BOUNDARY CONDITIONS APPLIED TO GEOSTUDIO MODEL USED TO MODEL DIAVIK WASTE ROCK TEST PILE

GEOSTUDIO SIMULATION

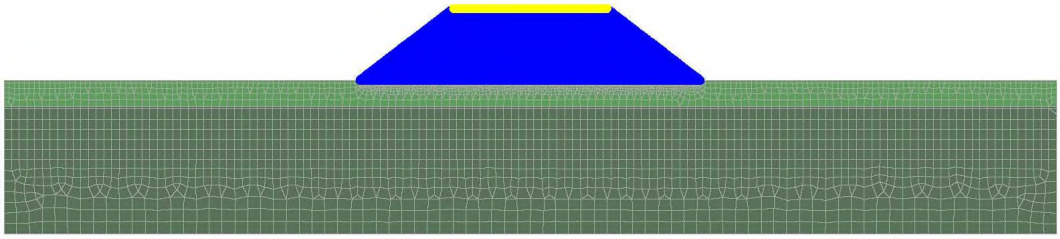

A) Steady state; 32,332 nodes and 32,840 elements

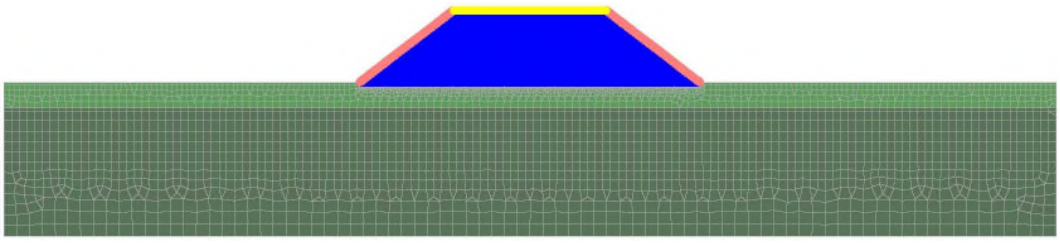

B) Transient state; 32,332 nodes and 32,840 elements

FIGURE I2: STEADY STATE AND TRANSIENT STATE TEMPERATURE BOUNDARY CONDITIONS APPLIED TO GEOSTUDIO MODEL USED TO MODEL DIAVIK WASTE ROCK TEST PILE

GEOSTUDIO SIMULATION

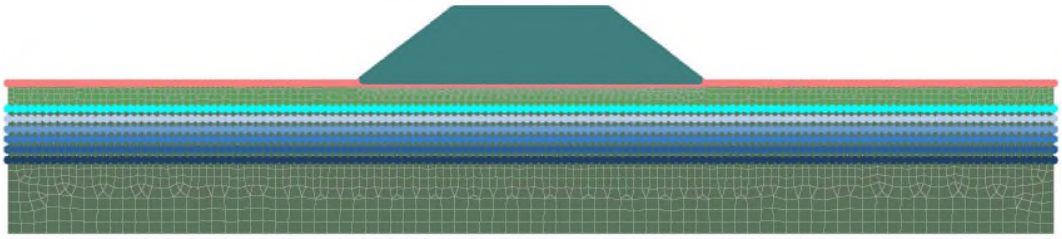

A) Steady state; 32,332 nodes and 32,840 elements

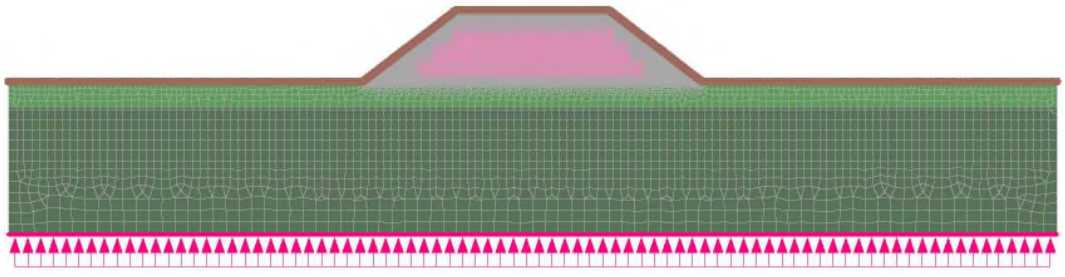

B) Transient state; 32,332 nodes and 32,840 elements